volume 2

EARTHQUAKE GEOTECHNICAL ENGINEERING

Edited by

P. Sêco e Pinto

EARTHQUAKE GEOTECHNICAL ENGINEERING
VOLUME 2

This Page Intentionally Left Blank

PROCEEDINGS OF THE SECOND INTERNATIONAL CONFERENCE ON EARTHQUAKE GEOTECHNICAL ENGINEERING/LISBOA/PORTUGAL/21-25 JUNE 1999

Earthquake Geotechnical Engineering

Edited by
Pedro S. Sêco e Pinto
Portuguese Society for Géotechnique (SPG), Lisboa, Portugal
National Laboratory of Civil Engineering (LNEC), Lisboa, Portugal

VOLUME 2
Underground and buried structures/Liquefaction/Slopes and embankments/Codes, standards and safety evaluation/Recent earthquakes

A.A. BALKEMA/ROTTERDAM/BROOKFIELD/1999

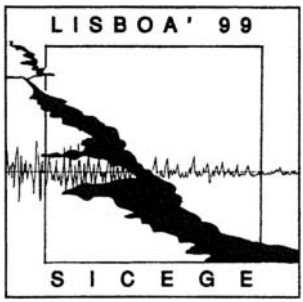

The financial support given by the Science and Technology Foundation for the publication of these Proceedings is greatly acknowledged.

The texts of the various papers in this volume were set individually by typists under the supervision of each of the authors concerned.

Published by
A.A. Balkema, P.O. Box 1675, 3000 BR Rotterdam, Netherlands
Fax: +31.10.413.5947; E-mail: balkema@balkema.nl; Internet site: www.balkema.nl
A.A. Balkema Publishers, Old Post Road, Brookfield, VT 05036-9704, USA
Fax: 802.276.3837; E-mail: info@ashgate.com

For the complete set of three volumes, ISBN 90 5809 116 3
For Volume 1, ISBN 90 5809 117 1
For Volume 2, ISBN 90 5809 118 X
For Volume 3, ISBN 90 5809 119 8

Printed in the Netherlands

Earthquake Geotechnical Engineering, Sêco e Pinto (ed.) © 1999 Balkema, Rotterdam, ISBN 90 5809 116 3

Table of contents

4 *Underground and buried structures*

5 *Liquefaction*

6 *Slopes and embankments*

7 *Codes, standards and safety evaluation*

8 *Recent earthquakes*

4 Underground and buried structures

This Page Intentionally Left Blank

Earthquake Geotechnical Engineering, Sêco e Pinto (ed.) © 1999 Balkema, Rotterdam, ISBN 90 5809 116 3

Designing tunnel linings upon seismic effects

N.N.Fotieva
Department of Materials Mechanics, Tula State University, Russia
N.S.Bulychev
Department of Underground Construction, Tula State University, Russia

ABSTRACT: This paper describes an original approach to the problem of designing tunnel linings against seismic effects consisting in the determination of most unfavourable lining stress state at different combinations and any directions of long longitudinal and shear waves propagating in the plane of the tunnel cross-section. The analytical methods based on that approach are developed for designing tunnel linings of arbitrary cross-sectional shape, including the linings constructed with the application of rock grouting, circular linings including the multi-layer ones of mutually influencing parallel tunnels. The proposed method is illustrated by examples of calculations,

1 INTRODUCTION

In the design and construction of underground structures in seismic regions, it is necessary to take into account that those structures may be subjected to earthquakes effects besides usual static loads. Those earthquakes effects consist of spreading long seismic longitudinal (compressive-tensile) and shear waves in the rock mass, the combinations and directions of which are unknown in advance respectively to the underground structure.

That is why an original approach to the problem of designing tunnel linings for earthquake effects has been developed at Tula State University (Fotieva, 1980). According to that approach, the design includes determining the most unfavourable lining stress state at any combinations and directions of long longitudinal and shear waves propagating in the plane of the tunnel cross-section. The above approach and the basic principles of designing tunnel linings upon seismic effects have been included in the standard [Instruction 1983] and widely applied in projects of transport and power-stations tunnels. On that base using different design schemes the analytical methods and corresponding computer programs have been created for designing tunnel linings of an arbitrary cross-sectional shape constructed with the application of grouting (Klimov 1993), linings from sprayed concrete (Fotieva, Bulychev 1996), monolithic and multi-layer linings of the complex of parallel mutually influencing circular tunnels including the determination of minimal safe distances between them [Fotieva, Kozlov 1992]. The approach will be illustrated in application to designing tunnel linings of a non-circular cross-section shape.

2 METHOD OF DESIGN

With the aim of determining the tunnel lining stress state caused by seismic effects two dimensional elasticity theory quasi-static contact problems are analysed, the design schemes of which are shown in Figure 1 a, b.

Here the infinite medium simulating the rock mass is characterised by the deformation modulus E_1 and the Poisson ratio ν_1. The external ring layer of thickness Δ_1, which has the deformation modulus E_2 and Poisson ratio ν_2 simulates the rock zone strengthened by grouting. The internal ring layer of thickness Δ_2 with characteristics E_3 and ν_3 simulates the tunnel lining.

The ring layers and the medium undergo deformation together, that is the conditions of continuity of stresses and displacements are fulfilled on the L_i $(i = 1, 2)$ contact lines. The L_3 internal outline is free from loads.

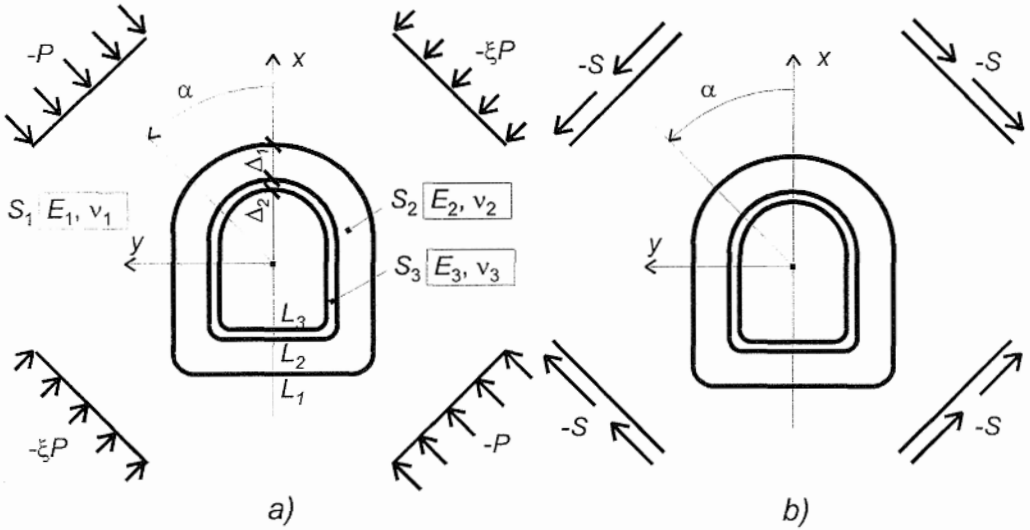

Figure 1. Schemes for designing tunnel lining upon the action of a long arbitrary directed longitudinal wave (a) and shear wave (b).

In the first problem (Figure 1, a) the medium is subjected in the far field to a double-axis compression with non-equal components oriented at an arbitrary angle α simulating the action of long arbitrary directed longitudinal wave in the compression phase. The stresses in the far field are expressed as follows:

$$P = \frac{1}{2\pi} A k_1 \gamma c_1 T_0, \quad \xi = \frac{\nu_1}{1-\nu_1} \tag{1}$$

where A is the coefficient corresponding to the earthquake intensity, k_1 is the coefficient taking into account admissible damages, γ is the rock unit weight, c_1 is the speed of longitudinal waves, T_0 is the prevailing period of the rock particles oscillations.

In the second problem (Figure 1, b) the medium is subjected to a pure shear in the far field simulating the action of long arbitrary directed shear wave. Here

$$S = \frac{1}{2\pi} A k_1 \gamma c_2 T_0, \tag{2}$$

where c_2 is the speed of shear waves.

From the solution of the first problem (Fig. 1, a) the $\sigma^{(P)}$ stresses (here the σ symbol signifies all components of stress tensor), which appear in the lining due to the action of a long longitudinal wave falling at an α arbitrary angle, are determined; from the solution of the second problem (Fig. 1, b) the $\sigma^{(S)}$ stresses, produced by a shear wave, are obtained.

Further, the sum and difference of analyticalal expressions for $\sigma_\theta^{(P)}$ and $\sigma_\theta^{(S)}$ normal tangential stresses, which characterise the lining stress state caused by mutual actions of longitudinal and shear waves passing simultaneously (the worst case) are investigated in every point of the internal outline L_3 on the extreme relatively the angle α. With this aim the following equations are solved

$$\frac{\partial}{\partial \alpha}[\sigma_\theta^{(P)} \pm \sigma_\theta^{(S)}] = 0 \tag{3}$$

and for every point such a combination of waves and such an angle of their falling at which normal tangential stresses in the points considered are maximal by their absolute are determined. It allows the envelope diagram of normal tangential stresses on the L_3 internal outline to by obtained analytically.

The stresses upon the external L_2 outline, the N longitudinal forces and the M bending moments in every lining normal section are deter-

mined at such a combination and such a direction of waves at which the σ_θ normal tangential stress in that section has a maximal absolute value.

The stresses and forces obtained that way are assumed to have the signs "plus" and "minus" and summed up with stresses and forces appearing due to other acting loads in their most unfavourable combinations. After that a sections strength test upon compression and tension is made.

If the lining is not anchored to the massif and is designed with an allowance of fissure forming we assume that the tensile normal loads are not transferred upon the lining. In this case the action of the longitudinal waves in the tension phase is not to be taken into account and the design is made on the base of two different envelope diagrams of normal tangential stresses, obtained using the maximal absolute values of the compressive (negative) stresses and tensile (positive) ones, called forth by mutual actions of shear waves and longitudinal waves in the compression phase. plane contact problems (Fig. 1, a, b) have been

The analytical solutions of the elasticity theory obtained by Klimov (1991) with the application of the complex variable analytic functions theory and apparatus of complex series.

3 EXAMPLES OF DESIGN

3.1 *Design of railway tunnel*

Results of designing the railway tunnel are given in Figure 2. The shape and sizes of the lining cross-section are shown in Figure 3.

Calculations were made at the following input data:

$\Delta_1 = 4\ m,\quad \Delta_2 = 0.4\ m,\quad E_1 = 1000\ MPa,$

$\nu_1 = 0.3,\quad E_2 = 1800\ MPa,\quad \nu_2 = 0.3,$

$E_3 = 23000\ MPa,$

$\nu_3 = 0.2,\quad \gamma = 23\ kN/m^3,\quad A = 0.4,$

$k_1 = 0.25,\quad T_0 = 0.5\ s.$

The lining is designed with the allowance of fissures.

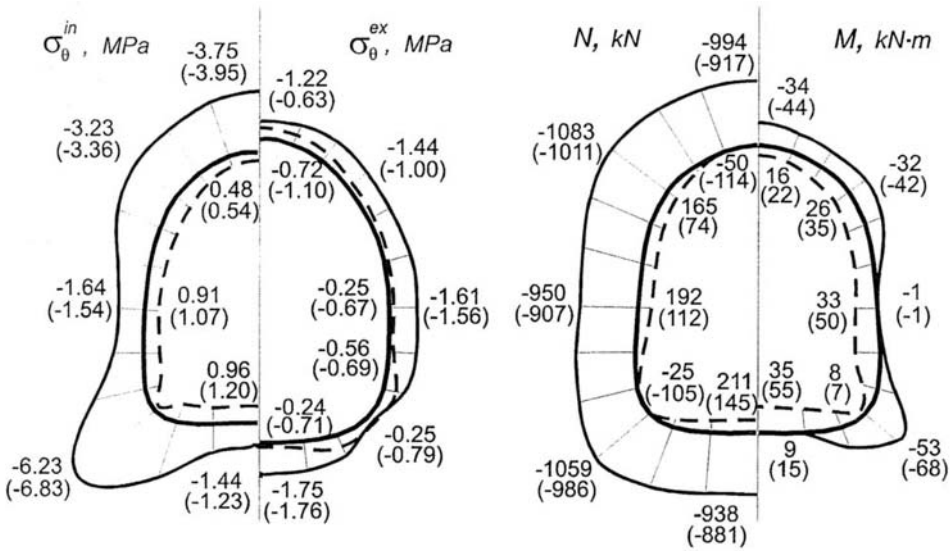

Figure 2. The results of the tunnel lining design.

The distributions of maximal compressive and tensile σ_θ^{in} normal tangential stresses on the internal outline of the lining cross-section, corresponding them σ_θ^{ex} normal tangential stresses on the external outline, the N longitudinal forces and the M bending moments are shown in Figure 2 by solid and dotted lines correspondingly.

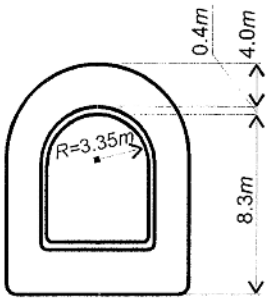

Figure 3. The lining cross-section.

For the comparison values of the same stresses and forces obtained in the case when the grouted soil zone is absent are given in brackets.

3.2 *Design of vertical turbine shafts of a power-station*

The linings from concrete with internal steel layer of six parallel vertical turbine pressure shafts of the Rogun power-station in Tadjikistan (the external radii of tunnels are 3.93 m, the distances between their centres are 26.3 m) have been designed with the application of the method by Fotieva, Kozlov (1992) mentioned above.

The design scheme of that method is a linearly deformable medium weakened by an arbitrary number of arbitrary located circular holes of different radii supported by multi-layer rings fulfilled from different materials. The medium is loaded on the infinity by the same stresses as in Figure 1 and two the same problems of the elasticity theory are considered. The most unfavourable stress state of the linings is determined by solving the equations similar to the (3) obtained for internal outlines of the every layer of the every lining.

The design of six parallel vertical shafts of the Rogun power station has been fulfilled taking into account the actions of the water internal head, the rock's own weight and the Earthquake effects.

The general input data are the following: thickness of the concrete layers is 0.4 m; thickness of the steel layers is 0.03 m (internal radii of the steel layers are 3.5 m); the concrete deformation modulus and the Poisson's ratio are correspondingly E_2 = 24000 MPa, ν_2 =0.15; the steel deformation modulus and the Poisson's ratio are correspondingly E_3 = 200000 MPa, ν_3 =0.3; the rock unit weight is γ =25.5 kN/m^3 ; the lateral pressure coefficient in an intact rock mass is λ = 1; the internal water pressure is p=2.5 MPa; the coefficient corresponding to the Earthquake intensity is A = 0.4; the coefficient taking into account the admissible damages is K_1 = 0.25; the prevailing period of the rock particles oscillation is T_0 = 0.5 s.

The calculations have been fulfilled for two kinds of the rocks with different E_1 deformation modules, ν_1 Poisson's ratios, initial stresses $\sigma_r^{(0)}$ in the intact rock mass and c_1 values of the long elastic waves velocity. Those characteristics are given in the Table 1.

Table 1. The variants of the input data

Parameters	Variants	
	I	II
E_1, MPa	30000	36000
ν_1	0.3	0.33
$\sigma_r^{(0)}$, MPa	14.0	17.0
c_1, m/s	4250	4600

Distributions of the σ_θ normal tangential stresses in the lining layers obtained as the results of calculations at the loads mentioned above are shown in Figures 4,a,b,c, and 5,a,b,c for both variants of the input data correspondingly (in Figures 4,c and 5,c the maximal compressive (negative) and tensile (positive) normal tangential stresses at different combinations of the mutually acting longitudinal and shear waves of any directions in the plane of the tunnels cross-section are given). Taking into account the symmetry the results are represented for three left tunnels; the stresses in the steel and concrete layers are shown in the upper and lower parts of figures correspondingly.

As follows from the results obtained for both variants the tensile σ_θ stresses in the concrete layers surpass the designed concrete strength on the tension R_{bt} = 0.75 MPa (Fig. 4,a and 5,a). That is why additional calculations have been fulfilled at the value of the E_2 concrete deformation modulus decreased up to E_2 = 11600 MPa taking into account the possible crack formation. Besides that taking into account that stresses appearing in steel layers are small their thickness has been decreased up to 0.02 m.

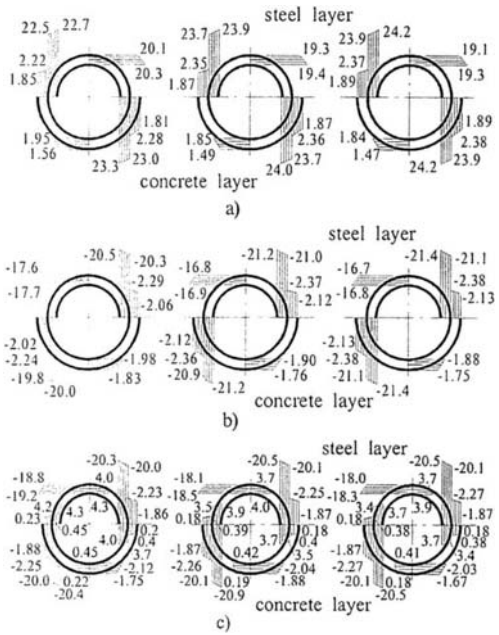

Figure 4. The σ_θ normal tangential stresses in the steel and concrete linings layers at the action of the internal water head (a), the rocks own weight (b) and the Earthquake effects (c) obtained for the first variant of the input data.

For additional control the calculations have been fulfilled at the steel layers thickness Δ_2 = 0.02 m and a still lower value E_1 = 7000 MPa of the concrete deformation modulus. Those calculations also confirmed the possibility of the steel layer thickness to be decreased.

So, with the aid of calculations fulfilled it was be shown that the bearing capacity of the lining of the vertical turbine pressure shafts of the Rogun power-station is being secured at the steel layers thickness of Δ_2 = 0.02 m.

In general the experience of applying the methods developed shows that those methods may be useful and effective at designing tunnel linings in seismic regions.

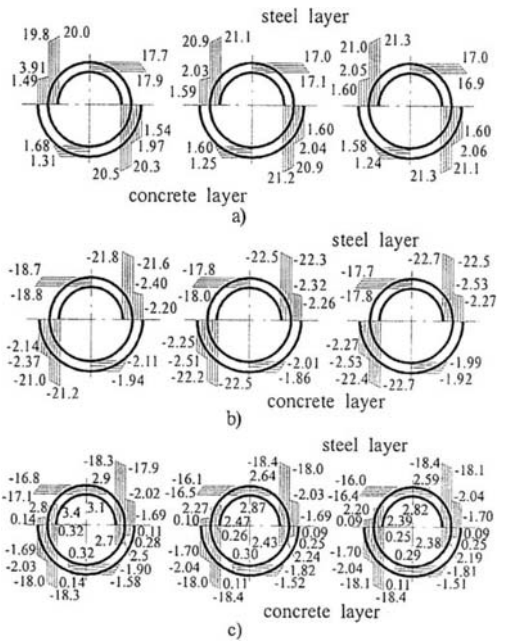

Figure 5. The σ_θ normal tangential stresses in the steel and concrete linings layers at the action of the internal water head (a), the rocks own weight (b) and the Earthquake effects (c) obtained for the second variant of the input data.

REFERENCES

Fotieva, N.N. 1980. *Design of underground structures support in seismically active regions.* Moscow: Nedra.

Fotieva, N.N. & A.N. Kozlov 1992. *Designing linings of parallel openings in seismic regions..* Moscow: Nedra.

Instruction to designing mining workings and linings calculation .1983. Moscow: Stroyizdat.

Klimov, Y.I. 1991. Designing tunnel linings undergoing seismic effects with rock grouting to be taken into account. *Underground Structures Mechanics,* Tula, Russia.

Muskhelishvili, N.I. 1966. *Some basic problems of mathematical elasticity theory.* Moscow: Nauka.

This Page Intentionally Left Blank

Earthquake Geotechnical Engineering, Sêco e Pinto (ed.) © 1999 Balkema, Rotterdam, ISBN 90 5809 116 3

Dynamic behaviour of a foundation-soil-artificial block system

Thomas Siemer
Ingenieurgesellschaft für Bautechnik mbH, Berlin, Germany

ABSTRACT: The centrifuge model technique proves to be an attractive method to investigate dynamic geotechnical problems with real prototype full-scale behaviour subjected to identical stress conditions in the model as in nature. The dynamic response of a transient loaded foundation located at the sand surface with an artificial block in the soil beneath is investigated in a number of centrifuge model tests. The experiments are carried out in a specially designed container with wave energy absorbing walls.
From the results of the experimental investigations it is found, that the response of the foundation is a function of the built-in depth of the artificial block. The investigations show further that the response of the foundation such as the spectral density and the resonance frequency increases with decreasing built-in depth of the artificial block.
The result of a field investigation is analyzed to verify the conclusions which are derived from the centrifuge model investigations.

1 INTRODUCTION

The excitation of buildings due to soil vibrations is occuring more frequently today and is getting more attention in engineer planning processes and design methods. Some examples are machine foundations and vibration and drop-hammers which act as vibration sources inducing dynamic forces in the soil. The resulting waves transport the energy from the load source, e. g. a foundation, and cause soil vibrations. If the waves reach a neighbouring foundation this foundation is passively excited.

An active vibration control method to reduce foundation oscillations planes to build an artificial block in the soil beneath the loaded foundation (Siemer and Jessberger 1994, Schmid et al. 1991). The authors show the effect of an artificial block beneath a loaded foundation as a wave screening element towards a neighbouring foundation.

In this work, the dynamic response of the foundation above the artificial block is experimentally investigated in a number of centrifuge model tests.

2 CENTRIFUGE MODEL TECHNIQUE

On a model which moves on a circular orbit with the radius "r" and the angular velocity "ω" (Figure 1) acts besides the earth gravity "g" a radial acceleration which can be expressed as a multiple of the earth gravity "ng" (Equ. 1):

$$n \bullet g = \omega^2 \bullet r \qquad (1)$$

If the model container is placed in a swinging basket (Figure 1) the surface of the model swings up in the direction of the resultant acceleration field. The "1g" component, 90° to the "ng" acceleration field, can be neglected.

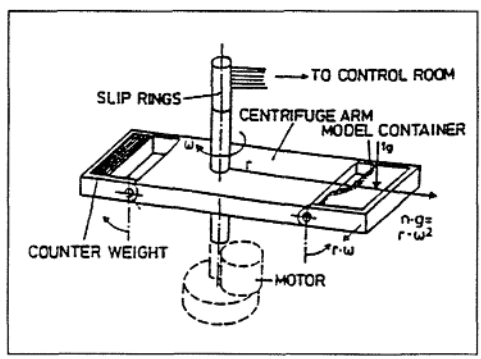

Figure 1. Principle of the centrifuge model technique

So the resultant acceleration can be set to "ng". If "n" is chosen to be the scaling factor of the model all mass forces of the model are increased "n" times.

That means the same stress condition for both model and prototype. As the stress-strain relationship of the soil is non-linear its dynamic stiffness increases also non-linear with depth. It is important for any study of soil structure interaction to consider the same stiffness in the model and in the prototype (full scale) at simular positions because the dynamic stiffness of the subsoil has a significant influence towards the propagation of waves.

In a centrifuge model test the stress-strain behaviour of the model and the prototype is identical.

Therefore this test method is able to model wave propagation and soil structure interaction to study the dynamic response of a transient loaded foundation located at the sand surface with an artificial block in the soil beneath.

Forces, displacements, accelerations, frequency etc. can be directly calculated from model to prototype scale using the scaling factors. Some of these scaling factors are summarized in Table 1.

Table 1: Scaling factors

Parameter	Prototype „1•g“	Model „n•g“
Length	1	1/n
Area	1	$1/n^2$
Volume	1	$1/n^3$
Stress	1	1
Strain	1	1
Shear modulus	1	1
Acceleration	1	n
Frequency	1	n
Time (dyn.)	1	1/n
Energy	1	$1/n^3$

3 CENTRIFUGE MODEL TESTS

3.1 Test facilities

The dynamic experiments are all performed at the centrifuge centre of the Institute for Soil Mechanics and Foundation Engineering, Ruhr-University Bochum, Germany, in a circular container as shown in Figure 2.

The steel container has a diameter of 1000 mm. A putty like damping material is applied to its wall and bottom to absorb most of the reflected wave energy.

The dry model sand is pluviated through a fine sieve by hand in the container, resulting in a density index $D_d = 97$ % on average.

The loading system is a falling-weight. This falling-weight was developed by the author. A detailed description of the falling-weight is given in Siemer (1996).

In the tests presented in this paper a stiff foundation at the soil surface with different ground areas (A and B) which represents a machine foundation in prototype scale is used.

The foundations are loaded transient by the falling-weight which represents a forge-hammer in prototype scale. The falling-height of the falling-weight and the frequency content of the load signals are continually controlled in order to introduce always the same dynamic forces into the foundation in the different tests.

An artificial block is located beneath the foundation in the soil in different depths ($h_E = 0.3$ m, $h_E = 0.6$ m and $h_E = 1.5$ m). The artificial block represents a concrete block in prototype scale.

The dimensions of the test foundations, the artificial block and the falling-weight are presented in Table 2.

Table 2: Dimensions of foundations, artificial block and falling-weight

Object	Dimension	Prototype scale
Foundation A	Length [m]	1.80
	Width [m]	1.80
	Hight [m]	1.32
	Mass [kg]	11624
Foundation B	Length [m]	2.40
	Width [m]	2.40
	Hight [m]	0.75
	Mass [kg]	11583
Artificial block	Length [m]	10.80
	Width [m]	10.80
	Hight [m]	1.50
	Mass [kg]	477900
Falling-weight	Mass [kg]	1134
	Falling-height [m]	
	min / max	0 / 1.80
	Energy [Nm]	
	min / max	0 / 667

The vertical component of the foundation vibration is measured by three accelerometers of type Bruel & Kjaer 4393 with very light weight and a resonance frequency of 55 kHz. The accelerometers and the foundation are coupled together with small threads. A plan view and a cross section is given in Figure 3.

The vertical component of the artificial block vibration is measured by five accelerometers of type Bruel & Kjaer 4393. The horizontal component of

the artificial block vibration is measured by four accelerometers of type Bruel & Kjaer 4393.

One accelerometer type Bruel & Kjaer 4374 is placed in the falling-weight for measuring a reference signal of the load input. This reference signal is analysed with the help of an oscilloscope.

The experiments are all run at a g-level of the centrifuge of n=30.

A sketch of the measurement system is given in Figure 4.

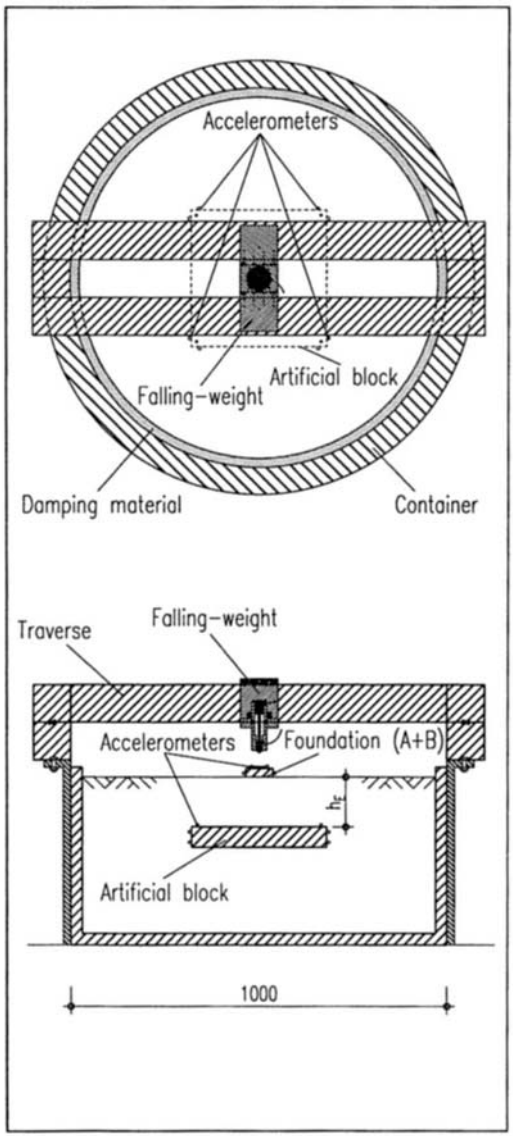

Figure 2. Plan view and cross section of the model container

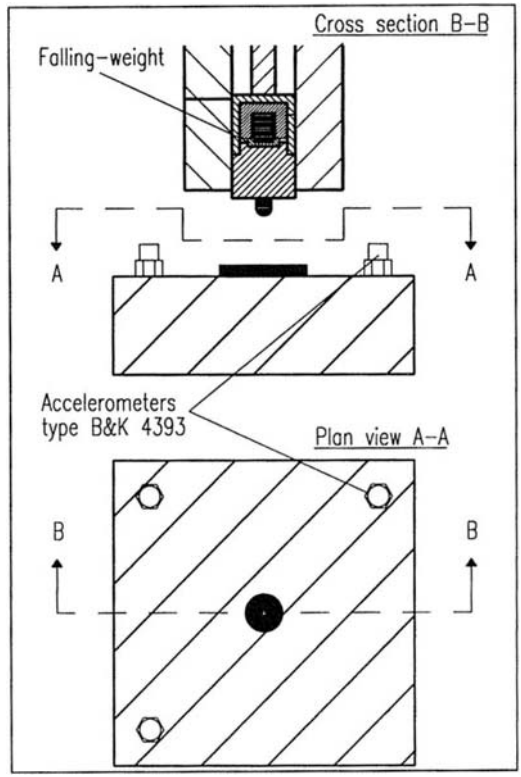

Figure 3. Plan view and cross section of foundation vibration tests

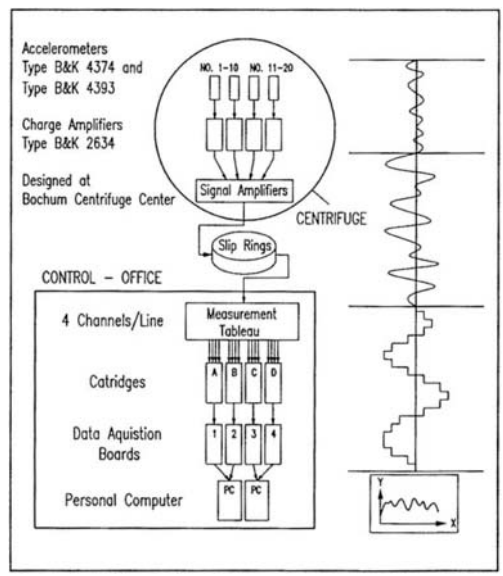

Figure 4. Measurement system

3.2 Test results

The results of centrifuge model tests towards the dynamic transmitting behaviour of rigid foundations at the soil surface in interaction with a horizontal artificial block in the soil beneath the foundation are presented.

In Figure 5 the spectral density of the foundation response of foundation B due to vertical load is shown for the situation without artificial block (tests wp6 and wp9, straight line) and with an artificial block in different depths (dotted lines). The results of the different experiments corresponding to the depth of the artificial block „h_E" are shown in Figure 5. The frequency „f" is plotted against the abscissa and the amount of the spectral density „$|G\ddot{y}\ddot{y}(\omega)|$ is plotted against the ordinate.

The influence of the artificial block in view of a shift in the resonance frequency and in different amounts of the spectral density of the foundation response is investigated. This kind of investigation is suitable with respect to the load input signals of the different experiments which are very similar in the frequency domain (frequency content and spectral density).

The test results of the resonance frequency and the spectral density corresponding to the different dephts of the artificial block are shown in Table 3.

If the artificial block is built in the soil beneath the foundation „B" the resonance frequency shifts in relation to the depth of the artificial block.

The lower the depth of the artificial block, the bigger the value for the resonance frequency of the foundation.

The amounts of the spectral density show the same dependency (see Table 3).

The frequency domain with smaller foundation responses for the situation with artificial block compared to the situation without artificial block is interesting. The bigger the resonance frequency for the situation with artificial block is, the bigger is this frequency domain.

Above the resonance frequency the amounts of the spectral density decrease quickly. The foundation responses are similar with the exception of the depth of the artificial block of $h_E = 0.30$ m. Small depths of the artificial block cause a deviation in the transfer behaviour in comparison to a one mass swinging system.

Table 3. Resonance frequency $f_{0,ZMV}$ and spectral density $|G\ddot{y}\ddot{y}(\omega)|$ with corresponding depths of the artificial block h_E

Test	h_E [m]	$f_{0,ZMV}$ [Hz]	$\|G\ddot{y}\ddot{y}(\omega)\|$ [m/s²]²
wp6 (B)	without	22.8	1.626
wp7 (B)	0.30	42.4	6.165
wp21 (B)	0.60	39.1	4.924
wp22 (B)	1.50	29.4	3.948
wp9 (A)	without	19.6	3.042
wp10 (A)	0.30	39.1 - 42.4	6.381
wp19 (A)	1.50	22.8	4.456

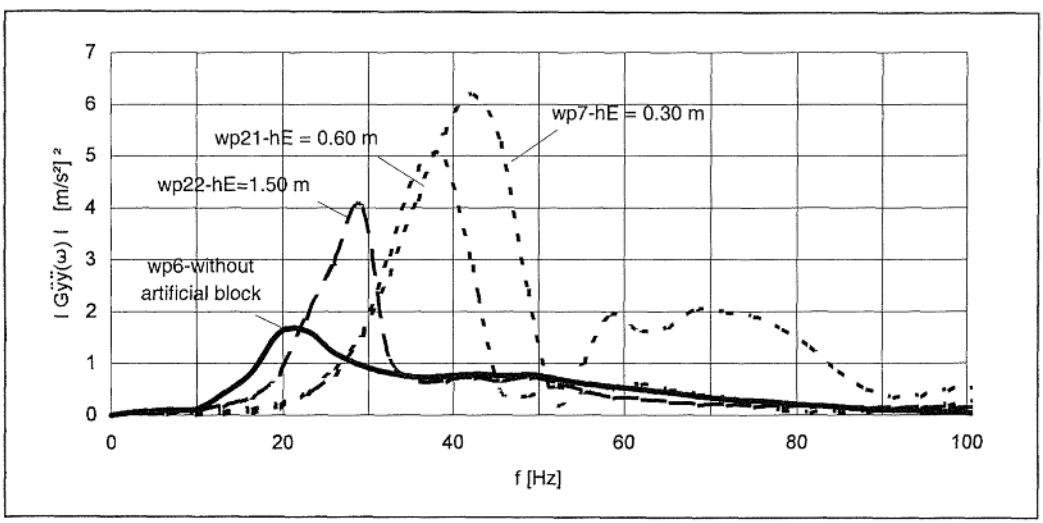

Figure 5. Spectral density of the foundation response (B) with different depths h_E of the artificial block

The measurements of the vertical and horizontal vibration components of the artificial block show its definite response in the resonance frequency of the foundation above. The vertical component is 50 times smaller and the horizontal component is 120 times smaller than the response of the foundation.

The experiments with foundation „A" differ from the experiments with foundation „B" towards the ground area. Foundation „B" has a ground area of 2.4 m * 2.4 m which corresponds to a radius $r_0 = \sqrt{[(l \bullet b)/\pi]} = 1.35$ m. Foundation „A" has a ground area of 1.8 m * 1.8 m which corresponds to a radius $r_0 = 1.02$ m.

The different depths of the artificial block beneath the foundation „A" in these experiments are the same as chosen in the experiments with foundation „B".

The results of the resonance frequencies and the spectral densities can be taken from Table 3.

The results show the same tendency towards the shift of the resonance frequency and the spectral density in dependency on the depth of the artificial block.

The resonance frequency shows smaller values for the situation with foundation „A" (tests wp10 and wp19) in comparison with foundation „B" (tests wp7 and wp22). The graphs for the spectral density show a similar tendency.

Figure 7 shows the dimensionless values of the resonance frequency of the foundation response „B", the foundation response „A" and the foundation response of a field test.

The results of the different experiments with foundation „A" and foundation „B" and respectively with the field test can be found in Figure 6.

The dimensionless value of the depth of the artificial block „h_E / λ_R" is plotted against the abscissa and the dimensionless value of the resonance frequency „$f_{0,with} / f_{0,without}$" is plotted against the ordinate. „h_E" is the depth of the artificial block beneath the foundation, „λ_R" is the wave length of the Rayleigh wave with $\lambda_R = 11$ m, „$f_{0,with}$" is the resonance frequency for the situation with and „$f_{0,without}$" is the resonance frequency for the situation without artificial block.

A connection between resonance behaviour of the foundation and depth of the artificial block can be derived from the test results. This connection shows the straight line in Figure 7. The graph (dotted line) is extrapolated for values „h_E / λ_R" greater than 0.15.

The test results with regard to foundation „A" and foundation „B" from centrifuge model tests are similar.

From there the dependency on the foundation ground area towards the diminsionless resonance frequency is assumed to be small.

The result of a field test in Berlin, Germany, is also shown in Figure 7. These field tests work with similar boundary conditions as found in the centrifuge model tests.

The dimensions of the foundation and the artificial block can be taken from Table 4. The depth of the artificial block is 1.0 m beneath the foundation.

The soil between the foundation and the artificial block is dry sand.

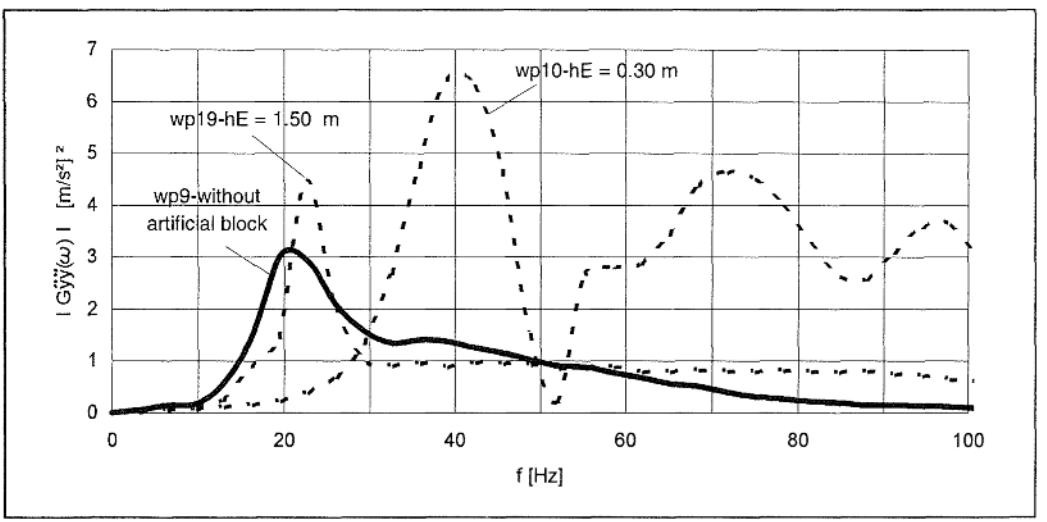

Figure 6. Spectral density of the foundation response (A) with different depths h_E of the artificial block

These field tests are also designed by the author. Some more details and test results can be taken from Forchap et al. (1994).

The result of the test result occures as a dot in Figure 7. The test result shows the same dependency on the diminsionless resonance frequency from the diminsionless depth of the artificial block.

Table 4: Field test - Dimensions of the foundation and the artificial block

Object	Dimension	Field test
Foundation	Length [m]	1.00
	Width [m]	1.00
	Hight [m]	0.50
	Mass [kg]	12.500
Artificial block	Length [m]	5.00
	Width [m]	5.00
	Hight [m]	0.60
	Mass [kg]	375.000

4 CONCLUSIONS

The following conclusions can be derived from the results of the centrifuge model tests:

- An artificial block beneath a foundation has a significant influence on the dynamic response of the foundation
- The resonance frequency of a foundation shifts in dependency on the depth of an artificial block beneath the foundation.
- The addition of an artificial block leads to an increasing of stiffness of the foundation-soil system.
- If „h_E / λ_R“ is equal to 1.0, the influence of the artificial block is insignificant.
- The dependency on the foundation ground area towards the diminsionless resonance frequency is assumed to be small.
- The results from field tests confirm the reults from centrifuge model tests.

REFERENCES

Forchap, E., Siemer, Th., Schmid, G. and Jessberger, H.L. 1994. Experiments to investigate the reduction of soil wave amplitudes using a built-in block. *2nd Intern. Conf. on Earthqu. Resistant Constr. and Design, Berlin, pp. 635 – 642.*

Schmid, G., Chouw, N. and Le, R. 1991. Shielding of structures from Soil Vibrations. *Soil Dyn. and Earthqu. Eng. V*, pp. 651 - 662.

Siemer, Th. 1993. Freifeldversuche zur Untersuchnung einer konstr. Maßnahme zur Reduzierung von Oberflächenversch. und Fundamentschwingungen. *Arbeitsbericht T1 SFB 151, Tp C6*, RUBochum.

Siemer, Th. 1996. Zentrifugenmodellversuche zur dynamischen Wechselwirkung zwischen Bauwerk und Baugrund infolge stoßartiger Belastung. *Heft 27 der Schriftenreihe des Instituts für Grundbau und Bodenmechanik*, Ruhr-Universität Bochum.

Siemer, Th. and Jessberger, H.L. 1994. Wave propagation and active vibration control in sand. *Proc. Intern. Conf. Centrifuge '94, Singapore*, pp.307-312.

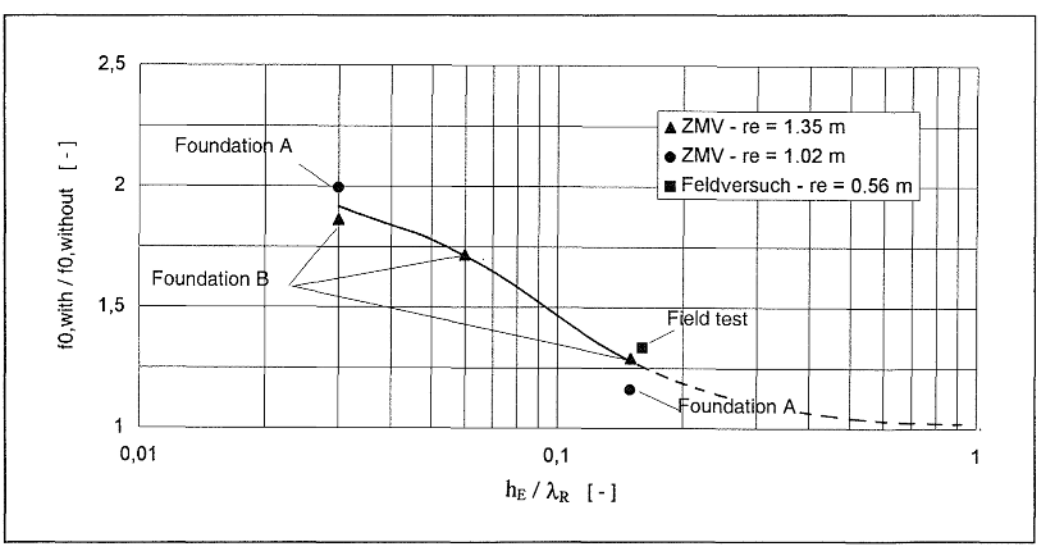

Figure 7. Dimensionless resonance frequency „$f_{0,with}$ / $f_{0,without}$“ in dependency on the dimensionless depth of the artificial block „h_E / λ_R“

Earthquake Geotechnical Engineering, Sêco e Pinto (ed.) © 1999 Balkema, Rotterdam, ISBN 90 5809 116 3

Stochastic analysis of underground structures subject to earthquake loading

H.R.Zhang & G.A.Cao
School of Civil Engineering, Northern Jiaotong University, Beijing, People's Republic of China
Z.P.Kuang
Department of Civil Engineering, Tongji University, Shanghai, People's Republic of China

ABSTRACT: The objective of the paper is to propose a simple numerical deterministic approach to analyze the stochastic response and dynamic reliability of underground structures under the action of stationary and non-stationary random seismic action. The method is based on general purpose FEM software for structure analysis where a numerically equivalent unit impulse function is used as the input of seismic load. After the impulse response function of the structure is obtained, the transfer relationship between the random excitation and response of the structure is adopted to calculate the mean square response and the peak response. On the basis of the proposed approach, the random seismic response of a tunnel is analyzed and a parametric study is presented. Both stationary and non-stationary responses are obtained and compared with each other. It is shown from the results that the stationary responses will under-estimate the dynamic reliability of the structure.

1 INTRODUCTION

The response behavior of underground structure to deterministic seismic loading had been investigated by a number of researchers (Akl et al 1989, Brancaleoni et al 1989, Kim et al 1995, Liao 1991, Pan et al 1987, Rowe 1992, Shao 1990, St John et al 1987, Sunil et al 1991, Takemmiya et al 1984). However, few of them took account of the random properties of the seismic excitation. Since the complicity in the behavior of fault and the travelling path of seismic wave, the seismic loading acting on structure should be considered as a random field or a random process. Therefore, it is necessary to deal with the seismic response of underground structure by the method of random vibration, and the soil-structure interaction should also be considered.

Lin proposed a virtual-excitation method to analyze the random response of structures by general purpose FEM software for structure analysis (Lin 1985, 1993, 1995).

The objective of this paper is to propose an alternative approach in which the impulse response functions of underground structure are calculated on the basis of δ function, using general purpose FEM software for structure analysis, and to investigate the peak response behavior of tunnels in various conditions.

2 FORMULATIONS

2.1 Calculation of impulse functions

The unit impulse function δ(t) should satisfy the following condition:

$$\int_a^b \delta(x-x_0)dx = \begin{cases} 0, & x_0 \notin (a,b) \\ 1, & x_0 \in (a,b) \end{cases} \quad (1)$$

Under the action of $\delta(t)$, the response of a structure system is called impulse response function $h(t)$.

To obtained $h(t)$ through numerical analysis software, we can use a discrete series of $\delta(t)$ as following

$$\delta(t) = \{\frac{1}{\Delta t}, 0, 0, 0, \cdots\cdots\} \quad (2)$$

as the excitation of the structure system, in which Δt is the time step in the dynamic analysis. It can be proved that the discrete Fourier Transform of Equation (2) is consistent to theoretical value of $\delta(t)$. This discrete series can be used as the input of FEM software to obtain the impulse response function at any point of a underground structure.

2.2 Stochastic Response of Structures

Considering the seismic excitation as an non-

stationary Gaussian process expressed by the following Fourier-Stieltjes integration:

$$\ddot{Y}(t) = \int_{-\infty}^{+\infty} A(t,\omega) e^{-i\omega t} dF_X(\omega) \tag{3}$$

where, $A(t,\omega)$ is a deterministic function of t and ω. If the power spectrum of the stationary process $X(t)$ is $\Phi_{XX}(\omega)$, The instant power spectrum of the non-stationary process $\ddot{Y}(t)$ is:

$$\Phi_{\ddot{Y}\ddot{Y}}(t,\omega) = |A(t,\omega)|^2 \Phi_{XX}(\omega) \tag{4}$$

In seismic analysis of structure, a special form of Equation (3), $\ddot{Y}(t) = \psi(t)X(t)$, is usually used to model a seismic excitation, where $X(t)$ is a stationary Gaussian process with mean value of zero, and $\psi(t)$ is a deterministic envelope function.

It is well known that the response of a linear time independent system to the excitation presented by Equation (3) is still a non-stationary Gaussian process with zero mean value. If the impulse response function of the system is $h(t)$, then the response of the system can be written as following:

$$u(t) = \int_{-\infty}^{+\infty} M(t,\omega) e^{-i\omega t} dS_X(\omega) \tag{5}$$

where,

$$M(t,\omega) = \int_{t_0}^{t} h(t-\tau) A(\tau,\omega) e^{i\omega(t-\tau)} d\tau \tag{6}$$

The power spectrum of the response is

$$\Phi_{uu}(\omega,t) = |M(t,\omega)|^2 \Phi_{XX}(\omega) \tag{7}$$

and the mean square of the response is

$$\sigma_u^2(t) = \int_{-\infty}^{+\infty} \Phi_{uu}(\omega,t) d\omega \tag{8}$$

The spectrum moment of the response can be written as:

$$\lambda_i = \int_{-\infty}^{+\infty} \omega^i \Phi_{uu}(\omega,t) d\omega \tag{9}$$

where, λ_i is the spectrum moment of the ith order.

The shape factor of the power spectrum is

$$q(t) = \sqrt{1 - \frac{\lambda_1^2(t)}{\lambda_0(t)\lambda_2(t)}} \tag{10}$$

Assuming the passage of the response process to a given level as a Poisson process, we can obtain the probability in which the response is within the limit of (-b,b) as following:

$$P(b,-b) = \exp\{-\frac{1}{2\pi}\int_0^T \omega_2(t) \exp[-\frac{b^2}{2\sigma^2(t)}]dt\} \tag{11}$$

An modified expression with Malkov assumption is

$$P(b_i - b) = \exp[-\int_0^T \alpha(t)dt] \tag{12}$$

where,

$$\sigma(t) = \sqrt{\lambda_0(t)} \tag{13}$$

$$\omega_2 = \left[\frac{\lambda_2(t)}{\lambda_0(t)}\right]^{1/2} \tag{14}$$

$$\alpha(t) = \frac{\omega_2(t)}{\pi} \exp[-\frac{r^2(t)}{2}] \frac{1 - \exp[\sqrt{\frac{\pi}{2}} q(t) r(t)]}{1 - \exp[-\frac{r^2(t)}{2}]} \tag{15}$$

If the non-stationary behavior can be ignored, the following simplified formulation for the stationary response can be obtained:

$$\lambda_i = \int_{-\infty}^{+\infty} \omega^i \Phi_{uu}(\omega) d\omega \tag{16}$$

$$q = \sqrt{1 - \frac{\lambda_1^2}{\lambda_0 \lambda_2}} \tag{17}$$

In this case, we can obtain the peak response factor under a given probability of non-exceedence.

For Poisson distribution,

$$r^2 = -2\ln[\frac{\pi}{T\omega_2} \ln p] \tag{18}$$

whereas under the assumption of Malkov distribution, we can obtain the following modified expression:

$$r^2 = 2\ln\left\{2n\left[1 - \exp\left(-q^{1.2}\sqrt{\pi \ln(2\pi)}\right)\right]\right\} \tag{19}$$

where, r is the peak response factor. T is the duration of earthquake; p is the probability of non-exceedence.

$$\omega_2 = \sqrt{\frac{\lambda_2}{\lambda_0}} \tag{20}$$

$$n = -\frac{\omega_2 T}{2\pi \ln p} \tag{21}$$

The peak response of the structure can be obtained by the following expression:

$$R_{\max} = r\sigma \tag{22}$$

where, σ is the root of the mean square of response.

Using the formulation given above, the stationary and non-stationary response of an underground structure can be calculated.

3 NUMERICAL EXAMPLE AND PARAMETER STUDY

3.1 Finite Element Model and Parameters

The seismic damage shows that the shape, size and

thickness of the lining of a underground structure, the mechanical behavior of the lining and the surrounding medium, the embedment of the structure and the thickness of the deposit between the structure and the bedrock are the main factors affecting the stability of the underground structure. To consider the influence of these factors five cases is compared in this paper. The finite element model of the structure and the surrounding soil is shown in Fig. 1. The parameters of the five cases are shown in Table 1. The mechanical parameters of the lining structure and the surrounding soil are shown in Table 2. The seismic wave is assumed to be propagate vertically with maximum acceleration of 0.32g.

Table 1 Outlines of the five cases

Case	Soil type	Lining thickness (m)	Embedment (m)*	Deposit thickness (m)**
1	Type 1	0.5	40	40
2	Type 1	0.5	40	20
3	Type 2	0.5	40	40
4	Type 1	0.5	20	40
5	Type 1	0.7	40	40

Notes:
* Distance between the ground surface and the top of the underground structure
** Distance between the Bottom of the structure and the surface of the bedrock

Table 2 Parameters of lining and soil

	E(kPa)	ρ(kg/m^3)	μ	ξ
Type 1	4.17×10^5	1900	0.35	0.08
Type 2	3.0×10^5	1900	0.35	0.08
Lining	2.7×10^7	2500	0.2	0.02

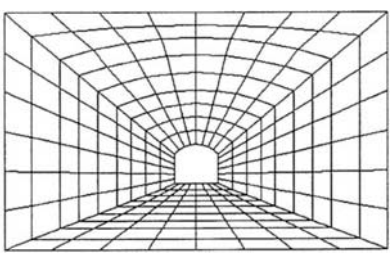

Fig. 1 Finite Element Model

3.2 Random Model for the Seismic Excitation

A model following Kanai (Kanai 1957) and Tajimi (Tajimi 1960) is adopted as the stationary power spectrum of the seismic acceleration:

$$\Phi_{XX} = \frac{1+4\xi_g^2\frac{\omega^2}{\omega_g^2}}{(1-\frac{\omega^2}{\omega_g^2})+4\xi_g^2\frac{\omega^2}{\omega_g^2}}\cdot\frac{4\xi_g\sigma_A^2}{\pi\omega_g\left(1+4\xi_g^2\right)} \quad (23)$$

where, ω_g is the natural frequency of the site, ξ_g is the damping ratio, σ_A is the mean square root of the acceleration (Wang et al 1997). The parameters in calculation is shown in Table 3.

Table 3 Parameters of the ground acceleration

ω_g	ξ_g	σ_A
16.5	0.8	1.0825

The envelope function for the non-stationary model is shown in Fig.2 (Cao et al 1998).

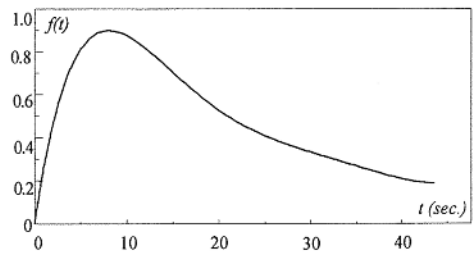

Fig.2 Envelope function for the seismic wave

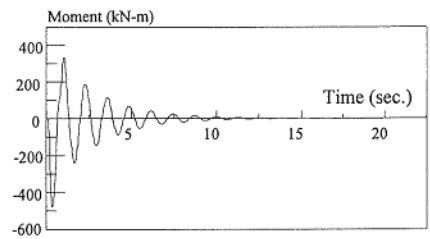

Fig.3 Impulse response of moment at top of lining

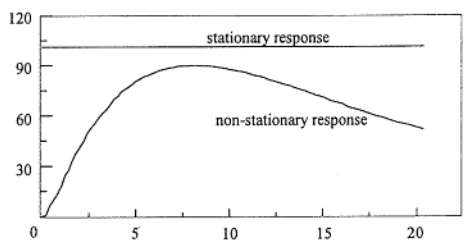

Fig.4 Mean square root of moment at top of lining

3.3 Results

The impulse response functions of moment at the spandrel of the lining for case 1 is shown in Fig.3. The

corresponding stationary and non-stationary mean square root of the moment response are given in Fig.4, where the horizontal lines are the stationary response which are independent to time.

It can be find in Fig.3 and Fig.4 that the stationary response of moments are larger than the corresponding non-stationary responses. Therefore, the reliability of the structure will be under estimated considerably if only the stationary response is considered.

To compare the influence of various factors on the response character of the structure, the mean square root of the response for all the five cases mentioned above are listed in Table 4.

Table 4 Stationary mean square roots for all the cases

Location	Case 1		Case 2		Case 3		Case 4		Case 5	
	Axial force (kN)	Moment (kN-m)	Axial force (kN)	Moment (kN-m)	Axial force (kN)	Moment (kN-m)	Axial force (kN)	Moment (kN-m)	Axial force (kN)	Moment (kN-m)
1*	45	45	47	45	43	43	33	34	51	60
2**	293	38	309	27	288	37	218	29	349	48
3***	19	313	39	330	14	310	10	225	18	463
4****	134	305	125	323	131	304	101	213	151	449
5*****	490	76	515	88	471	85	329	44	542	151
6******	89	101	94	102	85	104	57	70	99	153

Notes:
* The center of the bottom plate of the lining
** The lower corner of the lining
*** The middle of the side wall of the lining
**** The foot of the arch of the lining
***** The vault of the lining
****** The spandrel of the lining

It can be find from Table 4 that (compared with case 1):

(1) Decrease in the thickness of the deposit between the underground structure and the bedrock (case 2) will increase the maximum mean square response;

(2) Decrease in the stiffness of the surrounding soil (case 3) will decrease the maximum mean square response;

(3) Decrease the embedment of the underground structure (case 4) will decrease the maximum mean square response;

(4) Increase the stiffness of the underground structure lining (case 5) will increase the maximum mean square response.

It can also be find that the maximum mean square axial force produced in the lining of the underground structure arises at the vault of the lining, whereas the maximum mean square moment arises in the side wall of the lining.

To further compare the random response behavior of the underground structure, Table 5 to Table 9 show the peak responses of axial forces and the moments for all the five cases, at the reliability of 95% for Poisson and Malkov distributions.

Table 5 Peak response for case 1

Location	Stationary response				Non-stationary response			
	Poisson distribution		Malkov distribution		Poisson distribution		Malkov distribution	
	Axial force (kN)	Moment (kN-m)	Axial force (kN)	Moment (kN-m)	Axial force (kN)	Moment (kN-m)	Axial force (kN)	Moment (kN-m)
1*	162	165	159	161	66	68	62	63
2**	1063	140	1040	136	433	57	398	53
3***	69	1138	68	1113	31	465	29	428
4****	486	1112	475	1090	199	456	182	422
5*****	1785	278	1751	274	734	115	679	107
6******	325	368	317	360	134	151	124	140

Notes: Same as in Table 4.

Table 6 Peak response for case 2

Location	Stationary response				Non-stationary response			
	Poisson distribution		Malkov distribution		Poisson distribution		Malkov distribution	
	Axial force (kN)	Moment (kN-m)	Axial force (kN)	Moment (kN-m)	Axial force (kN)	Moment (kN-m)	Axial force (kN)	Moment (kN-m)
1*	173	166	168	162	74	71	66	65
2**	1138	101	1104	98	454	43	416	40
3***	143	1212	141	1177	62	510	59	465
4****	459	1190	446	1154	643	501	179	457
5*****	1894	323	1838	314	798	137	728	125
6******	345	376	336	366	99	159	134	146

Notes: Same as in Table 4.

Table 7 Peak response for case 3

Location	Stationary response				Non-stationary response			
	Poisson distribution		Malkov distribution		Poisson distribution		Malkov distribution	
	Axial force (kN)	Moment (kN-m)	Axial force (kN)	Moment (kN-m)	Axial force (kN)	Moment (kN-m)	Axial force (kN)	Moment (kN-m)
1*	154	156	150	152	60	62	56	57
2**	1032	132	1010	129	407	53	273	49
3***	53	1136	53	1111	24	448	22	413
4****	471	1108	460	1087	187	441	172	407
5*****	1695	305	1662	299	675	122	622	113
6******	308	375	301	367	122	149	113	137

Notes: Same as in Table 4.

Table 8 Peak response for case 4

Location	Stationary response				Non-stationary response			
	Poisson distribution		Malkov distribution		Poisson distribution		Malkov distribution	
	Axial force (kN)	Moment (kN-m)	Axial force (kN)	Moment (kN-m)	Axial force (kN)	Moment (kN-m)	Axial force (kN)	Moment (kN-m)
1*	123	127	121	124	53	54	50	52
2**	810	108	795	106	348	47	325	43
3***	37	836	37	823	18	365	16	337
4****	375	794	368	782	162	345	151	326
5*****	1229	165	1210	163	529	72	501	69
6******	214	260	212	256	94	113	88	106

Notes: Same as in Table 4.

Table 9 Peak response for case 5

Location	Stationary response				Non-stationary response			
	Poisson distribution		Malkov distribution		Poisson distribution		Malkov distribution	
	Axial force (kN)	Moment (kN-m)	Axial force (kN)	Moment (kN-m)	Axial force (kN)	Moment (kN-m)	Axial force (kN)	Moment (kN-m)
1*	183	220	179	214	75	90	69	82
2**	1266	176	1238	172	516	72	475	66
3***	67	1684	66	1642	28	687	25	629
4****	551	1633	539	1579	225	669	207	619
5*****	1972	550	1931	539	809	226	745	210
6******	360	555	353	543	147	228	137	209

Notes: Same as in Table 4.

It can be find from Table 5 to Table 9 that:

(1) The peak responses for stationary Poisson distribution are 2% to 4% larger than for Malkov distribution;

(2) The peak responses for non-stationary Poisson distribution are 8% to 10% larger than for non-stationary Malkov distribution;

(3) The peak responses for stationary Poisson and Malkov distribution are 130% to 150% larger than for non-stationary Poisson and Malkov distribution.

Therefore, it is too conservative to deal with the seismic excitation as stationary process. Moreover, it have to be noted that the Poisson distribution is suitable only when the peak response is larger enough to which the probability to exceed is very small.

4 CONCLUSION

The following conclusions can be obtained according to the analysis:

(1) The proposed method is suitable to the random vibration and peak response for underground structures;

(2) The maximum peak axial force produced in the lining of the underground structure arises at the vault of the lining, whereas the maximum peak moment arises in the side wall of the lining;

(3) The thickness of the lining, the embedment of the structure, the thickness of the deposit between the structure and the bedrock, and the stiffness of the lining and the surrounding medium, can affect the random response of the understructure significantly;

(4) Dealing with the seismic excitation as stationary process will result conservative design.

ACKNOWLEDGMENT

The research for this paper is supported by the National Science Foundation of China (Grant No. 59478042).

REFERENCES

Akl A.Y., Sobaih M. & Maher M.M. 1989. Behavior of tunnels under seismic loads, International Conference on Civil and Structural Engineering Computing: 81-87.

Brancaleoni F., Castellani A. & D'Asdia P. 1989. The response of submerged tunnels to their environment. Engineering Structures.Vol.11, No.1: 47-56.

Cao Guoan and Zhang Hongru 1998. An envelope function model for earthquake intensity. J. Northern Jiaotong University, Vol.22, No.1: 29-33.

John C. M. et al 1987. Aseismic design of underground structures. Tunneling and Underground Space Technology, No.2: 165-197.

Kanai K 1957. Seismic-empirical formula for seismic characteristics of the ground, Bull. Earthquake Res. Inst. Japan, No.35:309-325.

Kim Moon Kyum, Leigh Ilho & Keum Ho Oh 1995. Effect of structural types on vibration characteristics of railway tunnels, Proc. International Symposium on Public Infrastructure Systems Research: 283-289.

Liao Sam S.C. 1991. Seismic design issues for immersed tube tunnels, Proc. of 21st Century Construction Congress, ASCE, New York, NY, USA: 584-589.

Lin Jiahao 1985. A deterministic algorithm for random seismic response. Earthquake Engineering and Engineering Vibration. Vol.5, No.1: 89-93.

Lin Jiahao 1993. An effective accurate algorithm for non-stationary seismic response. Earthquake Engineering and Engineering Vibration. Vol.13, No.1: 24-29.

Lin Jiahao, Shen Weiping and Williams F.W. 1995. An accurate integration algorithm for the response of structures subjected to evolutionary random excitation. J. Dalian University of Science and Technology, Vol.35, No.5: 600-605.

Pan Changshi and Yang Li 1987. Seismic response analysis for tunnels in loess. Chinese J. Civil Engineering, Vol.20, No.2.

Rowe R 1992. Tunneling in seismic zones. Tunnels & Tunneling, Vol.24, No.12: 41-44.

Shao Dagen 1990. Study on the aseismic behavior of railway tunnel lining under intensive earthquakes. Research report, The China Academy for Railways, Beijing.

Sunil Sharma & William R.Judd 1991. Underground opening damage from earthquakes, Engineering Geology, Vol.30: 263-276.

Tajimi H 1960. A statistical method of determining the maximum response of a building structure during an earthquake, Proc. 2nd Word Conf. On Earthquake Eng., Japan

Takemmiya H., Yokoyama K. & Oishi H. 1984. Seismic analysis of an underground structure, Proc. International Symposium on Dynamic Soil-Structure Interaction: 65-74.

Wang Junjie and Wang Jinren 1997. A note on the stationary self power spectrum for seismic wave. World Earthquake Engineering, 13(2): 37-40.

Earthquake Geotechnical Engineering, Sêco e Pinto (ed.) © 1999 Balkema, Rotterdam, ISBN 90 5809 116 3

Seismic resistance and design of shield tunnel lining with a new internal lining

J.Tohda
Osaka City University, Japan
H.Yano
Sekisui Chemical Company Limited, Siga, Japan
J.Tomita
Sogo Engineering Incorporated, Osaka, Japan

ABSTRACT: A series of 1/50 scale seismic centrifuge model tests was conducted to compare earthquake resistances of two types of shield tunnel linings under seismic loading, one with a conventional internal concrete lining without reinforcing steel bars and the other with a new type of internal lining that is constructed by inserting thin and flexible FRPM pipes into a constructed external steel lining and filling the clearance between them with air-mortar. The centrifuge experiments revealed that the shield tunnel lining with the new internal lining has considerably higher earthquake resistance than that with the conventional internal concrete lining. A new design concept that considers external steel linings as temporary structures is proposed. Numerical calculations revealed that with the proposed design concept and the new internal lining, the size of the shield tunnel lining can be reduced significantly, resulting in considerable savings in the construction cost.

1 INTRODUCTION

In Japan, shield tunnels for sewage transport with internal diameters less than 3 m are commonly constructed by assembling steel segments as external linings and placing concrete without reinforcing steel bars inside the steel segments as internal linings. This type of shield tunnel lining is referred as R(Rigid)-lining here. The following problems have been identified for the R-lining: (1) inefficiency resulting from the batch construction system of internal concrete linings, (2) poor working environment due to an increase in temperature while concrete hardens during internal lining construction, (3) damage to internal concrete linings due to acidic sewage, (4) corrosion of external steel linings, (5) low resistance against seismic loading as observed after the 1995 Hyogoken-Nambu Earthquake, and (6) high cost as compared to pipe jacking methods.

A new type of internal lining system was developed to overcome the abovementioned problems of the R-lining, and is now increasingly adopted in Japan. In this system, thin and flexible FRPM (fiber reinforced plastic mortar) pipes are inserted into constructed external steel linings and the clearance between a pipe and an external lining is filled with low strength air-mortar. A shield tunnel lining with this new type of internal lining system is referred as F(Flexible)-lining here.

The FRPM pipes with high resistance against acidic sewage are used in the F-lining. They are continuously inserted from a vertical shaft. Also, these pipes are designed to support all external forces that would be transferred to them after their external steel linings are completely corroded. In addition, during the hardening of the air-mortar, the increase in temperature is smaller as compared to the R-lining. Thus, the F-lining overcomes problems (1) to (4) that were identified for the R-lining.

The structural system of the F-lining is much more flexible than that of the R-lining. The failure strain of FRPM pipes is about 200 times greater than that of concrete. Therefore, the F-lining is expected to have considerably higher earthquake resistance than the R-lining; however, this needs to be proven experimentally. Also, the construction cost of the F-lining is now almost comparable to the cost of the R-lining, which is achieved by reducing the size of a shield tunnel. However, it is still costlier in comparison with pipe jacking methods.

The effectiveness of the F-lining in overcoming the abovementioned problems (5) and (6) with the R-lining is evaluated in this paper. Results from a series of seismic centrifuge model tests are first presented. The tests were conducted to confirm that the F-lining is highly earthquake resistant. Then, a new design concept which reduces the tunnel size resulting in significant savings in the construction cost of the F-lining is presented.

2 SEISMIC RESISTANCE OF THE F-LINING

2.1 *Background*

Damage to shield tunnel linings of a total length of

about 20 km was observed in the Hanshin Area after the 1995 Hyogoken-Nambu Earthquake. They were used for sewage transport. The damage was observed in variety of shield tunnels ranging from 2 to 7 m in diameter and 5 to 25 m in burial depth. Documentation on the damage to shield tunnels as severe as that in the Hyogoken-Nambu Earthquake was not found in the earlier earthquake damage reports.

The damage mainly consisted of cracks in internal concrete linings along the longitudinal axes of the shield tunnels. The cracks were located at $\pm 45°$ from the tops and bottoms of the tunnels, forming X-letter-shaped pattern. Most of the cracks were accompanied with water leakage from the outside because of the opening of joints of the external linings. On the other hand, water leakage was not observed in the segments of shield tunnels under construction. The facts that no damage was observed in the shield tunnels without internal concrete linings and many shield tunnels with internal concrete linings experienced severe damage suggested that the existence of internal concrete linings caused the damage during the earthquake.

Full scale loading tests for the actual R- and F-linings of 2 m external diameter were performed to obtain their flexural stiffnesses. Then, a series of seismic centrifuge model tests was performed both to duplicate the cracking of the R-linings observed after the Hyogoken-Nambu Earthquake and to demonstrate higher seismic resistance of the F-lining. The size of the F-lining was not reduced in the tests so as to be able to compare its behavior with that of the R-lining directly.

2.2 *Full scale loading tests*

Schematics of the actual R- and F-linings used in the full scale loading tests are shown in Figure 1. Their internal (d) and external (D) diameters were 1.35 m and 2 m, respectively. Seven 75 cm long steel segment pieces were combined to form one ring of the external lining. Beam members (0.8 cm thick steel plates) of the segment structures were bolted to both ends of the external lining to simulate the deformation behavior of a long tunnel lining correctly.

The internal lining of the R-lining was constructed by placing concrete without reinforcing steel bars, as in the conventional construction. The internal lining of the F-lining was constructed by filling air-mortar in the clearance between the external lining and a 17.85 mm thick FRPM pipe. Table 1 shows mechanical properties of the internal lining materials.

A pair of line loads (P) were cyclically applied at diametrically opposite locations (top and bottom) of the lining and corresponding vertical deflection (δ) of the lining was measured. The P-δ relationships

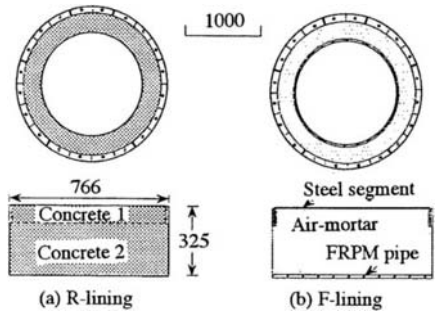

Figure 1. Schematics of the actual linings used in the full scale loading tests (dimensions are in mm).

Table 1. Mechanical properties of the internal lining materials.

	Concrete	Air-mortar	FRPM
Strength (kgf/cm^2)	313*	11.7*	2200**
E (kgf/cm^2)	300000	4586	181900
ν	0.24	0.25	0.30

*Compression, and **compresion and tension

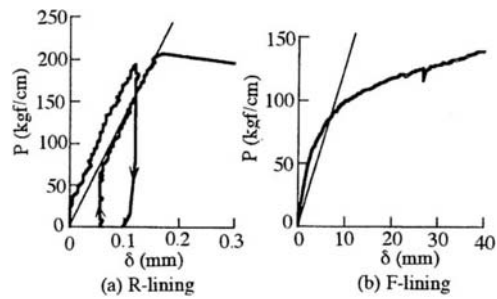

Figure 2. Measured and calculated P-δ relationships for actual R- and F-linings.

for the two linings are shown in Figure 2. The P-δ behavior of the R-lining was linear until cracks in the internal concrete lining were developed. On the other hand, P-δ behavior of the F-lining was non-linear because of cracking in the air-mortar in the vicinity of joints of the segment pieces. The FRPM pipe of the F-lining was intact even when δ reached 150 mm. The figure also indicated that the F-lining is considerably more flexible than the R-lining.

P-δ relationships for both R- and F-linings were calculated by considering the structural systems as a thick multi-layered cylinder for the R-lining and a thin multi-layered cylinder for the F-lining. The assumed interface conditions for both linings were: (1) the external linings (steel segments) and concrete or air-mortar were bonded in both R- and F-linings, and (2) the FRPM pipe and air-mortar could slide easily in the F-lining. The values of Young's moduli (E) of the concrete and air-mortar were determined as follows: For the R-lining, E of the concrete 1 (Fig. 1a) was assumed as 1,500,000 kgf/cm2 by considering an increase in the stiffness

of this area due to the existence of both joint steel plates and rib steel plates along the long axis of each segment. E of the concrete 2 (Fig. 1a) was adjusted to E of the concrete specimen (=300,000 kgf/cm^2). For the F-lining (Fig. 1b), E of the air-mortar was assumed as 1300 kgf/cm^2 corresponding to about 30 % of E=4586 kgf/cm^2 of the intact air-mortar by considering existence of the cracks.

The calculated P-δ relationship are shown as straight lines in Figures 2a and 2b. These lines compared fairly well with the measured P-δ curves. Flexural stiffnesses (S_p) of 2944 kgf/cm^2 for the R-lining and 19.6 kgf/cm^2 for the F-lining were determined from these two lines, and using equation: $\delta_M=0.149P/S_p$. Here, δ_M denotes deflection of the lining due to bending moment.

2.3 *Seismic centrifuge model tests*

Two pipes, made of aluminum (E=740,000 kgf/cm^2 and ν=0.3), were used as 1/50 scale model R- and F-linings in the centrifuge model tests. The external diameter (D) and length of both model linings were 4 cm and 14.8 cm, respectively. Their thicknesses (t, 6 mm for the model R-lining and 1.3 mm for the F-lining) were determined by using the equation: $S_p=Et^3/\{12(1-\nu^2)R^3\}$, to have the same S_p values as those of the actual linings (R=neutral radius of the model lining). Strain gages were mounted at 16 circumferential locations to measure bending strains produced in the wall of the model lining (ε_m).

Bending moments in the model linings (M_m) were calculated from measured model strains (ε_m) as: $M_m=\varepsilon_m Et^2/\{6(1-\nu^2)\}$. The actual bending moments (M_a) were extrapolated from M_m according to the scaling relation: $M_a=n^2M_m$, where n (=50) is the g-level at which the test was conducted. The prototype strains (ε_a) produced in the internal surface of the actual lining could then be calculated by applying M_a to the structural systems of the actual linings described in Section 2.2. The relationships between actual and model strains were determined to be $\varepsilon_a=1.65\varepsilon_m$ for the R-lining and $\varepsilon_a=0.39\varepsilon_m$ for the F-lining.

Figure 3 shows a typical centrifuge model configuration. The model linings were buried in decomposed-granite (G) or dry-sand (S). Ground-G was constructed by compaction (several 2 cm thick layers). The compaction was progressed vertically. Ground-S was constructed by dry pluviation. The pluviation was progressed in parallel to the long axis of the model lining. The properties of the model grounds are given in Table 2, in which G_D and G_L denote dense and loose decomposed-granite, respectively.

The experiments were conducted at 50 g (i.e. 50 times greater than the gravitational acceleration g). The base input motions (a typical one shown in Fig. 4) were generated using the servo-controlled,

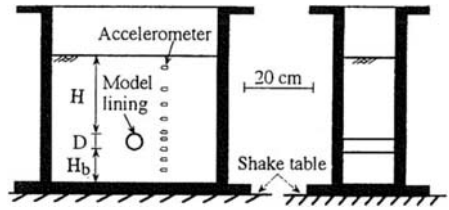

Figure 3. A typical centrifuge model configuration.

Table 2. Properties of model grounds.

Soil*	G_s	D_{max} mm	U_c	ρ_{dmax} g/cm^3	ρ_{dmin} g/cm^3	ρ_d g/cm^3	w %	c_d tf/m^2	ϕ_d Degree
G_D	2.71	2.0	70	1.92	1.37	1.70	10	2.3	38
G_L						1.50	10	0.9	38
S	2.65	0.43	1.8	1.78	1.47	1.72	0	0	43

*G_D and G_L respectively denote dense and loose decomposed granite, and S denotes dry silica sand.

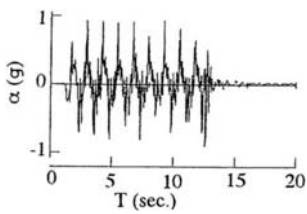

Figure 4. Time history of the base horizontal input acceleration in prototype scale.

Table 3. Test conditions.

Series	Lining	Ground	H/D	H_b/D
A	R and F	G_D	2.5, 5 and 7.5	2.5
B	R and F	G_D	5	0.25, 2.5 and 5
C	R and F	G_D, G_L, G_{LD}*, and S	5	2.5

*G_{LD} ground is composed of G_L at the shallower layer 19cm thick and G_D at the deeper layer 15cm thick.

electro-hydraulic shake table on-board the 400 g-ton centrifuge at the University of Colorado at Boulder. According to the prototype scale, the horizontal input motions were approximately sinusoidal with 10 cycles of $\pm$0.8 g amplitude at 1 Hz frequency. During the shaking, the data from strain gages of the model linings and accelerometers buried in the model grounds were collected for 1 second at a sampling rate of 2500 Hz.

A series of 16 tests was conducted to study the effects of cover depth (H), distance between the base and the bottom of the lining (H_b), density and type of the ground material, and flexibility of the tunnel lining. Pertinent test conditions are summarized in Table 3.

A typical set of measurements from the tests on the model R-lining in Ground-G_D for different H_b is presented in Figure 5. The graphs shown in these figures were generated for the particular time instances when the strain at the right-side shoulder

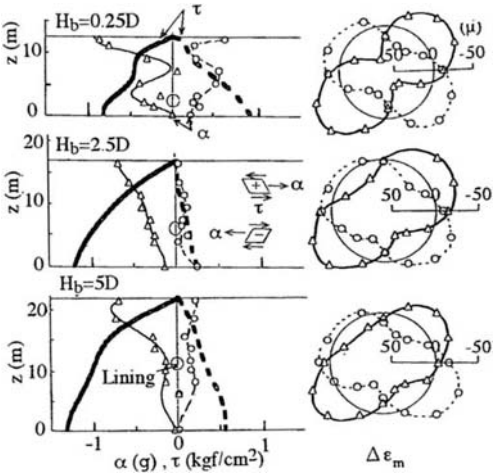

Figure 5. Measurements from a typical set of tests for different H_b (R-lining).

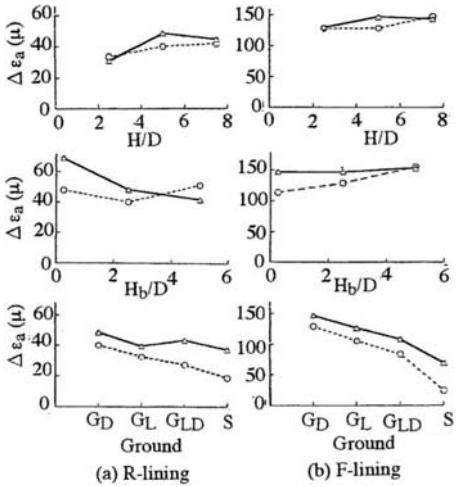

Figure 6. The maximum $\Delta\varepsilon_a$ produced in the actual linings.

of the model lining indicated the compressive and tensile peak values during the third cycle of the base input motion. The plots in Figure 5 that are on the left show the ground horizontal acceleration (α). In the same plots, thick curves represent the distributions of shear stress (τ) which were calculated by integrating the measured ground horizontal accelerations. The plots on the right illustrate the distributions of incremental bending strain due to the oscillation in polar coordinates ($\Delta\varepsilon_m$), in which $\Delta\varepsilon_m$ is counted as positive when the internal surface of the lining is extended. The following observations were made:

(1) The model R-lining produced the maximum tensile $\Delta\varepsilon_m$ at the internal four measuring points which were approximately $\pm 45°$ apart from the top and the bottom of the lining. The corresponding actual strains ($\Delta\varepsilon_a$) would generate cracks in the actual R-linings, as was observed after the 1995 Hyogoken-Nambu Earthquake.

(2) The absolute values of $-\tau$ in the ground were greater than those of $+\tau$. This generated a difference in the magnitude of measured $\Delta\varepsilon_m$ at the respective time instances.

(3) Similar results were obtained in other tests, except that $\Delta\varepsilon_m$ of the model F-lining were ten times greater than those of the model R-lining.

Figure 6 shows the change (due to the investigated factors) in the maximum increment of tensile strains $\Delta\varepsilon_a$ produced on the internal surfaces of the actual R- and F-linings at the same time instances as in Figure 5. The values of $\Delta\varepsilon_a$ were calculated as: $1.65\Delta\varepsilon_m$ for the R-lining and $0.39\Delta\varepsilon_m$ for the F-lining. Figure 6 indicates that:

(1) $\Delta\varepsilon_a$ of the R-lining were greater, when H was greater, H_b was smaller, and ground-G was denser. The change in $\Delta\varepsilon_a$ of the F-lining was similar to that of the R-lining, except when H_b was varied.

(2) $\Delta\varepsilon_a$ of the R-lining were in a range of 20-70 μ. The strain when cracks are generated in the actual internal concrete was estimated to be about 80 μ. The maximum value of $\Delta\varepsilon_a$ in the R-lining reached 70 μ, which was close to the failure strain. This confirms that internal concrete linings of the R-lining can get damaged easily during strong earthquakes, as was observed after the 1995 Hyogoken-Nambu Earthquake.

(3) The maximum $\Delta\varepsilon_a$ in the actual F-lining was around 150 μ, which was about 130 times smaller than the failure strain (=2 %) of the FRPM pipe. This confirms that the F-lining has considerably higher earthquake resistance than the R-lining.

3 NEW DESIGN CONCEPT FOR THE F-LINING

3.1 *Background*

The internal diameter of the F-lining can be made 1 size (about 10 %) smaller than that of the R-lining which would still allow the transport of the same volume of sewage as that of the R-lining, because the surface of the FRPM pipe is smoother than the internal concrete lining of the R-lining. In addition, the clearance between the pipes and steel segments can be minimized by making it just enough to still allow the insertion of the pipes into the external lining easily. Thus, the external diameter of the F-lining can be now made 2 sizes (about 15 %) smaller than that of the R-lining.

The current design standard in Japan for the R-lining (JSWAS 1990) specifies that the external lining supports external loads (earth pressures and external hydraulic pressures) entirely, i.e., the internal concrete lining does not contribute in supporting these external loads. On the other hand, the FRPM pipes in the F-lining are designed to support exter-

nal loads entirely when the steel segments are completely eliminated owing to corrosion. This means that both external and internal linings in the F-lining are designed as permanent structures in the current design practice, which is overconservative and also, the cost of construction is unnecessarily increased.

Therefore, a new design concept is proposed by the authors of this paper. Their method considers the external steel lining of the F-lining, whose long-term durability is not assured, as a temporary structure. To demonstrate the effectiveness of the proposed design method, a numerical example is presented in the following sections. In the example, a trial F-lining is designed according to the proposed design concept. Its performance is compared with that of the R- and F-linings which are designed according to the JSWAS standard to confirm that the new design concept can reduce both external diameter of the F-lining and the weight of the steel segments considerably.

The hypothetical R- and F-linings are designed for the following conditions: The ground is consisted of uniformly distributed sandy soil (mean N value=25, c_d=0, ϕ_d=35°, γ_t=γ_{sat}=1.8 tf/m^3, γ'=0.8 tf/m^3). The depth of the invert of the internal lining is 17 m below the ground surface. The ground water table is located at 6 m below the ground surface. The surface load is 1.25 tf/m^2. The minimum radius of the tunnel alignment (R_a) is 70 m.

3.2 *Design of the R-lining*

The R-lining is designed according to the JSWAS standard of steel segments for sewerage shield tunnels (JSWAS 1990) with 235 cm external diameter and 165 cm internal diameter. The external steel lining of the R-lining is constructed by assembling standard segments M9 (external diameter D_s=235 cm, internal diameter d_s=214.4 cm, and length L_s= 90 cm). The height (h_s) and thickness (t_s) of the main beams of M9 are 10 cm and 0.9 cm, respectively. The weight of the assembled M9 per unit length (W_s) is 549 kgf/m. The material of M9 is SM490A with allowable tensile and compressive strengths (σ_a) both to be equal to 1900 kgf/cm^2.

Calculated external loads on the external steel lining are shown in Figure 7. The vertical earth pressure p_v on the upper half of the external lining (=3.8 tf/m^2) is calculated through the equation: p_v=$\gamma'H_0$=$\gamma'2D_s$, where H_0 is equivalent to the height of the ground arch calculated by Terzaghi's theory. The lateral and reaction earth pressures (q_h and q_r) are calculated by using specified values of their coefficients (λ=0.5 and k=2 kgf/cm^3) as: q_h=λ(p_v+ $\gamma'z$) and q_r=kδ. Here, z is the depth measured from the top of the lining, and δ is the horizontal deflection of the lining at the springline. The pressures acting on the lower half of the lining consist of

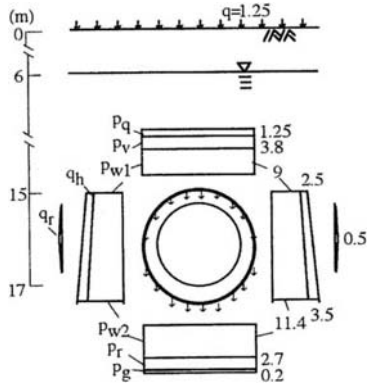

Figure 7. Design loads for the R-lining (tf/m^2).

hydraulic pressure (p_{w2}), reaction earth pressure (p_r), and reaction pressure against the lining weight (p_g). The value of p_r is calculated as: p_r=(p_q+p_v+ p_{w1})-p_{w2}, so as to satisfy the equilibrium of the vertical forces. When applying these external loads and weight of the segments, the absolute maximum fiber stress of the external steel lining is calculated as 1303 kgf/cm^2 (compression) on the internal edges of the segments at ±80° apart from the top of the lining. Since this value is smaller than σ_a=1900 kgf/cm^2, the R-lining is judged to be safe.

3.3 *Design of the F-lining*

First, the safety of the FRPM pipe is examined. The reduced internal diameter of the FRPM pipe used in the F-lining is 150 cm due to the smoother surface of the pipe. The external diameter, length, and wall thickness are 153.6 cm, 4 m, and 1.8 cm, respectively. The tensile and compressive allowable strengths of the pipe (σ_a) are specified both to be equal to 730 kgf/cm^2. Figure 8a shows the external loads on the pipe, which are calculated according to the JSWAS standard of steel segments. The absolute maximum fiber stress of the pipe is calculated for this load condition as 174 kgf/cm^2 (compression) on the external surface at the top of the pipe. This value is considerably smaller than σ_a. Also, the allowable external hydraulic pressure that the pipe can sustain without buckling is evaluated as 76 tf/m^2, which is considerably greater than the external hydraulic pressure acting on the upper half of the pipe (p_{w1}= 9.5 tf/m^2). The deflection of the pipe is calculated as 0.12 cm, which is negligible. Thus, the FRPM pipe is judged to be safe.

Then, the external steel lining is designed as a permanent structure according to the JSWAS standard. The minimum internal diameter of steel segments, into which the FRPM pipes with 4 m in length are inserted, becomes 169.6 cm for R_a=70 m. This internal diameter includes a clearance of 5 cm

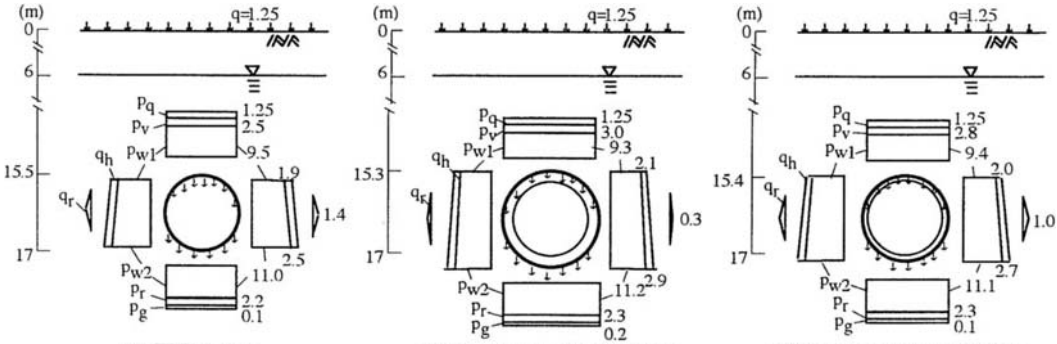

Figure 8. Design loads for the F-lining (dimensions are in tf/m^2).

all around the pipe to ease the insertion of the pipes into the lining. The segment M2 is selected among the standard steel segments provided in the JSWAS standard, because the internal diameter (d_s=174.4 cm) of M2 is the closest to 169.6 cm as calculated above, and also, its external diameter (D_s=190 cm) is the smallest. The other dimensions of M2 are specified as L_s= 75 cm, h_s=7.5 cm, t_s=0.8 cm, and W_s=380 kgf/cm. The absolute maximum fiber stress of M2 is calculated as 1200 kgf/cm^2 (compression) for the external loads shown in Figure 8b. Since this value is smaller than σ_a=1900 kgf/cm^2, the external lining M2 is judged to be safe.

Finally, the external lining is designed as a temporary structure according to the proposed design concept. In this case, the allowable strength of SM 490A (σ_a) is increased as 2850 kgf/cm^2, which is 1.5 times greater than 1900 kgf/cm^2 in the permanent structure case. The dimensions of the trial steel segment with d_s=169.6 cm are determined such that the segment generates the absolute maximum fiber stress smaller than σ_a=2850 kgf/cm^2 for the external loads shown in Figure 8c, as: D_s= 176.2 cm, L_s= 75 cm, h_s=3 cm, and t_s=0.7 cm. The value of W_s becomes 220 kgf/m. The absolute maximum fiber stress of the segment is calculated as 2603 kgf/cm^2.

3.4 *Comparison among the designed linings*

While using the current design standard, the external diameter of the F-lining is reduced from 235 cm of the R-lining to 190 cm. The effect of the reduction in size is expressed in terms of the ratios (the F-lining quantity to the R-lining quantity) of the excavated soil volumes (α) and the steel segment weights (β) as α=(190 cm/235 cm)^2=0.65 and β= (380 kgf/m)/(549 kgf/m)=0.69.

On the other hand, by using the new design concept, the F-lining can be reduced further from 190 cm to 176.2 cm in the tunnel size and from 380 kgf/m to 220 kgf/m in the segment weight. The values of α and β against the R-lining become α= (176.2 cm/235 cm)^2=0.56 and β=(220 kgf/m)/(549 kgf/m)=0.40. The savings in the cost due to the adoption of the proposed design concept are reflected in the ratios (α and β) of the F-lining quantities obtained according to the proposed design method to the F-lining quantities obtained according to the current design standard as α=(176.2 cm/190 cm)^2= 0.86 and β=(220 kgf/m)/(380 kgf/m)=0.58.

4 CONCLUSIONS

1. The centrifuge experiments confirmed that the commonly used shield tunnel lining with the internal concrete lining (R-lining) can get damaged easily during strong earthquakes, as was observed in the 1995 Hyogoken-Nambu Earthquake. The experiments also confirmed that the shield tunnel linings with the new internal lining system using FRPM pipes and air-mortar (F-lining) has considerably higher earthquake resistance than the R-lining.
2. Using the proposed design concept that considers external steel lining as a temporary structure, both the size of the shield tunnel and the weight of the steel segments can be reduced significantly, resulting in considerable further savings in the cost without compromising its stability as evident from the fiber stress calculations.
3. Thus, the F-lining designed according to the proposed design concept is effective in overcoming all the problems identified for the R-lining. Its adoption will contribute significantly to prevent damage to shield tunnels due to seismic loading.

REFERENCES

JSWAS. 1990. The standard steel segments for sewerage shield tunnels, JSWAS &JSCE.

Tohda, J., Yoshimura, H. & Li, L. 1996. Characteristic features of damage to the public sewerage systems in the Hanshin Area, *Special issue of soils and foundations*: 335-347, JGS.

Earthquake Geotechnical Engineering, Sêco e Pinto (ed.) © 1999 Balkema, Rotterdam, ISBN 90 5809 116 3

Experimental study on the effects of vertical shaking on the behavior of underground pipelines

Y. Mohri
National Research Institute of Agricultural Engineering, Japan

T. Kawabata
Pipe Engineering Department, Kubota Corporation, Japan

H. I. Ling
Department of Civil Engineering, Columbia University, USA

ABSTRACT: Soil liquefies during an earthquake resulting in flotation of buried pipelines to the ground surface. In order to reveal the uplift behavior of buried pipelines during earthquake, large-scale shaking tests were conducted on a pipeline installed under loose sand using a 3 dimensional shaking table. The effectiveness of four different types of stabilizing techniques against liquefaction was investigated. This paper discusses the effectiveness of each stabilizing technique.

1 INTRODUCTION

Buried pipelines are greatly influenced by the physical properties of the surrounding ground. Thus, the entire structure is usually stabilized by compacting the backfill materials of good quality. Field investigations of actual damage, vibration tests and numerical analyses have produced useful results pertaining to soil liquefaction of underground structures. To improve the accuracy of damage prediction and earthquake resistance of such buried pipes, it is important to identify the mechanism leading to liquefaction of backfill soil.

Some experimental studies have been conducted to identify the behavior of underground structures subject to ground liquefaction. Nevertheless, most of these studies involved small-diameter pipes, and only a limited studies have been conducted to investigate the methods of preventing large-diameter pipes from uplifting. In addition, there has been no study on the behavior of buried pipes subject to horizontal and vertical vibrations.

In this study, the authors investigated the influence of vertical motions on the behavior of buried pipes and the surrounding ground by conducting a series of one and two dimensional vibration tests. The effectiveness of mitigation technique to prevent buried pipes from uplifing is reported and discussed.

2 2-D SHAKING TEST

2.1 *Methodology*

The test was conducted using a three-dimensional vibration table with two types of excitation, i.e., excitation applied in a single direction (horizontal vibration only) and the other with excitation applied simultaneously in two directions (vertical and horizontal vibrations). The horizontal vibration was applied in the direction orthogonal to the pipe axis. The ratio of the maximum acceleration of vertical motion to that of horizontal motions was 0.5.

2.2 *Test Equipment*

The vibration table used for the test has plane dimensions of 6 m x 4 m, with the maximum loading capacity of 50 tf. The excitation was generated by hydraulic servo, which allowed independent control of three-dimensional vibration having six degrees of freedom.

The model was installed in a steel tank (4.6 m wide, 1.8 m high, and 1 m long) installed on the vibration table. The accelerometers, piezometers, and displacement transducers were used to monitor the performance. The scheme of instrumentation is shown in Figure 1.

Table 1. Models and input acceleration

	Input acceleration	WEST	CENTER	EAST
TEST-1	H=0.3g	MODEL_2	MODEL_1	MODEL_3
TEST-2	H=0.3g, V=0.15g	MODEL_2	MODEL_1	MODEL_3
TEST-3	H=0.3g, V=0.15g	MODEL_6		MODEL_5

2.3 *Model Ground*

The sand used in the test was homogeneous sand with a mean particle diameter (D_{50}) of 0.30 mm and the uniformity coefficient (Uc) of 2.49. To create the model sand ground, water was introduced into the test box up to a depth of around 50 cm, onto which wet sand was dropped from the water surface to create a loose ground. The relative density of the ground (Dr) was between 56% and 61%. A model pipe (a hard chloroethylene pipe with a diameter of 420 mm and a length of 970 mm) was buried at a depth of 40 cm from the ground surface. In each test, three models were constructed, as given in Table 1.

2.4 *Input Earthquake Motions*

To excite the model, input ground motion of 5.0 Hz was applied in the direction vertical to the pipe axis with a maximum acceleration of 300 gal in the horizontal direction. Vertical motion was input with the maximum acceleration of 150 gal. It was in phase with the horizontal motion. Figure 2 shows the acceleration waveforms measured on the vibration table.

2.5 *Test Conditions*

Table 1 shows the testing program. Model 1 is the reference test with a loose ground only, while Model 2 has a pipe installed at a designated location. In Model 3, crushed stones were filled around the upper half of the pipe and with a geogrid to form an integrated body. In Model 5, crushed stones were filled all around the pipe, while in Model 6, 15 cm wide vertical drain columns, made of crushed stones, were installed on the bottom and both sides of the pipe. The apparent unit weight of the pipe was 2.4 kN/m^3. The unit weight of the crushed stone section was 18.6 to 19.8 kN/m^3.

3 TEST RESULTS AND REMARKS

3.1 *Influence of Vertical Motions*

Figure 3 shows the amount of uplifting of the pipes. In Test 1, in which only horizontal excitation was applied, the pipe started to rise immediately after the commencement of excitation, and continued to rise by around 150 mm to 200 mm during excitation. In the case of Model 3, in which crushed stones were installed around the upper part of the pipe, the uplifting stopped immediately when excitation ended. The crushed stones proved effective in reducing flotation. In the case of Model 2, which is without reinforcement, the uplifting did not stop even after the end of excitation. The pipe rose to the ground surface two minutes after the end of vibrations.

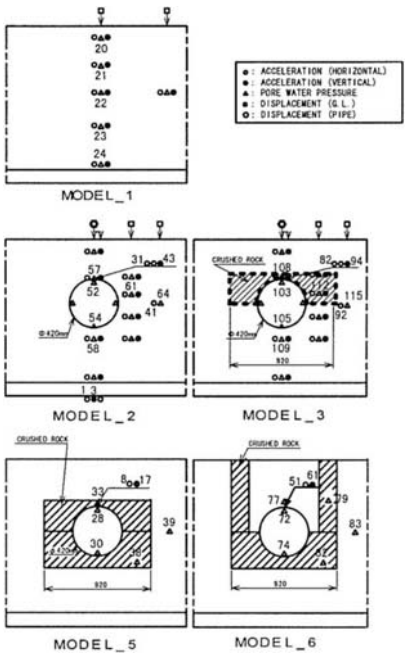

Fig. 1 Soil models for shaking table tests

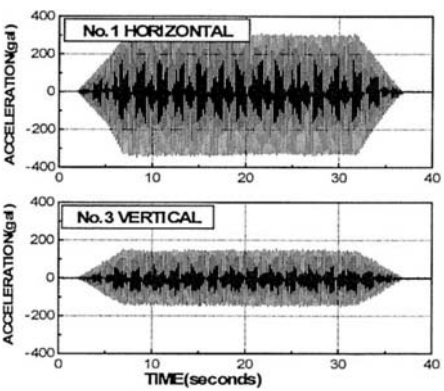

Fig.2 Time histories of acceleration of shaking table

In Test 2, in which excitation was applied both vertically and horizontally, the pipe rose at a speed two times as fast as that of the models having horizontal excitation only. In the case of Model 2, which was without reinforcement, the pipe rose up to the ground surface during excitation, while in the case of Model 3, the pipe did not rise conspicuously. The final amount of uplifting of this reinforced model was small, thus proving the effectiveness of reinforcement.

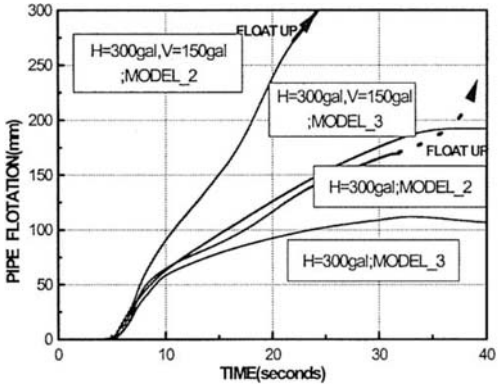

Fig.3 Time histories of floatation of pipes (MODEL_2&3)

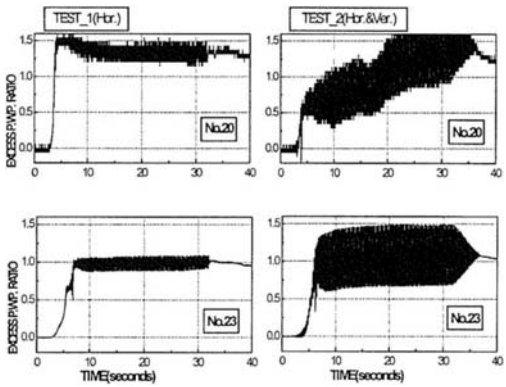

Fig.4 Time histories of excess pore water pressure (MODEL_1)

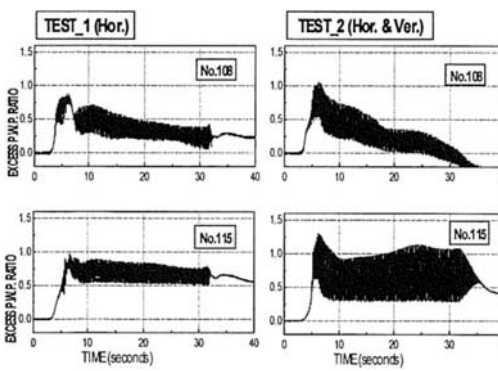

Fig.5 Time histories of excess pore water pressure (MODEL 3)

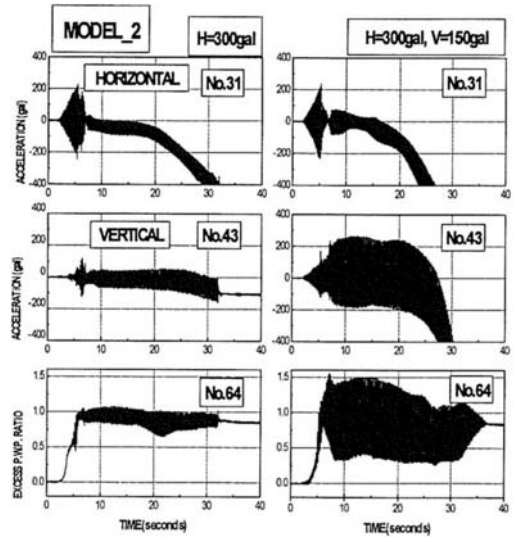

Fig.6a Time histories of acceleration of pipe (MODEL_2)

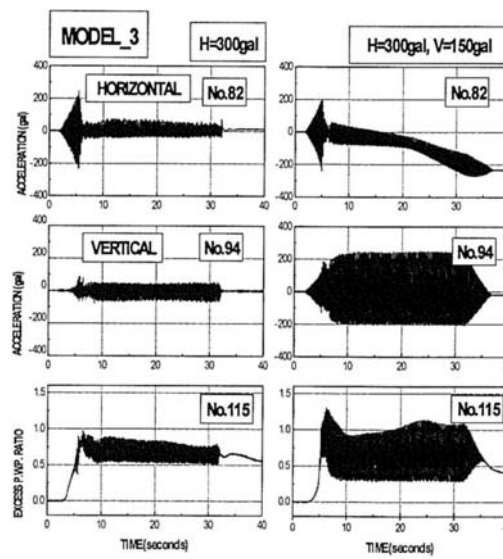

Fig.6b Time histories of acceleration of pipe (MODEL_3)

Figure 4 shows the response of pore water pressure of the ground. In the case of Model 1, there was a delay in the generation of excess pore water pressure at a position deeper in the ground (No. 23) than that near the ground surface (No. 20). The result shows that the liquefied area propagated from the ground surface into the interior. When vertical motions were input, the amplitude of the

response waveforms of the pore water pressure became great, which is attributed to the occurrence of excess pore water pressure generated through the influence of vertical inertia force of the ground. Note that the position of the pore pressure transducer is close to the ground surface, and the depth and effective stress may be affected by shaking. Thus the ratio calculated may be grater than 1.

Figure 5 shows the response of the pore water pressure around the pipe of a reinforced model (Model 3). Although the pipe behavior was basically the same as in the case of the model without reinforcement, the pore water pressure in the ground near the crushed stones (No. 108 and 115) did not increase as much, with which the excess pore water pressure ratio was 1.0 or lower. In the case when vertical motions were input, the excess pore water pressure ratio was equal to or less than 1.0. The response amplitude was greater than the model to which only horizontal motions were input.

Figure 6 shows the acceleration response of the pipes. As shown by the waveforms of the pore water pressure of the surrounding ground, it is common to all models that the acceleration of the pipes decreased sharply immediately after the ground has liquefied. When vertical motions were input, the pipes were subject to a large vertical acceleration greater than the input acceleration, even when the ground had liquefied and the horizontal acceleration of the pipes had decreased. Thus, when studying the uplifting of pipes, the influence of vertical motions must be taken into consideration.

3.2 *Effect of Countermeasures against uplifting of Pipes*

Figure 7 shows the amount of pipe uplifting in the models to which countermeasures were taken using crushed stones. Excitation was applied to the vibration table in the vertical direction in addition to the horizontal direction. In the case of Model 5, the pipe rose by 170 mm during excitation. It continued to rise slowly after the end of excitation, and reached the ground surface completely 30 minutes later. In the case of Model 6, the pipe rose by around 80 mm during excitation, but stopped rising at the instant excitation ceased, thus proving that the crushed stones helped to prevent the pipe from rising. The speed of pipe rising during excitation was half or less than that of Model 2, which was without any reinforcement. The results demonstrated the effectiveness of crush stones.

Figure 8 shows the location of the pipe and configuration of the crushed stones after the test. In the case of Model 6, the pipe itself did not move much, although the entire earth rose by around 43

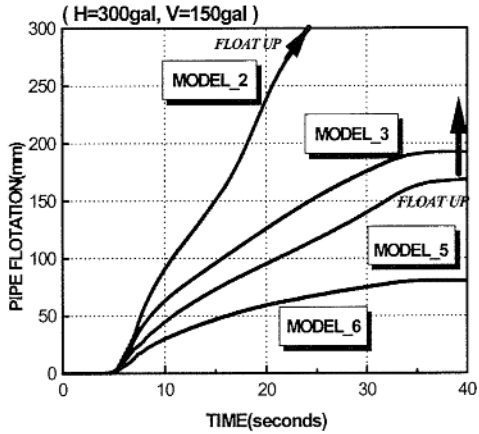

Fig.7 Time histories of

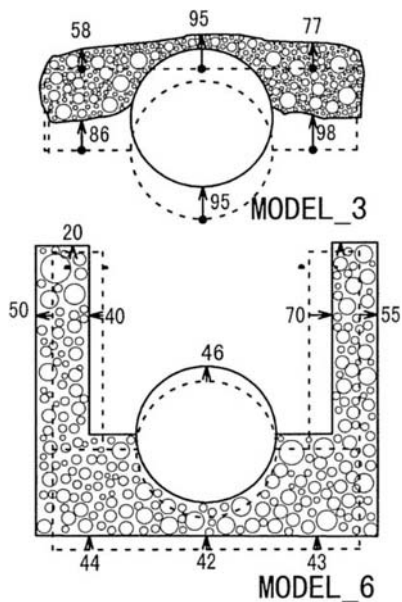

Fig.8 Deformation of pipe and surroundings (MODEL_3&6)

mm from the layer of crushed stones under the pipe. There was no major change in the shape of the vertical drains on both sides of the pipe, although the distance widened. Thus, the drains were proven to have prevented the flow of the sand ground above the pipe.

Figure 9 shows the response of excess pore water pressure of Model 5. Since vertical motions were input, the response amplitude was greater than that of horizontal acceleration alone. According to the response of underground pore water pressure (No. 39), the surrounding ground liquefied seven minutes after the start of excitation, and high pore water pressure was maintained in the ground during excitation. Although the water pressure inside the crushed stones (No. 38) during the initial phase of excitation showed the same behavior as in the surrounding ground (No. 39), the amount of increase of the pore water pressure was smaller than that of No. 39. The pore water pressure decreased gradually after reaching the maximum. In addition, the water pressure acting on the outer surface of the pipes (No. 28 and 30) decreased immediately after the ground liquefied. This was due to the fact that the depth of pipes became shallow after the pipe moved upward.

Figure 10 shows the response of excess pore water pressure in Model 6. The increasing acceleration in the initial phase of excitation showed the same behavior as in Model 5, and the pore water pressure in the surrounding ground (No. 83) decreased sharply right after ground liquefaction. The amount of increase of pore water pressure inside the layers of crushed stone drains (No. 79) was low, being half or less than that of No. 84. The results show that the vertical drains made of crushed stones were effective in mitigating pipe uplifting.

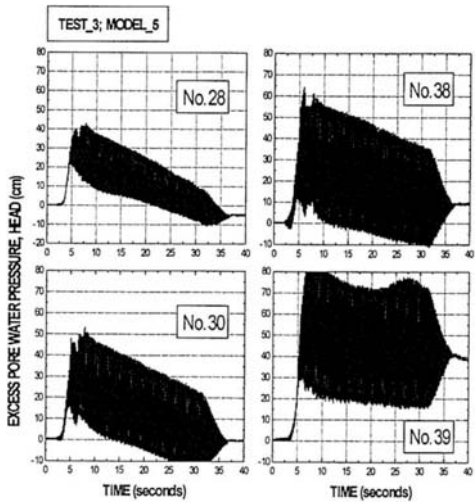

Fig.9 Time histories of excess pore water pressure (MODEL_5)

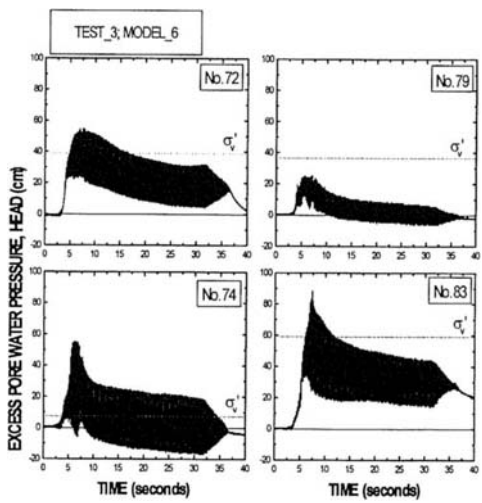

Fig.10 Time histories of excess pore water pressure (MODEL_6)

4 CONCLUSIONS

A series of model vibration tests were conducted to identify the influence of vertical input vibrations on the rising of buried pipes. The following points were clarified with respect to the effects of vertical accleration:

- The amplitude of the response of excess pore water pressure increased in the presence of vertical acceleration
- The response in the vertical direction was not reduced even after the response of the horizontal acceleration of pipes has decreased as a result of ground liquefaction.
- When vertical motions were applied along with horizontal motions, the speed of pipe rising was more than twice that of the pipes subjected to only horizontal motions.
- The models in which geogrid was applied on the upper part of the pipes to reinforce (constrain) the backfill materials around the pipes greatly prevented the pipes from uplifting.
- Installing vertical drain channels around a pipe using crushed stones greatly helped to prevent the pipes from uplifting.
- The influence of vertical motions must be taken into consideration when evaluating pipe uplifting.

REFERENCES

Koseki, J., Matsuo, O. and Koga, Y. (1997). Uplift Behavior of Underground Structures Caused by Liquefaction of Surrounding Soil during Earthquake. *Soils & Foundation,* Vol. 37, No. 1, 97-108

Sekiguchi, K. and Oishi, H. (1987). Experimental Study on the Effectiveness of Stabilizing Techniques of Underground Pipelines against Liquefaction. *Proc. of JSCE*, Vol. 382/3-7, 175-181. (in Japanese)
Katada, T. and Hakuno, M. (1981). Experimental Analysis on Dynamic Behavior of Underground Structures in the Liquefaction Process, *Proc. of JSCE*, Vol. 306, 1-10. (in Japanese)
Ishihara, K. (1996). *Soil Behavior in Earthquake Geotechnics*, Oxford Science Publications.

Earthquake Geotechnical Engineering, Sêco e Pinto (ed.) © 1999 Balkema, Rotterdam, ISBN 90 5809 116 3

Simulation analysis on countermeasure testing for underground pipeline

Y. Mohri – *National Research Institute of Agricultural Engineering, Japan*

A. Yuasa – *Advanced Analytical Technology Section, Analysis Consulting Service Incorporated, Japan*

T. Kawabata – *Pipe Engineering Section, Kubota Corporation, Japan*

H. I. Ling – *Department of Civil Engineering, Columbia University, USA*

ABSTRACT: Underground pipelines, such as water supply systems, suffer large damage during earthquakes by surfacing or meandering because of ground liquefaction. Several countermeasures against liquefaction have been proposed for earth structures, but these methods are not oriented towards underground pipelines. The simulation analysis of the shaking table test as presented herein was conducted with the aim of confirming the validity of a proposed countermeasure method. The effective stress analysis was conducted using FLIP. The analysis by FLIP simulated well the behavior of the underground pipe during an earthquake. The results of analysis offered insights into the behavior of pipeline with the proposed countermeasure during liquefaction. The countermeasure with the crushed gravel as substitute for soil at the vicinity of the pipeline proved effective in reducing damages during liquefaction.

1 INTRODUCTION

Water supply systems underwent significant damages during earthquakes because of ground liquefaction (e.g., Koseki et al., 1990). Surfacing and meandering are typical types of damages observed for pipelines. The mechanism of pipeline floating is currently interpreted in terms of the force balance between buoyancy and gravity. But in the current practice, the countermeasure method against liquefaction is not considered towards these underground structures.

The authors have initiated a series of studies to look into the liquefaction countermeasure method for pipeline flotation (Mohri et al., 1999). The simulation analysis of the shaking table test was conducted with the purpose of confirming the validity of proposed countermeasure method. An effective stress analysis was conducted using FLIP (Iai et al.,1992). The results of analysis are reported herein.

Table 1. Details of simulation.

	Experiment condition	Content of analysis
Case1	Soil alone	Setting up the dilatancy parameters
Case2	Soil with buried pipe	Confirming the flotation damage of the pipe
Case3	Countermeasure	Confirming the effectiveness of the countermeasure

2 DETAILS OF SIMULATION

The details of numerical simulation are shown in Table 1. Three Cases, were conducted:

Case 1 was conducted with the purpose of calibrating the dilatancy parameters from the experimental results. The dilatancy parameters used in the analysis may be identified directly from the liquefaction resistance of the laboratory test. However, it is difficult to conduct laboratory undrained cyclic triaxial test at very low confining pressure that resembles the stress states in a shaking table. The dilatancy parameters were selected by matching the numerical results with the excess pore water pressure measured in the actual test.

Case 2 aimed to duplicate numerically the flotation damage of a pipe.

Case 3 was conducted to confirm the effectiveness of the proposed countermeasure.

3 OUTLINE OF EXPERIMENT

A series of shaking table model tests were performed to study the uplift mechanism of pipeline (Mohri et al., 1999). A rigid soil box 480 cm long, 150 cm high and 100 cm deep was used. The soil layer was prepared from Kasumigaura sand with the following index properties: mean diameter D_{50}= 0.2998mm, uniformity coefficient Uc= 2.49, relative density Dr≒ 60%. The model pipe was installed in

the soil layer. It was manufactured from the polyvinyl chloride. The outside diameter, inside diameter and equivalent density of the pipe were 420 mm, 400 mm, and 2.689 kg/m^3, respectively. In the countermeasure, Case 3, a crushed gravel was used as substitute for the soil around the pipe (Figure 4). The soil box was shaken for a duration of 30 seconds by the sinusoidal wave of frequency 5 Hz as shown in Figure 1. This is the record from experiment, Case 1, and it is the input wave used in all analyses.

4 MODELS USED IN ANALYSIS

4.1 *Soil Model*

The effective stress soil model used in this study is composed of two parts; a stress-strain relation for shear mechanism and a mechanism for simulating the generation of excess pore water pressure. The shear mechanism adopted here consists of a multiple shear mechanism composed of virtual simple shear mechanism in arbitrary orientations; each virtual simple shear mechanism is assumed to follow the hyperbolic stress-strain relation with hysteresis characteristics (Towhata et al., 1985). The excess pore water pressure is simulated as a function of cumulative shear work (Iai et al., 1992). Effect of positive dilatancy is also included for taking into account the cyclic mobility behavior through the concept of liquefaction front defined in the effective stress space. The model can simulate the rapid or gradual increase in cyclic strain amplitude of the order of several percent under undrained cyclic loading. Outline of stress-strain model and excess pore water pressure model are shown Figures 2(a and b). It has to be emphasized that the program used in the analysis is based on the undrained condition.

4.2 *Pipe Model*

The pipe was modeled using a beam element with linear elastic properties.

5 ANALYTICAL CONDITIONS

5.1 *Value of Material Parameters*

The values of material parameters used in the analysis are shown in Table 2. Though typical values were adopted from the measurements obtained from the experiment or the laboratory tests, the initial shear modulus and the limiting virtual damping factor of the liquefaction soil was substituted using the test data of Toyoura standard sand (Iwasaki et al., 1978). The initial shear modulus of the crushed gravel was selected to be 10 time that of the liquefied soil.

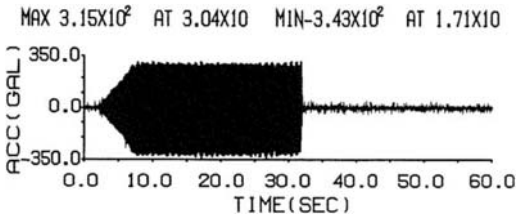

Figure 1. Input acceleration wave (Δt = 0.002 second).

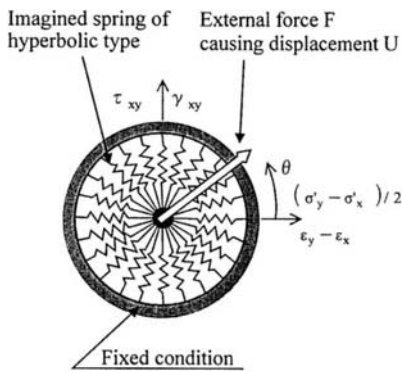

Figure 2a. Stress–strain model (Towhata et al.,1985).

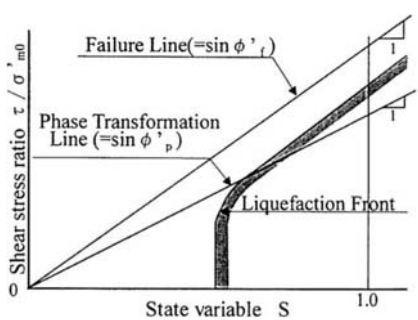

Figure 2b. Excess pore water pressure model (Iai et al.,1992).

Table 2. Value of Material Parameters

Parameters	γ * (tf/m³)	n*	h_{max}*	ϕ'_f * (deg)	C * (tf/m²)	G_0 * (tf/m²)	K_0 * (tf/m²)	ν *	K_f * (tf/m²)
Sand	1.96	0.440	0.25	34.7	0.0	9000	24,000	0.333	2.24×10^{-5}
Crushed gravel	2.04	0.386	0.28	40.0	0.0	90,000	240,000	0.333	2.24×10^{-5}

Parameters	G_p * (tf/m²)	E_p * (tf/m²)	ν_p *	γ_{eq} * (tf/m³)	A* (m²)	I_z * (m⁴)	Rayleigh damping
Pipe	111,111	300,000	0.35	2.689	0.01	8.3×10^{-8}	$\beta=7.5\times10^{-6}$

* γ : Density. n : Porosity. h_{max} : Maximum damping. ϕ'_f : Shear resistance angle. C : Cohesion. G_0 : Initial shear modulus in σ_{m0}'=6.66 tf/m². K_0 : Initial bulk modulus in σ_{m0}'=6.66 tf/m² . ν : Poisson ratio. K_f : Bulk modulus of pore water. G_p : shear modulus. E_p : Elastic modulus. ν_p : Poisson ratio. γ_{eq} : Density. A : Cross section. I_z : Geometrical moment of inertia.

Table 3. Parameters for dilatancy.

Layer	ϕ'_p *	S1 *	W1 *	P1 *	P2 *	C1 *
Sand	31.2°	0.005	12.0	1.995	0.50	1.0

* ϕ 'p: Phase transformation angle. S1 : Ultimate limit of dilatancy. W1 : Overall dilatancy. P1 : Initial phase of dilatancy. P2 : Final phase of dilatancy. C1 : Threshold limit.

5.2 *Dilatancy Parameters*

The dilatancy parameters used in the analysis are shown in Table 3, and the liquefaction resistance was calculated by the preliminary analysis using the parameters shown in Figure 3.

The analyses of Case 2 and Case 3 were proceeded using the input material parameters and dilatancy parameters decided from Case 1.

5.3 *Rayleigh Damping*

A parametric study was conducted, and the Rayleigh damping β was selected later in Section 6.2 based on accelerations records of Case1. The analysis of Case 2 and Case 3 used the Rayleigh damping properties chosen from Case 1.

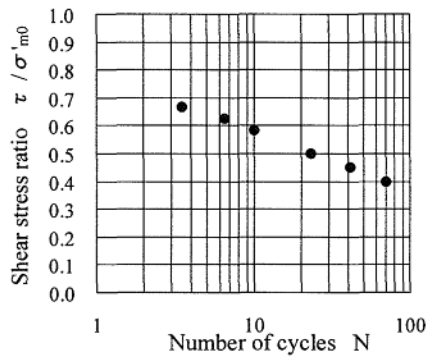

Figure 3. Liquefaction resistance by analysis.

5.4 *Finite Element Mesh and Boundary Conditions*

The finite element mesh used in the analysis is shown in Figure 4. As for the boundary conditions, the bottom is fixed, and the two sides were allowed to move vertically but were restrained horizontally.

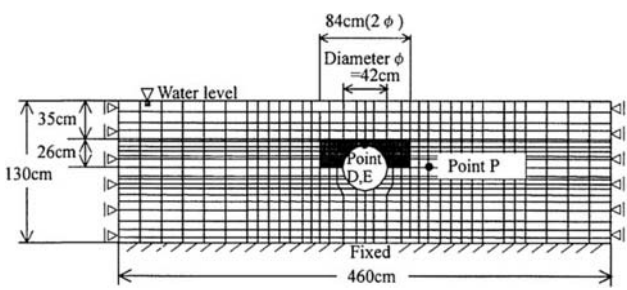

Figure 4. Finite element mesh and boundary condition.

6 ANALYTICAL RESULTS

6.1 *Self-Weight Analysis*

The self-weight analysis was conducted by applying a self weight to the soil. The self weight analytic results of Case 1 - Case 3 are shown in Figures 5(a to c) with the effective vertical stress σ_v. The initial stress condition is reproduced well in each case.

6.2 *Dynamic Analysis*

a) Case 1

The analysis of Case 1 decided the values of dilatancy parameters and Rayleigh damping β. The response values, which are influenced by this parameter, are the excess pore water pressure and the acceleration. The comparison of the analytical and experiment result is shown in Figures 6(a to c) and Figures 7(a to c). It is understood that the experimental results are well simulated by the parameters used in the analysis.

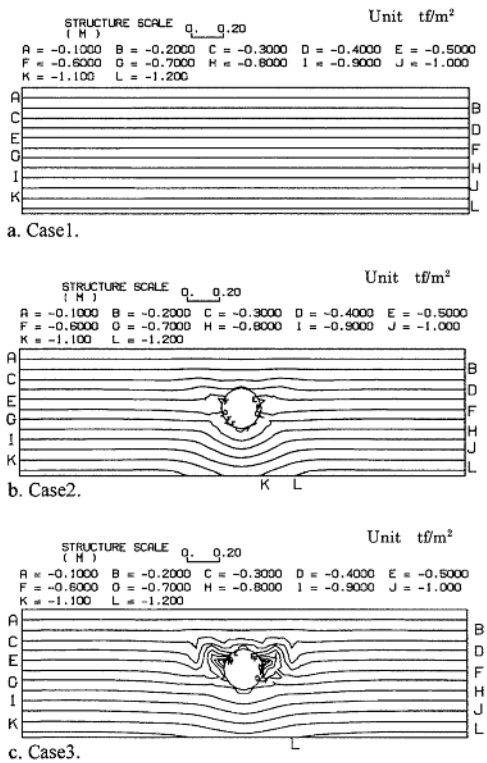

Figure 5. Effective vertical stress (σ_v) by self-weight analysis in Case 1 - Case 3.

b) Case 2

The deformation up to the end of calculation is shown in Figure 8. The deformation obtained from the analysis shows that the pipe flotation mode is reproduced. The comparison of the excess pore water pressure, the amount of pipe uplift, and the bending strain of the top of the pipe is shown in Figure 9.

The excess pore water pressure of analysis and measurements correspond well to each other until the time of undrained conditions (before t = 40 seconds). The amount of pipe flotation was 17 cm in the experiment and 13 cm in the analysis. The agreement was considered very satisfactory.

c) Case 3

The deformation to the end of calculation and the time response are shown in Figures 10 and 11, respectively. In the same manner as Case 2, The amount of pipe flotation was 10 cm in the experiment and 6 cm in the analysis. There are some differences in the experiment and the analysis for the time response. But it can be said that both results agreed well. In the analysis, the validity of the countermeasure method of the floating damage of the pipe can be confirmed from the above-described comparisons.

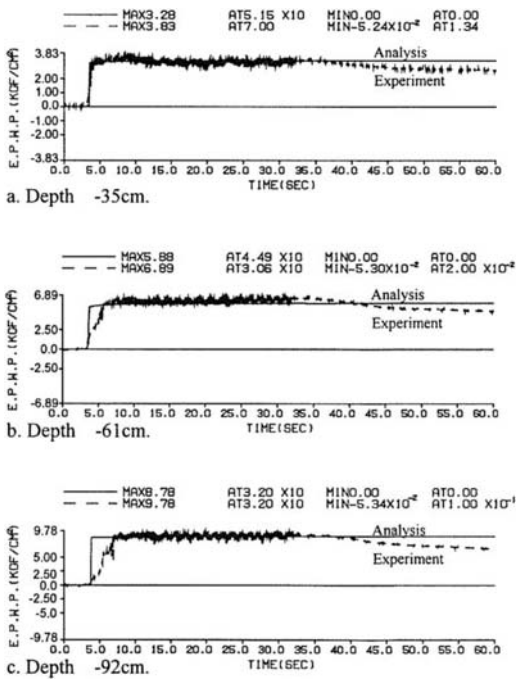

Figure 6. Excess pore water pressure response in Case 1.

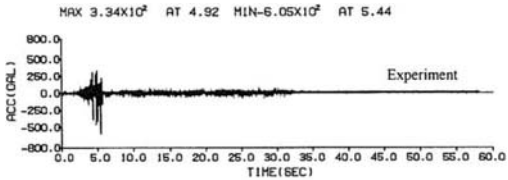

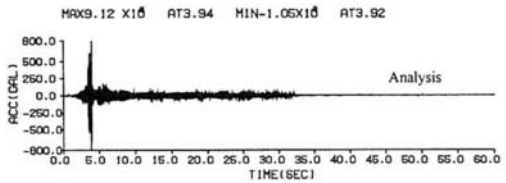

a. Depth -35cm.

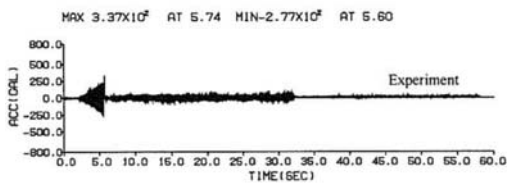

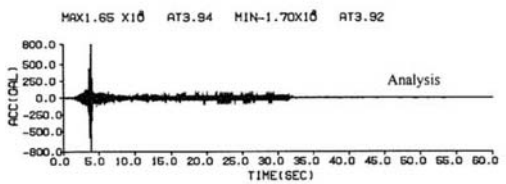

b. Depth -61cm.

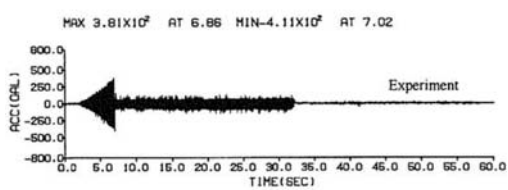

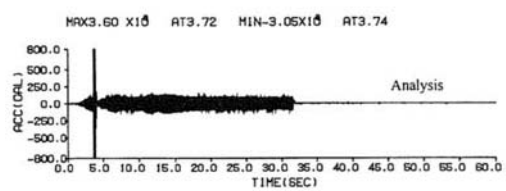

c. Depth -92cm.

Figure 7. Comparison of acceleration response in Case 1.

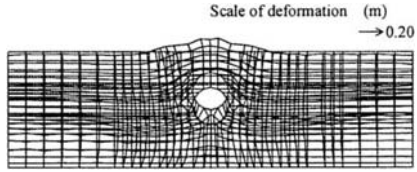

Figure 8. Deformation to end of the calculation in Case 2.

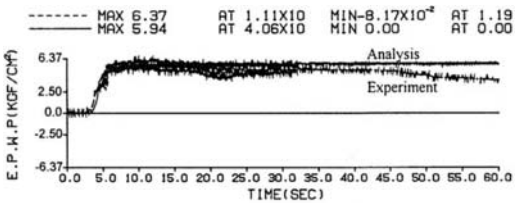

a. Excess pore water pressure at point P in Figure 4.

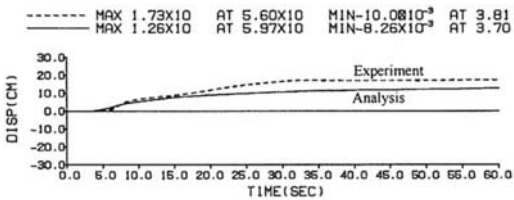

b. Amount of floating of the pipe at point D in Figure 4.

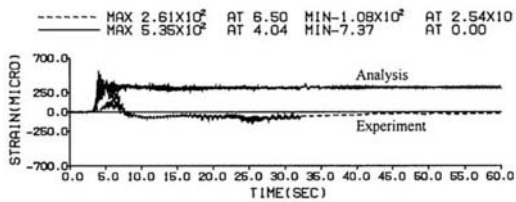

c. Bending strain of top of pipe at point E in Figure 4.

Figure 9. Comparison of time response in Case 2.

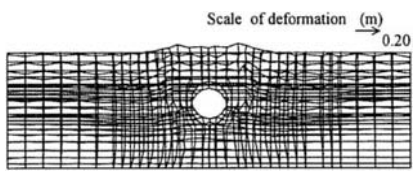

Figure 10. Deformation to end of the calculation in Case 3.

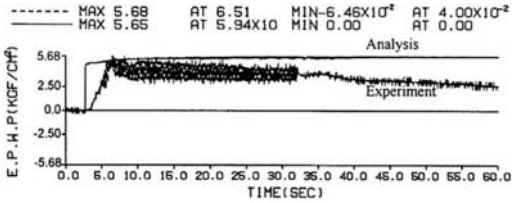

a. Excess pore water pressure at point P in Figure 4.

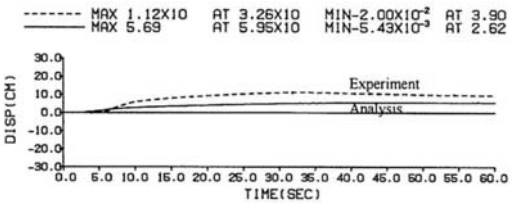

b. Amount of floating of the pipe at point D in Figure 4.

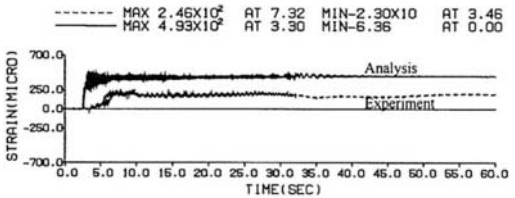

c. Bending strain of top of pipe at point E in Figure 4.

Figure 11. Comparison of time response in Case 3.

7 INFLUENCE OF COUNTERWEIGHT

The weights of the pipe and the countermeasure material, which resisted the floating of the pipe, were examined in the analysis. Each of the density was made equal to 70% and 130% of the experiment value, and the analysis was conducted under Case 2 or Case 3. The results are shown in Tables 4 (a and b).

It is understand that the amount of pipe flotation was affected by the magnitude of the weight from Tables 4. Thus the weight of the material has an influence, especially on the countermeasure.

8 CONCLUSIONS

An experiment on pipe flotation caused by liquefaction was simulated. The following conclusions were drawn from the results of analysis.

- FLIP simulated well the experiment results.
- It can be confirmed that the countermeasure with the crushed gravel as substitute for soil around the pipe is effective.
- The weight of the material attached to the pipe played a role as counterweight against flotation.

Table 4. Influence of weight in Case 2 - Case 3.

a. About pipe in Case 2.

Density (rate)	Amount of floating of pipe
1.882 tf/m³ (0.7 time)	15.7 cm
2.689 tf/m³ (1.0 times)	12.6 cm
3.496 tf/m³ (1.3 times)	11.1 cm

b. About crushed gravel in Case 3.

Density (rate)	Amount of floating of pipe
1.43 tf/m³ (0.7 time)	18.0 cm
2.04 tf/m³ (1.0 times)	5.7 cm
2.65 tf/m³ (1.3 times)	0.6 cm

REFERENCES

Iai, S. & Matsunaga, Y. & Kameoka, T. 1992. Analysis of undrained cyclic behavior of sand under anisotropic consolidation. *Soils and Foundations.* Vol.32, No.2, 16-20.

Iwasaki, T. & Tatsuoka, F. & Takagi, Y. 1978. Shear moduli of sands under cyclic torsional shear loading. *Soils and Foundations.* Vol.18, No.1, 39-56.

Koseki, J. & Koga, Y. 1990. Uplift of Semi-buried Structures in Liquefiable Sands during Earthquake. Proceedings of 8 th Japan Earthquake Engineering Symposium. Vol.1, 933-938.

Mohri, Y. & Kawabata, T. & Ling, H. I. 1999. Experimental study on the Effects of Vertical Shaking on the Behavior of Underground Pipelines. Second International Conference On Earthquake Geotechnical Engineering. June. Lisboa. Portugal.

Towhata, I. & Ishihara, K. 1985. Shear Work And Pore Water Pressure In Undrained Shear. *Soils and Foundations.* Vol.25, No.3, 73-84.

Earthquake Geotechnical Engineering, Sêco e Pinto (ed.) © 1999 Balkema, Rotterdam, ISBN 90 5809 116 3

Design spectra for the seismic deformation method defined on ground surface

Sumio Sawada
Disaster Prevention Research Institute, Kyoto University, Uji, Japan

Kenzo Toki
Graduate School of Civil Engineering, Kyoto University, Japan

Siro Takada
Department of Civil Engineering, Kobe University, Japan

ABSTRACT: The design spectra for Seismic Deformation Method (SDM) of underground structures have been given by the velocity response spectra defined on the seismic base layer (Vs > 300m/sec). In this paper, a new method is proposed to define the design spectra for SDM in terms of the acceleration response spectra defined on the ground surface. The proposed method makes possible to include the seismic and ground conditions in the design spectra of underground structures. In order to compare the proposed method with the conventional method, a conversion procedure of the spectrum defined on the ground surface into that for SDM is proposed. The procedure is applied to the seismic design spectrum of Earthquake Resistant Design of Bridges of Japan and the average response spectra which have been determined from 394 components of the strong motion records. The converted spectra are compared with the design spectra defined in various seismic design codes for underground structures.

1 INTRODUCTION

Response spectrum is widely used in earthquake resistant design of the most types of structures such as bridges, buildings, and so on. In the case of "Earthquake Resistant Design of Bridges (ERDB)" code (Japan Road Association 1990), the design response spectra are defined as shown in Figure 1 for fixed damping factor of 0.05, which is defined on ground surface. The ground condition is classified into 3 groups by soil types and the design spectra are defined for each ground type. Type I stands for the outcropped bedrock with 0.1 to 0.2 seconds of natural period of surface layer, type II is hard soil deposit with 0.2 to 0.6 seconds of natural period of surface layer, and type III is soft alluvium for which the natural period of surface layer is over 0.6 seconds.

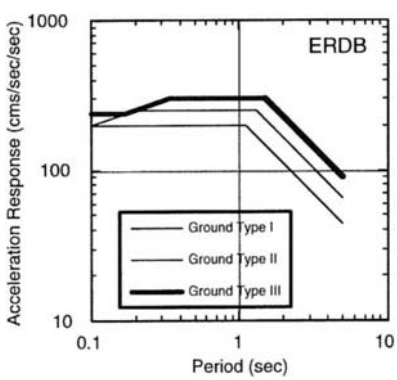

Figure 1 Design acceleration response spectrum defined in "Earthquake Resistant Design of Bridges" of Japan.

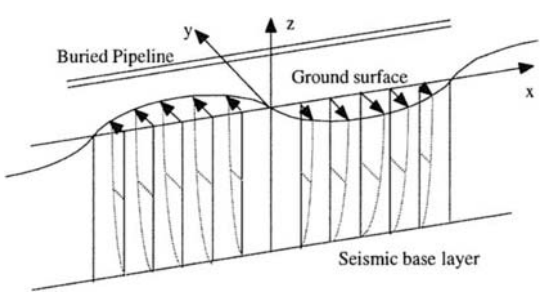

Figure 2 Schematic diagram of distribution of maximum displacement of subsurface ground.

On the other hand, Seismic Deformation Method (SDM) is applied to seismic design of underground structures, such as pipeline and submerged tunnels. This is a design method that the displacement of ground exerts seismic deformation on the structure. In Japan, "Technical Standard for Petroleum Pipelines (PPL)"(Japan Road Association 1974) is the first seismic design standard for underground structure using SDM. The design code for multi-service tunnels (MST, Japan Road Association 1986) is widely used for many types of underground structure. The design code for underground parking lot (UPL, Japan Road Association 1992) is the newest code for underground structure in Japan. In these codes for underground structure, vertical distribution of horizontal ground displacement in surface layer of which shear wave velocity is less than 300 m/sec is modeled by a quarter of cosine wave shape, as shown in Figure 2. The distribution of maximum displacement of the ground is given by Eq. 1.

$$U(z) = \frac{2}{\pi^2} S_V T_S \cos\frac{\pi z}{2H} \qquad (1)$$

where $U(z)$: horizontal maximum displacement amplitude at depth z, z: depth from the surface of the ground, T_s: natural period of surface layer, H: thickness of surface layer, S_v: response velocity spectrum.

In SDM, the seismic design spectrum S_V is defined on the interface between the surface ground and the seismic base layer(V_s > 300m/sec). Figure 3 shows the design spectra of PPL, MST and UPL. Note that the abscissa in Figure 3 is the natural period of "Surface Layer". The design spectra for SDM are not the response spectrum calculated from the records observed on the interface between the surface layer and the seismic base ground because the records on the interface are affected by the surface layer at the site. Those are also different from the response spectrum of the records observed on the outcropped seismic base layer because the spectrum must be affected by the surface layer if it exists on the seismic base layer. For these reasons, it is difficult to understand the meaning of the design spectrum for SDM. Thus, spectrum for SDM has the following drawbacks;

1) The physical meanings of the design spectrum is ambiguous so that there is no way to obtain the spectrum applicable to different site conditions and seismic environments.
2) Seismic design force is not specified for such structure that extends continuously above the ground surface from underground.
3) Seismic ground motion is not defined for structures laying in the ground deeper than the seismic base layer.

If the seismic design spectrum is defined on the ground surface and can be easily modified for the above-surface structures and underground structures, it is much easy to understand and to use the spectrum in seismic design. Fortunately we have large accumulation of strong motion records observed on the ground surface, which will provide enough dataset to specify the seismic ground motion on the ground surface. Moreover several methods have been proposed to modify the surface ground motion into the subsurface motion.

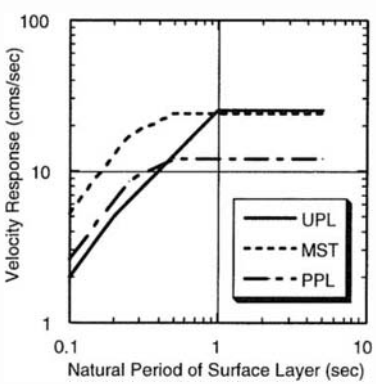

Figure 3 Design velocity response spectrum defined in the design codes using SDM.

In this paper, a new method is proposed to define the design spectra for SDM in terms of the acceleration response spectra on ground surface. In order to compare the proposed method with the conventional method, a conversion procedure of the spectrum defined on the ground surface into that for SDM is proposed. The procedure is applied to the seismic design spectrum of ERDB and the average response spectra which have been determined from 394 components of the strong motion records.

2. SIMPLE CONVERSION METHOD

As mentioned above, while the design response spectrum in ERDB is defined on the ground surface, the design response spectrum for SDM is defined on the interface between the surface ground and the seismic base layer(V_s > 300m/sec). We propose a conversion method from the spectrum on ground surface to the spectrum for SDM.

In SDM, amplitude of displacement wave at ground surface is given by Eq. 2, which is given by letting z = 0 in Eq. 1.

$$u(\omega) = \frac{4}{\pi} \cdot \frac{1}{\omega} S_V(\omega) \qquad (2)$$

Although the design spectrum of SDM is explained as the velocity response spectrum on the seismic base layer, it is considered that it simply represents the relationship between the natural period of surface layer and the amplitude of velocity wave on ground surface which is obtained by differential calculus of the displacement wave. The amplitude of displacement wave is the key parameter to design underground structures. It needs to develop a method that can convert the response spectrum defined on ground surface to the amplitude spectrum of displacement on ground surface.

If a stationary sinusoidal displacement wave $u(\omega)$ with angular frequency ω is applied to the one degree of freedom system with natural angular frequency n, the ratio of acceleration response amplitude $S_A(\omega)$ to $u(\omega)$ is given by Eq. 3.

$$\frac{S_A(n)}{u(\omega)} = \omega^2 \frac{(\omega/n)^2}{\sqrt{\left\{1-(\omega/n)^2\right\}^2 + 4h^2(\omega/n)^2}} \quad (3)$$

The maximum response ratio is obtained by letting $\omega = n$ in Eq. 3, as follows;

$$u(\omega) = \frac{2h}{\omega^2} S_A(\omega) \quad (4)$$

Then the relationship between $S_A(\omega)$ and $S_V(\omega)$ is obtained from Eqs. 2 and 4 as follows;

$$S_V(\omega) = \frac{\pi}{4} \cdot \frac{2h}{\omega} S_A(\omega) \quad (5)$$

Figure 4 shows the comparison with the spectra of SDM and the converted spectrum from ERDB spectra. The value of PPL is about two times larger, those of MST and UPL are about 4 times larger than that of ERDB in the period range over 1.0 second. These difference s can be explained by following two reasons.

The difference between envelope value and average value of response spectra of many strong motion record is an explanation. As shown in Figure 5, while the spectrum of ERDB is defined as an average of spectra obtained from many accelerograms, the response values of a record corresponding to the natural period of surface layer often exceeds the value of the ERDB spectrum. There is no problem for above-ground surface structure except the case that the natural period of surface layer is equal to that of the structure. On the other hand, the underground structure must be designed for the response value corresponding to the natural period of the surface layer. It is concluded that this factor represents the ratio between the peak value of response spectrum corresponding to the natural period of surface layer against the average spectrum.

The non-stationary properties of seismic motion must be another reason. Eq. 4 is inferred under the assumption that the input seismic motion is sinusoidal and stationary. There may be many cases the assumption is not satisfied. Figure 6 shows the response factor of single degree of

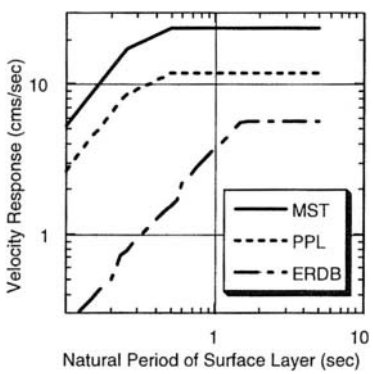

Figure 4 Comparison of the SDM spectra with the converted ERDB spectrum.

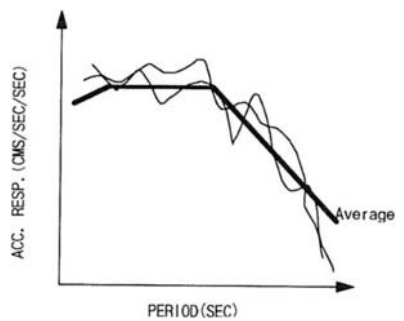

Figure 5 Schematic diagram of the relationship between the response spectra of strong motion record and averaged response spectrum.

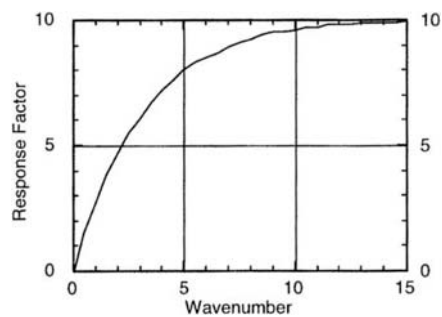

Figure 6 Relationship of input wavenumber and response factor of single degree of freedom system.

freedom system with damping factor of 0.05 excited by input sinusoidal motions with various wavenumber of which period is the same as the natural period of the system. Eq. 4 is exactly satisfied when the factor reaches 10.0. The factors are only 2.7 and 4.7 if the wavenumbers are 1.0 and 2.0, respectively. In the case that the response factor is 5.0, $u(\omega)$ in Eq. 4 must be multiplied by 2. This operation is needed for the non-stationary input motions.

Now we introduce the new parameters to Eq. 4 to consider the effects mentioned above.

$$u(\omega) = C_N \cdot C_A \cdot \frac{2h}{\omega^2} S_A(\omega) \qquad (6)$$

where, C_N is the parameter for indicating non-stationary properties of seismic motion, C_A the parameter for correcting the amplification factor of the site. If the product of C_N and C_A is about 4.0, the ERDB spectra agree with the MST and UPL spectra. If it is 2.0, the ERDB spectra correspond with the PPL spectrum.

The difference between MST and UPL spectra is discussed in the next section.

3. CONVERSION METHOD CONSIDERING DISPERSION OF PHASE VELOCITY

In the comparison mentioned above, only the seismic ground motion corresponding to the natural period of surface layer is considered. The observed ground motion records consist of not only the spectral component corresponding to the natural period of surface layer but also other frequency components which may cause damage on submerged structure. Thus the underground structure should be designed for the input ground motion which has wide frequency components. The seismic wave propagating horizontally consists mostly of surface wave which has dispersion characteristics. In such case, the apparent wave velocity of surface wave with longer period is greater than the shear wave velocity in surface layer.

Now, we propose a conversion method from acceleration response spectrum on ground surface to SDM spectrum considering dispersion of surface wave, as follows;

(i) Assume the structure of ground except for the surface layer.

(ii) Determine the natural angular frequency ω_s of the surface layer.

(iii) Displacement spectrum on ground surface $u(\omega)$ is calculated by Eq. 6 from the acceleration response spectrum of the ground type corresponding to ω_s.

(iv) Spectrum of phase velocity of Love wave $p(\omega)$ corresponding to the thickness of the surface layer corresponding ω_s and the profile of seismic base layer is determined.

(v) Strain spectrum $\varepsilon(\omega)$ is calculated by Eq. 7.

$$\varepsilon(\omega) = u(\omega)\frac{2\pi\omega}{p(\omega)} \qquad (7)$$

(vi) ε_{max}, maximum of $\varepsilon(\omega)$ in the frequency range less than ω_s, is obtained.

$$\varepsilon_{max} = \max\{\varepsilon(\omega); \omega \le \omega_s\} \qquad (8)$$

(vii) Value of $S_V(\omega_s)$ corresponding to ε_{max} is calculated by Eq. 9.

$$S_V(\omega_s) = \frac{\pi}{4} p(\omega_s)\varepsilon_{max} \qquad (9)$$

(viii) Repeat the procedure (ii) to (vii) for all frequency component.

The structure of base layer must be defined to apply the proposed method which considers the dispersion characteristics of phase velocity. We

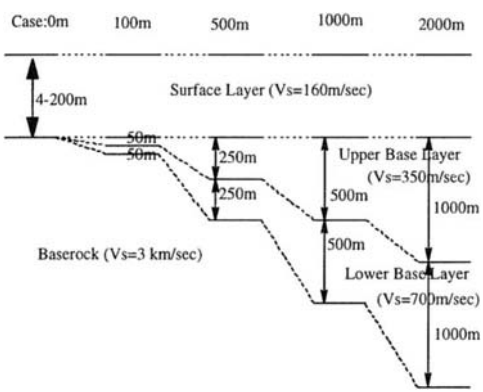

Figure 7 Cases analysed.

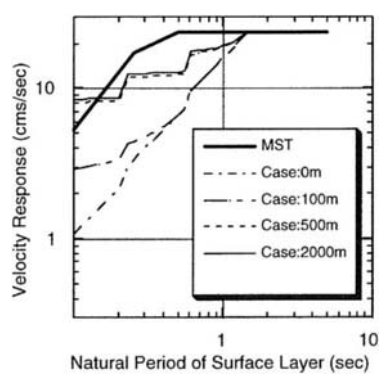

Figure 8 Comparison of MST spectrum with the converted ERDB spectrum considering dispersion of phase velocity.

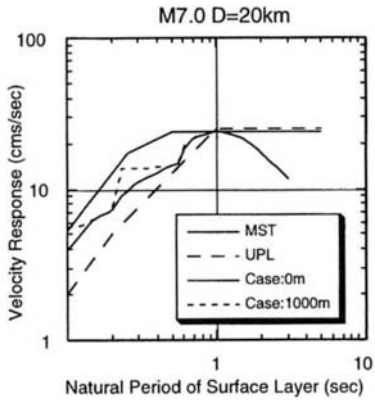

(a) The case of magnitude 7.0 and epicentral distance of 20 km.

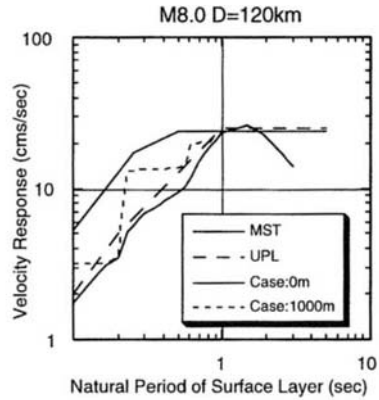

(b) The case of magnitude 8.0 and epicentral distance of 120 km.

Figure 9 Comparison of SDM spectra with the converted average acceleration spectra considering dispersion of phase velocity.

assumed 5 cases of base layer model, the thickness of seismic base layer is 0, 100, 500, 1000 and 2000 m, as shown in Figure 7. The shear wave velocity of the bedrock laying beneath the base layer is assumed to be 3 km/sec. The surface layer whose shear wave velocity is 160m/sec has various thickness of 4 m to 200 m corresponding to the natural period of surface layer of 0.1 sec to 5 sec. The parameters in Eq. 6 are set to C_N=2.0 and C_A=2.0.

Figure 8 is the comparison of MST spectrum with the converted ERDB spectra considering the dispersion of phase velocity. The spectra of the case of 1000 m and 2000 m thick of the base layer were so similar that only the case of 2000 m is plotted in Figure 8. The case of 0 m is the same with the result of the simple conversion method. The cases of 1000 m and 2000 m are well compared with the MST spectrum. The MST spectrum can be understood to be converted from the ERDB spectrum considering the effect of dispersion of surface wave corresponding to very deep deposit. On the other hand, the MST spectrum may overestimate the displacement of ground if it is applied to the ground of type I or II which has not thick base layers, like the cases of 0 m and 100 m.

In the case of the underground structure with vertical axis, such as shaft and small underground parking structure, it is not necessary to consider the effect of horizontal travel of seismic waves and therefore the simple conversion method is enough to estimate the vertical distribution of the maximum displacement beneath the ground surface. Thus, the UPL spectrum would provide a good estimate of the vertical strain distribution in subsurface soil layer for the seismic design of underground structure with vertical axis, and will underestimate the displacement of ground if it is applied to the underground structure with horizontal axis.

4. RELATIONSHIP BETWEEN AVERAGED ACCELERATION SPECTRA AND SDM SPECTRA

Many attenuation equations have been proposed for defining the average acceleration spectrum for given magnitude and epicentral distance. ERDB shows one of the attenuation equations, which is obtained by regression analysis on 394 components of strong motion records. The average acceleration spectra that is calculated by the ERDB attenuation equation for different magnitudes and epcentral distances are converted to SDM spectra by the method proposed in the previous section.

Figures 9(a)(b) show the converted spectra (case: 0 m and case: 1000 m) to compare with MST and UPL spectra. As discussed in previous chapter, the case of 0 m should be compared with the spectra for the underground structures with vertical axis, such as UPL. On the other hand the cases of 1000 m should be compared with the spectra for the underground structures with horizontal axis, such as MST. The converted spectra agree with the design spectra for SDM.

5. DESIGN METHOD USING ACCELERATION RESPONSE SPECTRUM ON GROUND SURFACE

We propose a new design method for underground structures based on the acceleration response spectrum defined on ground surface. The maximum displacement on ground surface, u_{max} , is obtained in terms of the acceleration spectrum on ground surface, $S_A(T)$, as follows;

$$u_{max} = C_N \cdot C_A \cdot 2h\left(\frac{T_S}{2\pi}\right)^2 S_A(T_S) \quad , \qquad (10)$$

where,

C_N: parameter for indicating non-stationary properties of seismic motion. In the case of stationary, the value must be 1.0.

C_A: parameter for correcting the amplification factor of the site.

h: damping factor of $S_A(T)$.

T_S: natural period of the surface layer.

If C_A=2.0 and C_N=2.0 are adopted, the ERDB spectra agree with the MST and UPL spectra.

The vertical distribution of displacement in the ground, $u(z)$, is given by

$$u(z) = u_{max} D_H(z) \quad , \qquad (11)$$

where, $D_H(z)$ is the function which represents the vertical distribution of displacement, z the depth from the ground surface. If the ground structure of the site is approximately represented by the simple model consisted of surface layer and seismic base layer, the function $D_H(z)$ can be written by

$$D_H(z) = \cos\frac{\pi z}{2H} \quad , \qquad (12)$$

where H is the thickness of the surface layer.

If the horizontal distribution of ground displacement is needed, the ground structure deeper than the seismic base layer must be considered. The spectrum of the maximum displacement of ground surface, $u_{max}(T)$, can be obtained by Eq. 10 for the longer period than T_S. The spectrum of ground strain at the given depth, $\varepsilon_z(T)$, is defined by

$$\varepsilon_Z(T) = u_{max}(T) \cdot D_H(z) \frac{2\pi}{T \cdot p(T)} \qquad (13)$$

where, $p(T)$ is the spectrum of phase velocity which is calculated from the ground structure. The maximum value of $\varepsilon_z(T)$ is considered as the horizontal ground strain for designing underground structure.

6. CONCLUSION

(1) A new design method for underground structures based on the acceleration response spectrum defined on ground surface is proposed.

(2) The design spectra which have been defined in the several design standards for underground structures agree with the spectra converted from the average response spectra by the proposed method.

(3) The spectra defined in the "Technical Standards of Petroleum Pipelines" or "Design Standards of Multi-service Tunnels" may overestimate the displacement of ground if it is applied to the underground structures with vertical axis such as a shaft within hard ground and shallow sedimentary layers.

ACKNOWLEDGMENTS

The computer program which determine the phase velocity of Love wave is written by Takao KAGAWA, Geo Research Institute, Osaka.

REFERENCES

Japan Road Association 1974. *Technical Standards of Petroleum Pipelines* (In Japanese).

Japan Road Association 1986. *Design Standards of Multi-service Tunnels* (In Japanese).

Japan Road Association 1990. *Earthquake Resistant Design of Bridges.*

Japan Road Association 1992. *Design and Execution Standards of Underground Parking Lot* (In Japanese).

5 Liquefaction

This Page Intentionally Left Blank

Earthquake Geotechnical Engineering, Sêco e Pinto (ed.) © 1999 Balkema, Rotterdam, ISBN 90 5809 116 3

Preventing tunnel flotation due to liquefaction

Birger Schmidt
Parsons Brinckerhoff Quade & Douglas, Inc., San Francisco, Calif., USA
Youssef M.A. Hashash
University of Illinois, Urbana-Champaign, Ill., USA

ABSTRACT: The mechanism of flotation of a buried structure due to liquefaction of the surrounding soil requires 1) the liquefaction of most or all of the ground surrounding the structure, 2) the structure is buoyant in the liquefied mass, 3) no foundations or hold-down installation prevents flotation, 4) the liquefied soil mass is free to flow under the structure as the structure floats. Traditional means include prevention of liquefaction by soil improvement or other means, or holding the structure in its place by structural means. In this paper explores prevention of the flow of liquefied soil under the structure, using the isolation principle. Walls are built around the structure to prevent the flow under the structure and maintain the in situ total stress under the structure unchanged. Reconsolidation of the liquefied material under the structure can, however, result in post-earthquake settlements.

1 INTRODUCTION

Pipelines, tunnels, underground tanks and other underground structures can rise out of the ground when the soil around and below liquefies. Case histories have shown tanks and pipelines rising out of the ground due to liquefaction, to be destroyed. No tunnels have yet been seen rising out of the ground, but that may only be a matter of luck. A pair of Californian tunnels may have the potential to rise tunnels, unless remedial measures are implemented before the next major earthquake. These are the Posey and Webster Street Tunnels, highway tunnels connecting the City of Oakland with the Alameda Island).

Figure 1 Posey & Webster St. Tubes, California

2 THE ALAMEDA TUBES

The Alameda Tubes are two 12-m diameter immersed tunnels, both about 1300 m long, placed in 1927 and in 1963 across the Alameda estuary, which is about 12 m deep.

Construction of these tunnels required the dredging of 14 m deep trenches in the channel bottom, floating in the tubes, one by one, connecting them, and backfilling the trench by dumping dredged material to fill the trench and cover the tubes (Figure 2). At that time there was no appreciation of the mechanisms of liquefaction, and no attempt was made to densify the soil. Hence, the backfill around the Webster Street Tunnel consists of loose sand, and that around the Posey Tunnel consists of mixed dredged backfill, soft clays and loose sands.

Evidence from the 1989 Loma Prieta earthquake (M=7.1, 160 km distant) clearly showed that portions of the trench backfill had liquefied. The maximum credible earthquake for the Alameda Tubes is a M_w=7.25 event at the Hayward Fault, only 6 km distant. Such an event most probably would result in flotation and virtual destruction of the Tubes.

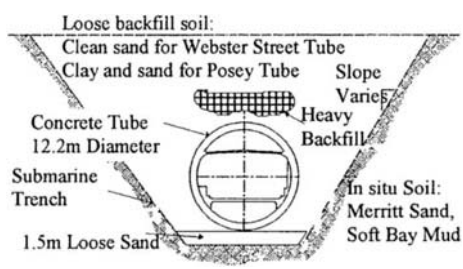

Figure 2 Typical Tube Section in Submarine Trench

The retrofit of these tunnels to prevent flotation posed a difficult problem, because most logical remedies appeared to be infeasible. It was therefore necessary to examine the fundamental principles of flotation due to liquefaction to find a feasible retrofit.

3 MECHANISM OF FLOTATION

In a liquefied soil mass, the maximum liquefied pressure is equal to the total overburden pressure. Flotation of a structure buoyant in the liquefied soil mass occurs when a flotation mechanism is created. This flotation mechanism requires freedom of the liquefied material to flow around and below (see Figure 3). For flotation to occur the following must happen:

1. Partial or full liquefaction of the surrounding soil
2. The structure must be lighter than the liquefied soil mass it displaces; it is buoyant in the liquefied soil mass
3. Nothing holds the structure from floating, piles, anchors, hold-downs
4. The liquefied material must have mobility and be able to flow as the structure rises.

The components of the flotation mechanism are each examined to determine a feasible way to prevent flotation. All four components must be active or present to cause flotation. The elimination of just one component will eliminate flotation.

4 PREVENTION OF LIQUEFACTION

If the problem is recognized at the time of the design of the structure, there are a number of means to choose from. The most effective ones would appear to prevent liquefaction altogether.

Conventional means to prevent liquefaction includes removal and replacement of offending material, improvement by densification or grouting, deep foundations, anchors or hold-downs. Another ground improvement method could consist of: permanent dewatering, most effective if the area is enclosed so that the pumping or drainage requirement is not excessive.

Ground improvement can be achieved by any one of a number of methods that may be applied before the structure is placed into the ground. Examples include:

1. Replacement of the offending material with non-liquefiable material
2. Densification of the material by vibroflotation, deep densification, compaction grouting or similar means
3. Changing the properties of the ground by injection grouting, jet grout column installation, or similar.

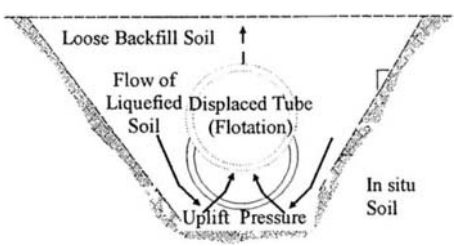

Figure 3 Backfill liquefaction and tube flotation

For the Alameda Tubes, soil material replacement was out of the question, because the tubes would be buoyant even in sea water, making the removal of the soil material around the tubes, even along short lengths, could result in flotation. Densification of the soil mass would be feasible, but reaching under the tubes to densify the soil beneath the tubes proved virtually impossible.

Grouting of the soil mass under the tubes would be technically feasible, through numerous grout holes drilled through the tube bottom from the lower air plenum. During this operation the tunnel could not be operated as a traffic tunnel, and each drill hole would have to be secured against a catastrophic inflow of soil and water at a pressure of some 20 m of water head. This risk was considered unacceptable.

Grouting beneath the tube could also be accomplished using directional drilling from floating equipment in the estuary. Low-angle drilling would be required, at great precision, and there would be a danger of damaging the exterior water proofing of the tubes. Besides, the Port of Oakland uses the estuary daily and would not look kindly at a continuous disruption of the navigable waters. This solution was therefore not considered attractive.

5 MECHANICAL MEANS TO PREVENT FLOTATION

If a structure is made denser than the potential liquefied soil mass it will not float. Foundation failure or excessive settlements, however, can result, unless the structure has deep foundations. Gravity dry-docks are designed to resist the buoyant force of water. For storage vessels and most tunnels or pipelines, this solution is usually not economical. For most existing structures, such as for example the Alameda Tubes, this solution is physically impossible.

For a potentially buoyant structure to be held in place in a liquefied soil mass, two components are usually needed: Anchors to prevent flotation and deep foundations to prevent sinking during reconsolidation of the liquefied soil mass. These remedies are reasonably easy to install at the time of initial construction, though sometimes expensive. In fact, dry-docks and some depressed highway structures have been built to incorporate permanent tie-down anchors. For the Alameda Tubes the buoyancy forces in a liquefied soil mass would be so great as to make this solution impractical.

These methods basically attack the first three elements of the flotation mechanism. A new concept to prevent flotation is presented in the following.

6 PREVENTING FLOTATION USING THE ISOLATION PRINCIPLE

This new concept attacks the fourth component of the flotation mechanism, the mobility of liquefied material. If not permitted to flow under the structure (the isolation principle) the maximum liquefied pressure under the structure is precisely equal to the weight of the structure and is thus in equilibrium, and the structure does not float. Barriers are created alongside the structure to prevent mobility of the liquefied material under the structure.

Many kinds of installations can be employed for isolation, provided that they can withstand the differential liquid pressures on the sides. The barrier also must not liquefy and permit flow. Suitable installations may include densified, non-liquefiable soil, grouted soil mass, diaphragm walls, sheet pile walls of sufficient strength and rigidity, and others.

The final design selected consists for the Webster Street Tube of soil densification using displacement gravel columns on both sides of the Tube (Figure 4). The displacement would cause adequate densification of the loose sand backfill to prevent liquefaction. The design of the stone columns was based on the method proposed by Onoue (1988). The gravel drains would also provide drainage of excess porewater pressures, quickly enough to prevent liquefaction. The backfill material around the Posey Tube consists of a mixture of sands and clays, not thought amenable to densification and drainage. Here the (more expensive) final design consists of two rows of jet-grout columns forming a wall on both sides of the Tube (Figure 5).

6.1 Applicability of isolation principle

The new concept is partly supported by centrifuge modelling tests and some field evidence from large earthquakes. This information is mostly from Japanese case histories and modeling (Boulanger et. al. 1997). In fact, based on the case histories, while flotation can be prevented, settlements may occur during or after the earthquake event. Eventual dissipation of excess porewater pressures and reconsolidation of the underlying material can result in some settlement of the structure as the soil reconsolidates. However, if the net weight of the structure is small, then the reconsolidation pressure is also small, and the settlement would be due mainly to the rearrangement of sand grains after liquefaction.

The settlement would then appear to be a function of the following factors:

1. The reconsolidation pressure existing under the structure after the earthquake event
2. The thickness and density of the liquefiable mass under the structure
3. Any additional supporting elements helping the structure staying in place

The consequences of any such settlements would depend on the relative flexibility and continuity of the structure. For the Alameda Tubes we consider the following factors:

1. While the sand fill under the tubes is assumed to be loose, the thickness is only about one m
2. The vertical effective (reconsolidation) stresses beneath the tubes are very small, as the tubes are very light
3. Individual tube elements are about 60 m long and individually quite rigid and able to resist longitudinal bending
4. Installation piles were placed at each tube joint, adding some resistance to settlement
5. The installation of the isolation walls lend some vertical shear capacity along the sides of the tubes

Needless to say, an estimate of the resulting settlement and its distribution would be difficult to prepare, considering the unknowns in this analysis. Assuming a possible reduction in the one-m thickness of the soil beneath the tubes and some resistance to settlements from the factors discussed, we estimate a maximum settlement of the order of 50 mm, considered acceptable. Considering the uncertainties of the analyses, however, some repairable cracking damage cannot be excluded.

7 CONCLUSION

These two applications of the isolation principle to counteract the flotation mechanism will be installed in 1999. However, we hope to wait many years to witness the final field verification of the concept.

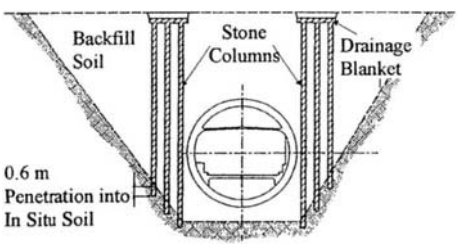

Figure 4 Stone columns, Webster Street Tube

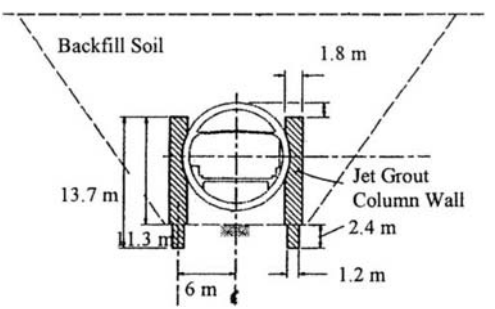

Figure 5 Jet Grouting for Posey Tube

8 ACKNOWLEDGEMENTS

The contents of this paper were prepared in cooperation with the State of California, Business, Transportation and Housing Agency, Department of Transportation. The contents of this paper reflect the views of the authors who are responsible for the facts and the accuracy of the data presented herein. The contents do not necessarily reflect the official views or policies of the State of California. This paper does not constitute a standard, specification, or regulation.

The authors wish to acknowledge the contributions of colleagues at Parsons Brinckerhoff, International Civil Engineering Consultants, Inc. (ICEC), SC Solutions, and Ben C. Gerwick, Inc

REFERENCES

Boulanger, R. W., Stewart, D. P., Idriss, I. M., Hashash, Y., and Schmidt, B. (1997). "Ground Improvement Issues for the Posey & Webster St. Tubes Seismic Retrofit Project: Lessons from Case Histories." *Report UCD/CGM-97/02*, Ctr. for Geot. Modeling, Dept. of Civil & Envir. Engrg., Univ. of Calif., Davis, 78 pp., April.

Onoue, A. (1988). "Diagrams considering well resistance for designing spacing ratio of gravel drains." *Soils and Foundations*, **28**(3), 160-168.

Earthquake Geotechnical Engineering, Sêco e Pinto (ed.) © 1999 Balkema, Rotterdam, ISBN 90 5809 116 3

Studies of the state parameter and liquefaction resistance of sands

Y.C.Chen & T.S.Liao
National Taiwan University of Science and Technology, Taipei, Taiwan

ABSTRACT: Steady state lines of remolded samples of Mailiao sands were obtained by performing undrained triaxial tests. The effects of stress path, fines content, and over-consolidation ratio (OCR) on the steady state line are studied. Liquefaction resistance was obtained by performing undrained cyclic triaxial tests. The relationship between state parameter and liquefaction resistance is investigated. Test results show that larger state parameter corresponds to lower liquefaction resistance. Linear relationship exists between state parameter and liquefaction resistance.

1 INTRODUCTION

The mechanical behavior of sand is mainly controlled by its density and confining stress. Other factors, such as fabric, grain properties, etc. also have minor effects. Relative density is commonly used to describe the state of sand. However, it is well known that relative density cannot fully describe the mechanical behavior of sand. Therefore a parameter, which can incorporate the density and stress state of soil, is needed to characterize the engineering behavior of sand. To establish a rational engineering approach to constructing structures on hydraulic sand fill, Been & Jefferies (1985) developed a state parameter concept to characterize the sand behavior. They found that significant engineering design parameters are dependent on the state parameter. Recently, quite a few hydraulic sand fill islands are being or will be constructed on the western coast of Taiwan to be used as industrial parks. Therefore, it would be beneficial to apply the state parameter concept in designing these islands.

Been & Jefferies (1985) propose to use the steady state line (SSL) on the e-log I' plane as the reference line. State parameter, Ψ, is defined as the difference between initial void ratio and the corresponding void ratio at the same stress level on the steady state line. State parameter combines the influence of density and stress so that it can reasonably characterize many important engineering behaviors of sand, as well as liquefaction resistance.

Initial liquefaction indicates a condition where, during the course of cyclic stress applications, the residual pore water pressure on completion of any full stress cycle becomes equal to the applied confining pressure. In this paper, liquefaction resistance is defined as the cyclic stress ratio required for soil to reach initial liquefaction at a certain number of cyclic loading.

Previous researches mostly concentrated on normally consolidated samples, very few studies were conducted on over-consolidated samples. Hydraulic-filled sand layers are usually in loose condition and vulnerable to liquefaction. Soil improvement is commonly applied to increase the relative density of soil so that the structures can be built safely. Therefore, the soil is usually in over-consolidated condition.

This paper will discuss the relationship between liquefaction resistance and state parameter under over-consolidated condition.

2 LITERATURE REVIEWS

Steady state of sand refers to the state that sand continuously deform at constant volume, constant effective stress, constant shear stress, and constant strain rate (Been & Jefferies, 1985, Been et al., 1991). Only until fabric is totally restructured, all influence of particle orientation is stable, and all crushing of particles is completed, a steady state can be achieved. Steady state line is the loci where soils reach steady state from various void ratios and stress states. The original structure of specimen only has minor effect on the stress-strain behavior during the

beginning stage of shearing. But 'flow' structure and its corresponding strength are independent of its initial structure. Major factors influencing steady state line of sand include fines content, particle shape, stress path, and magnitude of effective stresses. Some of the major previous research results are summarized in the following paragraphs.

Fines content affects the location and slope of steady state line on e-log I' plane. With increasing percentage of fines, steady state line moves leftward with changing slopes (Been & Jefferies, 1985, Dobry et al., 1985, Konard, 1990). It is also noted that well-rounded sand has falter slope of steady state line than sand of angular shape (Konard, 1990, Poulos et al., 1985). Some researches indicate that steady state line is independent of the stress path that soil specimens experienced during shearing (Been et al., 1991, Castro et al., 1992). However, there are other studies showing that different steady state lines can be obtained from different stress paths (Kuerbis et al., 1988, Vaid et al., 1990). It is generally agreed that either it is a stress-controlled or a strain-controlled test that steady state line is approximately the same (Castro et al., 1982). Rate of shearing also does not have any obvious influence on steady state line (Negussey et al., 1988).

Magnitude of effective stress affects the shape of steady state line (Been et al., 1991, Castro et al., 1992). With effective stress less than 5 kg/cm^2, steady state line is a straight line. Steady state line will curve downward when effective stress exceeds 10 kg/cm^2. The reason is that the sand particles crush at higher confining stress and the fines content increases. Anisotropic consolidation does not significantly influence the steady state line (Castro et al., 1992). When soil specimen reaches its steady state, initial fabric of sand is totally restructured. Thus, method of sample preparation does not have significant influence on steady state line (Been et al., 1991, Poulos, 1981, Poulos et al., 1985).

There are three major categories of saturated sand behaviors under cyclic undrained shearing, namely flow liquefaction, limited liquefaction and cyclic mobility (Vaid & Chern, 1985). These three types of liquefaction behaviors are closely related to the initial state of sand. If the initial state of sand is located on the right hand side of the steady state line (contraction side), flow liquefaction may occur. If the initial state of sand is located on the left hand side of the steady state line (dilation side), cyclic mobility may occur. If the initial state is very close to the steady state line, limited liquefaction may occur.

Chen & Tseng (1998) showed that the liquefaction resistance decreases with increasing state parameter in a more or less linear relationship. It is possible to estimate the in-situ liquefaction resistance by estimating the state parameter.

3 TEST PROGRAM

3.1 *Test Material and Equipment*

Soil samples were obtained from Mailiao industrial park on the southwestern coast of Taiwan. This industrial park is a hydraulic-filled reclamation site for the use of Sixth Cracking Project of Formosa Plastics Group. Because Taiwan is located on the western border of the Circum-Pacific Belt which has more than thousand times of earthquakes every year, reclaimed land especially needs to be assessed carefully and effective treatments are necessary to assure the safety of equipment and structures. Both dynamic compaction and vibro-replacement stone column methods were adopted to compact the loosely filled silty sands in Mailiao.

The soil particles of Mailiao sand are sub-angular and flat, which are the fragments of slate. Natural soil has fines contents between about 0 to 20%. The remolded samples used in this paper have fines content of 5, 10, and 15%. The physical properties of soil samples are shown in Table 1.

Triaxial tests were performed by using triaxial cell with enlarged lubricated ends to eliminate the effects of end restraints. Cyclic triaxial apparatus were used to perform undrained triaxial tests to investigate the liquefaction resistance of samples.

Table 1. The physical properties of soil samples

F.C. (%)	5	10	15
D_{60}	0.285	0.260	0.240
D_{50}	0.250	0.220	0.205
D_{30}	0.180	0.180	0.150
D_{10}	0.100	0.074	0.057
C_u	2.850	3.514	4.211
C_c	1.137	1.684	1.645
G_s	2.702	2.700	2.704
e_{max}	1.279	1.151	1.031
e_{min}	0.739	0.595	0.440

3.2 *Test Conditions*

Specimens of different relative densities were prepared either by dry tamping or moist tamping methods. The soil was poured into the mold in five equal layers to control the density and achieve uniformity. Specimens were circulated with CO_2 and de-aired water and subjected to a backpressure of 200 kPa to ensure good saturation.

For the steady state tests, specimens were consolidated at different effective confining pressures first, then subjected to either undrained compression or extension tests. This is to understand the effects of stress path on the steady state line. To investigate the effects of overconsolidation, specimens were con-

solidated to a higher effective confining pressure, then unloaded to a lower pressure to achieve the state of overconsolidation. Overconsolidation ratios (OCR) of 2 and 4 are chosen in this study. After specimens were consolidated at the desired OCR, they were subjected to undrained triaxial compression or extension tests to determine the steady state lines at different OCR.

For liquefaction tests, specimens were prepared and consolidated to have three kinds of relative density, 40, 55, and 70%. After consolidation, specimens were subjected to undrained cyclic triaxial tests until initial liquefaction achieved.

4 RESULTS AND DISCUSSIONS

4.1 *Results of Steady State Tests*

Both triaxial compression and extension tests were performed to investigate the effects of stress path on the steady state lines. Figure 1 shows the results of steady state lines obtained from triaxial compression and extension tests for Mailiao sand with 5% fines content. It is shown that the steady state line from extension tests is on the left side of the line from compression tests. This is the same behavior as obtained by Vaid et al. (1991) and Chen & Tseng (1998). The possible reason is as follows. The long axes of the particles of the samples are lying mostly on the horizontal direction due to the flat particle shape and the sample preparation methods. During undrained shearing, the anisotropic particle orientation could not be erased completely even at large strain condition.

Figure 2 shows the results of steady state shear strengths obtained from triaxial compression and extension tests for Mailiao sand with 5% fines content. It is shown that the steady state shear strength from compression tests is slightly larger than that from extension tests. The anisotropic particle orientation that has more particles lying on the horizontal direction at the steady state is more resistant to the vertical loading than the horizontal loading. This contributes to the higher steady state shear strength from compression tests.

Figure 3 shows the results of steady state lines of Mailiao sand with different fines content. It is shown that the steady state line will shift leftward and downward with increasing fines content. The slope of the steady state line will decrease with increasing fines content. It is the same behavior as been found by Dobry et al. (1985) and Chen & Chen (1996), but contradicts to Been & Jeffery (1985). Other factors will also affect the slope and location of the steady state line, such as gradation and particle size. Gradation and particle size will change when changing the fines content. It is very difficult to isolate the effects of fines content from other factors. So, when discuss the effects of fines content on the steady state line, the influences of other possible factors should also keep in mind.

Test results show that steady state shear strength will also decrease with increasing fines content.

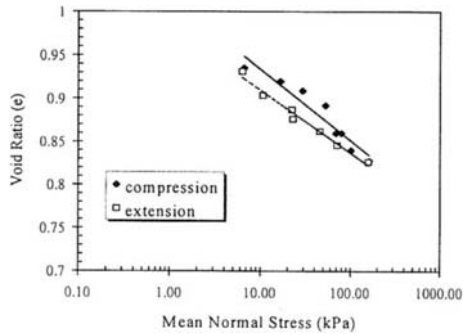

Figure 1. Steady state lines of Mailiao sand obtained from triaxial compression and extension tests.

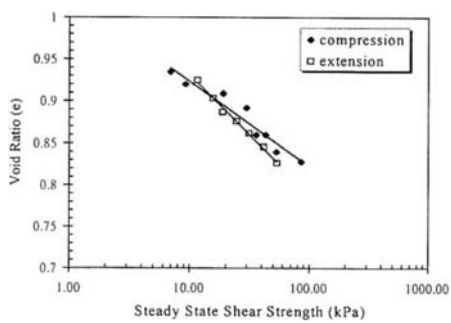

Figure 2. Effects of stress path on the steady state shear strength

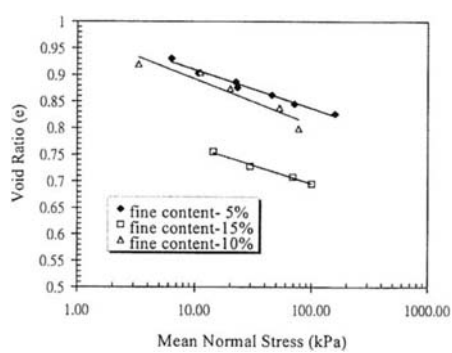

Figure 3. The steady state lines of Mailiao sand with different fines content

To investigate the effects of overconsolidation on the steady state line, samples were consolidated at higher confining stresses first, then unloaded to lower confining stresses. After consolidated at desired overconsolidation ratio, samples were subjected to either undrained triaxial compression or extension tests. Figure 4 shows the results of steady state line determined by triaxial extension tests for samples with 5% fines content. It is shown that overconsolidation ratio has no effects on the steady state line. Results of triaxial compression tests also show the same behavior. The steady state shear strength is also not affected by overconsolidation ratio.

The fabric induced by the overconsolidation would generally be erased completely by the process of steady state deformation. The steady state line as well as the steady state shear strength is, therefore, not affected by the overconsolidation ratio.

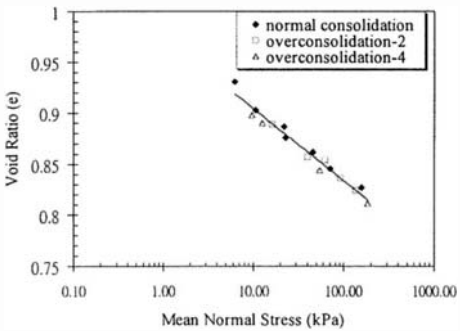

Figure 4. Effects of overconsolidation on the steady state line (triaxial extension tests, fines content=5%)

4.2 *Results of liquefaction resistance*

Figure 5 shows the results of liquefaction resistance for normally consolidated samples with confining pressure 98 kPa and 5% fines content. It is found that liquefaction resistance increases with increasing relative density more or less linearly for the range of 40 to 70%. The results of liquefaction resistance for samples with OCR= 2 and 4 have the same tendency as normally consolidated samples.

To study the effects of overconsolidation on the liquefaction resistance, samples were consolidated at OCR=2 and 4 but had the same relative densities as normally consolidated samples. Figure 6 shows the results of liquefaction resistance for samples with 40% relative density, 5% fines content and different OCR. It is shown that samples with higher OCR would have higher liquefaction resistance. Since relative density is same for all samples, other factors are responsible for the higher liquefaction resistance with higher OCR. Overconsolidation would increase the degree of cementation between particle contacts, would change the state of fabric (increasing average particle contact number), and would, therefore, increase the liquefaction resistance.

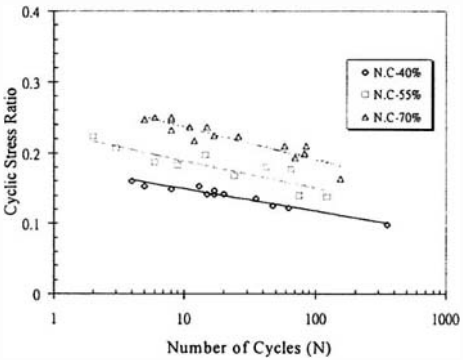

Figure 5. Liquefaction resistance for normally consolidated samples with confining pressure 98 kPa and 5% fines content.

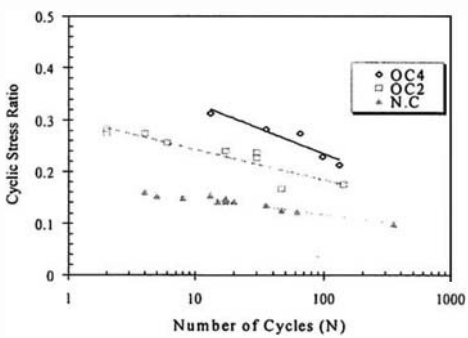

Figure 6. Results of liquefaction resistance for samples with 40% relative density and different OCR.

Figure 7 shows the effects of overconsolidation ratio on the liquefaction resistance of samples with 40% relative density and 98 kPa confining pressure. Similar results could be found for samples with 55% and 70% relative density and at different confining pressure. It is found that the relationship between liquefaction resistance and overconsolidation ratio is best represented by the following equation.

$$(\tau / \sigma')_{OCR} = (\tau / \sigma')_{NC} \times \sqrt{OCR} \qquad (1)$$

From equation 1, the liquefaction resistance for overconsolidated samples could be calculated by multiplying the liquefaction resistance for normally consolidated samples with the square root of OCR.

Figure 8 shows the results of liquefaction resistance for samples with different fines content and at 98 kPa confining pressure. It is shown in the figure that increasing fines content would decrease the liquefaction resistance.

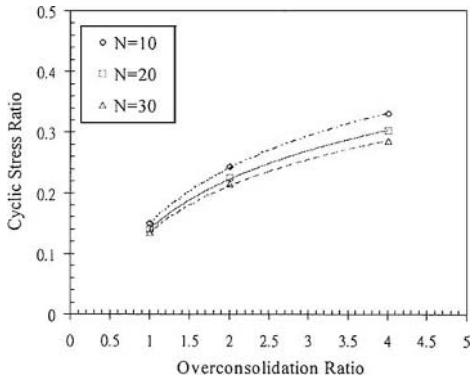

Figure 7. Effects of overconsolidation ratio on the liquefaction resistance of samples with 40% relative density and 98 kPa confining pressure.

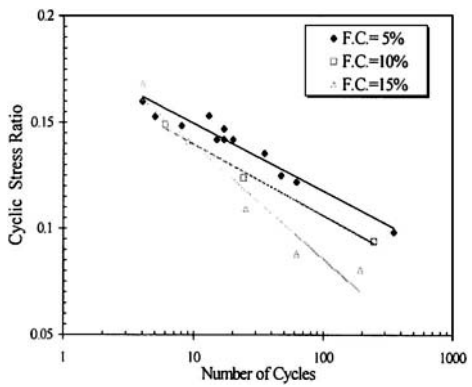

Figure 8. Effects of fines content on the liquefaction resistance for samples with 40% relative density and at 98 kPa confining pressure.

4.3 *State parameter and liquefaction resistance*

Figure 9 shows the relationship between state parameter and liquefaction resistance at 10 cycles for samples with different overconsolidation ratio. It is shown in the figure that at the condition of same overconsolidation ratio, liquefaction resistance decreases more or less linearly with increasing state parameter.

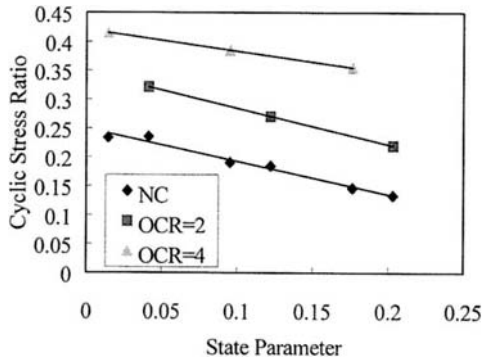

Figure 9. Relationship between state parameter and liquefaction resistance at 10 cycles

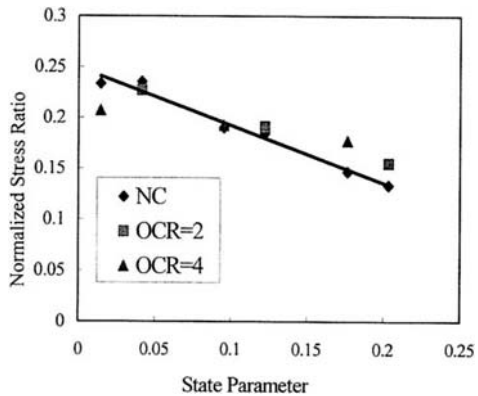

Figure 10. Relationship between state parameter and normalized stress ratio at 10 cycles.

The state parameter seems to be a good index to estimate the liquefaction resistance. The relationship between state parameter and liquefaction resistance is, however, affected by overconsolidation ratio. The reason is that overconsolidation has no effect on the steady state line but affects the liquefaction resistance a lot. To eliminate the effect of overconsolidation on the relationship between state parameter and liquefaction resistance, liquefaction resistance should be normalized by the square root of OCR. Figure 10 shows the results of normalized resistance versus state parameter. After normalization the relationship between state parameter and liquefaction resistance becomes unique.

5 CONCLUSIONS

This research performed triaxial tests and cyclic triaxial tests on remolded samples of Mailiao sand with different fines content, relative density, and overconsolidation ratio. The effects of stress path, fines content, and overconsolidation ratio on the steady state line are investigated. Liquefaction resistance under different overconsolidation ratio is obtained and the relationship between state parameter and liquefaction resistance is studied. Conclusions of this paper are as follows.

1. Stress path has some effect on the steady state line. Steady state line of triaxial extension test is located on the left side of the line obtained from triaxial compression test. The soil particle shape of the samples is very flat. This may contribute to the differences.
2. Overconsolidation has no effect on the location and slope of the steady state line.
3. Steady state line will shift leftward with increasing fines content, and the slope of the steady state line will decrease with increasing fines content.
4. Liquefaction resistance increases linearly with the square root of overconsolidation ratio.
5. Liquefaction resistance decreases with increasing fines content at the condition of same relative density.
6. A unique relationship exists between state parameter and liquefaction resistance if the liquefaction resistance is normalized by the square root of overconsolidation ratio. Liquefaction resistance decreases with increasing state parameter.

REFERENCES

Been, K. & M.G. Jefferies 1985. A State Parameter for Sands. *Geotechnique.* 35: 99-112.

Been, K., M.G. Jefferies & J. Hachey 1991. The Critical State of Sands. *Geotechnique.* 41: 365-381.

Castro, G., J.L. Enos, J.W. France & S.J. Poulos 1982. *Liquefaction Induced by Cyclic Loading.* Report to National Science Foundation, Washington, DC, No. NSF/CEE-82018.

Castro, G., R.B. Seed, T.O. Keller & H.B. Seed 1992. Steady-State Strength Analysis of Lower San Fernando Dam Slide. *Journal of the Geotechnical Engineering. Div., ASCE.* 118: 406-427.

Chen Y.C. & G.C. Chen 1996. Effects of several factors on the steady state line of sands. *Journal of the Chinese Institute of Civil and Hydraulic Engineering.* 8(2):161-169.

Chen, Y.C. & C.H. Tseng 1998. State Parameters and Liquefaction Resistance of Sand. *Journal of the Chinese Institute of Civil and Hydraulic Engineering.* 10(1):139-144.

Dobry, R., A. Vasquez-Herrera, R. Mohamad & M. Vucetic 1985. Liquefaction Flow Failure of Silty Sand by Torsional Cyclic Tests. *ASCE National Convention Session on Advances in the Art of Testing Soils under Cyclic Loading*, Detroit, 29-50.

Konard, J.M. 1990. Minimum Undrained Strength versus Steady-State Strength of Sands. *Journal of the Geotechnical Engineering. Div., ASCE.* 116: 948-963.

Kuerbis, R., D. Negussey & Y.P. Vaid 1988. Effect of Gradation and Fines Content on the Undrained Response of Sand. *ASCE Conference on Hydraulic Fill Structures*, Geotechnical Special Publication 21: 330-345.

Negussey, D., W.K.D. Wijewickreme & Y.P. Vaid 1988. Constant-Volume Friction Angle of Granular Materials. *Canadian Geotechnical Journal.* 25: 50-55.

Poulos, S.J. 1981. The Steady State of Deformation. *Journal of the Geotechnical Engineering. Div., ASCE.* 107: 553-562.

Poulos, S.J., G. Castro & J.W. France 1985. Liquefaction Evaluation Procedure. *Journal of the Geotechnical Engineering. Div., ASCE.* 111: 772-792.

Vaid, Y.P. & J.C. Chern 1985. Cyclic and Monotonic Undrained Response of Saturated Sands. *ASCE National Convention Session on Advances in the Art of Testing Soils under Cyclic Loading*, Detroit: 120-147.

Vaid, Y. P., E.K.F. Chung & R.H. Kuerbis 1990. Stress Path and Steady State. *Canadian Geotechnical Journal.* 27: 1-7.

Earthquake Geotechnical Engineering, Sêco e Pinto (ed.) © 1999 Balkema, Rotterdam, ISBN 90 5809 116 3

Liquefaction resistance based on the energy dissipation capacity

E. Yanagisawa, M. Kazama & T. Kagatani
Graduate School of Engineering, Tohoku University, Sendai, Japan

ABSTRACT: So far only a few attempts have been made to evaluate the liquefaction resistance from a ductility view point. The authors propose a new concept to evaluate the ductility of soils against liquefaction. This method is based on the energy dissipation capacity obtained from stress-strain relationships. This concept makes it possible to evaluate the liquefaction strength against big earthquakes like the 1995 Hyogoken-Nambu earthquake. The energy dissipation capacity for various soils were studied by using strain controlled cyclic triaxial test. To confirm the validity of the method proposed, we compare the results for Masado soil at Kobe Port Island obtained from elementary test, array observation data and seismic response analysis. Energy dissipation capacity obtained from above the three procedures shows very consistent results.

1 INTRODUCTION

Following the 1995 Hyogoken-Nambu Earthquake, it is well known that Port Island was covered with sand boils due to liquefaction. The reclaimed material used to construct the artificial island was decomposed granite soil. The soil called *Masado* is well-graded and an easy crushing of soil particles. So far, it is considered that the well-graded material such as the Masado causes no liquefaction (Port & Harbour Res. Inst. 1997).

This big earthquake gave us a new problem with relation to the liquefaction resistance of soil. One example is the liquefaction resistance for the soils that had been considered as non-liquefiable soils, such as clayey and gravelly material. The other is the liquefaction resistance subjected to an extra large stress loading with small number of cycles. In other words, it is necessary to estimate a ductility nature of soils.

Liquefaction strength of soils is currently evaluated by cyclic triaxial test under stress controlled conditions. In case of using the cyclic triaxial test under stress controlled conditions, liquefaction of soil is defined when the axial strain double amplitude reaches the value prescribed. Relations between shear stress ratio and the number of cycles is, as it is well known, called liquefaction strength curve or undrained cyclic shear strength, and gives the relation-like fatigue curve for the metal. So far, the following drawbacks of this concept pointed out were : (1) Difficulty in obtaining the strength of soil subjected to large stress loading with few cycles, (2) Variations in strain rate duing the test, and (3) Reliability of liquefaction behavior in extra large strain levels. However, the most essential drawback to such a concept is the impossibility for distinguishing the liquefaction of sandy soil with a sudden loss of shear strength from the fatigue failure in cohesive soils. As far as we use the current concept, a major concern is the alternative conclusion whether the soil will liquefy or not.

In this paper, the authors propose a new concept for evaluating the liquefaction resistance of soil from ductility viewpoint. Concepts proposed here will be explained by laboratory test results for various soils and a case study for Kobe Port Island during the 1995 Kobe earthquake (Kazama et al., 1998a,b).

2 LIQUEFACTION RESISTANCE BASED ON ENERGY DISSIAPTION CAPACITY

2.1 *Material used for laboratory testing*

The grain size distributions of the soils used in this study are shown in Fig.1. Toyoura sand is clean fine sand and its mean grain size is 0.1 to 0.2mm. Haneda soil is a reclamation soil used in the construction of New Tokyo International Airport, and has over 35% fines. Typical alluvial clay sampled from Inae district in Miyagi prefecture has a plastic index of 50%. Masado is the decomposed granite soil sampled from Kobe Port Island and liquefied completely during the 1995 Kobe earthquake. In the laboratory test for Masado, only material under 2mm in grain size was used. This treatment was necessary to avoid membrane penetration phenomena.

2.2 *Liquefaction behavior from ductility view point*

Figure 2 shows the results of the undrained cyclic triaxial test of Toyoura sand and alluvial clay under a constant strain controlled condition. When paying attention to the results of Toyoura sand, in continued cyclic shearing, the excess pore water pressure increase gradually, and reaches a value close to the applied initial hydrostatic pressure. Corresponding to this pore pressure build up, we can observe the decrease axial stress that is an indication of the resistant force of the soil specimen. Finally, the stress-strain relationship becomes flat. This stage is regarded as an ultimate stage of so called liquefaction.

In contrast, in case of alluvial clay, even if excess pore water pressure increases up to 80% of initial hydrostatic pressure, the shear resistance still remains 70% of initial shear resistance, and reaches steady state in cyclic shearing. This is typical behavior for clayey material. Therefore, if liquefaction is defined by a loss of shear resistance at the strain level prescribed, it is possible to conclude that this alluvial clay is non-liquefiable soil.

Fig.3 shows the secant shear modulus reduction with number of cycles for various soils obtained from the same tests. In Fig. 3, the vertical axis is the secant modulus normalized by a secant shear moduli G_1 at initial loading. As shown in this figure, the finer and the denser soil subjected to cyclic loading shows the smaller reduction of secant modulus.

When paying attention to the energy dissipation capacity in the material, we can estimate it by integrating the area covered with stress-strain loops. This example of cyclic triaxial test makes it clear that liquefaction corresponds to the final stage in which no more dissipation energy accumulated in soil. Therefore, a liquefiable soil has an upper limit of the energy dissipation capacity. On the other hand, alluvial clay accumulates constant energy as a material damping continuously. Thus, it can be said that this material has much more ductility nature compared with liquefiable sandy material. This is why the idea stands ductility point of view and energy dissipation capacity should be an index to represent the liquefaction resistance.

Over the past decade a considerable number of

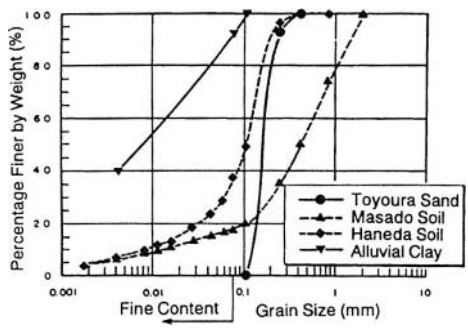

Fig. 1 Grain size distributions of the soils used here.

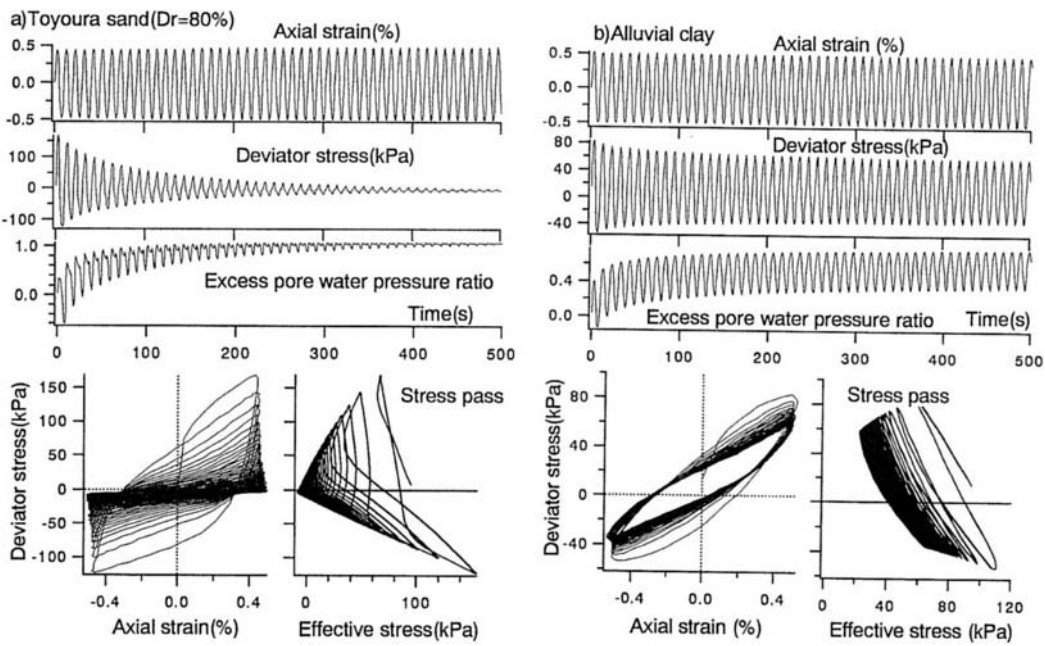

Fig. 2 Undrained cyclic triaxial test of Toyaura sand and alluvial clay under constant strain controlled condition. (Axial strain single amplitude = 0.5-0.55%, Frequency =0.1Hz)

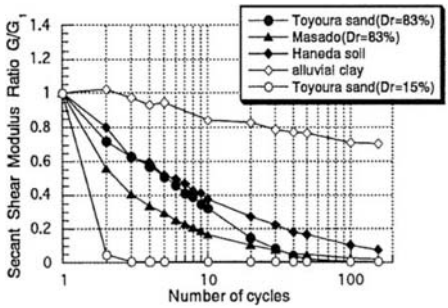

Fig. 3 Secant shear modulus reduction for various soils subjected to a constant cyclic shear strain.

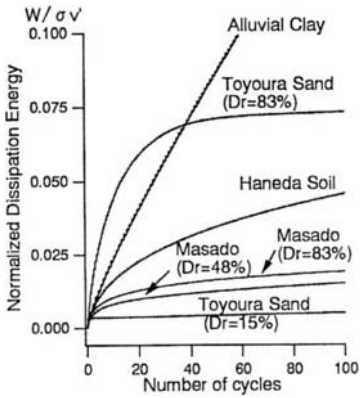

Fig. 4 Energy dissipation process for various soils subjected to constant cyclic shear strain.

studies have been made on energy dissipation, sometimes it is called a shear work (for example, Towhata, 1985, Sugano, 1992, Okada 1994). From these studies it has been found that the process of excess pore water pressure builds up corresponds to that of dissipation energy accumulation and that the stronger soils has a larger energy dissipation capacity.

Fig.4 shows the energy dissipation process obtained from the tests. For all sandy soils except for the clay, the dissipation energy is saturating gradually. Apparently for Haneda soil, the energy was still accumulated after 80 cycles were applied. The energy dissipation capacity for Toyoura sand is seriously dependent on the relative density. However, the energy dissipation capacity for Masado soil has a small dependency on the relative density. This point will be discussed in the following section.

Combining the result of Fig.3 and Fig.4, the relation between the dissipation energy and secant modulus reduction is obtained as shown in Fig.5. If an input earthquake motion will be given at a site and the dissipation energy generated due to the earthquake will be evaluated by response analysis, it is possible to evaluate the degree of liquefaction by using Fig.5.

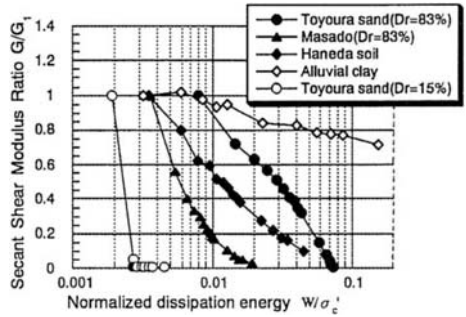

Fig. 5 Relation between secant shear modulus reduction and dissipation energy for various soils.

3 CASE STUDY FOR KOBE PORT ISLAND

3.1 *Liquefaction characteristics of Masado*

Many researchers has investigated liquefaction strength of Masado after the 1995 Kobe Earthquake. Zen & Yamazaki (1996) and Hatanaka et al. (1997) conducted large scale cyclic triaxial tests of Masado sampled from Port Island by undisturbed frozen sampling method. The dimensions of the specimens are 30cm $\phi \times$60cm and 15cm $\phi \times$30cm respectively. Comparing the results for the reconstituted Masado, liquefaction strength of undisturbed specimen was a little larger than that of the reconstituted specimen. In addition to this, many researchers also conducted the cyclic triaxial tests for the reconstituted Masado without gravel content.

According to these tests results, the following feature of Masado were found; (1) Masado has large particle size but low liquefaction strength, and nearly equal to that of Toyoura sand with a relative density of about 70%; (2) It is difficult to make a specimen with the specified relative density because of consolidation during saturation; (3) Liquefaction strength does not so increase with increasing relative density; and (4) Strain amplitude was incidentally developed comparing to fine clean sand. These results were discussed from undrained shear strength curve, so called liquefaction strength curve.

3.2 *Dissipation energy capacity inferred from array*

The authors (1996) had already studied stress-strain relationships by using strong motion array records at Port Island. The liquefaction process of the reclaimed ground has also been studied using cyclic simple shear testing controlled by the inferred stress time history. In this section we show the energy dissipation capacity inferred from the array records. Since there is no doubt on that the reclaimed Masado reached complete liquefaction during the main shock, the dis-

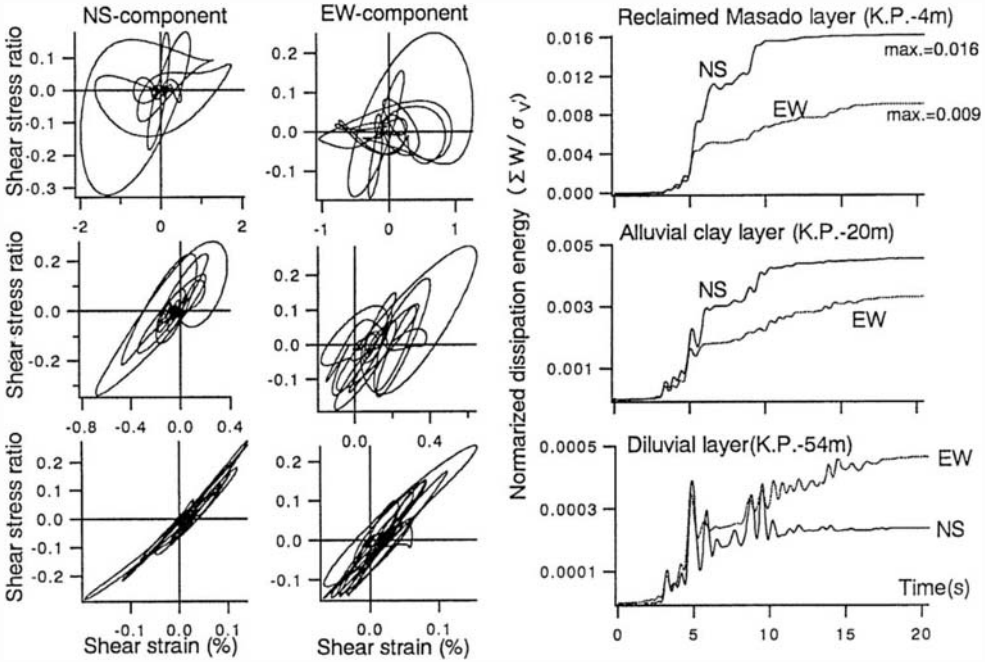

Fig. 6 Stress strain relationships and energy accumulation processes inferred from array records during the 1995 Kobe earthqukae at Kobe Port Island.

sipation energy accumulated in the ground due to the earthquake corresponds to the energy dissipation capacity of Masado.

When time histories of shear stress and shear strain are given, the dissipation energy accumulated is calculated as follows.

$$\Delta W(t) = \oint_f \tau(\gamma)d\gamma = \int_0^t \tau(\gamma)\,\gamma'(t)dt \qquad (3.1)$$

Applying this calculation to the stress-strain relationship inferred from the observed strong motion records, we estimate the energy dissipation capacity of the in-situ condition as shown in Fig.6. In Fig.6, we normalized the dissipation energy by its initial overburden pressure at the depth shear stress calculated. Comparing the dissipation energy accumulated in each layer, it is found that the upper layer behaves much more plastic and that the larger energy is dissipated as material damping. This is evidence that the behavior of Masado soil was beyond the elastic region. Regarding the dissipation energy in the reclaimed layer, it saturated at ten seconds before earthquake motion terminates. Therefore, the reclaimed ground reached the ultimate stage behaving like a liquid at 10 seconds, in which no more shear stress was transmitted to the upper layer as shown in Fig.7. The saturated values are 0.016 in NS component and 0.009 in EW component. If the energy in two directions can be superimposed, total dissipation energy

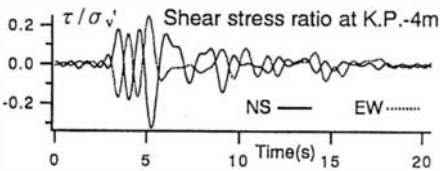

Fig. 7 Shear stress ratio at the depth of K.P -4m in reclaimed Masado layer inferred from array data.

will be 0.025.

3.2 *Energy dissipation capacity obtained from strain controlled cyclic triaxial test.*

The authors have conducted strain controlled cyclic triaxial test for obtaining the energy dissipation capacity. Table 1 shows the physical properties of soils used here. To compare the ordinary fine clean sand material, Toyoura sand was used as representative of standard clean sand. The relative density in initial dry state and after isotropic consolidation to 98kPa was shown in Table 2. It was found that the volumetric change of Masado specimen during water saturation and consolidation is considerably large compared with Toyoura sand. According to the previous study by the authors (Kazama et. al 1998b), only small compact energy is necessary for compacting Masado up to

Table 1. Physical properties of soils

	ρ_s (g/cm^3)	D_{50}(mm)	e_{max}*	e_{min}*	fines
Masado	2.644	0.57	1.045	0.535	18%
Toyoura sand	2.64	0.1-0.25	0.967	0.596	0%

*as defined by Japanese standards

Table 2. Test conditions

Masado				Toyoura sand			
No.	Dr_i(%)	Dr(%)	N	No.	Dr_i(%)	Dr(%)	N
MS1	20	40	0	TY1	6	10	0
MS2	37	51	0	TY2	18	18	0
MS3	41	51	0	TY3	36	37	15
MS4	54	68	2	TY4	38	38	60
MS5	72	83	5	TY5	45	47	100
MS6	68	79	10	TY6	46	48	200
MS7	70	80	10	TY7	56	57	*
MS8	75	77	15	TY8	72	73	*
MS9	75	88	15	TY9	78	80	*
MS10	76	86	20	TY10	79	81	*

Dr_i=initial relative density in dry state
N=number of weight drop per unit layer
*compacted by mallet

the void ratio in loosest state compared with Toyoura sand. It is likely to be a typical nature of well-graded soils.

Meanwhile, for sandy material, there is other important nature that shear resistance will recover in a large strain level due to its dilatancy characteristics. Energy dissipation capacity under certain strain level must be much smaller than the capacity under the larger strain level. Therefore, step loading procedure was used for all test, in which the strain double amplitude was from 0.7% to 20%. For one loading stage, cyclic load was continuously applied until the shear resistance decreases 10% of initial shear resistance or 100 times. During the loading stage undrained condition had been kept completely. Detailed testing procedure is shown in the other paper (Kazama et.al. 1998c).

Masado is regarded as a problematic soil due to the easy particle crushing. Before the step-loading test, single loading step tests were conducted for investigating effects of confining pressure varying from 98 to 294kPa on the dissipation energy. Its relative density after consolidation was from 88% to 97%. The unique relation was obtained from the test between the dissipation energy normalized by the confining pressure and the wave number applied, as shown in Fig.8. No effect due to the particle crushing was observed in this stress level.

Fig.9 shows the comparison of the dissipation energy accumulation in each strain step, the larger strain level is applied the larger energy dissipation capacity was observed. It is indication of a recovery of stiffness due to dilatancy. Increase of energy dissipation capacity of Masado with strain amplitude is relatively small compared with that of Toyoura sand. It relates the facts that only small compact energy is necessary to make dense Masado.

Fig.10 shows the relation between the relative density and dissipation energy capacity at shear strain

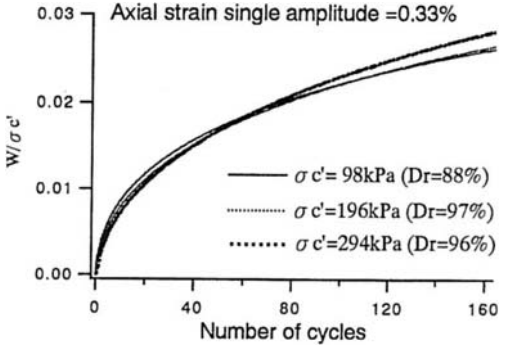

Fig.8 Comparison of the dependency of the dissipation energy capacity on the confining pressure.

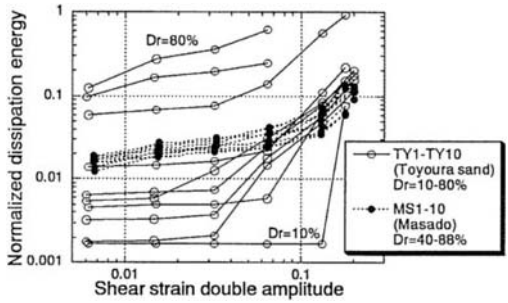

Fig.9 Dissipation energy capacity of soils with strain amplitude.

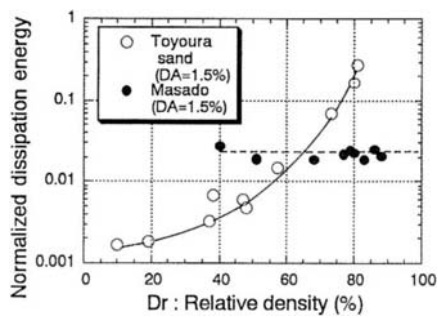

Fig.10 Comparison of the dependency of the dissipation energy capacity on a relative density.

level 1.5%. Apparently, the energy dissipation capacity for Toyoura sand is seriously dependent on the relative density. However, the energy dissipation capacity for Masado shows a small dependency on the relative density. In other words, energy dissipation capacity of the Masado in-situ condition should be the almost same value as the test results. We have to pay close attention to that the energy dissipation capacity of Masado is about 0.02-0.03. The range of the values is well consistent with the value inferred from array records.

3.3 *Dissipation energy obtained from seismic response analysis*

To use the liquefaction resistance proposed here, we have to estimate the dissipation energy generated by the design earthquake. In this section, a simple method for estimating the dissipation energy in the ground will be explained. Example is the Kobe Port Island array observation site during the 1995 earthquake.

In general, the dissipation energy can be calculated by a nonlinear seismic response analysis such as an effective stress analysis. However the effective stress analysis itself is liquefaction analysis, and then we will lose the motivation to calculate the dissipation energy for evaluating liquefaction potential. Furthermore, the result must strongly depend on the constitutive equations used in the analysis. Therefore, in this study, the energy dissipation was calculated by the equivalent linear analysis to be usually used in the design work.

There is the following relation between the elastic energy W_E and the plastic energy ΔW consumed as a material damping.

$$h_{eq} = \frac{1}{2\pi} \cdot \frac{\Delta W}{W_E} \tag{4.1}$$

where h_{eq} is damping ratio for the soil. Using this relation, we can estimate the dissipation energy accumulated during the shaking by summing up the elastic energy for each pulse as shown in equation (4.2).

$$\Delta W_{total} = \sum_{i=1}^{I} \Delta W_i = 2\pi h_{eq} \sum_{i=1}^{I} W_{E,i} \tag{4.2}$$

Fig.11 shows the dissipation energy of Kobe Port Island array site in depth direction calculated by the method written above. In this calculation we used the record observed at K.P.-28m in NS component as an input motion. As shown in Fig.11, the dissipation energy accumulated in the reclaimed Masado layer from 0m to -12m is about 0.02-0.03. These values are also well consistent with the results from array data and laboratory test previously.

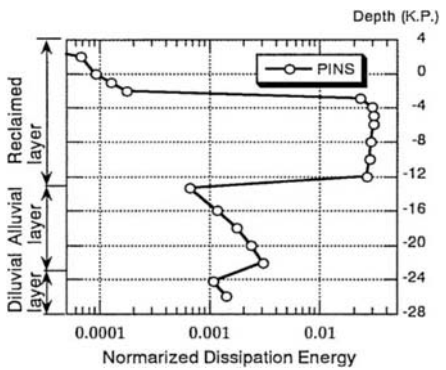

Fig.11. Comparison of the dependency of the dissipation energy capacity on a relative density.

4 CONCLUSION

The authors propose a new scheme for evaluation the liquefaction resistance from ductility view point. The conclusions obtained from this study are summarized as follows:

(1) Energy dissipation capacity proposed here is very effective index to represent the ductility of the soils against liquefaction.

(2) From case study of Kobe Port Island during the 1995 earthquake, the dissipation energy for Masado obtained from laboratory cyclic triaxial test under strain controlled condition, that inferred from array observation records and that calculated by seismic response analysis shows very consistent result.

REFERENCES

Hatanaka, M., Uchida, A. & Ohara, J. 1997. Liquefaction characteristics of a gravelly fill liquefied during the 1995 Hyogo-ken Nanbu Earthquake, *Soils and Foundations*, Vol.37, No.3, pp.107-115.

Kazama, M. et.al. 1996. Stress strain relationship in the ground at Kobe Port Island during the 1995 Hyogo-ken Nanbu Earthquake inferred from strong motion array records (in Japanese), Journal of Geotechnical Engineering, JSCE, No.547, pp.171-182.

Kazama, M. et al. 1998a. Evaluation of liquefaction resistance using strain controlled cyclic triaxial test (in Japanese), *TSUCHI-TO-KISO* , Vol.46, No.4, pp.21-24.

Kazama, M. et al. 1998b. Liquefaction strength of decomposed granite soil inferred from array records, *the 12th. Engineering Mechanics, ASCE*, pp.478-481.

Kazama, M., Kagatani, T. & Yanagisawa, E. 1998c. Liquefaction characteristics of decomposed granite soil at Kobe artificial island, *International Symposium on Problematic Soils, IS-Tohoku98 Balkema,* pp.411-414.

Okada, N. & Nemat-Nasser, S. 1994. Energy dissipation in inelastic flow of saturated cohesionless granular media, *Geotechnique* , Vol.44, No.1, pp.1-19.

Port & Harbour Res. Inst. Editor, 1997. Handbook on Liquefaction Remediation of Reclaimed Land, Balkema.

Sugano,T. & Yanagisawa, E. 1992. Cyclic Undrained Shear Behavior of Sand Under Surface Wave Stress Conditions, *Proc.of the 10th. WCEE*, pp.1323-1327.

Towhata, I. & Ishihara, K. 1985. Shear Work and Pore Water Pressure in Undrained Shear, *Soils and Foundations,* Vol.25, No.3, pp.73-84.

Zen, K. & Yamazaki, H. 1996. Liquefaction characteristics of Masado (decomposed granite soil) used for reclaimed land (in Japanese), *TSUCHI-TO-KISO*, Vol.44, No.2, pp.60-63.

Earthquake Geotechnical Engineering, Sêco e Pinto (ed.) © 1999 Balkema, Rotterdam, ISBN 90 5809 116 3

Liquefaction potential of sand by torsional shear test

M. Dehghani, G. Habibagahi & A. Ghahramani
Shiraz University, Iran

J. Berrill
University of Canterbury, Christchurch, New Zealand

ABSTRACT: The liquefaction potential of saturated sand is estimated by using torsional shear. Laboratory tests indicate distinct patterns between torsional moment and rotation angle of cylinder embedded in sand for contracting and dilative behavior. Using corresponding relations, shear stress versus shear strain of sand adjacent to cylindrical surface is evaluated. By slightly modifying the standard penetration test, torsion shear tests were carried out. The predictions of liquefaction potential by torsional shear compares favorably with the predictions of standard penetration tests for liquefaction potential.

1 INTRODUCTION

The liquefaction potential of saturated sand is basically estimated by using standard penetration tests (SPT) and cone penetration test (CPT or CPTU). These tests produce volumetric stresses in the soil and thus the generation of pore pressure due to shear is not directly measured. To overcome this difficulty recently Atkinson and Jessett (1990) and Charlie et al (1995) developed the piezovane. They were thus able to measure pore pressure decrease for dilative sand and pore pressure increase for contractive sand during torsion of the vane apparatus. The torsional in situ field test is desirable, because it produces basically shear strains and thus by measuring torque and rotation angle of the cylinder being subjected to rotation, the shear stress versus shear strain can be measured.

Laboratory tests were done on cylindrical bar of 2.5 cm diameter embedded in sand for a length of 20 cm for different relative densities of sand. Theoretical development relates torsion on the cylinder to shear stress on adjacent soil and rotation angle to shear strain. By plotting shear stress versus shear strain, distinct pattern of behavior is noticed for dilative and contractive sands.

Field torsional tests on SPT were carried out by modifying the SPT slightly. The pattern of sand behavior makes it possible to estimate the liquefaction potential for contractive behavior.

2 TORSONAL SHEAR TEST THEORY

If the cylindrical bar embedded in the soil is subjected to rotation as shown in Fig. 1, then for the soil at depth h assuming lateral stress to be p_0 and for fully elastic case ($r_c = r_0$) it can be shown that (Dehghani, 1998) as indicated in Fig. 2.

$$\tau_{r\vartheta} = \tau_0 \left(\frac{r_0}{r} \right)^2 \tag{1}$$

$$\varepsilon_r = \varepsilon_\theta = 0 \tag{2}$$

$$\gamma_{r\theta} = \frac{1}{r}\frac{\delta u_r}{\delta \theta} + \frac{\delta u_\theta}{\delta_r} - \frac{u_\theta}{r} = \frac{\tau_0}{G}\left(\frac{r_0}{r} \right)^2 \tag{3}$$

Where p_0 is lateral pressure, σ_r is radial stress , σ_θ is circumferential stress, $\tau_{r\theta}$ is shear stress, ε_r is radial strain, ε_θ is circumferential strain, $\gamma_{r\theta}$ is shear strain, G is the shear modulus, u is the displacement , r_0 is the bar radius, and r is the radial distance. τ_0 is the shear stress at the cylinder boundary.

It is interesting to note that the soil surrounding the cylindrical bar is behaving basically in pure shear and the change of volume is zero. Also from equation (3) , it can be seen that

$$\frac{u_\theta}{r} = \left(\frac{-\tau_0}{2G}\right)\left(\frac{r_0}{r}\right)^2 = -\frac{\delta_{r\theta}}{2} = \alpha \qquad (4)$$

Where α is the rotation angle. Thus the shear strain is twice the rotation angle.

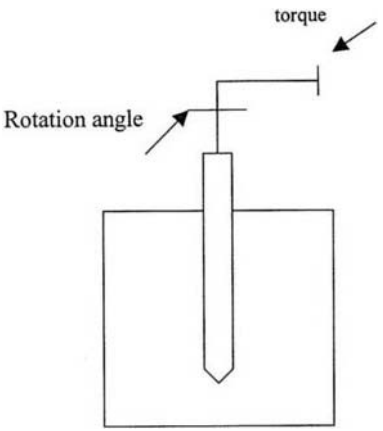

Figure 1. The torsional shear apparatus

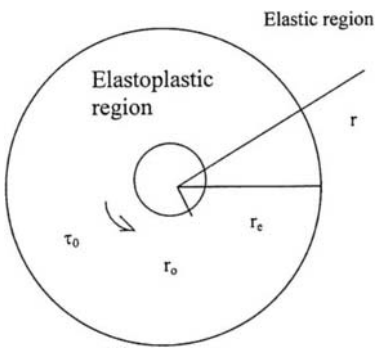

Figure 2 The elastic and elasto plastic region

In the elasto plastic region, assuming Mohr Coulomb failure criteria, it can be shown that

$$\sigma = p_i\left(\frac{r}{r_0}\right)^Q \qquad r_e = r_0\left(\frac{p_0}{p_i}\right)^{\left(\frac{1}{Q}\right)} \qquad Q = 2\tan^2\varphi$$

$$\tau = G\gamma \qquad when \quad \gamma \le \frac{p_0 \tan\varphi}{G} \qquad otherwise$$

$$\tau = \left(\frac{2(1+\nu)k_f \tan\varphi \tan\psi}{2(1+\nu)k_f \tan\varphi \tan\psi + (1-\nu)(1+k_f)}\right)x$$

$$G(\gamma - \gamma_0) + \tau_0 \qquad (5)$$

(Dehghani 1998)
It is also concluded that

$$\tau_0 = p_0 \tan\varphi \quad where \quad k_f = \left(\frac{1}{1+2\tan^2\varphi}\right) \qquad (6)$$

Where φ is the friction angle and ψ is the dilation angle. The general pattern is shown in Figure 3.

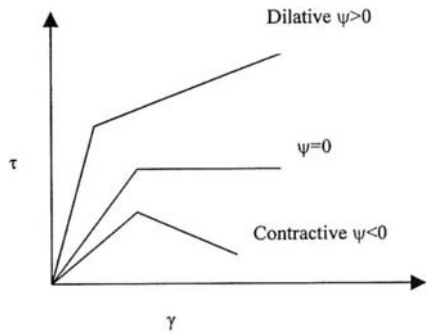

Figure 3. Contractive and dilative behavior

Thus it can be seen that for Mohr Coulomb soil, the soil adjacent to the cylindrical bar is acting in undrained behavior and thus shear stress is proportional to shear strain at the elastic range and it then decreases for Contractive soil and increases for dilative soil.

3 TORSIONAL SHEAR TEST LABORATORY TESTING.

During the laboratory testing the cylinder (roughened at the periphery to prevent slippage between the cylinder and the soil) equipped with a torquemeter and rotation angel measuring system as shown in Figure 1. Two sands were tested. The property of the sands is shown in Table1.

Table 1 The property of the two sands tested

Property	Sand 1	Sand 2
D_{50} mm	0.28	0.75
e max	0.93	0.89
e min	0.57	0.52
G	2.64	2.65
Cu	2.7	5.6
Cc	0.9	0.9

The grain size distribution of the two sands is shown in Figure 4.

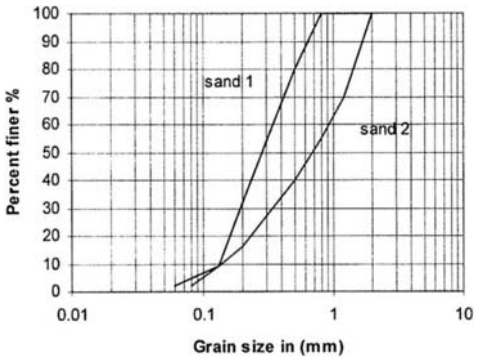

Figure 4 The grain size distribution of sands

Triaxial tests under undrained condition were run for the two sands on 5 by 12 cm samples. The steady state line for the two sands is shown on figure 5 and the steady state condition for the two sands is shown in figure 6.

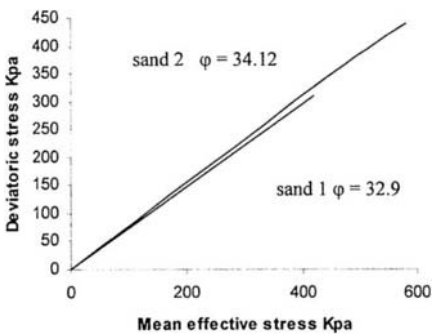

Figure 5 Steady state lines

After having measured the properties of the two sands under triaxial conditions torsional shear tests were carried out. The results of the tests are presented after converting the torque to shear stress and the rotation angle to shear strain. The test results for different relative densities for the tow sands are shown on Figure 7 and Figure 8.

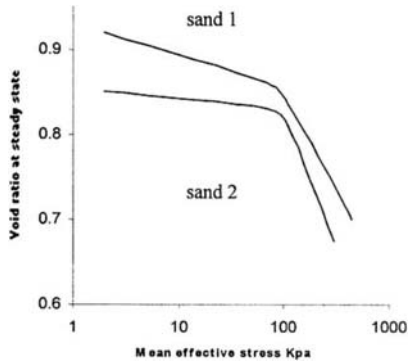

Figure 6 Steady state conditions

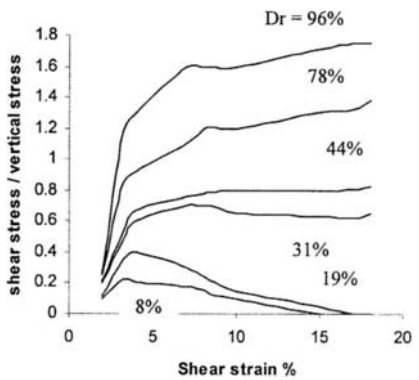

Figure 7 Torsional shear test on sand 1

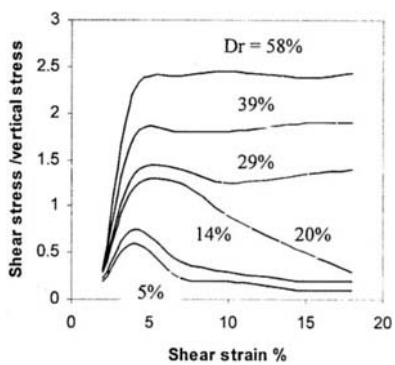

Figure 8 Torsional shear test on sand 2

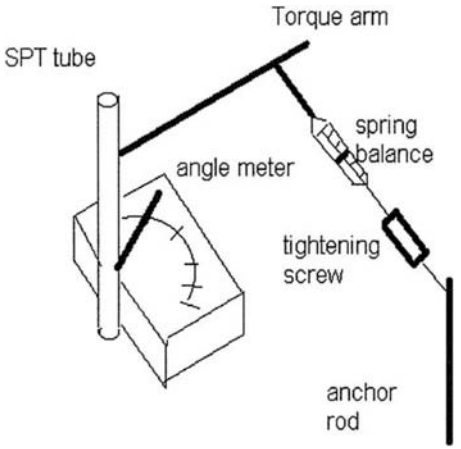

Figure 9 Torsional shear field test

4 TORSIONAL SHEAR TEST, FIELD TESTING

The field tests were carried out in southern part of Iran in Hormozgan University extension land. The area is covered by loose saturated sand up to the depth of 10 meters and is known to have liquefiable sand layers. Two boreholes were tested. After boring to the required depth and installing casing and filling the hole up with bentonite, Standard Penetration Test was carried out at the given depth. After SPT test, the torsional field shear was carried out. The schematic test setup is shown in Figure 9.

The test unit consists of the following parts:

A. A platform of 50 centimeter high and surface area of 100 centimeter by 150 centimeter with a 10 centimeter diameter hole in the middle to let the SPT sampler and tube pass from it.
B. A plate for measuring angles of rotation with graduation in degrees on it with 100centimeter diameter and 10 centimeter hole in the middle.
C. Steel arms of 100 and 50 centimeter lengths attached to the SPT tube for applying the torque to the SPT sampler.
D. Two spring balances of 30 and 50 kilogram range for measuring the force applied to the arm to create the torque on the SPT sampler.
E. A pointer attached to the tube to help in measuring the rotation angle.
F. An anchor rod inserted in the ground to be a fixed support for applying the force through the tightening screw attached to the spring balance.

The torsional shear was done in the following manner:

The platform was installed and the plate for angle measurement was fixed on it. The hole in the plate and the platform was centered with the SPT tube. Then the arm was fixed to the SPT tube at one meter high above the ground with the help of grippers. A vertical pointer was also applied to the arm to point to the graduations on the angel measurement plate. Another pointer was also applied to the tube at the level of the graduation plate. These tow pointers should measure the same angle during the application of the torque if there is no tilt in the tube. Then the spring balance was hooked to the torque arm and through the tightening screws to the anchor rod. By tightening the screw, a force was gradually applied to the torque arm. The spring balance measured the force and this force multiplied by the arm would give the magnitude of the torque. The rotation angle was measured by the pointer taking care during the test to have the two pointers pointing to the same rotation angle. It should be mentioned that the periphery of the SPT sampler was roughened to prevent slippage between the sampler and the sand and to introduce the shear in the sand. . After carrying the torsional shear test, the boring was continued to another depth and the procedure was repeated, thus doing SPT test first and torsional shear test afterwards at the same depth. The schematic test setup is shown on Figure 9.

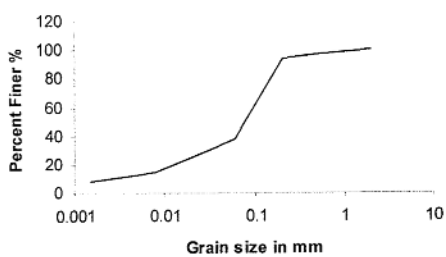

Figure 10 Grain size at depth 1.5m B.H.1

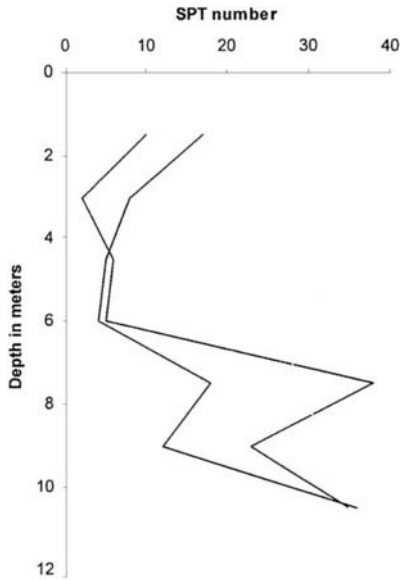

Figure 11 SPT variation with depth

This simple setup was chosen to be easily applicable to SPT test without major modification of the SPT test setup. The only modification was roughening the sides of the SPT cylinder to prevent slippage.

A sample grain size distribution of the sand in the field is shown in Figure 10 The variation of SPT with depth is shown on Figure 11 for both boreholes.

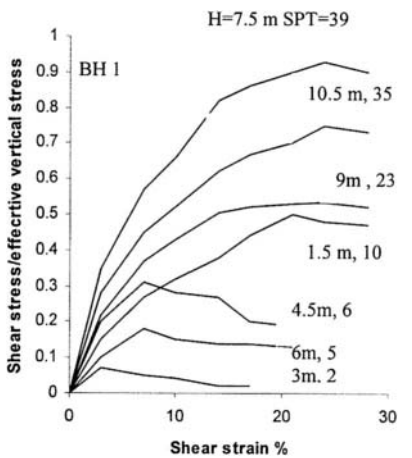

Figure 12 Torsional field test B.H No. 1

The torque measured during the torsional shear test was converted to shear stress and the rotation angle converted to shear strain. The shear stress in the soil at contact with SPT Sampler was made non dimensional by dividing it with respect to vertical effective stress. The results for Bore Hole No. 1 is shown in Figure 12 and for Bore Hole No. 2 is shown in Figure 13.

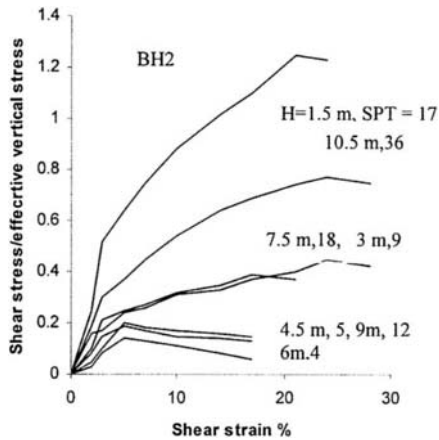

Figure 13 Torsional field test B.H No. 2

5 DISCUSSION OF RESULTS

The results of laboratory and field torsional shear tests were presented in Figures 7,8,12,13..

It is clear from laboratory tests that higher relative densities have dilative effect, this means that with the increase of shear strain, the shear stress is increased and up to large shear strains this trend is evident. At low relative densities, the contractive effect is evident and the shear stress reaches a maximum and it then declines with the increase of shear strain.

Also the results of field torsional shear tests indicate that at higher SPT values, the dilative behavior is also present in the field test and shear stress keeps increasing up to large shear strains. However at low SPT values, the contractive behavior is present and shear stress reaches a maximum and then declines with the increase of shear strain. It is also interesting to notice that at the same SPT , the shallower samples show more dilative behavior.

Thus torsional field shear test is another signature for the sandy soils after SPT for prediction of liquefaction potential.

6 CONCLUSIONS

Considering the theoretical development and the results of the laboratory and field torsional shear tests, it is concluded that

1. The torsional shear test is capable of predicting the contractive and the dilative behavior of the sand adjacent to the SPT sampler.

At the dilative behavior, the shear stress increases continuously up to large shear strains. When the behavior is contractive, the shear stress reaches a maximum and then decreases with the increase of the shear strain. At low relative densities or at low SPT values, the shear stress may reduce to almost zero.

2. It is possible after SPT test, with simple modification of test technique, to run torsional shear test in the field, thus giving another signature of the soil behavior to be used in liquefaction potential evaluation.

3. The predicted theoretical pattern of shear stress versus shear strain is followed both at laboratory torsional shear tests and at the filed torsional shear test.

ACKNOWLEDGEMENT

The authors would like to acknowledge the support of Shiraz University and Hormozgan University in Iran and the support of the University of Canterbury in New Zealand for preparation of this research. The authors would like to thank the International Panel of Reviewers for their valuable suggestions.

REFERENCES

Atkinson, J. H. and Jessett, J. H. (1990), Measurement of relative density of saturated sand using the piezovane, *Field testing in engineering Geology*, Engineering Geology Special Publication 6, pp. 229-233, London: Geological Society of London

Dehghani, M. (1998). Liquefaction potential of sand by torsional Shear test. PhD thesis, Shiraz University, Shiraz, Iran.

Charlie, W. A., Scott, C. El, Siller, T. J., Butler, L. W. and Doehring D. O. (1995). Estimating liquefaction potential of sand using the Piezovane, *Geotechnique*, 45, No. 1, 55-67

Earthquake Geotechnical Engineering, Sêco e Pinto (ed.) © 1999 Balkema, Rotterdam, ISBN 90 5809 116 3

Liquefaction of improved ground at Port Island, Japan, during the 1995 Hyogoken-nanbu earthquake

Nozomu Yoshida
Engineering Research Institute, Sato Kogyo Company Limited, Tokyo, Japan
Koji Ito
Technical Research Institute, Obayashi Corporation, Tokyo, Japan

Abstract: Liquefaction at an improved ground in Port Island, a man made island in Japan, during the 1995 Hyogoken-nambu earthquake is presented. The site was improved by the rod compaction method, and neither significant structural damage nor ground deformation was observed at the time of the earthquake. Detailed in-situ and laboratory tests were conducted at the site, which included dynamic deformation test and liquefaction strength test of frozen samples. In-situ investigation pointed out that the ground settlement of about 10 cm occurred during the earthquake. Two effective stress earthquake response analyses were conducted using the data from in-situ and laboratory tests. Both calculations showed that the ground near the water table did not liquefy, but the ground 7 meters below the ground surface (4 meters below the water table) liquefied. This result is in consistent with the observed fact.

1 INTRODUCTION

Significant liquefaction was observed in the fill area in Kobe City, Japan, and its vicinity during the 1995 Hyogoken-nambu earthquake. At the same time, this earthquake proved the effectiveness of the remedial works against liquefaction. The settlement of the ground was shown to depend on the degrees of improvement of the ground; settlement is smaller as improvement becomes more heavy (Yasuda et al., 1995).

Liquefaction in the Port Island, a man made island in Kobe City, was also severe. All the quay walls displaced toward the sea for about 1 to 5 meters (Inagaki et al., 1995). The entire island except improved region was covered by boiled sand and colored brown as shown in Figure 1.

Detailed in-situ and laboratory tests were conducted at a site in Port Island where the ground was improved by the rod compaction method. Evidence of the liquefaction such as sand boils and ground deformation was not observed at the site. In-situ investigation, however, pointed out that ground settlement of about 10 cm occurred during the earthquake as described later. Residual horizontal displacement was also observed (Hamada et al., 1995). This fact seems to be against the common sense; large ground settlement does not occur if liquefaction does not occur. In order to clarify this inconsistency, we conducted earthquake response analyses based on effective stress, which is reported in this paper.

2 LOCATION AND GROUND CONDITION

Port Island is a man made island developed in 1969 by filling the decomposed granite called Masado taken from the Rokko Mountain. Figure 1 shows the location of the investigated site. This site is located just neighboring to the vertical array observation site of Kobe City as shown in Figure 2. The area of about 150 × 150 m^2 was improved by the rod compaction method in 1977 and five one-storied factories (steel-framed structures used for warehouse and workshop) and a three-storied reinforced concrete control building were built. All factories

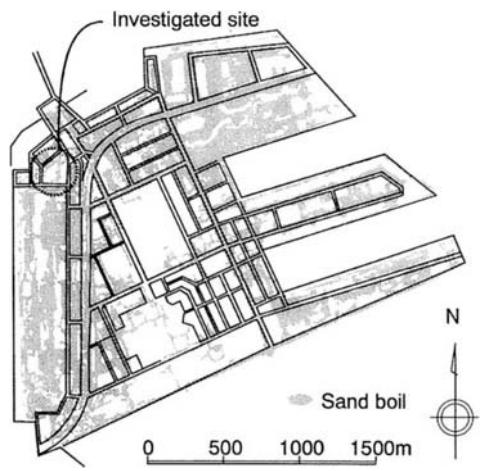

Figure 1. Location of the site in Port Island.

were supported by the spread foundation, and the control building was supported by the pile foundation. Details of the improved area and locations of the structures are shown in Figure 2.

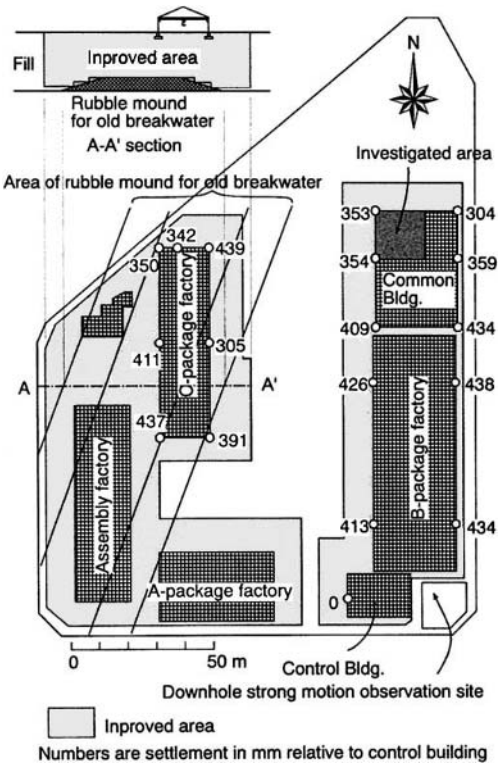

Figure 2. Details of the site.

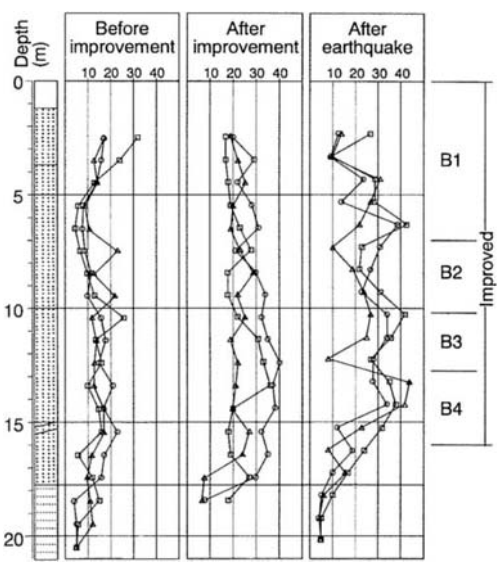

Figure 3. Soil profiles and SPT N-value before and after the improvement and after the earthquake.

Figure 3 shows soil profiles and SPT N-value before and just after the improvement, and after the earthquake. The fill was made on the marine clay layer called Ma13. The thickness of the fill is about 18 meters, among which upper 16m was improved by the rod compaction method, and the rest 2m was not improved because liquefaction was supposed not to occur as its fines contents was large.

After the 1995 Hyogoken-nambu earthquake, detailed investigation was made at this site by Geotechnical Research Collaboration Committee on the Hanshin-Awaji Earthquake Disaster. In situ tests such as PS logging by downhole and suspension methods, and standard penetration tests were conducted; frozen undisturbed samples were taken and both liquefaction strength and dynamic deformation characteristics were obtained in the laboratory tests; other various physical and mechanical tests were also conducted.

Depending on the SPT N-value distribution and other properties, improved ground is classified into four layers, named B1 to B4 layers. Liquefaction strength in each layer is shown in Figure 4.

3 DAMAGE AND SETTLTMENT DURING EARTHQUAKE

The ground in the vicinity of the site was covered by the boiled sand and mud water during the earthquake, but neither large ground deformation nor the sand boil was observed in the improved area. Relative settlement between the improved area and neighboring unimproved area reached several tens cm. The paved ground between improved areas sank about 10 to 30 cm, and mud water submerged it. No damage was observed at the A- and B-packing factories and the control building. Inner pavement of the C-packing factory and the assembly factory sank about 10 to 30 cm, and the ceiling crane became not to operate. Relative settlement between the control building and neighboring improved ground was observed to be about 20 cm as shown in Figure 5.

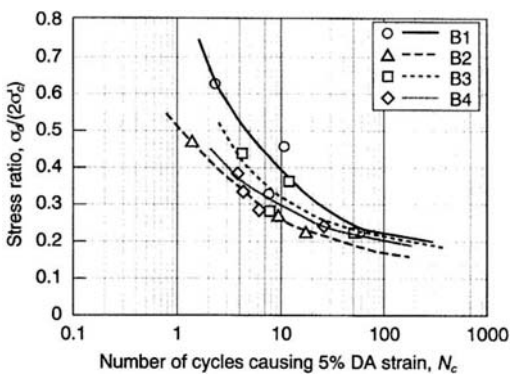

Figure 4. Liquefaction strength causing 5% DA strains.

After the earthquake, settlement of the improved area was measured. Since control building is supported by the pile foundation (PC pile with 500 mm in diameter and 34m in length. Number of piles is 35), settlement can be assumed not to occur. The difference of the elevation at the top of the footing of steel columns from the control building (reference point) is measured. Since the elevation difference when these structures were made is known from the design draft, settlement of each point relative to the control building can be computed by subtracting the elevation difference at the construction from the measured one. They are shown in Figure 2; relative settlements are about 30 to 40 cm.

Since obtained settlement includes settlement due to consolidation of Ma13 (clay layer), it must be subtracted in order to obtain the settlement at the time of the earthquake. Assuming the coefficient of consolidation to be 70 and 7 cm^2/day, settlement during 1977 and 1995 is evaluated to be 17.2 and 41.2cm, respectively. Taking the average value, settlement yields about 29 cm. These settlements are in consistent with the observed one at other places in Port Island. Finally, settlement at the time of the earthquake is evaluated to be about 14 cm at the B-package factory, 9 cm at the C-package factory, and 8 cm at the common factory.

Hamada et al. (1995) measured permanent displacement from the aerial photos taken before and after the earthquake. About 40 to 80cm horizontal displacement toward the northwest direction, direction toward the sea, is observed at this site.

These observed displacement and settlement indicate that large ground deformation might occur under the ground during the earthquake although there was no ground deformation at the ground surface. In order to investigate the reason, we conducted earthquake response analysis.

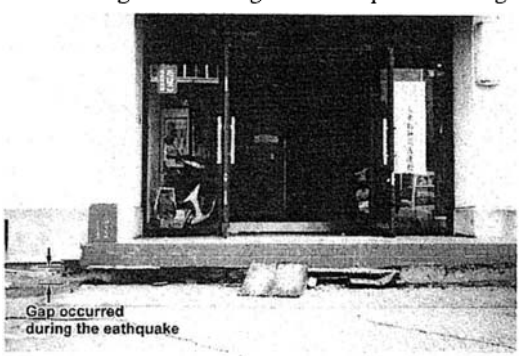

Figure 5. Relative settlement between control building and improved ground.

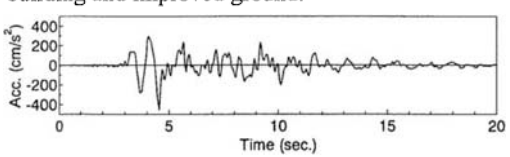

Figure 6. Incident wave at GL-32m (Principal direction)

4 METHOD OF ANALYSIS

Two computer codes, YUSAYUSA-2 (Yoshida and Towhata, 1991) and EFECT (Ito, 1995), are employed to grasp the behavior of the site during the earthquake. Both computer codes are based on the Biot's two-phase material theory as governing equation. YUSAYUSA-2 employs hyperbolic stress-strain model and stress path model for excess porewater pressure generation proposed by Ishihara and Towhata (1980). EFECT employs Matsuoka model, a multi-mechanism model that considers shear deformation, principal stress rotation and consolidation separately, and is expanded under cyclic loading. The ability of these codes to simulate the liquefaction of the unimproved site in Port Island is already proved (Yoshida, 1995; Geotechnical Research Collaboration Committee on the Hanshin-Awaji Earthquake Disaster, 1998)

The ground up to GL-32m is analyzed. Here GL-32m is a depth at which a seismograph was set up at the vertical array observation in Port Island that is located at about 100m south from the site as seen in Figure 2. The incident wave used in the analysis is computed by using the equivalent linear method with multiple reflection theory from the vertical array record. In the multiple reflection theory, continuity conditions of shear stress and displacement between the boundary of the layers, and 2 boundary conditions are used to solve the horizontally layered ground. In the ordinary equivalent linear method, the condition that incident wave and reflected wave are the same at the ground surface is used for one boundary condition, and input motion (observed motion at GL-32m) is used for another boundary condition in order to obtain the incident wave at GL-32m. The behavior near the ground surface will strongly reflects the downward wave at the base when this method is employed. Considering that, however, significant liquefaction occurred at the vertical array observation site, and the accuracy of the equivalent linear analysis is less at the liquefied site, this method may result in large error in the incident wave. In order to avoid the effect of the liquefaction in calculating the incident wave, the ground up to GL-83m at which another seismograph was set up is analyzed. Two ground motions, i.e., observed records at GL-32m and GL-83m, are used to be two boundary conditions and incident wave at GL-32m is retrieved. Obtained incident wave is shown in Figure 6.

The ground is modeled as shown in Figure 7 based on the borehole investigation. Here, as described previously, layers B1 to B4 were

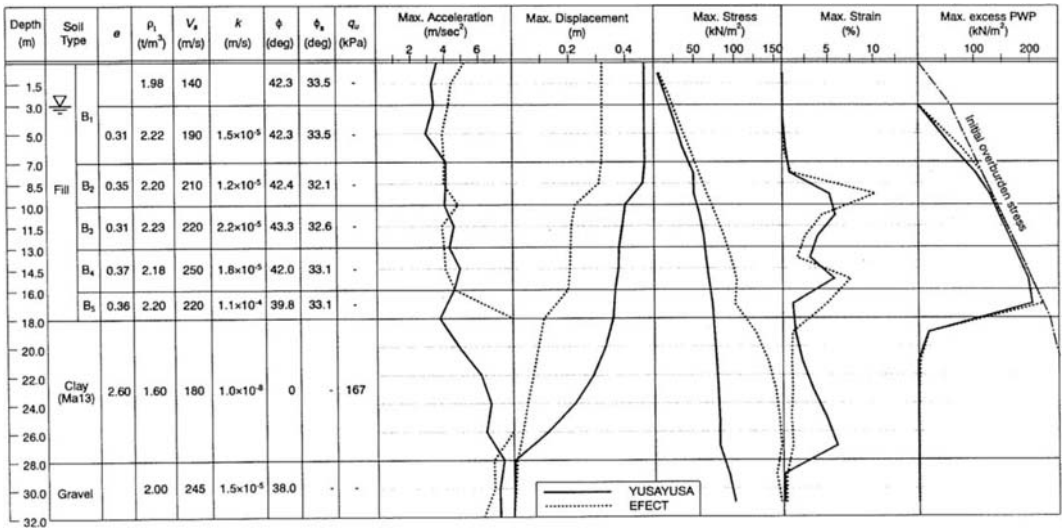

Figure 7. Ground condition for analysis and peak response. ρ_t is mass density, V_s is S-wave velocity, k is permeability, ϕ is internal friction angle, ϕ_s is phase transform angle, q_u is unconfined compressive strength. Peak acceleration greater than 8m/s^2 is omitted.

improved but layer B5 was not improved. Fundamental physical parameters are also shown in the figure.

The model parameters of the improved fill material are determined by simulating the liquefaction strength tests. Those for unimproved material (B5 layer) are determined based on the data by Suzuki et al. (1997) who conducted laboratory tests of frozen sample of the unimproved ground at Port Island that is located about 200m south from the site. Excess porewater pressure generation is not considered in the clay layer and below, but flow of water is taken into account. The hyperbolic stress-strain model is employed by YUSAYUSA-2 for clay layer. Constitutive model same with sand is used by EFECT by setting no excess porewater pressure generation. Results of the simulation of the liquefaction strength test are shown in Figure 8.

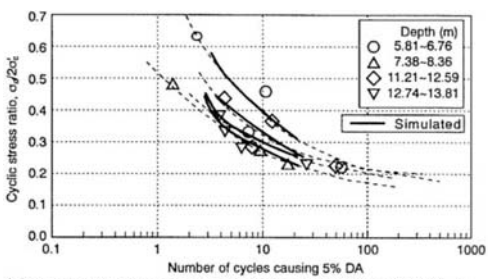

(a) Liquefaction strength test by YUSAYUSA-2

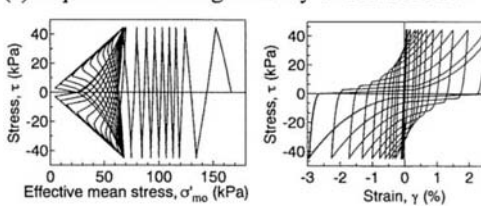

(b) Simulation by EFECT

Figure 8. Simulation of element test

5 RESULTS AND DISCUSSION

Peak responses are shown in Figure 7, acceleration time histories are shown in Figure 9, excess porewater pressure and excess porewater pressure ratio (excess porewater pressure divided by initial effective overburden stress) are shown in Figure 10, and stress path and stress-strain relationships are shown in Figure 11. Here calculations are conducted up to about 41 seconds, but only responses until 20 seconds are shown in the figure because response after that is less important in the discussion in this paper.

Acceleration at the ground surface becomes very small after 6 seconds in YUSAYUSA-2 and 10 seconds in EFECT. This indicates that liquefaction may occur under the ground. Actually, as seen in Figure 10, excess porewater pressure ratio reaches nearly unity at several layers at about 6 and 10 seconds, respectively. Maximum excess porewater pressure distribution in Figure 7 indicates that two layers just below the water table are not liquefied, but the rest layers liquefy.

If above two layers (4m thick) do not liquefy, thickness of the non-liquefied layer becomes 7m in total including the subsoil above the water table.

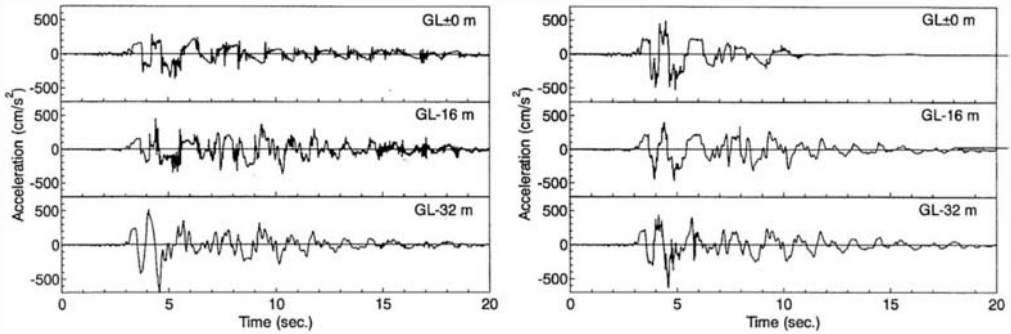

(a) YUSAYUSA (b) EFECT

Figure 9. Acceleration time history

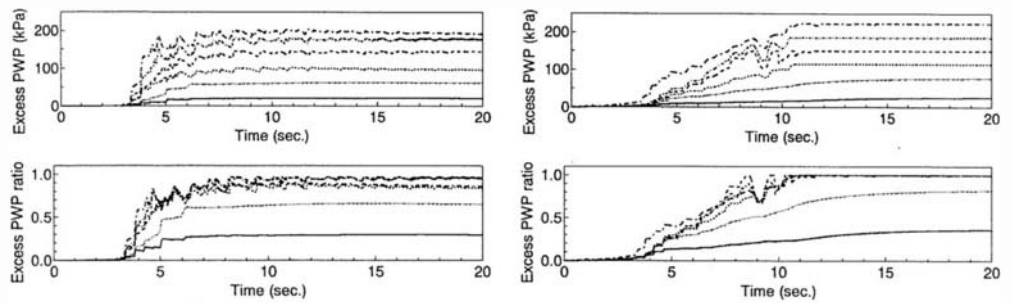

(a) YUSAYUSA (b) EFECT

Figure 10. Excess porewater pressure time history. Layers 3, 4, 5, 7, 9 and 11 are shown.

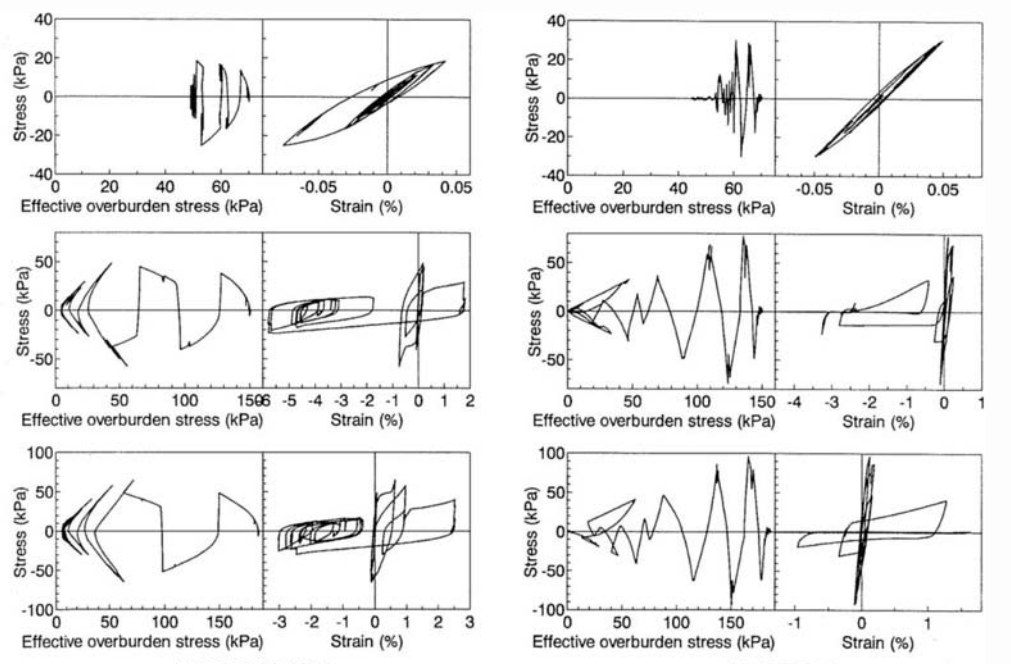

(a) YUSAYUSA (b) EFECT

Figure 11. Stress path and stress-strain relations. Layers 3, 7 and 9 from the above.

Therefore, it is not surprising that neither large ground deformation nor evidence of liquefaction such as sand boil was observed. Moreover, considering that all factories are one-storied structure therefore the weight is light, damage to factories may not be hardly observed. Differential settlement at the C-factory can be recognized if degrees of liquefaction is different because of the existence of old breakwater. It is noted that there may be another explanation on this damage. An employee reported that settlement became more severe at the rising tide with sound of water flow near the old breakwater on the day of the earthquake. The soil near the old breakwater may be washed out resulting in settlement. Even if this is true, it also indicates that something, probably large ground deformation, occurred in the subsoil because rising tide has been daily phenomena.

As seen in the stress-strain relationships and stress path in the third layer in Figure 11, layer 3 is recognized to be far from liquefaction. There may be two reasons why liquefaction did not occur near the water table. The one is that liquefaction strength is larger than the other, and the other is that input motion deamplified very much because lower layer liquefied quickly. As shown in Figure 4, liquefaction strength at B1 layer is the largest. At the same time, however, excess porewater pressure ratio increases faster in the lower layer. Therefore, both reasons worked so that liquefaction did not occur in the upper layers.

The behavior of the fill computed by two computer codes is nearly the same. Peak accelerations are about $4m/s^2$. Relative displacement within the improved thickness is about 10cm. Maximum shear strain is about 10 %. Shear strains are especially large at 6, 7 and 10th layers. There are some differences in the behavior in the clay layer, probably because of the difference of the constitutive model; maximum shear strain reaches about 5% and decreases upward in YUSAYUSA-2 whereas they are nearly constant to be a little less than 1% in EFECT. It is also interesting that maximum shear strain in B5 layer, unimproved layer, is less than above improved layer, which probably occurred because of the excess porewater pressure dissipation.

6 CONCLUDING REMARKS

Liquefaction on the improved ground in Port Island is investigated. Through the numerical analysis, it is concluded that liquefaction occurred at the deep layer of the improved region, but it did not occur near the water table. Because the thickness of the non-liquefied layer including layers above the water table was about 7 meters, it is not surprising that evidence of liquefaction did not appear at the ground surface and factories was not damaged even if liquefaction occurred. It is also noted that displacement is much smaller in the improved area than that in the unimproved area (Geotechnical Research Collaboration Committee, 1998) although liquefaction occurred at both sites. These observations indicate that soil improvement by compaction is effective to reduce liquefaction-induced damage.

AKNOWLEDGEMENT

This research was conducted as a part of the activity in the Geotechnical Research Collaboration Committee on the Hanshin-Awaji Earthquake Disaster. The authors with to thank those who discussed in the committee.

REFERENCES

Geotechnical Research Collaboration Committee on the Hanshin-Awaji Earthquake Disaster. 1998: Report of Activity, 347p. (in Japanese)

Hamada, M., Isoyama, R. & Wakamatsu, K. 1995. The 1995 Hyogoken-Nanbu (Kobe) earthquake, liquefaction, ground displacement and soil condition in Hanshin area, *ADEP*, 194p.

Inagaki, H., Iai, S., Sugano, T., Yamazaki, H. & Inatomi, T. 1996. Performance of caisson type quay walls at Kobe port, Special Issue on Geotechnical Aspects of the January 17 1995 Hyogoken-Nanbu Earthquake, *Soils and Foundations*: 119-136

Ishihara, K. & Towhata, I. 1980. One-dimensional Soil Response Analysis during Earthquake Based on Effective Stress Method, *Journal of the Faculty of Engineering, The University of Tokyo,* XXXV (4),. 656-700

Ito, K. 1995. EFECT: the code of effective stress analysis (Part I) - basic theory and constitutive model of soils, *Obayashi Corp. Technical Research Report*, 51: 7-14 (in Japanese)

Suzuki, Y., Hatanaka, M. & Uchida, A. 1997. Drained and undrained shear strengths of a gravelly fill of weathered granite from Kobe Port Island, *Jour. of Structural and Construction Engineering, Transactions of AIJ*, 498: 67-73 (in Japanese)

Yasuda, S., Ishihara, K., Harada, K. and Shinkawa, N. 1995. Effect of soil improvement on ground subsidence due to liquefaction, *Special Issue on geotechnical aspects of the January 17 1995 Hyogoken-Nambu earthquake, Soils and Foundations*, 99-107

Yoshida, N. and Towhata, I. (1991): YUSAYUSA-2 and SIMMDL-2, theory and usage, *Sato Kogyo and University of Tokyo*, revised in 1995

Yoshida, N. (1995): Earthquake Response Analysis at Port Island during the 1995 Hyogoken-nanbu Earthquake, *Tsuchi-to-Kiso*, 43 (10): 49-54 (in Japanese)

Earthquake Geotechnical Engineering, Sêco e Pinto (ed.) © 1999 Balkema, Rotterdam, ISBN 90 5809 116 3

Prototype piezovibrocone for evaluating soil liquefaction susceptibility

Craig M. Wise
Black and Veatch, Overland Park, Kans., USA

Paul W. Mayne & James A. Schneider
Civil and Environmental Engineering, Georgia Institute of Technology, Atlanta, Ga., USA

Keywords: liquefaction, earthquake, CPT, cone penetration test, piezocone, vibrocone, in-situ testing

ABSTRACT: A piezovibrocone has been developed for the evaluation of soil liquefaction susceptibility by inducing localized cyclic pore pressures while concurrently measuring dynamic resistances. The device couples a triple-element penetrometer with a pneumatic solenoid. This piezovibrocone offers a number of advantages over its predecessors including downhole vertical oscillation, adjustable dynamic force and frequency of excitation, and the simultaneous measurement of porewater pressures at multiple positions. Initial field trials in the historic earthquake region of Charleston, South Carolina indicate the unit is capable of generating and measuring excess cyclic pore pressures in liquefiable soils.

1 INTRODUCTION

Current geotechnical practices for identifying liquefiable soil strata involve empirical relationships based on databases specific to narrow geographic regions. Due to the large uncertainties involved in selecting the proper correction factors, those analyses often result in low confidence levels. The piezovibrocone penetrometer is intended to improve geotechnical earthquake hazard analyses by directly measuring the free-field dynamic soil response in-situ. It is intended that the vibrocone will provide a rational means of evaluating soil liquefaction susceptibility, as well as the post-cyclic residual undrained shear strength.

2 CURRENT METHODS OF EVALUATING SOIL LIQUEFACTION POTENTIAL

Seismic analyses of soil deposits include laboratory testing and field investigation. Laboratory cyclic triaxial and cyclic simple shear tests on cohesionless materials rely on obtaining high-quality samples. Preservation of the soil structure by freezing is very costly and not readily available for use on routine projects. Moreover, the utilization of cyclic lab tests relies on a number of empirical modifiers that attempt to account for initial stress state (K_o), overburden stress level (K_σ), depth effect, number of cycles to failure (N_f), and accumulated strains. Effects of aging, sampling disturbance, inherent fabric, and re-establishment of the in-situ stress state are difficult to take into account.

Accordingly, for most projects, the greatest weight in the assessment of liquefaction potential is given to the results of field in-situ tests. To date, the standard penetration test (SPT) has been most widely used for this purpose. Unfortunately, the number of corrections that must be made to the raw data from even the most carefully conducted tests leads to similar difficulties as noted for lab methods. The SPT-N value must be modified to include corrections for energy efficiency, overburden stress level, fines content, borehole diameter, barrel liner, rod lengths, aging, and other factors (Skempton 1986; Kulhawy & Mayne 1990; Robertson & Wride 1997).

For liquefaction analysis, Seed et al. (1975) established a relationship between the adjusted $(N_1)_{60}$ and cyclic stress ratio (CSR = cyclic shear stress normalized to vertical effective stress). The CSR relates earthquake acceleration to the dynamic shear stress of the soil and can be obtained through a simplified procedure by Seed and Idriss (1971):

$$CSR = \frac{\tau_{cyc}}{\sigma'_{vo}} = \frac{\tau_{ave}}{\sigma'_{vo}} \approx 0.65 \frac{a_{max}}{g} \frac{\sigma_v}{\sigma'_{vo}} r_d \qquad (1)$$

where τ_{cyc} = equivalent uniform cyclic shear stress, τ_{ave} = average cyclic shear stress, σ_{vo}' = effective vertical stress, σ_v = total vertical stress, a_{max} = peak ground acceleration, g = gravitational constant, and r_d = stress reduction coefficient accounting for the stiffness of the soil column. The energy-corrected SPT value, normalized to a stress level of one bar and designated $(N_1)_{60}$, is used in the well-known curves for a binary assessment of either "liquefaction" or "no liquefaction" (e.g. Glaser & Chung, 1995; Robertson & Wride, 1997).

More recently, interest has focused on development of CSR curves from the cone penetration test (CPT) for the in-situ evaluation of liquefiable soils (e.g., Suzuki, et al., 1995; Stark and Olson, 1995). The CPT offers several advantages over the SPT including better standardization, a continuous record with depth, and the ability to measure several parameters, including: tip stress q_t, sleeve friction f_s, porewater pressure u_b, and vertical inclination i. However, modification factors for overburden stress level, aging, and fines content are still necessary.

Other in-situ tests have been correlated for use in liquefaction assessment, including the flat plate dilatometer test (Reyna and Chameau, 1991) and shear wave velocity (Andrus and Stokoe, 1996). The seismic cone (Campanella, 1994) produces four measurements, including tip resistance and shear wave, thus allowing two independent evaluation of liquefaction potential. However, since each of the above approaches provide only an empirical indirect assessment, a more rational and direct method was sought using a vibrocone.

3 VIBROCONE CONCEPT

The basic concept of a vibrocone consists of a cone penetrometer with trailing vibrator unit, as shown by Figure 1. Prior versions of a vibrocone device were developed in Japan, Italy, and Canada, and a detailed review is given by Wise (1998). The original model of Japanese vibrocone was built by the Public Works Research Institute (PWRI) that applied a downole horizontal centrifugal force of 32 kgf and operated at a set frequency of 200 Hz (Sasaki and Koga, 1982). Each test required two sister soundings, one static and one dynamic. This was followed by later designs with dynamic forces of 80 and 160 kgf at 200 Hz (Teparaksa, 1987). A similar model developed at ISMES in Italy also used horizontal vibration (Piccoli, 1993).

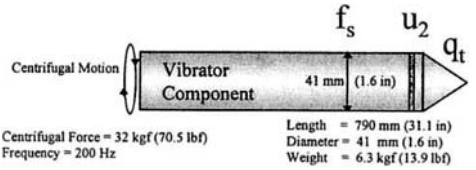

Figure 1. Schematic of the Original Vibratory Piezocone (Sasaki and Koga, 1982)

Previous field studies used simple side-by-side comparisons of static tip resistance (q_{cs}) with the dynamic tip resistance (q_{cd}). Figure 2 illustrates the recorded profiles of q_{cs} and q_{cd} from vibrocone tests at two Japanese sites. For site 1 which historically shows no evidence of sand boils or settlements following earthquakes, both the static and dynamic tip resistances are relatively similar (except for a small localized zone about 3 m deep), inferring no major liquefaction problems. In contrast, the results of vibrocone tests at site 2, which is known to have liquefied repeatedly, illustrate that the dynamic resistance is considerably reduced at depths between 2 to 5 meters, reflecting the contractive nature of the sand deposit and high likelihood of liquefaction.

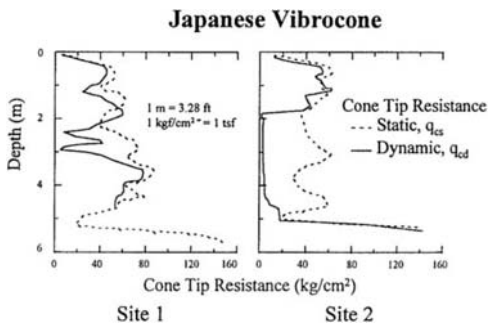

Figure 2. Vibrocone tests (a) at site 1 which shows no apparent damage during seismic events and (b) at site 2 with historical liquefaction evidence following seismic events (modified after Sasaki et al., 1984).

A UBC vibrocone (Moore, 1987) was constructed using an uphole vertical vibrator consisting of an oscillating pair of eccentric counter-weights to the actuator assembly above-hole in the cone rig. The

Table 1. Contributions to the Development of the Vibrocone

Country	Author(s)	Details	Results
Japan	Sasaki & Koga, 1982 Sasaki et al., 1984 (PWRI)	• Down-hole vibration at 200 Hz • 32 kgf horizontal centrifugal force	Reduction in q_c reflected possible liquefiable zones
Japan	Teparaksa, 1987 (PWRI)	• Down-hole vibration at 200 Hz • 80 kgf horizontal centrifugal force	Compared sister sets of static and dynamic soundings
Canada	Moore, 1987 (UBC)	• Vibration applied at top of rods • Vertical force at 75 Hz frequency	Shoulder pore pressures did not identify liquefiable layers
Italy	Mitchell, 1988 Piccoli, 1993 (ISMES)	• Down-hole horizontal vibration • 200 Hz	Qualitative interpretation

electric power for the vibrator was coupled with the rig power, causing fluctuations in the operating frequency. Tests in a silt showed a reduction in q_c, but a shoulder element did not show evidence of excess pore pressures.

4 VIBROCONE DESIGN

Under funding from the USGS and NSF, the development and calibration of a piezovibrocone penetrometer has been initiated in a joint research program at Georgia Tech and Virginia Tech (Wise, 1998). The new vibrocone is an improvement over prior vibrocones for the following reasons:

- Dynamic motion is downhole to prevent energy losses associated with uphole vibrators, as used on the prior UBC version.
- Motion is directed vertically to prevent gapping at the soil-cone interface, as the horizontal centrifugal oscillations of the prior PWRI and ISMES vibrocones likely compromised the axial CPT measurements.
- Midface (u_1) and shoulder (u_2) porewater pressures are measured together.
- The unit allows for control of dynamic force at lower frequencies (5 to 30 Hz).

Seismic strong motion records from most earthquakes show a spike in their power spectra at frequencies of 1 to 5 Hz, yet previous vibrocones operate at frequencies of 75 to 200 Hz, which are considerably higher. Therefore, from an operational standpoint, a lower frequency vibro-unit was desired having adjustable force excitation.

For the initial design, a downhole pneumatic system was built to offer simplicity in operation and economy in construction. Impulse-type loading was used for the initial trials. Two units were needed, one for field use by Georgia Tech and one for CPT calibration chamber testing at Virginia Tech. For chamber calibration tests, a 15-cm^2 triple-element piezocone was donated by Fugro Geosciences. This allows for the simultaneous measurement of cumulative cyclic pore pressures at three locations: midface (u_1), behind the tip (u_2 or u_b), and behind the sleeve (u_3). For initial field trials, a 10-cm^2 Davey-type piezocone with a single midface (u_1) porous element was used.

The fabricated prototype attached to the triple-element piezocone is illustrated in figure 3. Key resistance parameters are measured, including tip resistance (q_c), sleeve friction (f_s), multiple porewater pressures (u), and frequency content of excitation. Both an HP oscilloscope and spectrum analyzer have been used for the latter.

The vibratory module consists of a solenoid valve, air cylinder, an impact mass, velocity geophone, a housing assembly, and nitrogen gas. An electronic timer provides electrical pulses to a solenoid valve which opens and closes at the rate dictated by the timer setting. The solenoid pressurizes the air piston which in turn drives the excitation. Two modes of excitation are available to increase the versatility of the unit and range of applicability of the results. One mode is driven by a spring-mass oscillation and another uses impulse with an impacting mass. To measure the applied force and frequency, a small OYO Model 14-L9 geophone is installed in the unit. In future designs, an inexpensive micromechanical system (MEMS) will be used to measure dynamic accelerations. In lieu of an oscilloscope or analyzer, the MEMS can be read directly using a notebook computer.

Without reconfiguring the vibrator, the dynamic force can be adjusted at the control panel by increasing or decreasing the pressure from the tank or compressor. The air cylinder in the prototype has a bore size of 2.7 cm corresponding to a force of 100 kgf at 1.7 MPa pressure. The frequency of excitation can be varied by simply changing the timer setting which is capable of duty cycles from 0.001 seconds to 9999 hours and varied by incre-

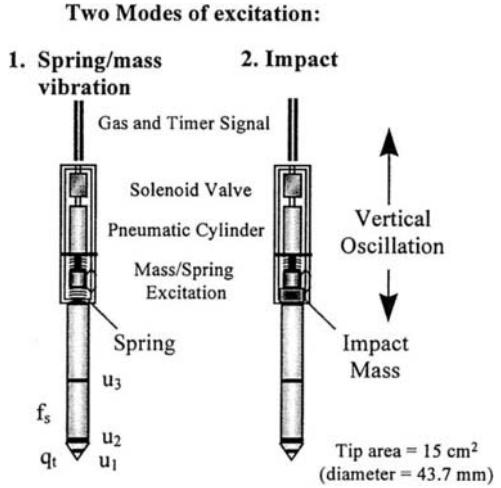

Figure 3. Prototype Pneumatic Impulse Generator and Triple Element Piezocone.

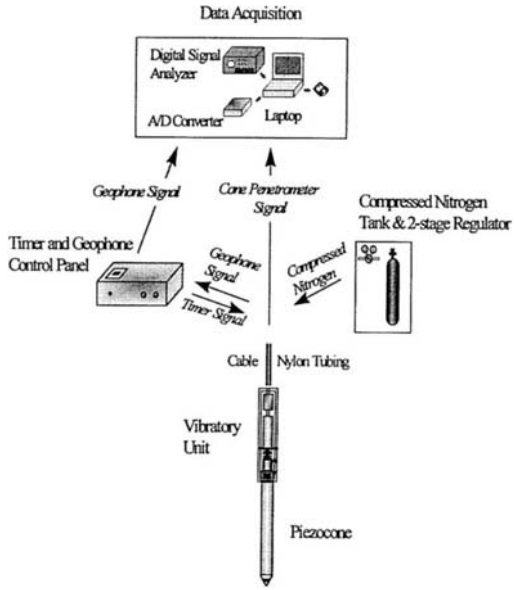

Figure 4. Components of the Vibrocone System

ments of 0.001 seconds. The solenoid is rated to perform adequately at duty cycles down to 60 per second. Note that calling the timer setting a 'frequency' is not quite accurate. The timer setting is actually a duty cycle for which the frequency content of the system can be determined by performing a Fourier analysis on the voltage versus time data. A spectrum analyzers has also been used to determine the frequency content in real-time. Figure 4 illustrates the various piezovibrocone components.

5 FIELD PERFORMANCE

The impulse vibrocone system has been tested to check its ability in generating excess porewater pressures. The device was advance in historically-liquefiable sands in a series of soundings near Charleston, South Carolina, USA. This seismic region was selected for trial soundings with the piezovibrocone due to the noted abundance of mapped paleoliquefaction features resulting from the Charleston Earthquake of 1886 with M = 7.5 to 7.7 (Martin & Clough, 1994).

The specific test site locations were based upon the prior documentation of accessible sites where prior SPT, CPT, and grain size information was reported (Martin & Clough, 1990). Gregg In-Situ, Inc. of Aiken, South Carolina provided a 25-tonne cone truck and an electronic 10-cm^2 seismic piezocone with a porous element at the u_2 (shoulder) position. These data provided a baseline reference for comparison with both static and dynamic soundings for the vibrocone penetration test (VCPT).

The Charleston site selected was the Thompson Industrial Services in the Atlantic coastal plain region of South Carolina. The area is of minimal relief and low elevation and comprised of sandy sediments deposited between 130,000 to 230,000 years ago. The water table was within 1.5 m of the ground surface. Based on published first-hand accounts and field reconnaissance, the extent of liquefaction due to the Charleston Earthquake had been characterized as extensive and moderate at the Ten Mile Hill and Eleven Mile Post sites, respectively (Martin and Clough, 1994).

Static reference soundings were performed with both with an electronic ConeTec (type 2) piezocone and the electric Davey (type 1) piezovibrocone (see Figure 5). The tip stresses and sleeve resistances indicate favorable comparisons between the two soundings. The midface u_1 readings mirrored the shoulder u_2 measurements, yet midface pressures were generally above hydrostatic while shoulder pressures were slightly below hydrostatic conditions.

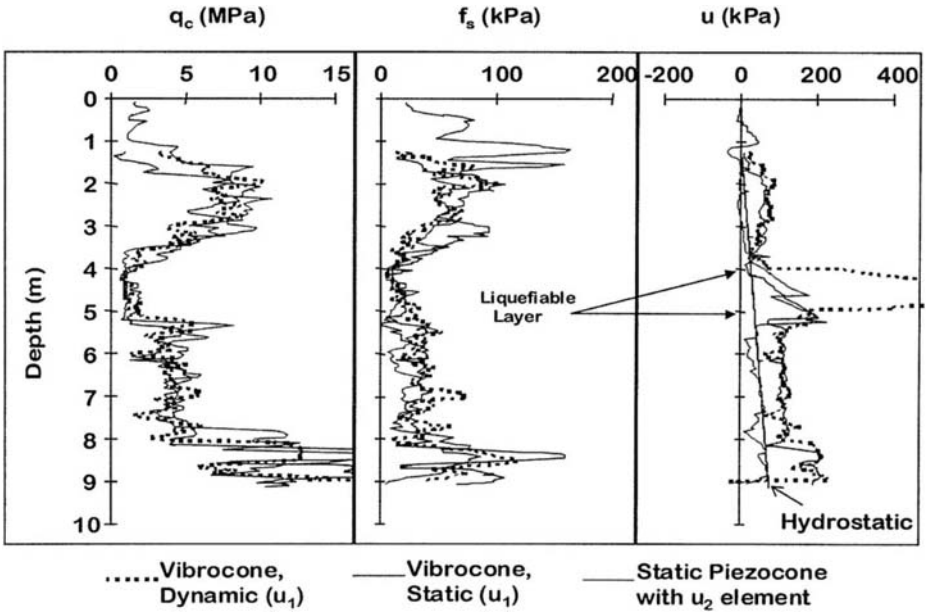

Figure 5. Vibrocone Results Compared with Reference Type 1 and Type 2 Piezocone Soundings at the Thompson Industrial Site in Charleston, South Carolina, USA.

This observation is consistent with static piezocone results reported in clean sands (Robertson, et al. 1986).

Adjacent to these two static tests, a dynamic sounding was also performed using the vibro-unit at 5 Hz, thus completing a VCPT. At depths of between 3.5 to 5.1 meters, Fig. 5 shows a significant spike in the porewater pressure response of the dynamic sounding. It is believed that this indicates a zone of liquefiable soil. Moreover, it can be seen that tip resistances for all three soundings were relatively low in this zone, but the dynamic tip resistance (VCPT) does not noticeably fall below either of the tip resistances from the two PCPTs. Noteably, however, a complete and rational interpretation for the VCPT will require a complex consideration of all possible responses for the loading conditions, including those due to static liquefaction, steady-state, quasi-liquefaction, cyclic mobility, as well as dilatant behavior of soils, as planned in future studies (Schneider et al. 1998). The measured q_t and u readings, in fact, may reflect totally different portions of the induced effective stress paths.

6 SUMMARY

A specialzed in-situ tool, termed the piezo-vibrocone, has been constructed for the direct evaluation of soil liquefaction potential on site-specific projects. The device utilizes a multi-element piezocone coupled with a downhole impulse vibro-unit operating vertically at low frequencies. Preliminary trials in historically-liquefied sands of the Charleston seismic region show generation of cyclically-induced porewater pressures. Additional improvements are ongoing in producing more uniform and sinusoidal forces, dynamic stress measurements, and controlled soil conditions involving large calibration chamber testing.

7 ACKNOWLEDGMENTS

The authors thank Dr. John Unger of USGS and Dr. Cliff Astill of NSF for funding this project. Appreciation is also due to Recep Yilmaz and Rick Klopp at Fugro Geosciences, Brad Pemberton at Gregg In-Situ, and Tracy Hendren at GT, as well as our VT colleagues, J.K. Mitchell, T.L. Brandon, and J. Bonita.

REFERENCES

Andrus, R.D. and Stokoe, K.H. (1997), "Liquefaction resistance based on shear wave velocity. *Proceedings*, Workshop on Evaluation of Liquefaction Resistance, Report NCEER-97-0022, Buffalo, NY, 89-128.

Campanella, R.G. and Robertson, P.K., (1988). "Current Status of the Piezocone Test," *Penetration Testing 1998 (ISOPT-1,* Orlando), Vol. 1, Balkema, Rotterdam, 93-116.

Campanella, R.G. (1994). "Field Methods for Dynamic Geotechnical Testing", *Dynamic Geotechnical Testing II,* (STP 1213), ASTM, West Conshohocken, PA, 3-23.

Glaser, S.D., and Chung, R.M., (1995). "Estimation of Liquefaction Potential In-Situ," *Earthquake Spectra,* Vol. 11, No. 3, 431-455.

Kulhawy, F.H., and Mayne, P.W., (1990). "Manual on Estimating Soil Properties for Foundation Design," *Report EL-6800,* Electric Power Research Institute, Palo Alto, 306 pp.

Martin, J.R., and Clough, G.W. (1990). "Implications from a Geotechnical Investigation of Liquefaction Phenomena Associated with Seismic Events in the Charleston, SC Area," *USGS Report,* No. 14-08-001-G-1348, 414 p.

Martin, J.R. and Clough, G.W. (1994). "Seismic Parameters from Liquefaction Evidence". *Jour. of Geotechnical Engrg.* 120 (8), 1345-1361.

Mitchell, J.K. (1988). "New Developments in Penetration Tests & Equipment", *Penetration Testing 1988*, Vol. 1, Balkema, Rotterdam, 245.

Mitchell, J.K., and Brandon, T.L., (1998). "Analysis & Use of CPT in Earthquake and Environmental Engrg.," *Geotechnical Site Characterization*, Vol. 1, Balkema, Rotterdam, 69-97.

Moore, D.M. , (1987). "Evaluation of the Cone Penetrometer & Its Effect on Cone Bearing and Pore Pressure," *BS Thesis,* Civil Engineering, Univ. of British Columbia, Vancouver, 73 pp.

Piccoli, S., (1993). "ISMES Vibrocone," *Personal correspondence* from ISMES, Bergamo, Italy.

Reyna, F. and Chameau, J.L., (1991). "Dilatometer Based Liquefaction Potential of Sites in the Imperial Valley" *Proceedings*, 2nd Intl. Conf. on Recent Advances in Geotechnical Earthquake Engineering and Soil Dynamics, St. Louis, Vol. 1, 385-392.

Robertson, P.K., and Wride, C.E., (1997). "Cyclic Liquefaction Potential and Its Evaluation Based on the SPT and CPT," *Proceedings,* Workshop on Evaluation of Liquefaction Resistance, NCEER-97-0022, Buffalo, NY, 41-87.

Robertson, P.K., Campanella, R.G., Gillespie, D., and Greig, J., (1986). "Use of Piezometer Cone Data," *Use of In Situ Tests in Geotechnical Engineering*, (GSP 6), ASCE, Reston, VA, 1263-1280.

Sasaki, Y., and Koga, Y., (1982). "Vibratory Cone Penetrometer to Assess the Liquefaction Potential of the Ground," *Proceedings*, 14th U.S.-Japan Panel on Wind and Seismic Effect, NBS Special Pub. 651, Washington D.C., 541-555.

Sasaki, Y., Itoh, Y., and Shimazu, T., (1984). "A Study of the Relationship Between the Results of Vibratory Cone Penetration Tests and Earthquake-Induced Settlement," *Proceedings,* 19th Annual Meeting of Japanese Society of Soil Mechanics & Foundation Engrg., Tokyo.

Schneider, J.A., Mayne, P.W., Hendren, T.L., and Wise, C.M. (1998). "Initial Development of an Impulse Piezovibrocone for Liquefaction Evaluation". Proceedings, Intl. Workshop on Physics & Mechanics of Liquefaction, Johns Hopkins Univ., Balkema, Rotterdam.

Seed, H.B., and Idriss, I.M., (1971). "Simplified Procedure for Evaluating Soil Liquefaction Potential," *Journal of Geotechnical Engineering,* Vol. 97, No. 9, 1249-1273.

Seed, H.B., Idriss, I.M., Makdisi, F., and Banerjee, N., (1975). "Representation of Irregular Stress Time Histories by Uniform Equivalent Series in Liquefaction Analysis," *Report No. EERC-75-29,* University of California, Berkeley, 40 pp.

Skempton, A.W., (1986). "Standard Penetration Test Procedures & Effects in Sands of Overburden Pressure, Relative Density, Particle Size, Aging, and OCR," *Geotechnique,* Vol. 36 (3), 425-447.

Stark, T.D. and Olson, S.M. (1995). "Liquefaction Resistance Using CPT and Field Case Histories". *Jour. of Geotechnical Engrg.* 121 (12), 856-869.

Suzuki, Y., Tokimatsu, K., et al. (1995). "Field Correlation of Soil Liquefaction Based on CPT Data, *Proceedings, CPT'95*, Vol. 2, Linkoping, Swedish Geotechnical Society, 583-588.

Teparaksa, W., (1987). "Use and Application of Penetration Tests to Assess Liquefaction Potential of Soils," *Ph.D. Dissertation, Department of Civil Engineering, Kyoto University*, Japan, December.

Wise, C.M., (1998). "Development of a Prototype Piezovibrocone for In-Situ Evaluation of Soil Liquefaction Susceptibility.," *MS Thesis,* Civil & Environmental Engrg., Georgia Tech, Atlanta, March, 176 p.

Earthquake Geotechnical Engineering, Sêco e Pinto (ed.) © 1999 Balkema, Rotterdam, ISBN 90 5809 116 3

Prediction of liquefaction-induced deformations of river embankments

S.Okada, R.P.Orense & Y.Kasahara
Kosi-jiban Consultant Company Limited, Tokyo, Japan

I.Towhata
University of Tokyo, Japan

ABSTRACT: An analytical method that can predict the deformation of liquefied ground is presented which is based on three variational principles of mechanics, i.e., principle of minimum potential energy at state of force equilibrium, the Lagrangean equation of motion, and the Hamilton's principle. The prediction method consists basically of closed-form solutions and requires limited number of input data and short computation time, facilitating its use for practical purposes. Procedures to evaluate the duration of flow and critical damping ratio, two necessary input parameters for the model, are also discussed. The method is applied to simulate the settlement of river embankments during large earthquakes, and the results show a good agreement with observed values. Furthermore, the effectiveness of various countermeasures is assessed using the proposed model.

1 INTRODUCTION

River embankments resting on loose cohesionless soil deposits are highly susceptible to liquefaction-induced damage during earthquakes. Settlements and lateral spreading in the order of several hundreds of centimeters have been observed during recent large earthquakes in Japan, such as the 1993 Hokkaido Nansei-oki Earthquake and the 1995 Hyogoken Nanbu Earthquake. Since the height of river embankment is important in preventing flooding after the occurrence of an earthquake, methodologies to predict the magnitude of liquefaction-induced deformation of river embankments as well as to assess the effectiveness of countermeasures to mitigate such damage are very important.

This paper presents an analytical tool to predict ground deformation caused by sub-soil liquefaction. The proposed method is characterized by its closed-form solution derived by combining observations from shaking table tests and the principle of minimum potential energy. This method requires limited number of input data which are easily obtainable within the framework of existing field investigation for liquefaction potential, making it a practical tool to predict the potential seismic hazards induced by liquefaction-induced deformation.

To illustrate its capability, the method is employed to simulate the settlements observed in several dikes which were damaged during recent earthquakes in Japan. Moreover, the effectiveness of various liquefaction countermeasures are investigated.

2 THEORETICAL BACKGROUND

2.1 *Model ground*

The closed form solution of the maximum possible displacement is derived for a simple subsoil model shown in Figure 1. The variation of the elevation of the unliquefied stable base, B, the thickness of liquefiable layer, H, the thickness of the surface unsaturated layer, T, and the magnitude of the surcharge which is inclusive of the weight of surface soil, P, vary linearly with the horizontal coordinate, x. Note that the thickness and depth of liquefiable sandy layer can be determined by using SPT N-values and other data through liquefaction potential evaluation procedures as outlined in various design codes (e.g., the Specifications for Highway Bridges, 1996).

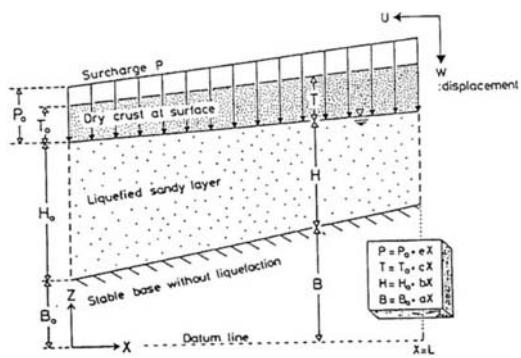

Figure 1 - Model Ground

2.2 *Ultimate displacement*

The lateral displacement of the liquefied soil is assumed to follow a sinusoidal distribution in the vertical section as given by

$$U(x,z) = F(x)\sin\frac{\pi(z-B)}{2H} \tag{1}$$

where $U(x,z)$ is the maximum possible lateral displacement, and $F(x)$ is the lateral displacement at the surface. Conversely, the maximum possible vertical displacement $W(x,z)$ is calculated based on constant volume condition. The settlement caused by consolidation of liquefied sand is calculated separately (e.g., by assuming one-dimensional consolidation).

The surface unsaturated layer behaves as an elastic bar resisting against lateral compression. This layer and the surcharge move together with the top of the liquefied subsoil without slip. The liquefied soil behaves like liquid with negligible shear modulus.

In general, ground with irregular profile is often encountered instead of one with a regular shape as shown in Figure 1. For the method to be directly useful, the irregular section is divided into piece-wise linear segments considering displacement continuity at the interface of the segments. Next, the total potential energy of the ground, Q, is formulated by summing up the strain and gravity components of energy in the liquefied layer and surface unsaturated layer for each segment. After simplification, the total potential energy of the ground, Q, can be derived as a function of the surface displacement $F(x)$, its derivative and the coordinate x.

The principle of minimum potential energy requires the total energy, Q, to be minimum for the true displacement $F(x)$. Therefore, it becomes a typical problem in calculus of variation where the function $F(x)$ which makes the energy functional Q minimum is to be determined. For details of the derivation, the readers are referred to the works by Towhata et al. (1992) and Orense (1992).

2.3 *Time history of displacement*

The maximum possible displacement outlined above refers to the case when a state of lateral flow continues for a sufficiently long period of time. In most cases, however, since the soil flow ceases when seismic shaking stops, the real displacement is smaller than the maximum possible one. Hence, there is a need to consider the effect of time on the displacement. For this purpose, the method of dynamic analysis, schematically shown in Figure 2, is employed in the analysis of the development of displacement with time. Because of space limitation, only the essential features are discussed here, and readers are referred to the papers by Towhata (1995) and Towhata et al. (1997) for details.

The displacement of the liquefied ground at any

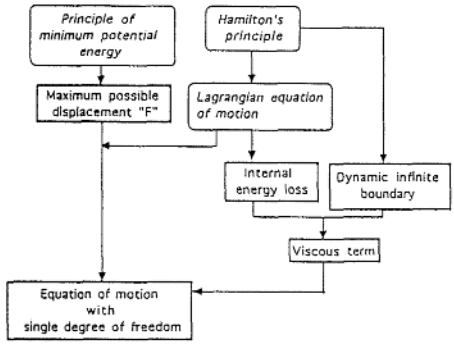

Figure 2: Summary of analytical method

time t is expressed as

$$u(x,z,t) = \lambda(t)U(x,z)$$
$$w(x,z,t) = \lambda(t)W(x,z) \tag{2}$$

where u and w are the horizontal and vertical displacements, respectively. Since the maximum displacements U and W are already obtained from static analysis, the only unknown is the scalar function $\lambda(t)$. The value of λ ranges from zero at $t=0$ (initial condition) to one at $t=\infty$ (flow continues for a long period of time). Thus, the effect of time is separated and the equation of motion for a single degree of freedom system can be developed. The kinetic energy K contributed by both the liquefied subsoil and surface layer can be calculated from Eqn. (2).

The theory of Lagrangean equation of motion for a single degree of freedom system is given by

$$\frac{d}{dt}\left[\frac{\partial\{K-(Q+I)\}}{\partial(d\lambda/dt)}\right]-\frac{\partial\{K-(Q+I)\}}{\partial\lambda}=0 \tag{3}$$

in which K and Q represent the kinetic and potential energies, respectively, I is the energy contribution of the inertial force, and λ is the generalized coordinate. Since u and w are functions of λ, all the energy components can be expressed in terms of λ. Upon simplification, Eqn. (3) can be written as

$$m\frac{d^2\lambda}{dt^2}+k\lambda=-f-r-n\frac{d^2u_b}{dt^2} \tag{4}$$

where m, k, f, r and n are parameters through which the various energy components are expressed, and $d^2(u_b)/dt^2$ is the base acceleration. Note that $k+f+r=0$ because the ultimate stability is attained with $\lambda=1$. Eqn. (4) is a second-order differential equation and can be solved easily.

2.4 *Consideration for energy dissipation*

The analysis of flow using Eqn (4) significantly overestimates the rate of soil movement, and therefore, some sort of energy dissipation mechanism should be incorporated into the above equation. Since shaking

table tests suggest that flow of liquefied ground has a rate-dependent nature (Towhata, 1995), a viscous term given by $c \times d\lambda/dt$ is added to Eqn (4). When liquefied sand is assumed to have a viscosity coefficient η, the viscous term is given by

$$c = \frac{\eta\pi^2}{8}\int_0^L \frac{F^2}{H}dx \qquad (5)$$

Since much is not known regarding the apparent viscous nature of liquefied ground, it is difficult to determine η and use Eqn (5) in practice. As a rational alternative, the value of c is determined by using a critical damping ratio, instead, i.e.,

$$m\frac{d^2\lambda}{dt^2} + c\frac{d\lambda}{dt} + k\lambda = -f - r - n\frac{d^2u_b}{dt^2} \qquad (6)$$

in which

$$c = h \times 2\sqrt{mk} \qquad (7)$$

where h stands for the critical damping ratio. The value of h used in the present analysis will be discussed later.

3 APPLICATION TO RIVER EMBANKMENTS

3.1 *Cases and Input Parameters*

The method outlined in the preceding section is employed in the analysis of the settlements observed in river embankments in two sites, namely: the Shiribeshi-toshibetsu River (1993 Hokkaido Nansei-oki Earthquake) and Yodo River (1995 Hyogoken Nanbu Earthquake). In total, eleven sections were analyzed, six along the Shiribeshi-toshibetsu River, and five adjacent to Yodo River. To facilitate the analysis, each section is divided into two along the centerline of the embankment, and the river-side and land-side sections are analyzed independently.

The relevant input parameters employed in the analyses are listed in Table 1. In the analysis, the liquefied sand is treated as liquid with zero shear modulus and zero residual strength. The thickness of the liquefied layers is determined using the revised liquefaction potential evaluation procedure as outlined in the Specifications for Highway Bridges (1996), with the maximum surface accelerations set as the same as those recorded at nearby stations when the actual earthquakes occurred.

3.2 *Duration time of liquefaction*

The evaluation of the appropriate duration time of liquefaction through which flow can occur is very difficult. Shaking table tests as well as centrifuge tests show that movement stops when seismic shaking ceases. Hence, for the purpose of this study, it is assumed that the duration time of flow, designated as T_{ul}, corresponds to the interval between the occurrence of peak acceleration (corresponding to liquefaction) and the last acceleration peak having a value greater than 50gals (dissipation of pore pressure). This is shown in Figure 3. By analyzing strong motion time histories, a study of the values of T_{ul} computed from many strong motion records might lead to correlations which would further simplify the estimation of appropriate values of T_{ul} for different design earthquakes. To this end, 145 acceleration time histories for 20 earthquakes (6 American earthquakes and 14 Japanese earthquakes) recorded at or near the ground surface were obtained and analyzed to determine the value of T_{ul} indicated for each record.

Table 1: Parameters used in the Analysis

Soil and Earthquake Parameters	Shiribeshi-Toshibetsu	Yodo
Unit Wt. of Surface Layer, γ_t (kN/m^3)	15.7	17.6
Unit Wt. of Liq. Layer, γ_l (kN/m^3)	16.7	17.6
Mod. Of Elasticity, E (kN/m^2)	2060	4800
Earthquake Magnitude, M	7.8	7.2
Critical damping ratio, h	16.5	6.8
Duration of flow, t (sec)	58	25

The values of T_{ul} computed based on the above criterion are plotted and examined with respect to various seismic parameters, such as epicentral distance, earthquake magnitude and magnitude of peak ground acceleration, as well as the soil type (i.e., Type I - $T_G < 0.2$sec; Type II - $0.2\text{sec} \leqq T_G < 0.6$sec; Type III - $T_G \geqq 0.6$sec, where T_G is the predominant period of the ground). The results show that among these parameters, T_{ul} correlates best with earthquake magnitude, and the plot is shown in Figure 4. Also shown is the upper bound for all the data. Since this line provides a reasonable method of estimating the maximum duration of T_{ul}, this line is considered in this study. For comparison purposes, the relations proposed by Lee (1972) and Housner (1965), who also investigated the duration of significant shaking using other criteria, are also shown.

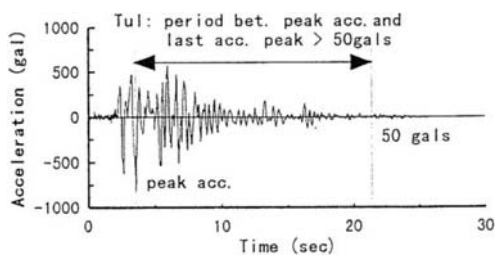

Figure 3: Definition of duration time of flow, T_{ul}

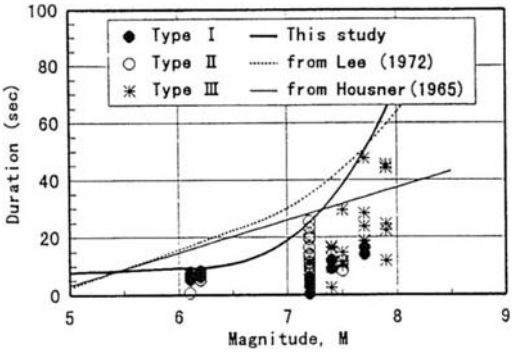

Figure 4: Relation between magnitude and T_{ul}

3.3 *Damping Ratio*

Another parameter required in the analysis but which is difficult to evaluate is the value of the critical damping ratio. This is not an inherent property of the material and should not be confused with hysteretic type of damping usually employed in dynamic analysis. Toyota (1995) performed shaking table tests on very loose sand deposits ($D_r < -10\%$) to determine the values of h which make the calculated displacements fit the observation. His results showed that when flow is induced by impact-type of loading, a value of 0.63 is suitable, whereas when the flow is induced by cyclic shaking, the suitable value of h is dependent on the value of input motion and void ratio of the liquefied sand, as depicted in Figure 5.

In the present analysis, the Lagrangean equation of motion for a single degree of freedom system and given in Eqn. (6) is employed. When the usual case of overdamping ($h > 1$) is considered, the solution to Eqn. (6) is given by

$$\lambda = Ae^{(-h+\sqrt{h^2-1})\omega_o t} + Be^{(-h-\sqrt{h^2-1})\omega_o t} + 1 \quad (8)$$

where $\omega_o = \sqrt{k/m}$. Now, considering the initial condition of $\lambda = d\lambda/dt = 0$ at $t=0$, the constants in Eqn.

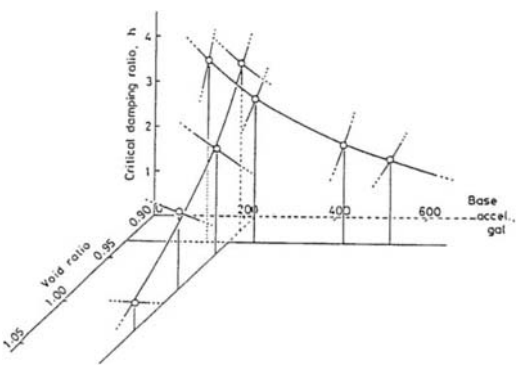

Figure 5: Variation of critical damping with shaking acceleration and void ratio (From Toyota, 1995)

(4) can be solved as

$$\begin{bmatrix} A \\ B \end{bmatrix} = -\frac{1}{2}\left(1 \pm \frac{h}{\sqrt{h^2-1}}\right) \quad (9)$$

From Eqns. (8) and (9), it is noted that there is a linear relation between damping ratio and the factor $\omega_o \times t$ for a specified value of λ. This theory is considered in the analysis of the sites mentioned above. The magnitude of λ is known beforehand, with values ranging from $\lambda = 0.2 \sim 0.8$ for Shiribeshi-toshibetsu River (S-T), and $\lambda = 0.4 \sim 0.5$ for Yodo River. Instead of plotting the factor $\omega_o \times t$ against h, the duration time of liquefaction, T_{ul}, is considered. The variation of damping ratio h with duration time T_{ul} for the sites under consideration is shown in Figure 6. Note that in addition to the sites analyzed, two sections of embankments near Hachirogata River (H-G) which were damaged during the 1983 Nihonkai-Chubu Earthquake are included in the analyses. It is worth mentioning that a longer flow duration is required to achieve a given λ when the damping ratio is high. Although it can be seen that there is a general scatter between the lines representing the sites, the general relation can be represented by the average of these lines, as shown by the bold line in Figure 6. It is hoped that a better line will be obtained in the future when more case studies are performed.

Hence, the duration time of flow and critical damping ratio can be determined from the earthquake magnitude through the use of Figures 4 and 6.

3.4 *Results of analysis*

The boundary conditions used are as follows: (a) at the top of the slope (i.e., at the center of embankment), the lateral displacement is fixed; (b) at the bottom of the slope, infinite condition for the landside, and a fixed boundary at the center of the river on the riverside.

Figures 7 and 8 show the comparison of the observed and calculated settlements for Section No. 1 near Shiribeshi-toshibetsu River and Section No. 2

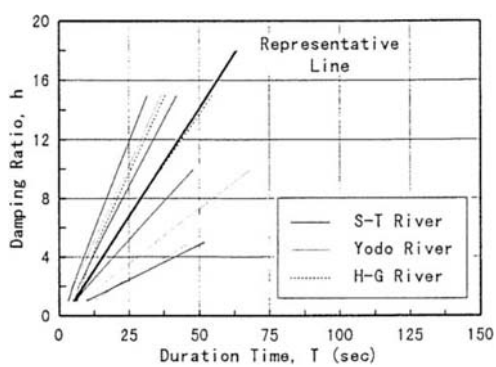

Figure 6: Relation between T_{ul} and damping ratio

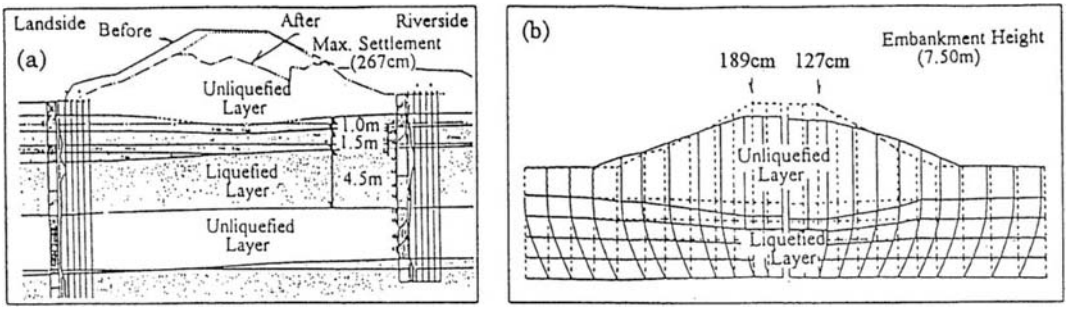

Figure 7: Deformed shape for Section No. 1 of Shiribeshi-toshibetsu River (a) observed ; (b) calculated

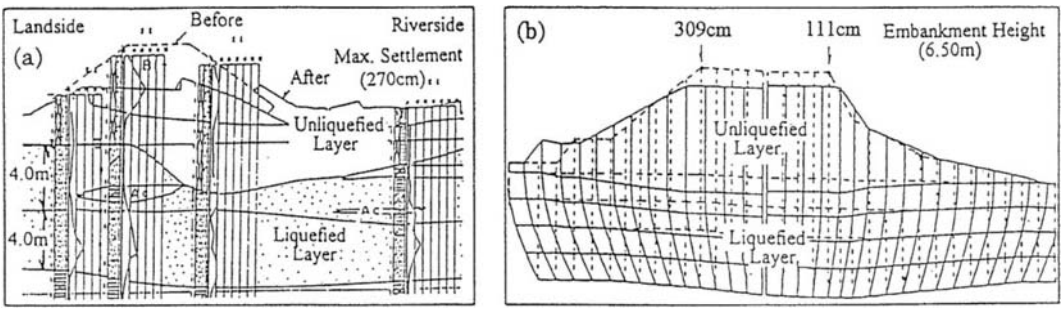

Figure 8: Deformed shape for Section No. 2 of Yodo River (a) observed ; (b) calculated

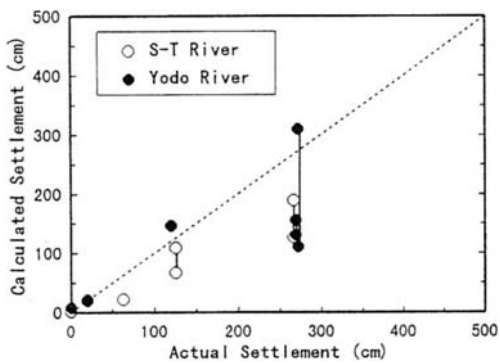

Figure 9: Comparison of actual and calculated values

adjacent to Yodo River, respectively. These cross-sections show the largest observed settlements, i.e., 2.7m. It can be seen that the calculated patterns of displacement are well-simulated and the method was able to simulate such large amount of settlement.

On the other hand, Figure 9 shows a comparison of the observed and calculated settlements at the top of the embankment for the cross-sections analyzed. As mentioned above, two calculated values are presented, one for each half of the cross section. It can be seen that although there is a wide range of calculated values, there is generally a 1:1 relation between the actual and calculated settlements, indicating the applicability of the model.

4 EFFECTIVENESS OF REMEDIAL MEASURES

In addition, the present model is also employed to take into account the presence of various measures usually employed to mitigate damage to river embankments. The presence of such countermeasures can easily be incorporated into the model by adding the strain energy that develops in these structures as a result of flow to the total energy of the whole ground.

4.1 *Cases considered*

In the analysis, Section No. 2 of the Yodo River is considered as the model ground. Seven remedial measures are examined and these are listed in Table 2, together with the input parameters. The boundary conditions are similar to those discussed earlier. Two levels of ground accelerations are employed: Level 1 - 221 gals representing the actual earthquake; and Level 2 - 600 gals for a large-scale earthquake. Note that the earthquake level affects the thickness of liquefiable layer, as well as h and T_{ul}. The duration of liquefaction is set at 20sec for Level 1 and 10sec for Level 2. Critical damping ratios of 1, 2, and 5 are considered.

4.2 *Results of analysis*

A comparison of the results of the analyses in terms of settlement normalized with respect to that of the embankment top for the case of no countermeasure

Table 2: Parameters for analysis of countermeasures

Countermeasure	Type	Soil Parameters	Earthquake Parameters
No Countermeasure (NC)	----------	Unit wt. of surface layer, γ_t=17.6 kN/m^3 Unit wt. of liquefied layer, γ_l=17.6kN/m^3 Modulus of Elasticity, E=4800kN/m^2	Level 1 Eq.: Acc=221gal T_{ul}=20sec Level 2 Eq.: Acc=600gal T_{ul}=10sec
Berm (BC)	50m long, 4m high berm		
Sheetpile (SP)	Type III sheetpile, EI=33750kN-m^2/m		
Berm + Sheetpile (BC+SP)	50m long, 4m high berm + Type III sheetpile, EI=33750 kN-m^2/m		
Compaction Method (SC)	6.4m improved width, ϕ 700mm piles, G=4611kPa		
Solidification Method (HD)	6.4m improved width, G=7652kPa		
Sand Drain Method (SD)	6.4m improved width, τ_r=49kPa		

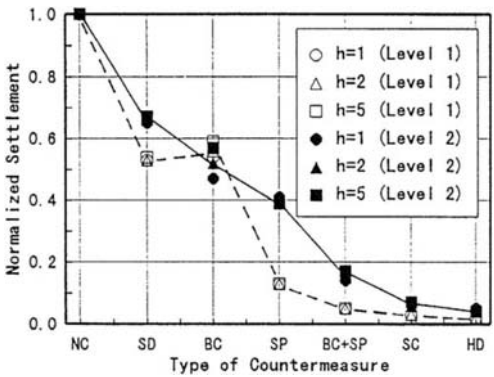

Figure 10: Relation between type of countermeasure and normalized settlement

(NC) is shown in Figure 10. It can be seen that, considering the features of the countermeasures employed in the analysis as listed in Table 2, the settlement at the top of the embankment decreases in the following order: no countermeasure, sand drain, with berm, sheetpile, berm + sheetpile, compaction, and solidification methods. The effectiveness of compaction and solidification methods to mitigate the settlement of river embankments is very evident. In the analysis, the shear moduli of the compacted and solidified portion are set to 4611kPa and 7652kPa. Obviously, any change in the magnitude of the shear modulus of the compacted or solidified ground will reflect on the magnitude of the embankment settlement. Moreover, the residual strength τ_r of the sand drains is set at 49kPa, and the results showed that the computed settlement is in the same order as that of with berm. This assumed value of residual strength may change depending on the permeability and method of construction, and therefore, difference in computed settlement may also occur.

It can also be seen that for both earthquake levels, the effect of damping ratio h on the normalized settlement is negligible. The presence of the berm limited the settlement to only 45~60% of that which would occur without countermeasure, while the sheetpile wall and compaction method reduce the settlement to only 15~40% and 2~8%, respectively, for both Level 1 and Level 2 earthquakes.

5 CONCLUDING REMARKS

A theory of prediction of ground displacement induced by soil liquefaction is presented based on three variational principles: minimum potential energy, Lagrangean equation of motion and Hamilton's principle. The method is applied to the analysis of settlements of river embankments observed during recent earthquakes, and the calculations show generally good agreement with the measured values. Also, the applicability of the method when employed for the evaluation of the effectiveness of various liquefaction countermeasures is also presented.

REFERENCES

Japan Road Association (1996). Specifications for Highway Bridges, Part V: Earthquake Resistant Design (in Japanese)

Housner, G.W. (1965). "Intensity of Earthquake Ground Shaking Near the Causative Fault," Proc. 3rd WCEE, Vol. III, 94-115.

Lee, K.L. (1972). "Number of Equivalent Significant Cycles in Strong Motion Earthquake," Proc., International Conference on Microzonation, Seattle, 609-627.

Orense, R. (1992). Modeling of Permanent Displacement of Liquefied Ground and its Effects on Structures," Doctoral Thesis, University of Tokyo.

Towhata, I., Orense, R. and Toyota, H. (1997) Mathematical Principles in Prediction of Lateral Ground displacement Induced by Seismic Liquefaction," Soils and Foundations (accepted for publ.).

Towhata I, Sasaki Y., Tokida, K., Matsumoto, H., Tamari, Y., and Saya, A. (1992). "Prediction of Permanent Displacement of Liquefied Ground by Means of Minimum Energy Principle," Soils and Foundations, Vol.32, No.3, 97-116.

Towhata, I. (1995). "Liquefaction and Associated Phenomena," Theme Lecture, First International Conference on Earthquake Geotechnical Engineering, Tokyo, Vol. 3, 1411- 1434.

Toyota, H. (1995). "Shaking Table Tests and Analytical Prediction on Lateral Flow of Liquefied Ground, " Doctoral Thesis, University of Tokyo.

Earthquake Geotechnical Engineering, Sêco e Pinto (ed.) © 1999 Balkema, Rotterdam, ISBN 90 5809 116 3

Resistance against liquefaction of ground improved by sand compaction pile method

J.Ohbayashi, K.Harada & M.Yamamoto
Geo Engineering Division, Fudo Construction Company Limited, Japan

ABSTRACT: This paper describes a quantitative evaluation of the resistance against liquefaction of ground improved by sand compaction pile (SCP) method, based on data of ground behavior at sites that have suffered large scale earthquakes. Further, as factors behind the differences seen between improved and non-improved ground in earthquake-caused damage, it examines the coefficient of earth pressure at rest in SCP-improved ground and the distribution of ground strength in sand piles and the surrounding compacted ground. It also reviews the evaluation of the resistance against liquefaction of ground improved by SCP method.

1 INTRODUCTION

Compaction methods have been widely used as a countermeasure against liquefaction in Japan. Sand compaction pile (SCP) method is considered one of the most reliable of these methods and it has been widely adopted for ground improvement. Its effectiveness has been confirmed at sites that have suffered earthquakes in recent past, as shown in Fig. 1. However, in the evaluation of the earthquake-resistance of ground compacted by SCP method, much remains unclear.

This paper makes a quantitative estimation of the liquefaction-resistance of ground improved by compaction, using data, including earthquake intensity and SPT N-values (N-values), from sites that have suffered a large scale earthquake in the recent past. An investigation was also carried out into differences between improved and unimproved ground, and the factors contributing to them.

Further, as the cause for such differences, the increase in earth pressure (coefficient of earth pressure at rest, K_0) specific to ground improved by SCP method was examined, as well as the distribution in strength across improved ground comprising sand piles and compacted ground.

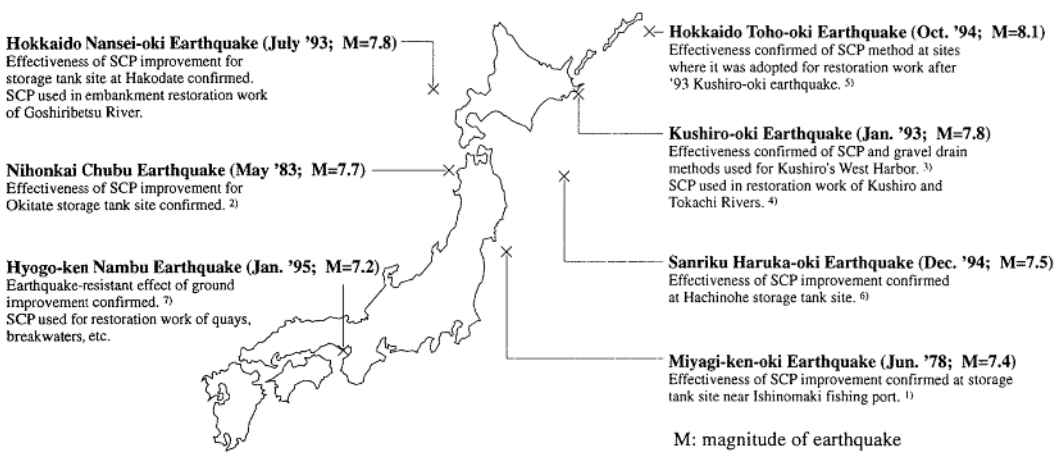

Fig. 1 Sites suffered recent past large scale earthquakes and SCP improvement works

2 EVALUATION OF IMPROVED GROUND BY SCP METHOD

As Fig 1 shows, the effectiveness of SCP method of ground improvement as a countermeasure against liquefaction has been demonstrated at sites that have suffered large scale earthquakes. Although liquefaction has been observed in surrounding ground, the fact that no damage has been observed in the improved ground has largely been made as a qualitative assessment, and only in very few cases has a quantitative evaluation been made of the degree to which the ground improvement has shown resistance against liquefaction.

On the resistance against liquefaction of ground compacted by SCP method, Tokimatsu et al[8] have collected the in-situ frozen sample (high-quality undisturbed sample) and undertaken cyclic triaxial tests. Based on these results, Yoshimi[9] has shown ductile behavior in that strain amplitude in the sand increases only moderately when the intensity of earthquake ground motion is increased significantly beyond a design value. Thus, compared with actual ground (or laboratory specimens) with the same level of relative density, sandy ground compacted by SCP method shows a much greater resistance against liquefaction. The factors contributing to this increase in resistance against liquefaction due to SCP method are thought to be: 1 an increase in density, 2 an increase in horizontal effective stress, and 3 the stabilizing of the microscopic structure through cyclic shear.

Table 1 Data of sites suffered recent past large scale earthquakes

Earthquake	Max. acceleration at ground surface (gal)		Number of boring	Improvement specs: △ triangular grid □ square grid
Nihonkai Chubu	200		1	SCP △ 2.0 m
Sanriku-Haruka-oki	A	440	1	SCP □ 1.5 m
	B	600	2	SCP △ 1.9 m
	C	600	3	SCP △ 1.9 m
	D	600	6	SCP △ 1.9 m
Hokkaido Nansei-oki	220		3	SCP □ 1.5 m
Hokkaido Toho-oki	200		4	SCP □ 1.7 m

Table 1 gives data on ground improvement sites that have suffered recent past large scale earthquakes, and Fig. 2 shows depth distributions of N-values for compacted ground at those sites where there was no

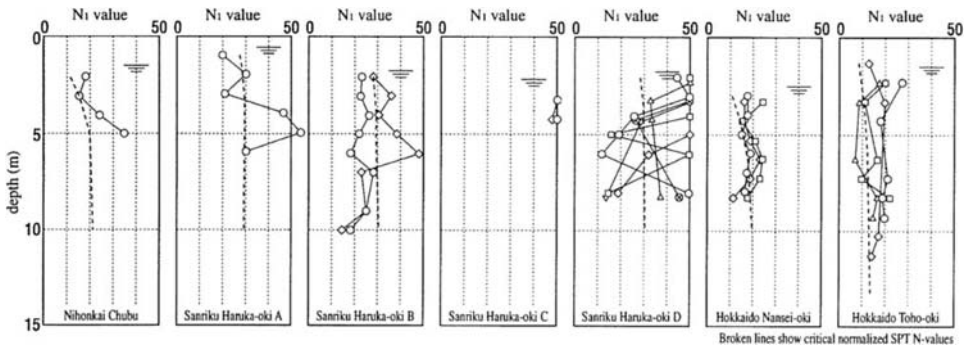

Fig. 2 Distribution of normalized SPT N-values (after improvement)

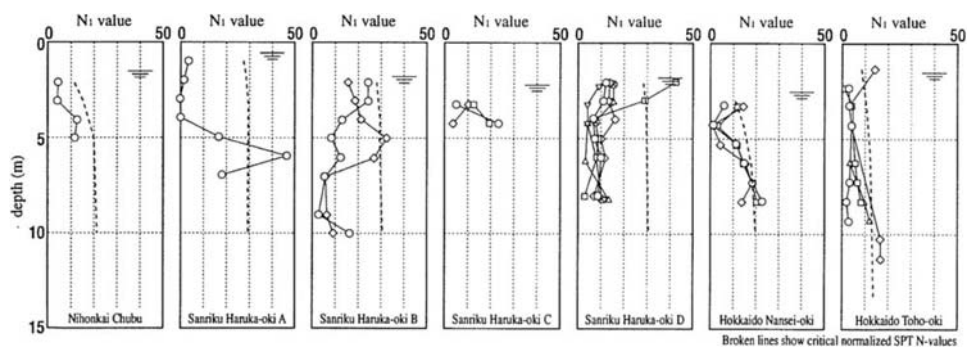

Fig. 3 Distribution of normalized SPT N-values (before improvement)

evidence of liquefaction. The N-values were taken for compacted ground of inbetween sand piles, relatively soon (between 1 and 4 weeks) after the compaction work, and to avoid the influence of confining effective stress, equation (1) was used to standardize the figures per 98 kN/m^2 (1kgf/cm^2) to N_1 (normalized SPT N-values). The data shown is limited to that for which the ratio of fine content is less than 20%. Boring data from the same sites before improvement is shown in Fig. 3. The figures show that the effect of the SCP work was to increase N-values by roughly 10 to 20. Figs. 2 and 3 also show a depth distribution of critical N-values. These were calculated from the relation between N_1 values and resistance strength against liquefaction in alluvial sandy ground shown by Matsuo[10], and its relation to the dynamic shear stress ratio obtained using equation (2) from the maximum surface acceleration recorded near each site.

$$N_1 = \frac{1.7N}{\frac{\sigma_v'}{98} + 0.7} \quad (1)$$

$$\frac{\tau_{max}}{\sigma_v} = (1 - 0.015z)\ \frac{\alpha_{max}}{g}\ \frac{\sigma_v'}{\sigma_v} \quad (2)$$

where,

τ_{max} : maximum cyclic shear stress (kN/m^2)

σ_v : total overburden pressure (kN/m^2)

σ_v' : effective overburden pressure (kN/m^2)

z : depth (m)

α_{max} : maximum surface acceleration (gal)

g : acceleration gravity (=980gal)

In the before-improvement state, almost all values ar consistently lower than the critical N-values, wherea after improvement some exceed the critical N-value

In order to clarify this relation, Figs 4 and 5 sho the relation between N_1 values and the dynamic shea stress ratio estimated to have applied at that point, be fore and after improvement. These figures show N values for alluvial sandy ground established by Matsu and a suggested line marking the strength of resistanc against liquefaction. Comparing the two, as for th strength before improvement, there are many plots i the area where liquefaction is likely to occur (left o the suggested line), and this conforms with the fac that traces of liquefaction were observed at points out side the improved area when recordings were made For the improved ground where there were no trace that liquefaction had occurred, there are plots in th area to the left of the suggested line where liquefac tion might have been expected. But even though ther are plots in this area, if they represent isolated point within the ground, they will not directly lead to lique faction or residual signs of it in the ground as a whole and so to distinguish the plots in Fig. 2 that are lowe than critical N_1 values at depths greater than 3m con sistently, they are shown in black in Fig. 5. This mean

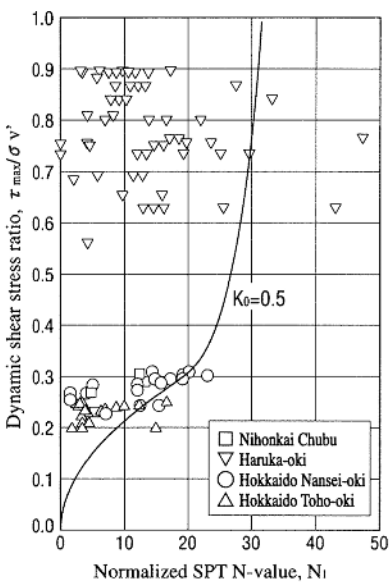

Fig. 4 Relation between shear stress ratio and normalized SPT N-values (before improvement)

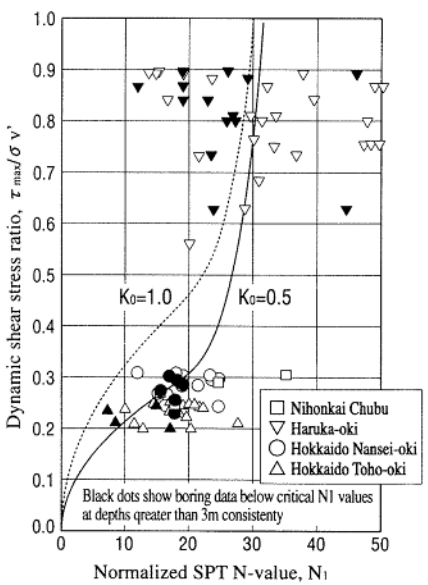

Fig. 5 Relation between shear stress ratio and normalized SPT N-values (after improvement)

that even though consistent distributions are shown for sites B and D that suffered the Sanriku Haruka-oki earthquake and the site that suffered the Hokkaido Nansei-oki earthquake, no traces of liquefaction are observable in the improved ground. Put another way, this result suggests the possibility that ground compacted by SCP method has considerable resistance against liquefaction compared with alluvial sandy ground. The fact that its behavior in relation to liquefaction is different even though it shows similar N-values to unimproved ground has also been reported by Yamazaki[11].

The reason for this, besides the effect of Yoshimi's studies mentioned earlier, can be thought of as the effect of characteristics brought about by the increased rigidity of the composite ground consisting up of sand piles and compacted ground.

3 CHARACTERISTICS OF GROUND IMPROVED BY SCP METHOD

Of the characteristics of ground improved by SCP method, the results of a study of the coefficient of earth pressure at rest that shows the increase in horizontal effective stress, and results of compiling variations in strength for composite ground that contains sand piles, are considered.

3.1 Increase in coefficient of earth pressure at rest

Fig. 6 shows K_0 values taken from borehole horizontal loading tests that were carried out before and after the ground was improved by SCP method. K_0 Values that were around 0.5 before the ground improvement rose to between 1.0 and 2.0 after improvement. A further survey at site A carried out two years after the improvement indicated no fall in K_0 values. It has been shown that the strength of the ground to resist liquefaction increases with a rise in K_0 values[12], and so the effect of ground improvement by SCP in boosting K_0 values can be regarded as one factor behind the strength of such ground in resisting liquefaction.

At the time the suggested line was created in Fig. 5, the results of the cyclic triaxial tests carried out on samples under isotropical condition ($K_0 = 1.0$) were adjusted to the equivalent of $K_0 = 0.5$. If these results are adjusted to $K_0 = 1.0$, the suggested line more closely conforms with the recorded data, as the broken line in Fig. 5 shows.

3.2 *Evaluation of composite ground*

Evaluation of ground improved by SCP method has always been carried out at a point furthest removed from the sand piles (inbetween sand piles), as shown in Fig. 7. As the figure shows, in unimproved ground the distribution of N-values obtained through boring closely matches the distribution throughout the whole ground, however in improved ground it cannot be assumed that the distribution represents the ground as a whole. It further can be assumed that in reality there are the distribution of ground strength around the sand piles[13]. The distribution of ground strength of the sand piles and the distribution of ground strength in the surrounding ground were therefore examined from the results of past SCP improvement work.

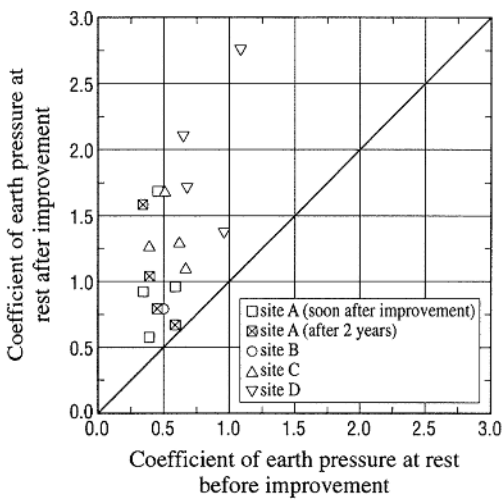

Fig. 6 Coefficient of earth pressure at rest before and after improvement

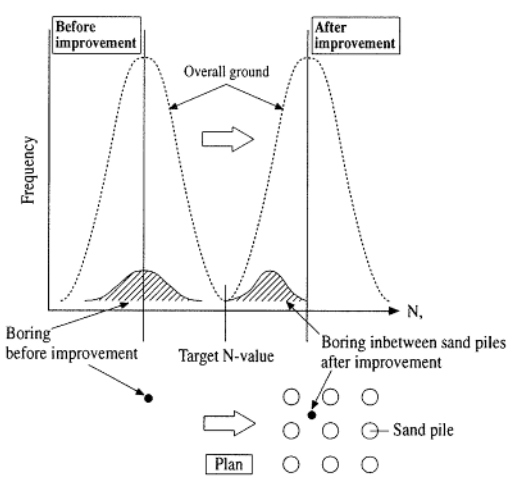

Fig. 7 Schematic figure of evaluation before and after improvement

In Fig. 8 shows the influence of fine content on N_1 values for inbetween piles and those for pile center, based on data from 16 ground improvement sites. As the figure shows, the disparity between the two sets of N_1 values grows as the fine content increases, and to evaluate the improved ground as a whole, the use of N-values for inbetween piles gives safer results. Furthermore, from the standpoint of the strength distribution in ground around sand piles, as Fig. 9a shows, the increase in ΔNsw (Nsw is calculated by Swedish weight sounding), declines with increasing distance. In Fig. 9b the results of tests taken of ground between sand piles after improvement by SCP method to calculating from improvement ratios are shown as the distance from sand pile center plotted against the increase in N-value for ranges of fine content[15]. The figure reveals that when the fine content exceeds 40%, there is no remarkable difference in the strength of the ground related to the distance from the sand pile. But below 40%, a trend can be identified whereby variations to strength correlate with the distance from the sand pile, and when the fine content is below 20%, this becomes considerably more marked. The results of cone penetration tests on site at differing distances between sand piles, shown in Fig. 9c (data by Non-vibratory SCP method), give the similar results.

The fine content of the original ground has little effect on the strength of the sand piles, which on average gives N_1 values of between 25 and 30 as shown in Fig. 8. The sand piles constitute between 10% and 20% of the total area of the ground, but it can be assumed that highly rigid sand piles will have some influence on the strength of the ground as a whole to resist liquefaction.

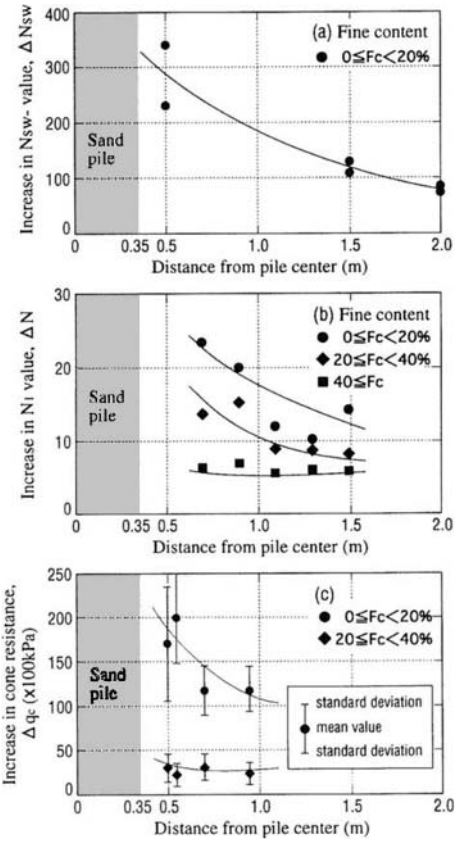

Fig. 9 Relation between distance from pile center and increase in three strength parameters

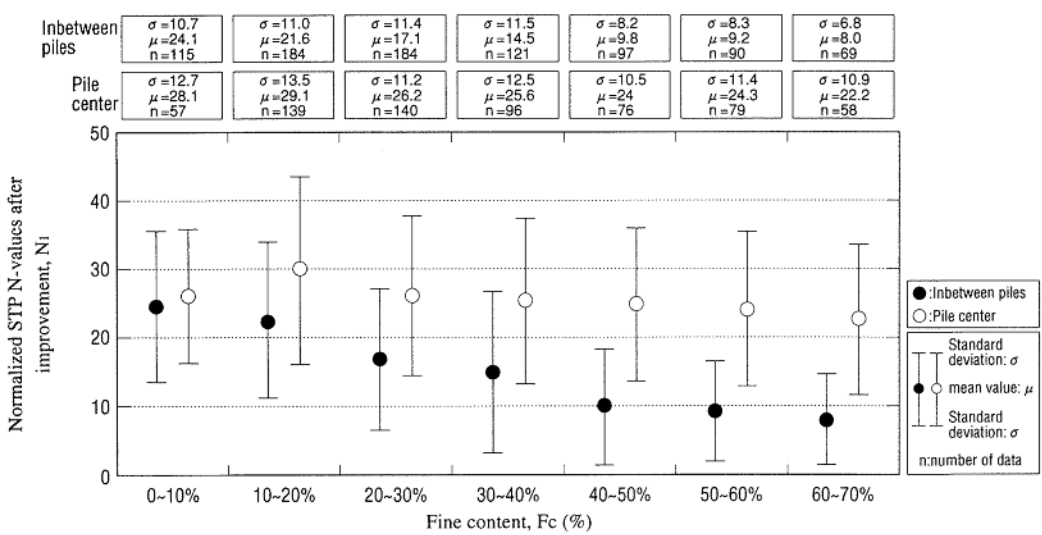

Fig. 8 Influence of the fine content on normalized SPT N-values of inbetween piles and pile center

These results show that the resistance of the ground against liquefaction was usually evaluated from N-values obtained from the furthest point from sand piles, it is possible that the evaluations tended to the side of safety.

4 CONCLUSION

In this paper the strength to resist liquefaction in improved ground compacted by SCP method is estimated from data and survey results taken from improved ground that has suffered a large scale earthquake and the dynamic shear stress ratio thought to have applied, and shows it is comparatively strong in resisting liquefaction. Furthermore, the increase in the horizontal effective stress, thought to be a relevant factor in this, and evaluation of the strength of the composite ground as a whole were reviewed based on existing survey results.

In connection with the characteristics of ground compacted with SCP method, there are many aspects apart from those mentioned above that remain unclear, such as changes to the microscopic structure and increased rigidity of total compacted ground due to the presence of sand piles, and these will require further study.

REFERENCES

1) Ishihara, K., Kawase, Y. and Nakajima, M. (1980), '*Liquefaction Characteristics of Sand Deposits at Oil Tank Site during the Miyagiken-oki Earthquake*', Soils and Foundations, Vol. 20, No. 2, pp. 97-111.
2) The Japanese Society of Civil Engineering (eds) (1986), *Survey Report on Damage Caused by 1983 Nihonkai Chubu Earthquake.* (in Japanese)
3) Iai, S., Matsunaga, Y., Morita, T., Miyata, M., Sakurai, H., Ohishi, H., Ogura, H., Ando, Y., Tanaka, T. and Kato, M. (1994), '*Effects of Remedial Measures against Liquefaction at 1993 Kushiro-oki Earthquake*', Proceedings of 5th US-Japan Workshop on Earthquake Resistant Design of Lifeline Facilities and Countermeasures Against Soil Liquefaction
4) Sasaki, Y., Tamura, K., Yamamoto, M. and Ohbayashi, J. (1995), '*Soil Improvement Work for River Embankments Damaged by 1993 Kushiro-oki Earthquake*', Proceedings of 1st International Conference on Earthquake Geotechnical Engineering, Vol. 1, pp. 43-48.
5) Nishikawa, J., Kamata, T. and Kaji, M. (1995), '*Damage to Roads, Railways and River Embankments Caused by 1994 Hokkaido Toho-oki Earthquake*,' Soils and Foundations, Vol. 43, No. 4, pp. 7-10.
6) Japanese Geotechnical Society (eds) (1996), '*Survey Report on Damage Caused by 1994 Sanriku Haruka-oki Earthquake.*' (in Japanese)
7) Yasuda, S., Ishihara, K., Harada, K. and Shinkawa, N. (1996), 'Special issue of *Effect of Soil Improvement on Ground Subsidence due to Liquefaction*', Soils and Foundations, pp. 99-107.
8) Tokimatsu, K., Uchida, A. and Ariizumi, K. (1983), '*Strength of Liquefaction-Resistance of Sandy Ground Improved by the Sand Pile Compaction Method*', Proceedings of 33rd Symposium on Soil Engineering, pp. 19-22. (in Japanese)
9) Yoshimi, Y. (1990), '*Evaluation Norms for "Cohesive Strength" in Liquefaction Countermeasures*', Tsuchi-to-Kiso, Vol. 38, No. 6, pp33-38.
10) Matsuo, O. (1996), '*On Strength to Resist Liquefaction of Various Sandy Soils*', Proceeding of 31st Japanese Conference on Geotechnical Engineering, pp. 1035-36. (in Japanese)
11) Yamazaki, H. (1996), '*Earthquake-Resistant Design of Ports and Harbors, Special supplement on Earthquake-Resistant Design and Soil Surveys*', Soil Mechanics and Research, pp. 27-33. (in Japanese)
12) Ishihara, K., Iwamoto, A., Yasuda, S. and Takatsu, H. (1977), '*Liquefaction of Anisotropically Consolidated Sand*', Proceedings of 9th International Conference on Soil Mechanics and Foundation Engineering, pp. 11-15.
13) Harada, K., Yamamoto, M. and Ohbayashi, J. (1998), '*On the Evaluation of Density Increase in Improved Ground Compacted by the Non-vibratory Sand Compaction Pile Method*', Proceeding of 33rd Japanese Conference on Geotechnical Engineering, pp. 2155-56. (in Japanese)
14) Sakaguchi, S. (1965), "*On the Stabilization Method for Sandy Ground in Architechtural Foundations,* Tsuchi-toKiso, Vol. 13-2, JSSMFE. (in Japanese)
15) Ohbayashi, J., Yanagida, T., Harada, K. and Murakami, K. (1998), '*Strength Distribution in Compacted Ground*', Annual Meeting of Civil Engineering Society in Chugoku Region, pp. 347-348. (in Japanese).

Earthquake Geotechnical Engineering, Sêco e Pinto (ed.) © 1999 Balkema, Rotterdam, ISBN 90 5809 116 3

A simplified method to evaluate liquefaction-induced deformation

S. Yasuda – *Tokyo Denki University, Japan*

N. Yoshida & H. Kiku – *Sato Kogyo Company Limited, Tokyo, Japan*

K. Adachi – *Jiban Soft Factory Company Limited, Japan*

S. Gose – *Katahira and Engineering Incorporated, Japan*

ABSTRACT: A simplified procedure for the analysis of liquefaction-induced residual deformation was proposed based on the testing method for stress-strain relationships of liquefied sands developed by the authors. In this procedure, the authors assumed that residual deformation would occur in liquefied ground due to the reduction of shear modulus. The authors applied this method to the grounds behind quaywalls, a gentle slope and a river dike in Kobe, Noshiro and Hokkaido, respectively, where very severe damages occurred during past earthquakes, to demonstrate the adaptability of this procedure. The results showed the fairly well adaptability.

1 INTRODUCTION

Liquefaction brings very large residual deformation of grounds and earth structures such as ground flow behind quaywalls and settlement of embankments. Evaluation of the liquefaction-induced deformation is necessary for precise seismic design. However, it is hard to evaluate large deformation by almost all seismic response analytical codes because large strain cannot be considered in these codes.

The authors developed a simplified method to evaluate the liquefaction-induced large deformation. The code of the developed method is named "ALID" (Analysis for Liquefaction-induced Deformation). In the method, the authors assumed that residual deformation would occur in liquefied ground due to the reduction of shear modulus. In this paper, the reduction of shear modulus studied by laboratory tests are showed at first. Then principal of the method and some applications are presented.

2 TORSIONAL SHEAR TESTS TO STUDY POST LIQEFIEFACTION BEHAVIOR

2.1 *Test apparatus and procedures*

Torsional shear test apparatuses were used to study the post liquefaction behavior. Toyoura sand which is a clean sand was used at first to study the effects of density, confining pressure and severity of liquefaction. Then several sands were tested to study the effect of fines content. (Yasuda et al., 1998)

Specimens were saturated, applied back pressure and consolidated. Then a prescribed number or prescribed amplitude of cyclic loadings was applied in undrained condition. Safety factor against liquefaction, F_L, which implies severity of liquefaction was controlled by the number of cycles or amplitude of the cyclic loadings. After that a monotonic loading was applied under undrained condition with a relatively high speed of γ=10 % in a minute, as shown in Figure 1. Relationships among shear stress, τ, excess pore pressure, Δu, and shear strain, γ in the monotonic loading were measured.

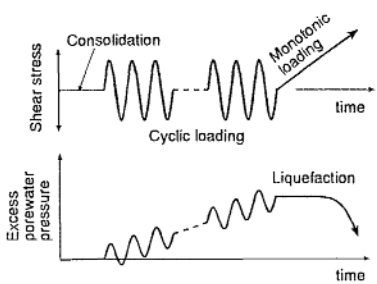

Fig.1 Procedure of cyclic and monotonic loading

2.2 *Typical test results and definition of G_{0i}, G_N, , G_l and γ_L*

Figure 2 shows stress-strain curves and excess porewater pressure-strain curves in the case of

Toyoura sand with different relative densities, *Dr*. Scales of axes in Figure 2(c) are enlarged one of Figure 2(a). Shear strain increased with very low shear stress up to very large strain. Then, after a resistance transformation point, the shear stress increased comparatively rapidly with shear strain, following the decrease of pore water pressure. As shown in Figure 2(c), shear strain up to the resistance transformation point increased with the decrease of *Dr*. And, shear modulus up to the resistance transformation point decreased with the decrease of *Dr*.

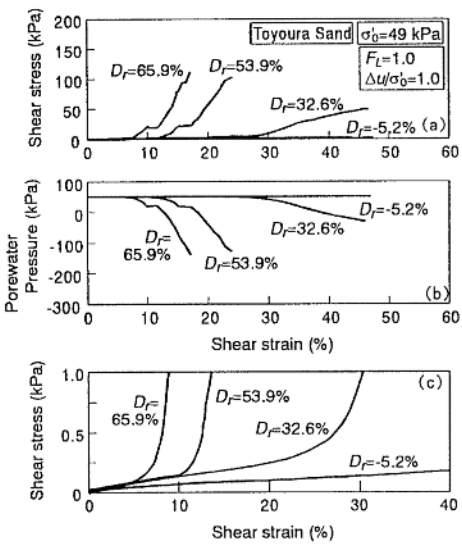

Fig.2 Stress-strain and strain-porewater pressure curves for Toyoura sand

As shown in Figures 2, shear stress increased comparatively rapidly after a resistance transformation point. The amount of strain up to the resistance transformation point is called the "reference strain at resistance transformation, γ_L" as shown in Figure 3. Stress-strain curves before and after the reference transformation point can be presented approximately by a bilinear model with G_1, G_2 and γ_L:

$$\tau = G_1 \gamma \quad \text{for } \gamma < \gamma_L \qquad (1)$$

$$\tau = G_1 \gamma_L + G_2(\gamma - \gamma_L) \quad \text{for } \gamma \geqq \gamma_L \qquad (2)$$

where G_1 and G_2 are the shear moduli before and after the reference transformation point, respectively.

To know the reduction rate of shear mudulus due to liquefaction, the rate of shear modulus G_1/G_0, which is the ratio of shear modulus after and before liquefaction, was calculated. Two types of G_0 were selected : ① $G_{0,i}$: secant modulus of stress-strain curves at γ=0.1 % in the case of without cyclic loading ($\Delta u/\sigma_v'$ =0) and ② G_N : estimated from SPT *N*-value by the formula of G_N=28*N*. In the first shear modulus, 0.1 % of shear strain was selected because the strain of soils which occurs in the ground due to overburden pressure is estimates as around γ =0.1 % in usual case. The second one is widely used for the design of foundation in Japan.

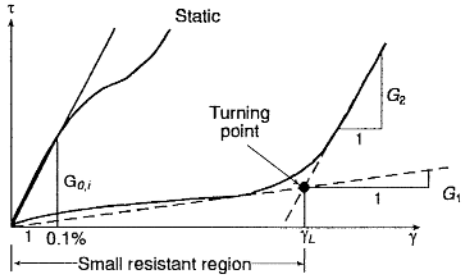

Fig.3 Definition of G_{0i}, G_1, G_2 and γ_L

2.3 *Relationships among shear modulus ratio, F_L and fines contents*

Relationships between the shear modulus ratio, $G_1/G_{0,i}$ and fines content less than 75 μ m, *Fc*, in the range of F_L =0.9 to 1.0 were plotted in Fig 4. The ratio $G_1/G_{0,i}$ increased with *Fc*. Though figures are not shown here, $G_1/G_{0,i}$ decreased with F_L. Based on the test results, relationships among shear modulus ratio, F_L and *Fc* are summarized as shown in Fig.5.

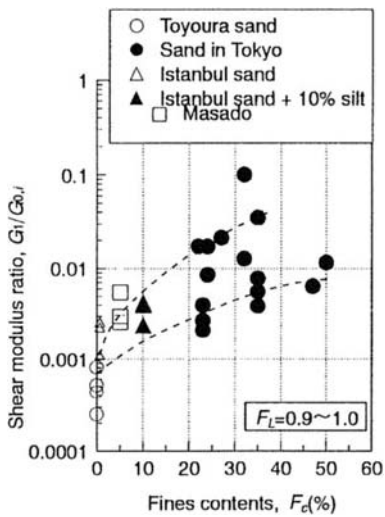

Fig.4 Relationships between shear modulus ratio and fines contents

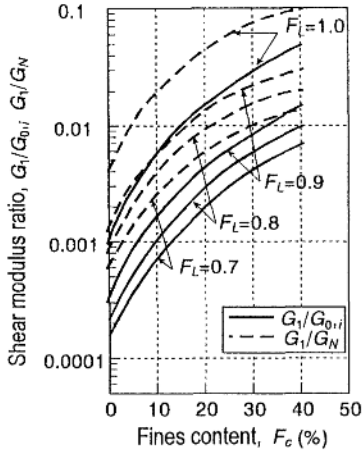

Fig.5 Summary of relationships among shear modulus ratio, F_L and fines contents

3 OUTLINE OF THE PROPOSED METHOD

3.1 *Concept of the proposed method*

Figure 6 shows the concept of the stress-strain curves which are used in the proposed method for liquefaction-induced deformation. Line ℓ denotes a backbone curve at the beginning of the earthquake. Point A in Fig.6 is supposed to be initial state of a soil element in the ground. When excess porewater pressure generates, material properties such as shear strength and elastic moduli change. Suppose that the backbone curve moves from ℓ to m due to liquefaction, then strain should increases in order to hold the driving stress. Since driving stress, however, decreases according to the change of geometry, actual strain increment from state ℓ to m is from A to C. Namely, strain increment caused by the change of material property is $\gamma_C - \gamma_A$. Ground flow stops when new material property comes to balance with a new driving stress, which is shown as point C in the figure. In the proposed method here, two paths : ① A to C through B and ② O to C through B are assumed though the actual path is A to C because of simplification.

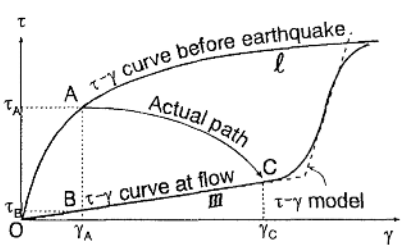

Fig.6 Schematic of stress-stain curves

If the two paths are assumed, two procedures to analyze the liquefaction-induced deformation are available:

a)Stress relaxation method

In the first stage, state before the earthquake is calculated by the FEM using stress-strain curve ℓ. Then by holding the strain, stress-strain curve is changed to m. In this stage, external stress and internal stress are not balanced because the strain is fixed. Therefore it is necessary to relax the unbalanced stress. During the process of the relaxation , increment of shear strain due to liquefaction, $\gamma_C - \gamma_A$ and liquefaction-induced deformation of the ground can be calculated.

b)Self weight method

In the first stage, deformation of the ground is calculated by the FEM using stress-strain curve ℓ same as the stress relaxation method. Then the same gravity force is applied to the same model again by using the stress-strain curve m. Deformation due to liquefaction-induced flow can be evaluated by deducing the deformation form the second one to the first one.

Both methods have merits and demerits. Stress relaxation method is reliable and any stress-strain curve can be applied. However, special modification is necessary from the conventional FEM codes. Self weight method can not take into account the change of the driving force, but arbitary FEM program can be used. In the following analyses, the self weight method are employed with linear stress-strain relationships.

3.2 *Modeling of the ground*

In the modeling of the liquefied soil layers, F_L of liquefiable layer is evaluated at first by some method. Then the rate of reduction of shear modulus due to liquefaction is estimated by laboratory tests or Fig.5. Shear modulus of the upper unliquefiable layers had better to be reduced because frequently cracks are induced in the unliquefiable layers during the liquefaction-induced flow. Shear modulus ten times larger than that in the liquefiable layer was applied in the following analyses based on several back analyses during past earthquakes.

If the boundary between ground and caisson or sheet pile walls is connected directly, the ground just behind the walls cannot settle. Therefore, it is recommended to use joint elements or double nodes which move together in the horizontal direction but move independently in the vertical direction.

Subsidence of the ground surface occurs by two mechanism : geometrical change due to the flow and densification due to dissipation of excess porewater pressure. The subsidence by the first mechanism is

evaluated automatically in this analysis. Some additional analyses are necessary to evaluate the subsidence due to the second mechanism. Though an analytical procedure in FEM is available to evaluate the subsidence, simple estimation, for example estimation by the Ishihara and Yoshimine's method (1992), is recommended because modification of standard programs is not so easy.

3.3 *Note for locking of element*

Because undrained behavior is assumed in the analysis of liquefaction-induced flow, apparent bulk modulus or total bulk modulus of the liquefied sand can become very large, resulting in Poisson's ratio to be close to 0.5, In such a situation, it is known that deformation of the element is constrained as Poisson's ratio reaches to 0.5 if two point Gauss-Legendre integral that is commonly used in the finite analysis is employed in computing the element stiffness matrix. This phenomena is known to be locking of element. Reduced integral technique is known to be effective to avoid locking effect, but it creates another problems, i.e., hourglass instability. This problem can be avoided by employing the anti-hourglass stiffness. In this section, we examined various methods to compute element stiffness matrix in order to make the effect clear.

Element stiffness matrix was computed by the following four methods:

1) Two point Gausse-Legendre integral
2) Reduced integral (one point Gausse-Legendre integral)
3) Reduced integral with anti-hourglass stiffness (Yoshida, 1989)
4) Condense from four triangular element

Two point Gauss-Legendre integral is the most common method in the finite element analysis. The quadrilateral element is divided into four elements by making a new node at the center of the element in the condense method. Element stiffness matrix of the quadrilateral element is made by eliminating the internal node internally. This condense dose not affect the result, therefore, if a computer code does not have this function, one can divid the quadrilateral element into four triangular element by hand. It is not recommended to divide a quadrilateral element into two triangular elements because stiffness has direction dependent characteristic.

The Uozakihama site shown later was used. The results are show in Fig.7, and can be summarized as follows:

a) A conventional method, i.e., two point Gauss-Legendre integration underestimate displacement very much. Therefore this method is not recommended.

b) Distinct hourglass mode deformation is observed if only reduced integration is employed. Therefore, deformation pattern of each element sometimes seems extraordinary. The average deformation, however, nearly the same with following two cases.

c) Both reduced integral with anti-hourglass stiffness and condense from triangular element show nearly the same displacements.

Therefore reduced integral with anti-hourglass stiffness is the best method because amount of calculation is smaller. If the computer code does not have anti-hourglass stiffness, one can use triangular elements by dividing a quadrilateral element into four triangular elements. If one does not mind the deformation of each element but want only global feature, one can use reduced integral, too.

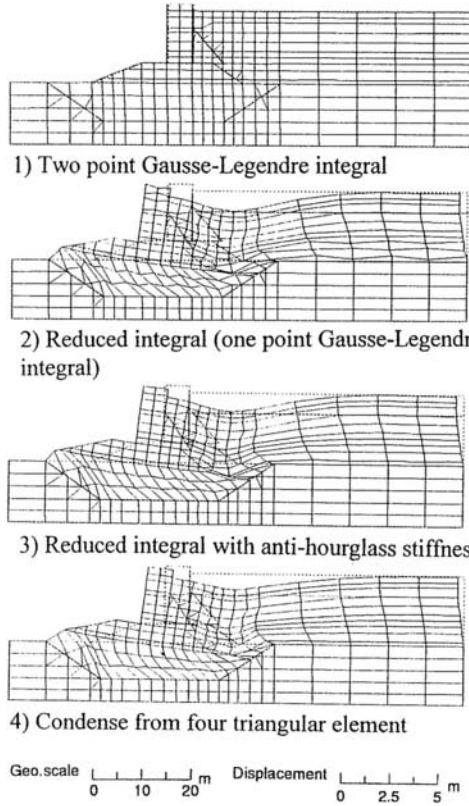

Fig.7 Comparison of deformation computed by four methods

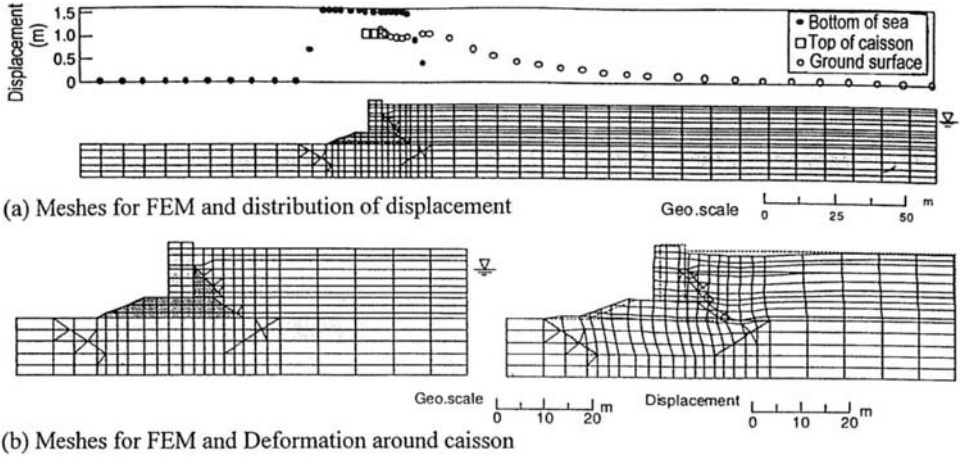

(a) Meshes for FEM and distribution of displacement

(b) Meshes for FEM and Deformation around caisson

Fig.8 Deformation of the ground behind a quay wall

4 TYPICAL ANALYSED RESULTS

The proposed method "ALID" was applied to several structures which were damaged during past earthquakes, to demonstrate the adaptability of the method. Among them three cases are shown in this paper. In the analyses, shear modulus before the earthquake were estimated by SPT N-values, and F_L was evaluated by the method introduced in the Specification for Highway Bridges (1996).

4.1 *A caisson type quay wall at Uozakihama*

A caisson type quay wall moved toward the sea and the ground behind the wall flowed at Uozakihama in Kobe during the 1995 Hyogoken-nambu earthquake. Horizontal displacement of the wall was 2.0 m and the flow extended to more than 100 m from the wall. Fig.8 shows the analyzed result. Horizontal displacement of the wall was 1.2 m and the flow extended more than 100 m. It can be said that analyzed results agree well with the actual damage.

4.2 *A gentle slope at Aoba-cho*

A very gentle slope with the gradient of about 1 % flowed due to liquefaction at Aoba-cho in Noshiro City during the 1983 Nihonkai-chubu earthquake. Analyzed deformation is shown in Fig.9. Figure 10 compares the distribution of horizontal displacement. As shown in this figure, average displacement is

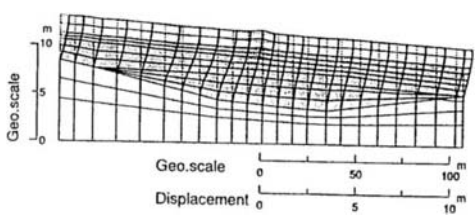

Fig.9 Deformation of a gentle slope

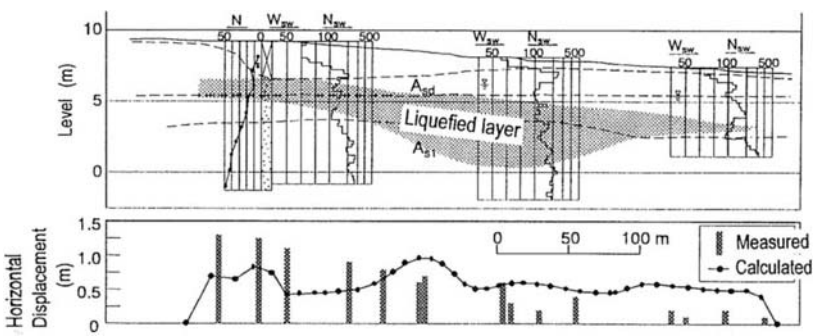

Fig.10 Distribution of displacements on the ground surface

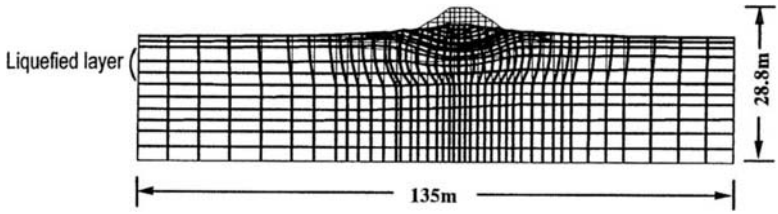

Fig.11 Deformation of a river dike

fairly coinceded with the actual displacement. Exactly speaking, however, displacement is underestimated in the left side in the cross section. Two reasons may exist : ① a steep slope which is located at left outside from this figure pushed the soil layer to right direction and ② nodal points at left boundary cannot move in the horizontal direction in the analysis.

4.3 *A river dike in Hokkaido*

River dikes of the Siribeshi-toshibetsu river were damaged due to liquefaction during the 1993 Hokkaido-nansei-oki earthquake. Settlement of the dike at near Shin-ei Bridge was 2.6 m. Two shear moduli were assumed for the embankment in the analyses: ① shear modulus does not decrease ② shear modulus decrease as same as the unliquefiable layer. Figure 11 shows the deformation analyzed under the second assumption. Analyzed settlement on the top of the embankment was 0.9 m and 3.2 m, respectively. Therefore, some reduction of shear modulus of embankment may be necessary.

5 CONCLUSIONS

A simplified method to evaluate liquefaction-induced deformation was proposed. Then adaptability of the method was confirmed by several case studies. As the proposed method is very sensitive for reduction of shear modulus, it is recommended to conduct laboratory tests. Moreover, special attention is necessary for locking effect. Reduced integral with anti-hourglass stiffness is the best method to avoid the locking effect. However, if the code does not have anti-hourglass stiffness, triangular elements by dividing a quadrilateral element into four triangular elements are also available.

ACKNOWLEDGEMENT

Cyclic torsional shear tests were conducted by Mr. T. Terauchi and Mr. H. Morimoto. Soil data at the dike was provided by a technical committee organized by Japan Institute of Construction Engineering. The authors would like to express their thanks to them.

PREFERENCES

Ishihara,K. and M. Yoshimine 1992. Evaluation of settlements in sand deposits following liquefaction during earthquakes, *Soils and Foundations*, 32: 173-188.

The Japan Road Association 1996. Specifications for Highway Bridges.

Yasuda, S., T. Terauchi, H. Morimoto, A. Erken & N. Yoshida 1998. Post liquefaction behavior of several sands, *Proc. of the 11th European Conference on Earthquake Engineering.*

Yoshida, N. 1989. Finite displacement analysis on liquefaction-induced large ground displacements, *Proc., 2nd Japan-US Workshop on Liquefaction, Large Ground Deformation and Their Effects on Lifeline Facilities*, : 207-217.

Earthquake Geotechnical Engineering, Sêco e Pinto (ed.) © 1999 Balkema, Rotterdam, ISBN 90 5809 116 3

Zoning for liquefaction risk in an Italian coastal area using CPT

Teresa Crespellani, Claudia Madiai & Giovanni Vannucchi
Department of Civil Engineering, University of Florence, Italy

ABSTRACT: With a view to drawing up digitised maps of liquefaction risk along the Romagna coast, for which about eight hundred cone penetration tests (CPT) are available, four different methods based on CPT to evaluate safety factor profiles are analysed and compared. The methods considered are those proposed by (1) Robertson and Wride (1997), (2) Suzuki et al. (1997), (3) Shibata and Teparaska (1988), and (4) Olsen (1997). The synthetic index introduced by Iwasaki et al. (1978), representative of the liquefaction potential in correspondence with every profile explored by means of CPT, was employed for drawing up the digitised liquefaction risk maps. Up until now, one hundred mechanical cone penetration tests have been digitised. The aforesaid four methods have been applied to these tests. A comparison of these methods points out a substantial agreement between the results.

1. INTRODUCTION

With the aim of zoning the seismic geotechnical hazards in the territory of several municipalities on the northern Italian Adriatic coast, a study for the assessment of soil liquefaction risk has been carried out within the framework of a research promoted and supported by the Emilia – Romagna Region.

An analysis of the regional seismicity has indicated that in the site the seismic conditions for liquefaction exist (Rebez et al., 1996; Marcellini et al., 1998). Moreover, historical investigation has shown that some effects of past earthquakes observed by eye-witnesses on the beaches, deltas and river channels (cracks in the ground with seepage of water and sand or mud, sand boils, etc.), can be interpreted as liquefaction signs (Serpieri, 1889; Galli and Meloni, 1993).

The best approach in mapping seismic risk of a large and urbanised area is to utilise as much as possible existing geotechnical information (TC4, 1993). Therefore a bank of existing geotechnical data has been created. In the area under study a great amount of mechanical CPT tests were available. Thus, to evaluate the liquefaction risk, reference was made to procedures that use this type of test. At the present state of the research, 100 CPT tests have been digitised which concern an area of approximately 10 square km.

Studies of regional geology and historical seismicity have been also carried out.

Of course, the reliability of the final product, i.e. the microzoning map, depends on both the procedure used to process the data and also on the density and quality of the experimental data, that is due also to the type of probe used in the CPT (mechanical or electrical). As far as the first aspect is concerned, four of the most recent analysis procedures have been applied to 100 CPT profiles, and a comparison of the results was made. As to the second aspect, integrative research is under way that is aimed at controlling the quality of the available geotechnical data and checking the uncertainty introduced by using the interpretative procedures developed for an electrical CPT to process the data obtained by means of a mechanical probe.

2. LIQUEFACTION POTENTIAL INDEX

For mapping the liquefaction risk, a single numerical value must be associated with each profile examined. A synthetic index representative of the liquefaction risk was introduced by Iwasaki et al. (1978). It is the liquefaction potential index, P_L, defined as follows:

$$P_L = \int_0^{20} F(z) \cdot w(z) \cdot dz \qquad (1)$$

in which z is the depth below the ground surface, measured in meters and defined up to the value of 20 m beyond which liquefaction phenomena can be excluded, F(z) is a function of the liquefaction resistance factor, FSL, which assumes a value of zero for FSL>1, and is the complement to 1 for FSL<1; w(z) = 10 - 0.5 z is a linearly-decreasing function of depth z.

The P_L values range from 0 to 100 but Iwasaki et al. (1978) demonstrated that P_L values greater than 15 identify a high susceptibility to liquefaction damage. This index can be applied to all the methods that involve the calculation of liquefaction resistance factor, FSL.

In a given depth of a generic soil profile, FSL is by definition the ratio between the capacity of resistance against liquefaction (CRR = Cyclic Resistance Ratio) and the demand for resistance to liquefaction (CSR = Cyclic Stress Ratio):

$$FSL = \frac{CRR}{CSR} \qquad (2)$$

To calculate the FSL safety factor, the two variables, CSR and CRR, must be evaluated separately.

The results of in situ tests, and particularly of the CPT test, may be used for estimating the capacity of resistance to liquefaction, CRR.

Instead, the demand for resistance to liquefaction, CSR, is a parameter of seismic load. For an earthquake with a magnitude of 7.5, this is normally estimated by means of the following semi-empirical equation, which was proposed by Seed and Idriss (1971):

$$CSR = \left(\frac{\tau_{av}}{\sigma'_{v0}}\right) = 0.65 \cdot \left(\frac{a_{max}}{g}\right) \cdot \left(\frac{\sigma_{v0}}{\sigma'_{v0}}\right) \cdot r_d \qquad (3)$$

in which:

- a_{max} is the horizontal peak acceleration at the surface of the deposit;
- g is the acceleration of gravity;
- σ_{v0} and σ'_{v0} are, respectively, the total and effective vertical lithostatic stresses;
- r_d is a stiffness reduction which, in simplified procedures, are assumed to vary only with the depth.

At present, the most reliable equations for the estimate of r_d (NCEER, 1996) are the following:

$r_d = 1 - 0.00765\ z$ for $z \le 9.15$m
$r_d = 1.174 - 0.0267\ z$ for $9.15 < z \le 23$m
$r_d = 0.774 - 0.008\ z$ for $23 < z \le 30$m
$r_d = 0.5$ for $z > 30$m.

The liquefaction potential index, P_L can be easily mapped, either by partitioning the area under consideration into cells and averaging the P_L values over each cell (Iwasaki et al., 1982), or by contouring the point data obtained for each profile explored. In the present paper the latter way was taken, and, according to Iwasaki et al. (1978), the four classes of risk severity, which are indicated in Table I, were assumed.

Table I: Liquefaction index and associated risk level

Value of P_L	Liquefaction risk
$P_L = 0$	very low
$0 < P_L \le 5$	low
$5 < P_L \le 15$	high
$15 < P_L$	very high

3. USE OF CPT TESTS FOR EVALUATING THE CYCLIC RESISTANCE RATIO, CRR

The reason for the success of CPT in evaluating the susceptibility to liquefaction of soils may be found in the greater accuracy and repeatability of this test compared to SPT, as well as in its low cost, and in the possibility of having continuous records with the depth of two independent measurements of soil resistance: the cone resistance, q_C, and the local friction resistance, f_S. The greatest limitation of the CPT lies in the fact that, differently from the SPT, it does not permit taking soil samples.

The early techniques for analysing liquefaction risk using CPT were developed in the 1980's. They utilised the procedures based on the SPT test, using available correlations between SPT and CPT and converting the q_c-values to N_{SPT}-values. By this means the charts to evaluate liquefaction resistance based on N_{SPT} can be used (Seed and Idriss, 1982). But these procedures called for additional field investigation, because - as already noted - the presence of a non negligible fine content (FC > 5%) has considerable influence on the cyclic resistance ratio of sandy soil. This condition frustrated a good part of the CPT test's advantages, as integrative soundings, the extraction of numerous soil samples for grain size analyses and the use of empirical correlations (whose reliability is generally uncertain), were required for the assessment of soil conditions.

In recent years, the growth in the CPT statistical data base has made it possible to develop techniques for analysing the liquefaction potential directly

based on CPT. Several of these procedures not only do not require a prior knowledge of the grain size distribution, but also take into account the other factors connected with the presence of a clay fraction (plasticity, stress history, soil structure).

4. PROCEDURES USED

The four procedures used to evaluate the liquefaction potential are described in detail in the works of:

1) Robertson e Wride (1997),
2) Suzuki et al. (1997),
3) Shibata e Teparaska (1988),
4) Olsen (1997).

For every profile, their use require:

a) an estimate of the profile with depth of the resistance to liquefaction, expressed in terms of cyclic resistance ratio (CRR) or of normalised cone penetration resistance (q_{c1N}); this resistance is derived from the results of the CPT test;
b) an estimate of the profile of the expected seismic action expressed in terms of the cyclic stress ratio (CSR) or of the critical normalised resistance ($q_{c1N,cr}$); this action is expressed as a function of the seismic parameters of the expected earthquake (peak acceleration a_{max} and magnitude M) and of the tensional state at the testing depth;
c) a calculation of the profile of the factor of liquefaction resistance, FSL, down to a depth beyond which the possible occurrence of liquefaction phenomena can be excluded.

The aforementioned simplified procedures are based on field observations referring to earthquakes of magnitude M=7.5. To apply them for liquefaction analysis with earthquakes having a magnitude other than 7.5, a magnitude scale factor, MSF, is utilised, which is a multiplier of the cyclic resistance ratio $CRR_{7.5}$ (even if it would be more logical to use it as a divisor of the cyclic stress ratio, CSR). For a long time, the value to be attributed to MSF was calculated with the equation:

$$MSF = \frac{0.65}{0.1 \cdot (M - 1)} \qquad (4)$$

which analytically reproduces the numerical values proposed by Seed and Idriss (1982).

More recently, with a larger and more significant data base, many researchers have demonstrated that application of equation (4) leads to an overestimation of the liquefaction risk when the magnitude is less than 7.5, and to an underestimation of the risk when the magnitude is greater than 7.5. They have, therefore, proposed alternative equations.

For earthquakes of a magnitude greater than 7.5, the recent NCEER recommendations (Youd, 1997) suggest employing MSF values given by the equation (Idriss, 1990):

$$MSF = \frac{10^{2.24}}{M^{2.56}} \qquad (5)$$

and for earthquakes of a magnitude of less than 7.5, intermediate MSF values between those of equation (5) and those calculated with the following equation (Andrus and Stokoe, 1997):

$$MSF = \left(\frac{M}{7.5}\right)^{-3.3} \qquad (6)$$

Table II contains a comparison of the traditional MSF values by Seed and Idriss (eq. 4) with those of the NCEER recommendations.

Table II: Comparison of the scale factor values of the MSF magnitude according to Seed and Idriss (1982) with those of the NCEER recommendations (Youd, 1997)

M	5.5	6	6.5	7	7.5	8	8.5
Eq. (4)	1.44	1.30	1.18	1.08	1.00	0.93	0.87
NCEER	2.50	1.93	1.52	1.22	1.00	0.85	0.73

In the case under study, the magnitude of the design earthquake was M = 6, and the difference between the two scale-factor values of the magnitude was very great. In a previous study, a map of the seismic liquefaction risk of the same zone (Crespellani et al., 1997a) was obtained with the same CPT data base, but utilising equation (4). The contouring lines of the liquefaction potential index obtained in the two studies had a similar form, but correspond to very different values of risk; in practice; by employing equation (4) as the magnitude scale factor instead of the value suggested by the NCEER recommendations, the areas classified as "low risk" passed to the "high risk" category, and the "high risk" ones passed to the "very high risk" category.

The above four procedures were applied to the first 100 digitised CPT tests. The penetration profiles that reached depths of more than 20 m were cut off at that depth. As design seismic data a magnitude of M = 6 and a peak acceleration of a_{max} = 0.275g were assumed. For each profile, a saturated volume weight of γ_{sat} = 19 kN/m^3 and a depth of water table

(where not measured) of z_w = 1.5 m were considered.

The mean, minimum and maximum values and the standard deviation of P_L and the total thickness of the layers that can liquefy ΣH (m) obtained with the four aforementioned procedures are indicated in Table III.

Table III: Comparison of the results obtained using the four procedures

	P_L				ΣH			
	(1)	(2)	(3)	(4)	(1)	(2)	(3)	(4)
Min.	0	0	0	0	0	0	0	0
Max.	7.42	8.99	9.51	3.76	4.40	3.80	3.80	1.80
Mean	1.95	1.65	1.72	0.39	1.39	1.26	1.13	0.30
S.D.	2.01	1.92	1.97	0.67	1.26	1.22	1.09	0.45

In figures 1a, 1b and 1c, the values of the liquefaction potential index in the design seismic conditions obtained, respectively, using procedures 2, 3 and 4, are compared separately with the values obtained using procedure 1 assumed as reference (in the abscissa in the graphs). In figures 2a, 2b and 2c, the values of the total thickness of the liquefiable layers in the design seismic conditions, obtained respectively by using procedures 2, 3 and 4, are compared separately with the values obtained in procedure 1 assumed as reference (in the abscissa in the graphs). Compared to the values obtained with the reference procedure, procedure 4 led to a systematic underestimation of the liquefaction potential index, while procedures 2 and 3 led to estimates that diverged unsystematically and independently of the value of P_L. The mean value of P_L in procedure 1 was the highest. The overall mean thickness of liquefiable layers was not much different with that obtained applying the procedures 1, 2 and 3, and was distinctly less when procedure 4 was used. As the results obtained by applying the first three procedures were, compared to those obtained with procedure 4, more conservative, very similar and did not lead to different classes of liquefaction risk, only a procedure was used in order to extend the analysis to other CPT tests and for mapping liquefaction risk. In particular, because of its greater completeness and reliability, the Robertson and Wride procedure (1997) was chosen for the subsequent analyses.

5. MAP OF LIQUEFACTION RISK

The values of the liquefaction potential indexes, associated with to each of the profiles explored by means of CPT, were located in a two-dimensional map and contoured with interpolation lines, linking the points having equal values of P_L. The map obtained is shown in figure 3. The contour lines have a distance of $\Delta P_L = 2$, and the intensity of the grid is proportional to liquefaction risk level according to Table I. It is possible to observe that the pattern of the points investigated is not regular, and therefore the accuracy of the result varies from zone to zone.

6. CONCLUSIONS

Several conclusions can be drawn from the analysis made.

As far as the procedures for evaluating the liquefaction risk from CPT tests are concerned, it can be observed that:

1. Three of the four procedures used gave results that were essentially equivalent and, in the specific case, did not modify the risk class.
2. The procedure of Robertson and Wride (1997) is the most complete one, and was therefore chosen for drawing up the liquefaction risk maps.
3. The results of the analysis were much more influenced by the value of the scale factor of magnitude than by the calculation procedure.

As far as liquefaction risk in the area under study is concerned (figure 3), it can be noted that:

1. The geological, morphological and geotechnical conditions in the coastal zone correspond to those of the soils susceptible to liquefaction.
2. The seismic conditions that exist in the area are such that cyclic liquefaction phenomena may occur, as the earthquakes expected with a return period of 475 years are characterised by an intensity of I = VIII MCS and a peak acceleration of a_{max} = 0.24g.
3. From the risk map obtained, it can be inferred that, according to Iwasaki's classification (1978), the risk class is "high" level in the delta of the river Rubicone, and "low" in the remaining part of the coast.
4. The phenomena observed during several historic earthquakes can be attributed to the cyclic liquefaction of the soil.
5. In consideration of the high population density and the damages of liquefaction, a precise risk analysis is of great importance for urban planning and earthquake protection in the area. Therefore, further research must be devoted to the estimate of amplification site effects as well as to the assessment of non linear behaviour of soils.

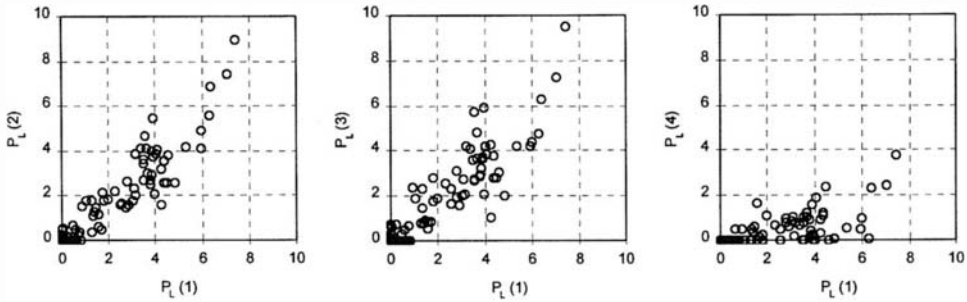

Figure 1 : Comparison of the values of the liquefaction potential index, P_L, obtained using the four methods

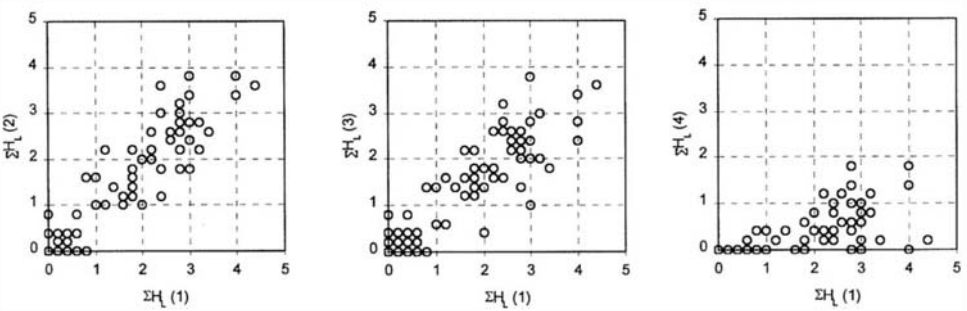

Figure 2 : Comparison of the thickness of liquefiable layers obtained using the four procedures

ACKNOWLEDGEMENTS

The work was promoted and supported by the Emilia - Romagna Region.

REFERENCES

Andrus, R.D., Stokoe, K.H. (1997) "Liquefaction resistance based on shear wave velocity". NCEER Workshop on Evaluation of Liquefaction Resistance of Soils, Technical Report NCEER-97-0022, National Centre for Earthquake Engineering Research, Buffalo, NY

Crespellani T., Madiai C., Vannucchi, G., Marcellini, A., Martelli, L., Frassineti, G. (1997a) "Analisi del rischio di liquefazione nell'area costiera fra Cesenatico e Bellaria - Igea Marina". Geologia delle Grandi Aree Urbane, Progetto Strategico CNR, Bologna, 4-5 novembre 1997

Crespellani, T., Madiai, C., Vannucchi, G. (1997b) "Valutazione del potenziale di liquefazione di vaste aree mediante prove CPT". Atti del VIII° Convegno Naz. "L'Ingegneria Sismica in Italia", vol. 3, Taormina

Galli, P., Meloni, F. (1993) "Nuovo catalogo nazionale dei processi di liquefazione avvenuti in occasione dei terremoti storici in Italia". Il Quaternario , 6 (2), 271-292

Idriss, I.M. (1990) "Response of soft soil sites during earthquakes". Proc. of H.B. Seed Memorial Symposium, vol. 2, BiTech Publ. Ltd, Vancouver, B.C. Canada, 273-290

Iwasaki, T., Tatsuoka, F., Tokida, K., Yasuda, S. (1978) "A practical method for assessing soil liquefaction potential based on case studies at various sites in Japan". Proc. 2nd Int. Conf. on Microzonation for Safer Construction - Research and Application, San Francisco, California, vol. 2, 885-896

Iwasaki, T., Tokida, K., Tatsuoka, F., Watanabe, S., Yasuda, S. and Sato, H. (1982) "Microzonation for Soil Liquefaction Potential Using Simplified methods". Proc. 3rd Int. Conf. On Microzonation, Seattle, Vol. 3, 1319-1330

Marcellini, A., Daminelli, R., Pagani, M., Riva, F., Crespellani, T., Madiai, C., Vannucchi, G., Frassineti, G., Martelli, L., Palumbo, D., Viel, G. (1998). " Seismic microzonation of some Municipalities of the Rubicone area (Emilia-Romagna Region)". 11th European Conference on Earthquake Engineering, Paris, 6-11 September

Olsen, R.S. (1997) sito web: http://www.liquefaction.com.

Rebez, A., Peruzza, L. e Slejko, D. (1996) "Characterisation of the seismic input in the seis-

mic hazard assessment of Italian territory". Thorkelsson B. (ed), Seismology in Europe, Icelandic Meteorological Office, Reykjavik, 327 - 332

Robertson, P.K., Wride (Fear), C.E. (1997) "Cyclic liquefaction and its evaluation based on SPT and CPT". NCEER Workshop on Evaluation of Liquefaction Resistance of Soils, Technical Report NCEER-97-0022, National Centre for Earthquake Engineering Research, Buffalo, NY

Seed, H.B., Idriss, I.M. (1971) "Simplified procedure for evaluating soil liquefaction potential". JSMFD, ASCE, vol. 97, SM9, 1249-1273

Seed, H.B., Idriss, I.M. (1982) "Ground motions and soil liquefaction during earthquakes". Earthquake Engineering Research Institute Monograph.

Serpieri, A. (1889) "Scritti di sismologia, Parte II, I terremoti del 18 Marzo 1875 e del 28 Luglio 1883". Tipografia Editrice Calasanziana, Firenze.

Shibata, T., Teparaksa, W., (1988) "Evaluation of liquefaction potentials of soils using cone penetration tests". Soils and Foundations, Vol. 28, N.2, 49-60

Suzuki, Y., Koyamada, K., Tokimatsu, K. (1997) "Prediction of liquefaction resistance based on CPT tip resistance and sleeve friction". Proc. of XIV ICSMFE, vol. 1, 603-606, Hamburg.

Technical Committee for Earthquake Geotechnical Engineering TC4 - ISSMFE (1993). Manual for Zonation on Seismic Geotechnical Hazard. The Japanese Society of Soil Mechanics and Foundation Engineering

Youd, T.L., Idriss, I.M., Eds. (1997) - Proceedings of the NCEER Workshop on Evaluation of Liquefaction Resistance of Soils, Technical Report NCEER-97-0022, National Centre for Earthquake Engineering Research, Buffalo, NY

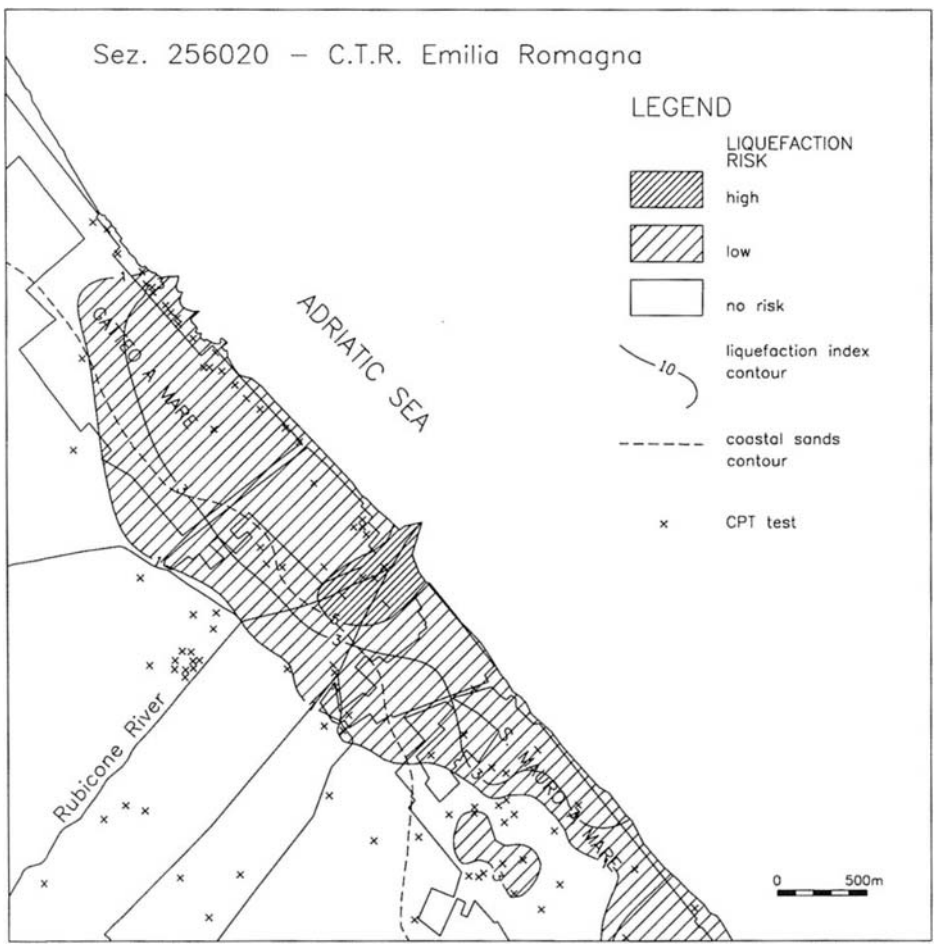

Figure 3: Liquefaction risk map

Earthquake Geotechnical Engineering, Sêco e Pinto (ed.) © 1999 Balkema, Rotterdam, ISBN 90 5809 116 3

Analysis of full-scale tests on piles in deposits subjected to liquefaction

M.Cubrinovski
Kiso-Jiban Consultants Company Limited, Japan

K. Ishihara & K. Furukawazono
Department of Civil Engineering, Science University of Tokyo, Japan

ABSTRACT: This paper describes results and analysis of shaking table tests on a prototype-scale soil-pile model. A model of pile foundations embedded in saturated sand was used to investigate the performance of piles when surrounding soils undergo liquefaction during earthquakes. It is shown that the lateral displacement of liquefied layer and pile-head fixity condition are key factors influencing the pile response. A reasonably good agreement is found between the experimental results and theoretical predictions by an effective stress method of analysis.

1 INTRODUCTION

Performance of pile foundations may significantly be affected when surrounding soils undergo liquefaction during earthquakes. This observation is abundantly confirmed by well documented case histories from the 1995 Kobe earthquake where a number of piles has been found damaged or collapsed as a result of soil liquefaction (Tokimatsu and Asaka, 1998; Ishihara and Cubrinovski, 1998). Essentially, the liquefaction-related damage to piles is caused by an excessive lateral movement of the liquefied soil layer. Here, lateral ground displacements associated with two manifestations of liquefaction have to be recognized, i.e., cyclic displacements in the course of dynamic softening of the soil, and permanent displacements due to lateral spreading of liquefied deposits.

In an effort to gain fundamental understanding of the mechanism that brings large vulnerability to piles when surrounding soils liquefy, a number of studies utilizing 1-g and centrifuge shaking table tests on soil-pile models have been recently carried out in Japan. This paper presents results and analysis of a unique liquefaction experiment on a prototype-scale soil-pile model. The level ground model discussed herein was designed to investigate the cyclic phase of the interaction, and therefore it excludes the effects of lateral spreading.

2 FULL-SCALE LIQUEFACTION TESTS

The soil-pile model was prepared in a laminar box with plan dimensions of 12 by 3.5 meters, and height of 6 meters. The laminar box was bottom-fixed at a large shaking table. A 5.2 m thick deposit of saturated sand was prepared by pouring the sand into the laminar box through a water layer with a height of about 60 cm. The relative density of the sand layer prepared in the above manner is assessed to be in the range between 50 and 55 %. Shear wave velocity measurements along two vertical profiles indicated values of about 90 m/sec and 110 m/sec for the shallow and deep parts of the sand layer, respectively.

Three independent pile foundation systems aligned in the direction of shaking were used in this model test. Each foundation consisted of a group of four piles connected at their tops in a model footing with a mass of 8 tons. Two of the foundations were of prestressed high-strength concrete (PHC) piles and one was of steel piles. This paper presents only the results and analysis of the PHC-pile foundations.

The PHC piles were 5 m long and 20 cm in diameter. They had hollow-cylindrical cross section, with a wall-thickness of 4 cm and prestress level of 10 MPa. Each pile was bolted at the base of the laminar box whereas the pile tops where either fixed or pinned in the footing. Figure 1 shows a side view of the soil-pile model and layout of the instrumentation used. For the sand layer, pore pressure transducers and accelerometers were installed in several vertical arrays. In addition, lateral displacements and settlements of the ground surface were measured at two locations. The piles were instrumented with accelerometers along the depth and displacement transducers at their tops. Pairs of strain gauges were attached along the pile body for measuring bending moments.

The soil-pile model was shaken with a series of sinusoidal motions applied at the base of the laminar box. The first two shaking events which are referred in the following as Test 1 and Test 2 are discussed herein. The base acceleration time histories applied in

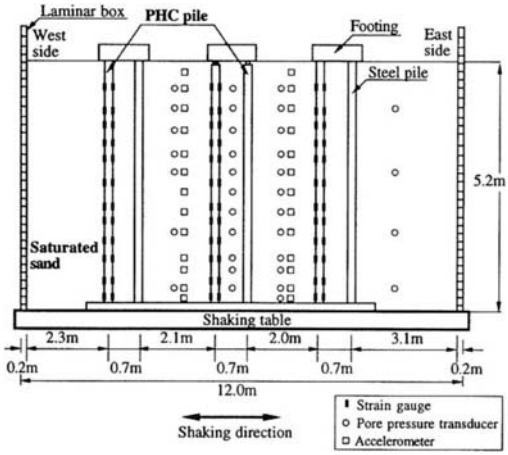

Figure 1. Cross-sectional view of the model and layout of the instrumentation

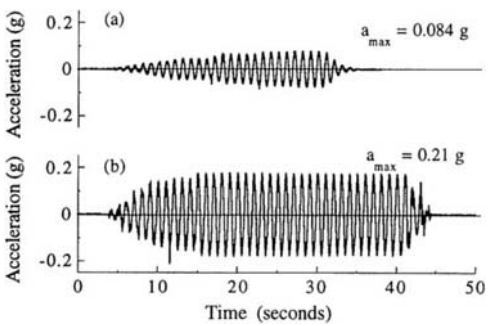

Figure 2. Base input motions: (a) Test 1, a_{max} = 0.084 g; (b) Test 2, a_{max} = 0.21 g

Test 1 and Test 2 are shown in Figure 2. The motions have a frequency of 1 Hz and peak accelerations of 0.084 g and 0.21 g respectively.

3 KASUMIGAURA SAND

The test soil used, Kasumigaura sand, is a well-graded sand with a mean grain size of D_{50} = 0.265 mm and fines content of about 3 % by weight. It was found to have a specific gravity of 2.71, maximum void ratio of e_{max} = 0.966 and minimum void ratio of e_{min} = 0.569.

Multiple series of laboratory tests on saturated soil samples were conducted to investigate the deformation characteristics of Kasumigaura sand. The majority of the tests were conducted on samples prepared by the water sedimentation method (WS) since it was assumed that this method of sample preparation provides the most representative fabric for the soil deposit of the model test. In addition, tests on

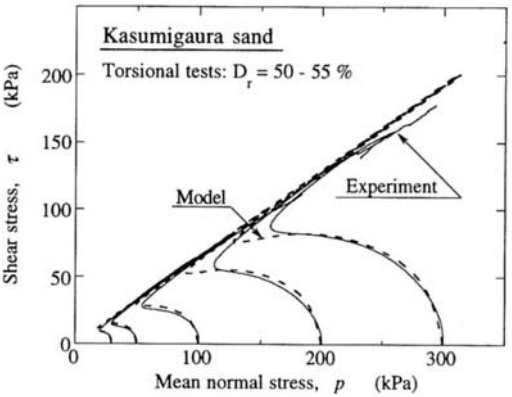

Figure 3. Effective stress paths in undrained tests

samples prepared by wet tamping (WT) were used to investigate the steady state and stress-strain characteristics of the sand with different fabrics. Selected results of tests which were used for analytical modelling and are illustrative of the deformation characteristics of Kasumigaura sand are introduced below.

3.1 *Monotonic undrained behaviour*

Effective stress paths measured in monotonic undrained torsional tests are shown with the solid lines in Figure 3. In these tests, water-sedimented samples were isotropically consolidated to a confining stress of 30, 50, 100, 200 or 300 kPa, achieving relative densities of 50, 51, 53, 54 and 55 % respectively. It is worth noting that these relative densities are in the same range with those of the deposit in the laminar box. It may be seen in Figure 3 that the effective stress path is nearly flat prior to the phase transformation, exhibiting marginal behaviour between drop and no-drop in the shear stress. This behaviour is typical of a loose sand.

The steady states obtained in monotonic undrained tests are plotted in the void ratio - mean effective stress diagram in Figure 4. Here, each symbol represents the ultimate state of a sample attained in triaxial compression (TC), triaxial extension (TE) or torsional mode of loading. A reasonably well defined steady state line is seen to exist though the modes of deformation and fabrics of Kasumigaura sand are different.

3.2 *Cyclic strength*

Five series of cyclic undrained tests on water-sedimented samples were conducted to determine the liquefaction resistance of Kasumigaura sand. The cyclic strength for different relative densities of the sand is displayed in Figure 5 in a typical plot showing the relationship between the uniform cyclic stress ratio and the number of cycles causing 5 % or 7.5 %

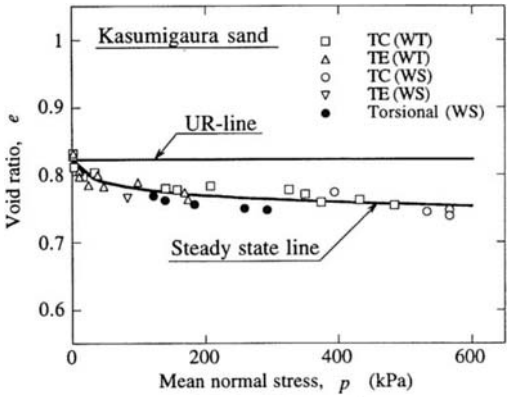

Figure 4. Steady states and reference lines

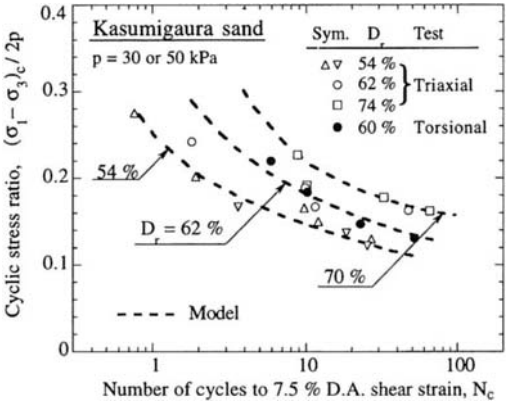

Figure 5. Cyclic strength for various relative densities

double amplitude axial or shear strain respectively. Apparently, Kasumigaura sand has relatively low cyclic strength, with 10 cycles of 0.145 cyclic stress ratio or only a single cycle of 0.25 stress ratio being sufficient to cause liquefaction and induce large shear strains for samples with a relative density of 54 %. As expected, the cyclic strength of the sand increases with increasing relative density. It is interesting to note that the cyclic strengths measured in the triaxial and torsional tests were found to be similar for samples having comparable relative densities.

4 NUMERICAL ANALYSIS

A fully coupled effective stress method of analysis of saturated soil was used to analyze the soil-pile model. The finite element mesh consisted of four node solid elements and beam elements representing the soil and the piles respectively. It was estimated that the interaction of the adjacent pile systems may be neglected in the analysis, and therefore, numerical models with a single pile foundation system placed nearly at the center of the laminar box were adopted. Lateral boundaries of the numerical model were tied to share identical displacements in order to model the lateral constraint imposed by the laminar box. Both soil and piles were modeled as elastoplastic materials.

4. 1 *Constitutive model for sand*

An elastoplastic deformation law for sands which is based on a state concept interpretation of sand behaviour was employed in the analysis. The use of the state concept for sand modelling is described in Cubrinovski and Ishihara (1998a) whereas the elastoplastic formulation of the model is given in Cubrinovski and Ishihara (1998b). Here, only some features of the model are highlighted and brief description of the determination of the material parameters of Kasumigaura sand is given.

4.2 *Material parameters*

The key feature used in the state concept description of soil behaviour is that shear behaviour is related to the initial state of the sand in the void ratio - mean effective stress diagram. Here, what counts is the relative initial state with respect to some reference states in the e - p diagram. The particular reference lines used in this model are those shown in Figure 4 where the UR-line is defined by the void ratio at which the steady state line intersects the ordinate.

In addition to the reference lines, the model requires three groups of material parameters to be determined, as indicated in Table 1 where the material parameters of Kasumigaura sand are listed. The elastic parameter A was evaluated from the measured shear wave velocity of the deposit in the laminar box while the values of n and ν were assumed. The stress-strain parameters were determined from relationships of the peak stress ratio and initial shear moduli with the state index I_s (Ishihara, 1993), as shown in Figure 6. These relationships were defined by using normalized stress-strain curves of five drained p-constant torsional tests. Finally, the dilatancy parameters μ_o and S_c were determined through simulations of behaviour observed in monotonic and cyclic undrained tests respectively, whereas the critical stress ratio M was assessed from the tests shown in Figure 3.

By using the values of the material parameters listed in Table 1, it is possible to model both monotonic and cyclic behaviour of Kasumigaura sand for any relative density and initial confining stress. This feature of the modelling is demonstrated in Figures 3 and 5 where model predictions, indicated with the dashed lines, are comparatively shown with tests results. It may be seen in Figure 5 that accurate predictions of the cyclic strength were achieved for various relative densities of Kasumigaura sand. The void ratio was the only parameter that would be varied in these three simulations.

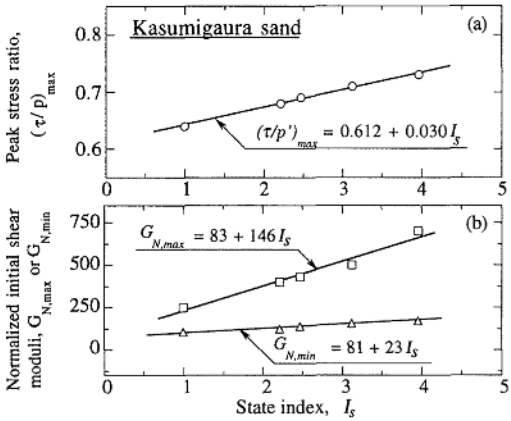

Figure 6. Stress-strain parameters versus state index: (a) peak stress ratio, (b) initial shear moduli

Table 1. Material parameters of Kasumigaura sand

Elastic	A = 250	n = 0.80	ν = 0.17
Stress-strain	$(\tau / p')_{max}$	$G_{N,max}$	$G_{N,min}$
	$a_1 = 0.612$	$a_2 = 83$	$a_3 = 81$
	$b_1 = 0.030$	$b_2 = 146$	$b_3 = 23$
Reference lines	UR-line	Steady state line	
	$e_o = 0.820$	$e_s = 0.845 - 0.033 \log p'$	
Dilatancy	$\mu_o = 0.17$	M = 0.622	$S_c = 0.005$

Table 2. Moment-curvature parameters of the piles

	Cracking (C)	Yielding (Y)	Failure (F)
Moment (kN-m)	13.3	26.7	29.8
Curvature (1/m)	0.0046	0.0283	0.0407

4.3 *Moment-curvature relationship of the piles*

Flexural properties of the PHC piles were modeled by a nonlinear moment-curvature relationship. The parameters of the equivalent trilinear M-ϕ relation are given in Table 2 where the kink points are defined as: C - concrete cracking at the extreme tension fiber; Y - yielding of the tension bars, and F - concrete crushing at the extreme compression fiber.

5 RESULTS AND DISCUSSION

5. 1 *Ground response*

In spite of the small base accelerations of less than 0.1 g, the sand layer liquefied throughout its entire depth in Test 1. Measured and predicted excess pore pressures at three depths of the sand layer are shown in Figure 7a where it may be seen that the pore pressure build-up was fairly uniform throughout the deposit. Computed effective stress paths in the analysis of Test 1 have indicated that after the initially negligible pore pressures induced when the cyclic stress ratios were less than 0.1, a sudden rise in the pore pressures was caused once the stress ratios reached values in the range between 0.15 and 0.20. The number of cycles required to liquefy the sand layer was found to agree fairly well with the liquefaction resistance shown in Figure 5. It is important to note that the relative density used in the analysis was from 50 to 57 %, and was distributed through the depth of the sand deposit as shown in Figure 9c.

Approximately one hour after Test 1, the second test was conducted. At that time, the excess pore

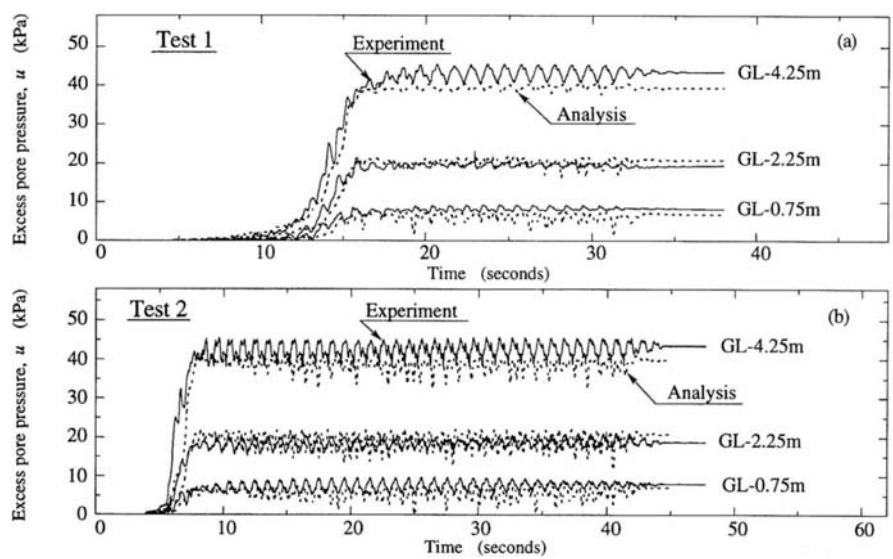

Figure 7. Measured and computed excess pore pressures: (a) Test 1, (b) Test 2

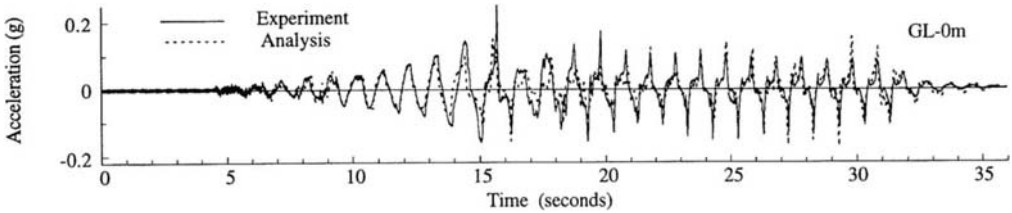

Figure 8. Recorded and computed accelerations at the surface of the sand deposit in Test 1

pressures which were induced in Test 1 were fully dissipated. As shown in Figure 7b, the liquefaction of the sand layer in Test 2 was faster and more sudden than that of Test 1. This response is in accordance with the increased input accelerations applied in Test 2. Good agreement between the measured and computed excess pore pressures may be seen in Figure 7 for both tests. The small discrepancy in the final values of the excess pore pressures is due to differences in the locations of the actual transducers and computational points. To further illustrate the accuracy of the analysis, computed and recorded acceleration time histories at the surface of the sand layer in Test 1 are comparatively shown in Figure 8.

Comparisons between measured and computed horizontal accelerations and displacements of the sand layer are shown in Figure 9. For purpose of comparison, the spikes in the accelerations shown in this figure were removed by low-pass filtering. Apparently, the maximum accelerations are fairly uniform through the depth of the layer in Test 1 whereas those of Test 2 attenuate towards the surface of the deposit. The largest scatter was found in the measurements of the ground displacement, and hence, it was the most difficult parameter for interpretation. The displacements of the experiment shown in Figure 9b were obtained by a double integration of the acceleration records and are those at the time of the peak ground surface displacement. The maximum displacements at the ground surface of about 5 cm for Test 1 and 8 cm for Test 2 indicate an average shear strain of about 1 % and 1.5 % respectively. Again, a reasonably good agreement between the measured and computed ground responses may be seen in Figure 9.

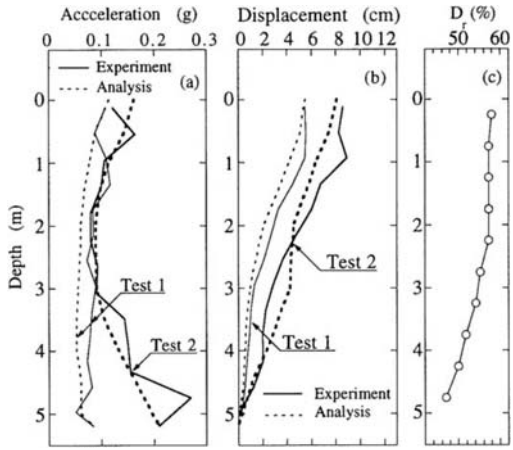

Figure 9. Measured and computed ground responses: (a) maximum accelerations, (b) relative displacements, (c) relative densities used in the analysis

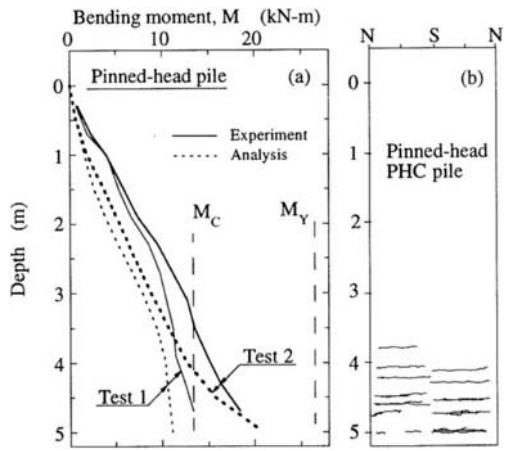

Figure 10. Pinned-head pile: (a) Computed and measured maximum bending moments,(b) observed cracks

5.2 *Pile response*

Once the testing was finished, the sand was removed from the laminar box, and damage to the piles was inspected. Figures 10b and 11b show the distribution of the observed cracks for the pinned-head and fixed-head piles respectively. Larger damage to the fixed-head piles was found, with a pronounced influence of the head fixity condition on both distribution and extent of the damage. It may be seen in Figures 10a and 11a that the maximum bending moments for both piles were much smaller in Test 1. Essentially, these bending moments were less than the cracking moment. Thus, it appears that all of the damage to the piles was inflicted during Test 2. Caution is needed here however, since a final test was conducted after Test 2,

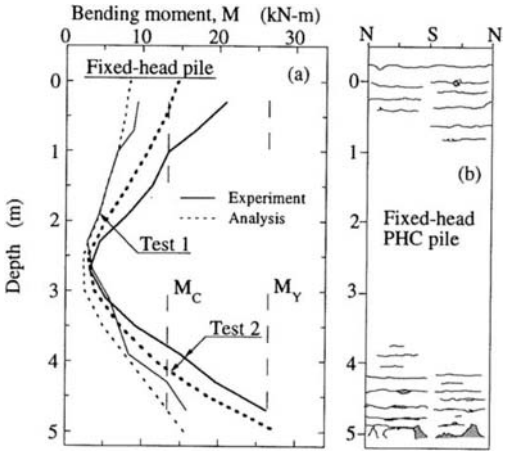

Figure 11. Fixed-head pile: (a) Computed and measured maximum bending moments,(b) observed cracks

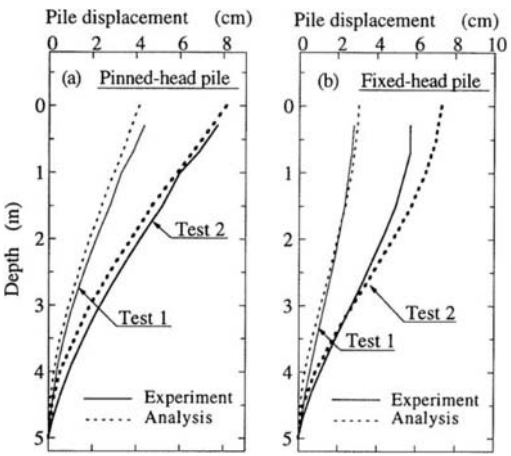

Figure 12. Maximum lateral displacements of the piles: (a) pinned-head pile, (b) fixed-head pile

in which the acceleration level was additionally increased for about 30 %. It may be seen in Figure 11 that the bending moments of the fixed-head piles reached the yielding level at the tip of the piles. It is interesting to note that the damage of the piles as described above is in accordance with a number of case histories on pile foundations from the 1995 Kobe earthquake where it has been found that the damage to the piles was concentrated in two zones: (a) in the zone of the interface between the liquefied layer and underlying unliquefied layer, and (b) at the pile-top.

The maximum lateral displacements of the piles shown in Figure 12 indicate that the peak displacements of the pinned-head pile-top were either similar or slightly smaller than the peak displacements of the ground surface. Due to constrains at the top of the fixed-head piles however, the corresponding displacements of these piles were smaller than the peak ground surface displacements for approximately 2-3 cm.

It may be seen in Figures 10 to 12 that predictions of the analyses are in good agreement with the experimental results. In essence, the analysis captured all important aspects of the response of the piles.

6 CONCLUSIONS

Results and analyses of liquefaction tests on a prototype-scale soil-pile model are presented. The key findings can be summarized as follows:

1. The large difference in the performance of piles in Test 1 and Test 2 despite the equally induced excess pore pressures and liquefaction in both tests, clearly demonstrates the importance of the lateral ground displacements for the pile response.

2. The pile head fixity condition was found to be another key parameter influencing both the degree and the distribution of the pile damage.

3. Predictions of the ground and pile responses by an effective stress method of analysis were found to be in good agreement with the measured values.

ACKNOWLEDGMENTS

The tests presented in this paper were sponsored by the High-Pressure Gas Safety Institute of Japan and were conducted using the large shaking table of the National Research Institute for Earth Science and Disaster Prevention (NIED), Tsukuba, Japan. The authors would like to acknowledge the permission of these two agencies for using the test data. The cooperation of Dr. N. Ogawa and C. Minowa, NIED, is greatly appreciated. Appreciation also goes to Mr. I. Morimoto and Dr. R. Orense, Kiso-Jiban Consultants Co. Ltd., Tokyo, for providing some of the test results and general cooperation.

REFERENCES

Cubrinovski, M. & K. Ishihara 1998a. Modelling of sand behaviour based on state concept. *Soils and Foundations* 38(3): 115-127.

Cubrinovski, M. & K. Ishihara 1998b. State concept and modified elastoplasticity for sand modelling. *Soils and Foundations* (to be published).

Ishihara, K. 1993. Liquefaction and flow failure during earthquakes. 33-rd Rankine lecture,*Geotechnicque* 43(3): 351-415.

Ishihara, K. & M. Cubrinovski 1998. Soil-pile interaction in liquefied deposits undergoing lateral spreading. *Proc. XI Danube-European Conf., Geotechnical Hazards* : 51-64.

Report of the High-Pressure Gas Safety Institute of Japan on large-scale shaking table tests on piles in liquefiable soil.

Tokimatsu K. and Asaka 1998. Effects of liquefaction-induced ground displacement on pile performance in the 1995 Hyogoken-Nambu Earthquake. *Soils and Foundations, Special Issue No.* 2 : 163-177.

Earthquake Geotechnical Engineering, Sêco e Pinto (ed.) © 1999 Balkema, Rotterdam, ISBN 90 5809 116 3

A study on liquefaction strength characteristics of sand mixed with gravel

H. Nagase & A. Hiro-oka
Kyushu Institute of Technology, Kitakyushu, Japan
Y. Kuriya
Kumamoto Prefectural Office, Japan

ABSTRACT: Sandy gravel ground is considered stable for the construction of structures. However, liquefaction occurred in sandy gravel deposits during the 1993 Hokkaido-Nansei-Oki Earthquake and 1995 Hyogoken-Nambu Earthquake. The liquefaction characteristics of sandy gravel deposits, especially during a great earthquake, should be clarified. In the present study, several series of cyclic undrained triaxial tests were performed on two kinds of sand mixed with four kinds of gravel, in order to study the effects of several parameters to express the state of packing in the specimen on the liquefaction strength of sand-gravel composites. It was found that liquefaction strength had a positive correlation with the parameters, with a scattering, though some problems in the evaluation method remain.

1. INTRODUCTION

During the 1995 Hyogoken-Nambu Earthquake, reclamed lands of sandy soil deposit containing gravel along the coastal areas of Kobe City, which consists of decomposed granite soil, liquefied on a large scale and highway bridges, shore structures and other structures were severely damaged (Ishihara et al. 1996, Towhata et al. 1996). It was also reported that a layer with a gravel content of about 80% liquefied during the 1993 Hokkaido-Nansei-Oki Earthquake (Kokusho et al. 1994). Liquefaction in such sandy gravel deposits has been a significant problem for the determination of renewal seismic design methods since the 1995 Earthquake. Sandy gravel ground has a high bearing capacity and is considered stable for the construction of structures. However, it was proved in the earthquake disasters that liquefaction can occur in sandy gravel deposits due to huge earthquake motion, even if the deposits do not have a low permeability. Moreover, it seems to be possible for liquefaction to occur in sandy gravel deposits covered with a clayey soil layer with a low permeability. Therefore, it is needed to investigate liquefaction characteristics of sandy gravel deposits.

Structures generally become instable when sandy ground around them liquefies. Therefore, it is necessary to accurately assess the liquefaction strength of sandy soil to discuss stability. Several parameters have been proposed to assess the liquefaction strength of sandy gravel. However, it is not clear what parameters are suitable for the assessment of liquefaction strength.

In the present study, several series of liquefaction tests were performed on Toyoura sand, and Chikugo river sand, whose mean diameter is larger and grain size distribution is better graded than Toyoura sand, compounded with some kinds of gravel of different grain size and grain shape. The method of assessing the liquefaction strength of sand-gravel composites was discussed using four density parameters.

2. SAMPLE MATERIALS AND TEST PROCEDURES

Figure 1 shows grain size distribution curves of soil samples used in the tests, which were Toyoura sand and Chikugo river sand mixed with four kinds of gravel. The gravel content ratio, GC, was 0%, 10%, 30% and 50%. Round gravel (2:3) means a sample combining a round gravel of 2mm to 4.76mm in diameter with a round gravel of 4.76mm to 9.50mm in diameter at a two-three ratio. Table 1 shows the test condition in this study.

The specimens used for the undrained cyclic triaxial tests were 15cm in diameter and 30cm in height. The density of the specimens was maintained according to procedure described below. The average relative density of the sand part, Dr_{matrix}, as defined in Fig.2, was 39% to 53%, as shown in Table 1. In the case of GC=0%, Toyoura sand with a relative density, Dr , or Dr_{matrix} of 70% and Chikugo river sand with Dr or Dr_{matrix} of 80% were also used

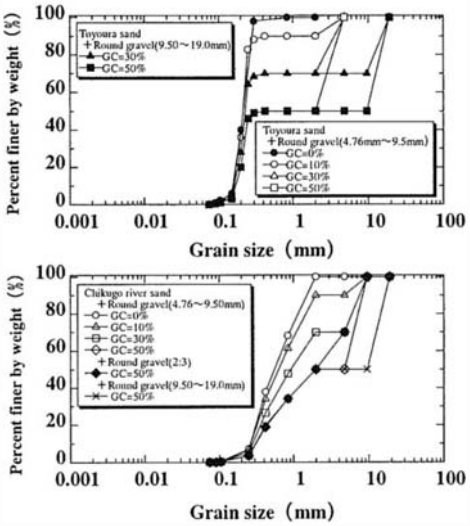

Fig.1 Grain size distribution curves

Table 1 Test condition

Sample	GC(%)	Dr_{matrix}(%)
Toyoura sand	0	50
//	0	70
Totoura sand +Round gravel (4.76~9.50mm)	10	49
//	30	46
//	50	41
+Round gravel (9.50~19.0mm)	30	51
//	50	52
+Angular gravel (4.60~9.50mm)	30	47
//	50	44
Chikugo river sand	0	50
//	0	80
Chikugo river sand +Round gravel (4.76~9.50mm)	30	45
//	50	39
+Round gravel (9.50~19.0mm)	50	53
+Round gravel (2:3)	50	48

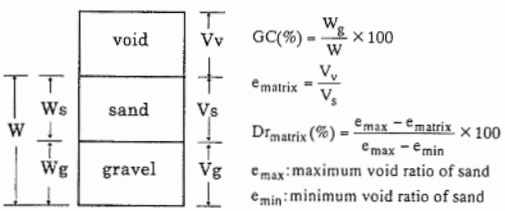

Fig.2 Explanation of GC and Dr_{matrix}

for the test.

The specimens were prepared from samples of unsaturated sand by a freezing method, which is explained in detail in Nagase et al. (1995). The preparation method involved pasting unsaturated sand and flattening the surface of the specimen to prevent membrane penetration. It also seemed to prevent sample segregation.

After the specimen was placed in a cell and defrosted, carbon dioxide (CO_2) gas was percolated through it to ensure the desired degree of saturation. Deaired water was then circulated and a back pressure of 196 kPa was applied to achieve a B-value in excess of 0.95. The specimen was then isotropically consolidated under a pressure of 49kPa. Following consolidation, axial stress was cyclically loaded at a frequency of 0.1 Hz while keeping the cell pressure constant.

Several examinations were performed on procedures in the liquefaction strength test on sand-gravel composites. The maximum density of the sample, excess pore water pressure generated at the top and bottom of specimen and distribution of axial strain induced by undrained cyclic triaxial test were investigated in the examination. The following behaviors were observed. The results are shown in detail in Kuriya (1998).

(1) According to the results obtained by observing a section of specimen after the maximum density test on Toyoura sand combined with a round gravel, segregation took place slightly in the vicinity of the top of the specimen, while segregation in the whole specimen did not occur remarkably.

(2) From the results on the process of excess pore water pressures observed at the top and bottom of the specimen, there was no difference between both pressure values. Therefore, that difference did not seem to be the reason for constriction of the specimen.

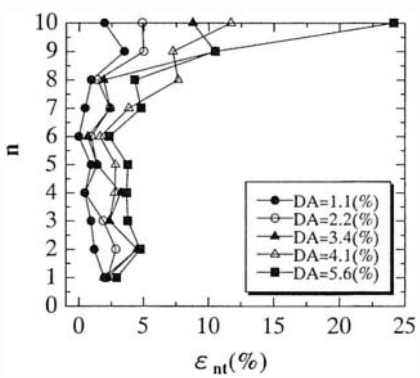

Fig.3 Distributions of double amplitude axial strain ε_{nt}

(3) The distribution of axial strain in the vertical direction was measured to examine a reliable sphere of the strain in the liquefaction strength test. If the double amplitude axial strain, DA, was smaller than 2%, the non-uniformity in the deformation of the specimen was tiny, as shown in Fig.3, and it was judged that the liquefaction strength test is reliable within the strain.

3. ESTIMATION OF LIQUEFACTION

3.1 The estimation due to Dr

Figures 4(a) and 4(b) indicate the relationships between the cyclic stress ratio, $R=\sigma_d/2\sigma_0'$, and the number of cycles, Nc, to a double amplitude axial strain, DA, of 2% using the data from tests on the specimens of Toyoura sand and Chikugo river sand mixed with gravel, respectively. The liquefaction strength ratio, R_{l20}, which is the cyclic stress ratio at 20 cycles, read from Fig.4, was plotted versus the relative density of the whole specimen, Dr, in Fig.5. It may be seen from Fig.5 that the liquefaction strength depends on the relative density, Dr, even if grain size or grain shape of gravel mixed with both sands was changed. The relationships have a good positive correlation, especially for the data on Toyoura sand. There seems to be a positive correlation in the relationships on Chikugo river sand, although there is much scatter in the data.

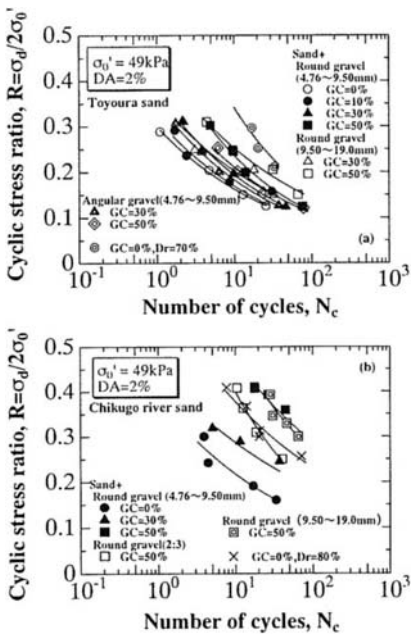

Fig.4 Cyclic stress ratio R versus number of cycles Nc to DA=2% relationships

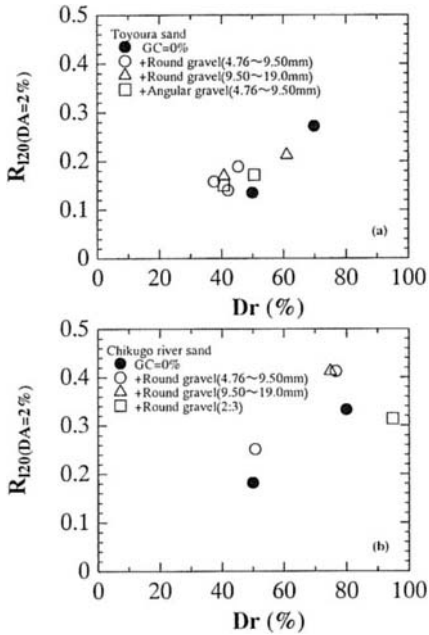

Fig.5 Liquefaction strength ratio, R_{l20}, versus relative density, Dr, relationships

3.2 The estimation due to Dr_{matrix}

Figure 6 indicates the liquefaction strength ratio, R_{l20}, versus the average relative density of the part of sand, Dr_{matrix}, obtained from the data, shown in Fig.4. For Toyoura sand mixed with gravel, it is recognized that the liquefaction strength ratio, R_{l20}, decreases as the relative density, Dr_{matrix}, increases. Therefore, the liquefaction strength does not depend on Dr_{matrix}. There appears a positive correlation for Toyoura sand mixed with round gravel of 9.50mm to 19.0mm in diameter, but the trend is different from that on Toyoura sand combined with no gravel, GC=0%. Thus, there seems to be a good correlation between the liquefaction ratio, R_{l20}, and the relative density of Dr_{matrix}, entirely, but the tendency is denied in the detail of the data.

On the contrary, R_{l20} obviously decreases as Dr_{matrix} increases for Chikugo river sand combined with a round gravel of 4.76mm to 9.50mm in diameter. R_{l20} does not depend on Dr_{matrix}, and different tendencies are observed between the data on Chikugo river sand with and without gravel. Therefore, it can be considered that it is different to estimate the liquefaction strength from the relative density of Dr_{matrix}.

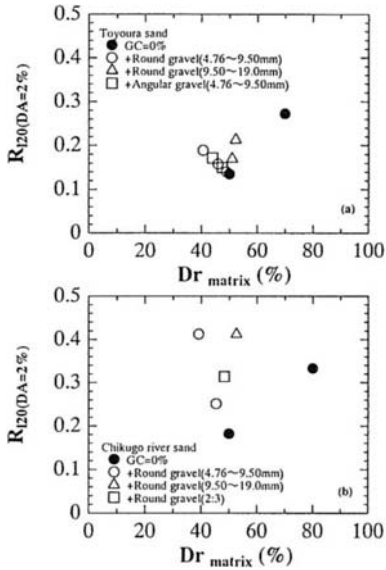

Fig.6 Liquefaction strength ratio, R_{l20}, versus relative density, Dr_{matrix}, relationships

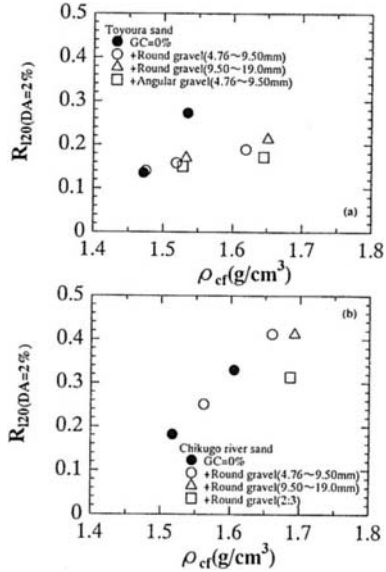

Fig.7 Liquefaction strength ratio, R_{l20}, versus equivalent fraction density, ρ_{cf}, relationships

3.3 The estimation due to equivalent fraction density

The estimation of the liquefaction strength was attempted using equivalent fraction density, ρ_{cf}, defined by the following formula.

$$\rho_{cf} = \frac{1}{\frac{GC}{\rho_c} + \frac{1-GC}{\rho_m}} = \frac{\rho_c}{1+GC(1-\frac{\rho_c}{G_{sg}})} \qquad (1)$$

where, ρ_c : density of sand-gravel composite (t/m^3)
ρ_m: density of sand part (t/m^3)
GC: gravel content ratio
G_{sg}: specific gravity of gravel particle

The liquefaction strength ratio, R_{l20}, versus equivalent fraction density, ρ_{cf}, relationships are shown in Fig.7. For Toyoura sand mixed with gravel, the data are plotted nearly on a straight line except for GC=0%. A straight line can also be drawn on the basis of the data on Chikugo river sand combined with gravel and no gravel. Thus, there seems to be a good correlation between R_{l20} and ρ_{cf}; it may indicate a limitation of ρ_{cf} for the estimation that R_{l20} versus ρ_{cf} relationships on Toyoura sand with GC=0% was quite different from that on the other data.

3.4 The estimation due to $Dr_{far\text{-}field\ matrix}$

Fragaszy et al.(1990) pointed out a theory on packing of sand and gravel particles, where the near-field matrix composed of small particles around oversize particles is generally looser than the far-field matrix consisting of small particles far from oversize particles. Figure 8 shows a schematic illustration of the idea. It was supposed in this study that oversize particles were gravel whose grain size was larger than 2mm and small particles forming the matrix was sand. And the authors tried to estimate the liquefaction strength from the relative density in the far-field matrix, $Dr_{far\text{-}field\ matrix}$. The relative density, $Dr_{far\text{-}field\ matrix}$ is expressed in the following formula. It was also assumed in this study that the average void ratio, e_{matrix}, is initially substituted for void ratio, e.

$$\left.\begin{aligned} \alpha &= \frac{1}{1+\beta\kappa} \\ \beta &= 1.333\ (e-0.1) \\ \kappa &= \frac{D_m C_m S_m}{D_0 C_0 S_0} \end{aligned}\right\}$$

where D_m, D_o: mean diameter, D_{50}, of sand and gravel
C_m, C_o: uniformity coefficient, U_c, of sand and gravel
S_m, S_o: grain shape coefficient of sand and gravel

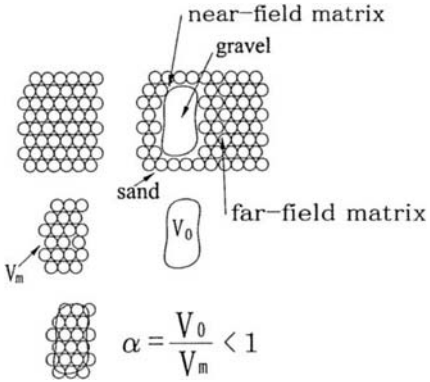

Fig.8 Explanation of α

$Dr_{\text{far-field matrix}}$ is calculated by assuming that the volume of gravel is equal to V_o/α, where V_o denotes the true volume of gravel and α is obtained from Eq.(2). The void ratio, $e_{\text{far-field matrix}}$, obtained from the relative density, $Dr_{\text{far-field matrix}}$, was substituted again for void ratio, e, in Eq.(2), until the calculated value corresponded to the substituted value.

The value of S_m was supposed to be 1 and the value of S_o was decided by averaging the ratio of the shortest length of gravel particle, c, to the longest length, a, whose values were measured from 50 extracted gravel particles. This assumption was done for an estimation of grain shape of gravel, in which the sand particles have a spherical shape and gravel particles are always more angular than sand particles. The value of S_o was obtained as 0.603, 0.555 and 0.390 for round gravel of 4.76mm to 9.50mm in diameter and 9.50mm to 19.0mm in diameter and an angular gravel of 4.76mm to 9.50mm in diameter, respectively. Figure 9 shows the relationships between the liquefaction strength ratio, R_{l20}, and the relative density, $Dr_{\text{far-field matrix}}$. There is a unique relation between R_{l20} and $Dr_{\text{far-field matrix}}$ for Toyoura sand mixed with gravel, while the data on Toyoura sand combined with angular gravel slightly separates from the other results. It is also recognized in the results on Chikugo river sand mixed with gravel that the R_{l20} versus $Dr_{\text{far-field matrix}}$ relationships have a positive correlation, although there is some scatter in the data.

For the equation of κ, proposed by Fragaszy et al. (1990), the term D_m/D_o is proved geometrically and the terms of C_m/C_o and S_m/S_o are expressed in the same manner as that of D_m/D_o because the value of α is affected by the form of grain size distribution curve and grain shape. However, it was not clarified in the paper why the equation of κ is required to have three such terms in that form. When the grain size distribution curve of sand was not changed, but that of gravel was changed, as in the present study, it can be seen that the volume of

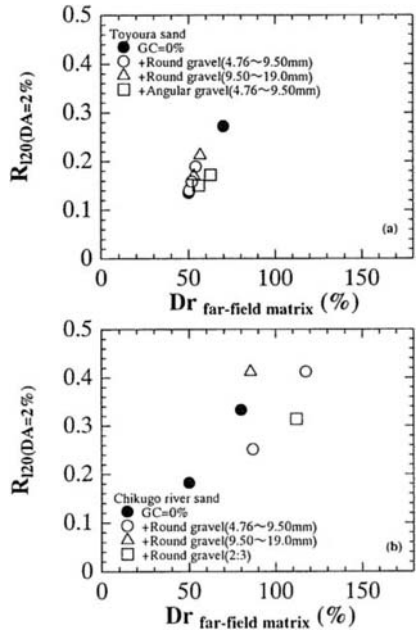

Fig.9 Liquefaction strength ratio, R_{l20}, versus relative density, $Dr_{\text{far-field matrix}}$, relationships

the near-field matrix increases as the uniformity coefficient, U_c, decreases and the surface area of gravel increases. On the basis of this idea, the relative density, $Dr_{\text{far-field matrix}}$, increases if the average void ratio of the sand part, e_{matrix}, is constant. In this case, $Dr_{\text{far-field matrix}}$ is considerably affected by the composition of gravel particles. Similarly, the surface area of gravel increases and $Dr_{\text{far-field matrix}}$ increases, when the gravel particles become angular and the value of S_o decreases. Thus, uniformity coefficient, U_c, and grain shape are closely related with the surface area of the particles. In this study, an equation form of $\sqrt{C_m}/\sqrt{C_o}$ and $\sqrt{S_m}/\sqrt{S_o}$ were utilized to obtain the value of κ, because the terms C_m/C_o and S_m/S_o are closely related with the ratio of the area of sand particle to that of grave particle and these terms were changed into the ratio of length as D_m/D_o. Figure 10 shows the relationships between the liquefaction strength ratio, R_{l20}, and the relative density, $Dr_{\text{far-field matrix}}$, obtained on the basis of the idea described above. It can be seen in Fig.10 that R_{l20} versus $Dr_{\text{far-field matrix}}$ relationships have a good correlation. Thus, it can be considered that the relationships shown in Fig.10 will have a high correlation, if grain size distribution and grain shape can be quantified as well as grain size and these quantities can be reflected in the value of α. In this view, it is quite significant to consider physical meanings when the value is decided. Although the method for deciding the value of α using the terms

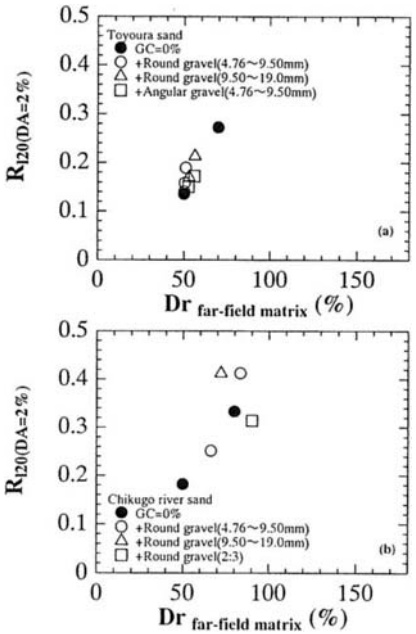

Fig.10 Liquefaction strength ratio, R_{120}, versus relative density, $Dr_{\text{far-field matrix}}$ relationship

$\sqrt{C_u}/\sqrt{C_0}$ and $\sqrt{S_q}/\sqrt{S_0}$ may not be the best one, a physical meaning is somewhat considered in the value of α.

4. CONCLUSIONS

Several series of liquefaction tests on Toyoura sand and Chikugo river sand mixed with gravel of different grain size, grain shape and grain size distribution were conducted using cyclic triaxial apparatus, in order to estimate the liquefaction strength using relative densities, Dr, D_{matrix}, $Dr_{\text{far-field matrix}}$ and equivalent fraction density, ρ_{cf}. The following behaviors were observed.

(1) The liquefaction strength increased as the relative density, Dr, calculated from the maximum and minimum dry density of the sand-gravel composites increased with a certain scattering, especially in the data on Chikugo river sand with a mean grain size larger than that of the Toyoura sand.
(2) The liquefaction strength versus the average relative density of the sand part, Dr_{matrix}, did not have a good correlation.
(3) Using the relative density in the part of sand far from gravel particles, $Dr_{\text{far-field matrix}}$, the liquefaction strength versus relative density relationships had a good correlation with a little scattering, if the effects of grain gradation and grain shape on the value of α were also properly considered in the calculation of $Dr_{\text{far-field matrix}}$.
(4) The liquefaction strength versus equivalent fraction density, ρ_{cf}, relationships also had a relatively good correlation, except for the data on Toyoura sand mixed with no gravel.
(5) Most of the sand-gravel composites used in this study are gap graded. Therefore, it is necessary to estimate the liquefaction strength of natural sandy gravels, which generally are not gap graded, using the relative density, $Dr_{\text{far-field matrix}}$, in order to confirm whether the density parameter is useful.

REFERENCES

Evans, M.D. and Zhou, S.: Liquefaction behavior of sand-gravel composites, *Journal of Geotechnical Engineering Division*, ASCE, Vol.121, No.3, pp.287-298, 1995.

Fragaszy, R.J., Su, W. and Siddigi, F.H.: Effects of oversized particles on the density of clean granular soils, *Geotechnical Testing Journal*, Vol.13, No.2, pp.106-114, 1990.

Ishihara, K., Yasuda, S. and Nagase, H.: Soil Characteristics and Ground Damage, *Special Issue of Soils and Foundations*, pp.109-118, 1996.

Kokusho, T., Tanaka, Y. et al.: Liquefaction of Gravelly Debris Avalanche Layer during Hokkaido-Nansei-Oki Earthquake – General Site Characterization and Geophysical Exploration, *Proc. of the 29th Japan National Conference on Soil Mechanics and Foundation Engineering*, pp.783-784, 1994 (in Japanese).

Kuriya, Y.: A Study on Liquefaction Strength Characteristics of Sand-Gravel Composites, *Master's Thesis at Kyushu Institute of Technology*, 1998 (in Japanese).

Nagase, H., Yanagihata, T. and Yasuda, S.: Liquefaction Characteristics of Very Loose Sand by Triaxial Compression Tests, *Proc. of the 1st International Conference on Earthquake Geotechnical Engineering*, IS-Tokyo'95, pp.805-810, 1995.

Towhata, I., Ghalandarzadeh, A., Sundarraj, K.P. and Vargas-Monge, W.: Dynamic Failures of Subsoils Observed in Waterfront Areas, *Special Issue of Soils and Foundations*, pp.149-160, 1996.

Earthquake Geotechnical Engineering, Sêco e Pinto (ed.) © 1999 Balkema, Rotterdam, ISBN 90 5809 116 3

Decrease of liquefaction susceptibility by preloading, measured in simple-shear tests

C.A. Stamatopoulos, A.C. Stamatopoulos & P.C. Kotzias
Kotzias-Stamatopoulos Consulting Engineers, Athens, Greece

ABSTRACT : Cyclic simple-shear tests simulate the soil response under conditions of level ground and horizontal earthquake loading. A series of such tests illustrated a marked increase of the cyclic strength of silty sands with preloading. The increase of the cyclic shear strength with the overconsolidation ratio in these tests was compared with the increase in tests given by other researchers, and was found to be similar. Relationships giving the increase of the cyclic strength with the overconsolidation ratio are proposed. The applicability of these relationships in the field to predict effects of preloading on level ground is discussed.

1 INTRODUCTION

Ground deformations caused by earthquakes are of great concern for aseismic design of structures on saturated soft soil [6]. Soil improvement is an effective way to mitigate the risk of excessive seismic ground deformations [8].

Preloading is a temporary loading applied at a construction site to improve subsurface soils by increasing density and lateral stress. The method is frequently used to improve poor soil conditions and sustain large static loads [11]. Compared to other methods of soil improvement, preloading is less expensive and requires simpler equipment. It is significant that, whereas other methods of soil improvement apply to particular soil types, preloading does not have any such restrictions [11]. Other advantages of preloading are that it is possible to directly observe its progress in the field, by measuring ground settlements, and to assess its effects in the laboratory, as illustrated below.

Most applications and publications on preloading consider the improvement of static properties of soil without, however, examining the corresponding improvement of dynamic properties. A soil parameter illustrating the susceptibility of level ground to large seismic deformations is the cyclic soil strength. This paper investigates the effect of preloading on the cyclic soil strength, using results of cyclic laboratory tests.

2 CYCLIC SOIL STRENGTH AND OVER-CONSOLIDATION RATIO ON LEVEL GROUND

2.1 Cyclic soil strength of level ground

In level ground, the vertical effective stress σ'_v equals the overburden effective pressure, and the ratio of the effective horizontal stress to the effective vertical stress is given by the factor K_o. Earthquake loading is primarily applied in the form of horizontal shaking causing cyclic shear stress τ_{cyc}. For these conditions, cyclic stress ratio SR is defined as the ratio of the cyclic (half the peak-to-peak change) shear stress τ_{cyc} to the effective vertical stress, σ'_v. It can be noted that a cyclic stress ratio SR corresponds to a horizontal acceleration (SR*g), where g is the acceleration of gravity.

During dynamic shaking of saturated level ground positive strains develops for positive τ, and negative for negative τ. The amplitude of strain increases with cycle number. Cyclic strength SR_{10} is defined as the value of the cyclic stress ratio SR causing double-amplitude cyclic shear strain exceeding the value of 5% in 10 uniform cycles of dynamic loading. Similarly, cyclic strength SR_N is defined as the cyclic stress ratio SR causing double-amplitude cyclic shear strain exceeding the value of 5% in N uniform cycles.

Cyclic soil strength is measured in the laboratory by cyclic tests using various devices and procedures, described below.

2.2 Laboratory tests where horizontal displacement is not allowed

This condition exists in the simple-shear device, where horizontal strain in the base of the apparatus is zero. In this device, during consolidation, similarly to level ground in the field, lateral movement is not allowed, and the stress ratio initially equals K_o, a property of the soil. As a result of cyclic loading with constant volume and without static shear stress τ, similarly to the seismic response of level ground, static shear stress q decreases, pore

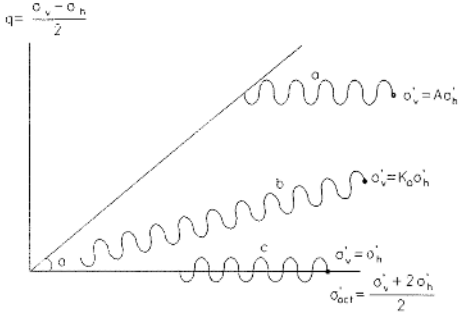

a anisotropically-consolidated triaxial test
b simple-shear test, or Ko-consolidated torsional shear test
c isotropically-consolidated triaxial test or isotropically-consolidated torsional shear test
K_a is the ratio of the effective horizontal by the vertical stress (a property of the soil)
A is the ratio of the applied effective vertical by horizontal stress during consolidation
• state after consolidation

Fig. 1: Illustration of differences in the stress path in cyclic undrained tests using different devices.

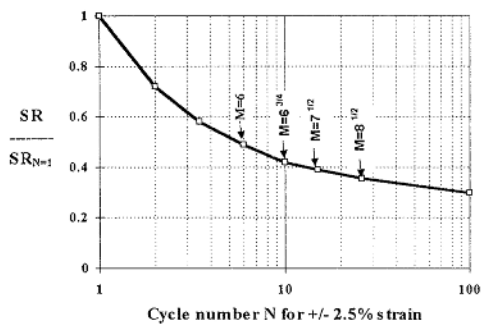

Fig. 2: Typical shape of the relationship between SR and number of cycles to ± 2.5% strain and relationship between number of cycles and earthquake magnitude (Seed et al, 1983).

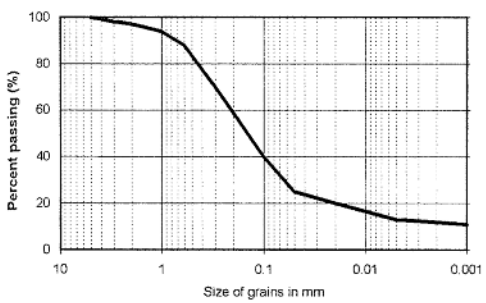

Fig .3: Grain size disribution of the silty-sand from Langadas.

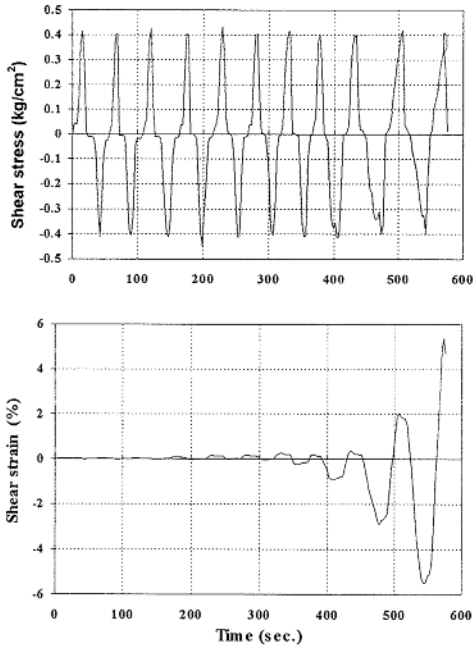

Fig. 4: Measured shear stress and shear strain versus time in a typical cyclic simple-shear test on the silty sand from Langadas (OCR=1).

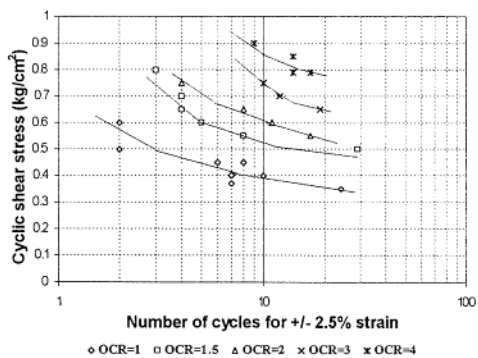

Fig.5: Effect of prestress on he liquefaction curves, in samples of the silty-sand from Langadas, measured in cyclic simple-shear tests (σ_v = 3.0 Kg/cm²).

pressure and cyclic strain builds up, and liquefaction develops (fig. 1-b). Prior to liquefaction, residual horizontal strain is about zero [9]. In the triaxial chamber it is also possible to perform tests where no lateral movement is allowed during consolidation, and at the end of each cycle of cyclic loading, by adjusting the cell pressure σ'_h accordingly. In these tests, the response is similar to the response of the cyclic simple-shear tests.

2.3 *Laboratory tests where the cell pressure is kept constant*

During cyclic undrained triaxial tests, usually the cell pressure remains constant and cyclic loading is applied as $\sigma_{v\text{-}cyc}$. Under these conditions, for soil samples that are not very loose, pore pressure cannot exceed the value determined by the horizontal distance between the initial state and the failure line in fig. 1. In anisotropically-consolidated tests, as a result of cyclic loading, permanent shear strain accumulates, but cyclic shear strain may not change considerably with cycle number, and liquefaction may not develop (fig. 1-a) [13]. In undrained isotropically-consolidated cyclic tests, similarly to the response of cyclic simple-shear tests described above, as the number of cycles increases, pore pressure builds up, cyclic shear strain increases and liquefaction develops (fig. 1-c). In addition, permanent shear strain is about zero prior to liquefaction [13].

2.4 *Discussion*

From the above it is concluded that the cyclic soil strength can be measured in tests with cyclic loading (a) in anisotropically consolidated conditions where the horizontal strain in the base of the apparatus is zero, (b) in conditions of isotropic consolidation. The tests of type (a) are usually performed in the simple-shear device, while the tests of type (b) in the triaxial cell. Unlike the tests of type (b), the tests of type (a) with initial prestress under different vertical stresses simulate the increase of density and horizontal stress (and K_o) that is caused by preloading in horizontal ground in the field. The cyclic loading that follows simulates the seismic response of a soil element of a level ground under a horizontal earthquake. Analysis of such tests gives the effect of preloading in cyclic soil strength of level ground.

The Overconsolidation Ratio OCR is defined as $\{\sigma'_{v\text{-}max}/\sigma'_v\}$, where $\sigma'_{v\text{-}max}$ is the maximum past effective vertical stress that has been applied, and σ'_v is the current overburden effective vertical stress. In standard practice in soil mechanics, the Overconsolidation Ratio (OCR) is used to describe the effect of preloading in soils.

Seed et. al. [10] give the typical shape of liquefaction curves measured in cyclic laboratory tests; i.e., the normalised cyclic stress ratio SR causing liquefaction in N cycles of uniform cyclic loading, SR_N, as a function of the cycle number (fig. 2). Thus, between different liquefaction curves, the proportional change of the cyclic shear strength SR_N between curves is more-or-less unique and does not depend on the cycle number for which the cyclic strength is taken.

For these reasons, the change of SR_{10} in cyclic simple-shear tests and the OCR will be used below as indexes in studying the effect of preloading on the cyclic soil strength of level ground.

3 PROGRAM OF CYCLIC SIMPLE-SHEAR TESTS

The material used in the laboratory tests of the present study was a mixture of silty sand samples, obtained from borings near Langadas in Northern Greece. The content of fines in the mixture was 30% (fig. 3), and the plasticity of the material was practically zero. The specimens were prepared at a dry density equal to 1.64 T/m^3. Oedometer tests showed that the apparent overcconsolidation pressure of the specimens was about 1.5 Kg/cm^2. The specimens were saturated and consolidated in the simple-shear device at a vertical stress σ'_v of 3.0, 4.5, 6.0, 9.0 or 12 Kg/cm^2. Prior to the application of cyclic loading, the vertical stress was decreased in all specimens to 3.0 Kg/cm^2. The corresponding OCR values are 1, 1.5, 2, 3 and 4, respectively. For each of these five cases, at least three cyclic constant-volume tests were performed with different values of cyclic shear stress.

Fig. 4 gives the shear stress and shear strain versus time of a typical test. Fig. 5 gives the measured effect of preloading on the number of cycles causing liquefaction (double-amplitude cyclic shear strain exceeding the value of 5 %) for various cyclic stresses and OCR values.

4 CYCLIC STRENGTH VERSUS OVERCONSOLIDATION RATIO IN TESTS SIMULATING THE SEISMIC RESPONSE OF LEVEL GROUND

4.1 *Correlations*

Table 1 summarises test programs found in the literature that study the effect of preloading on the cyclic soil strength of soils in conditions simulating the seismic response of level ground. In addition to programs using the simple-shear device, a program using the torsional-shear device is given, in which, similarly to the simple-shear tests, horizontal strain was kept zero during consolidation, preloading, and the subsequent cyclic loading.

Fig. 6a plots the effect of OCR on the cyclic strength SR_{10} of the studies of table 1, as a function of soil type (according to the categories sands, clays). The following may be observed: Overconsolidation has a definite effect in increasing the cyclic strength of the specimens. This effect is similar for all test programs, and becomes more pronounced for clays. The proportional increase of the cyclic strength with OCR on a logarithmic scale is not linear, and its rate decreases with OCR.

An empirical correlation giving the increase in cyclic strength with OCR, for OCR<10, is

$$\{ SR_{10\text{-}oc}/SR_{10\text{-}nc} \} = OCR^{\Lambda} \quad (1a)$$

where $\Lambda = a\,(1 - b \times \log(OCR))$ (1b)

Table 1. Studies and results of the effect of preloading on the cyclic soil strength in cyclic tests without horizontal strain.

No	REFERENCE	TYPE OF TEST	% FINES	N	SR (ocr=1)	SR (ocr) /SR (ocr=1) OCR= 1.5	2.0	3.0	4.0	8.0	10
in sands, silty sands											
1	Seed and Peekock (1971)	simple-shear	0	10 20	0.07 0.05				2.1 2.7	3.4 4.5	
2	Ishihara and Takatsu (1979)	torsional shear	0	20	0.17		1.7				
3	Finn (1981)	simple-shear	0	10 20	0.10 0.08		1.6 1.7		2.4 2.4		
4	present study (fig. 5)	simple-shear	30	10 20	0.13 0.12	1.3 1.3	1.5 1.5	1.9 1.9	2.2 2.2		
in clays											
5	Andersen et al (1980)	direct simple-shear	100	10 20	0.17 0.17				2.7 2.7		4.4 4.4
6	Malek (1987)	direct simple-shear	100	20	0.16		1.8		2.7		

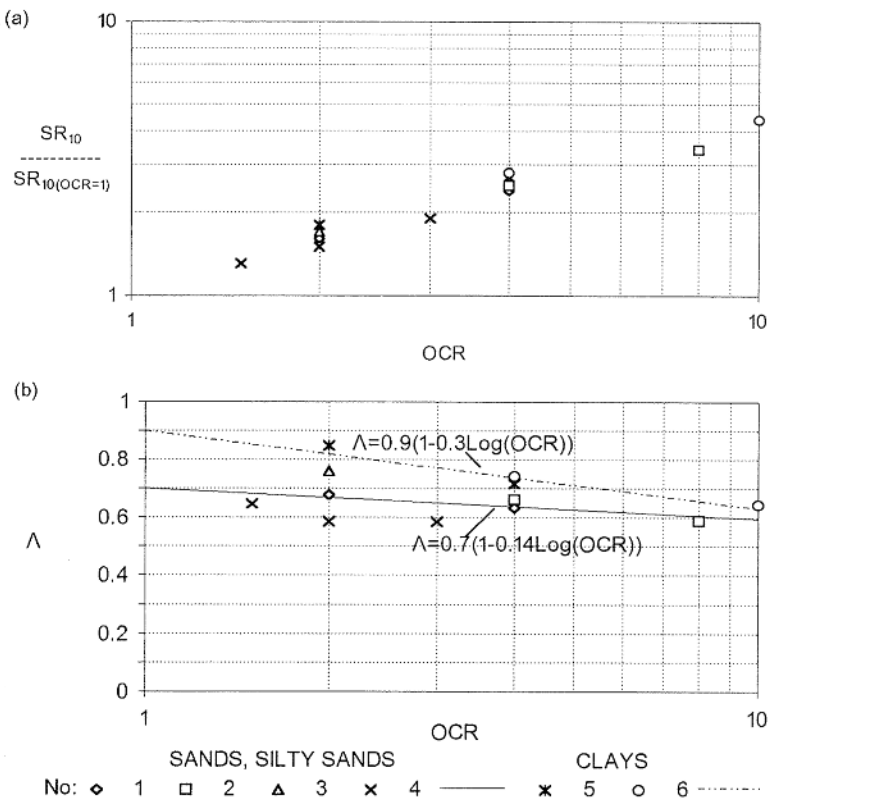

Fig 6: The proportional increase of the cyclic strength and the factor Λ (equation 2b) with OCR, as measured in the cyclic tests of Table 1.

where the subscripts "oc" and "nc" denote overconsolidated and normally consolidated states and the parameters a and b depend on the soil type. Fig. 6b gives the factor Λ, for the results of fig. 6a. Linear regression gives that for sands a=0.7 and b=0.14, while for clays a=0.9 and b=0.3. The coefficient of correlation R^2 for sands equals 0.4, while for clays 0.9.

4.2 Verification from results of isotropically-consolidated tests

The considerable increase of the cyclic strength with the overconsolidation ratio has also been measured in cyclic undrained tests with isotropic consolidation [4, 12]. Similarly to tests in the simple-shear device, (a) similarities are observed between the tests in the increase of cyclic soil strength with the overconsolidation ratio for similar soils, and (b) the effect is larger in clays than in sands [12]. However, the relative increase of the cyclic soil strength in terms of OCR was smaller than that in the simple-shear device (fig. 6), presumably because of the increase of the horizontal stress with preloading, prior to the application of the cyclic stress in the simple-shear tests (unlike the isotropically-consolidated tests).

As was discussed previously, consolidation of a horizontal soil layer, differs from that of laboratory tests with isotropic consolidation. In the field the horizontal stress σ'_h is not equal to the vertical stress σ'_v, but is given by $K_o \sigma'_v$, where the lateral stress ratio K_o depends (increases) with the Overconsolidation Ratio. These conditions correspond to the conditions of the simple-shear tests. Thus, to predict the increase of cyclic soil strength of level ground with the OCR, with results of isotropically-consolidated cyclic tests, assumptions are needed for (a) the increase of the horizontal stress with preloading and (b) the increase of cyclic soil strength with the horizontal stress. It is concluded that for the prediction of the increase of cyclic soil strength of level saturated ground with preloading, tests with isotropic consolidation can not be quantitatively as accurate as relationships obtained from cyclic simple-shear tests, and thus are not examined in detail.

4.3 Form of equation (1)

Some proposed relationship that has been proposed correlating the cyclic soil strength with the OCR in simple-shear conditions was not found in the literature. Ishihara and Takatsu [6] propose for the increase of cyclic strength with OCR in conditions of isotropic consolidation for sands the relationship

$$\{SR_{oc}/SR_{nc}\} = OCR^{0.5} \qquad (2)$$

As anticipated (from the previous discussion) the parameter 0.5 is smaller than the measured increase of cyclic soil strength in the simple-shear device of fig. 6.

The relationship (2) indicates that the factor Λ of equation (1b) does not depend on the overconsolidation ratio. However, in the relationship of the cyclic soil strength with the OCR in conditions of simple-shear, the effect of the factor Λ with the OCR is considerable, especially for clays (fig. 6), and thus the form of equation (1b) is necessary.

5 DISCUSSION

5.1 Applicability in the free-field

The increase in cyclic strength by preloading of soft and/or loose horizontal deposits could be obtained by estimating the increase of OCR with depth by a preloading surcharge, OCR_{after}, by elastic analyses, and the increase of the cyclic strength with OCR, by equation (1). However, caution should be used when using equation (1) to estimate the increase of the cyclic shear strength in the field with OCR_{after}. Unlike laboratory tests used to derive relationship (1), in the field, as a result of ageing and secondary consolidation, the in situ Overconsolidation Ratio may be greater than unity, even for soft deposits.

A possible way to consider this effect is to predict the increase of the cyclic shear strength in the field by :

$$\{SR_{N\text{-after}}/SR_{N\text{-bef.}}\} = \{SR_{N\text{-after}}/SR_{N\text{-nc}}\}\{SR_{N\text{-nc}}/SR_{N\text{-bef.}}\} \qquad (3)$$

where both terms of equation (3) can be evaluated by equation (1). The value of the baseline overconsolidation ratio $OCR_{bef.}$, required to obtain the factor $\{SR_{N\text{-nc}}/SR_{N\text{-bef.}}\}$, could be measured by laboratory oedometer tests on undisturbed samples from borings, or from field measurements.

It should be noted that the cyclic soil strength in equation (3) is defined in terms of the N "significant" cycles of earthquake loading, unlike the cycle 10 in equation (2), but this is permissible because of the (approximately) unique relationship of fig. 2, that was described in section 2.4.

5.2 Factor of safety against large ground deformations

The factor of safety of level ground against large seismic movements, for a given depth z, FS(z), can be assessed by a simple comparison of the seismically induced shear stress with the similarly expressed cyclic shear strength required to cause initial liquefaction, or, equivalently, using:

$FS(z) = SR_N(z)\, g / a(z)$

where the cyclic strength SR_N is defined in chapter 2, g is the acceleration due to gravity and a(z) is the "average" horizontal applied acceleration in terms of depth for the N "significant" cycles of the earthquake [6].

Preloading increases the above factor of safety by increasing, for any given depth, the cyclic soil

strength SR_N, as discussed in section 5.1. However, preloading may cause stiffening of the soil and hence amplification of seismic acceleration a(z). This effect may be studied by performing dynamic 1-dimensional analyses, using different values of dynamic soil parameters (e.g. the shear modulus Go) before and after preloading.

6 CONCLUSIONS

Cyclic simple-shear tests with different prestress levels and no initial shear stress τ model the increase in density and horizontal stress by preloading on level ground, and the pore-pressure and shear deformation build-up by a subsequent horizontal shaking. Such tests illustrated that preloading has a definite effect in increasing the cyclic strength of soft/loose soil. Comparison of the results of these tests with various other data found in the literature illustrated that the proportional effect of overconsolidation on cyclic soil strength is similar for all test results, and becomes more pronounced for clays. An empirical correlation giving the increase in cyclic strength with OCR is proposed (equations (1)).

Equations (1) should be used with caution when investigating the effect of preloading in reducing the potential of large seismic ground deformations in the field because (a) in the field, unlike in the soil specimens, as a result of aging, the Overconsolidation Ratio prior to the application of the surcharge may be greater than unity, even for soft deposits and (b) seismic acceleration may be higher after preloading, due to stiffening of the soil.

ACKNOWLEDGMENT

This work was supported by the European Commission, DG XII for Science, Research and Development, Climate and Natural risks (project "Cost-effective Soil Improvement Methods to Mitigate Seismic Risk"). C. Mavridis and A. Xenakis assisted in the performance, while civil engineer L. Balla in the analysis of the tests presented in the present article.

REFERENCES

1. Andersen, K. H., Pool J. H., Brown S. F., Rosenbrand W. F. "Cyclic and Static Laboratory Tests on Drammen Clay", Journal of the Geotechnical Engineering Division, ASCE, 1980, Vol. 106, No. 5, pp 499-529.
2. Campanella G., Lim B. S., "Liquefaction Characteristics of Undisturbed Soils", Intern. Conf. on Recent Advances in Geotech. Earthq. Engin. and Soil Dynamics, University of Missouri-Rolla, Missouri, USA, 1981, pp 227-230.
3. Finn W. D. L. "Liquefaction Potential: Developments Since 1976", Intern. Conf. on Recent Advances in Geotechn. Earthq. Engin. and Soil Dynamics, University of Missouri-Rolla, U.S.A., 1981, pp 655- 675.
4. Ishihara K. and Takatsu H. "Effects of overconsolidation and K_o conditions on the liquefaction characteristics of sands", Soils and Foundations, Japanese Society of Soil Mechanics and Foundation Engineering, 1979, Vol 19, No 4, pp 59-68.
5. Ishihara K., Sodekawa M. and Tanaka Y. "Effects of Overconsolidation on Liquefaction Characteristics of Sands Containing Fines", Dynamic Geotech. Testing, ASTM STP 654, American Society for Testing and Materials, 1978, pp 246-264.
6. Ishihara, K. "Liquefaction and Flow Failure During Earthquakes", 33rd Rankine Lecture, Geotechnique, 1993, Vol. 43, No. 3, pp 351-415.
7. Malek A. M. "Cyclic behavior of clay in undrained simple shearing and application to offshore tension piles", thesis for Doctor of Science, Department of Civil Engineering, Massachussetts Institute of Technology, Cambridge, USA, 1987.
8. Mitchell J. K., Baxter C. D., Munson T. C. "Performance of improved ground during earthquakes", Soil Improvement for Earthquake Hazard Mitigation, ASCE, Geotechnical Special Publication No. 49, 1995, pp 1-36.
9. Seed, H. B. and Peacock, W. H. "Test procedures for measuring soil liquefaction characteristics", Journal of the Geotechnical Engineering Division, ASCE. 1971, Vol. 97 , No. 8, pp 1099-1119.
10. Seed, H. B., Idriss I. M., and Arango I. "Evaluation of Liquefaction Potential Using Field Performance Data", Journal of Geotechnical Engineering, ASCE, 1983, Vol. 109, No. 3, pp 458-482.
11. Stamatopoulos A. C and Kotzias P. C., Soil Improvement by Preloading , John Wiley & Sons, 1985, 261 pages.
12. Stamatopoulos, C. A., Stamatopoulos, A. C., Kotzias, P.C. (1995) "Effect of prestress on the liquefaction potential of silty sands", Soil Dynamics and Earthquake Engineering VII, Computational Mechanics Publications, Southampton, pp. 181-188.
13. Stamatopoulos, C. A., Bouckovalas, G., and Whitman, R. V. "Analytical Prediction of the Earthquake-Induced Permanent Deformations", Journal of the Geotechnical Division, ASCE, 1991, Vol. 117, No. 10, pp 1471-1491.

Earthquake Geotechnical Engineering, Sêco e Pinto (ed.) © 1999 Balkema, Rotterdam, ISBN 90 5809 116 3

Microzonation for liquefaction in northern coast of Anazali lagoon, Iran

S. M. Mir Mohammad Hosseini
Amir Kabir University of Technology, Tehran, Iran

ABSTRACT: One of the most common causes of ground failure during heavy earthquakes is the liquefaction Phenomenon which has produced severe damages so far all over the world. Zonation of active seismic region against liquefaction is usually one of the common methods to mitigate the seismic hazards. In this paper according to the availabe geological and geotechnical data in the northern coast of Anzali lagoon in an area which serves the main road in the coastal band of the Caspian sea and connects the most eastern province to the most western one of Iran, a microzonation against liquefaction was carried out. Using different analyses methods, the liquefaction potential of the area was investigated. Finally the microzonation maps of the area based on grade 2 methods were produced.

1 INTRODUCTION

There have been significant development in understanding the nature and consequences of the liquefaction Phenomenon since it was recongnized as a main cause of many damages during heavy earthquakes in the mid 1960s . Because in some cases the ground loses its strength completely, servere damages may impose to buildings , lifelines , ports , bridges , roads and other urban facilities in this conditions.

In order to mitigate the seismic hazards , one of the effective way is to determine the land use based on the zonation maps provided with respect to the probability of occurrence of the phenomenon and the level of damages induced in these circumstances.

In this study a great attempt has been made to determine the most suitable method for evaluating liquefaction potential of suceptible zones in the northern coast of Anzali Lagoon (in the north of Iran) , according to geological and geotechnical characteristics as well as the seismicity of the region, and to provide zonation maps with some degrees of accuracy.

2 DIFFERENT METHODS FOR EVALUATION LIQUEFACTION POTENTIAL

Several analyses methods for evaluating liquefaction potential of saturated and loose sands have been developed during recent years. In these methods usually cyclic shear stresses induced during an earthquake are estimated and compared with cyclic shear strengths of the soil layers.

The main laboratory tests to obtain the cyclic strength of the soils are cyclic triaxial and cyclic simple shear tests, which need the undisturbed samples to be tested under field conditions . Due to some difficulties in taking undisturbed samples particularly for loose granular soils which is the case in liquefaction phenomenon, the insitu tests have been more commonly used for obtaining the cyclic strength of the soil layers. Among them the SPT(Standard Penetration Test) , CPT (Cone Penetration Test) and the shear wave velocity measurements are the most popular ones which have been extensively used all over the world.

The evaluation of liquefaction potential is initially carried out at a single borehole in different depths. Then its consequeces on the ground surface are investigated. In the next step an overall assessment are made for a series of boreholes within a selected zone.

Since there have been many field data available from the SPT sutdies in the region under consideration , in this section the main and important methods for analyzing liquefaction potential based on the results of SPT have been reviewed and described. Because of different specifications and procedures of the SPT, it is of great importance to uniform all test results obtained from site investigation carried out in different conditions . In this respect appropriate correction factors are applied to the test results.

There are many methods by which the liquefaction potential can be estimated , among them the following ones which have been used in this study are mentioned.

2.1. Seed et al. method (1971)

Based on the SPT obtained at each depth , N , the corrected number can be obtained using equation (1):

$$(N_1)_{60} = C_N \frac{ER_m}{60} (N) \quad (1)$$

Where , N is the SPT number, ER_m is the energy efficiency used to penetrate the SPT rod into the ground , and C_N is the overburden correction factor which can be obtained either from the graph or equations shown below:

$$C_N = \frac{1}{\sqrt{\sigma'_0}} \quad (2)$$

$$C_N = 0.77 \log \frac{20}{\sigma'_0} \quad (3)$$

The cyclic shear strength ratio :$R = \pi_{av}/\sigma'_0$ can be obtained from the empirical graphs developed by Seed et al. (1985) using the corrected SPT number, N_1, which has to be compared with the shear stress ratio causing liquefaction, L_s:

$$L = \frac{\alpha_{max}}{g} r_d \frac{\sigma_0}{\sigma'_0} \quad (4)$$

Where $r_d = 1\text{-}0.015Z$. The safety factor against liquefaction may be calculated from the following equation:

$$FL = \frac{R}{0.65\ L} \quad (5)$$

The values of ER_m for different testing systems and procedures may change between 45 to 78 (%) .

2.2 Ishihara method (1990)

The cyclic shear strength of the soil layers may be obtained from the following equation:

$$R = 0.0676 \sqrt{N_1} + 0.0035\ F_c \quad (6)$$

Where Fc, is the fine content of the soil and N1 is the corrected SPT number:

$N_1 = (1.67/\sigma'_0)N.$

2.3 Iwasaki et al. method (1978)

The cyclic shear strength of the soil can be estimated based on the following equations which have been outlined in the Japanese Bridge code (Japan Road Association , 1991):

$$R = R_1 + R_2 + R_3 \quad (7)$$

Where:

$$R_1 = 0.0882 \sqrt{N' / (\sigma'_0 + 0.7)} \quad \text{in which } N' = 0.838\ N \quad (8)$$

$$R_2 = \begin{cases} 0.19 & \text{For } 0.02 \text{ mm} \le D_{50} \le 0.05 \text{ mm} \\ 0.225 \lg(\frac{0.35}{D_{50}}) & \text{For } 0.05 \text{ mm} \le D_{50} \le 0.6 \text{ mm} \\ -0.05 & \text{For } 0.6 \text{ mm} \le D_{50} \le 2\text{mm} \end{cases} \quad (9)$$

$$R_3 = \begin{cases} 0.0 & \text{For } \%0 \le F_c \le \%40 \\ 0.004\ F_c - 0.16 & \text{For } \%40 < F_c \le \%100 \end{cases} \quad (10)$$

2.4 Chinese Criterion

In this method a critical SPT number has been defined, below which the sand layers may liquefy . The critical SPT number which can be considered as a criterion for liquefaction occurrence may be estimated from the following equation:

$$N_{cr} = \bar{N}[1 + 0.125(d_s - 3) - 0.05\ (d_w - 2) - 0.07\ F_c] \quad (11)$$

Where dw, is the depth of the water table , ds is the depth of the sand layer , $\bar{N}$ is a function of earthquake shaking intensity and Fc is the percent of clay content.

3 EVALUATION OF LIQUEFACTION EFFECTS ON THE GROUND SURFACE

Since the liquefaction of subsurface layers may not cause, considerable damages to buildings and superstructures, as far as the ground surface is not influenced remarkably, the liquefaction by itself is not of great importance. In the liquefaction potential evaluation method suggested by Iwasaki (1982), a parameter called liquefacrtion potential indes, PL, has been defined as below:

$$PL = \int_0^{20} F(z)\ W(z)\ dz \quad (12)$$

Where z is the depth of the layer, F(z) is function of the liquefaction safety factor which can be substituted by the following equation:

$$F(z) = 1\text{-}FL \quad \text{For } FL \le 1 \quad (13)$$

$$F(z) = 0 \quad \text{For } FL \ge 1 \quad (14)$$

$$\text{and } W(z) = 10\text{-}0.5\ z \quad (15)$$

The PL has been categorized in 3 classes as below:

$0<PL\leq5$	belong to areas with low risk
$5\leq PL\leq15$	belong to areas with high risk
$PL>15$	belong to area with very high risk

4 THE GENERAL CHARACTERISTICS OF THE REGION

The coastal flat of Gilan province has faced with so many times of rising and falling the Caspian sea water level at different points during its geological history. A general glance to the sides of existing rivers and lagoons in the region through out the coastal bands of the Caspian sea, from south of the Chamkhaleh to the end of the Anzali lagoon, leads to the fact that after each rising the sea water a new sedimental layer has fromed and covered the affected areas. The materials covered northern part of the Anzali lagoon specially from Taleb-Abad to Koolivar are mostly consisted of sand layers between which some roots and debirs of old trees can be observed . Increasing the seidmentation on the Anzali lagoon due to spreading the sea water, has caused many plants and vegetables to be buried and gradually desolved and produced an interlayer texture of such loose and weak lenses in the area.

According to geotechnical and geological data obtained from about 20 boreholes in the area under consideration , the soil depostis up to 10 meters depths have mainly consisted of fine sands namely SP , SM and SP-SM in the Unified soil classification system. These sedimentations in different depths have some shell segments inside, and in some cases thin lenses of clay (CL) or silt (ML) by thickness of less than 1 meter are evident.

On the whole the more getting far from Lijarki (in the east) toward the Kooliver (in the west), the more decreasing in the percent of the fine materials happens in the surficial layers. The soil layer up to 15 metters depth consisted of sand with thin lenses of clay materials. The general plan of the region with the selected area for liquefaction studies is shown in figure 1.

5- THE SEISMICITY OF THE REGION:

The area under study is located in the Gilan province. This province is one of the northern province of Iran which have surrounded by the Caspian sea in the north and the highly folded areas of Alborz Chains of mountains in the south. Although there are not so many evidences and recorded documents available concerning past erthquakes in the region, the heavy Manjil earthquake occured in 1990 by an epicentral distance of about 75 km. from the area under consideration caused strong ground motion in the Anzali area and severe damages to city of Rasht (the capital of the province). During this earthquake many areas in the province suffered from flow liquefac–tion. Some other important earthquakes have happened in the far past which have been caused by the activities of many faults existing in the Alborz folded areas.

Since the record of such seismic activities and historical earthquakes in the region have not collected properly and instalation of seismic instruments has mainly carried out after Manjil earthquake, the records of the instrumented earthquakes in the region is little and young.Therefore a comprehensive study about seismicity of the region and risk analysis in the area have not performed so far. For this reason in the present study a relatively wide range of peak ground accelerations have been chosen to cover the different probability of seismic risks in the area. The peak ground acceleration used in this study were 0.2 g, 0. 3 g, 0.4g and 0.5 g for most heavy earthquakes in the area.

6 THE GEOTECHNICAL DATA AND ANALYSIS RESULTS

The geotechnical information used in this study were all collected from different organizations through out the area. The whole data belong to 20 boreholes and 6 test pits carried out for different engineering purposes in different points of the area.

The types of available information for each borehole are the SPT numbers at mainly 1.5 meters and in some cases 3 meters maximum distances for which the specifications of the equipment are fully described . Also the measurement of the under-ground water table for all points have been carried out . According to these data the water table in the area is very high and varies only between .5 and 1.5 meters. The density of the soil in different layers, mean particle size, D_{50} , percentage of the fine materials, plastic index,PI, and the soil classification in the unified system have been estimated and determined.

The distribution of the geotechnical data obtained from above sources in the area is relatively uniform and covers nearly all point with different characteristics, so they allow to provide a microzonation map in grade 2 by an acceptable accuracy.The zonations carried out in this study are based on the liquefaction potential analyses methods mentioned in section 2. A special computer program was developed to do all analyses and calculation for different depths at different points by various methods. The effects of the liquefied layers on the ground surface have been determined by

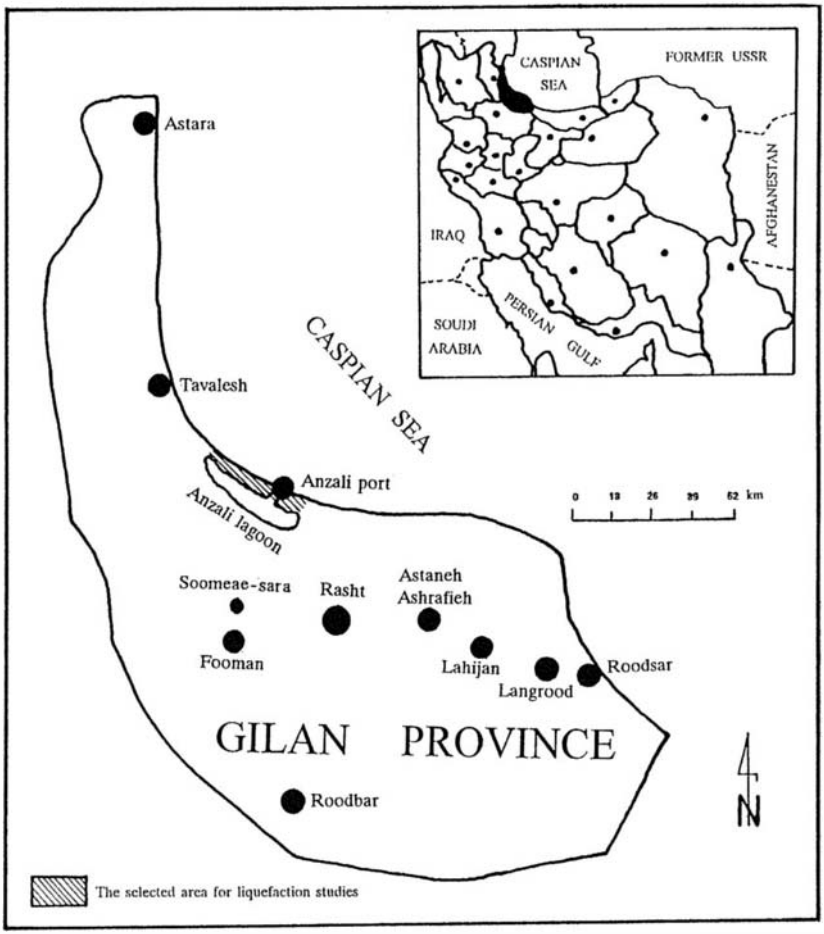

Figure 1 - The general plan of the region with the selected area for liquefaction studies.

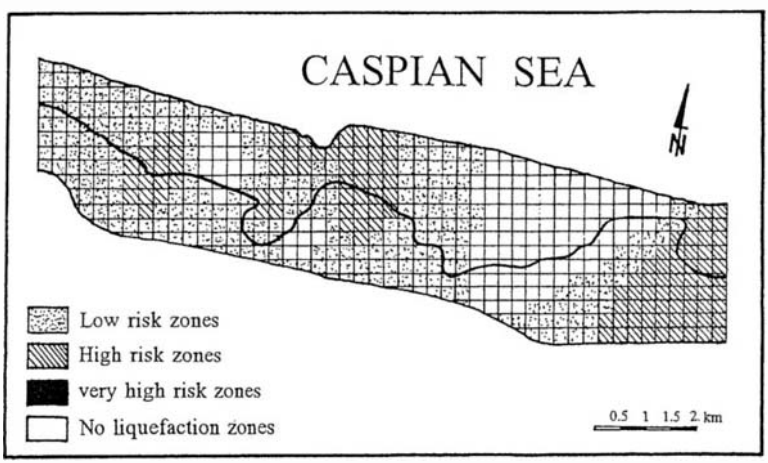

Figure 2 - Microzonation map of the selected area for a_{max}=0.2g

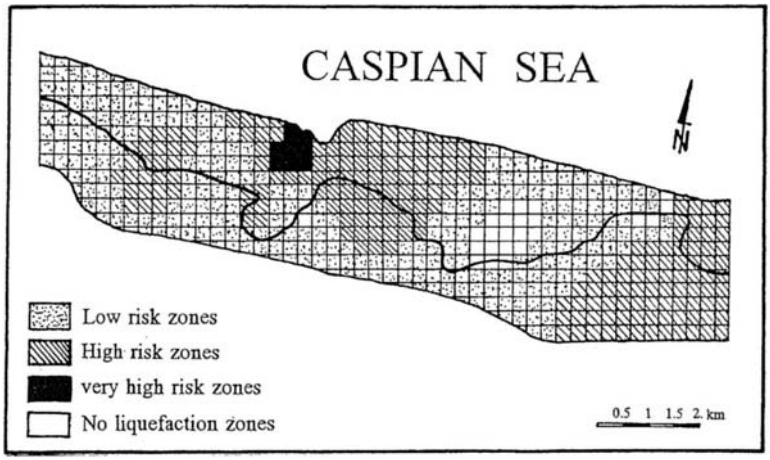

Figure 3 - Microzonation map of the selected area for a_{max}=0.3g

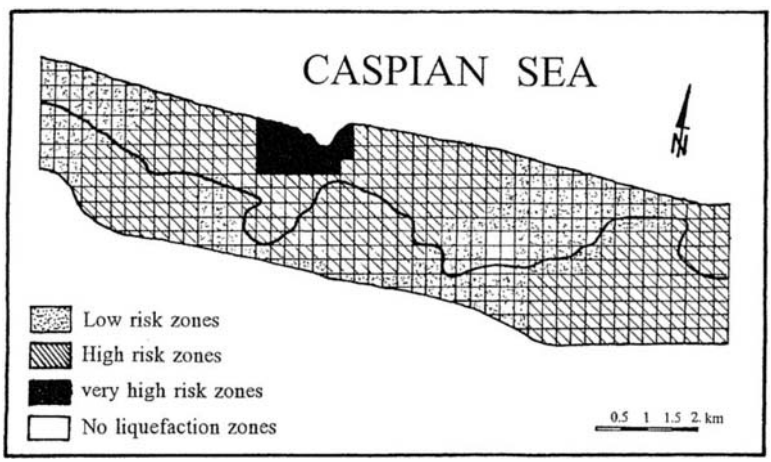

Figure 4 - Microzonation map of the selected area for a_{max}=0.4g

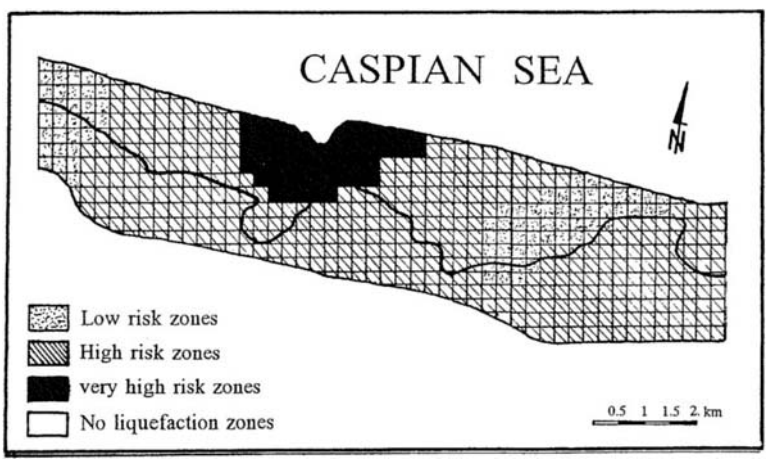

Figure 5 - Microzonation map of the selected area for a_{max}=0.5 g

calculations of the liquefaction potential index (PL). The microzonation maps of the northern coast of the anzali Lagoon for selected peak ground accelerations are presented in figures 2 to 5.

7 SUMMARY AND CONCLUSIONS

The liquefaction potential of an important zone located in the northern coast of Anzali lagoon was investigated. This zone which is positioned in the Gilan province (one of the most northern province of Iran) serves the main connection road between the most eastern and the most western cities in the coastal band of the Caspian sea.

Geotechnical and geological data from 20 boreholes and 6 test pits were collected through out the area and used in this study . Four different peak ground accelerations from 0.2 to 0.5 g were selected and used. Different analyses methods were attempted and the microzonation maps for each level of ground acceleration were provided based on the most critical results.

Among different methods used in this study the Seed et.all method is very sensitive to SPT numbers and the Ishihara method is the most conservative one. The proximity between different methods decreases as the fine content of the sand layers increases. The areas near the Anzali port and in the northern west of the Anzali lagoon are among those with high risk of liquefaction occurence even for the least peak ground acceleration 0.2g, selected in this study.

8 REFERENCES

Bour,M.et al,1998.Seismotectionic and Seismic Zonations of metropolitan France for the application of French regulations relating to critical facilities. Proc. of the 11th European conf. on Earthquake Eng.-Paris.

Ishihara, k. 1993. Liquefaction and flow failure during earthquakes, J of Geotechnique , vol . 43, No 3.

Seed,R.B. & Harder, L.F. 1990 SPT based analysis ofcyclic pore pressure generation and undrained residual strength. In J. M. duncan (ed), Proceedings, H.Bolton-Seed memorial symposium, Univ. of California , Berkeley,Vol.2,PP. 351-376

Seed , H.B.Idriss, I.M. & Arango, I . 1983 , Evaluation of liquefaction potential using field performance data, J. of Geotech.Eng.ASCE 109(3)

Technical committee for earthquake Geotech. Eng.TC4 of the ISSMFE,1993. Manual for zonation on seismic geotechnical hazards. Japanese society of SMFE.

Youd, T.L.& Garris , C.T.1995. Liquefaction - induced ground surface disruption. J of Geotech. Eng., ASCE Vol.121,No.11

Youd, T.L.1991 . Mapping of earthquake - induced liquefaction for seismic zonation. Proc. of 4th . Int. conf on seismic zonation, Earthquake Eng. research Inst. Stanford Univ. Vol.I,PP. III-147

Zlatovic , S. & Ishihara, K.1995 . on the influence of nonplastic fines on residual strength . proc. of the 1st. Int. conf. on Earthquake Geotechnical eng. Tokyo, 14-16 Nov.

Earthquake Geotechnical Engineering, Sêco e Pinto (ed.) © 1999 Balkema, Rotterdam, ISBN 90 5809 116 3

Geotechnical seismic retrofit evaluation I-57 Bridge over Illinois State Route 3

George M.S. Manyando & Thomas L. Cooling
URS Greiner Woodward Clyde, St. Louis, Mo., USA

Scott M. Olson
Department of Civil Engineering, University of Illinois, Urbana Champaign, USA

Joseph Zdankiewicz
Illinois Department of Transportation, Carbondale, Ill., USA

ABSTRACT: A seismic retrofit evaluation was conducted for the existing Interstate 57 Bridge over Illinois State Route 3. The bridge is located within the New Madrid Seismic Zone. It is about 919 m long, has 30 spans and was designed in the 1970s with minimal seismic considerations,. The bridge has concrete filled pipe-pile foundations bearing in medium to very dense granular soils. The estimated bedrock acceleration at the site is 0.22g (AASHTO). For the given site conditions, liquefaction is probable and could reduce foundation capacity in the southern half of the structure. Initially, underpinning with pin-piles and soil improvement were the recommended mitigation design options at the south abutment. A re-analyses using estimated residual strengths in liquefied soils for stability analyses indicated soil improvement would be unnecessary at the south abutment. The cost of foundation retrofit using pin piles was estimated to be about $225 - $365 per linear meter.

INTRODUCTION

The Illinois Department of Transportation (IDOT) completed the original geotechnical study and constructed the Interstate 57 (I-57) bridge over Illinois State Route 3 (Rt. 3) during the 1970s. A preliminary seismic evaluation of the bridge was conducted in 1992 (Woodward-Clyde 1992) using the geotechnical data and construction records from the original design. Based on the findings of the preliminary study, IDOT planned to perform a detailed seismic retrofit study of the bridge. This paper presents some aspects of the detailed seismic retrofit study, the retrofit options considered, and the foundation retrofit recommendations.

SITE LOCATION AND BRIDGE DESCRIPTION

The I-57/Rt. 3 bridge is located in the Mississippi River floodplain about 5 km north/northwest of Cairo, Illinois and about 1.5 km north of the Mississippi River, near the northern tip of the New Madrid Seismic Zone (Figure 1). The design bedrock acceleration for this site is approximately 0.22g based on AASHTO guidelines for a return period of 500 years.

The bridge is about 919 m long. It includes a northbound and southbound structure, and carries I-57 over Rt. 3, the Gulf-Mobile and Ohio Railroad, the Missouri-Pacific Railroad, and the United States Army Corps of Engineers' levee. The bridge has 30 spans, varying in length from 25 to 46 m, with a

Figure 1. Bridge Location and AASHTO Acceleration (%g)

typical length of about 30.5 m. The deck of each structure is 13 m wide. The bridge piers are supported on concrete filled pipe-piles bearing in medium to very dense granular soils between 10 to 20 m below grade. The approach embankments are about 5 m high at the north abutment and about 8 m high at the south abutment. The abutments are also supported on piles bearing approximately 10 to 20 m below original grade. The bridge is in AASHTO Seismic Performance Category C.

FIELD INVESTIGATION AND LABORATORY TESTING

A geotechnical field investigation program was performed to evaluate subsurface soil conditions and estimate soil properties. It consisted of 12 test borings, including two that were used for downhole geophysical shear wave velocity measurements, 24 piezocone penetration soundings, and standard penetration test (SPT) hammer energy efficiency measurements on two IDOT drill rigs.

The test borings were advanced using hollow-stem augers above the water table and rotary wash methods below the water table. Soil samples were obtained using a split spoon sampler according to ASTM D-1586 and thin-walled (Shelby) sample tubes according to ASTM D-1587.

Cone penetration test (CPT) soundings were made in accordance with procedures in ASTM D-3441 using an electronic piezocone with the pore pressure sensor located directly behind the tip.

Downhole shear wave velocity measurements were made in two of the 12 borings to provide estimates of shear modulus for use in the site response analysis. Measurements were made to depths of 43.5 and 47.9 m. The seismic data were collected using a conventional downhole technique (Crice 1980).

Standard penetration test energy measurements were performed to estimate the SPT hammer-transfer energy for both the CME 75 and the CME 55 drill rigs used at the site. The results were used to correct the field SPT N-values to the standardized SPT $(N_1)_{60}$ values for use in liquefaction assessment. The results indicated a hammer energy efficiency of about 75 percent for the automatic trip hammers used for both rigs.

Laboratory tests were performed by IDOT on selected soil samples. The tests included visual classification, water content, dry unit weight, liquid and plastic limits, unconfined compressive strength tests, and unconsolidated-undrained triaxial tests.

SITE AND SUBSURFACE CONDITIONS

Subsurface conditions along the bridge alignment varied significantly between the north half and south half of the bridge. A U.S. Army COE levee crosses the bridge alignment and divides it into two parts; the north stretch from the north abutment to the levee and the south stretch from the levee to the south abutment. A relict stream channel was identified within the southern half of the alignment. A generalized soil profile along the bridge alignment is shown in Figure 2.

In general, three primary strata are present at this site: Cahokia Alluvium, Henry Formation, and Mississippi Embayment deposits which extend to bedrock. Bedrock is estimated to be about 150 to 185m below grade (Figure 2).

The Cahokia Alluvium extends from ground surface to depths of approximately 10 m below grade in some locations. The alluvium consists primarily of soft to firm, high plasticity clays with occasional zones of low plasticity clay and silt and loose silty fine sands. The undrained shear strength of the Cahokia clays was estimated to be about 24 kPa. The standard penetration test $(N_1)_{60}$-values were quite variable, ranging from about 2 to 10 blows per 30 cm. The average measured shear wave velocity was about 140 m/sec.

The Henry Formation underlies the Cahokia Alluvium and extends to approximately 12 to 17 m below grade. It generally consists of medium dense to very dense clean sand (SP, SW). The soils were generally dense to very dense with $(N_1)_{60}$ values greater than 30 in the northern half and medium dense to dense the southern half of the alignment. The average measured shear wave is about 250 m/sec.

The Mississippi Embayment deposits underlie the Henry Formation and extend to bedrock. These deposits typically consist of very dense sand and gravel, and hard, gravely clay. Generally, $(N_1)_{60}$ values were 50 or more in these deposits and the average measured shear wave velocity was about 375 m/sec to a depth of about 45 m.

The embankments at each abutment, the railroad embankments and the levee were reported to have been constructed of a stiff, gray, low plasticity clay. The undrained shear strength of the abutment fills, based on cone penetration tests and laboratory tests, averaged about 72 kPa.

Groundwater was generally encountered between 3 and 5 m below grade.

GEOTECHNICAL SEISMIC EVALUATION

The geotechnical evaluation focused on the following: 1) dynamic site response, 2) liquefaction evaluation, 3) slope stability and lateral displacements, and 4) seismic damage mitigation options.

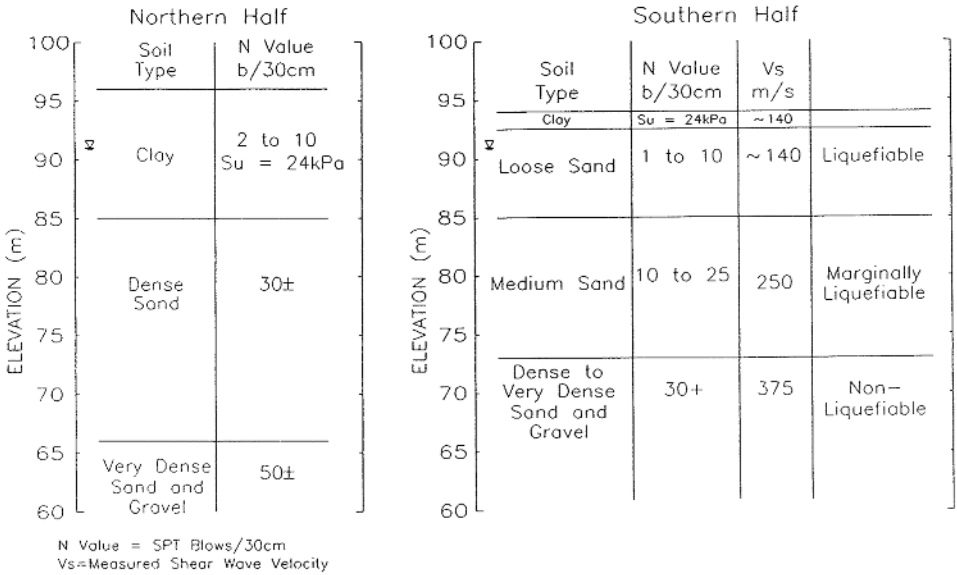

Figure 2. Generalized Subsurface Soil Profile

Site Response

Site specific dynamic response analyses were performed using SHAKE 91 (Idriss and Sun, 1992) to develop site response spectra at the north abutment, the relict stream channel, and the south abutment. Acceleration-time histories scaled to the zero-period bedrock acceleration (0.22g) at the site were used as input motion. The input motions were modified from the horizontal components of two earthquakes: the (1985) Nahanni earthquake at Station No. 3, and the (1988) Saguenay earthquake at Station No. 16, resulting in four input motions. These motions were modified and scaled to match the recommended rock spectrum shown in Figure 3. These earthquake records are two of the few available moderate magnitude records from eastern North America, and were judged to be appropriate for this project site.

Response analyses were carried out at each location using three different shear wave velocities: the average of the measured shear velocity for the site and ±10 percent of the average measured shear wave velocity to obtain a range of likely response.

Site specific response spectra developed for the north abutment and the former stream channel are shown in Figure 3. The recommended spectra are more conservative than the calculated spectra to account for uncertainties in the analysis, especially at periods above one second where the calculated motions are judged to be less accurate. The additional conservatism at long periods was judged to be prudent since base isolation may be used to increase the period of the bridge. A response spectrum was not developed for the south abutment since liquefaction was predicted to occur in that reach.

Results of the response analyses at the stream channel indicated a ground surface acceleration of 0.35g. The bedrock acceleration for this site is 0.22g, thus, the resulting surface motion was about 1.5 times the bedrock motion. No significant amplification was indicated at the north abutment.

Liquefaction Evaluation

Liquefaction resistance was evaluated using both the SPT and CPT approach using the "simplified"

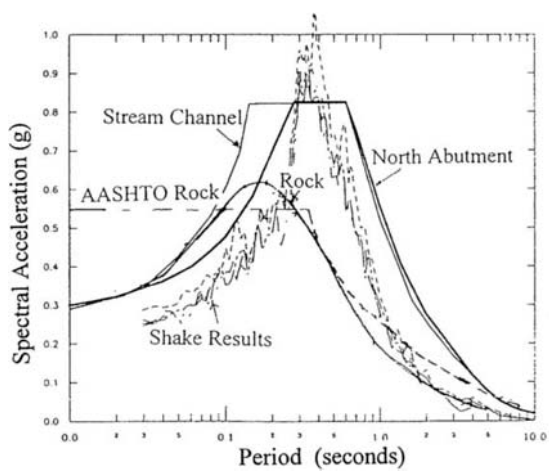

Figure 3. Site Specific Response Spectra

procedure developed by Seed and Idriss (1971), and updated by Seed and Harder (1990). A magnitude 6.5 earthquake and ground surface acceleration of 0.35g were used. For the SPT approach the Seed et al.(1985) relationships and a hammer efficiency of 75 percent were used. For the CPT approach, liquefaction resistance was estimated from relationships developed by Stark and Olson (1995), Mitchell and Tseng (1990, Shibata and Teparaksa (1988), Seed and De Alba (1986), and Robertson and Campanella (1985). The following observations were made:

The liquefaction analyses indicated that the potential for liquefaction is low in the northern half of the bridge and the risk of damage was judged to be negligible. Consequently for calculation purposes, the bearing capacity of the piles was not reduced in that section. Liquefaction was predicted to occur in the southern half of the bridge alignment. Generally, the lowest values of factor of safety against liquefaction were obtained in the upper 10 m in the silts and medium dense sands of the subsurface profile (Figure 2). The average factor of safety against liquefaction obtained in the cohesionless soils near the south abutment was about 0.75.

It was anticipated that the pile capacity in the southern reach of the bridge would be significantly reduced by down-drag from the upper clayey soils and liquefaction in the bearing zone. Consequently, bearing capacity failure and/or significant settlement of the bridge piers was judged to be probable in this area unless mitigation was undertaken. The recommended mitigation options are discussed subsequently.

Slope Stability Analysis

Pseudo-static slope stability analyses were performed and lateral displacements were estimated for the north abutment, south abutment and the levee. Displacements were estimated using the Makdisi-Seed (1978) approach in areas where liquefaction was not predicted to occur. Where liquefaction was predicted to occur in the vicinity of south embankment, residual strengths were used with gravity forces in the slope stability analyses. Inertia forces were excluded in the residual strength stability analysis. Results of the slope stability analyses and the estimated lateral displacements are summarized in Table 1. Lateral displacements for liquefied conditions were estimated from the strain required to mobilize the residual strength (Seed et al. 1985).

Discussion of Results

Based on the results in Table 1, the lateral displacements estimated at the north abutment and the levee under seismic conditions were judged to be acceptable and tolerable. Therefore, mitigation was not required. For the south abutment, liquefaction was anticipated and a detailed analysis considering the residual strength in the liquefied soil was necessary.

Initial calculations using the lower bound residual strength curve in Figure 4 (Seed and Harder 1990) resulted in factor of safety of 1.1. Another analysis using residual strength estimated from Stark and Mesri (1992) provided a factor of safety 1.2 against slope failure. These factors of safety suggest that flow failure is unlikely, however, lateral displacements are probable. Once liquefaction has occurred, the resulting lateral displacement are difficult to quantify without performing non-linear analyses such as FLAC (1995) which was beyond the scope of work. While the factors of safety obtained could result in tolerable displacements in embankment dams, it was judged that the displacements would be large enough to impact the integrity of the bridge structure. Consequently, it was initially recommended that liquefaction mitigation be done. Subsequent stability analyses with residual strength values in the mid-range of Figure 4 provided a factor of safety of 1.3 against slope failure. The use of residual strength in the mid-range of Figure 4 was judged appropriate because the $(N_1)_{60}$ residual strength value used in the analysis represented a minimum value for the liquefied layer. For this factor of safety, the estimated displacements were judged not to be excessive for the integrity of the bridge.

However, if the factor of safety with the more conservative residual strength analyses was less than 1.2, obtained in the previous analyses, a more detailed study would have been recommended. Considering the high estimated cost of mitigation, and the conservatism in the residual strength analysis, it was finally decided that soil improvement would not be required at the south abutment.

LIQUEFACTION MITIGATION OPTIONS AT SOUTH ABUTMENT

Two alternatives were considered to mitigate liquefaction at the south abutment: 1) construction of a stabilizing berm, and 2) insitu soil improvement to create a non-liquefiable soil "plug" near the toe of the slope. A factor of safety of 1.4 (significantly greater than unity) assuming no residual strength in the liquefiable soils was used as a design target for which lateral deformations would be tolerable (Seed 1987).

Stabilizing Berm

Several berm sizes were analyzed considering both circular and non-circular failure surfaces but a targeted factor of safety of 1.4 could not be achieved. This improvement technique would have been

Table 1: Results of Slope Stability and Displacement Analyses

Feature	Case 1 FS_{pscudo}	Case 1 K_y (g)	Case 1 U (mm)	Case 2 FS	Case 3 FS
North Embankment	0.9	0.171	2 - 20	N/A	N/A
South Embankment	1.6	0.42	0	1.3	1.4
Levee- Northward	0.6	0.124	10 - 100	N/A	N/A
Levee - Southward	0.7	0.13	10 - 90	N/A	N/A

Ground Surface Acceleration = 0.35 g

FS_{pscudo} = Pseudo-Static Factor of Safety

FS = Factor of Safety for Slope Stability against Gravity Loads

K_y = Yield Acceleration (g)

U = Lateral Displacement (mm) (Makdisi and Seed 1978)

Case 1 = Undrained Strength in Soils

Case 2 = Residual Strength in Liquefied Soils

Case 3 = Retrofit with Zero Residual Strength in Upper Liquefied Soil

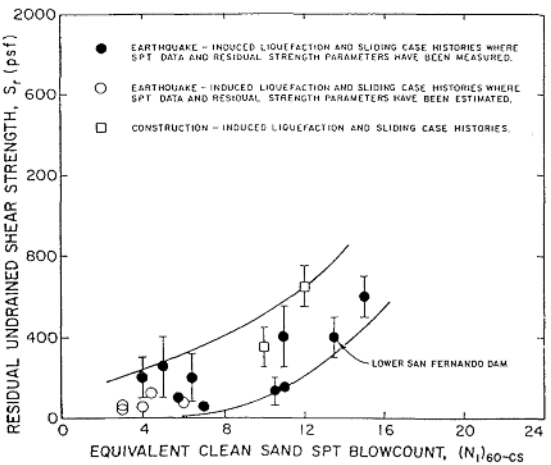

Figure 4. Residual Undrained Shear Strength vs. Clean Sand $(N_1)_{60-CS}$

effective had some residual strength been used in the liquefied soils, however, some lateral displacements would accompany the mobilization of the residual strength. Therefore the berm option was rejected.

Soil Improvement

Generally, the soil improvement technique selected depends on the soil to be treated, constructability, and cost. The fines content of the loose sandy soils at this site is about 35 to 40 percent. Common densification techniques such as vibro-compaction and compaction grouting were judged to be less effective than vibro-replacement or stone columns where the soils have a relatively high fines content. Stone columns have been used successfully to mitigate consequences of liquefaction in soils with a large amount of fines (Mitchell et al. 1995). For this project, soil improvement using stone columns was initially recommended.

It was recommended that the stone columns extend 1.5 m below the liquefiable zone into the underlying non-liquefiable layer, and that the improved soil zone be located near the toe of the slope as shown in Figure 5. The stone columns were anticipated to strengthen the soil and provide drainage during shaking. For slope stability analysis, the strengthened zone created by the stone column was assumed to have an average friction angle of 32 degrees. To implement this option, compaction grouting or deep-soil mixing would have to be used directly below the structure because of the restricted headroom.

Cost Estimates

For design and cost estimating purposes, a mitigation scheme consisting of 0.9 m diameter stone columns, spaced on 2.1 m centers extending 1.5 m into the non-liquefiable sands was considered. The estimated cost for stone columns was $120 per linear meter based on previous IDOT studies. For this project, the estimated total cost for soil improvement was about $600,000 to $700,000. This amount did not include the cost of temporary excavation to prepare a work pad, or other incidental construction.

As aforementioned, after additional slope stability analysis, this liquefaction mitigation option was deemed unnecessary resulting in significant savings to the overall seismic retrofit costs for this bridge.

FOUNDATION RETROFIT

Foundation capacity from the north abutment to the levee was judged not to be significantly affected by earthquake shaking. Consequently, foundation retrofit north of the levee was not recommended unless the capacity of existing foundations were not

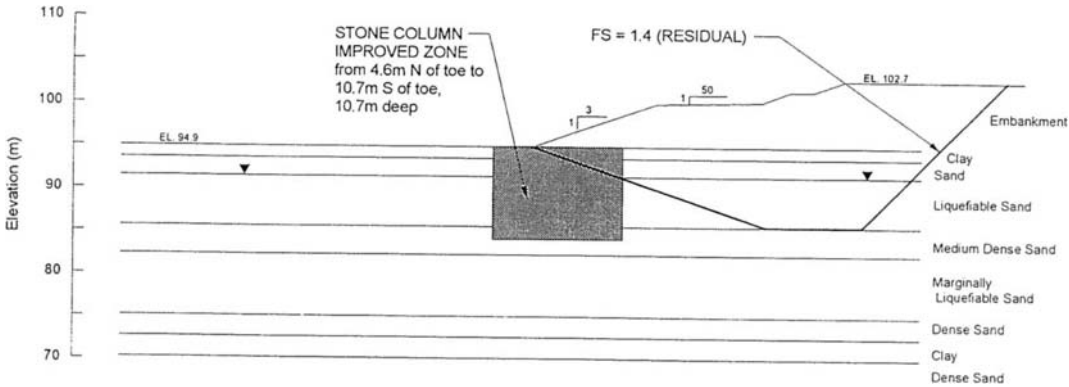

Figure 5. South Abutment Initially Recommended Retrofit

adequate for seismic loads. Liquefaction south of the levee is expected to significantly reduce existing foundation capacity. For the south half of the bridge, two general techniques for retrofit were considered: 1) soil improvement at pier locations to prevent liquefaction, and 2) foundation underpinning to transfer loads to the non-liquefiable strata below the liquefiable zone. Based on a cost analysis and constructability, underpinning was recommended. A schematic of the underpinning is shown in Figure 6.

Two options, driven piles (pipe and H-sections) and pin-piles were considered. Driven piles have two major disadvantages: 1) they are difficult and expensive to install where head room is limited, and 2) pile driving could potentially cause settlement of the existing bridge. In contrast, when properly installed, pin-piles can used at sites with limited head room without being detrimental to the safety of the existing bridge. Generally, pin-piles are more costly than driven piles where headroom can accommodate pile driving. The cost for each option was estimated considering that piles of about 30 to 35 m long will be required for ultimate capacities of about 1.79 MN. The cost estimates are presented in Table 2.

The estimated unit cost for pin piles is slightly more than that for driven piles. However, the small premium was viewed to be a worthwhile trade-off considering the possible detrimental effects driven piles could have on the existing bridge. Pin-piles were therefore the recommended foundation retrofit option for this project.

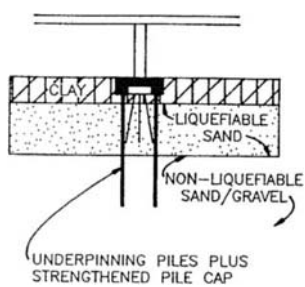

Figure 6. Retrofit by Underpinning Piles and Strengthened Pile Cap

Table 2: Cost Estimates

Pile Type	Ultimate Capacity MN	Cost Per Linear meter		
		Contractor A	Contractor B	Contractor C
HP 14 x 89	1.79	$203	$262 - $328	
12.75 OD x 0.5" pipe	1.79	$240	$262-$328	
Pin Pile	1.79	$226	$230*	$295 - $361

* For 1.07 -MN ultimate capacity pin pile.

CONCLUSIONS AND REMARKS

In this project, a factor of safety of 1.3 obtained using a conservative estimate of the residual strength in the liquefied zone was accepted in favor of a potentially costly liquefaction mitigation option for the south abutment. The residual strength used to evaluate slope stability and lateral displacements where liquefaction is predicted to occur is a key issue in seismic retrofit studies. Slope stability and resulting displacements are very sensitive to the residual strength assigned to the liquefiable zone. Currently, there is no consensus on a procedure for the selection of residual strengths in liquefied soils. Consequently, when reliable site specific laboratory data such as tests on insitu frozen samples are not available, the selection of residual strength should be based on available correlations of back-calculated residual strengths from field case histories of liquefied failures. The cost of retrofit options is usually significantly higher than that of performing detailed displacement analysis using nonlinear methods. Therefore, it may be advantageous to perform non-linear analyses in seismic retrofit studies for bridge abutments.

REFERENCES

American Association of State Highway and Transportation Officials (AASHTO) (1991). "Standard Specifications for Seismic Design of Highway Bridges." AASHTO.

Crice, dB, (1980). Seismic Applications for Shallow Exploration Seismographs, in Practical Geophysics, Northwest Mining Association.

Idriss, I. M. & Sun, J. (1992). "SHAKE91 - A Computer Program For Conducting Equivalent Linear Seismic Response Analyses of Horizontally Layered Soil Deposits." Center for Geotechnical Modeling, Dept. of Civil and Environmental Engineering, University of California, Davis, California, November.

Mitchell, J.K.; et al, (1995). "Performance of Improved Ground During Earthquakes." Proceedings, Soil Improvement for Earthquake Hazard Mitigation, Ed. Hryciw, R.D., Geotechnical Special Publication No. 49, ASCE, October 22-26

Mitchell, J.K. & Tseng, D.J. (1990). "Assessment of Liquefaction Potential by Cone Penetration Resistance." Proceedings, H.B. Seed Memorial Symposium, BiTech Publishing, J. Michael Duncan, ed., Vol. 2, pp. 335-350.

Robertson, P.K. & Campanella, R.G. (1985). "Liquefaction Potential of Sands Using the CPT." JGED, ASCE, Vol. 111, No. 3, pp. 384-403.

Seed, H.B. & De Alba, P. (1986). "Use of SPT and CPT Tests for Evaluating the Liquefaction Resistance of Sands." Proceedings, INSITU '86, ASCE Specialty Conference on Use of In Situ Testing in Geotechnical Engineering, Virginia Tech, Blacksburg, Virginia, Geotechnical Specialty Publication No. 6, pp. 281-302.

Seed, H. B. & Makdisi, F.I. (1978). "Simplified Procedure for Estimating Dam and Embankment Earthquake-Induced Deformations." JGED, ASCE, Vol. 104, No. GT 7, pp. 967-994.

Seed, H. B., et al (1985). "Influence of SPT Procedures in Soil Liquefaction Resistance Evaluations." JGED, ASCE, Vol. 111, No. 12, pp. 1425 -1445.

Seed, H.B. (1987). "Design Problems in Soil Liquefaction." JGED, ASCE, Vol. 113, No. 8, pp. 827-845.

Seed, R.B., & Harder, L. F. (1990). "SPT-Based Analysis of Cyclic Pore Pressure Generation and Undrained Residual Strength," Proceedings of H. Bolton Seed Memorial Symposium, BiTech Publications, J. Michael Duncan, ed., Vol. 2, pp. 351-376.

Shibata, T. & Teparaksa, W. (1988). "Evaluation of Liquefaction Potentials of Soils Using Cone Penetration Tests." Soils and Foundations, Vol. 28, No. 2, pp. 49-60.

Stark, T. M. & Mesri, G. (1992). "Undrained Shear Strength of Liquefied Sands For Stability Analysis." JGED, Vol. 118, No 11, pp. 1727-1747.

Stark, T.D. & Olson, S.M. (1995). "Liquefaction Resistance Using CPT and Field Case Histories." JGED, ASCE, Vol. 121, No. 12, pp. 856-1747

Woodward-Clyde Consultants, (1992). "Seismic Condition Study. PSB 65/40," prepared for Illinois Department of Transportation, Bureau of Bridges and Structures, by Woodward-Clyde Consultants, St. Louis, Missouri, Project No. 89C8623.

This Page Intentionally Left Blank

Earthquake Geotechnical Engineering, Sêco e Pinto (ed.) © 1999 Balkema, Rotterdam, ISBN 90 5809 116 3

Dynamic interaction at an embankment dam base and estimation of incident seismic waves using observations at dam base

T. Iwashita
Public Works Research Institute, Ministry of Construction, Tsukuba, Japan (Currently: Department of Civil and Environmental Engineering, University of California, Berkeley, Calif., USA)

T. Ine
NEWJEC Incorporated, Osaka, Japan (Formerly: Public Works Research Institute, Ministry of Construction, Tsukuba, Japan)

H. Yoshida
Public Works Research Institute, Ministry of Construction, Tsukuba, Japan

ABSTRACT: Many earthquake motions have been observed at the bedrock of embankment dams. The observed waves are affected by the dynamic interaction between the dam and its foundation. The effects of the frequency contents of the input waves and the impedance ratio on the dynamic interaction at the dams base were evaluated using FEM analyses. The change of the dynamic interaction on the footprint of dams was represented analytically. The analytical results agreed with the earthquake observations and the microtremor measurements at dam sites. Moreover, a simplified analytical procedure that the estimated incident seismic wave on the basement layer from the within wave observed at the base of an embankment dam was proposed. The procedure was applied to the estimation of the incident wave at a rockfill dam site during the Kobe Earthquake.

1 INTRODUCTION

Earthquake observations at the bedrock of dam sites are precious data of earthquake motions at the hard rock site condition, for which the S-wave velocity is over about 800 m/s. There are few earthquake observational stations situated at hard rock site in Japan, except for dams and nuclear power plants. In most dams of Japan in particular, seismographs have been installed in the inspection gallery at the base of embankment dams or at the bottom of concrete dams for the purpose of safety control against earthquakes. Most dams in Japan, except for small earth dams, are constructed directly on the excavated bedrock of riverbeds and abutments. The lower part of a massive dam is, thus, roughly considered to behave approximately in the same way as its bedrock and rock abutment during earthquakes. However, earthquake response of a dam is affected by the dynamic interaction of dam-foundation-reservoir system. The earthquake waves observed at the dam base or at the dam bottom are interacted especially with its foundation. In other words, the earthquake waves at the dam base are the combination of the incident waves through the foundation and the radiation waves through the dam body. They are, therefore, different from the waves at the free-field, i.e. outcrop. In order to make practical use of the observations at the dam base of the many dams where seismometers have already been installed, it is necessary to evaluate the quantitative difference of the earthquake wave at the dam base with that at the free-field.

The effects of the dynamic interaction between a dam and its foundation are evaluated by wave energy dissipation through the dam to the foundation or by radiation damping. Analytical evaluations of radiation damping of embankment dams have been performed (Chopra & Perumalswami 1969, Ohmachi 1980, Yanagisawa 1982, Hirata 1989, Tohei & Ohmachi 1990). In these evaluations, analytical procedures were mainly used and few comparative evaluations with actual dam observations were conducted.

In this paper, we evaluate the effects of frequency contents of input waves and the impedance ratio on the dynamic interaction between an embankment dam and its foundation. A little effect of reservoir for an embankment is not considered. The evaluations are performed using both FEM numerical analysis and the earthquake observations at an existing dam. Moreover, we propose a simplified analytical procedure that estimates the incident seismic wave on the basement layer without the dynamic interaction effects from the observations at the base of an embankment dam.

2 DYNAMIC INTERACTION AT BASE OF AN EMBANKMENT DAM

2.1 *Analytical method and cases*

We analyzed the two-dimensional FE model of the Miho Dam in Japan, a rockfill dam with a central core, shown in figure 1. The physical and dynamic properties of the dam were determined from in-situ tests and laboratory tests using the fill materials of this dam. We used the

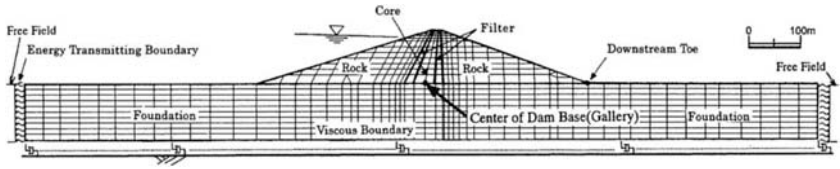

Fig. 1. Finite element model of the Miho Dam.

complex dynamic response analysis program DINAS, which employs equivalent linear dynamic soil modeling.

We performed analyses on the five cases shown in Table 1. In Cases 1A and 1B, the effect of the frequency contents of the input wave on the dynamic interaction was evaluated. In Case 1A, the acceleration wave, which has a maximum of 138gal and is shown in figure 2, observed at the downstream toe of the Miho Dam during the event of March 6, 1996 (JMA magnitude of 5.8) was input. In Case 1B, the same wave as in Case 1A only with the time axis stretched by a factor of two, that is with twice calculation period, was input. The predominant frequency of the input wave of Case 1B was consistent with the natural frequency of the dam body. In Cases 1B, 2-4, the effects of the impedance ratio between the dam body and its foundation were evaluated by changing the shear stiffness of the foundation.

2.2 *Results of the analysis*

a) Effects of frequency contents of input waves

The amplification spectra of the response waves at the crest and at the center of the dam base against the input wave for Case 1A are shown in figure 3. The amplification spectrum for the dam base dips at a slightly higher frequency than the natural frequency that is indicated as the predominant frequency of the amplification spectrum at the crest. The amplification spectrum for the dam base in figure 3 shows that the seismic wave at the dam base reduces the seismic power at the frequency range of the natural frequencies of the dam considerably.

Figure 4 shows the Fourier amplitude spectra of the acceleration at the center of the dam base and at the free-field for Case 1A. The amplitude spectrum for the dam base is smaller than that for the free-field for the second and third natural frequencies of the dam (around 3 Hz). This is because the spectrum of the input wave has large amplitudes around the second and third natural frequencies of the dam. The Fourier amplitude spectra for Case 1B are shown in figure 5. The amplitude spectrum for the dam base is extremely smaller than that for the free-field around the first natural frequency of 1.7Hz. When an incident wave that has large energy power around the natural frequency of a dam is input, dynamic interaction between the dam and its foundation makes the spectral amplitude of the response acceleration at the dam base decrease around this frequency.

b) Effects of impedance ratio

Table 1. Analytical cases.

	S-wave Vel. for Foundation Vs_F(m/s)	Impedance Ratio α	Calculation Period Δt(s)	Items Investigated
CASE 1A	1950	0.29	0.01	Frequency contents of input waves
CASE 1B	1950	0.29	0.02	
CASE 2	1380	0.41	0.02	Impedance ratio $\alpha = \frac{\rho_D \cdot V_{SD}}{\rho_F \cdot V_{SF}}$
CASE 3	975	0.57	0.02	
CASE 4	690	0.81	0.02	

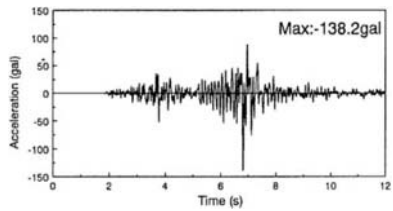

Fig. 2 (a). Input acceleration-time history for Case 1A.

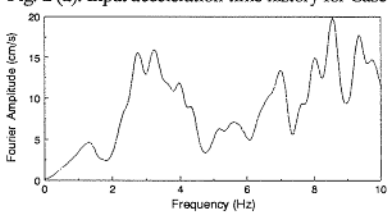

Fig. 2 (b). Fourier amplitude spectrum of input acceleration for Case 1A.

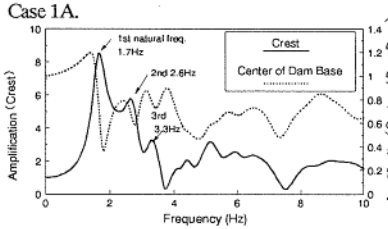

Fig. 3. Amplification spectra for Case 1A.

The amplification spectrum ratio Ar, which is the amplification spectrum for the dam base divided by the amplification spectrum for the free-field, was calculated. The amplification spectrum ratio Ar shows the difference between the seismic response at the dam base and that at the free-field. Figure 6 shows the amplification spectrum ratios for the central part of the dam base for Cases 1B, 2 to 4. Figure 7 shows the amplification spectrum for the crest. Figure 8 shows the relationship between the frequency where the amplification spectrum ratio for the dam base sinks in figure 6 and the predominant frequency of the amplification spectrum for the crest in figure 7. Figure 8 shows that each sinking frequency for

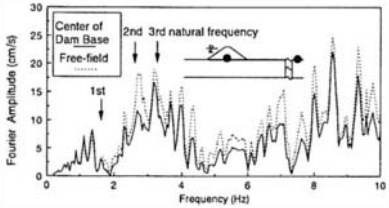

Fig. 4. Fourier amplitude spectra of acceleration at dam base and at free-field (Case 1A).

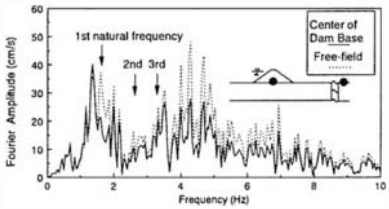

Fig. 5. Fourier amplitude spectra of acceleration at dam base and at free-field (Case 1B).

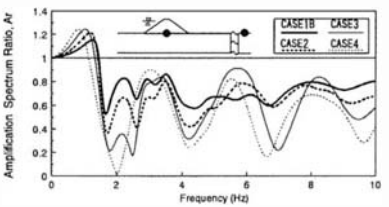

Fig. 6. Amplification spectrum ratio for dam base.

the dam base is slightly higher than the corresponding predominant frequency for the crest. In figure 6, the larger the impedance ratio, the larger the dip in the amplification spectrum ratio. In other words, the larger the impedance ratio, the larger the effect of dynamic interaction. Figure 7 shows that the response magnification of the dam becomes larger as the impedance ratio becomes smaller. This indicates that the smaller the impedance ratio, the larger the non-linearity of the dam body and the lower its natural frequency. It is, therefore, suggested that the sinking frequency for each amplification spectrum ratio shown in figure 6 becomes lower as the impedance ratio becomes smaller.

Figure 9 shows the distribution of maximum acceleration, which is normalized by dividing by the maximum acceleration at a free-field, along the dam base and on the downstream ground surface for each of the analytical cases. The maximum accelerations are smallest at the center of the dam base and recover as you move toward the downstream toe. The maximum accelerations at the downstream toe are only about ten percent less than the maximum accelerations at the free-field. The larger the impedance ratio, the more the maximum accelerations at the dam base drop and the larger the dynamic interaction between the dam and the foundation.

The residual of the amplification spectrum ratio was integrated from $0.5f_1$ to $2.5f_1$, where f_1 is the first natural frequency. The mean residual e shown in equation (1)

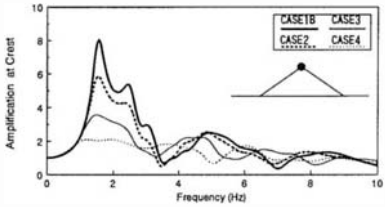

Fig. 7. Amplification spectrum for crest.

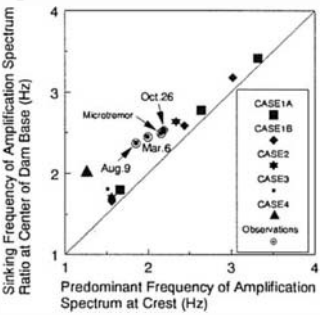

Fig. 8. Comparison between sinking frequency of transfer function ratio for dam base and predominant frequency of transfer function for crest.

represents the ratio of the energy loss at the dam base due to the dynamic interaction.

$$e = \frac{1}{2f_1}\int_{0.5f_1}^{2.5f_1}(1 - Ar(f))df \qquad (1)$$

Figure 10 shows the distribution of the mean residual e along the dam base (footprint) and on the downstream ground surface for each of the analytical cases. The mean residual e is large around the center of the dam base and becomes smaller as you move toward the downstream toe. Furthermore, the larger the impedance ratio, the larger the mean residual, i.e. the larger the energy loss due to dynamic interaction. The values of the mean residual e are only about 0.1 around the downstream toe for all the cases.

Figures 9 and 10 indicate that the effect of dynamic interaction on earthquake response is low around the downstream toe, regardless of the impedance ratio. There is negligible effect of dynamic interaction due to the dam on the seismic response at the point about half a dam's width away from the downstream toe.

2.3 *Verification of analytical results using observations*

The characteristic of the earthquake motions at the dam base obtained from the analytical procedures in section 2.2 above were verified using the earthquake observations during three events and the data of microtremor measurements at the Miho Dam. We calculated the ratio of the Fourier amplitude spectrum of the waves observed at the crest to that at the outcrop. We also calculated the ratio of the Fourier amplitude spectrum of the waves observed at the center of the dam base to that at the outcrop. The relationships between the

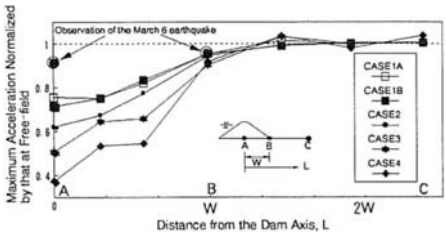

Fig. 9. Distribution of maximum acceleration at dam base and downstream ground surface.

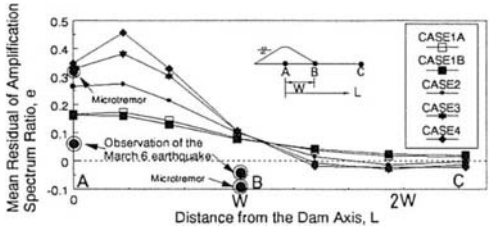

Fig. 10. Distribution of mean residual of amplification spectrum ratio for dam base and downstream ground surface.

sinking frequency of the Fourier amplitude spectrum ratio for the center of the dam base and the predominant frequency for the crest obtained from the observations and the microtremor data have been added to figure 8. The points appear slightly above the 45-degree line that represents the case where the sinking frequency for the dam base is equal to the predominant frequency for the crest. In other words, the sinking frequency for the dam base is slightly higher than the corresponding predominant frequency for the crest, which agrees well with the analytical results in section 2.2 above.

The normalized maximum acceleration and the mean residual of the amplification spectrum ratio from the earthquake observations during the event of March 6, 1996 and the microtremor data measured at the center of the dam base and the downstream toe have been added to figures 9 and 10 respectively. The waves observed at the outcrop were used as the reference wave records. The maximum acceleration at the center of the dam base is smaller than that at the downstream toe. The mean residual e at the center of the dam base is larger than that at the downstream toe. These trends agree with those seen in the analytical results.

3 ESTIMATION OF SEISMIC WAVE INCIDENT ON BASEMENT LAYER

3.1 *Estimation procedure*

As stated in the previous chapter, earthquake waves observed at the dam base are interacted with the dam body. Hence, we propose a simplified procedure for estimating the wave incident on the basement layer from observations at the base of an embankment dam analytically. Ohmachi & Kataoka (1995) estimated the incident seismic waves from the observations at the base of a concrete dam using the procedure that involved dividing the frequency characteristics of the observations at the dam base by the transfer function. However, an earth structure such as an embankment dam has the high earthquake-induced non-linearity of the soil and rockfill materials. This is the major difference from a concrete dam with regard to the estimation of the incident wave for earth structure. For this reason, we performed dynamic equivalent linear pre-analysis on the model of an embankment dam with a rigid foundation. The reason why a rigid foundation model is analyzed is that the wave observed at the dam base must be input. This dynamic pre-analysis gives the shear modulus of the dam reached in the inelastic region during shaking. Furthermore, a comparison between the analytical response results and other observations at the dam enables the accuracy of the dam model to be verified.

The estimation procedure is as follows:

1. The dynamic pre-analysis of the embankment dam model with a rigid foundation is performed using the equivalent linear soil modeling method. The distribution of the shear modulus of the dam in the final iterative calculation step is obtained.

2. The transfer function for the dam base is calculated using the above shear modulus of the dam.

3. The Fourier spectrum, which involves the characteristics of both amplitude and phase, of the wave incident on the basement layer is obtained by dividing the Fourier spectrum of the wave observed at the dam base by the above transfer function.

4. The Fourier inverse transform of the Fourier spectrum calculated above gives the seismic wave incident on the basement layer.

An observed wave consists of the coupled response of horizontal and vertical vibrations. In this simplified procedure, however, we consider only the horizontal transfer function for the horizontal input motion and only the vertical transfer function for the vertical input motion.

3.2 *Dam analyzed and its model*

We applied this procedure to the earthquake observations at the Minoogawa Dam during the Kobe Earthquake of 1995. The Minoogawa Dam, a 47.0 m-high rockfill dam, was located about ten kilometers northeast of the earthquake fault. The seismometers installed in the inspection gallery at the base of the dam and at the dam crest recorded acceleration waves during the excitation. Their maximum horizontal accelerations perpendicular to the dam axis were 135 gal in the gallery and 242 gal at the crest. The dam foundation is hard bedrock that has an elastic wave velocity of about 4 km/s. The impedance ratio between the dam and the foundation is about 0.3.

We prepared the 2-D FE model of the cross section

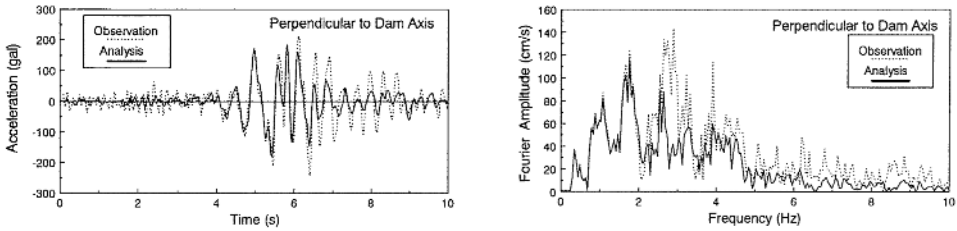

Fig. 11. Comparison between observed acceleration at crest with analytical results (pre-analysis of the Minoogawa Dam model with a rigid foundation).

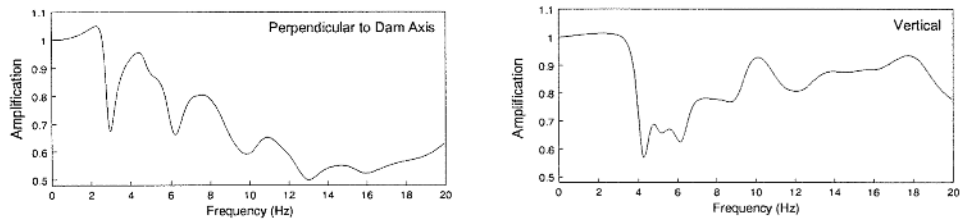

Fig. 12. Amplification spectra for the center of the dam base of the Minoogawa Dam model.

of the Minoogawa Dam. The properties of the dam materials were determined from the results of execution control tests in the time of the construction and the laboratory tests using the fill materials of this dam. We verified the accuracy of the vibration characteristics of the model by comparing the natural frequency of the model with that from earthquake observations and microtremor measurements (Iwashita & Yoshida 1997). In the pre-analysis of the rigid foundation model, the effects of energy dissipation by dynamic interaction were assumed to be represented by the equivalent radiation damping ratio that was added to the hysteresis damping ratio of the dam materials.

3.3 *Calculation of an incident wave*

Firstly, we analyzed the rigid foundation model and obtained the shear modulus of the dam during excitation. Figures 11 show comparisons of the observed response acceleration at the crest with that obtained through the dynamic pre-analysis. Looking at the acceleration-time history, during the first half of the principal motion (t = 4 - 6 sec) the analytical results agree well with the observations, but during the second half (over 6 sec) the analytical results are smaller than the observed values. With regard to the Fourier amplitude spectrum, the analytical results in the low frequency range under 2 Hz agree well with the observations, but the analytical results are smaller than the observed values around the natural frequency during shaking of 3 Hz. In spite of the rigid foundation model analysis, the analytical results give relatively good agreement with the observations. This confirms that the model describes the non-linearity of the dam well during the earthquake.

Secondly, the transfer functions for the dam base were calculated using the shear modulus of the dam, which is the output from the above pre-analysis on the rigid foundation model. The amplification spectra shown in figure 12 have a significant sinking at 3 Hz for the direction perpendicular to the dam axis and at about 4Hz for the vertical direction.

Finally, we estimated the wave incident on the basement layer of the Minoogawa Dam site using the steps 3 and 4 of the above-mentioned procedure, with the earthquake observations in the inspection gallery built on the dam base and its transfer functions. The estimated incident wave time history and Fourier amplitude spectrum are shown in figures 13. The wave observed at the inspection gallery is also shown in the figures for the shake of comparison. The horizontal maximum accelerations of the incident wave and the wave observed in the gallery are 137 gal and 135 gal respectively; the vertical maximum accelerations are 89 gal and 80 gal respectively. The amplitude spectrum of the incident wave is larger than that for the wave observed at the gallery at the natural frequencies (the range around 3 Hz for the horizontal direction and 4 to 5 Hz for the vertical direction) because of the dynamic interaction effects descrived in chapter 2.

3.4 *Verification of the estimated incident wave*

We performed dynamic analysis on the Minoogawa Dam model with a compliance foundation. The incident wave estimated in the previous section was input under the basement boundary of the compliance foundation model. Figures 14 show the comparisons of the acceleration-time histories and Fourier amplitude spectra of the analytical response horizontal acceleration at the crest with those of the observed acceleration at the crest. The results of the analysis agree well with the observations for both the time history and the Fourier

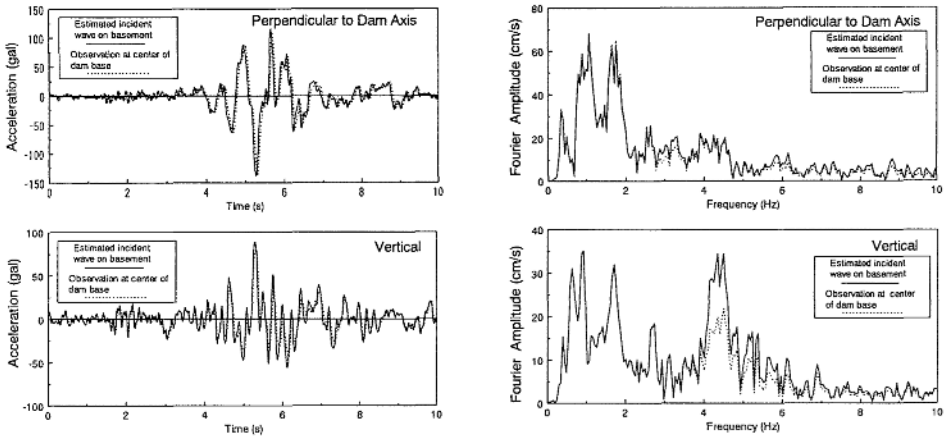

Fig. 13. Estimated incident acceleration on basement layer and observed acceleration at dam base.

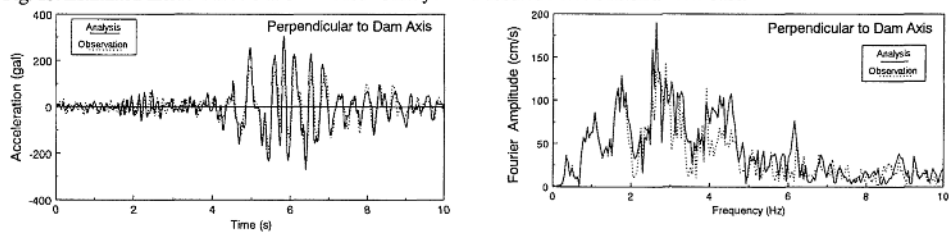

Fig. 14. Comparison of observed acceleration at crest with analytical results (analysis on the Minoogawa Dam model with a compliant foundation, on which the estimated incident wave was input).

spectrum. Of particular note is the good agreement of the time histories even for the second half of the principal motion and of the Fourier amplitudes at around 3 Hz. In the above range, the results from the simulation of the rigid foundation model analysis did not agree with the observations, as was shown in figures11.

4 CONCLUSIONS

1. Due to the dynamic interaction between an embankment dam and its foundation, the Fourier amplitude of the seismic waves at the dam base at the natural frequency is smaller than that at the free-field. It was demonstrated from FEM analysis and observations at an existing dam that the sinking frequency is slightly higher than the corresponding predominant frequencies for the response wave at the crest.

2. The larger the Fourier amplitude of the incident seismic wave for the natural frequency of the dam and the larger the impedance ratio of the dam and its foundation, the larger the dynamic interaction effects become.

3. Dynamic interaction effects such as reductions in maximum acceleration and wave energy are largest at the center of the dam base and decrease as you move towards the downstream toe. These interaction effects are fairly small by time you reach the toe. The effects at a point about half a dam's width from the downstream toe are about the same as those at a free-field.

4. A simplified procedure for estimating the incident wave from the observations at the dam base was proposed. This procedure was demonstrated by estimating the waves incident on the basement layer at the Minoogawa Dam site during the Kobe Earthquake.

REFERENCES

Chopra, A.K. & P.R. Perumalswami 1969. Dam-foundation interaction during earthquakes. *Proc. 4th World Conf. on Earthquake Engineering*: 37-52.

Hirata, K. 1989. Estimation of radiation damping in dynamic analysis of fill dams. *Report of Central Research Institute of Electric Power Industry*. U88061. Abiko: CRIEPI.

Iwashita, T. & H. Yoshida 1997. Earthquake response analysis and seismic stability of a rockfill dam –Behavior of the Minoogawa Dam during the Kobe Earthquake–. *Engineering for Dams*. 126: 27-35. Tokyo: Japan Dam Engineering Center.

Ohmachi, T. 1980. A fundamental study on dynamic interactions with a rockfill dam and the foundation deposit. *Tsuchi-to-Kiso*. 1191: 31-36. Tokyo: JSSMFE.

Ohmachi, T. & S. Kataoka 1995. Evaluation of dynamic interaction effects of 2-D dam-foundation-reservoir systems. *Proc. of the Japan Society of Civil Engineers*. 519: 199-209. Tokyo: JSCE.

Tohei, M. & T. Ohmachi 1990. Model analysis procedure using a FE-BE method in time domain and its application to a dam-foundation system. *Proc. of the Japan Society of Civil Engineers*. 416: 429-438. Tokyo: JSCE.

Yanagisawa, E. 1982. Effect of ground condition on vibrational characteristics of earth structure. *Proc. of the Japan Society of Civil Engineers*. 317: 101-110. Tokyo: JSCE.

Earthquake Geotechnical Engineering, Sêco e Pinto (ed.) © 1999 Balkema, Rotterdam, ISBN 90 5809 116 3

Stone column and vibro-compaction of liquefiable deposits at a bridge approach

J. Zdankiewcz & R. M. Wahab
Illinois Department of Transportation, Springfield, Ill., USA

ABSTRACT: The foundation soils for a bridge approach and abutment were identified as liquefiable soils. The subsurface soils consist of alluvial deposits comprising 4.5 to 6 m of soft silt over 21 m of loose sand. Vibro-replacement stone columns (0.9 m diameter) were used to improve the top silt deposit. Vibro-compaction was used to densify the top 11 m of the underlying loose sand. The standard penetration test (SPT) was used as an acceptance criterion for vibro-compaction. Out of 370 SPTs conducted, 350 exceeded the minimum required blow count. Liquefaction and slope stability analyses were conducted before and after ground improvement. Significant improvements in soil strength, density and factor of safety against liquefaction, were achieved for both the soft silt and loose sand deposits. The short- and long-term slope stabilities were also improved.

1 INTRODUCTION

A Cable-stayed bridge is currently under construction on the Mississippi River along Illinois State Highway IL 146, at Cape Girardeau (Illinois and Missouri states). The project is located in seismically active area, where the bedrock acceleration is estimated to be 0.36g, with an earthquake magnitude of approximately 8.5. On the Illinois side, a bridge abutment and a 10 m high by 62 m long approach embankment were constructed by Illinois department of Transportation (IDOT). The end slope was designed for 0.24g, with no deformation and no liquefaction. The foundation soils consisted of alluvial deposits which comprise 4.5 to 6 m of soft silt over 21 m of loose sand. The top 15 m of alluvial deposits were identified as highly liquefiable soils.

Several ground improvement alternatives were considered for the project. These include deep dynamic compaction, preloading, removal of silt and replacement with acceptable material, and the vibro-replacement and vibro-compaction techniques. Experience (Lukas, 1995) indicated that the top silt layer, with a plasticity index of 0 to 26, may present an "unfavorable" condition for dynamic compaction. Also, the relatively large depth of influence (about 27 m) would require a high energy input which would make dynamic compaction costly. The preloading was not a viable option because of project schedule. Removal and replacement was estimated to be the most costly alternative.

Vibro-replacement stone columns (0.91 m diameter) were used to improve the top silt deposit. Vibro-compaction was used to densify the top 11 m of the underlying loose sand. In both cases, coarse crushed stone was used as a backfill material. Compaction points were arranged in a uniform triangular grid.

Twenty eight (28) quality assurance soil borings were performed, at an average of 1 boring for every 30 compaction points. The standard penetration test (SPT) was used as an acceptance criterion for vibro-compaction. Approximately, 370 SPT tests were conducted, of which 350 exceeded the minimum required blow count.

Liquefaction analyses were conducted before and after ground improvement using Seed and Idriss' (1982) simplified procedure. Also, static and pseudo-static seismic slope stability analyses were conducted using the simplified Bishop slices method. The computer program SHAKE91 (Idriss and Sun, 1992) was used to identify ground motion. Significant improvements in soil strength, density and factor of safety against liquefaction, were achieved for both the soft silt and loose sand deposits. Slope stabilities were also improved.

2 SITE INFORMATION

Ground modification was accomplished on the east side of the Mississippi River Bridge along Highway IL 146 at Cape Girardo, Illinois (Figure 1) to improve the foundation soils for the bridge approach and abutment. The east side of the project will be referred to as the "site".

2.1 Subsurface Soil Condition

The subsurface investigation at the site, prior to ground modification, indicated that the foundation soils consisted of 4.5 to 6 m of very soft sandy silt to

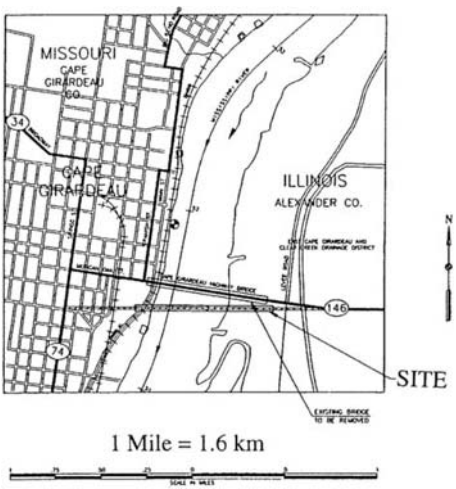

Figure 1: Location map for the site where ground modification was conducted.

silt over 21 m of loose, fine to coarse silty sand to sand. The silt to silty loam layer consisted, on the average, of 50% to 70% silt, 20% to 30% sand and 5% to 20% clay. A typical particle size distribution for this silty soil is shown on Figure 2. The majority of the silty soil samples were non-plastic; however, a few samples with the high clay content showed plasticity index (PI) ranging from 6 to 23. The moisture content ranged from 20% to 50% Consolidated-drained (CD) and consolidated-undrained (CU) triaxial tests were conducted on typical silty soil samples. Based on the CD tests, The average effective cohesion (c') and friction angle (φ') values for the silty soils were 8 kPa and 31° , respectively. Based on the CU tests, the average c' and φ' values were 3 kPa and 17°, respectively. The average N-value, from the SPT tests, for the underlying 21 m of sandy layer ranged from 3 to 27 blows per 0.3 m penetration at various depths. The average moisture content ranged from 25% to 35%. The ground water was encountered at an average depth of 2.5 m below existing grade for all borings.

2.2 Liquefaction Analysis

The liquefaction potential of the foundation soils was evaluated using the *Simplified Procedure* originally developed by Seed and Idriss (1982). This method is based on documented field performance of soils subjected to earthquakes, and it

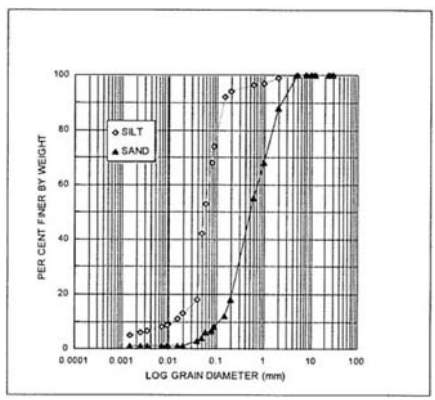

Figure 2. Typical grain size distribution curves for the upper silty soil and the underlying sandy soil.

uses the SPT N-value to estimate the cyclic stress required to cause liquefaction, called the *critical* cyclic stress. This stress is then compared to the cyclic stress induced by the design earthquake, to estimate the factor of safety against liquefaction (FOSL). Corrections to the procedure were made for SPT hammer energy and overburden pressure. Also, corrections for the site earthquake magnitude of 8.5 was made. The average corrected N-values, used in the liquefaction analysis, were 5 and 15 for the upper 4.5 to 6 m silty soil and the underlying 21 m sandy soil, respectively. An average ground water depth of 2.5 m below existing grade was used in the analysis. Based on the analysis, it was concluded that the FOSLs for the upper 4.5 to 6 m silty soil and the underlying 21 m sandy soil were 0.4 and 0.7, respectively.

2.3 *Slope Stability Analysis*

In order to conduct slope stability analysis, the bedrock acceleration at the embankment base was estimated, using SHAKE91 program (Idriss and Sun, 1992). This program is based on a one-dimensional equivalent-linear site response analysis. The average soil parameters used in this program for the upper 4.5 to 6 m silty soil and the underlying 21 m sandy soil, respectively, were: shear moduli of 43 MPa and 66 MPa, mass densities of 1900 and 2000 kg/m^3, and an average equivalent viscous damping ratio of 0.04 used for both layers based on an effective strain factor of 0.65 (Kavazanjian et al., 1998). The bedrock acceleration at the site is estimated to be 0.16g for a return period of 475 years (90% non-exceedence in 50 years) and 0.36g for a return period of 2400 years (90% non-exceedence in 250 yrs.). Results of the SHAKE91 analysis indicate amplification of the bedrock motion to be about 0.24g at the base of the embankment for the lower return period. The SHAKE91 analysis did not indicate amplification of the bedrock motion for the higher return period.

Static slope stability analysis was conducted for the side slopes, using a slope stability analysis program called XSTABL (Sharma, 1994). XSTABL is based on the limit equilibrium approach, using the simplified Bishop slices method. Also, pseudo-static seismic stability analysis was conducted for the endslope, using XSTABL and assuming the earthquake loads are applied at the centroid of each individual slice.

Table 1. Summary of slope stability analyses before ground modification.

Condition	Soil Parameters	FOS
End of Construction (Static: K = 0.0g) UU Tests	Silt: c' = 17 kPa, φ = 0 Sand: c' = 0, φ = 30°	0.82
Long-Term (Static: K = 0.0g) CD Tests	Silt: c' = 0, φ' = 31° Sand: c = 0, φ' = 30°	1.74
Long-Term (Seismic: K_y = 0.24g) CU Tests	Silt: c' = 0, φ' = 17° Sand: c' = 0, φ' = 30°	0.79
Long-Term (Seismic: K_y = 0.36g) CU Tests	Silt: c = 0, φ' = 17° Sand: c = 0, φ' = 30°	0.65

The end slope was designed to have no deformation at a yield base acceleration of 0.24g, for a factor of safety (FOS) of 1. For base accelerations greater than 0.24g and the FOS is less than 1, the permanent seismic deformation was estimated using the procedure developed by Makdisi and Seed (1978). The procedure is based on two-dimensional finite element analysis of embankments. The end slope was designed to have a tolerable deformation less than 15 cm for earthquakes producing up to 0.36g base acceleration. A cohesive silty clay soil, with an average cohesion of 50 kPa and zero friction angle, was use for the 18.6 m approach embankment. The end and side slopes were constructed at 2H:1V and 3H:1V, respectively, in all analyses. A summary of the subsurface soil parameters, used in the stability analyses for different conditions, and the resulting FOS are summarized in Table 1.

3 CONSTRUCTION PROCEDURES

The objective of ground modification at the site was to improve the shear strength of the upper 4.5 to 6 m silty layer and densify the underlying 21 m of loose sandy layer. This was accomplished by using the vibro-replacement method for the soft silty layer and the vibro-compaction method for the loose sandy layer. As shown on Figure 3, both methods covered the entire area, except vibro-compaction extended 9 m to the west beyond the limits of vibro-replacement to cover the entire end slope. The analyses indicated that stone columns beyond the mid-point of the end slope did not significantly influence the different factors of safety. In the common (shaded) area, both methods were performed as a continuous operation at the same modification points (locations) as shown on Figure 4. All modification points were arranged in a 2.4 m equilateral triangular grid as shown on Figure 5.

The backfill material (stone) used for both vibro-replacement and vibro-compaction holes was an IDOT-specified coarse aggregate, designated as CA-05. This material consists of 97±3% passing US sieve size 37.5 mm, 40±25% passing US sieve size 25 mm, 5±5% passing US sieve size 12.5 mm and 3±3% passing US sieve size 4.75 mm (No. 4). The stone was tested for gradation (AASHTO T 27), specific gravity (ASTM C 127) and the minimum and maximum densities (ASTM C 29). The same stone was also used in a 1-m thick drainage blanket/working platform over the existing ground.

The downhole vibratory probe used in both methods was a 16-metric ton gyratory probe with an average

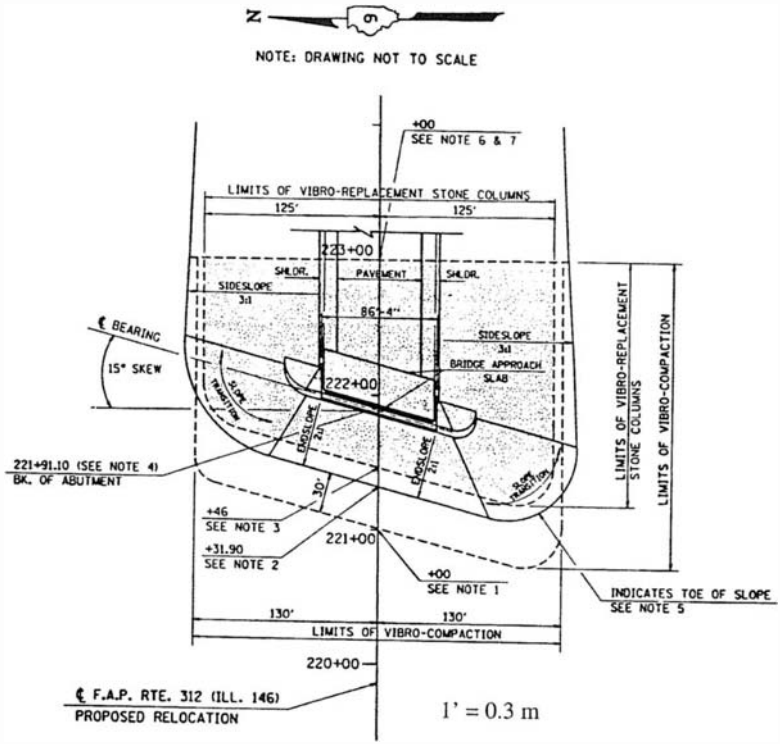

Figure 3. Limits of vibro-replacement and vibro-compaction.

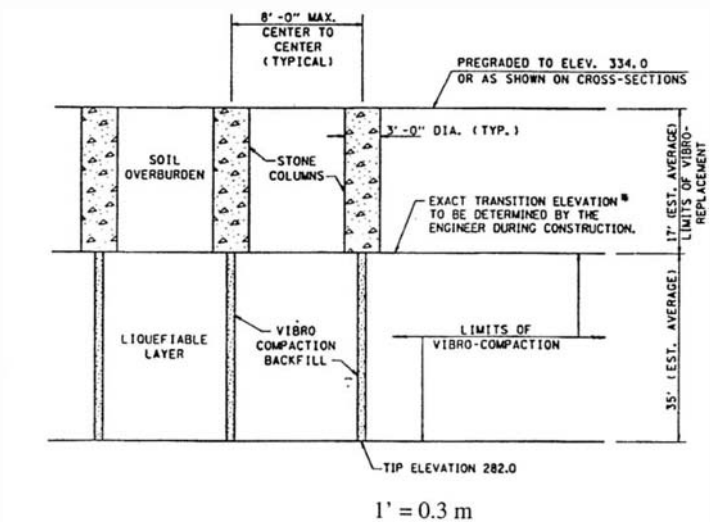

Figure 4: Cross-section through ground modification points where vibro-replacement stone columns and vibro-compaction were applied.

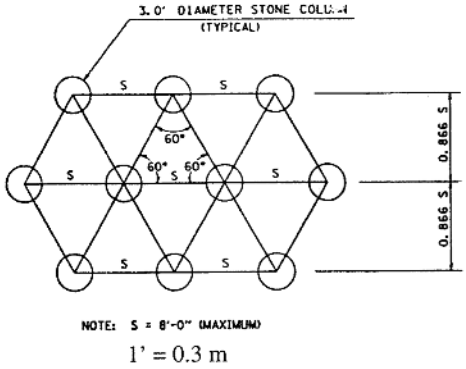

Figure 5: Equilateral triangular grid arrangement of ground modification points

frequency of 2300 rpm. The axes of modification points (or vibration centers) were near vertical, not exceeding 5° inclination from the vertical or a maximum of 0.3 m from the assigned location. No subsurface obstructions were encountered, during the modification operations, to cause any significant deviation in the location of the modification points.

3.1 Vibro-Compaction

Vibro-compaction commenced at the specified locations by full penetration of the vibratory probe through the treatment zone. Afterthat, the probe was slowly retrieved in 0.6 to 1.2 m increments to allow backfill placement. The backfill stone was then repenetrated at least twice by the probe, in order to densify and force the stone radially into the surrounding insitu soil. The diameter of vibro-compaction holes ranged from 0.45 to 0.6 m.

SPT soil borings were performed concurrently with the vibro-compaction operation, at a frequency of one boring every 30 compaction points. This was done to provide test results as quickly as possible, verify the minimum target blow count of 25 blows per 0.3 m and to perform the necessary corrective measure at the spots not meeting this criterion, while the compaction equipment was on the site.

3.2 Vibro-Replacement Stone Columns

Vibro-replacement commenced at the specified locations, after the vibro-compaction operation at each location. Water was applied at the tip of the vibratory probe to widen the diameter of the stone columns to the required 0.9 m. The flow of water from the bottom jet was maintained at all times during backfilling to prevent caving or collapse of the hole, and to provide a clean stone column. The stone columns were constructed by slowly retrieving the vibratory probe in 0.6 to 1.2 m increments and allowing the stone placement. Also, the backfill stone was then repenetrated at least twice by the probe, in order to densify and force the stone radially into the surrounding insitu soil.

Quality assurance was achieved by maintaining a minimum area replacement ratio [0.907(column diameter/column spacing)^2] of 0.128. This ratio was considered critical to the embankment stability, according to Barksdale and Bachus (1982). The average effective stone column diameter was calculated, using the in-place density of the stone and the weight of the stone used to fill a given length of the hole. The in-place density was assumed to equal 95% of the compacted stone density as determined by laboratory testing (ASTM C 29). The weight of the stone required to fill a column was based on the equivalent number of full buckets of stone placed in the hole and the loose stone density determined in the laboratory (ASTM C 29).

4 RESULTS AND DISCUSSION

The shear strength of the upper 4.5 to 6 m of soft silty soil and the density of the underlying 21 m loose sandy soil were both significantly improved by the vibro-replacement and the vibro-compaction methods, respectively. The improvement in the shear strength of the silty soil was estimated using the weighted average shear strength method recommended by Barksdale and Bachus (1982). In this method, the stone columns in row were converted into an equivalent strip whose width is proportional to the total volume of stone in that strip. The stone and soil friction angles were converted into an equivalent shear strength for the entire layer, taking into consideration the effective overburden pressure acting on the potential sliding surface, inclination of this surface, soil plasticity and any possible stress concentration. Based on average friction angles of 45° and 31° assumed for the in-place stone and the silty soil, respectively, the equivalent weighted average undrained shear strength of the improved soil was estimated to be 68 kPa (compared to the unimproved 17 kPa) for no stress concentration condition.

The improvement in the sandy layer was measured in terms of the increase in the SPT blow count. Based on the liquefaction analysis, the minimum required (corrected) N values at different elevations

were as specified on Figure 6 for a FOSL of 1.3. As shown on this figure, the observed N values for the improved sandy soil significantly exceeded the specified values at all depths. Therefore, a friction angle of 35° was conservatively assumed for the improved sandy soil in all analyses.

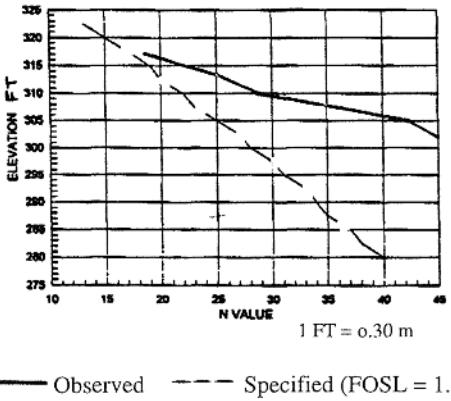

Figure 6. Specified and observed SPT N value curves after ground improvement.

Liquefaction and slope stability analyses were conducted after accomplishing ground improvement. The liquefaction FOSL increased to the minimum required value of 1.3 for both layers. Also, the FOS against slope failure increased for the different conditions analyzed as shown in Table 2. For the UU condition, the weighted average undrained shear strength of 68 kPa for the silt/stone layer was used. For the CU and CD conditions, the actual friction angles corresponding to each condition for the silt and stone were used as shown in Table 2.

Table 2. Summary of slope stability analyses after ground modification.

Condition	Soil Parameters	FOS
End of Construction (Static: K = 0.0g) UU Tests	Silt/stone: c = 68 kPa, φ = 0 Sand: c = 0, φ = 35°	1.52
Long-Term (Static: K = 0.0g) CD Tests	Silt/stone: c'=0, φ' = 31°/45° Sand: c' = 0, φ' = 35°	2.31
Long-Term (Seismic: K_y = 0.24g) CU Tests	Silt/stone: c' = 0, φ'= 17°/45° Sand: c' = 0, φ' = 35°	1.00
Long-Term (Seismic: K_y = 0.36g) CU Tests	Silt/stone: c'=0, φ' =17°/45° Sand: c' = 0, φ' = 35°	0.81*

* With tolerable deformation of 15 cm.

5 CONCLUSIONS

The foundations soils of a bridge approach and abutment were identified as liquefiable soils. Vibro-replacement (stone columns) method was used increase the shear strength of the upper silty soil, and vibro-compaction was used to densify the underlying loose sandy soil. Liquefaction and slope stability analyses were conducted before and after the ground improvement. The factors of safety against liquefaction and slope failure, both significantly increased after the ground improvement. The two methods proved to be effective for the types of soils considered in this project.

6 REFERENCES

Barksdale, R.D. and Bachus, R.C. (1982). "Design and Construction of Stone Columns." FHWA Publication No. FHWA/RD-83/026.

Idriss, I.M. and Sun, J.I. (1992). "User's Manual for SHAKE91." Center for Geotechnical Modeling, Department of Civil and Environmental Engineering, University of California, Davis, California, 13 p. (plus Appendices).

Seed, H.B. and Idriss, I.M. (1982). "Ground Motion and Soil Liquefaction During Earthquakes." Monograph No. 5, Earthquake Research Institute, Berkeley, California, 134p.

Sharma, S. (1995). XSTABL Reference Manual. Version 5. Interactive Software Designs, Inc. Moscow, Idaho.

Earthquake Geotechnical Engineering, Sêco e Pinto (ed.) © 1999 Balkema, Rotterdam, ISBN 90 5809 116 3

How liquefiable are cohesive soils?

Vlad G. Perlea
US Army Corps of Engineers, Kansas City, Mo., USA

Joseph P. Koester
US Army Waterways Experiment Station, Vicksburg, Miss., USA

Shamsher Prakash
University of Missouri-Rolla, Mo., USA

ABSTRACT: Although most clayey soils are not vulnerable to liquefaction during earthquakes, certain types of clayey materials, that meet the so-called "Chinese Criteria", are susceptible to significant strength loss during seismic action. If for sandy soils there are currently reliable procedures to determine the level of shaking intensity that may trigger liquefaction and their post-liquefaction residual strength, there are not widely accepted criteria for quantifying clayey soil behavior under seismic loading. Prudent engineering practice requires more conservatism in seismic design when cohesive soils meeting the "Chinese Criteria" are present in the foundation of structures than in respect to sandy soils, although sandy soils are recognized as more susceptible to triggering of liquefaction. The authors summarize some data in literature and findings of their research in an attempt to lowering the degree of conservatism in dealing with cohesive soils subjected to earthquake shaking.

1 INTRODUCTION

Liquefaction of sand, clean or with some fines content, has been extensively studied over the last three decades and is currently a phenomenon reasonably predictable. The liquefaction of relatively loose saturated sandy soils under cyclic loading is attributed to the increase in pore pressure due to the tendencies of the soil particles to re-arrange into a denser state. The most disturbing effect of sandy soil liquefaction, i.e. its significant loss of shear strength, is a direct consequence of the release of contacts between particles following the decrease of the effective confining pressure. Although cyclic undrained loading would increase the pore pressure in cohesive soils as well, their "cohesion" prevents separation of particles and, therefore, the loss of shear strength is less dramatic than in the cohesionless soil case.

Since observations during strong earthquakes in China from 1966 through 1976 and publication of the so-called "Chinese Criteria" (Wang, 1979), some clayey silts, silty clays, or lean clays are considered susceptible to significant strength loss during cyclic loading, in particular due to the seismic action. The induced loss of strength may even lead to a state similar to liquefaction as observed in cohesionless soils. There is, however, no available information (based on observations in China) on the ground motion characteristics required to trigger this behavior, except that occurrences were reported for earthquakes ranging in Modified Mercalli intensity from VII to IX.

In post-earthquake deformation and stability analyses it is currently common practice to assume that these somewhat cohesive soils, if anticipated to liquefy, behave like remolded sensitive clay, so that only their residual strength can be mobilized. On the other part, the modern approach using steady state or residual strength of liquefied sands (instead of zero strength) reduces the conservatism formerly applied in dealing with cohesionless soils. Therefore, current practice may result in a judgement that some clayey materials in the foundation of structures subjected to seismic action are more dangerous than liquefiable sands, i.e. they may possess shear strength comparable to or even less than liquefiable sands do under similar circumstances. It is the authors' opinion that the automatic assumption of significant loss of strength in cohesive materials during seismic action, indifferent of the duration of shaking and expected deformation, may be unwarranted and should be revised.

2 CHARACTERISTICS OF LIQUEFIABLE COHESIVE SOILS

The first reputable reference in the american technical literature on liquefiability of some cohesive soils is due to Seed et al. (1983):

> *"Consider some clay soils as being vulnerable to significant losses in strength. Based on Chinese data, these soils would appear to have the following characteristics: percent finer than 0.005 mm < 15%, liquid limit, LL < 35, and water content > 0.9 LL. The best way*

to handle these soils, if they plot above the A-line, would be to determine their liquefaction characteristics by tests."

It is, however, extremely difficult to obtain undisturbed samples of these soils and to test them. Therefore, it would be very profitable if empirical criteria or correlations with penetration results, available for cohesionless soils, can be extended to cohesive soils.

2.1 *Evidence of liquefiability of some cohesive soils*

The observations in China that lead to development of the "Chinese Criteria" are summarized in Figure 1 (after Wang, 1979, 1981). Two characteristics of the liquefied deposits that are not usually considered in the Chinese criteria were: plasticity index, $I_P < 14$ and liquidity index, $I_L \geq 0.75$. (See notation in Table 1.)

From the domains with liquefaction cases shown in Figures 1a, b, some portions correspond to coarse-grained or silty soils with no or low plasticity, that can be evaluated with procedures developed for sands: sand size (0.075 to 4.75 mm) ≥ 50%, plasticity index, PI < 4, soils that plot below the A-line. On the other part, clayey soils with more than 15% (or, conservatively, 20%) clay size particles (smaller than 5 μm) or with the plasticity index, PI > 13 were not observed to liquefy.

Liquefaction of fine-grained soils (defined in ASTM D 2487 as having 50% or more fines, i.e. particles passing the 75-μm sieve) have also been observed in Japan. For example:

- Kishida (1969) reported liquefaction of soils with up to 70% fines and 10% clay fraction;
- Tohno & Yasuda (1981) reported liquefaction of soils with up to 90% fines and 18% clay fraction due to the 1968, Tokachi-Oki earthquake;
- Miura et al. (1995) noted liquefaction of soils with up to 48% fines and 18% clay fraction due to the 1993, Hokkaido Nansai-Oki earthquake.

Japanese norms, based on studies by H. Tsuchida of liquefactions in 1964 in Niigata, consider easily liquefiable soils with up to 100% fines and 25% clay fraction (Japan Soc. of Civil Engrs, 1977).

In the United States, the upstream flow slide failure of the Lower San Fernando Dam, consequent to the 1971 San Fernando earthquake, has been attributed to liquefaction of "very silty" hydraulic fill sands (Seed et al. 1989). Liquefaction in soils containing silty or clayey fines is likely, though not well documented, to have occurred as a result of the 1886 Charleston, South Carolina earthquake (Obermeier et al. 1985). Alternating layers of silty and/or clayey glaciomarine sand deposits have been contended to have liquefied during several northeastern USA earthquakes (Tuttle & Seeber 1989). Wesnousky et al. (1989) detail a comprehensive evaluation of geologic

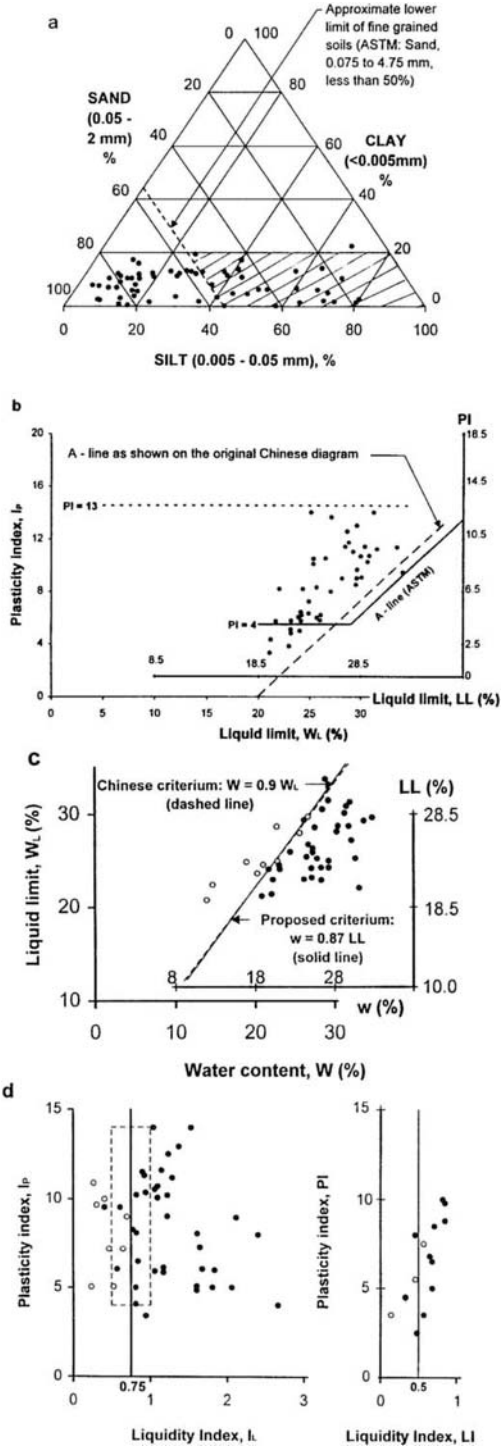

Figure 1. Plot of liquefied fine-grained soils in China during strong earthquakes (MM intensity VII and IX): solid circles = liquefied; open circles = non-liquefied. (After Wang, 1981.)

evidence of extensive liquefaction and massive sliding of loessial bluff soils throughout the Mississippi embayment as a result of 1811-12 New Madrid, Missouri series of very strong earthquakes. Youd et al. (1985) reported liquefaction of soil with 70% fines and 20% clay fraction (< 5 μm) at the Whiskey Springs site (2 km from epicenter) during the M = 7.3 Borah Peak, Idaho earthquake.

Ishihara et al. (1990) report that an earthquake of magnitude 5.5 shook the Dushanbe region of Tadjikistan in 1989, whereupon wetted, low-plasticity loess (80% silt, 15% clay, LL = 30, PI = 10, w = 40%) slumped and flowed as far as 2 km. However, the authors state that *"this event seems to be unique and previously unknown phenomenon"* and *"the loess deposit between the depths of about 7 and 17 m appear to have been in a state of impending hydraulic collapse even prior to the advent of the earthquake"*.

Susceptibility to liquefaction of fine-grained or cohesive soils was confirmed by laboratory tests. Lee and Fitton (1968) tested both sands and silts, and included in the category of "most liquefiable in laboratory" soils having up to 95% fines. Ishihara (1985) found that lean clay from the El Cobre, Chile, No.4 dike (95% fines, 20% clay fraction, PI = 11) has the resistance to liquefaction comparable with reconstituted samples of clean sand with a relative density of 40%. Actually, many clay or silt deposits with low plasticity index, such as tailings material, have been found to be as vulnerable to liquefaction as are loose clean sands.

2.2 *Generalization of "Chinese Criteria"*

According to Wang (1979), the following criteria are included in the Chinese Code of Aseismic Design of Hydraulic Structures: "any silty soil which contain less than 15% to 20% clay particles (less than 5 μm in diameter) and has plasticity index I_P greater than 3 is possible to reach liquefaction during strong earthquake if its water content W is higher than nine-tenths of its liquid limit W_L". However, the Chinese practice of determining clay fraction, I_P, W_L, and W differs from procedures used in USA and many other countries for determination of clay fraction (in accordance with ASTM D 422), liquid limit, LL, plastic limit, PL, plasticity index, PI (ASTM D 4318), and moisture content, w (ASTM D 2216).

Based on a parametric study of practices in consistency limits, water content and gradation measurements performed at Vicksburg District of the US Army Corps of Engineers and preliminary studies by Koester, Finn (1993) recommended an adjustment of the index properties as determined using the USA standards, prior to applying the Chinese criteria: (1) decrease fines content by 5%, (2) increase liquid limit by 1% and (3) increase water content by 2%. The author suggested the criterium based on liquidity index be ignored.

Koester (1992a) directed a comprehensive study on the influence of test techniques on the correlation of Atterberg limits with liquefaction occurrence in fine-grained soils. The major difference between soil characterization in USA and People Republic of China (PRC) is due to fundamentally different methods used to determine the plasticity limits: percution test in the Casagrande device for LL and rod-rolling method for PL in USA, as compared with fall-cone in laboratory penetrometer for both W_L and W_P, procedure described in the PRC Soil Testing Standard SD 128-007-84.

Considering the comparative tests of this study (USA vs. PRC procedures) only for soils in the range of interest (PRC defined $W_L \leq 35$ and $I_P \leq 14$, plotted above the A-line), LL was found 1 to 2 units (percent water content) lower than W_L. This finding suggests that a more appropriate adjustment would be to increase LL by 1.5% for obtaining an equivalent W_L, or $LL = W_L - 1.5$. Although the scatter of data was relatively high, no systematic difference was observed between PL and W_P; i.e. $PL \approx W_P$. Therefore, an appropriate conservative adjustment would also be $I_P = PI + 1.5$. Table 1 summarizes the difference between soil parameters as defined in PRC and USA (ASTM):

Table 1. Soil characterization parameters.

Parameter	Notation PRC	Notation USA	Relationship
Liquid limit, %	W_L	LL	$LL = W_L - 1.5$
Plastic limit, %	W_P	PL	$PL \approx W_P$
Plasticity index	I_P	PI	$PI = I_P - 1.5$
Moisture content, %	W	w	$w = W - 2$
Liquidity index	I_L	LI	$LI = (I_L I_P - 2)/(I_P - 1.5)$

The triangular diagram in Figure 1a is based on the Chinese Code fraction limits. The hatched zone corresponds approximately to fine grained soils (with ASTM defined sand size less than 50% and ASTM defined clay fraction less than 20%) that can be slightly cohesive.

The diagrams in Figures 1b&c have dual axes: I_P, W_L, W per Chinese Code and PI, LL, w per ASTM. Replacing Chinese by ASTM designations on graph 1c, $LL = W_L - 1.5$ and $w = W - 2$, a reasonable boundary between points corresponding to liquefaction and non-liquefaction (shown on the graph by a broken line) corresponds to the equation: $w = 0.87\ LL$.

The original Chinese graph in Figure 1d (left) has been replotted with LI vs PI axes (right) for points in the domain defined by $I_L = 0.5$ to 1.0 and $I_P = 4$ to 14. The criterium based on liquidity index ($I_L \geq 0.75$) becomes too comprehensive ($LI \geq 0.5$) and can be dropped.

In conclusion, the recommended "Chinese criteria" applied to index properties as obtained using US standards or similar, would be as shown on Figure 2. Another modification of the original Chinese criteria should be noted: the significant parameter to be

related to LL is the saturated moisture content, not the water content at the time of the investigation, when the potentially liquefiable deposit may not be saturated.

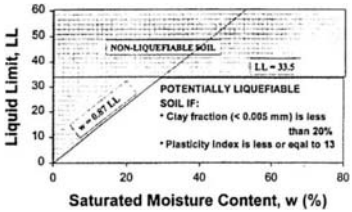

Figure 2. Chinese criteria adapted to ASTM definition of soil properties.

3 ASSESSMENT OF COHESIVE SOIL LIQUEFIABILITY

3.1 *Correlation with shaking intensity*

The intensity of shaking at a site, which can be directly related to the probability of liquefaction, is generally a function of earthquake magnitude and epicentral distance. Since Kuribayashi & Tatsuoka (1975) proposed an empirical relationship between magnitude, M and the maximum epicentral distance of liquefied sites, R ($\log_{10}R$ = 0.77 M - 3.6), many adjustments of this relationship have been proposed, based on more reported liquefaction events. For example, US Bureau of Reclamation (1984) proposed "the lower bound, below which no liquefaction should occur" shown in Figure 3.

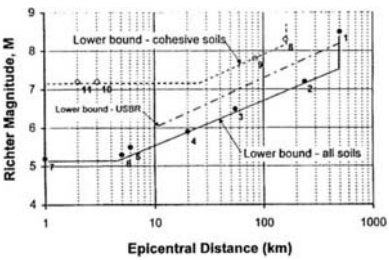

Figure 3. Seismic potential at site vs. empirical liquefaction occurrence. Numbers correspond to events in Tables 2 & 3.

The following events, plotted on Figure 3, justify an even lower threshold:

Table 2. Events near the threshold line.

Earthquake/Year	M	R (km)	Reference
1 Alaska, USA/1964	8.5	500	Youd 1977
2 Vrancea, Rom./1977	7.2	240	Perlea & Perlea 1985
3 Borrego, USA/1968	6.5	55	Youd 1977
4 Cairo, Egypt/1992	5.9	20	Elgamal et al. 1993
5 Chiapas, Mex./1975	5.5	6	Flores-Berrones 1977
6 Daly City, USA/1957	5.3	5	Youd 1977
7 Nagaoka, Japan/1961	5.2	1	Kuribayashi & Tats. 1975

In Table 2 and Figure 3 the intention was to use Richter (or local) magnitude. However, if this has been done is not sure, especially with older events. On the other hand, even if the magnitude definition would have been consistent for all events, they differ in energy transmission characteristics of earthquakes, or attenuation relationships. The graph in Figure 3 should, therefore, be considered for qualitative evaluation only.

Table 3 lists some events credited to induce liquefaction in cohesive soils [Kishida 1966 (8 & 10), Zhou 1981 (9), Youd et al. 1985 (11)]. The case history of loess liquefaction in Tajikistan (Ishihara et al, 1990) was disregarded because the soil deposit was already on the verge of hydraulic collapse before the earthquake.

Table 3. Events credited to induce cohesive soil liquefaction.

Earthquake/Year	M	R(km)	Soil type
8 Tohnankai, Japan 1944	8.3	160	Silt
9 Tangshan, China 1976	7.8	84	Sandy silt, 50% fines
10 Fukui, Japan 1948	7.2	3	Silt
11 Borah Peak, USA 1983	7.2	2	75% fines, 20% clay

Comparing the two threshold lines in Figure 3 that correspond to Table 2 and Table 3, respectively, (for any soil, including sands and for silty or clayey soils only) it is evident that triggering liquefaction in cohesive soils requires more energy than in sands. No liquefaction of cohesive soil was observed following earthquakes with Richter (local) magnitude less than 7.2. Such seismic events have durations of about 30 seconds or longer; it is believed that cohesive soils need more time than sands for incremental deformations to cumulate until liquefaction state is reached. Actually, Tables 2 and 3 are based on observations at the ground surface, so that, strictly speaking, the comparison of the two threshold lines shows that cohesive soils, compared to cohesionless soils, are either more resistant to liquefaction, or more difficult to be ejected to surface and be observed, or both (the last variant being the most probable).

Earthquake magnitude and epicentral distance control both amplitude and the duration of shaking. A parameter that incorporates the effects of both parameters, i.e. a measure of seismic energy at the site, is Arias intensity, I_h. Kayen & Mitchell (1997) derived the following relationship applicable to alluvial sites, which are the most susceptible to liquefaction:

$$\log I_h = M_w - 3.8 - 2 \log r \pm 0.61 \qquad (1)$$

where I_h is the Arial intensity at ground surface, M_w is the moment magnitude, r is the hypocentral distance (source-site), and *0.61* one standard deviation about the mean (it is assumed that subtracting one standard deviation is necessary for modeling an envelope). Assuming a depth of 6 to 8 m to the middle of liquefied layers, the Arias intensity depth-of-burial

reduction parameter, r_d, is approximately 0.5 (Kayen & Mitchell, 1997) and the Arias intensity at depth of liquefaction is approximately $I_{hb} = r_b\ I_h = 0.5\ I_h$. Figure 4 is a graphical representation of this approximate relationship.

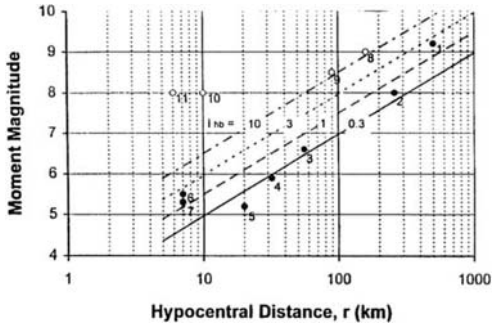

Figure 4. Estimated Arias intensity of some seismic events known to induce liquefaction.

According to Kayen & Mitchell (1997) $I_{hb} = 0.3$ is needed for liquefaction be induced in relatively loose clean sand deposits (less than 5% fines) with an average corrected blow count $(N_1)_{60} = 8$ and in a silty sand deposit (35% fines content) with $(N_1)_{60} = 2$. The corresponding $(N_1)_{60}$ threshold values are 22 and 15 for $I_{hb} = 1$ and 26 and 19 for $I_{hb} = 5$. Evidence of liquefaction of cohesive deposits was reported at locations where I_{hb} was of the order of 10; it is concluded, therefore, that the seismic action required to trigger liquefaction in the easiest liquefiable cohesive deposits is comparable to that capable to liquefy dense sandy deposits.

3.2 *Correlation with Standard Penetration Test (SPT) results*

The main advantage of SPT in liquefaction evaluation is that both SPT and liquefaction resistance are affected in the same direction (increase or decrease) by variation of relative density, soil fabric, deposit age, K_0, OCR, seismic history. However, the increase in fines content generally increases the resistance to liquefaction but decreases SPT blow count. The same effect, in opposite directions, has the plasticity index when in excess of about 10.

The most widely accepted method of accounting for the influence of fines on liquefiability is that by Seed et al. (1985). The relationship between stress ratio causing liquefaction and corrected SPT blow count for 35% fines is a conservative value for any cohesionless soil with fines content in excess of 35. However, it may give too conservative or non-conservative results when cohesive soils with low plasticity are evaluated. Fortunately, SPT furnishes also samples and anytime plasticity is observed different criteria should be used in evaluation.

3.3 *Correlation with static Cone Penetration Test (CPT) results*

There are several empirical methods of liquefiability evaluation using correlations with CPT results. However, they were developed based on field observations in sands and silty sands, so they should not be applied to cohesive soils.

In order to determine the area of application of these available procedures, electric cone penetration tests and identification tests on samples from adjacent borings have been performed in a liquefiable deposit near Manhattan, Kansas. The results of tests are presented in Figure 5.

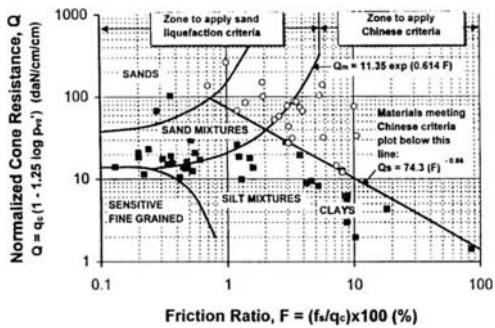

Figure 5. Cone penetration parameters of sensitive soils (meeting "Chinese criteria") plotted with solid squares. (Q_m-line after Robertson, 1990.)

Materials meeting both the two conditions: $Q \le Q_s$ and $Q \le Q_m$ should be considered vulnerable to significant loss of strength due to earthquake shaking, probably meeting the Chinese criteria. Materials with: $Q > Q_s$ or $Q > Q_m$ can be evaluated using criteria for sands and sandy soils. It should also not be forgotten that the graph in Figure 5 was based on data from one site only and may not be generalized.

3.4 *Laboratory testing evidence*

Unfortunately, the results of various studies are affected by particular conditions and can not usually be processed together or generalized. Sampling and trimming methods for obtaining specimens considered undisturbed, or procedures used to prepare remolded samples may induce a big scatter in results. Very rarely an author specifies if cyclic triaxial tests, for example, were performed in compression/extension or compression only, which dramatically affect the results. Therefore, most of published results provide only qualitative information on cohesive soil behavior under cyclic loading.

Early tests by Lee & Fitton (1968) as well as other numerous tests in the following 30 years showed undoubtedly that the most easily liquefiable cohesionless soils have some fines content. Qiu et al. (1988) reported that cyclic strength decreased to a

lower bound value when the clay content of an artificially prepared mixture reached about 9% and increased thereafter. Ishihara (1985) showed that although significant fines content generally increases the resistance to liquefaction, it does not if the silt- or clay-sized fines have low plasticity. Cyclic strength ratio, CSR (defined for 5% double amplitude axial strain in 20 cycles) was found not influenced by PI in soils with PI < 5, but increasing as a strong function of PI beyond this value and almost doubling at PI = 50 (Ishihara, 1993). Puri (1984) confirmed this trend over the range PI = 10 to 20; he also observed that cyclic axial strains sometimes greater than 10% developed prior to 100% pore water pressure response. This observation suggests that criteria based on cyclic strain are more appropriate than initial liquefaction index when the influence of fines content and/or their plasticity is studied. Relative density, D_r, is also a parameter difficult to determine when the fines content is large, so that correlations with void ratio, e, are preferred when the influence of fines on CSR is investigated.

Torsional simple shear tests were conducted in the hollow cylinder testing device of the University of Colorado in Denver (Chen, 1988) on remolded samples using the moist compaction method. For comparison, the test results were adjusted to D_r = 50% (e = 0.73) for clean sand specimens and to the same post-consolidation void ratio for mixtures. CSR dropped from 0.3 to 0.4 for clean sand to about 0.1 when up to 45% fines (fraction ≤ 0.074 mm) where added, of which 6 to 20% were clay, as shown in Figure 6 (Koester, 1992b). On the other part, the post-liquefaction shear strength increased dramatically with the percentage of clay fraction.

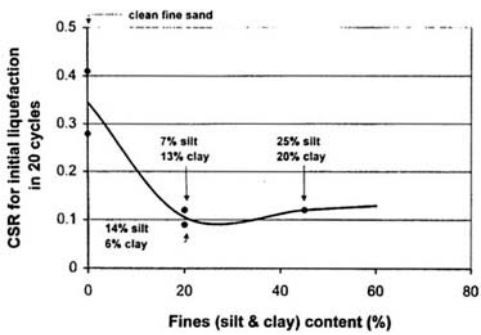

Figure 6. Results of cyclic torsional simple shear tests.

Koester (1992b) made a detailed description of the results of about 500 stress-controlled cyclic triaxial tests on isotopically consolidated specimens. Fines of varying plasticity (PI = 4 to 40) were added to each of three synthetically blended parent sands (medium uniform, fine uniform, and well graded). All specimens were prepared by moist compaction and most of them had a void ratio approximately equal to that of the parent sand at D_r = 50%. The specimens were prepared and tested at the University of Colorado in Denver under a contract with the Waterways Experiment Station of the Corps of Engineers. The complete account of this program, as well as a synthesis of cyclic triaxial test data from complimentary research on gradation effects on cyclic strength of soil was given by Chang (1990). The following conclusions have been drawn from this study:

- The cyclic strength of the parent sand decreases with addition of fines up to about 20 to 30% fines content, indifferent of the proportion of clay; thereafter, it starts to increase.
- Low plasticity index, of the order of 4, was associated to the lowest values of the cyclic strength; slight but continuous increase of the strength was observed for PI = 10 and greater.

Unfortunately, the scatter of results was significant so that reliable quantitative correlations between various parameters could not be derived. However, when groups of tests are considered independently, without requiring normalization of some parameters, the influence of fines becomes more evident. For example, Figure 7 presents the results of tests on mixtures of medium uniform sand with up to 60% fines; only results obtained on specimens with approximately the same void ratio (corresponding to relative density of 50% of the parent sand) and consolidated under the same chamber pressure (100 kPa) have been plotted.

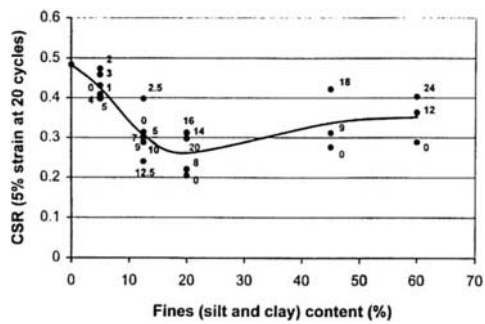

Figure 7. Results of cyclic triaxial tests on isotopically consolidated specimens of medium uniform sand mixed with various amounts of silt and clay fractions. Numbers show the percentage of clay. The curve is average variation of CSR with fines, indifferent of clay content.

From Figure 7 it is evident that the presence of fines up to about 20% decreases the CSR; thereafter, increasing fines content increases CSR. The influence of the clay fraction is different when the fines content is lower or higher than approximately 15%: at lower fines content the presence of clay decreases CSR, with the lowest value obtained when all fines were clay particles; at higher percentages of fines the effect is opposite, i.e. the lowest CSR was observed when no clay particles were present.

Prakash et al. (1998) examined results of tests by Hosri et al. (1984) on undisturbed samples of silts with either zero clay content or between 22 and 40% clay (< 5 μm). It was found that for this range of clay fraction the resistance to liquefaction (defined by CSR for initial liquefaction in 20 cycles) is clearly a function of the plasticity index (PI) if the results are normalized for the same void ratio. It was observed that CSR decreased slightly with an increasing PI up to about 5 and increased with increasing PI beyond this critical value. the lowest CSR was measured on a specimen with PI = 5, or a clay content (< 5 μm) of 22%. Similar results were obtained when reconstituted specimens of silt with PI ranging from zero to 20% were tested in the cyclic triaxial.

Puri et al. (1996) tested in triaxial reconstituted specimens with PI in the range 10 to 20; an increase of CSR with increasing PI in this range was observed. It was also observed that specimens having PI of 15 or higher did not attain the state of initial liquefaction (pore pressure equal to the initial effective confining stress, or $r_u = 100\%$) although they experienced cyclic axial strain in excess of 5%, or even 10%.

4 CONCLUSIONS

In general, cohesive soils appear to be much more resistant to liquefaction than fine sands when their states of denseness are similar. However, their residual strength, near the end of the earthquake shaking, may be significantly lower. Therefore, there are two aspects of major interest with reference to cohesive soil behavior under seismic action: (1) level of seismic action capable to trigger significant loss of strength and (2) residual strength mobilizable close to the end of the seismic action. This paper discusses the first aspect only.

Significant loss of strength in slightly cohesive soil deposits occurred during strong earthquakes, in zones with moderate shaking intensity. The characteristics of these soils range within the limits of "Chinese criteria". Because of differences in definition and testing procedures as compared with Chinese practice, the recommended criteria to be considered when soil parameters have been determined in accordance with ASTM or similar standards are shown in Figure 2.

Liquefaction or similar behavior of cohesive soils with low plasticity occurred in zones of moderate seismic intensity but due to strong earthquakes. Therefore, cohesive soils appear more dependent on magnitude (and indirectly on duration of shaking, or number of equivalent uniform cycles) than cohesionless soils. Based on case histories, liquefaction of non-sensitive cohesive soils is not expected if the earthquake Richter (local) magnitude is less than 7.2 or if the epicentral distance is greater than 160 km for any magnitude (see Figure 3). Qualitatively, the behavior during earthquakes of loose deposits of cohesive soils with low plasticity is similar to that of dense sand deposits (see Figure 4).

The most reliable simplified method for evaluation of liquefaction triggering in cohesionless soils is Seed et al. (1985) procedure. The threshold line for 35% fines can conservatively be used for evaluation of non-plastic materials with higher fines content, but should not be used for plastic (cohesive) soils (approximately located in the hatched zone of Figure 1a). With cohesive soils Chinese criteria should be used (see Figure 2). Unfortunately these criteria do not include dependence on earthquake parameters. The authors suggest to consider non-liquefiable any cohesive soil (PI > 4) if the design earthquake has a Richter (local) magnitude less than 7.2 or the seismic source zone is located farther than 160 km and if the deposit is not already on the verge of collapse. It is noted also that excess pore pressure (which may determine partial loss of strength) can be transmitted into a non-liquefiable layer if an adjacent cohesionless layer liquefies.

Liquefaction assessment based on CPT data is also available for cohesionless soils. Figure 5 indicates the domain where the criteria developed for cohesionless soils are applicable and the boundary between cohesive materials meeting or not the Chinese criteria, for a particular site.

Laboratory tests are, theoretically, the best way to assess liquefiability of soils meeting Chinese criteria for specific earthquake parameters. Unfortunately, it is so difficult to sample, to handle samples, and to test such materials, that the results of testing are seldom reliable. Therefore, judgement is usually the base of liquefiability assessment for these soils. For either test scheduling or judgement, the following observations may be useful:

- Initial liquefaction is rarely observed in cohesive soils although they may experience significant deformation. It is recommended to define failure based on the cyclic deformation level (e.g. 5 or 10% axial double amplitude deformation).
- The increase in fines content decreases the strength against liquefaction down to a minimum when the fines content is approximately 20%; thereafter the strength increases with increasing fines content, but slightly.
- The presence of clay fraction within fines has little influence on liquefiability when the fines content is low (less than 15%) and probably decreases the soil strength against liquefaction. When the soil contains 20% fines or more, increasing clay content significantly increases the soil strength against liquefaction.
- The most relevant parameter affecting liquefiability of silty clays or clayey silts is the plasticity of fines (both silt and clay fractions). The lowest resistance to liquefaction was observed on soils with PI = 4 to 5. Soils with PI > 14 may be considered non-liquefiable.

ACKNOWLEDGMENT

The tests described and the resulting data presented herein, unless otherwise noted, were obtained from research conducted under the Civil Works Investigative Study (Work Unit 32255 - Liquefaction Potential of Fine-Grained Soils) and Dam Safety Assurance programs of the United States Army Corps of Engineers. Permission was granted by the Chief of Engineers to publish this information.

REFERENCES

Chang, N.Y. 1990. *Influence of fines content and plasticity on earthquake-induced soil liquefaction.* Contract Report to US Army Engineer WES, Vicksburg, Mississippi.

Chen, J.W. 1988. *Stress path effect on static and cyclic behavior of Monterey No. 0/30 sand.* Ph.D. Thesis, University of Colorado, Boulder.

Elgamal, A.W., M. Amer & K. Adalier 1993. Liquefaction during the October 12, 1992 Egyptian Dahsure earthquake. *Proc. Third Int. Conf. on Case Histories in Geot. Engg. St. Louis, Missouri.*

Finn, Liam W.D. 1993. Evaluation of liquefaction potential. *Soil Dynamics and Geotechnical Earthquake Engineering, Seco e Pinto (ed.), Balkema.* 127-157.

Flores-Berrones, R.J. & A.W. Dawson 1977. A liquefaction case history, Chiapas, Mexico. *Proc. Ninth Int. Conf. on Soil Mech. and Found. Engg., Moscow,* 2:237-240.

Hosri, M.S. El, J. Biarez & P.Y. Hicher 1984. Liquefaction characteristics of silty clay. *Proc. Eighth Conf. on Earthquake Engg. San Francisco, California,* 3: 277-284.

Ishihara, K. 1985. Stability of natural deposits during earthquakes. *Proc. 11th Int. Conf. on Soil Mechanics and Foundation Engg., San Francisco,* 1: 321-376.

Ishihara, K. 1993. Liquefaction and flow failure during earthquakes. The Rankine Lecture. *Geotechnique,* 43(3): 351-415.

Ishihara, K., S. Okusa, N. Oyagi & A. Ischuk 1990. Liquefaction induced flow slide in the collapsible loess deposit in Soviet Tadjik. *Soils and Foundations,* 30(4): 73-89.

Japan Society of Civil Engineers 1977. *Earthquake resistant design for civil engineering structures. Earth structures and foundations in Japan.*

Kayen, R.E. & J.K. Mitchell 1997. Assessment of liquefaction potential during earthquakes by Arias intensity. *Journal of Geotechnical Engg, ASCE,* 123(12): 1162-1174.

Kishida, H. 1966. Characteristics of liquefaction sands during Mino-Owari, Tohnankai, and Fukui earthquakes. *Soils and Foundations,* 3(2).

Kishida, H. 1969. Characteristics of liquefied sands during Mino-Owari, Tohnankai and Fukui earthquakes. *Soils and Foundations,* 9(1): 75-92.

Koester, J.P. 1992a. The influence of test procedure on correlation of Atterberg limits with liquefaction in fine-grained soils. *Geotechnical Testing Journal,* 15(4): 352-361.

Koester, J.P. 1992b. *Cyclic strength and pore pressure generation characteristics of fine-grained soils.* Ph.D. Thesis, University of Colorado, Denver.

Kuribayashi, E. & F. Tatsuoka 1975. Brief review of liquefaction during earthquakes in Japan. *Soils and Foundations,* 15(4): 81-92.

Lee, K.L. & J.A. Fitton 1968. Factors affecting the cyclic loading strength of soil. *First Annual Meeting ASTM: Vibration effects of earthquakes on soils and foundations.* ASTM STP 450.

Miura, S., S. Kawamura & K. Yagi 1995. Liquefaction damage of sandy and volcanic grounds in the 1993 Hokkaido Nansei-Oki earthquake. *Proc. 3rd Int. Conf. on Recent Advances in Geotechnical Earthq. Engg. and Soil Dynamics, St. Louis, MO,* 1: 193-196.

Obermeier, S.F., G.S. Gohn, R.E. Weems, R.L. Gelinas & M. Rubin 1985. Geologic evidence for recurrent moderate to large earthquakes near Charleston, South Carolina. *Science,* 1(227):408-411.

Perlea, V. & M. Perlea 1985. *Dynamic stability of sandy soils.* (In Romanian) Bucharest: Ed. Tehnica, 336 pp.

Prakash, S., T. Guo & S. Kumar 1998. Liquefaction of silts and silt-clay mixtures. *Proc. 1998 Spec. Conf. on Geotechnical Earthq. Engg. and Soil Dynamics, Seattle, WA.,* 1: 327-348.

Puri, V.K. 1984. *Liquefaction behavior and dynamic properties of loessial (silty) soils.* Ph. D. Thesis, University of Missouri-Rolla.

Puri, V.K., B.M. Das & S. Prakash 1996. Liquefaction of silty soils. *Int. J. of Offshore and Polar Engg.* 6(4): 308-312.

Qiu, Y., S. Fan & W. Fan 1988. Some aspects of liquefaction potential of dynamically compacted loess-like sandy loam. *Proc. Ninth World Conf. on Earthquake Engg, Tokyo-Kyoto, Japan,* 3: 225-230.

Robertson, P. K. 1990. Soil classification using the cone penetration test. *Canadian Geotechnical Journal,* 27(1): 151-158.

Seed, H.B., I.M. Idriss & I. Arango 1983. Evaluation of liquefaction potential using field performance data. *Journal of Geotechnical Engg, ASCE,* 109(3): 458-482.

Seed, H.B., H. Tokimatsu, L.F. Harder, & R.M. Chung 1985. Influence of SPT procedures in soil liquefaction resistance evaluations. *Journal of Geotechnical Engg, ASCE,* 111(12):1425-1445.

Seed, H.B., R.B. Seed, L.F. Harder & H.L. Jong 1989. Re-evaluation of the Lower San Fernando dam - Report 2: Examination of the post-earthquake slide of February 9, 1971. *Contract Report GL-89-2, US Army Engr WES, Vicksburg, Mississippi.*

Tohno, I. & S. Yasuda 1981. Liquefaction of the ground during the 1978 Miyagiken-Oki earthquake. *Soils and Foundations,* 21(3): 18-34.

Tuttle, M.P. & L. Seeber 1989. Earthquake-induced liquefaction in the northeastern United States: historical effects and geological constraints. *Earthquake Hazards and the Design of Constructed Facilities in the Eastern US, Annals of the New York Academy of Sciences,* 558: 196-207.

US Bureau of Reclamation 1984. *Design Standard No. 13, Embankment Dams - Chapter 13, Seismic design and analysis.*

Wang, W. 1979. Some findings in soil liquefaction. *Water Conservancy and Hydroelectric Power Scientific Research Institute, Beijing, Cina.*

Wang, W. 1981. Foundation problems in aseismatic design of hydraulic structures. *Proc. of the Joint U.S.-P.R.C. Microzonation Workshop, Harbin, China:* 15/1-15/13.

Wesnousky, S.G., E.S. Schweig & S.K. Pezzopane 1989. Extent and character of soil liquefaction during the 1811-1812-New Madrid earthquakes. *Earthquake Hazards and the Design of Constructed Facilities in the Eastern US, Annals of the New York Academy of Sciences,* 558: 208-216.

Youd, T.L. 1977. Discussion of "Brief review of liquefaction during earthquakes in Japan" by E. Kuribayashi and F. Tatsuoka. *Soils and Foundations,* 17(1): 82-85.

Youd, T.L., E.L. Harp, D.K. Keefer, & R.C. Wilson 1985. The Borah Peak, Idaho earthquake of October 28, 1983--liquefaction. *Earthquake Spectra, Earthquake Engg. Res. Inst.,* 2(1): 71-89.

Zhu, S.G. 1981. Influence of fines on evaluating liquefaction of sand by CPT. *Proc. Int. Conf. on Recent Advances in Geotechnical Engg, St. Louis, Missouri,* 1: 167-172.

Earthquake Geotechnical Engineering, Sêco e Pinto (ed.) © 1999 Balkema, Rotterdam, ISBN 90 5809 116 3

Liquefaction of silty soils

Braja M. Das
California State University, Sacramento, Calif., USA
Vijay K. Puri
Southern Illinois University, Carbondale, Ill., USA
Shamsher Prakash
University of Missouri-Rolla, Mo., USA

ABSTRACT: Fine-grained soils such as silts, silty sands, and clays have generally be considered nonliquifiable. Recent studies have shown that fine-grained soils, especially silts, may be prone to liquefaction in certain situations. This paper presents the results of an experimental investigation to determine the liquefaction behavior of a silty soil using cyclic triaxial test equipment. Undisturbed and reconstituted specimens were used for this purpose. The results of the study indicate that low plasticity specimens used in this test program were susceptible to failure by large axial deformations even though liquefaction defined in terms of loss of initial effective confining pressure may not occur.

1 INTRODUCTION

Liquefaction of saturated soils during earthquakes has often been the primary cause of extensive damage to property, environment, and loss of human life. During the past three decades, major research efforts have been devoted to the study of liquefaction behavior of saturated cohesionless soils in the United States, Canada, Japan, and India. Laboratory investigations to study the important parameters influencing the phenomenon of liquefaction were conducted using the cyclic triaxial equipment (Seed and Lee 1966), cyclic simple shear equipment (Peacock and Seed 1968), and large size shake table tests (DeAlba et al. 1975, Finn 1982, Prakash 1981, and Silver and Seed 1971). Using the results of these tests and the observed performance of sand deposits during past earthquakes, procedures were developed to assess the liquefaction potential of saturated cohesionless soils (Seed 1976, 1979; Seed and Idriss 1981; Seed et al. 1975, 1983; and Gupta and Prakash 1984). The current research on liquefaction behavior of cohesionless soil has progressed to a stage where reasonable estimates of liquefaction potential of such soils can be made based on laboratory investigations, or on simple *in situ* characteristics such as standard penetration resistance or cone penetration resistance.

In contrast to cohesionless soils, the majority of clayey soils do no liquefy. Clays and silts of low plasticity may, however, be prone to liquefaction if their characteristics meet the following criteria (Seed and Idriss 1981 and Seed et al. 1983):

Percent finer than 0.005 mm < 15%
Liquid limit < 35%
Natural water content > (0.9)(liquid limit)

Liquefaction characteristics of soil falling in the above category need to be ascertained by carefully-conducted tests. Silty soil deposits at several locations in the United States have their characteristics in the range mentioned above. A limited number of tests were undertaken to evaluate the liquefaction behavior of a typical silty soil obtained from a selected location near Memphis, Tennessee, USA.

2 LABORATORY TESTS

The index properties of the soil used for the tests are given in Table 1. Cyclic triaxial tests were performed

Table 1. Index properties of the soil used for the laboratory tests

Property	Quantity
Passing No. 200 U.S. sieve	93-98%
Natural water content	18-26%
Liquid limit	32-36%
Plastic limit	21-25%
Plasticity index	9-14%
Clay content (finer than 2μ)	2-7.2%
Dry unit weight	14.7-15.2 kN/m^3

Table 2. Test parameters for cyclic strength studies of silty soil

Type of specimen	Test parameters	Values of parameter
Undisturbed saturated	Cyclic stress ratio, $\sigma_d/2\sigma_3$	0.15, 0.20, 0.25, 0.30, 0.35, 0.40, 0.45, 0.50
	Effective confining pressure, σ_3	69.0, 103.5, 138.0 kN/m^2
	Overconsolidation ratio, *OCR*	1, 2, 4 (σ_3 at *OCR* of 1 = 103.5 kN/m^2)
Reconstituted saturated	Cyclic stress ratio, $\sigma_d/2\sigma_3$	0.15, 0.20, 0.25, 0.30, 0.35, 0.40, 0.45,0.50
	Effective confining pressure, σ_3	103.5 kN/m^2
	Plasticity index, *PI*	10-20 (at σ_3 = 103.5 kN/m^2)

Note: σ_3 = initial effective confining pressure; σ_d = cyclic axial stress

on specimens having a diameter of 73.65 mm and a height of 147.3 mm. Both undisturbed and reconstituted specimens were used. The range of parameters for these tests is given in Table 2.

Samples for undisturbed tests were carefully obtained from the site and transported to the laboratory with minimum possible disturbance. Care was also exercised in extracting the samples from the Shelby tubes. Reconstructed specimens were prepared at the same initial moisture content and unit weight as the undisturbed specimens. The plasticity index of the reconstituted specimens was altered by adding varying amounts of the soil fraction finer than 2μ.

Cyclic triaxial tests were conducted following standard test procedures. Specimen saturation was ensured by measuring the *B* coefficient to be equal to 0.985 or more prior to the application of cyclic load. The tests were continued until the pore water pressure became equal to the initial effective confining pressure or until the axial strain became 20%.

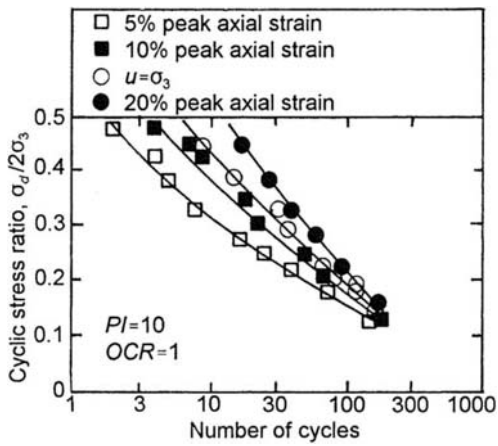

Figure 1. Cyclic stress ratio vs. number of cycles for undisturbed saturated specimens (σ_3 = 69 kN/m^2)

3 TEST RESULTS FOR UNDISTURBED SPECIMENS

Typical results of the cyclic stress ratio ($\sigma_d/2\sigma_3$) versus number of load cycles for developing pore water pressure $u = \sigma_3$, and axial strains of 5%, 10%, and 20% are shown in Figure 1 (σ_3 = 69 kN/m^2). It can be seen from this figure that the values of cyclic stress ratios causing a state of initial liquefaction ($u = \sigma_3$) in 10, 20, and 30 cycles are 0.425, 0.37, and 0.31, respectively. The cyclic stress ratios inducing 5% axial strain in 10, 20, and 30 cycles are 0.31, 0.275, and 0.24, respectively, and for inducing 10% axial strain in the same number of cycles are 0.38, 0.335, and 0.29, respectively. The failure defined by 5% or 10% axial strain in a given number of cycles thus occurs at relatively smaller values of cyclic stress ratio than those required to develop a state of initial liquefaction ($u = \sigma_3$) in the same number of loading cycles. This is in sharp contrast to

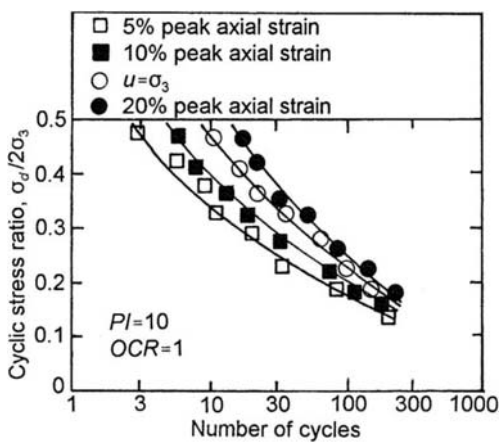

Figure 2. Cyclic stress ratio vs. number of cycles for undisturbed saturated specimens (σ_3 = 103.5 kN/m^2)

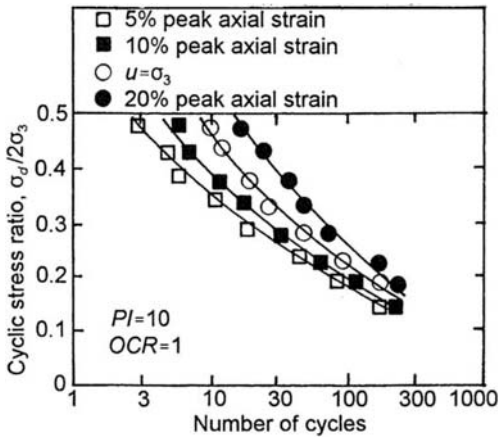

Figure 3. Cyclic stress ratio vs. number of cycles for undisturbed saturated specimens (σ_3=138 kN/m^2)

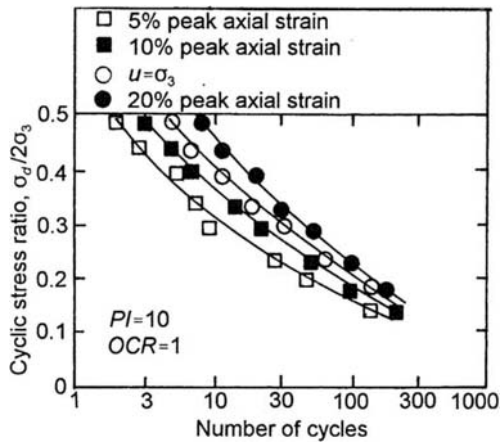

Figure 5. Cyclic stress ratio vs. number of cycles for reconstituted saturated specimens (σ_3=103.5 kN/m^2)

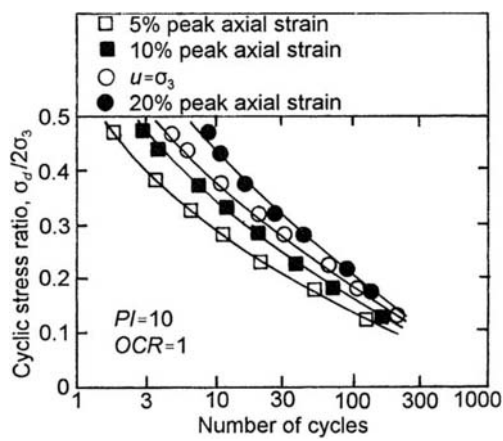

Figure 4. Cyclic stress ratio vs. number of cycles for reconstituted saturated specimens (σ_3=69 kN/m^2)

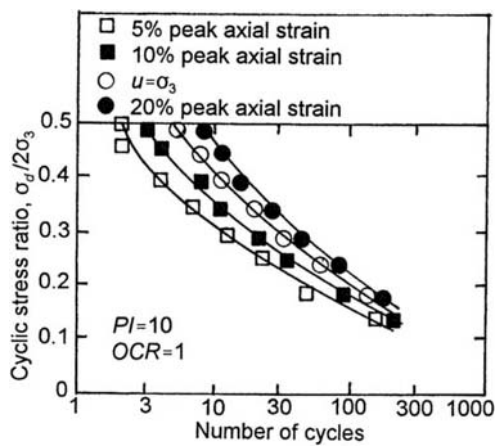

Figure 6. Cyclic stress ratio vs. number of cycles for reconstituted saturated specimens (σ_3=138 kN/m^2)

the behavior of loose saturated sands where large strains generally develop following the stage of initial liquefaction. The same trend was observed during tests on undisturbed specimens using initial effective confining pressures of 103.5 and 138 kN/m^2 as shown in Figures 2 and 3, respectively. The state of 20% axial strain usually developed several cycles after the stage of initial liquefaction.

4 TEST RESULTS FOR RECONSTITUTED SPECIMENS

The data of cyclic stress ratio and number of cycles for the reconstituted saturated specimens using σ_3 = 69, 103.5, and 138 kN/m^2 are plotted in Figs. 4, 5, and 6, respectively. The general trend of the data for all tests on reconstituted saturated specimens was similar to that of undisturbed specimens. Following is a comparison of the behavior of undisturbed and reconstituted specimens.

4.1 *Cyclic strength of Undisturbed and Reconstituted Specimens*

The effect of specimen disturbance on the cyclic strength of silts may be ascertained by comparing the observed behavior of undisturbed and reconstituted

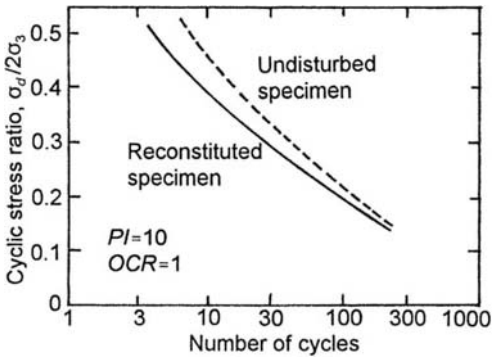

Figure 7. Comparison of cyclic stress ratio vs. number of cycles for undisturbed and reconstituted saturated specimens (condition of initial liquefaction, $u=\sigma_3$

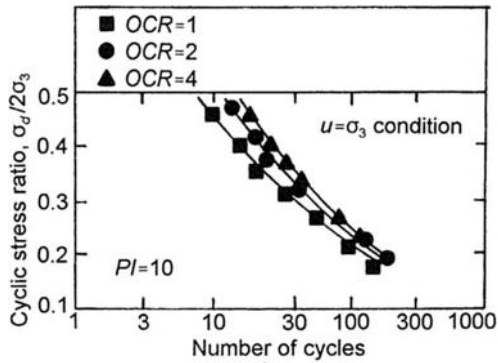

Figure 8. Cyclic stress ratio vs. number of cycles for different *OCR* values—undisturbed saturated specimens (σ_3=103.5 kN/m^2)

specimens. Plots of the cyclic stress ratio versus number of cycles for $u = \sigma_3$ condition for the undisturbed and reconstituted specimens are shown in Figure 7. The plots in Figure 7 represent the average for all test specimens for the σ_3 values used in these tests. It can be seen from this figure that, for a given value of cyclic stress ratio, the number of cycles inducing a condition of initial liquefaction ($u = \sigma_3$) is lower for reconstituted specimens compared to those causing the same condition in the undisturbed test specimens. Alternately, for a given number of stress cycles inducing the $u = \sigma_3$ condition, the cyclic stress ratio will be higher for undisturbed speci-mens than for the reconstituted specimens. This trend indicates that silts are sensitive to disturbance. Thus reasonable estimates of cyclic strength in such cases can be obtained from tests on undisturbed specimens only.

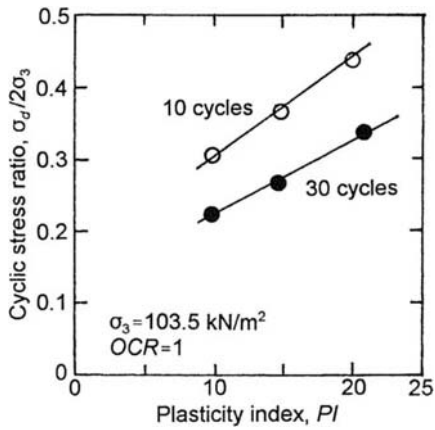

Figure 9. Effect of plasticity index on cyclic stress ratio inducing 5% peak axial strain in 10 and 30 cycles—reconstituted saturated specimens

4.2 *Effect of Overconsolidation Ratio*

A typical plot of cyclic stress versus number of cycles for inducing $u = \sigma_3$ condition for *OCR* = 1,2, and 4 for the case of undisturbed specimens of silt used for this study is shown in Figure 8. An increase in the *OCR* value increases the cyclic strength in relation to buildup of pore water pressure. Similar observations were made regarding the deformation of the undisturbed specimens under cyclic loads. Also, the effect of *OCR* on cyclic strength behavior was similar for the cases of undisturbed and reconstituted specimens. This suggests the importance of stress history which should be simulated as far as possible in evaluating the cyclic strength of silty soils.

4.3 *Effect of Plasticity of Silt*

The effect of increase in plasticity on liquefaction behavior of this silty soil was investigated on reconstituted specimens only. The effect of plasticity index on the cyclic stress ratio inducing 5% peak axial strain in 10 and 30 cycles is shown in Figure 9. Increased plasticity generally results in an increased cyclic strength. It was observed during the course of this investigation that, for soil specimens having a plasticity index (*PI*) of 15% or more and for values of cyclic stress ratios used in these tests, the state of $u = \sigma_3$ never developed. An increase in soil plasticity retards the buildup of pore water pressure. However, the cyclic axial strains may exceed 5% or 10% after application

of a certain number of stress pulses depending on the characteristics of the soil being subjected to cyclic loading.

5 CONCLUSIONS

Based on the results of limited tests conducted to investigate the liquefaction behavior of this silt, it was observed that, as a results of application of cyclic loads,

1. Pore water pressure builds up and may become equal to the initial effective confining pressure and axial deformations of 5%, 10%, or 20% may be induced in the soil.
2. Failure defined by 5% and 10% peak axial strain generally occurs earlier than the $u = \sigma_3$ condition developed. The failure condition of 20% peak axial strain usually developed after the $u = \sigma_3$ condition.
3. An increase in the overconsolidation ratio results in an increase in the cyclic strength of the silt. Time history effects are thus important in liquefaction studies of silty soils.

6 REFERENCES

DeAlba, P., C.K. Chan & H.B. Seed 1975. *Determination of soil liquefaction characteristics by large scale laboratory tests.* Report No.75-14, Earthquake Engineering Research Center, University of California, Berkeley.

Finn, W.D.L. 1982. Dynamic analysis and liquefaction —emerging trends. *Proc. 3rd International Earthquake Microzonation Conf.*, III, Seattle, USA.

Gupta, M.K. & S. Prakash 1984. Liquefaction of a soil deposit during an earthquake. *Proc. Int. Conf. Case Histories in Geotech. Engg.* St. Louis, USA, III,: 689-708.

Peacock, W.H. & H.B. Seed 1968. Sand liquefaction under cyclic loading simple shear conditions. *J. Soil Mech. Found. Div.*, ASCE, 94(3):689-708.

Prakash, S. 1981. *Soil dynamics*, McGraw-Hill, New York.

Seed, H.B. 1976. Evaluation of soil liquefaction effects on level ground during earthquakes. *Preprint No. 2752, Liquefaction problems in geotechnical engineering*, ASCE Annual Convention, Philadelphia:1-104.

Seed, H.B. 1979. Soil liquefaction and cyclic mobility evaluation of level ground during earthquakes. *J. Geotech. Engg.*, ASCE, 105(27):201-255.

Seed, H.B. & I.M. Idriss 1981. Evaluation of liquefaction potential of sand deposits based on observation of performance in previous earthquakes. *Preprint No. 81-544, In situ testing to evaluate liquefaction susceptibility*, ASCE Annual Convention, St. Louis.

Seed, H.B., I.M. Idriss & I. Ignacio 1983. Evaluation of liquefaction potential using field performance data, *J. Geotech. Engg. Div.*, ASCE, 109(3):458-482.

Seed, H.B. & K. L. Lee 1966. Liquefaction of saturated sands during cyclic loading. *J. Soil Mech. Found. Div.*, ASCE, 92(6):105-134.

Silver, M.L. & H.B. Seed 1971(a). Deformation characteristics of sands under cyclic loading. *J. Soil Mech. Found. Div.*, ASCE, 97(8):1081-1097.

Silver, M.L. & H.B. Seed 1971(b). Volume changes in sands during cyclic loading. *J. Soil Mech. Found. Div.*, ASCE, 97(9): 1171-1192.

This Page Intentionally Left Blank

Earthquake Geotechnical Engineering, Sêco e Pinto (ed.) © 1999 Balkema, Rotterdam, ISBN 90 5809 116 3

Case study for pile foundation damaged by soil liquefaction at inland site of artificial island

Noriaki Sento – *Kumagaigumi Company Limited, Ibaraki, Japan*
Koji Goto – *Chuo Kaihatsu Corporation, Tokyo, Japan*
Shinsuke Namba – *Arai Gumi Company Limited, Hyougo, Japan*
Katsumi Kobayashi – *Fujita Corporation, Kanagawa, Japan*
Hiroshi Oh-oka – *Building Research Institute, Ministry of Construction, Ibaraki, Japan*
Kohji Tokimatsu – *Tokyo Institute of Technology, Japan*

ABSTRACT: Plumb measuring, television observation, and pile inclinometer survey are conducted for PHC piles (Prestressed High strength Concrete piles) supporting a two-story building that experienced severe tilt due to soil liquefaction of reclaimed fill on Port Island in the 1995 Hyogoken-Nambu earthquake. A pseudo-static analysis is conducted in which the ground displacement profile estimated by one-dimensional effective stress analysis is applied to the pile through p-y springs. It is shown that: (1) the piles suffer extensive damage, with a horizontal displacement of about 0.4 m at the pile head and with horizontal gaps at about 3 m below the pile cap, (2) the horizontal gaps of the piles occurred in the plane parallel to the major direction of the earthquake ground motion, while the residual lateral deformation of the piles within the liquefied reclaimed fill occurred in a different direction, (3) most of the cracks in the piles occurred in the liquefied reclaimed fill, and (4) the analytical results showed a good agreement with those obtained by field investigations.

1 INTRODUCTION

During the 1995 Hyogoken-Nambu earthquake, soil liquefaction and laterally spreading that occurred in the reclaimed land areas caused extensive damage to pile foundations. Investigation and analyses of damaged foundations have shown that the damage to piles occurred under two different site conditions: one adjacent to a quay wall (Tokimatsu et al., 1997; Nakazawa et al., 1996) where large permanent horizontal ground movement occurred after soil liquefaction, and the other away from a quay wall (Isemoto et al., 1997, Shamoto et al., 1996) where soil liquefaction occurred with negligible or moderate permanent ground displacement. The extent and position of pile damage varied depending on the site conditions.

The building investigated in this study was located on Port Island, 260 m away from a quay wall. In addition to geological and geophysical site investigations, the failure and deformation of the piles were observed and measured using a plumb bob, and a television camera and inclinometer. The television camera and inclinometer were inserted into the hollow spaces of the piles down to a depth of 34 m, which resulted in the failure modes of the piles below the excavated ground.

The object of this paper is to present a set of reliable data that serves for the purpose of soil-structure interaction analysis and to clarify the mechanism of pile damage in a liquefied fill during the earthquake.

2 OUTLINE OF INVESTIGATIONS

2.1 Outline of damage to superstructure and foundation

The investigated building was located on the fill, 260 m away from a quay wall in the northeast portion of Kobe Port Island. Intensive liquefaction phenomena were observed around the site because soil improvement works had not been performed. A two-story reinforced concrete building built in 1978 was supported by prestressed high strength concrete piles (PHC piles) of A-type, which were made according to specifications of Japanese Industrial Standard, JIS A 5337. These piles had been driven to a Pleistocene gravelly sand layer by a diesel hammer. The pile heads were embedded into the pile caps by 10 cm and were strengthened with reinforced concrete filled into the hollow spaces over a length of 60 cm below the bottom of the pile caps. Fig. 1 shows the foundation plan. The building tilted towards northwest by 1/30 after the 1995 Hyogoken-Nambu earthquake.

2.2 Subsurface investigation

Before the investigation of damage to piles, Standard Penetration Test, PS logging, density logging and grain

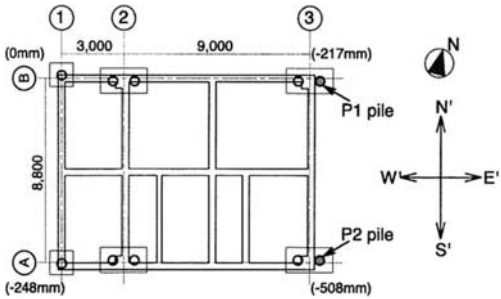

Fig.1 Plan of the foundation

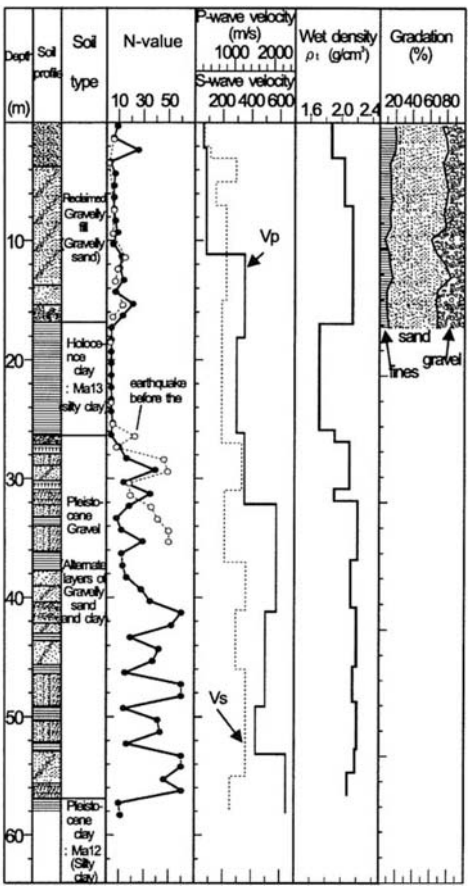

Fig.2 Results of subsurface investigation

size analysis were performed to a depth of about 60 m below the ground surface. Fig. 2 shows the N- values obtained before and after the earthquake. The gravelly sandy fill about 15 to 16 m thick has a fine content of 10 to 20 % and N-values of 5 to 15. This reclaimed fill consisting of well-graded decomposed granite soil (locally called Masado) can be considered to have liquefied during the earthquake. A Holocene clay layer locally called Ma13 layer about 9 m thick has an N-

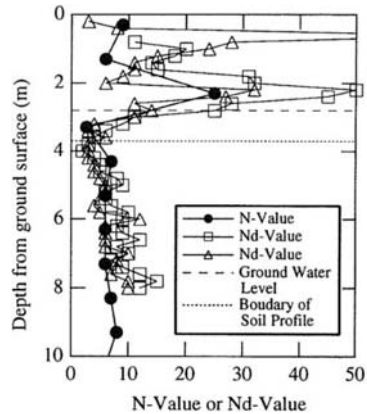

Fig.3 SPT N-values and N_d-values in the reclaimed soil

value of about 4. The piles had been driven into a Pleistocene gravelly sand deposit as point bearing piles.

The ground water level lies 2.8m below the ground surface and 1 m above the average sea water level. An automatic ram sounding was performed since the N-value at a depth of about 3 m was remarkably larger than that of other sites. Fig.3 compares Nd-values obtained by automatic ram sounding and the SPT N-values. It is conceivable that the reclaimed fill from the ground surface to a depth of 3.7 m is very stiff and might not have liquefied during the earthquake.

2.3 Investigation of damaged pile

After excavation and direct observation of the piles near the ground surface, detailed investigations including plumb measuring, television observation, and inclinometer surveys, were conducted for two piles labeled P1 and P2 as shown in Fig. 1. The numbers in the parenthesis indicates relative settlements of the foundation with respect to the northwest one.

Marked cutoffs were observed at 4-m depth of the two piles, as shown in Fig. 4. Pile P1 was cut off horizontally, while Pile P2 was cut off diagonally. The maximum horizontal gap between the upper and lower parts of the piles was 125 mm. The upper parts of the piles were shifted towards northwest or west with respect to the lower parts of the piles, the direction of which is parallel with one of the walls of the building.

To obtain the failure modes of the piles, television observation was conducted by inserting a remote controllable television camera into the hollow spaces of the piles. Fig. 5 shows the detected failure modes of the piles. Most of the cracks occurred in the reclaimed fill that is considered to have liquefied during the earthquake. Vital failures at a depth of 3 m below the bottom of the pile caps correspond to the gaps shown in Fig.4. Wide horizontal cracks also occurred at depths of 7-9 m and 16 m below the ground surface.

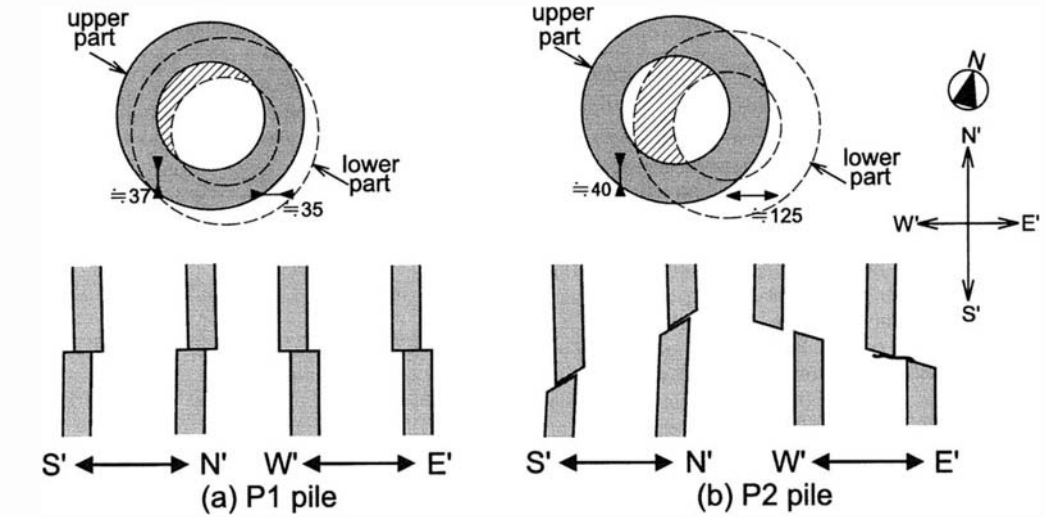

Fig.4 Marked lateral gaps and vertical section of the piles (unit:mm)

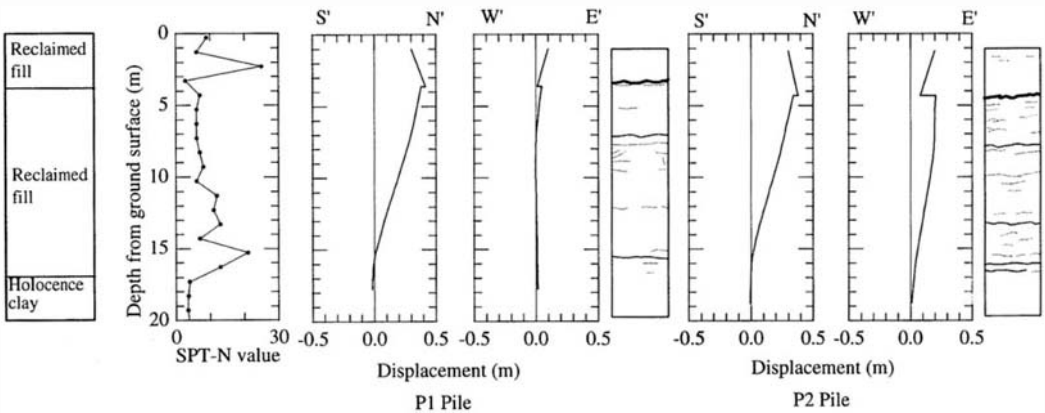

Fig.5 The residual deformation modes of piles and results of crack observation

The former corresponds to the middle of the reclaimed fill, while the latter corresponds to the boundary between the fill and the underlying Holocene clay layer.

The inclinometer survey using newly developed instrument also provides the residual deformation modes of the piles. It is capable of passing easily through a narrower space (see Oh-oka et al., 1996) or a gap such as shown in Fig. 4. Fig.5 shows the residual deformation modes that were obtained by integrating upwards the corrected slope angles of the piles. The corrections of the slope angles were made, based on the two assumptions:

(1)The horizontal displacements of the pile heads of P1 and P2 are equal since neither failure at the footing beam nor slips between the pile caps and the pile heads were observed; and

(2)Deformations of the piles due to the earthquake occurred only in the reclaimed fill since all the cracks of the piles were limited within the fill. (For further details of the method for correction, see Oh-nishi et al., 1996).

Fig. 5 shows that the residual horizontal displacement of the pile head is about 0.4 m towards the northeast and that the piles deform only within the fill, with large curvatures near the top and the bottom of the fill. The detected deformation modes of the piles are consistent with the cracks obtained by the television observations. It seems, therefore, that soil liquefaction of the reclaimed fill had significant effects on the failure and deformation modes of the piles, although the failure process is unknown.

3 FAILURE MECHANISM OF PILE

3.1 Relationship between pile foundation damage and earthquake ground motion

In this chapter, the relationship between the damage to the pile foundation and the earthquake ground motion are studied based on numerical analyses. The accelerograms obtained at the strong motion downhole array station in Port Island during the 1995 event are used. The strong motion station is located only 800 m away from the site, and its soil profile is similar to that of the site under investigation. Fig. 6 shows the orbit of the earthquake ground motion at the ground surface and the residual deformation of the damaged piles. It is noted that the direction of the horizontal gaps at 3 m below the bottom of the pile cap agrees with the major axis of the earthquake ground motion. The direction of the residual deformation of the piles is however different from the major axis of the earthquake ground motion.

3.2 Stress of piles during the earthquake

To study when cracks and remarkable failure of piles occurred, pseudo-static p-y analysis of pile foundation was conducted, using the ground deformation, excess pore water pressure ratio and acceleration response estimated by one dimensional effective stress analysis. The effective stress analysis program FLIP (Iai et al., 1992) was used. The soil profile and physical properties of soils including dilatancy parameters are shown in Table 1. The soil profile is modeled based on the result of the subsurface investigation shown in Fig. 2 and dilatancy parameters are determined by a simplified method (Morita et al., 1997) using an adjusted N-value (AIJ, 1998) of 14 ,based on the 10% fine content of the reclaimed fill. The liquefaction resistance (τ / σ_v') of the fill materials is estimated to be 0.14.

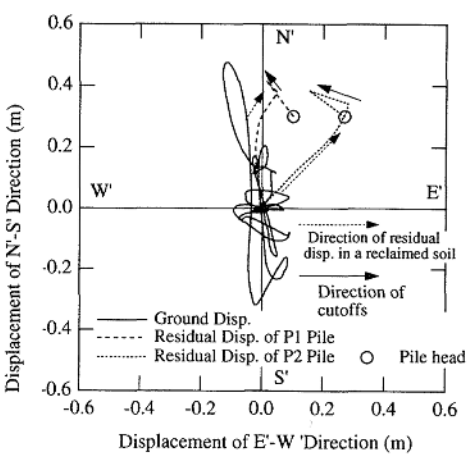

Fig.6 Earthquake ground motion at ground surface and residual pile deformation

Table 1 Parameters for 1 dimensional effective stress analysis

Soil profile	Depth (m)	Density (t/m^3)	G_{ma} (kPa)	σ_a (kPa)	ϕ_f (deg.)	ϕ_p (deg.)
		dilatancy patameter				
		S1	w1	p1	p2	c1
Reclaimed fill	0~3.7	1.9	83300	98	38	
Reclaimed fill	3.7~16.0	2.1	83300	98	38	28
		0.005	8.3	0.5	0.98	1.6
Holocence clay	16.0~26.0	1.7	47040	98	15 (c=98kPa)	
Pleistocene gravel	26.0-30.0	2.1	122500	98	38	
Pleistocene gravel	30.0-32.0	1.9	49000	98	35	

G_{ma}: Initial shear modulus, σ_a : Reference effective confining pressure, ϕ_f : Shear resistance angle, ϕ_p : Phase transformation angle, c: Cohesion

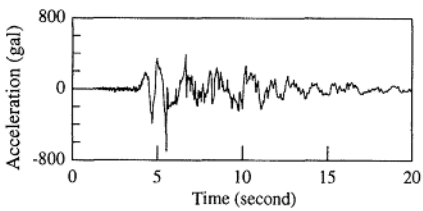

Fig.7 Input acceleration

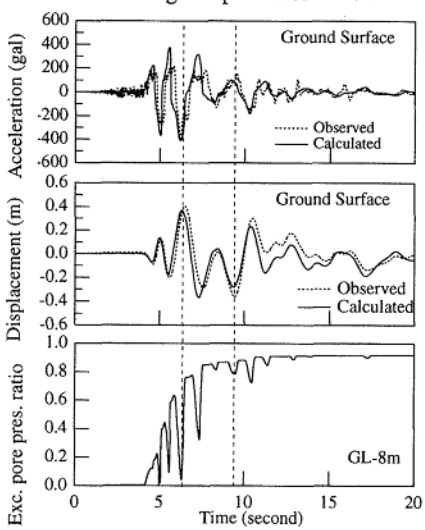

Fig.8 Time histoy of acceleration, relative displacement and excess pore water pressure ratio

Fig.7 shows the major axis component of the recorded at a depth of 32 m of the strong motion station, which is used as an input motion to the rigid base of the soil

column located at a depth of 32 m. It is assumed that soil liquefaction is unlikely to occur above a depth of 3.7 m because of the large N-values.

The calculated time history of acceleration, displacement relative to the base and excess pore water pressure are shown in Fig.8. It seems that the calculated acceleration and relative displacement show good agreement with the observed records. The broken lines in Fig. 8 indicate two time phases at which the ground surface displacement becomes the largest either before or after the excess pore pressure becomes unity. The distributions of relative displacement, excess pore water pressure ratio at these time phases are shown in Fig.9, which are used for the pseudo-static analysis.

Fig. 9 also shows the model used in the pseudo-static analysis. The pile is considered to be a non-linear beam with a tri-linear moment-curvature relation (M_c=110.7kN•m, M_u=186.2kN•m), and the beam is supported by non-linear springs defined by the following equations (see AIJ, 1998):

$$E_0=7N \quad (1)$$

$$K_h=0.8E_0B^{-0.75} \quad (2)$$

$$K_h=K_{h1}y^{-0.5} \quad (3)$$

To take into account the effect of soil liquefaction, Kh in equation (3) is reduced using a scaling factor defined as:

$$D_E=1-u \quad (4)$$

Where, E_0: Young's modulus of soil
K_h: Coefficient of horizontal sub-grade reaction
K_{h1}: Coefficient of horizontal sub-grade reaction at soil spring displacement of 1 cm
y: Displacement of soil spring
D_E: Scaling factor for coefficient of sub-grade reaction of liquefied soil
u : excess pore water pressure ratio.

The computed ground displacement profile shown in Fig. 9 is applied to the pile through the soil springs placed at every 0.5-m interval in the reclaimed fill and at every 1-m spacing in the remaining soil layers. The inertia force acting on the pile head from the superstructure is taken into account. The average N-value of the non-liquefied layer near the ground surface is regarded as 30.

The distribution of the computed bending moment in the pile is compared in Fig. 10 with the observed cracks shown in Fig. 5. The bending moments at 6.36 and 9.42 s exceed the crack moment at depths between 3 m and 8 m and between14 m and 17 m, which appears consistent with the observed pattern of cracks. However, it is unclear why the remarkable damage at the 4-m depth below the ground occurred. To investigate possible effects of the damage, another computation is made assuming that the distribution of ground displacement is trapezoidal at depths between 3 m and 16 m, as shown in Fig. 9 in the dashed dot line. The distribution of the computed bending moment is shown in Fig 10. The computed bending moment at the 4-m depth becomes close to the ultimate bending moment M_u, showing that the ground displacement profile can be a critical factor controlling the damage pattern of the pile. Probably, the high rigidity of the soil springs in the non-liquefied layer near the ground surface is also an important factor controlling the damage to the pile.

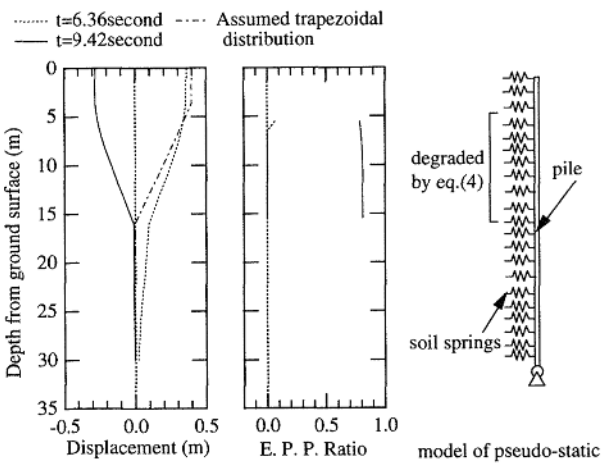

Fig.9 Distribution of relative dispalacement and excess pore water pressure ratio and model of pseudo - static p-y analysis

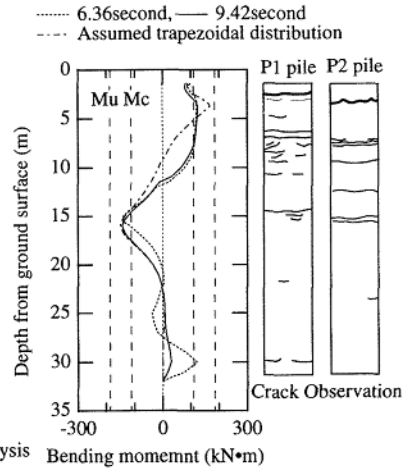

Fig.10 Calculated moment of piles

3.3 Study on residual deformation of pile

The above analyses and discussions suggest that: (1)The gaps at a depth of about 4 m was caused by the major component of shaking in the early phase, (2)The permanent ground displacements was accumulated in the other direction during the later phase of shaking, producing the observed permanent displacement of the piles in the same direction, but (3)The residual displacement of the piles was almost equal to the maximum cyclic ground displacement during the earthquake.

4. CONCLUSION

Based on the field investigations and analysis of the two-story building supported by PHC piles that experienced severe tilt after the 1995 Hyougoken-Nambu earthquake, the following conclusions may be made.

1) Although the building was located 260m away from quay walls, the pile heads of the building were displaced horizontally by about 0.4m which is equivalent to the maximum relative ground displacement during the earthquake.

2) The lateral gaps of the piles occurred in the major direction of the earthquake ground motion, while the residual lateral deformation of the piles in the liquefied reclaimed fill occurred in the different direction.

3) Most of the cracks and failures in the piles, including horizontal gaps, occurred at depths between 3m and 16 m in the liquefied fill.

4) The analytical results showed a good agreement with the field observations.

ACKNOWLEDGEMENT

This study and investigation were conducted by the ad hoc committee on " Building Foundation Technology against Liquefaction and Lateral Spreading" headed by Professor Kohji Tokimatsu of Tokyo Institute of Technology.

REFERENCES

TOKIMATSU, K., OH-OKA, H., SHAMOTO, Y., ASAKA, Y. 1997. Failure and deformation modes of piles due to liquefaction-induced lateral spreading in 1995 hyogoken-nambu earthquakes, Journal of structural and construction engineering AIJ, NO.495,, pp.95-100 (in Japanese)

NAKAZAWA, N., SOTETSU, A., NANBA, S., NAKAZAWA, Y. 1996 Investigation on pile foundations of a building damaged by Hyogken-Nanbu-earthquake (A Case In Ashiya City), AIJ J. Technol.Des. AIJ. No.3, pp.77-82 (in Japanese)

ISEMOTO, N., KANEKO, O., SATO, Y., ARAI, T. 1997 Investigations and Analysis of Pile Foundations Damaged by Soil Liquefaction during Hyogoken-Nanbu Earthquake(Part1: Damage Investigation), Proceeding of the 32th Japan National Conference on Geotechnical Engineering JGS, Vol.2,pp.919-920 (in Japanese)

SHAMOTO, Y., SATO, M., ABE, A., SHIMAZU, S. 1996 A Site Investigation of Post-Liquefaction Lateral Displacement of Pile Foundation in Reclaimed Land, Tsuchi-to-Kiso JGS, Vol.44 No.3 Ser. No.458 pp.25-27 (in Japanese)

OH-OKA, H., ONISHI, K., NANBA, S. MORI, T., ISHIKAWA, K., KOYAMA, S., SHIMAZU, S. 1997 Liquefaction-Induced Failure of Piles in 1995 Kobe Earthquake, Geotechnical Engineering in Recover from Urban Erathquake Disaster The Kansai Branch of JGS, pp.192-201

ONISHI, K., NANBA, S., SENTOH, N., HORII, K. 1997 Investigation of Failure and Deformation Modes of Piles throughout Overall Length at Inland Site in Port Island, Tsuchi-to-Kiso JGS, Vol.45 No.3 Ser.No.470, pp.24-26 (in Japanese)

IAI, S., MATSUNAGA, Y., KAMEOKA, T. 1992 Strain Space Plasticity Model for Cyclic Mobility, SOILS AND FOUNDATIONS JSSMFE Vol.32, No.2, pp.1-15

MORITA, T., IAI, S., LIU, H., ICHII, K., SATO, Y. 1997 Simplified Method to Determine Parameter of FLIP, Technical Note of the Port and Harbour Research Institute Ministry of Transportation. Japan, No.869 (in Japanese)

ARCHITECTURAL INSTITUTE OF JAPAN 1988 Recommendations for Design of Building Foundations (in Japanese)

Earthquake Geotechnical Engineering, Sêco e Pinto (ed.) © 1999 Balkema, Rotterdam, ISBN 90 5809 116 3

Liquefaction-induced failure of a bridge embankment

Th.Tika & K.Pitilakis
Department of Civil Engineering, Aristotle University of Thessaloniki, Greece

ABSTRACT: The 1995 Kozani-Grevena earthquake caused failure of Rimnio bridge embankment. The paper presents a study of the liquefaction induced failure of the embankment and a back-analysis of its permanent displacement. This case study yields valuable information about the dynamic response of embankments subjected to near-source ground motion.

1 INTRODUCTION

The Kozani-Grevena destructive earthquake of May 13, 1995, occurred in a region of North-Western Greece, previously considered as aseismic (M_s=6 and R=10Km, Papazachos et al. 1995), Figure 1. The most impressive damage, observed in geotechnical structures was the failure of the Rimnio bridge embankment. The 800m long embankment connects the village of Rimnio with the bridge crossing the northwest section of Polifito artificial lake. It was constructed in Seventy's with a height of 14 to 15m, a width of 12 to 14m at the crest and its sides, which are protected with rockfill, sloping at an inclination of 1:2.

The embankment has not shown any significant deformation since its construction. During the earthquake, however, it suffered serious damage. The pavement to a great length settled by 1 to 2m, while extensive cracking and deformation were observed at other parts of the embankment. According to the survey, carried out after the earthquake, the maximum horizontal displacement was of the order of 0.8 to 2m, depending on the location, Figure 2.

The subject of this paper is the study of the failure mechanism of the embankment and the back-analysis of its permanent displacement.

2 GEOTECHNICAL INVESTIGATION

An extensive geotechnical investigation was carried out after the earthquake in order to find out the causes of the embankment failure. This included boreholes for soil sampling, geophysical surveys and laboratory testing, Figure 3. The geotechnical investigation showed that the embankment is constructed from compacted clayey-sandy gravel and it is founded on a 3.5 to 4m thick layer of loose silty sand, which extents beyond the embankment toe. Then follows a 7.5 m thick layer of dense sandy gravel and cobbles and a layer of marly clay. The latter extends to the bedrock with an increasing stiffness.

The minimum number of SPT blows measured at the silty sand layer and the embankment central axis on May 23, i.e. ten days after the earthquake, was N_{SPT}=18. Also, the piezometric ground water table at the silty sand layer at the same date was 4m above the pavement, indicating the existence of a significant yet undissipated excess pore water pressure. Surficial effects of liquefaction, such as ground and pavement cracking, lateral spread and sand boils were observed, Figure 4 & 5.

These field observations indicated that failure was induced by the liquefation of the silty sand layer. The significant rise of pore water pressure in the silty sand layer caused the reduction of shear strength of the soil on which the embankment was founded. This in connection with the earthquake-induced stresses caused the embankment failure. The liquefaction of the silty sand layer was expectable, according to the existing empirical relationships between epicentral distance and distance to liquefiable soils (Ambraseys 1988, Manual of zonation on seismic geotechnical hazards 1993).

The effective vertical stress at the middle of the silty sand layer and the embankment central axis is σ'_v=243.5kPa. The minimum number of SPT blows, N_{SPT}=18, corrected for the overburden pressure to an effective vertical stress of 100kPa and the fines content at the residual state, becomes $(N_1)_{60}$=14 which corresponds to a void ratio of e=0.734 (Seed

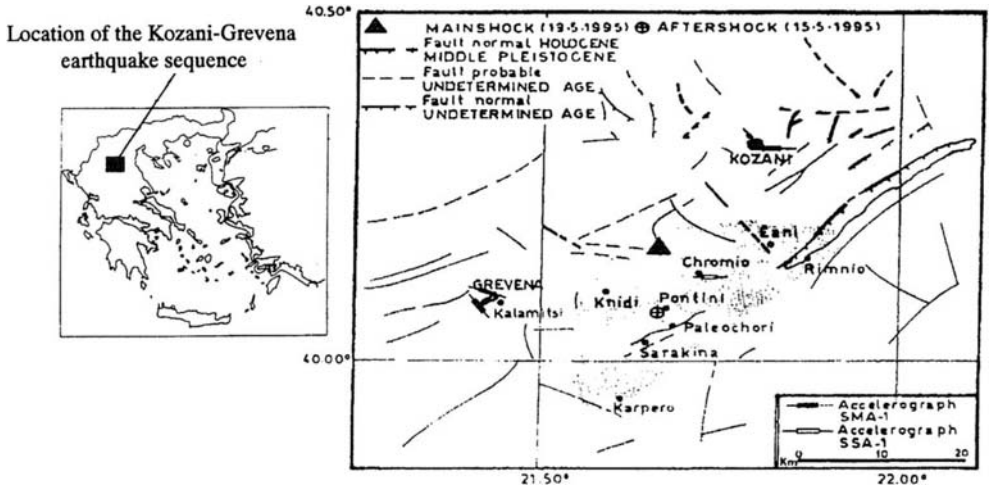

Figure 1. Map of the area affected by the 1995 Kozani-Grevena earthquake

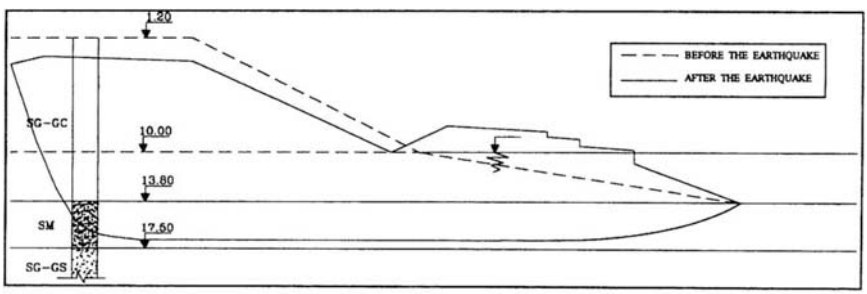

Figure 2. Embankment cross-section before and after the earthquake

1987, Skempton 1985). This in conjunction with the observation of the pore water pressure on May 23, indicated that the in-situ void ratio prior to earthquake was even higher. The average effective vertical stress on the sliding surface of the embankment is estimated to be of the order σ'_v=116kPa.

Figure 6 presents results from an undrained monotonic triaxial test (CU) on the silty sand. As shown in the above Figure, the undrained residual strength of the silty sand is $s_{us}=q_s \cos\varphi_{us}$ = 26.2-33.1kPa (average value 29.6 kPa) and its ratio to vertical effective stress is s_{us}/σ'_v=0.149-0.188, assuming that the sand is normally-consolidated.

The above value of the undrained residual strength is of the same order of magnitude with the value estimated from the empirical relation correlating the undrained residual strength of liquefiable soils and number of SPT blows $(N_1)_{60}$ (Seed & Harder 1990).

3 SEISMIC RESPONSE OF THE EMBANKMENT

A one-dimensional (1D) nonlinear effective stress analysis was carried out in order to evaluate the seismic response of the embankment. The computer program DESRA-2C was used (Lee & Finn 1997). This program models a horizontally layered soil profile as a lumped mass multidegree of freedom system and allows the profile to be excited by an earthquake acceleration time-history, input at an assumed bedrock. It incorporates a hyperbolic stress-strain relationship with hysteretic damping, pore water pressure increase (Byrne 1991), strain-dependent degradation of soil stiffness and strength, caused by the pore water pressure increase, and pore water pressure dissipation and redistribution.

The use of a 1D model to represent the seismic response of on embankment fill has been discussed by Bray et al. (1995). They found that for an embankment sliding on its base, which is the case in this study due to the liquefaction of the foundation layer, the dynamic shear stresses near the base of

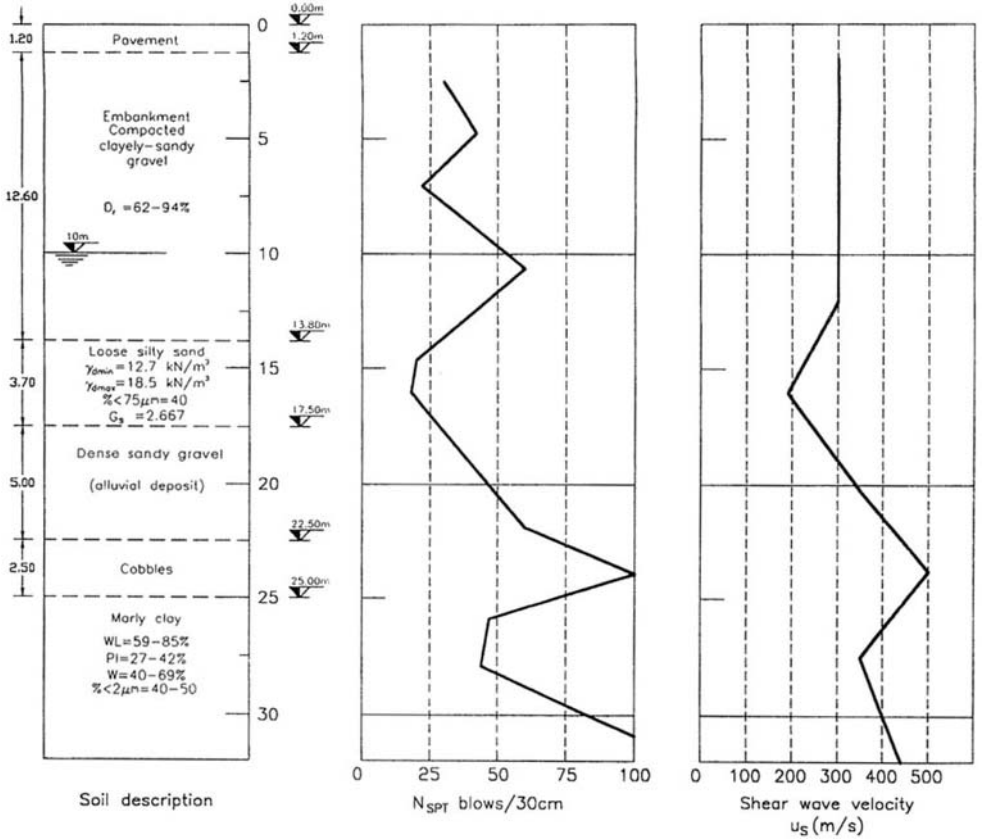

Figure 3. Soil profile

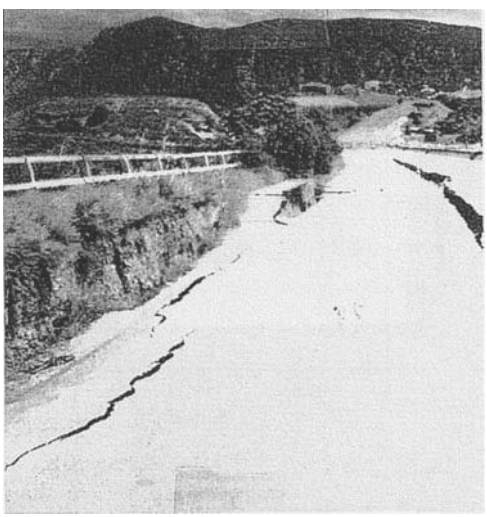

Figure 4. Soil and pavement cracks at the embankment crest

Figure 5. Sand boils at the toe of the west bank of the embankment

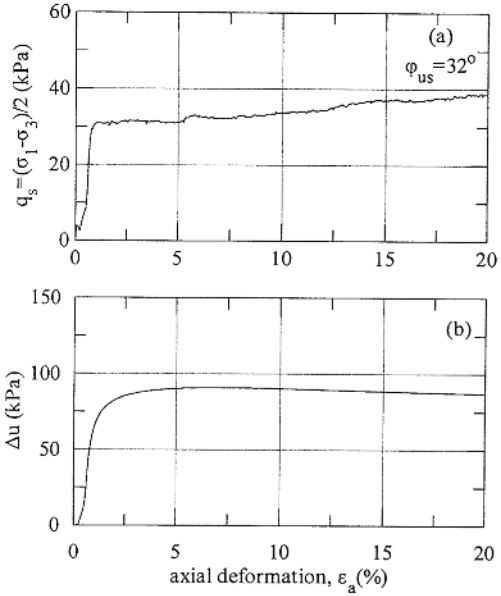

Figure 6. Results of undrained triaxial compression on silty sand (σ'_c=114.3kPa, e=0.785)

a two-dimensional (2D) embankment fill can be approximated reasonably well with 1D analysis. Given the uncertainties associated with the evaluation of dynamic properties of the embankment fill, the underlying soil and bedrock, and the design input motion, the use of 1D analytical method is considered to be appropriate.

As input excitation at the bedrock level, the synthetic accelerogram of the May, 13, strong motion was used (Tolis & Pitilakis 1993). The maximum value of the shear modulus, G_{max}, was calculated from the shear waves velocity, Vs, estimated by the surface waves inversion method (Lontzetidis et al. 1997). In the analysis the shear modulus and hysteritic damping were varied with shear strain, according to the relations, proposed by Hatanaka & Uchida (1995) for the embankment fill, the sandy gravel and cobbles layers and by Vucetic & Dobry (1991) for the marly clay. Resonant-column tests were performed for the evaluation of shear modulus and damping ratio of silty sand through a wide range of shear strains. Figure 7 shows the synthetic acceleration input motion, as well as the acceleration time-histories computed by the analysis.

4 ESTIMATION OF PERMANENT DISPLACEMENT OF THE EMBANKMENT

A sliding block analysis was implemented for the estimation of the permanent displacement of the

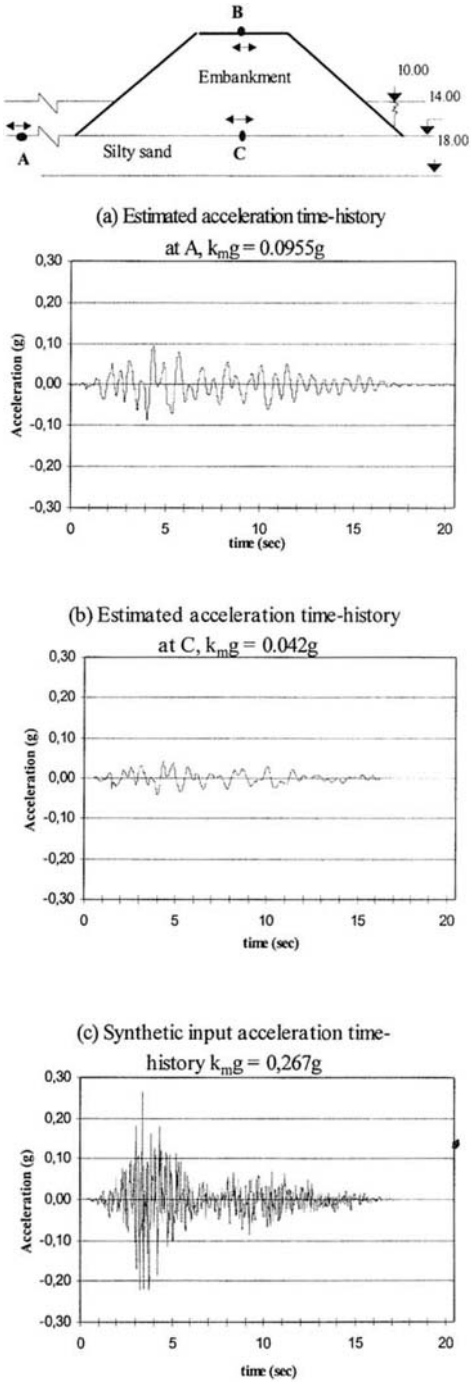

Figure 7. Acceleration time-histories computed by 1D seismic response analysis (a and b) and synthetic input acceleration (c)

embankment (Newmark 1965). According to this method, the sliding mass is considered as a rigid block moving on an inclined plane. The method takes into account the history of ground acceleration and two other parameters, the critical acceleration, $k_c g$, and the maximum ground acceleration, $k_m g$. The critical acceleration is the minimum ground acceleration, required for the initiation of the movement. It depends on the geometry of the sliding mass, the shear strength parameters of the soil and it corresponds to a factor of safety equal to one.

As input ground acceleration in the sliding block method the acceleration time-histories at the ground surface, calculated by the previously described seismic response analysis, were used (points A & C). A 2D conventional stability analysis was used for the estimation of the critical acceleration, $k_c g$=0.325g at the start of earthquake shaking. After the liquefaction of the silty sand and during the earthquake shaking, it can be calculated from the following expression (Tika-Vassilikos et al. 1993):

$$k_c g=((s_{us}/\sigma'_v)-\tan\beta)/g \qquad (4.1)$$

where (s_{us}/σ'_v)=0.149-0.188 is the ratio of the undrained residual strength to the effective vertical stress, determined from the results of undrained triaxial tests, and $\tan\beta$=0.187. The critical acceleration of the embankment during the earthquake was therefore negligible. Figure 8 shows the permanent displacement, u_{rmax}, as a function of the ratio of critical acceleration to the maximum ground acceleration, k_c/k_m. From Figure 8 for negligible critical acceleration, the permanent displacement is u_{rmax}=1.5 to 2.2m, which is of the same order magnitude as the observed horizontal movement after the earthquake.

5 CONCLUSIONS

During the Kozani-Grevena destructive earthquake of May 13, 1995, lateral spreading of the Rimnio bridge embankment was observed. The failure was induced by the liquefaction of the silty sand layer on which the embankment was founded. The observed settlement of the embankment was 1 to 2m and the horizontal displacement 0.8 to 2m. The horizontal displacement is of the same order magnitude as the one back-calculated. This study proves to be useful for the verification of the analytical methods used for the seismic analysis of earth dams and embankments.

ACKNOWLEDGMENTS

The authors wish to thank Dr. A. Anastasiadis, Mr G. Koninis, Mr. K. Lontzeditis, Miss K. Makra, and Dr. D. Raptakis for their help in the study of this case-history.

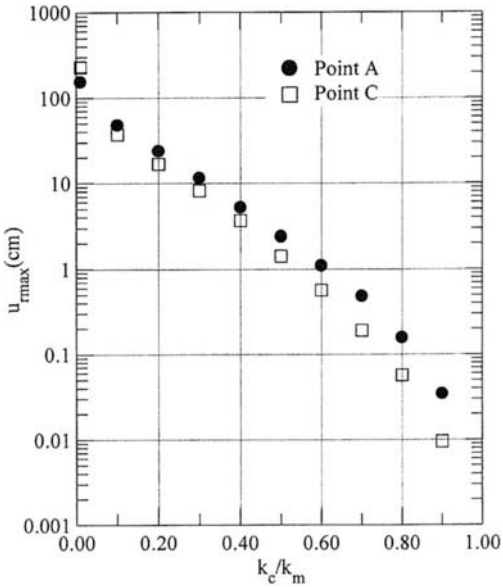

Figure 8. Permanent displacements, u_{rmax}, versus critical acceleration ratio, k_c/k_m

REFERENCES

Bray, J.D., Augello, A.J., Leonards, G.A., Repetto, P.C. & Byrne, R.J. (1995). Seismic stability procedures for solid waste landfills. J. of Geotech. Engrg., ASCE, Vol. 121, No. 2: 139-151.

Byrne, P.M. (1991). A cyclic Shear-Volume Coupling and Pore Pressure Model for Sand. Proc., 2nd Int. Conf. On Recent Advances in Geotechnical Earthquake Engineering and Soil Dynamics, University of Missouri, Rolla, Vol.1: 47-56.

Lontzetidis, K. Raptakis, D. & Pitilakis, K. (1997). Correlation Relationships Vs-Nspt of Greek Soils, Proc. of the 3rd Hellenic Conf. on Geotechnical Engineering, Vol. 1, pp. 419-425 (in Greek).

Tolis, St. & Pitilakis, D. (1993), "Quake: an algorithm for the construction of synthetic accelerograms at the bedrock", Proc. of 2nd Conference of Greek Geophysists, Vol. 1, pp.236-247 (in Greek).

Ambraseys, N.N., (1988), Engineering Seismology Journal of Earthquake Engineering and Structural Dynamics, Vol. 17, No 1, 1-105.

Hatanaka, M. and Uchida, A. (1995), "Effects of test methods on cyclic deformation

characteristics of high quality undisturbed gravel samples", Proceeding of session on static and dynamic properties of gravel soils, ASCE Geotechnical Special Publication No 56.
Lee, M.K.W. & Finn, L.W.D. (1997). Desra-2C program manual.
Manual for Zonation on seismic geotechnical hazards, (1993), Technical Committee for Earthquake Geotechnical Engineering, TC4, International Society of Soil Mechanics and Foundation Engineering (ISSMFE).
Newmark, N.M., (1965), "Effects of earthquakes on embankments and dams", Geotechnique,London, UK, 15(2), 60-139.
Papazachos, B.C., Panagiotopoulos, D.G., Scordilis, E.M., Karakaisis, G.F., Papaioanou, Ch.A., Karakostas, B.G., Papadimitriou, E.E., Kiratzi, A.A., Hatzidimitriou, P.M., Leventakis, G.N., Voidomatis, Ph.S., Peftitselis, K.I., Savaidis, A., Tsapanos, T.M., (1995), "Focal properties of the 13th May 1995 large (M_s=6,6) earthquake in the Kozani area (North Greece)", Proc. XV Congress of the Carpatho-Balkan Geological Association, Athens, Greece.
Seed, H.B., (1987), "Design problems in soil liquefaction", J, Geotech. Engrg., ASCE, 113(8), 827-845.
Seed, R.B., & Harper, L.F. (1990). SPT-mased analysis of cyclic pore pressure generation and undrained residual strength. Proc., Memorial H.B. Seed Symp., Vol.2:351-76.BiTech Publishers, British Columbia, Canada.
Skempton, A.W. (1986). Standard penetration test procedures and the effects in sands of overburden pressure, relative density, particle size, ageing and overconsolidation. Geotechnique, Vol. 36, No. 3, 425-447.
Tika-Vassilikos, T.E., Sarma, S.K. and Ambraseys, N.N., (1993), "Seismic displacements on shear surfaces in cohesive soils", J. of Earthquake Engineering and Structural Dynamics, Vol. 22, No 8, 709-721.
Vucetic, M. and Dobry, R., (1991), "Effect of soil plasticity on cyclic response", J. Geotech. Engrg., ASCE, 117(1), 89-107.

Earthquake Geotechnical Engineering, Sêco e Pinto (ed.) © 1999 Balkema, Rotterdam, ISBN 90 5809 116 3

A simulation study on liquefaction using DEM

Hitoshi Nakase
Tokyo Electric Power Services Company Limited, Japan

Tomoyoshi Takeda
Tokyo Electric Power Company, Japan

Masanobu Oda
Saitama University, Japan

ABSTRACT: Liquefaction analysis using Distinct Element Method (Cundall, 1979) is developed. Laboratory liquefaction tests are numerically simulated by the proposed method. The results show the method can simulate the general characteristics of liquefaction of saturated soils under cyclic loading.

1 INTRODUCTION

In order to simulate the micromechanics for liquefaction of sandy soil using DEM, it must consider interaction between soil particles and water. Hakuno et a1.(1988) succeeded in simulating the gradual increase in excessive pore pressure during shaking of a saturated loose assembly. However, their program code was not convenient for general use because of its enormous calculation time. The present objective is, therefore, to improve Hakuno's DEM for liquefaction analyses with special emphasis on how to model the phenomenon as simply as possible without losing the general characteristics.

2 DESCRIPTION OF LIQUEFACTION ANALYSIS USING DEM

How to deal with the effects of pore water is of particular importance in the simulation analysis of liquefaction by DEM. To do this, the following problems must be solved: i) change of pore volume due to movement of particles, ii) excess pore pressure caused by change of pore volume, iii) forces acting on the particles due to the excess pore pressure, and iv) dissipation of excess pore pressure.

2.1 *Change of pore volume*

The disks in Fig.1 represent soil particles. Hakuno et al. (1988) dealt with all pores formed by neighboring particles. The volume change due to the displacements of these particles was calculated for each pore. This method made the calculation and subsequent manipulation very complicated. To improve this problem, the pore volume change inside a small square (called a cell hereafter) is only considered in the present simulation. The dimensions of the cell, dx and dy, are chosen such that there are about 15 disks whose centers are located inside the cell. Then the volume change $\Delta V^{(i,j)}$ of pores in the cell (i, j) is calculated from the weighted average displacement of particles in the four neighboring cells $(i\text{-}1,j)$, $(i+1,j)$, $(i,j\text{-}1)$ and $(i,j+1)$ as following.

$$\Delta V^{(i,j)} = \Delta V^{(i,j)}_{(i-1,j)} + \Delta V^{(i,j)}_{(i+1,j)} + \Delta V^{(i,j)}_{(i,j-1)} + \Delta V^{(i,j)}_{(i,j+1)}$$

$$\Delta V^{(i,j)}_{(i-1,j)} = -dy \times \sum_{l} \Delta x^{(l)} v^{(l)} / \sum_{l} v^{(l)}$$

$$\Delta V^{(i,j)}_{(i+1,j)} = dy \times \sum_{m} \Delta x^{(m)} v^{(m)} / \sum_{m} v^{(m)}$$

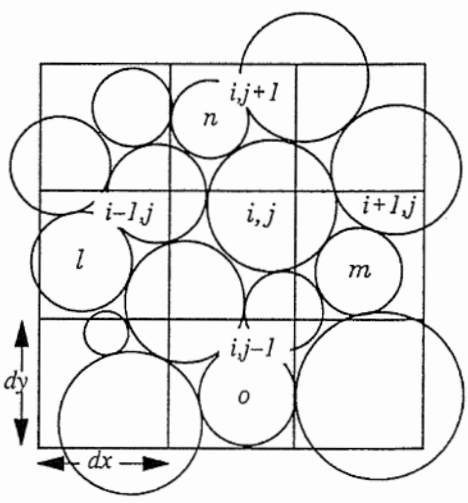

Fig.1 Volume change in a cell (i,j)

$$\Delta V_{(i,j-1)}^{(i,j)} = -dx \times \sum_n \Delta y^{(n)} v^{(n)} / \sum_n v^{(n)}$$

$$\Delta V_{(i,j+1)}^{(i,j)} = dx \times \sum_o \Delta y^{(o)} v^{(o)} / \sum_o v^{(o)} \quad (1)$$

where $\Delta V_{(i-1,j)}^{(i,j)}$, $\Delta V_{(i+1,j)}^{(i,j)}$, $\Delta V_{(i,j-1)}^{(i,j)}$ and $\Delta V_{(i,j+1)}^{(i,j)}$ are contributions of the neighboring cells to the volume change. $\Delta x^{(l)}, \Delta y^{(l)}$ and $v^{(l)}$ are the incremental displacement in the x-, y-directions and the volume of the l-th particle respectively. The summation, $\sum_l$ is performed from one to the total number of the particles in the cell (i, j). This operation keeps $\Delta V^{(i,j)}$ to zero when a particle flow takes place with the relative positions of particles unchanged.

2.2 *Excess pore pressure*

Assuming that the change of excess pore pressure $\Delta u_w^{(i,j)}$ is proportional to the decrease of the pore volume, we obtain:

$$\Delta u_w^{(i,j)} = \gamma_w \Delta V^{(i,j)} \frac{1}{dxdy\kappa^{(i,j)}} \quad (2)$$

where γ_w is the unit weight of water, and $\kappa^{(i,j)}$ is the storage coefficient of the cell (i, j) which is inversely proportional to the elastic bulk modulus of water in the condition that the bulk modulus of the particles equals that of water.

2.3 *Forces acting on particles*

Let $u_w^{(i,j)}$ be the excess pore pressure acting at the center of the cell (i, j) at time t. The pressure gradient between the neighboring cells generates the body forces $B_x^{(k)(i,j;t)}$ and $B_y^{(k)(i,j;t)}$ in x- and y-directions respectively to the k-th particle in the cell (i, j).

$$B_x^{(k)(i,j;t)} = \frac{u_w^{(i+1,j;t)} - u_w^{(i-1,j;t)}}{2dx} v^{(k)} \quad \text{and}$$

$$B_y^{(k)(i,j;t)} = \frac{u_w^{(i,j+1;t)} - u_w^{(i,j-1;t)}}{2dy} v^{(k)} \quad (3)$$

where 2 appears in each denominator since the excess pore pressure is defined at the center of each cell. These body forces are used in the equilibrium equations of the particle system, to calculate their movements as well as the conventional DEM.

2.4 *Dissipation of the excess pore pressure*

The gradient of the excess pore pressure between the cells also causes flow of pore water. The excess pore pressure dissipates through the water flow. A finite difference method for the seepage analysis through porous media is used to analyze the dissipation. If the flow of pore water takes place as shown in Fig. 2, the equation of continuity of water in a cell (i, j) is given by:

$$\sum_{k=1}^{4} Q_k \gamma_w \Delta t = (\overline{u}_w^{(i,j;t+\Delta t)} - u_w^{(i,j;t)}) \kappa^{(i,j)} dxdy \quad (4)$$

where Q_k (k=1,2..4) are the water volumes per unit time flowing out (or in) from the neighboring cells (i, j+1), (i+1, j), (i, j-1) and (i-1, j) to the cell (i, j), respectively (Fig. 2), and $\overline{u}_w^{(i,j;t+\Delta t)}$ is the excess pore pressure in the cell (i, j) at time $t+\Delta t$ when the pressure changes due to water flow.

Using Darcy's law, for example, Q_1 is written as:

$$Q_1 = k_1 \frac{u_w^{(i,j;t)} - u_w^{(i,j+1;t)}}{\gamma_w dy} dx \quad (5)$$

where k_1 is the coefficient of permeability in the y-direction which is determined, if necessary, by the average void ratio in the cells (i, j+1) and (i, j), and $u_w^{(i,j;t)}$ is written as

$$u_w^{(i,j;t)} = \frac{1}{2}(\overline{u}_w^{(i,j;t+\Delta t)} + u_w^{(i,j;t)}) \quad (6)$$

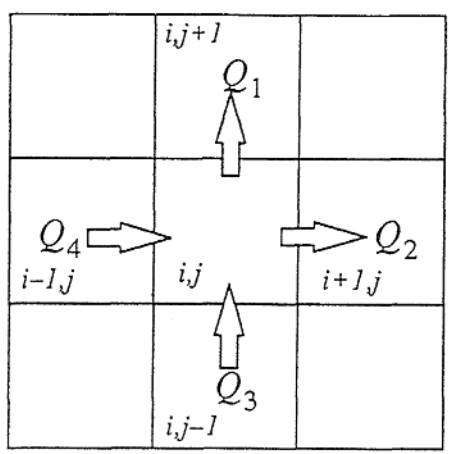

Fig.2 Pore water flow between the cells

Similar equations for Q_2, Q_3 and Q_4 can be written. Substituting these equations into (4) and rearranging for each cell, we obtain linear equations concerning the unknown values $\overline{u}_w^{(i,j;t+\Delta t)}$ by taking into account the boundary conditions and the given value $u_w^{(i,j;t)}$ at t. Finally, the total excess pore pressure $u_w^{(i,j;t+\Delta t)}$ at $t+\Delta t$ is determined by:

$$u_w^{(i,j;t+\Delta t)} = \overline{u}_w^{(i,j;t+\Delta t)} + \Delta u_w^{(i,j)} \quad (7)$$

The excess pore pressure thus determined is substituted into (3) to calculate the forces distributed to the particles.

3 *AN EXAMPLE OF SIMULATION*

In order to provide an initial configuration for each simulation test, about 3000 circular disks with diameters ranging from 2.4 mm to 6.6 mm with a mean D_{50} of 5.0 mm were numerically packed in a two-dimensional space 13.7 cm high and 41.2 cm wide under the gravity. The unit weight of the disks was 26.0 kN/m^3. The spring coefficient and the friction at contact were selected to be 3.6×10^7 N/m and 27°, respectively. The permeability coefficient of the assembly was set to 2.0×10^{-2} cm/sec. The value corresponds to that of typical sand. The storage coefficient was taken to be 1.0×10^{-5} from the elastic bulk modulus of water. Frequency of the cyclic loading was set to 2Hz tentatively to save computation time. In order to avoid the influence of inertia force due to higher speed of loading than 0.1Hz in general laboratory test, we compulsorily reduced the particle velocity to the maximum loading velocity if the particle velocity exceeds the maximum loading velocity. From comparing to numerical test with 0.1Hz cyclic loading frequency, it was found that the manipulation had no significant effect on the final results.

Two vertical boundaries of both sides consist of the so-called periodic boundaries, and the shear force was periodically applied through a top rigid boundary (Fig.3). The both sides of the assembly are analytically connected at rhe periodic boundaruy. The shear force was periodically applied through the top rigid boundary to enforce its load displacement in lateral direction. The top rigid boundary changes its vertical position slighty to keep the constant consolidation pressure (σ_c=98kPa). The bottom rigid boundary is immovable. Two assemblies were used: a dense assembly (void ratio e =0.225) and a loose one (e =0.249). To obtain high internal friction angles corresponding to natural granular soils, no rolling was allowed at any contact during the simulation tests.

The results are summarized in Fig.4 and Fig.5, where time histories of the shear stress τ, shear strain γ, excess pore pressure u_w normalized by the consolidation pressure σ_c, the stress path and the stress-strain relationships are shown for the dense and the loose assembly.

As described above, the cyclic shear stress was applied in a completely sinusoidal form on the top boundary. It is important to note here that τ in Fig.4 denotes the corresponding shear stress calculated at the bottom. The shear stress-time curve thus obtained was distorted when liquefaction started, as shown in Figs.4 (a) and (e). In the dense

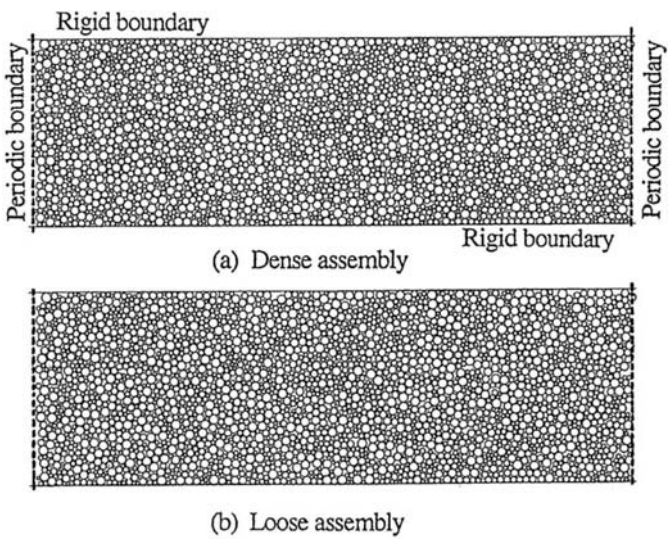

Fig.3 Numerical model of liquefaction test

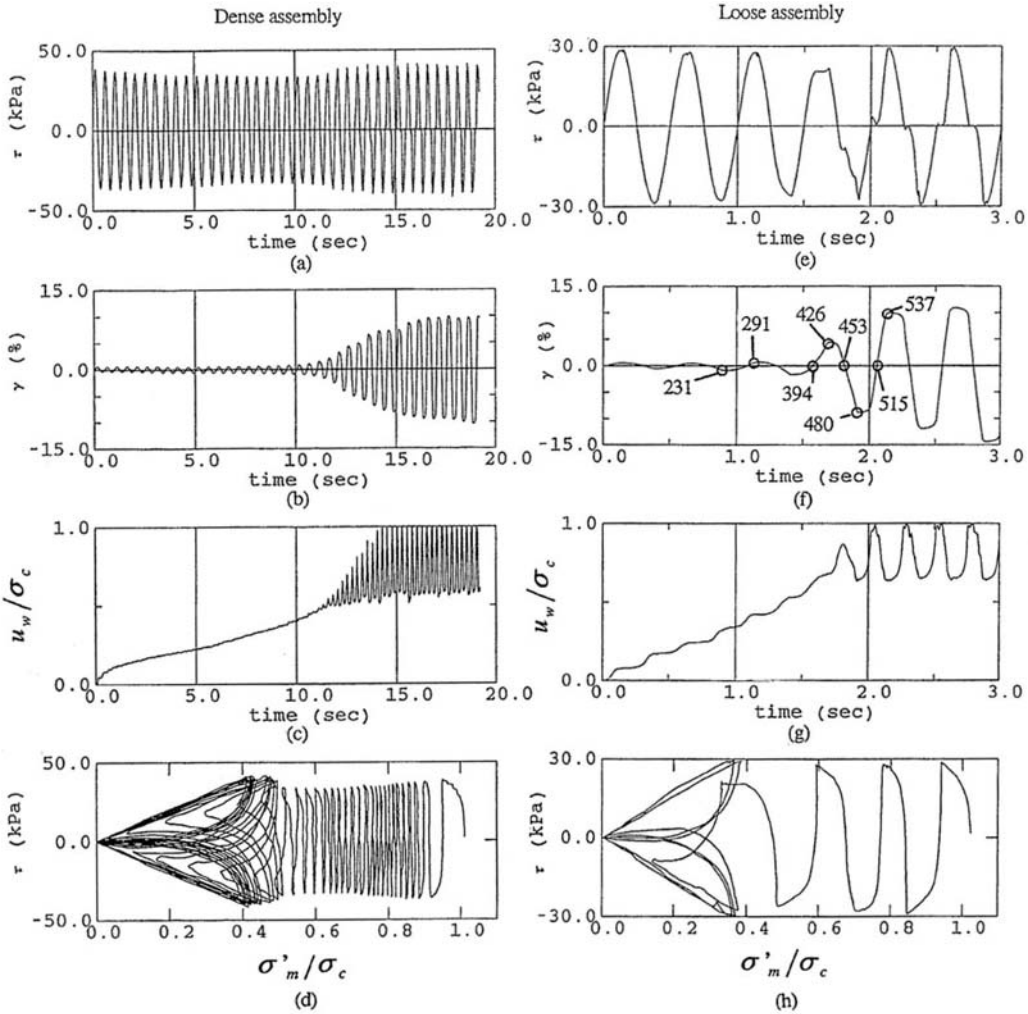

Fig.4 The results of the numerical analysis.
Time histories of average shear stress at bottom boundary (a), (e); average shear strain calculated from the lateral displacement of top boundary (b), (f);
normalized pore pressure averaged at bottom boundary(c), (g) and stress path (d), (h) drawn by using the data of (a),(c) and (e),(g)

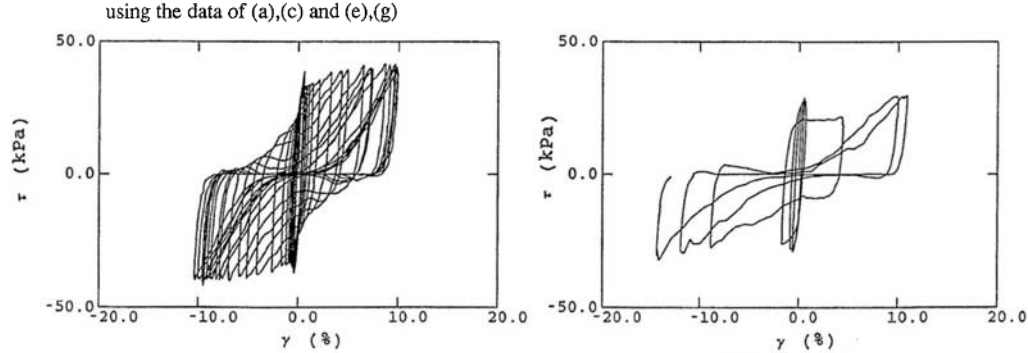

Fig.5 Stress-strain relationship

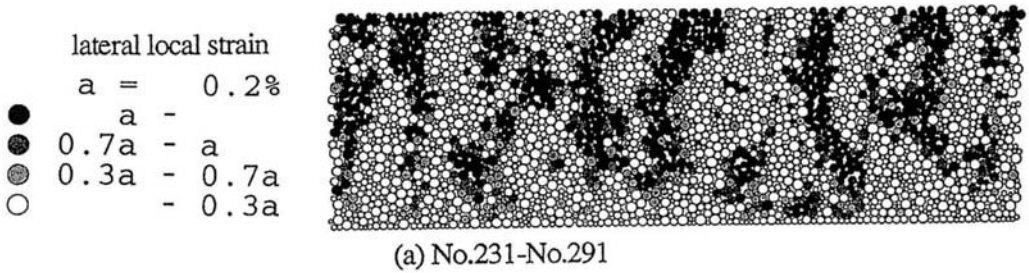

(a) No.231-No.291

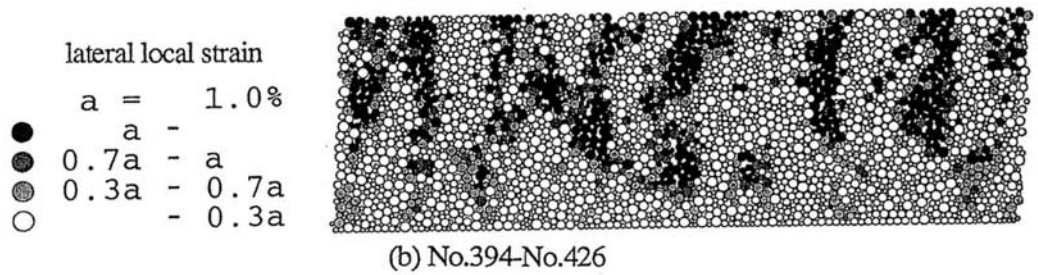

(b) No.394-No.426

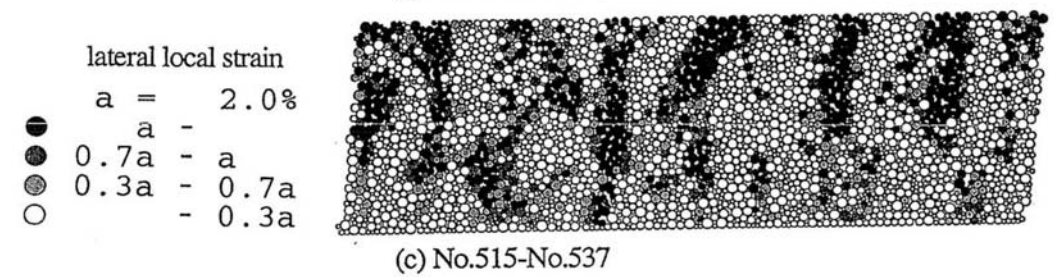

(c) No.515-No.537

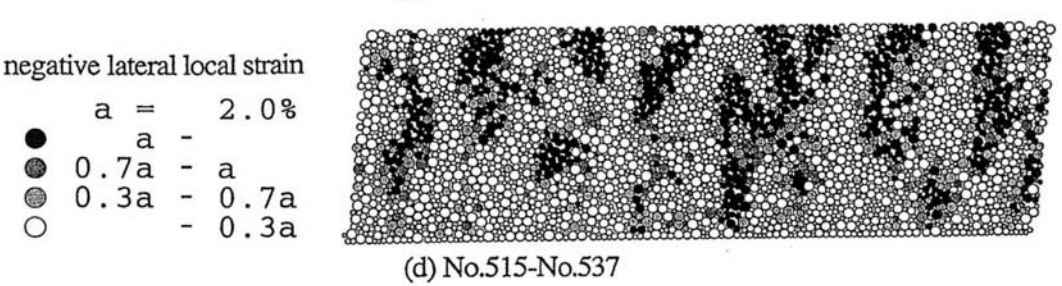

(d) No.515-No.537

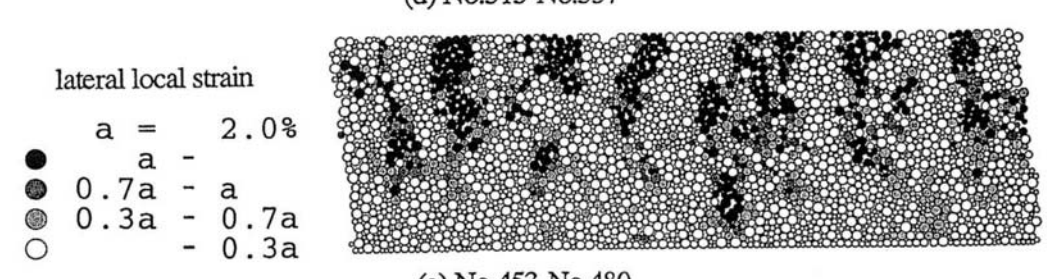

(e) No.453-No.480

Fig.6 Distribution of lateral local strain

assembly, the excess pore pressure increased gradually, and the shear strain increased suddenly after 22 cyclic loading steps. Then finally, the so-called cyclic mobility condition is reached after about 32 cyclic loading steps.

In the loose assembly, on the other hand, complete liquefaction took place after only four cycles with smaller applied shear stress than that of dense assembly.

It should be noted that such a change in liquefaction resistance due to the packing density is quite similar to that of natural sands.

4 STRAIN LOCALIZATION RECORD DUE TO A TURN OF LOADING

The strain localization in the loose assembly is observed in the following stady.

To denote visually distribution of the strained potion in the specimen, an index is introduced. The index, is named 'lateral local strain' here after, is given by the following equation,

$$\overline{\varepsilon_{xi}} = \sum_{j=1}^{N} \frac{x_j - x_i}{|x_j - x_i|} \Delta x_j \Big/ rN \qquad (8)$$

where ε_{xi} is lateral local strain around particle i, x_i, x_j are coordinates in the x direction of particle i, j, Δx_j is increment of lateral displacement of particle j and N is total number of particles inside the circle of radius r (2cm) whose center is located at the center of particle i. The value of the index is calculated for each particle. However the value does not show the magnitude of the strain of the own particle but the average lateral expanding movement of the particles around the particle i.

The distribution of the strained potion in the specimen at the maximum or minimum points, No.291, No.426, No.480 and No.537 in the Fig.4 (f) of strain time history, are shown in Fig.6. Lateral local strain in Fig.6(a) is calculated during half cyclic loading step, from No.231 to No291, before liquefaction. The degree of shading of each particle shows the magnitude of the lateral local strain. The most dark particle shows the area around the particle is laterally strained more than the threshold value of a, say 0.2% in this figure. Lateral local strain in (b) and (c) are due to the following cyclic loading in the same direction as (a), from No.394 to No.426 and from No.515 to No.537, respectively, of during quarter cyclic loading step after liquefaction. The patterns of distribution of the strained potion in (a), (b) and (c) are almost same each other not depending on the generation of liquefaction.

Distribution of negative lateral local strain during the same cyclic loading step as (c) is shown in (d). The dark particles show the compression area around the particle. Distribution of dark particles of (c) and that of (d) are complement each other in the specimen. Figure (e) shows lateral local strain due to shear stress in the opposite direction to that in the former figures, from No.453 to No. 480. It is interesting that distribution of the dark particles of (e) corresponds to that of (d).

5 CONCLUSION

The present computer program using DEM simulates the general characteristics of liquefaction of saturated soils under cyclic loading. The result of the simulation is natural as compared with the effective stress analysis using FEM. It take about 5 hour (CPU, work station) of calculation time for the simulation about the liquefaction phenomena in the loose assembly consisting of 3000 disks during 20 second excitation.

The detail analysis on the simulation result gives the following observations. Once the portion is strained by a turn of loading, almost the same portion is strained by following loading in the same direction, and the same potion is compressed by following loading in the opposite direction. This tendency does not depend on the generation of liquefaction.

REFERENCE

Cundall, P.A. & Strack, O.D.L.(1979).: A discrete numerical model for granular assemblies, Geotechnique 29, No. 1,47-65

Hakuno, M., Tarumi, Y.(1988):A granular assembly simulation for the seismic liquefaction of sand, Proc. Of JSCE No.398/I-10, pp129-138

Earthquake Geotechnical Engineering, Sêco e Pinto (ed.) © 1999 Balkema, Rotterdam, ISBN 90 5809 116 3

Behaviour of reinforced sand under liquefaction

S. Saran & O. P Singh
Civil Engineering Department, University of Roorkee, India
M. K. Gupta
Earthquake Engineering Department, University of Roorkee, India

Synopsis

The proposed investigation deals with the liquefaction study of a fine locally available SOLANI SAND deposited in a test tank 1.05m x 0.6m x 0.6m high and subjected to sinusoidal vibrations. Geogrid, Horizontal filter and Vertical Drains of gravel have been tried to control liquefaction. Geogrid at two different horizontal spacings of 50mm and 100mm, has been tested. Vertical drains of 50mm diameter (d), at three different spacing of 2.5d, 3d and 4d have been employed. The frequency of the vibration, has been fixed at 4 cps,.the acceleration range being from 10%g to 40%g. The relative density (initial) of 20% has been maintained for all the tests. It was observed that Geogrid can control liquefaction. But more effective method, to reduce the liquefaction potential, is by providing Horizontal Filter and Vertical Drains of gravel.

Introduction

Liquefaction of saturated sand has often been the main cause of catastrophic damages to the structures resulting in loss of life and property. Their occurrence of damage becomes more imminent, when the mechanical properties of soil are liable to undergo considerable changes due to dynamic loads. This is true for SANDS when they are loose, fine and saturated. Structures resting on such deposits may experience large scale tilt and movements due to the liquefaction of the foundation soil.

A large number of Earthquakes have been reported which have witnessed phenomenon of liquefaction and damages of small or large magnitude (Seed, 1968). The Obra dam in UP, Bansas dam in Gujarat and many more faced similar situation in which the foundation material of the dam is liable to liquefy due to an Earthquake.

Liquefaction often appears in the form of sand fountains and a large number of such fountains have been observed during the Bihar Earthquake of 1934, Dhubri Earthquake (Assam) of 1930. But 1964 Earthquake of Alaska, Nilgata Earthquake 1964 (Kawasumi, 1968), Loma Prieta Earthquake (1988) and the most recent Koyna Earthquake of 1995, are the best illustrations of liquefaction phenomenon causing catastrophic damages to structures and resulting in loss of life and property due to:

(a) Large settlements and tilts and even over toppling of structures.
(b) Floating up of buried structures like septic tanks, sewers, piles etc.
(c) Settlements, tilting and lateral movements of piers and abutments of bridges and land sliders
(d) Slumping of slopes and embankments and sinking of super structures.

In Koyna city (1995), a bridge, just overturned without cracking. No damage occurred to the super structure, though the buildings settled vertically by a couple of meters, Highway and Railway lines were damaged extensively, which proved that extra precaution taken in the design of the superstructure would not be of any help during the Earthquakes. It therefore extremely important, that the possibility of liquefaction of soils at the sites, during an anticipated Earthquake must be determined, before the construction activity commences and a suitable treatment of foundation soil must be carried out, if necessary.

A number of field and laboratory investigations (Kuwabara and Yoshmi, 1973: Yosufumi et.al., 1980; Yasushi and Taniguchi, 1982; Wang, 1984; Omaha Yamamoto, 1987) have been reported so far proposing various theoretical and practical aspects using gravel drains under surcharge load and the use of geotextiles (woven and nonwoven). Geotextiles are used fairly widely in surface and subsurface installations (Krishnaswamy and Issac, 1984). Crushed stone wrapped in geotextiles have often been used as surface and subsurface drains. Perforated plastic pipes too may be used for this purpose. They may be filled with crushed stones, if necessary. No large scale tests using GEOGRID have been reported to reduce the Liquefaction potential. Keeping this in view large scale tests have been performed on SHAKE TABLE on SOLANI SAND reinforced with GEOGRID.

This present study has been further extended to the use of gravel drains with both vertical filter drains and a horizontal blanket at top to study their behaviour in controlling the liquefaction of sand.

Development of Programme

The present investigations were carried out on vibration table, which can be excited in horizontal direction under steady state vibrations. The test tank of size 1.05 m x 0.60m x 0.60 was mounted on the shake table. Locally available SOLANI SAND (C_u = 1.7, C_c = 0.94, e_{max} = 0.835., e_{min} = 0.48, K = 9.34 x 10 m/s) has been used. The shake table is fed with sinusoidal vibrations. Soil sample was prepared by filling the sand under water by rainfall method. Tests have been performed at constant frequency of 4 cps. Tests were carried out on four types of saturated sand samples in following conditions:

(a) Tests without any reinforcement
(b) Tests with GEORID at a vertical spacing of 50 mm and 100 mm
(c) Tests with a horizontal blanket of gravel of 20 mm.
(d) Tests with vertical gravel drains of diameter (d) = 50mm, at varying spacing of 2.5d,3d and 4d. The range of acceleration chosen was 10%, 20%, 30% and 40%.

The initial relative density, D_n of 20% and height of sample was 420 mm was maintained in all the tests. Piezometers were used for measuring pore were pressure. These are installed at three different depths of 80 mm and 260 mm from the base of the tank, with the help of 20 mm diameter steel pipe which is projected through the side walls of the tank upto the centre.

Netlon geogrid CE-121, has been used for reinforcing the soil. It has a maximum load capacity of 7.68 kN/m. the mesh aperture size 80 mm x 6mm (diamond shaped) and the thickness of mesh being 3.3 mm.

Table 1 listed the different tests performed in this study

All the data are on presented in Table 2. Columns 4, 5 and 6 of this table represent the pore pressure values at depth of 160 mm, 230 mm and 240 mm respectively. In column no. 7, number of cycles required for pore pressure to reach the peak values are given. Number of cycles taken for the pore pressure to get completely dissipated are listed in Col. 8. Table 3 shows the values of pore pressure ratio r_u. i.e. the ratio of the value of pore pressure to the effective over burden pressure.

Interpretation

It can be observed from Table 2 that pore pressure increases with increase in acceleration, but the difference of absolute values decreases, as the values of acceleration increase. This has been observed in all types of tests

Table 1 – Tests Performed

S.No	Test Condition	Acceleration (% g)	No. of tests	Remarks
1.	Unreinforced soil	10,20,30,40	4	1. Frequency of vibrations was fixed as 4-cycles per sec.
2.	Reinforced soil at geogrid spacing = 100 mm	10,20,30,40	4	
3.	Reinforced soil at geogrid spacing = 50 mm	10,20,30,40	4	
4.	Soil sample with 2 mm horizontal gravel blanket at top surface	10,20,30,40	4	2. Initial relative density was maintained in all the tests
5.	Soil sample with 2 mm horizontal gravel blanket and vertical gravel drains at 2.5d spacing	10,30	2	
6.	Soil sample + Horizontal filter + vertical drains at 3d spacing	10,20,30,40	4	
7.	Soil sample + Horizontal filter + vertical drains at 4d spacing	10,30	2	
Total tests performed			24	

Table 2–Values of Dynamic Pore Water Pressure Developed Alongwith their Time for Dissipation, for Different Depths and Acceleration Values.

S.No	Type of set up	Acceleration (%g)	Dynamic Pore Water Pressure Rise Values u(N/m^2), at depth of 160mm	230 mm	340 mm	T_1(Cycles)	T_2 (Cycles)
(1)	(2)	(3)	(4)	(5)	(6)	(7)	(8)
1..	Unreinforced soil	10	1373.4	2109.2	3090.2	17	800
		20	1569.6	2354.5	3335.4	15	780
		30	1716.5	2501.5	3433.5	13	780
		40	1814.9	2600.0	3482.6	12	760
2(a)	Netlon Reinforced soil. Netlon spacing = 100 mm	10	1226.3	1962.0	2992.1	21	700
		20	1471.5	2158.2	3237.3	19	648
		30	1569.6	2256.3	3335.4	17	592
		40	1618.7	2305.3	3409.0	15	516
2(b)	Netlon Spacing = 50 mm	10	1177.2	1962.0	2943.0	23	735
		20	1373.4	2109.2	3237.3	22	635
		30	1471.5	2158.2	3335.4	21	565
		40	1417.5	2158.2	3384.5	19	510
3	Soil with Horizontal filter (20mm at top)	10	1128.2	1913.0	2746.8	18	760
		20	1373.4	2109.2	2943.0	16	684
		30	1471.5	2158.2	3041.1	15	610
		40	1520.6	2182.7	3065.6	15	556
4	Soil with Horizontal filter and vertical drains at						
	(a) 2.5d spacing	10	1079.1	1814.9	2697.8	12	488
		30	1373.4	2011.1	2943.0	14	442
	(b) 3d spacing Soil	10	931.9	1716.8	2560.0	10	360
		20	1128.2	1913.0	2869.4	10	308
		30	1226.3	1986.5	2992.1	11	280
		40	1275.3	2035.6	2992.1	12	180
	(c) 4d spacing	10	1030.1	1790.3	2771.3	12	472
		30	1373.4	2011.1	2943.0	14	416

i.e. whether the soil is unreinforced or reinforced with Geogrid or even if the drainage characteristic of the soil sample are improved by providing a Horizontal Gravel Filter and or a vertical gravel drain.

Since the piezometers are installed at fixed heights, the effective overburden pressure values for all the tests remains the same. hence the pore pressure ratio (r_u) values (Table 3) are directly dependent on the dynamic pore water pressure rise (u) values developed.

It can also be observed that the pore pressure attains its peak values, the rise being very rapid (in about) 10-25 cycles or 3-6 s from the onset of vibrations, depending upon the types of deposit-reinforced or not. The pore pressure remains constant for the next 2-3 s and thereafter starts dissipating. The dissipation being extremely rapid (about 10-12 secs.), if the vibration stops and varying from 455 to 180s in case the vibrations continue. This time reduces with the provision of reinforcement and increase in acceleration, due to the improved drainage conditions and soil deposit attaining a state of maximum value of dry density.

When the Geogrid is provided, the pore pressure (u) values and therefore pore pressure ratio (r_u) values, also decrease. The pore pressure takes longer time to rise to the maximum value, but the dissipation of pore pressure is little than for the unreinforced soil. The effect is not very pronounced, if we reduce the geogrid spacing from 100 m to 50 mm. Thus the liquefaction potential of a geogrid reinforced soil, is lower than that of an unreinforced one, but not safe against liquefaction.

When Horizontal Gravel filter (20mm) is provided at the top of soil sample, the pore pressure (u) values and pore pressure ratio (r_u) values, decrease, thereby reducing the liquefaction potential of the deposit. The time required for the generation and dissipation of the pore pressure also reduces.

Table 3 – Values of Pore Water Pressure Ratio (r_u) Calculated for Different Depths and Acceleration Values

S.No	Type of set up	Acceleration (%g)	Dynamic Pore Water Pressure Ratio (ru) at depths			Av. Values
			180 mm	230mm	340 mm	
(1)	(2)	(3)	(4)	(5)	(6)	(7)
1..	Unreinforced soil	10	0.91	0.97	0.96	0.95
		20	1.04	1.08	1.04	1.05
		30	1.13	1.15	1.07	1.12
		40	1.2	1.19	1.08	1.16
2(a)	Netlon Reinforced soil. Netlon spacing = 100 mm	10	0.81	0.9	0.93	0.88
		20	0.97	0.99	1.01	0.99
		30	1.04	1.04	1.04	1.04
		40	1.07	1.07	1.15	1.10
2(b)	Netlon Spacing = 50 mm	10	0.78	0.9	0.91	0.86
		20	0.91	0.97	1.01	0.96
		30	0.97	0.99	1.04	1.0
		40	0.97	0.99	1.05	1.0
3	Soil with Horizontal filter (20mm at top)	10	0.75	0.88	0.85	0.83
		20	0.91	0.97	0.91	0.93
		30	0.97	0.99	0.95	0.97
		40	1.01	1.01	0.95	0.99
4	Soil with Horizontal filter and vertical drains at					
	(a) 2.5d spacing	10	0.71	0.83	0.84	0.79
		30	0.91	0.92	0.91	0.91
	(b) 3d spacing	10	0.62	0.79	0.81	0.74
		20	0.75	0.88	0.89	0.84
		30	0.81	0.91	0.93	0.88
		40	0.84	0.93	0.95	0.91
	(c) 4d spacing	10	0.68	0.82	0.86	0.79
		30	0.91	0.92	0.91	0.91

If we place a Vertical Gravel Drain also alongwith a Horizontal filter, then the pore pressure rise (u) values are observed to be the least. The time required for pore pressure generation is reduced and the time for pore pressure dissipation is considerably reduced. The liquefaction potential of such a deposit also ramains subscritical i.e. the complete liquefaction never occurs and the soil is safe against liquefaction problem. As the vibrations continuing, even after the pore pressure values have reached their peak, the soil settles to a denser state, process of consolidation starts. The reason for pore pressure dissipation being slower is that, as the vibrations continue, soil settles and void ratio reduces and hence the permeability of soil reduces, thereby slowing down the pore pressure dissipation process. Out of the three vertical drain spacings provided, the one with the 3d spacing of drain grids gives the best results in comparison to 2.5d and 4d spacing of drains. The possible reason for this could be that at higher spacing, the permeability characteristics of the deposit reduce and the effect of gravel drains thereby lessened. But, at a low spacing, the interference effect due to the proximity of drains may be inhibiting the overall effectiveness of the system. Thus 3d spacing, of the gravel drains is the optimum spacing for a 50mm gravel drains.

The possible movements of structures are largely influenced by the time during which the soil is in the liquefied state. Since the pore pressure start dissipating almost immediately (2-3 S after attaining the peak values), the chances of the problem of larger movements of structures are less and the problem of liquefaction may not be that severe. However to stabilise a potentially liquefied sand deposit, the counter measures of providing Horizontal Gravel Filter and a Vertical Gravel Filter are effective for even a very high intensity of Earthquake and of large duration i.e. more than a minute. The increase in values of acceleration do not nullify the counter measures of reinforcing soil against liquefaction, although the absolute values of pore pressure rise (u) and hence the pore pressure ratio (r_u) values increase with increased accelerations.

The development and dissipation of pore pressure is much quicker when the grid of vertical drains are provided. The r_u values also drop from 1.1 to 0.7, but at higher acceleration values and higher depths the r_u values are still around 0.9, which is not a safe value to be considered from the liquefaction point of view. However, if a surcharge weight is also taken, then the values will fall drastically and the soil deposit be safe against liquefaction. Thus the combination of gravel drains and surcharge weight will surely be an effective liquefaction method.

Conclusions

1. The dynamic pore water pressure (u) and pore pressure ratio (r_u), increase with increase in acceleration. The rate of increase in pore water pressure, is higher at lower values of acceleration and vice-versa.

2. The pore pressures, reach the peak in 3-5 secs, remain at the peak for only 2-3 secs and thereafter start falling.

3. The pore pressures dissipate quickly, therefore chances of large movements in structures are less, for the type of sand used.

4. The rate of pore pressure dissipation, increases with increase in acceleration i.e. with increase in acceleration values, the pore pressure dissipation is faster.

5. The rate of pore pressure development is slower due to reinforcement provided in the soil sample.

6. The provision of Geogrid do not appear to be safe against liquefaction.

7. Provision of Horizontal Gravel Filter (20 mm at top) only, does not effectively control the complete liquefaction to occur, although the dissipation of pore pressure becomes faster.

8. Out of the three different spacings of vertical Gravel Drains provided, the one with a spacing equal to three times the diameter of the drain (50 mm), is the most effective, as in this case the pore pressure values attained are the least and the dissipation of pore water pressure, the quickest.

9. The arrangement of providing a Vertical Gravel Drain, at 3d spacing, alongwith a Horizontal Gravel Filter (20 mm), at the top of soil sample, is the most effective, for reducing the liquefaction potential of a deposit of sand.

References

1. Kawasumi, H. (1968), "General Report on Nilgata Earthquake of 1964", Tokyo Electrical Engg. College Press.

2. Kuwabara, F. and Yoshumi, Y. (1973), "Effect of Sub Surface Liquefaction on Strength of Surface Soil", ASCE, JGE, Vol.19, No.2, June 1973.

3. O-hara, S. and T. Yamaoto (1987), "Fundamental Study on Gravel Pile Method for Preventing Liquefaction", ECEE87, pp. 41-48.

4. Sead, H.B. (1968), "The Fourth Terzaghi Lecture "Landslides during Earthquake due to Liquefaction", J. Soil Mech. Found Divn., ASCE, Vol. 94, SM5, pp. 1053-1122.

5. Wang, S. (1984), "Experimental Study on Liquefaction Inhibiting Effect of Gravel Drains", Proc. VIII WCEE, California, Vol. I, pp. 207-214.

6. Yasushi, S. and Tanguchi, T. (1982), "Large Scale Shaking Table Tests on the Effectiveness of Gravel Drains", Earthquake Engg. Conference, Southampton, pp. 843-847.

7. Yosufumi, T., Kokusho, G. and Matsui (1984), "On Preventing Liquefaction of Level Ground Using Gravel Piles", Proc. JSCE, No. 352, pp. 89-98.

6 Slopes and embankments

This Page Intentionally Left Blank

Earthquake Geotechnical Engineering, Sêco e Pinto (ed.) © 1999 Balkema, Rotterdam, ISBN 90 5809 116 3

Seismic behaviour of dams subjected to earthquake induced hydro-dynamic forces

S.P.Gopal Madabhushi
Department of Engineering, University of Cambridge, UK

ABSTRACT: Dynamic behavior of large dams is of a major concern during and immediately after a major earthquake event. These dams will be subjected to large hydro-dynamic pressures on their upstream faces during the earthquake loading, in addition to the usual hydrostatic pressures. This paper concerns itself with the understanding of the generation of these hydro-dynamic pressures and their effects on the dynamic response of the dam. Dynamic centrifuge modeling involves testing reduced-scale physical models under the increased gravity field of a geotechnical centrifuge, so that prototype stresses are recreated in the model. Subjecting these scale models to lateral shaking, in-flight, i.e. while they are spinning around in the centrifuge simulates the earthquake loading. This technique is used in this study to investigate the effects of earthquake induced hydro-dynamic pressures on dams. The dynamic interaction effects between the dam and the impounded water in the reservoir are automatically accounted for, in this technique. In this paper, results from a series of dynamic centrifuge experiments carried out on model dams aboard the Cambridge University 10m beam centrifuge are presented. The dynamic response of the dam and the hydro-dynamic pressure data recorded in these experiments are presented. Comparison of the observed hydro-dynamic pressures and the hydro-dynamic pressures predicted by the conventional analytical solutions is presented.

1 INTRODUCTION

Safety of dams during and immediately after major earthquakes is always a significant concern. Large dams experience extensive stresses due to the lateral inertial forces induced by the earthquake shaking. In addition to this the impounded water induces large hydro-dynamic pressures over and above the usual hydrostatic pressures. In establishing the safety of such dams we need to estimate the magnitude of the hydro-dynamic pressures and understand the effect of these pressures on the overall response of the dam.

During the Los Angeles earthquake of 1971 and more recently in the Northridge earthquake of 1994, the Pacoima arch dam near Los Angeles suffered significant damage, Scott, (1994), Blakeborough, Daniel and Madabhushi (1994). Fortunately during both these earthquakes the impounded water level behind the dam was relatively low. However, seismic risk assessment of such structures requires us to predict the dynamic behavior of such dams under strong earthquakes, with full designed level of impounded water. This necessitates the estimation of hydro-dynamic pressures on the dam. In the conventional analyses of such dams, the hydro-dynamic pressures are estimated using analytical approaches similar to the one suggested by Westergaard. However, in using this approach the dynamic interaction of the dam structure and the impounded water is largely neglected.

In this paper, the results from a series of dynamic centrifuge tests on model dams subjected to earthquake loading will be presented. First, the technique of dynamic centrifuge modeling is introduced, briefly. Following this the experimental set up and the testing procedure are explained. Results from the typical experiments and the analysis of these results will be presented next. These experimental results are then compared to more conventional estimates like the Westergaard's method will be presented at the end.

2 DYNAMIC CENTRIFUGE MODELLING

Dynamic centrifuge modeling has established over the past decade as a powerful technique to study various soil-structure interaction problems. This technique involves testing reduced-scale physical models under the increased gravity field of a geotechnical centrifuge, so that prototype stresses are recreated in the model at homologous points. Prototype stresses are induced in the model when the gravity is increased by the same factor by which the geometry of the prototype is scaled down. Earthquake loading is simulated by subjected these scale models to lateral shaking, in-flight, i.e. while they are spinning around in the centrifuge. Schofield (1980, 81) derived a set of scaling laws which relate the behavior of the centrifuge model to the equivalent prototype. Some of the typical scaling laws are presented in Table 1.

Table 1 Scaling laws

Parameter	Ratio of model to prototype
Length	1/n
Area	$1/n^2$
Volume	$1/n^3$
Stress	1
Strain	1
Force	$1/n^2$
Velocity	1
Acceleration	n
Frequency	n
Time (dynamic)	1/n
Time (consolidation)	$1/n^2$

It is possible to use this technique to investigate the effects of earthquake induced hydro-dynamic pressures on dams. According to the scaling laws in Table 1, both the hydrostatic and the hydro-dynamic pressures on the dam will be the same as those on a prototype dam 'n' times larger than the model dam. The scaling factor 'n' in the dynamic centrifuge experiments will be in the range of 50 to 80 times the normal gravity (and consequently the model dams are $1/50^{th}$ or $1/80^{th}$ the size of the prototype dam. The dynamic interaction effects between the dam and the impounded water in the reservoir are automatically accounted for, when this technique is employed. In order to simulate the earthquake loading, the model container in the centrifuge is subjected to lateral shaking in-flight. This is explained next.

3 EARTHQUAKE LOADING

The lateral shaking of the model container while the centrifuge is in flight was achieved by using a mechanical actuator called the bumpy road system, Kutter (1982). A sinusoidal track is fixed to the centrifuge chamber wall. When the earthquake loading is required, a wheel on the end of the centrifuge is made to come into contact with the sinusoidal track using pneumatic valves. The radial movement of the wheel is converted to lateral movement of the package by means of a bell-crank mechanism. This actuator imparts 10 cycles of approximately sinusoidal base motion to the model container and has been widely used to test several centrifuge models at the Cambridge University Geotechnical Centrifuge Centre. The experiments were carried out using the Cambridge Equivalent Shear Beam (ESB) container, Schofield and Zeng, (1992), which has end walls which simulate the deformations of the soil during the earthquake. This prevents any reflection of stress waves from the end walls and simulates the length of the reservoir behind the dam wall.

The scaling laws dictate that the model earthquake has a frequency 'n' times greater than the prototype earthquake. Also the duration of the earthquake is '1/n' (see Table 1). The experiments reported in this paper were carried out at 50 g's. The bumpy road actuator produces an earthquake with a driving frequency of about 95 Hz for a duration of 160 ms. This event corresponds to a prototype earthquake of 1.9 Hz lasting for 8 seconds.

4 EXPERIMENTAL CONFIGURATION & TESTING PROCEDURE

Model dams were built from strong, pine wood for ease of construction, and were fixed rigidly to the base of the ESB model container. The Young's modulus of this material was determined experimentally as 9.45×10^6 kN/m^2 and the density of wood was taken as 5.29 kN/m^3. A typical section showing this configuration is presented in Fig.1.

In Fig.2 the location of the miniature accelerometers and the pressure transducers is shown schematically. During the earthquake the model container and hence the dam and the reservoir are subjected to lateral shaking in the plane of the paper. Three different model dams were tested in this series of experiments. However, only typical data are presented in this paper.

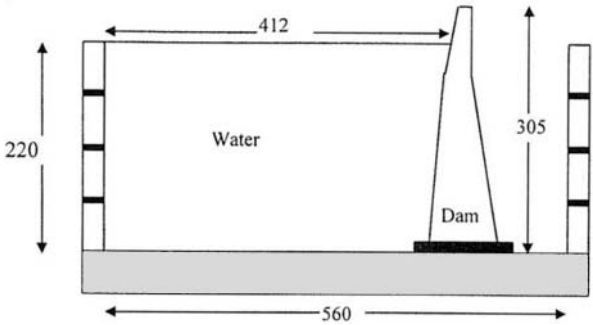

Figure 1 Configuration of the centrifuge tests

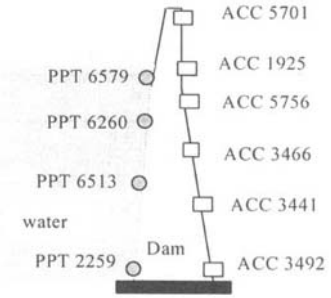

Figure 2 Schematic diagram showing the locations of the instruments

The test procedure adopted was as follows. The model dam was fixed to the ESB container and the centrifugal acceleration was increased to 50g's. Three to four earthquakes of increasing intensity were fired at this stage with reservoir empty. Data from the accelerometers shown in Fig.2 were recorded. This was used determine the dynamic response of the dam structure itself. Following this, the reservoir was filled up, by letting water flow through the fluid slip rings of the centrifuge and filling up the reservoir behind the dam. Once the reservoir was filled to the desired level, further earthquakes again of increasing intensity were fired. During these earthquakes, both the acceleration-time histories as well as the pressure-time histories from the PPT's (seen in Fig.2) were recorded.

5 CENTRIFUGE TEST DATA

The acceleration time histories and the hydro-dynamic pressure histories were recorded in all the earthquakes. For convenience, accelerations are expressed as a percentage of the centrifugal acceleration. The hydro-dynamic pressures are expressed in kPa.

5.1 Acceleration-time histories

In Fig.3 the acceleration-time histories recorded during earthquake 2 in centrifuge test PM-1 are presented. During this earthquake the reservoir was empty. In this figure we can see that the base accelerometer 3492 recorded a peak acceleration of about 31%. This corresponds to a prototype event with PGA of 0.3g. Looking at this figure we can see that the base acceleration recorded by ACC 3492 is amplified as the stress waves propagate upwards through the dam and subject the dam structure to bending stresses. ACC 3441 recorded a peak acceleration of 84.9 %, while ACC 3466 recorded a peak acceleration of 133.6%. This is further amplified at the location of ACC 1925 to 141 %. A peak acceleration of 158.9 % was recorded by ACC 5701 at the crest of the dam. ACC 5756 did not function well in this centrifuge test.

In Fig.4 the acceleration-time histories recorded during earthquake 8 are presented. During this earthquake the reservoir behind the dam was filled up in-flight using the fluid slip rings of the centrifuge. In this figure we can see that the base accelerometer 3492 recorded a peak acceleration of about 20.5%. This again corresponds to a prototype event with PGA of 0.21g. Looking at Fig. 4 we can see that the base acceleration is amplified more as stress waves travel up the dam compared to the reservoir empty case (comparing Figs.3 and 4). ACC 3441 recorded a peak acceleration of 60.1 %, while ACC 3466 recorded a peak acceleration of 115.9%. This is further amplified at the location of ACC 1925 to 112.9%. A peak acceleration of 158.2% was recorded by ACC 5701 at the crest of the dam.

Since the earthquake strengths were changed in each of the earthquake event, the amplification of accelerations is better understood by normalizing the accelerations at any given height in the dam with the acceleration recorded at the base of the dam. In Table 2 these normalized accelerations are presented for three earthquakes when the reservoir was empty and for three other earthquakes with full reservoir behind the dam. Comparing the amplifications in this table we may infer that the amplifications increase significantly when the reservoir behind the dam is full. The hydro-dynamic pressures acting on the dam wall have played an important role on the seismic behavior of the dam. It may also be observed that with the increase in the earthquake strength the amplifications reduce for both reservoir full and reservoir empty cases. In the next section, we shall look at these hydro-dynamic pressures.

5.2 Hydro-dynamic pressures on the dam

Fluid pressures were recorded in each earthquake when the reservoir was full using miniature pressure transducers (PPT's) at four levels (see Fig.2). It must be pointed out that the hydro-dynamic pressures discussed in this section are over and above the hydrostatic fluid pressures. The scaling laws in Table 1 dictate that the fluid pressures felt

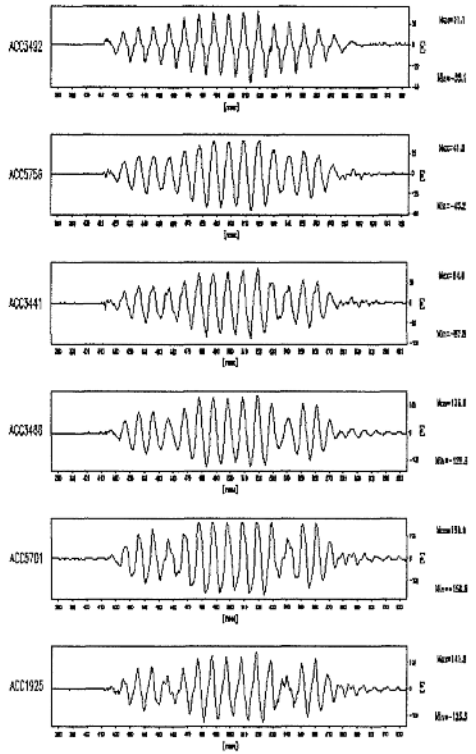

Figure 3 Acceleration-time histories during earthquake 2 in the centrifuge test PM-1 (reservoir behind the dam was empty in this event)

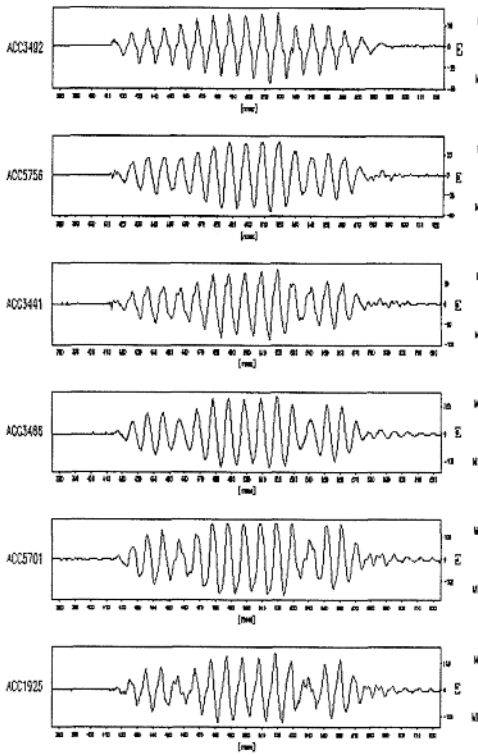

Figure 4. Acceleration-time histories during earthquake 8 in the centrifuge test PM-1 (reservoir behind the dam was full in this event)

Table 2 Amplification of accelerations in the dam during various earthquakes

Instrument	Ratio of peak acceleration at instrument level to the peak acceleration at the base of the dam					
	EQ –1	EQ-2	EQ-3	EQ-7	EQ-8	EQ-9
	(reservoir empty in these earthquakes)			(reservoir full in these earthquakes)		
ACC 5701	5.65	5.11	4.00	9.82	7.72	7.24
ACC 1925	4.01	4.53	3.67	6.60	5.51	5.29
ACC 3466	3.84	4.30	3.58	7.54	5.65	5.22
ACC 3441	2.17	2.73	2.49	4.40	2.93	2.93

behind the model dam will be the same as those felt by a prototype 'n' times larger than the model dam.

In Fig.5 the hydro-dynamic pressures recorded during earthquake 8 are presented. From this figure we can see that the shape of the hydro-dynamic pressure traces closely emulates the input earthquake shape. The peak hydro-dynamic pressures observed tend to increase from the base to the crest, which is consistent with the acceleration amplifications seen in the Sec.5.1. For example, referring to Fig.5, the peak hydro-dynamic pressure at the base of the dam was recorded by PPT 2259 as 14.6 kPa. This increases to a peak hydro-dynamic pressure of about 17.4 kPa recorded by PPT 6579. Larger peak hydro-dynamic pressure of 19.2 kPa was recorded by PPT 6260. We can estimate the hydro-dynamic force on the dam using an average hydro-dynamic

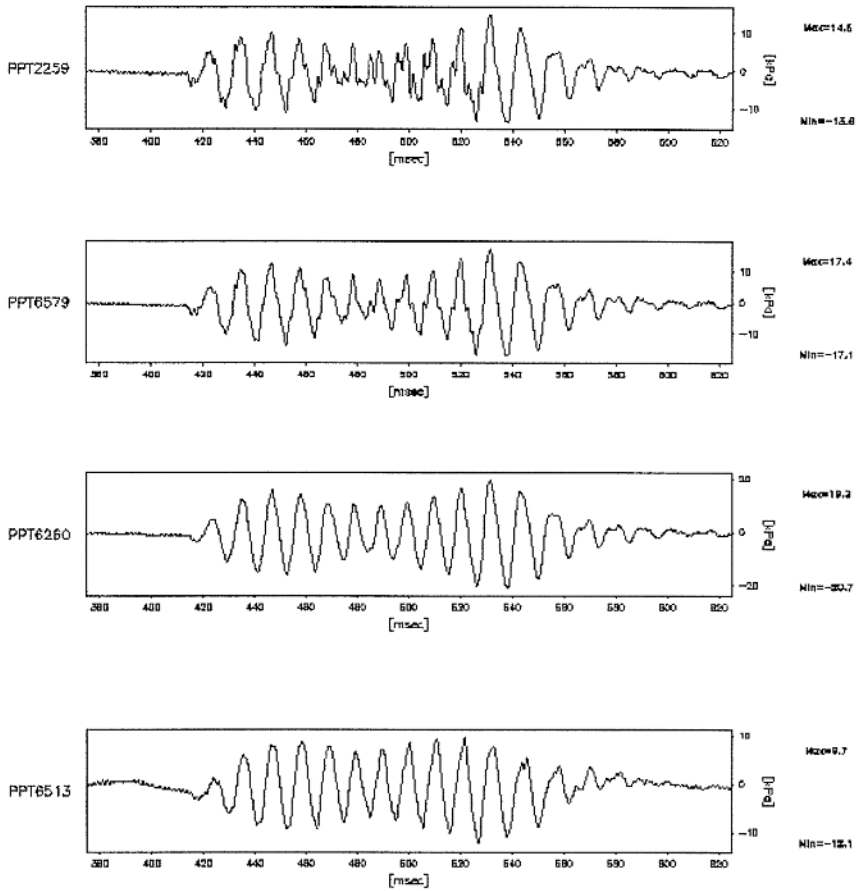

Figure 5 Hydro-dynamic pressures behind the dam during earthquake 2 in centrifuge test PM-1

pressure recorded by all the four PPT's as a first estimate. Noting that the scaling factor for force in Table 1 is n^2, we can calculate the hydro-dynamic force that would be felt by the prototype dam to be 8.37 MN/m run of the dam in this 0.21g event. The hydro-dynamic pressures recorded in all the earthquake events and the corresponding hydro-dynamic forces are presented in Table 3.

6 CALCULATED HYDRO-DYNAMIC FORCES

Westergaard (1933) suggested the following equation to estimate hydro-dynamic pressures on upstream face of dams during earthquakes, assuming that the body of the dam to be a rigid body;

$$p_h = 0.74\, k_c\, \gamma_o\, h \qquad \ldots (1)$$

where, k_c is the seismic co-efficient (ratio of peak ground acceleration to earth's gravity), h is the height of water at the point where the hydro-dynamic pressure is being computed and γ_o is the density of water. Using Eq.1 we can estimate the hydro-dynamic pressures and the hydro-dynamic force acting on the dam during any earthquake event.

In Table 4, the calculated hydro-dynamic pressures and estimated hydro-dynamic forces are presented. It must be noted that these calculations were carried out at the location where instruments were present in the centrifuge test. Comparing Tables 3 and 4, we can see that the Westergaard's approach is yielding lower hydro-dynamic forces in all cases. The reason for this is that Eq.1 is based on the approximation of the dam wall being rigid. However, based on the amplifications observed in Sec.5.1, we can see that the dam wall was not behaving as a rigid body, with significant amplifications in all earthquakes. Hence, the experimentally observed hydro-dynamic pressures and forces are larger than those estimated using Westergaard's approach.

Table 3 Hydro-dynamic forces in all the earthquake events

Event →	EQ4	EQ5	EQ6	EQ7	EQ8
ACC 3492	0.3g	0.4g	0.51g	0.083g	0.205g
PPT 2259 (kPa)	28.2	29.3	26.1	8.7	14.6
PPT 6513 (kPa)	18.5	22.3	22.8	7.1	9.7
PPT 6260 (kPa)	24.1	42.9	44.2	12.4	19.2
PPT 6579 (kPa)	32.4	37.4	34.3	11.6	17.4
Hydro-dynamic force (MN/m)	14.19	18.14	17.52	5.47	8.37

Table 4 Estimated Hydro-dynamic forces using Westergaard's approach

Event →	EQ4	EQ5	EQ6	EQ7	EQ8
ACC 3492	0.3g	0.4g	0.51g	0.083g	0.205g
PPT 2259 (kPa)	22.20	29.60	37.74	6.14	15.17
PPT 6513 (kPa)	12.77	17.02	21.70	3.53	8.72
PPT 6260 (kPa)	6.11	8.14	10.38	1.69	4.17
PPT 6579 (kPa)	2.22	2.96	3.77	0.61	1.52
Hydro-dynamic force (MN/m)	5.95	7.94	10.12	1.65	4.07

7 CONCLUSIONS

Hydro-dynamic pressures behind the dam wall need to be investigated in order to establish the seismic safety of large dams. Dynamic centrifuge experiments were carried out to study the generation of hydro-dynamic pressures. The interaction between the dam wall and the reservoir are automatically accounted for in this technique. Earthquakes were fired on model dams firstly, when the reservoir was empty and later when the reservoir was full. Based on the recorded acceleration traces, it was seen that the amplification of the ground motion in the dam was much higher when the reservoir was full compared to when the reservoir was empty. The recorded hydro-dynamic pressures closely followed the shape of the input motion. Based on the peak hydro-dynamic pressures observed in the experiment, the hydro-dynamic forces on an equivalent prototype structure were estimated. These values were compared to the calculations made by more traditional approach suggested by Westergaard. The comparison of the hydro-dynamic forces obtained by both these techniques seem to suggest that the Westergaard approach is under predicting the hydro-dynamic force that may be experienced by the dam during an earthquake event.

REFERENCES

Blakeborough, A., Daniel, W. and Madabhushi, S.P.G., (1994), Safety of Dams during the Northridge Earthquake, Earthquake Engineering Field Investigation Team (EEFIT) Report, Institute of Structural Engineers, London, UK.

Schofield, A.N.,(1980), Cambridge geotechnical centrifuge operations, Geotechnique, Vol.25., No.4, pp 743-761.

Schofield, A.N.,(1981), Dynamic and Earthquake geotechnical centrifuge modelling, Proc. Recent advances in Geotech. Earthquake Eng. Soil dynamics and earthquake eng., Univ. of Missouri-Rolla, Rolla.

Scott, R.F., (1994), Geotechnical Aspects of the Northridge Earthquake, EERI Report, California Institute of Technology, Pasedena, USA.

Shul'man, S.G., (1987), Seismic pressure of water on hydraulic structures, Russian Translations series, Balkema, Rotterdam.

Westergaard, H.M., (1931), Water pressures on Dams during earthquakes, Proc. ASCE, Vol.59, Trans.No.98.

Earthquake Geotechnical Engineering, Sêco e Pinto (ed.) © 1999 Balkema, Rotterdam, ISBN 90 5809 116 3

Two dimensional seismic response of solid-waste landfills

E. M. Rathje
University of Texas, Austin, Tex., USA

J. D. Bray
University of California, Berkeley, Calif., USA

ABSTRACT: Results from two dimensional finite element analyses are used to evaluate the reliability of one dimensional analyses to provide conservative estimates of seismic loading for base and cover liner systems of solid-waste landfills. The variation of seismic loading with normalized cover slope length is presented, and recommendations are made with respect to the use of one and two dimensional analyses to estimate the seismic loading for landfill systems.

INTRODUCTION

One dimensional (1D) seismic response programs are commonly used to analyze the response of municipal solid-waste landfills (MSWLFs) during earthquakes. Due to the commonly large aerial extent of MSWLFs and their propensity to have relatively shallow side slopes, engineers often assume that 1D analyses can capture the key response characteristics of what is truly a three dimensional (3D) problem. However, it remains questionable whether 1D analyses can calculate accurately the response of waste fills near the surface of these structures.

A major design concern for MSWLFs is the stability of the cover system. Geosynthetic interfaces within the cover have relatively low strengths due to the low confining stresses that act normal to these interfaces, suggesting that the performance of the cover system is an important consideration in the design of a MSWLF. The seismic loading for the cover system is closely represented by the acceleration-time history developed near the surface of the landfill. Therefore, the adequacy of 1D analysis to predict accurately the acceleration-time history along the slope and top deck of the landfill is investigated.

PREVIOUS WORK

A comparison of the maximum dynamic shear stresses calculated by 1D and 2D analyses was reported by Vrymoed & Calzascia (1978). The shear stresses through the upstream, crest, and downstream sections of nine earth dams were calculated with the equivalent-linear viscoelastic computer programs QUAD-4 (Idriss et al. 1973) and SHAKE (Schnabel et al. 1972). Many of these dam cross sections are similar to 2D MSWLF configurations. The maximum shear stresses calculated by the two programs agreed favorably for the sections analyzed. The authors concluded from this study that: "the simplified technique (i.e. SHAKE) can be used to adequately determine the dynamic stresses in an earth dam during earthquake loading." Elton et al. (1991) used FLUSH (Lysmer et al. 1975) and SHAKE to calculate the dynamic stresses within a triangular embankment. While a triangular embankment does not resemble common landfill configurations, useful observations can be gained from this investigation. The two programs predicted similar shear stresses at depths greater than 10 m, but 2D analysis calculated larger stresses near the surface. However, the absolute numerical difference between the shear stresses near the surface was relatively small. Bray et al. (1996) presented results from the analysis of a typical landfill cross section with QUAD4M (Hudson et al. 1994) and SHAKE91 (Idriss & Sun 1992). Again, the 1D analysis provided reasonable estimates of the maximum dynamic shear stresses at depth calculated by 2D analysis. However, the authors emphasized that the use of 1D analysis to study MSWLF cover system performance should be studied further.

Sitar & Clough (1983) performed linear viscoelastic and equivalent-linear viscoelastic analyses on steep slopes (i.e. slope angles greater than 70°) using FLUSH. The results showed amplification of acceleration near the slope face, but the crest accelerations were only slightly larger than those in the free-field behind the crest. Therefore,

the authors concluded that topographic amplification is small compared to free-field site amplification. Ashford et al. (1997) studied the seismic response of steep (i.e. greater than 60°) and shallow slopes using the generalized hyperelement method (Deng 1991). The authors reported that, on average, the acceleration at the crest of a steep slope is amplified by 50% over the free-field acceleration behind the crest, and concluded that even for steep slopes: "site amplification has a greater effect than topographic amplification."

ANALYTICAL PROCEDURES

QUAD4M Program

The 2D dynamic analysis program QUAD4M was used to analyze the response of several typical landfill configurations. QUAD4M uses the finite element formulation to solve the dynamic equations of equilibrium in the time domain and includes a compliant base. Similar to SHAKE91, the earth materials are modeled as equivalent-linear viscoelastic. QUAD4M includes the capability of calculating the seismic coefficient, k_{max}, for 2D sliding surfaces with the procedure outlined by Chopra (1967). This procedure involves using the shear and normal stresses along the sliding surface to calculate the force on the sliding mass, and dividing this force by the weight of the sliding mass to calculate k_{max}. However, the k_{max} calculation in QUAD4M has been found reliable for only deeper sliding surfaces. Hence, for cover sliding, the acceleration-time histories were calculated by QUAD4M along the top of the landfill and averaged through a mass-weighted averaging scheme in the time domain to evaluate the maximum horizontal equivalent acceleration (MHEA).

Landfill Configurations

Four baseline landfill configurations, shown in Figure 1, were used in this study. Configurations 1 and 2 represent above-ground/below-ground waste fills, with a slope height of 30 m (a total height of 45 m) and side slopes of 3H:1V and 2H:1V, respectively. Configurations 3 and 4 represent side-hill fill landfills. Configuration 3 is 60 m in height with a 2H:1V side slope. Configuration 4 has a more gentle slope than Configuration 3 (5H:1V) and a height of 45 m. In addition, five configurations from landfills in the Los Angeles area (Operating Industries, Inc. (OII), Lopez Canyon and Chiquita Canyon landfills), shaken by the 1994 Northridge earthquake, were analyzed as part of this study (Augello et al. 1995). Cross section HH of the OII landfill is similar to Configuration 1, cross sections AA and CC of the Lopez Canyon landfill resemble

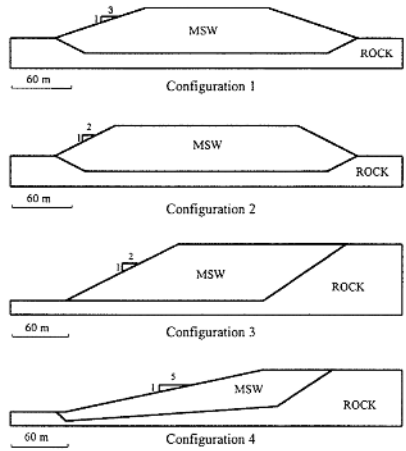

Figure 1. Landfill Configurations Used in this Study.

the side-hill fill geometry of Configuration 3, and cross sections CC and DD of the Chiquita Canyon landfill are comparable to Configuration 4 because of their gentle slope angles.

The shear wave velocity profile used for municipal solid waste (MSW) in this study is based on the range presented in Kavazanjian et al. (1996). Based on Augello et al. (1998), shear modulus reduction and damping curves for a soil with PI = 30 (Vucetic & Dobry 1991) were used to describe the dynamic material properties of MSW. The foundation bedrock (V_s=900 m/s) is overlain by 6 m of weathered rock (V_s=450-750 m/s), and a half space is incorporated below the model (V_s=1200 m/s). The base and cover liner systems have shear wave velocities of 240 m/s and 450 m/s, respectively, and use the shear modulus reduction and damping curves for a PI=15 clay (Vucetic & Dobry 1991). A Poisson's ratio of 0.3 was used for all materials.

Several outcropping rock motions were chosen for use as input for the dynamic analyses. These motions include two recordings from the 1989 M_w=6.9 Loma Prieta earthquake, two recordings from the 1994 M_w=6.7 Northridge earthquake, and two synthetic records for M_w 7 and 8 events. These motions are listed in Table 1.

RESULTS

Seismic Coefficients for Deep Sliding

Previous studies (e.g. Vrymoed & Calzascia 1978, Elton et al. 1991, Bray et al. 1996) indicate that 1D analysis generally predicts larger stresses,

Table 1. Input Motions Used in this Study.

Record	MHA (g)	T_m (s)	D_{5-95} (s)
Lick Observatory	0.45	0.28	9.5
Gilroy#1 090	0.47	0.47	3.7
Pacoima Dam Dnstrm	0.42	0.47	4.3
Topanga Canyon	0.36	0.32	8.7
Synthetic 1	0.36	0.49	9.0
Synthetic 2	0.30	0.45	34.5

MHA = maximum horizontal acceleration
T_m = mean period (Rathje et al. 1998)
D_{5-95} = significant duration (Dobry et al. 1978)

particularly at depth, than 2D analysis for earth dams and landfills. Hence, 1D analysis should also calculate conservative values of the seismic coefficient (k_{max}) for deep sliding, because k_{max} represents the maximum dynamic shear stresses along the sliding surface. Figure 2 shows the ratio of k_{max} calculated by 1D and 2D analyses (i.e. $k_{max,1D}/k_{max,2D}$) for the four baseline landfill configurations and the Los Angeles landfills, along with the median value for each configuration. The 2D values of k_{max} were calculated by QUAD4M. The 1D values of k_{max} were evaluated by calculating k_{max} at the elevation of the base of the waste for several 1D columns within the sliding mass and weighting these values by the percentage of the sliding mass upon which they act. This procedure necessarily assumes that these values of k_{max} occur at the same time, which is a generally conservative assumption.

For each landfill configuration, the 1D analysis typically calculates larger values of k_{max} (i.e. $k_{max,1D}/k_{max,2D} > 1.0$), with Configuration 4 producing the most conservative results. Data points that fall below one are generally for shallower sliding surfaces (i.e. within 7.5 m of the surface), where the 2D shear stresses may be slightly larger than those predicted by 1D analysis. However, the results indicate that, in general, the maximum seismic loading for base sliding within a landfill can be estimated conservatively with 1D analysis.

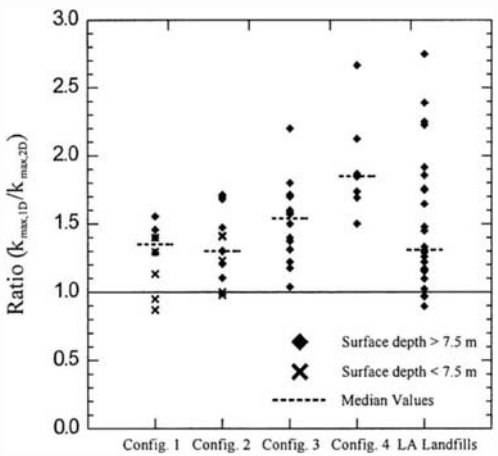

Figure 2. Comparison of k_{max} for Deep Sliding Calculated by 1D and 2D Analyses.

Surface Accelerations from 1D and 2D Analyses

The maximum horizontal accelerations (MHA) calculated by QUAD4M at the surface of Configurations 1 and 4 are found in Figure 3, along with the surface MHAs calculated from several 1D columns through the landfill. The Gilroy#1 090 motion was used as the input rock motion for the results shown.

Figure 3 shows that 1D analyses do not always capture the acceleration distribution along the waste fill surface adequately. For Configuration 1 (Figure 3(a)), 2D analytical results indicate zones of relatively higher MHA values along the slope and at the crest of the landfill. The details of the calculated

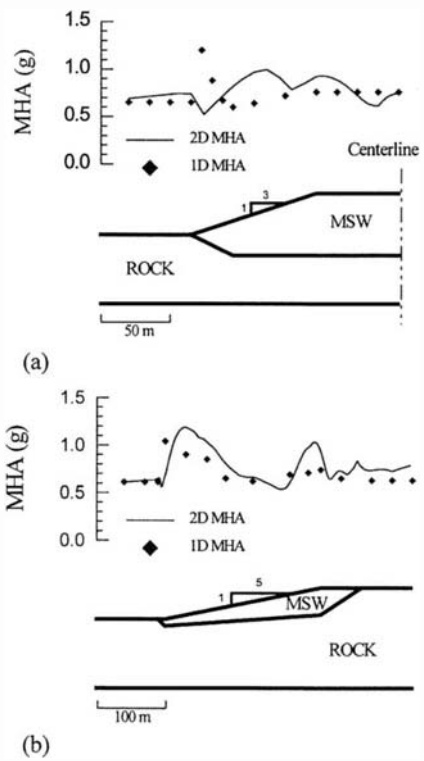

Figure 3. 1D and 2D MHAs Along the Surface of (a) Configuration 1 and (b) Configuration 4 Using the Gilroy#1 090 Input Rock Motion.

2D response are not captured well by the 1D analyses, although the average magnitudes of the calculated 1D MHAs are roughly of the same order of magnitude as the 2D values. Figure 3(a) reveals that the 1D analyses tend to calculate larger MHA values only for shallow columns of MSW near the toe, where "resonance" occurs between the soil column and input rock motion. However, the 2D MHAs near the toe tend to be significantly smaller, which agrees with previous researchers who observed deamplification of acceleration near the toe of slopes (Idriss & Seed 1967). The 1D analysis does not capture the larger MHA values calculated by 2D analysis at the crest of the landfill slope face. Generally, 1D analysis agrees best with 2D analysis along the top deck, further from the crest of the slope. However, landfills with narrow top decks can experience topographic effects along the entire deck of the landfill, as topographic amplification due to the slope has been calculated up to 1 to 2 slope heights back from the crest (Sitar & Clough 1983). Other above-ground/below-ground waste fill configurations showed similar results.

Results from the 2D analysis of Configuration 4 (Figure 3(b)), which has a moderately shallow slope angle, show relatively large MHA values along the landfill slope compared with those calculated at the crest. The zone of larger 1D MHAs near the toe for Configuration 4 coincides with the area of larger MHAs from the 2D analysis, suggesting that 1D resonance is the source of amplification in this area. Other side-hill fill landfill configurations showed similar results.

The influence of the shear modulus reduction and damping curves used to represent the strain-dependent material properties of MSW on the seismic response of Configuration 3 is shown in Figure 4. This figure compares the 1D and 2D MHAs calculated using the shear modulus reduction and damping curves for PI=30 clay and PI=0 clay (Vucetic & Dobry 1991). The 1D and 2D MHAs computed along the surface of the landfill using the PI=0 curves are significantly smaller than those computed with the PI=30 curves, which emphasizes the relative importance of waste fill characterization. Although the modulus reduction and damping curves affect the calculated response significantly, the comparisons between 1D and 2D MHAs are still valid. The 2D results remain underpredicted along the slope and near the crest, while 1D and 2D results compare favorably along the landfill top deck. Additionally, the results for PI=30 curves in Figure 4 reveal that the topography of the base rock can increase the MHAs along the deck of the landfill, and base rock topography cannot be explicitly accounted for using 1D analysis.

A summary of the results from 1D and 2D analyses is found in Figure 5. The ratio of 1D to 2D results is reported for MHAs calculated along the slope (i.e. along the bottom quarter of the slope, close to the toe), near the crest, and along the deck. For MHAs along the slope, on average, the 1D and 2D results roughly agree ($1D/2D_{median}$=0.91), but there are many ratios that indicate that the 1D MHA may be unconservative. Most of the data points that fall below 0.7 correspond to Configuration 4, where significant amplification occurs near the toe and results in the unconservative 1D values of MHA. 1D analysis generally provides unconservative estimates of MHA at the crest ($1D/2D_{median}$=0.81) due to topographic amplification near the crest of the slope. All of the landfill configurations predict some ratios of 1D/2D less than one for the crest; however, the majority of the crest data that falls below a value

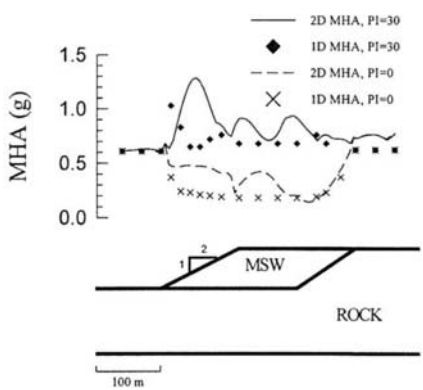

Figure 4. 1D and 2D Surface MHAs Calculated for Configuration 3 Using Vucetic & Dobry (1991) PI=30 and PI=0 Modulus Reduction and Damping Curves for MSW.

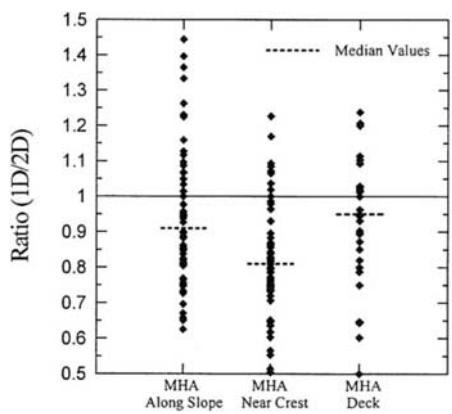

Figure 5. Comparison of MHAs Calculated by 1D and 2D Analyses.

of 0.7 represents Configuration 3 where base rock topography may be a factor. Surprisingly, conservative 1D values of MHA along the deck of a landfill cannot be guaranteed ($1D/2D_{median}$=0.95). Again, Configuration 3 contributes most of the data below 0.7, due to the 2D amplification along the deck attributed to the base rock topography. However, for landfills with wide top decks, 1D analysis should provide an MHA appropriate for the analysis of cover stability.

Cover Averaging

Commonly, the seismic loading for a cover system is estimated as the MHA at the surface of the landfill calculated from a 1D analysis. However, this acceleration acts at only one point along the potential sliding mass within the cover. The previous section has demonstrated that the accelerations along a slope vary, and thus, the seismic loading on the cover should vary with the length of the potential sliding mass. The incoherence of the waves results in parts of the slope experiencing an acceleration in one direction, while other parts of the slope are accelerating in the opposite direction. This incoherence is a result of typical spatial incoherence of ground motions and a systematic wave passage effect as the predominantly vertically propagating horizontal shear waves travel up the landfill slope.

The reduction in the normalized maximum equivalent acceleration ($MHEA/MHA_{crest}$) with normalized slope cover sliding mass length (L/L_s, where L = length of sliding mass and L_s = entire length of slope) for the baseline and Los Angeles landfill configurations subjected to the input motions listed in Table 1 is shown in Figure 6. More sophisticated normalizations that account for the full length of the slope cover and the predominant earthquake wavelength were attempted, but did not significantly reduce the scatter in the data. Figure 6 reveals that slightly less averaging occurs for shallow slopes, as evidenced by the data points from Configuration 4, with a slope of 5H:1V. A linear regression of the data is included in Figure 6 and indicates that, on average, the MHEA for the full slope cover is only about 40% of the crest MHA. Therefore, as a potential sliding mass along the cover increases in length, the MHEA decreases due to the incoherence of the waves along the slope. Hence, although 1D analysis may underpredict the MHA at the crest of a landfill, it may provide a conservative estimate of the MHEA for the full cover, because it does not account for the averaging of accelerations along the cover slope.

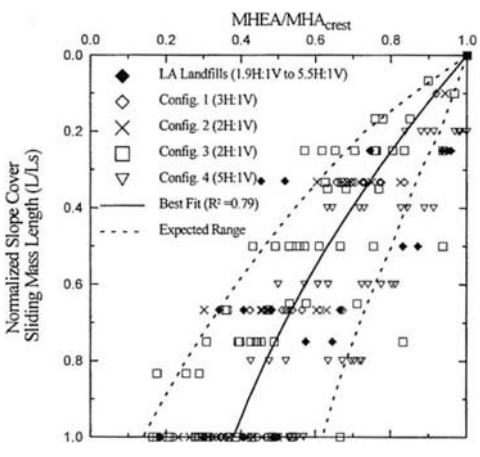

Figure 6. Variation of Normalized Cover MHEA with Normalized Slope Cover Sliding Mass Length.

FINDINGS

Because of the relative simplicity, availability, and perceived reliability of 1D analysis techniques, 1D analysis is often employed to evaluate the seismic reponse of 2D sections within solid-waste landfills. The results from this study reveal that 1D analysis provides generally conservative estimates of k_{max} for deep sliding surfaces, such as those along the base liner system. However, the results from this study indicate that 1D analysis underpredicts the surface MHAs along the slope of a landfill by 10%, on average, and by as much as 40%. At the crest, 1D analysis consistently underpredicts the MHA, such that $MHA_{crest} \approx (1/0.81)MHA_{1D} = (1.25)MHA_{1D}$. Along the deck, the 1D analysis is only moderately unconservative. The accelerations along the deck can be affected by base rock topography, and this effect is not captured with 1D analysis. The shear modulus reduction and damping curves used to represent the strain-dependent properties of MSW also affect the MHAs calculated along the surface of a landfill significantly, which re-emphisizes the relative importance of dynamic material property characterization.

The incoherence of waves along the slope of a landfill reduces the magnitude of the equivalent accelerations for cover systems. As a larger percentage of the slope cover is considered in the evaluation of the MHEA, the accelerations along the slope tend to partially cancel each other out and result in smaller values of MHEA. When the full cover is considered, the MHEA is generally less than 50% of MHA_{crest}. Therefore, a smaller sliding surface along the cover system may control cover design, even if this surface is not the most critical in terms of yield acceleration, due to less averaging over the shorter cover sliding mass distance.

However, for the analysis of full cover sliding, 1D analysis may provide a conservative estimate of MHEA, because it does not capture the cover averaging effect. For full cover sliding, one could use MHEA = (0.5)MHA_{crest} = (0.5)(1.25)MHA_{1D} = 0.65 MHA_{1D}.

While this comparison of 1D and 2D analyses has provided insights into the use of 1D analysis to model 2D structures, this study has focused solely on the seismic loading in terms of equivalent accelerations for base and cover liner systems. Generally, when assessing the likely seismic performance of a solid-waste landfill, the earthquake-induced displacements for base and cover liner sliding are calculated. Hence, the suitability of using 1D analysis to model the 2D geometry of a landfill should also be studied through a comparison of the seismically induced displacements calculated from the results of each calculational procedure.

ACKNOWLEDGEMENTS

Financial support was provided by the David and Lucile Packard Foundation and the National Science Foundation (BCS-9157083). This support is gratefully acknowledged.

REFERENCES

Ashford, S., Sitar, N., Lysmer, J., & Deng, N. (1997) "Topographic Effects on the Seismic Response of Steep Slopes", Bull. of the Seism. Soc. of Amer., 87(3), pp. 701-709.

Augello, A., Matasovic, N., Bray, J., Kavazanjian, E., & Seed, R. (1995) "Evaluation of Solid-Waste Landfill Performance During the Northridge Earthquake", Earthquake Design and Perf. of Solid Waste Landfills, ASCE Specialty Pub. 54, M. Yegian and W. Finn, eds., pp. 17-50.

Augello, A., Bray, J., Abrahamson, N., & Seed, R. (1998) "Dynamic Properties of Solid Waste based on Back-Analysis of the OII Landfill", J. of Geotech. Eng., ASCE, 124(3), pp. 211-222.

Bray, J., Augello, A., Leonards, G., Repetto, P., & Byrne, R. (1996) "Seismic Stability Procedures for Solid-Waste Landfills-Closure", J. of Geotech. Eng., ASCE, 122(11), pp. 952-954.

Chopra, A. (1967) "Earthquake Response of Earth Dams", J. of the Soil Mech. and Foun. Eng. Div., ASCE, 93(SM2), pp. 65-81.

Deng, N. (1991) "Two Dimensional Site Response Analyses", Ph.D. Dissertation, Univ. of Cal., Berkeley, CA.

Dobry, R., Idriss, I., & Ng, E. (1978) "Duration Characteristics of Horizontal Components of Strong-Motion Earthquake Records", Bull. of the Seism. Soc. of Amer., 68(5), pp. 1487-1520.

Elton, D., Shie, C., & Hadj-Hamou, T. (1991) "One- and Two-Dimensional Analysis of Earth Dams", Proc., 2nd Int. Conf. on Recent Adv. in Geotech. Earthquake Eng. and Soil Dyn., St. Louis, MO, pp. 1043-1049.

Hudson, M., Idriss, I., & Beikae, M. (1994) "QUAD4M- A Computer Program to Evaluate the Seismic Response of Soil Structures using Finite Element Procedures and Incorporating a Compliant Base", Center for Geotech. Modeling, Univ. of Cal., Davis, CA.

Idriss, I. & Seed, H. (1967) "Response of Earth Banks during Earthquakes", J. of the Soil Mech. and Foun. Eng. Div., ASCE, 93(SM3), pp. 61-82.

Idriss, I., Lysmer, J., Hwang, R., & Seed, H. (1973) "QUAD-4 – A Computer Program for Evaluating the Seismic Response of Soil Structures by Variable Damping Finite Element Procedures", EERC 73-16, Univ. of Cal., Berkeley, CA.

Idriss, I. & Sun, J. (1992) " User's Manual for SHAKE91", Center for Geotech. Modeling, Univ. of Cal., Davis, CA.

Kavazanjian, E., Matasovic, N., Stokoe, K., & Bray, J. (1996) "In Situ Shear Wave Velocity of Solid Waste from Surface Wave Measurements", Proc., 2nd Int. Conf. on Envir. Geotechnics, Osaka, Japan, pp. 97-102.

Lysmer, J., Udaka, T., Tsai, C., & Seed, H. (1975) "FLUSH- A Computer Program for Approximate 3D Analysis of Soil-Structure Interaction Problems", EERC 75-30, Univ. of Cal., Berkeley, CA.

Rathje, E., Abrahamson, N., & Bray, J. (1998) "Simplified Frequency Content Estimates of Earthquake Ground Motions", J. of Geotech. Eng., ASCE, 124(2), pp. 150-159.

Schnabel, P., Lysmer, J., & Seed, H. (1972) "SHAKE- A Computer Program for Earthquake Response Analysis of Horizontally Layered Sites", EERC 72-12, Univ. of Cal., Berkeley, CA.

Sitar, N. & Clough, G. (1983) "Seismic Response of Steep Slopes in Cemented Soils", J. of Geotech. Engrg., ASCE, 109(2), pp. 210-227.

Vucetic, M. & Dobry, R. (1991) "Effect of Soil Plasticity on Cyclic Response", J. of Geotech. Eng., ASCE, 117(1), pp. 89-107.

Vrymoed, J. & Calzascia, E. (1978) "Simplified Determination of Dynamic Stresses in Earth Dams", Proc., Earthquake Eng. and Soil Dyn. Conf., ASCE, pp. 991-1006.

Earthquake Geotechnical Engineering, Sêco e Pinto (ed.) © 1999 Balkema, Rotterdam, ISBN 90 5809 116 3

Seismic behaviour of solid waste Grândola landfill

P.Sêco e Pinto & A.Vieira
National Laboratory of Civil Engineering (LNEC), Lisboa, Portugal

A. Mendonça
Soares da Costa, S.A., Portugal

L. Lopes
Faculty of Engineering, University of Oporto, Portugal

ABSTRACT: In this paper an analysis of Grândola landfill located in zone A of Portugal seismic risk map is presented. The geotechnical characterization of the foundations and the geotechnical characteristics of waste materials are described.

The results of the stability analysis and the amplification analysis performed for Grândola landfill are discussed.

1 INTRODUCTION

For the analysis of seismic behavior of solid waste Grândola landfill both pseudo-static and deformational methods were used. For the geotechnical characteristics of foundation boreholes and identification tests were performed. The waste materials properties were based on density tests, dynamic penetrometer tests and shear wave velocities.

Also for the seismic response of Grândola landfill a 1D code, assuming an equivalent linear behaviour for the material, was used.

2 ANALYSIS OF GRÂNDOLA LANDFILL

2.1 Description of the landfill

The Grândola landfill is located in the south zone of Portugal map. This landfill comprises a mixture of domestic trash, construction demolition debris and other wastes.

The landfill has a maximum height of 12m and an inclination of 2.5(H):1(V). The deck is at level 83.5m and the volume of landfill is 664 000 m3.

The cover system comprises a mineral barrier with 1.50 m of thickness and a topsoil material with 0.20 m.

The bottom lining system consists of a drainage layer with 0.40 m of thickness, a geotextile (200g/m) a HDPE geomembrane (1.5mm), another geotextile (200 g/m^2) and clay material with 0.10 m thickness.

The layout of the Grândola landfill is shown in Figure 1.

The trash is dumped from trucks and spread with heavy equipment which achieves reasonable compaction of the materials.

2.2 General geological characteristics

To assess the geological characteristics of the foundation materials four trenches were opened. From the visual inspection sandy clay materials and fine sands materials were identified.

2.3 Geotechnical characterization of foundation

The three boreholes have identified sandy clay material with fine sands materials disseminated. The classification tests have given the following results:
Percentage of fines between 6.1 and 36.6%;
Liquid limit between 31% and none;
Plasticity limit between 17 % to none;
Plasticity index between 4% to none.

The classification of the materials was SC-SW.

The SPT results were increasing with depth with values between 40 to 60 blows.

The log and the obtained results are shown in Figure 2.

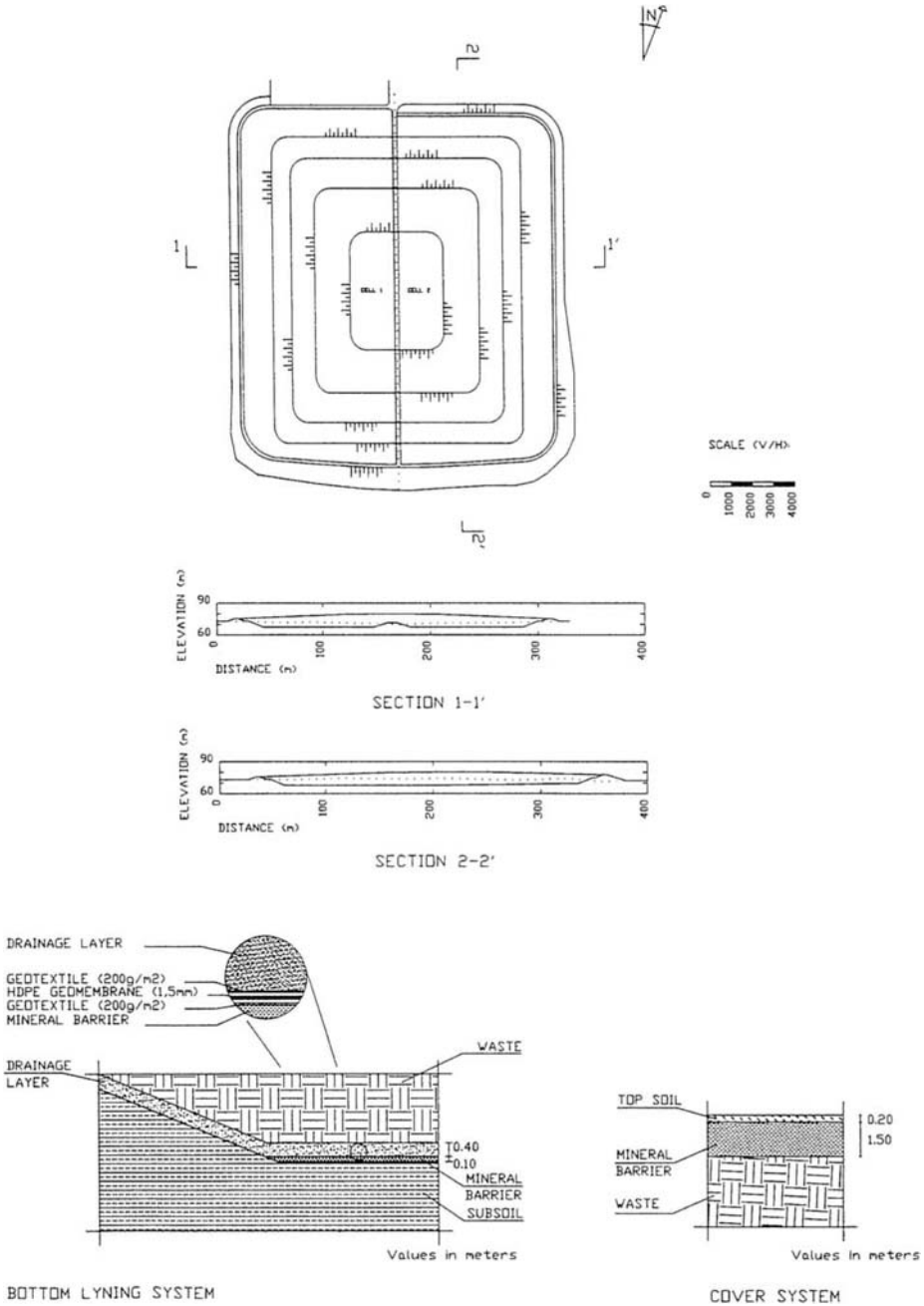

Figure 1 Layout of the Greendale landfill

2.4 Material properties

The particle size distribution of Grândola landfill wastes and the particle size distribution of municipal solid wastes is shown in Figure 3.

The shear strength properties of waste landfills are not easily determined since the physical composition of the mixture makes it unsuitable for

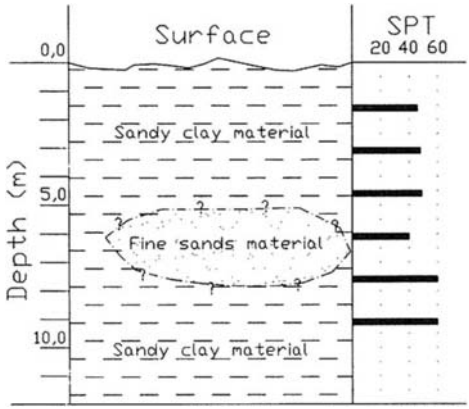

Figure 2 Geotechnical profile of foundation

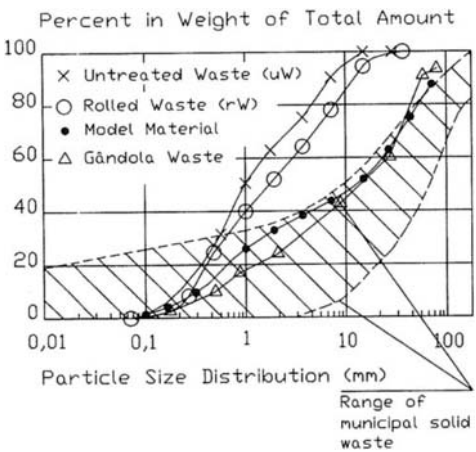

Figure 3 Particle size distribution of waste

the conventional laboratory strength testing. The size of testing equipment is too small relative to the normal size of the refuse. Also the shear parameters of municipal solid waste show a broad variety and a differentiation between fresh and old wastes.

In order to overcome this situation and to characterize the strength of the materials dynamic penetrometer tests were performed (Figure.4) and the obtained results are shown in Figure 5.

For the dry density of the waste materials have given results from 13 to 16 kN/m3 (Figure 6) and water contents from 14. 2 to 16%.

Based on the data proposed by Jessberg (1994) the following values were assumed for Grândola waste materials: cohesion = 10 kPa and friction angle = 25°.

Figure 4 Dynamic penetrometer tests

The measurement of the shear wave velocity by crosshole and downhole techniques need drilling boreholes in landfills. Spectral analysis surface waves (SAWS) provide relatively accurate Vs profiles without the need for drilling and sampling the landfill material. Taking this into consideration geophysical measurements to estimate dynamic strain-dependent materials of solid wastes were implemented (Figure 7).

For the Grândola waste materials a value of shear waves velocities between 330 - 350 m/ s was obtained (Figure 8).

The obtained results have not shown a variation of shear wave velocities with depth, probably due the

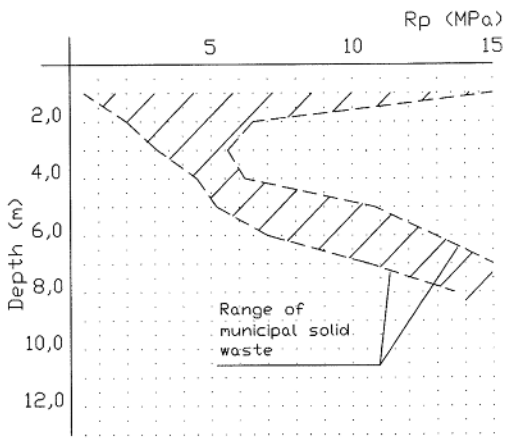

Figure 5 Results of dynamic penetrometer tests

Figure 6 Determination of solid waste density

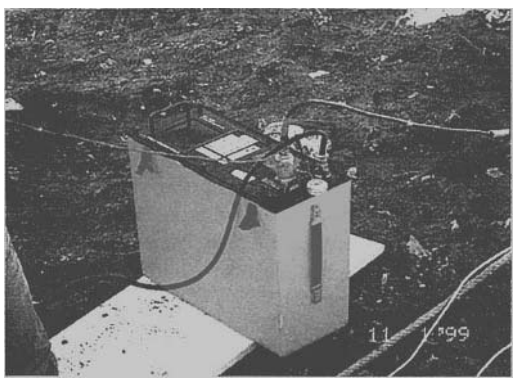

Figure 7 Determination of shear wave velocities

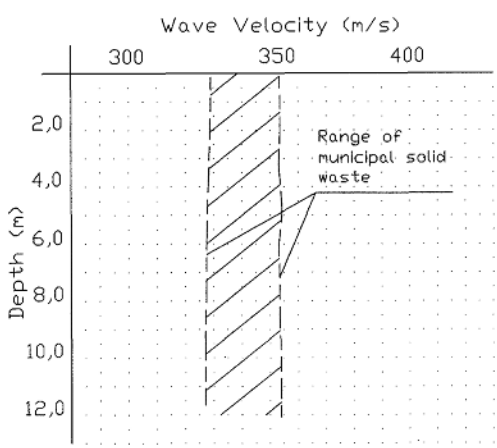

Figure 8 Shear wave velocities of Grândola solid wastes

height of landfill is only 12m, and are in reasonable agreement with the results reported by Kavazanjian et al. (1995).

2.5 Stability analysis

The slope stability of waste landfills is generally evaluated by limit equilibrium slope stability analyses.

A computer code was used and the minimum static safety factor for circular surface was 2.6.

Following Portuguese Code (RSA, 1983) the seismic actions should be defined for near sources and far sources. Considering that the landfill is located in zone A of Portugal seismic map, for the near sources (related with continental faults and magnitude 6.9 to 7.5) the peak ground acceleration is 170 gal and for the far sources (related with offshore faults and magnitude 8.5 - 9.0) the peak ground acceleration is 100 gal.

From the Portugal seismic map, which is based on the rocked outcrop motion the peak ground acceleration value is 170 gal.

For the pseudo-static analyses a seismic coefficient value equivalent to the peak ground acceleration divided by 1.5 can be considered (Sêco e Pinto et al., 1998).

For the pseudo-static analyses the minimum computed safety factor for circular surfaces was 1.9.

For the Makdisi-Seed method (1977) and for the Sarma (1975) method the computed permanent displacements were lower than 10 mm.

2.6 Amplification analysis

The seismic response was also obtained by a computer finite element 1D program ESTOC developed in FORTRAN 77 (Vieira, 1995).

Input motions are incorporated by base horizontal and vertical acceleration power spectra. These can be obtained by direct records of seismic motions by response spectra or by trilogaritme diagram.

This analysis is based on the solution of the equation of motion considering a homogenous and continuous soil deposit composed by horizontal soil layers and assuming a vertical propagation of shear waves.

For the soil behaviour the equivalent linear methods is used and the shear modulus and damping ratio are adjusted in each iteration until convergence has occurred.

The main profile for three foundation geometries (30m, 40m and 50m depths), in order to check this

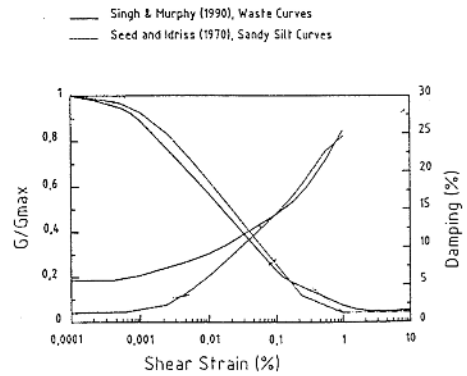

Figure 9 Waste modulus degradation and damping

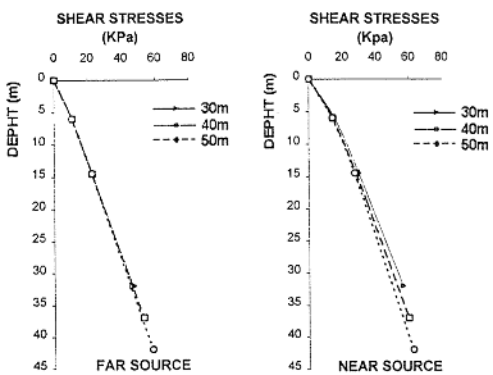

Figure 10 Shear stresses distribution

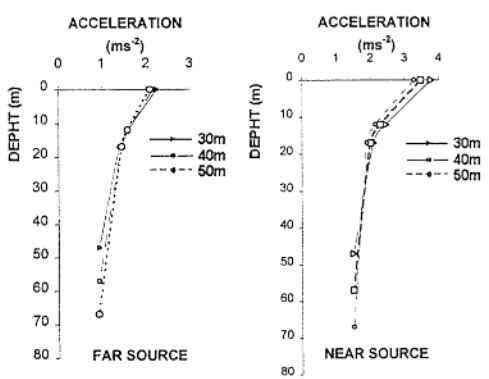

Figure 11 Acceleration distribution

influence, and for the seismic actions near and far source was analysed.

The variation of shear modulus and damping characteristics of waste materials and sandy silt material, with shear strain, is shown in Figure 9 (Singh and Murphy, 1990).

Table 1 - Summary of the seismic analyses results

	Near Source			Far Source		
H(m)	30	40	50	30	40	50
TRFA	3.51	3.22	3.05	3.43	3.18	3.03
T_F (s)	0.35	0.43	0.51	0.35	0.43	0.51
MaxA (m/s^2)	3.78	3.47	3.27	2.24	2.16	2.09
A (m/s^2)	0.95	1.49	1.49	0.94	0.93	0.92
AR	2.54	2.33	2.19	2.38	2.32	2.27

Due the geometry of the landfill (height and slopes) the effect of the HDPE geomembrane /geotextile liner was ignored, i.e. the dynamic properties of the geosynthetic liner was not replaced by the dynamic properties of the equivalent soil layer.

The shear stresses distribution and the acceleration distribution are presented in Figures 10 and 11.

The Table 1 summarizes for near source and far source the transference functions of acceleration (TFRA) between the bedrock and the ground level, the fundamental period of the layer (T_F), the maximum acceleration at the deck (MaxA), the acceleration at the bedrock (A) and the amplification ratio (AR).

3 INTERPRETATION OF THE RESULTS

The computed displacements values are in good agreement with the back analyses performed by Buranek and Prasad (1991) to analyse the solid waste landfill performance during the Loma Prieta earhquake and show that the Makdisi - Seed and Sarma simplified procedures for predicting permanent displacements appear to be appropriate for evaluating the seismic performance of solid waste landfills.

It can be noticed that the amplification effects for the near source and for the far source are of the same order. The shear wave velocities of waste materials play an important role on the amplifications effects.

The values of TFRA decrease with the increasing of the thickness of foundation layer.

The fundamental period values increase with the increasing of the thickness of foundation layer.

4 CONCLUSIONS

1) The measured shear wave velocities for the waste materials between 330m to 350m have not shown a variation with depth.
2) The pseudo-static analysis for circular surfaces gave a minimum safety factor of 1.9.
3) The Makdisi-Seed method and Sarma method can predict reasonable the performance of landfills during earthquakes.
4) The amplification of peak ground acceleration, using 1D model, was near 2.3 times, for both near source and far source.
5) For the three different geometry foundations conditions (30, 40 and 50m thickness) the amplification values of peak ground acceleration were similar.
6) The obtained results are in good agreement with the seismic performance of solid waste landfills.
7) As the shear wave velocities of solid waste materials play an important role on the amplifications effects a new program for characterization of these materials by geophysical tests is in progress.

REFERENCES

Buranek, D. and Prasad, S. 1991. Sanitary landfill performance during the Loma Prieta earthquake. Proc. 2nd ICRAGEESD, St. Louis, Vol. 2, pp. 1655- 1660.

Jessberg, H. L. 1994. Emerging problems and practices in environmental geotechnology. Proc. XIII ICSMFE Vol. 1, pp. 271- 281.

Kavazanjian, E., Jr., Matasovic, N. Bonaparte, R. and Schmertmann, G. R. 1995. Evaluation of MSW properties for seismic analysis. Proc. Geoenvironment 2000, ASCE Specialty Conference, New Orleans, Louisiana, 22-24, February.

Makdisi, F.I. and Seed, H.B. 1977. A Simplified procedure for estimating earthquake-induced deformations in dams and embankments. Report N° EERC 79-19. University of California, Berkeley.

RSA 1983 "Regulamento de segurança e acções para estruturas de edifícios e pontes"(portuguese code).

Sarma, S.K. 1975. Seismic stability of earth dams and embankments. Geotechnique, Vol. 25, N° 4, pp. 743--761.

Sêco e Pinto, P.S., Mendonça, A. Lopes, L. and Vieira, A. 1998.Seismic Behavior of Solid Waste Landfills. Proceedings of the 3rd International Congress on Environmental Geotechnics, Vol. 1, pp. 293-300. Edited by Pedro S. Sêco e Pinto. Published by A. Balkema.

Singh, S. and Murphy, B. 1990. Evaluation of the stability of sanitary landfills. ASTM STP 1070 Geotechnics of Waste Landfills- Theory and Practice. A. Landva, and G.D. Knowles, eds. ASTM, Philadelphia, Pa. pp. 240-258.

Vieira, A. 1995. Amplification of seismic movements for horizontal soil layers. Master thesis (in portuguese). University New of Lisbon.

Earthquake Geotechnical Engineering, Sêco e Pinto (ed.) © 1999 Balkema, Rotterdam, ISBN 90 5809 116 3

Static stability, pseudo-static seismic stability and deformation analysis of end slopes

R. M. Wahab & G. B. Heckel
Illinois Department of Transportation, Springfield, Ill., USA

ABSTRACT: Static and pseudo-static seismic slope stability analyses were conducted for 51 projects, using both the simplified Bishop and simplified Janbu methods. A comparison between the two methods, for seismic coefficients k_h of 0.0 and 0.3g, indicated that the Janbu factor of safety (FOS) exceeded the Bishop FOS by an average of 8% and 2%, respectively, assuming the same critical slip circle for both k_h= 0.0g and k_h= 0.3g conditions. The analysis was repeated assuming different slip circles in either case, by conducting a separate search for the seismic critical slip circle at k_h=0.3g for each method. The results indicated that the FOS decreased by an average of 8% to 9%, for both Janbu and Bishop methods. Also, based on the separate search, the Janbu FOS exceeded the Bishop FOS by the same average of 2% at k_h=0.3g . Deformation analyses were conducted, when the FOS was less than 1. For FOS ranging from 0.53 to 0.95, the deformations ranged from 1 cm to 250 cm.

1 INTRODUCTION

Illinois Department of Transportation (IDOT) currently uses software, called XSTABL, for slope stability analysis. XSTABL is based on the limiting equilibrium approach, using the slices method. For seismic stability analysis, XSTABL computes the FOS using the pseudo-static method, in which the earthquake loads are assumed to act at the centroid of each individual slice. The software also provides options for several methods, including the simplified Janbu and Bishop methods. Both methods satisfy vertical force equilibrium and ignore the inter-slice shear forces. The simplified Janbu method satisfies the horizontal force equilibrium for the entire mass. The simplified Bishop method satisfies the overall moment equilibrium about the center of each trial slip circle.

The simplified Janbu and Bishop methods are frequently used at IDOT, and other transportation agencies, for their simplicity and suitability for conducting a search for the critical slip circle. Based on some individual case histories, differences in the FOS from the two methods are anticipated, due to the analytical differences as well as some numerical problems associated with the two methods. Duncan (1992) presented an excellent discussion of the various methods of stability and deformation analyses. However, for these two methods which are widely used in engineering practice, the differences in FOS have not been fully quantified for a wide range of embankment, loading and subsurface soil conditions.

In this paper, slope stability data files for 51 select IDOT projects (between 1994 and 1998) were analyzed, using both the simplified Janbu and the simplified Bishop methods. The projects involved a wide range of embankment, loading and subsurface soil conditions for end slopes of bridge abutments at various locations in Illinois. Static stability and pseudo-static seismic stability analyses were conducted for each project, using the simplified Janbu and Bishop methods.

When the pseudo-static seismic FOS is less than 1, the slope is expected to fail under the maximum anticipated seismic condition. In this case, knowledge of the amount of deformation is important to make a decision regarding design changes. In this paper, simplified deformation analyses were conducted when the seismic FOS was less than 1. In each case, two methods were used. The first method determined permanent deformation using a chart prepared by Hynes and Franklin (1984) which is based on the Newmark (1965) sliding block model. The second method determined permanent deformation using a chart prepared by Makdisi and Seed (1978) which is based on a two-dimensional finite element analysis of embankments.

2 INPUT DATA

The 51 project files analyzed in this study included a wide range of embankment, loading and subsurface conditions. These projects, collectively, represent a large spectrum of case histories which are encountered in the day-to-day engineering practice at IDOT and some other transportation agencies. Most of the embankments analyzed were constructed of cohesive soils, generally classified as silty clay. It is an acceptable practice at IDOT to conservatively assume a cohesion value of 50 kPa and zero friction angle, for the cohesive embankment material. All end or side slopes are constructed at 2H:1V or flatter. One embankment was constructed of granular (sandy) materials. In this case, a friction angle of 30°, was assumed for the embankment material. Also, for granular embankments, the end or side slopes are constructed at 2.5H:1V or flatter.

For pseudo-static seismic stability analysis, a maximum horizontal seismic coefficient (k_h) of 0.3g was used. The highest k_h value anticipated in Illinois during a 50-year design period is 0.2g. Using 0.2g in the analysis did not produce enough cases with FOS less than 1, needed for the deformation analysis. Therefore, a value of 0.3g was used, which provided enough data for analytical purposes.

The subsurface soil data for the different projects were based on the laboratory testing of relatively undisturbed soil samples obtained for each project. The depths of soil borings varied from 1 to 3 times the embankment height, depending on the site geologic condition. Generally, about 60% of the projects included primarily cohesive subsurface soils, with an average cohesion of 30 kPa. About 10% of the projects included primarily cohesionless subsurface soils, with an average friction angle of 30°. The remainder 40% of analyzed projects included subsurface soils with both an average cohesion of 25 kPa and an average friction angle of 20°. The effects of local site seismic conditions were not considered in this study.

3 RESULTS AND DISCUSSION

3.1 Factor of Safety Analysis

This study consisted of three types of stability analyses: 1) Type A, in which the FOS was computed for the static (k_h = 0g) condition, using both the simplified Janbu and Bishop methods; 2) Type B, in which the FOS was computed for the seismic condition with k_h = 0.3g, using the slip circle identified in the Type A analysis, for both the Janbu and Bishop methods; and 3) Type C, in which the FOS was computed for both the Janbu and Bishop methods, using a different critical slip circle for k_h = 0.3g than the static circle. A comparison was made between the FOS, obtained from the three types of analyses for the Janbu and the Bishop methods. Figures 1 through 3 show Janbu FOS versus Bishop FOS for each type of analysis.

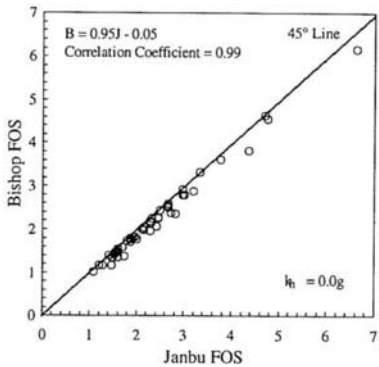

Figure 1. Bishop FOS vs. Janbu FOS for a Type A Analysis.

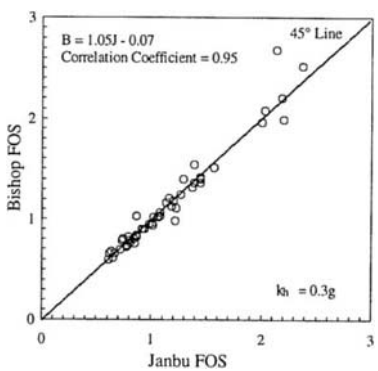

Figure 2. Bishop FOS vs. Janbu FOS for a Type B Analysis.

The data in Figures 1 through 3 indicates the difference between the simplified Janbu and Bishop methods appears to be insignificant for all practical purposes. For marginal cases, when the FOS is close to 1, the analysis method should be selected based on which is more appropriate for the specific conditions. A linear regression analysis was performed for each type of stability analysis. The resulting equations, with the corresponding correlation coefficients, are shown in the upper left hand corner of each figure.

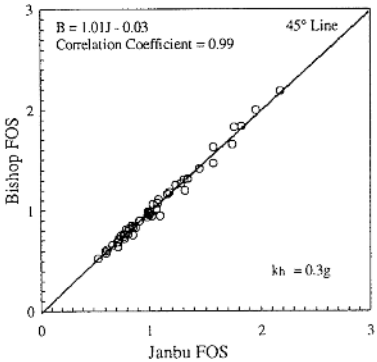

Figure 3. Bishop FOS vs. Janbu FOS for a Type C Analysis.

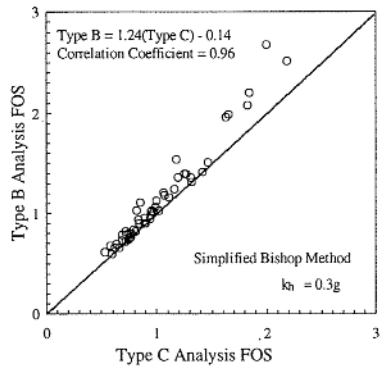

Figure 4. Type B FOS vs. Type C FOS Using the Simplified Bishop Method.

Unfortunately, the tabulated data is too extensive to be concisely presented in this report. The analysis shows: 1) Janbu FOS exceeds Bishop FOS by an average of 8.2% for a Type A analysis; 2) Janbu FOS exceeds Bishop FOS by an average of 1.6% for a Type B analysis; and 3) Janbu FOS exceeds Bishop FOS by an average of 2.3% for a Type C analysis.

3.2 Comparison of Type B and Type C Analyses

Figures 4 and 5 compare the data obtained from the Type B and Type C stability analyses, for both simplified Bishop and Janbu methods, respectively.

The data in Figures 4 and 5 shows that a Type C analysis, using either method, results in lower FOS values than Type B analysis. Therefore, it is more conservative to conduct a separate search for the critical seismic slip circle to obtain the seismic FOS. This is particularly significant when the seismic FOS is close to 1.0. A linear regression analysis was performed for each type of stability analysis. The resulting equations, and correlation coefficients, are shown in the upper left hand corner of each figure.

The statistical analysis shows: 1) Type B FOS exceeds Type C FOS by an average of 9.3% using the simplified Bishop method; and 2) Type B FOS exceeds Type C FOS by an average of 8.4% using the simplified Janbu method.

3.3 Deformation Analysis

The permanent seismic deformation was estimated for each project, in which the seismic FOS was less than 1 at k_h = 0.3g, using two methods. In the first method, a simplified chart developed by Hynes and

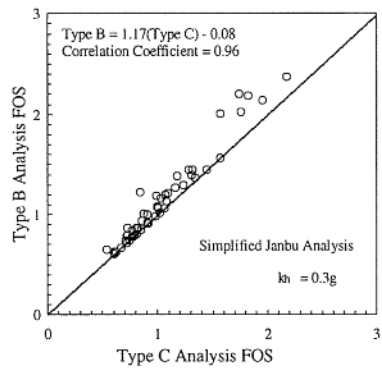

Figure 5. Type B FOS vs. Type C FOS Using the Simplified Janbu Method.

Franklin (1984) was used in this study. The chart is based on Newmark's (1965) sliding block model. Newmark computed the displacement, from the ground velocity, earthquake acceleration, and the soil mass's resistance to acceleration, using a block sliding on an inclined plane as a model. Newmark successfully compared the theoretical displacements with actual field observations from four earthquakes in California during the 1940s and 1950s. The chart developed by Hynes and Franklin does not include the effects of embankment amplification or earthquake magnitude.

The second method of deformation analysis, in this study, was based on the average data in a chart developed by Makdisi and Seed (1978). The chart was derived from two-dimensional finite element analysis of embankments. Also, the chart includes the effects of embankment amplification and earthquake magnitude. In, Illinois the maximum earthquake moment magnitude is anticipated to be 7.5 (Kavazanjian, et. al., 1998).

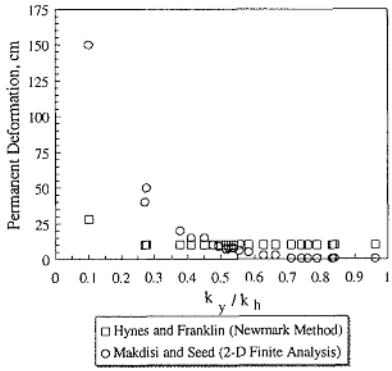

Figure 6. Typical Permanent Deformation vs. k_y / k_h Using Simplified Janbu Data from the Type B Analysis.

The results of the deformation analysis for both methods are summarized on Figure 6, where k_y represents the yield coefficient corresponding to a seismic FOS of 1 (using either Janbu or Bishop method). When the applied coefficient (k_h) exceeds the yield coefficient (k_y), the slope develops a deformation which increases as the ratio (k_y/k_h) decreases.

Figure 6 shows that the Hynes and Franklin method provides relatively constant small deformation (10 cm is the lower limit of the mean data provided by Hynes and Franklin) for a wide range of k_y/k_h ratios (0.25 to 0.95). For k_y/k_h ratios below 0.25, the deformation begins to increase gradually. The Makdisi and Seed method provides a small, gradual increase in deformation as the k_y/k_h ratio decreases from 1 to 0.25, below which the deformation increases rapidly. A similar trend was observed for the Type C analysis, using the Janbu method. Also, similar trends were observed for both Types B and C analyses, using the simplified Bishop method.

4 CONCLUSIONS

Slope stability data files for 51 select IDOT projects were analyzed, using both the simplified Janbu and the simplified Bishop methods. Three types of analyses were used: the static, the pseudo-static seismic using the static critical slip circle, and the pseudo-static seismic analysis using a separate search for the seismic critical slip circle. Permanent deformation was determined, for both Janbu and Bishop methods, based on Newmark's sliding block analysis and two-dimensional finite element analysis. The following conclusions have been drawn from the analyses:

1) For all practical purposes, the simplified Janbu and Bishop methods give approximately the same results for the static and pseudo-static seismic FOS. However, the simplified Bishop method generally resulted in a slightly lower FOS than the simplified Janbu method.

2) For both Janbu and Bishop methods, the seismic FOS based on a separate search for the critical slip circle is slightly less than that based on the static critical slip circle.

3) For both the Janbu and Bishop methods, when the seismic FOS is less than 1, the slope deformations based on Makdisi and Seed's chart were larger than those based on Hynes and Franklin's chart.

5 REFERENCES

Abramson, L., Boyce, G., Lee, T., and Sharma, S. (1993). Advanced Technology for Soil Slope Stability. Vol. 1, Slope Stability Manual. FHWA Publication No. SA-94-005.

Duncan, J.M. (1992). "State-Of-The-Art: Static Stability and Deformation Analysis." Proceedings: Stability and Performance of Slopes and Embankments II. Berkely CA, June 29 to July 1, 1992. ASCE Geotechnical Special Publication No. 31. Vol 1.

Hynes, M.E. and Franklin, A.G. (1984). "Rationalizing the Seismic Coefficient Method." Misc. Paper GL-84-13. US Army Engineer Waterways Experiment Station, Vicksburg, Mississippi.

Kavazanjian, E., Matasovic, N., Hadj-Hamou, T., and Wang, J. (1998). Earthquake Engineering. FHWA National Highway Institute training course participant's manual. Course No. 13239 - Module 9. Vol. 1

Makdisi, F.I. and Seed, H.B. (1978). "Simplified Procedure for Estimating Dam and Embankment Earthquake-Induced Deformations." Journal of the Geotechnical Engineering Division, ASCE. Vol. 104, No. GT7. pp.849-867.

Newmark, N.M. (1965). "Effects of Earthquakes on Dams and Embankments." Geotechnique. Vol. 15, No. 2, pp. 139-160.

Sharma, S. (1995). XSTABL Reference Manual. Version 5. Interactive Software Designs, Inc. Moscow, Idaho.

policies of IDOT. This paper does not constitute a standard, specification or regulation at IDOT. Trademark or proprietary names appear in this paper only because they are considered essential to the object of this document; their use does not constitute an endorsement by IDOT.

This Page Intentionally Left Blank

Earthquake Geotechnical Engineering, Sêco e Pinto (ed.) © 1999 Balkema, Rotterdam, ISBN 90 5809 116 3

Laboratory evaluation of the Newmark procedure for assessing seismically-induced slope deformations

J. Wartman, R. B. Seed, J. D. Bray & M. F. Riemer
University of California, Berkeley, Calif., USA

E. M. Rathje
University of Texas, Austin, Tex., USA

ABSTRACT: Results of studies to evaluate the accuracy and applicability of the Newmark procedure for calculating seismically-induced slope deformations are presented. Data are presented from shaking table tests on rigid and deformable sliding masses on an inclined plane, and a small-scale clay slope. Analyses of the tests, including numerical modeling of the inclined plane experiments, are presented and discussed. Important findings of this study include: (a) Newmark's rigid block assumption is unconservative when frequency content of the input motion is at or less than the natural frequency of the sliding mass across the range of frequencies tested, (b) displacement of a small-scale slope subjected to strong shaking was intermediate to those calculated by the Newmark procedure using peak and residual strengths, and (c) seismically-induced displacements in clay slopes may result from both sliding along distinct shear surfaces and internal deviatoric straining of the sliding mass.

INTRODUCTION

It is common practice in geotechnical earthquake engineering to estimate seismically induced permanent deformations in slopes and embankments using the Newmark procedure [e.g., Newmark (1965), Goodman and Seed (1966), Franklin and Chang (1977), Marcuson et al. (1992)]. This analytical procedure is formulated using the analogy of a rigid block sliding on a horizontal plane. No relative movement between the block and plane occurs until the yield acceleration is exceeded. For a rigid block, the acceleration is equal at all times to the ground acceleration (until the slip phase of motion); hence, the acceleration-time history of the earthquake motion is integrated directly to calculate the displacements. "Classical" Newmark deformation analyses are based on several simplifying assumptions: 1) the soil responds in a rigid, perfectly plastic manner; 2) displacements occur along a single, well-defined slip surface; and 3) the soil does not undergo significant strength loss as a result of shaking.

This paper discusses a 1-g shaking table-based study that examines the validity and applicability of the Newmark procedure. Results from numerical modeling of the shaking table tests are also presented. The current study (see also Wartman et al. 1998) expands upon earlier research efforts in this area [e.g., Goodman and Seed (1966), Kutter (1982), Elgamal et al. (1990), and Kramer and Smith (1997)]. The shaking table work is being conducted in two phases. Phase I examines an important fundamental assumption of the Newmark procedure by considering shaking-induced sliding of both a rigid block and a deformable soil column on an inclined plane. Phase II considers shaking-induced deformations that occur in small-scale clay slopes under earthquake–type excitations.

LABORATORY FACILITY

Tests were conducted on a 1.2 m by 1.0 m single-degree-of-freedom shaking table at the University of California, Berkeley. The table consists of an aluminum plate and beams bolted to two parallel horizonal tracks defining the direction of table movement. Each track consists of two Teflon linear motion bearings that rest on 5.1 cm diameter steel rods. The steel rods are anchored to a concrete block supported on an independent foundation to isolate the table from machine-induced vibrations. The shaking table is driven by a 22,000 kg, 15.2 cm displacement hydraulic actuator ported by a 95 liter-per-minute servovalve. An *MTS 406*

hydraulic control unit directs the servovalve based on a displacement feedback signal from the actuator and command signal.

INCLINED PLANE TESTS

General

The inclined plane consists of a 2.5 cm thick, 114 cm long steel plate supported by a rigid steel frame (Figure 1). At its lower end, the steel plate is attached to a bearing secured to the shaking table by a pillow block-base plate assembly. A steel frame, consisting of four vertically-mounted, 16.5 cm wide, 1.2 cm thick steel uprights, supports the middle and upper portions of the steel plate. The inclined steel plate is secured to the uprights by 8 bolts in slotted connections. The slotted connections allow the steel plane to be inclined from 0 to 40 degrees above horizontal. Free vibration tests indicate the inclined plane has a natural frequency of about 75 Hz.

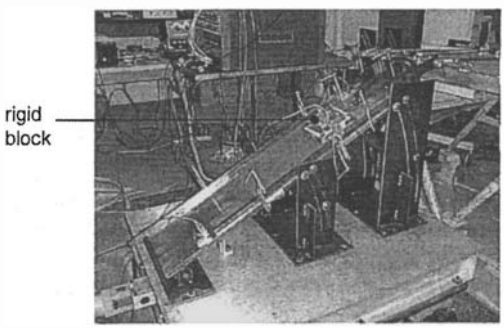

Figure 1 – Rigid block shown on inclined plane

Rigid Block Tests

A 12.7 cm square, 2.5 cm thick steel block was placed on the inclined plane and subjected to shaking. The bottom of the block was covered with a non-woven needle-punched geotextile. The geotextile was in contact with a 1.02 mm thick high-density polyethylene (HDPE) geomembrane that was secured to the upper side of the inclined plane. The static interface friction angle was assessed by raising the inclined plane until the block began to slide. The raised plane tests, performed both before and after shaking table experiments, indicated that the geotextile/geomembrane static interface friction angle was approximately 11.7 degrees. The dynamic interface friction angle for each test was back-calculated based on the observed yield acceleration and found to vary as a function of input motion frequency and total displacement. The dynamic interface friction angle typically ranged between 14 and 19 degrees. The block, inclined plane and shaking table were instrumented with accelerometers and displacement transducers. Tests were performed at inclinations ranging from about 9 to 11 degrees using ramped sinusoid, frequency sweep, and recorded earthquake input motions.

For the tests in which displacement occurred, the acceleration-time histories recorded on the block were truncated as a result of sliding when the yield acceleration was exceeded. Elgamal et al. (1990) made similar observations during their shaking table studies of seismically-induced slope deformations. The truncated sections of the acceleration-time history were noted to correspond with distinct pulses of permanent downslope displacement.

Deformable Soil Column

Tests performed with the rigid block were repeated using two cylindrical deformable soil columns measuring 15.2 cm and 25.3 cm in diameter. The smaller soil column consisted of a 1.9 cm thick Lucite disk over 15.5 cm of clay underlain by another 1.9 cm Lucite disk. A textured HDPE geomembrane was attached to one side of the lucite disks to minimize movement between the disk and the clay. The bottom of the lower disk was covered with same geotextile used for the rigid block tests. A latex membrane was used to contain the clay and maintain its water content during testing. The larger soil column (Figure 2) was 16 cm high (excluding the end disks) and was otherwise identical in profile to its smaller counterpart column. The clay consisted of a mixture of 3 parts kaolinite to 1 part bentonite with a water content of about 110%. This clay mixture has been used in previous physical model experiments [e.g., Lazarte and Bray(1996), and Wartman (1996)]. Both soil columns were instrumented with accelerometers and displacement transducers at the top and bottom disks. The natural frequency of the soil columns was estimated by free vibration tests (low strain test) and observation of

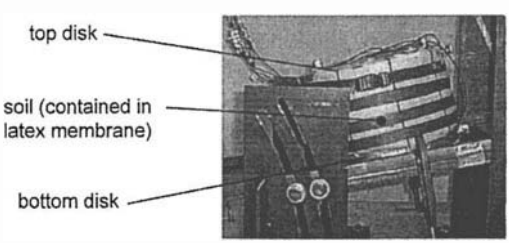

Figure 2 – 25.3 cm diameter soil column shown on inclined plane

natural period at stronger shaking levels (representative of relatively high strains during testing). The small and high strain natural frequency of the 15.2 cm diameter soil column was 5.2 and 4.7 Hz, respectively; whereas, the natural frequency of the 25.3 cm diameter soil column was 9.1 and 7.8 Hz, respectively.

Sliding Block Test Results

Figure 3 shows sliding displacement as a function of excitation frequency for the rigid block and 25.3 cm diameter deformable soil column using a sinusoidal input motion with a peak acceleration in the range of 0.15 g to 0.18 g and a 5 second duration. Only one set of tests are presented because of space limitations, however, the trends shown in Figure 3 were generally observed for all of the experimental data. Other tests were performed using sinusoidal input motions with peak accelerations ranging from 0.1 g to 0.36 g. For sinusoidal input motions, the soil column slips more than the rigid block when the excitation frequency is at or below the natural frequency of the soil column across the range of input frequencies tested. This additional sliding displacement of the deformable soil column may be substantial, often exceeding rigid block displacements by 50 to 500 percent. In these instances, Newmark's rigid block assumption is unconservative. The rigid block generally displaces more than the deformable soil column when the excitation frequency is significantly greater than the natural frequency of the soil column. For these cases, the absolute difference between rigid block and soil column displacement is generally small.

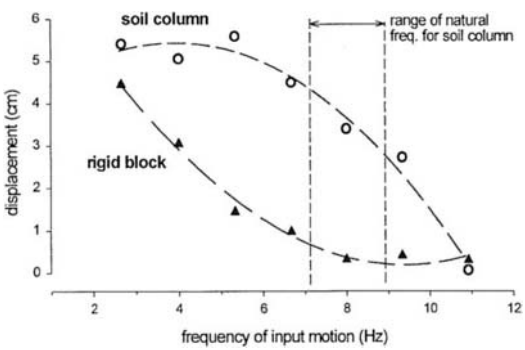

Figure 3 – Rigid block and large deformable soil column displacements for ramped sinusoidal input motions with peak accelerations in the range of 0.15g to 0.18g

Numerical Modeling of Inclined Plane Tests

The Newmark sliding block analytical procedure was adapted to include an inclined plane and used to model the rigid block tests. Figure 4 compares the recorded sliding displacement of the rigid block with the sliding displacement calculated by the modified Newmark procedure. A five-second, 8 Hz sinusoidal motion was used as input for these tests and the interface friction angle between the geotextile and geomembrane was 16 degrees. The analytical results and test results show very good agreement.

An analytical model was developed that calculates the sliding displacement of a deformable soil column on an inclined plane. Often when calculating the sliding displacement of a deformable soil column, the dynamic analysis of the system is performed separately from the sliding analysis (e.g. Makdisi and Seed 1978). This procedure is a decoupled displacement analysis and does not accurately model the forces along the sliding interface. The analytical procedure developed as part of this study uses linear elastic, modal analyses to model the dynamic response of the soil column and the appropriate mode shape for a one-dimensional soil deposit is implemented (Idriss and Seed 1968). Sliding is modeled during the dynamic analysis; therefore this procedure is considered a coupled displacement analysis. A similar model has been applied to gravity concrete dams (Chopra and Zhang 1991). The numerical formulation for the coupled sliding displacement model for earth embankments can be found elsewhere (Rathje and Bray 1999) and is beyond the scope of this paper.

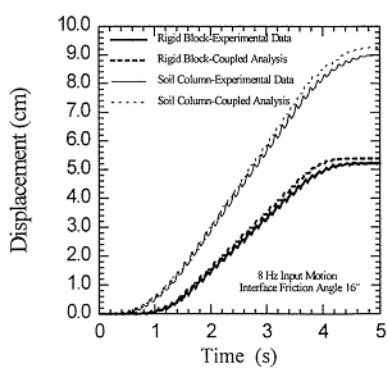

Figure 4 – Experimental data for 8 Hz sinusoidal input motion with calculated displacements from Rathje and Bray (1998) coupled model.

A comparison between the recorded sliding displacement of the soil column and the calculated sliding displacement from the coupled analysis is also shown in Figure 4. As with the rigid block tests, a five-second, 8 Hz sinusoidal motion was used as input and the interface friction angle at the base was maintained at 16 degrees. The coupled analysis accurately predicts the initiation of sliding at 0.4 s and the final calculated displacement is within 3 percent of the experimental value.

SMALL-SCALE SOIL SLOPE

General

As part of the Phase II study, a small scale slope was constructed in an 96 cm wide by 160 cm long Plexiglas box bolted to the shaking table. Stiffeners were attached to the outside of the box to minimize front and back wall deflections. The inside sidewalls were lubricated with canola oil to reduce friction along the sidewall-clay interface. The small-scale slope was comprised of soft clay that measured 18.4 cm in height with a face slope of 1.3 horizonal:1 vertical (Figure 5a). The slope was underlain by a 3.8 cm stiff clay layer. The top of the slope was flat and extended 85.5 cm beyond the front slope crest. The back of the slope was composed of stiff clay inclined at 2 horizonal:1 vertical. The toe of the slope was located 21.3 cm from the front of the containment box. Instrumentation consisting of six accelerometers and eight linear potentiometers were placed as the slope was constructed. In addition to the mechanical instrumentation, 75 strands of uncooked capellini number 9 (0.8 mm diameter) spaghetti noodles were pushed vertically into the slope along several profiles. Once hydrated, the pasta strands became soft and pliable and served as slope inclinometers.

The clay was composed of 3 parts kaolinite to 1 part bentonite at water contents ranging from 105% for the stiff clay and 128% for the soft clay. The liquid and plastic limits of the clay were 133 and 27, respectively. In situ mechanized vane shear tests that were performed immediately after the test indicate that the soft clay had static peak and residual strengths of 2.46 kPa (±0.05 kPa) and 1.80 kPa (±0.1 kPa), respectively. Based on these strengths, the slope had peak and residual yield acceleration values of 1.42g and 1.0g. The stiff clay had a peak strength of 4.18 kPa (±0.05 kPa).

The input motion was an acceleration-scaled, time-compressed version of a recording from a depth of 79 m at Kobe Port Island obtained during the 1995 Hyogoken-Nanbu Earthquake. The scaled input motion had a maximum horizontal acceleration of 3.0 g. The motion was selected and scaled to ensure that it would fall into the performance range of the shaking table while producing realistically

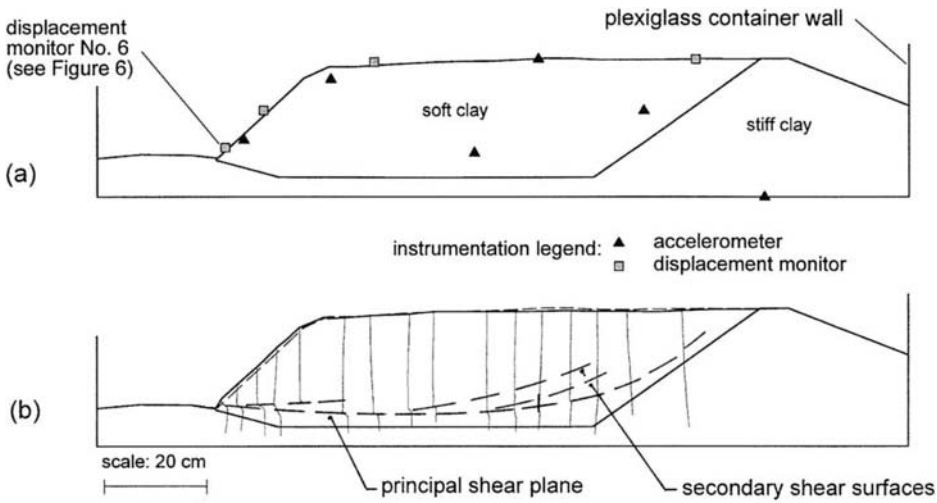

Figure 5 – Small scale slope: (a) pre-shaking geometry and instrumentation plan; (b) post-shaking profile showing deformed clay surface and pasta strands, and slip surfaces (pre-shaking profile shown with short dashed lines, slip surfaces shown with long dashed lines)

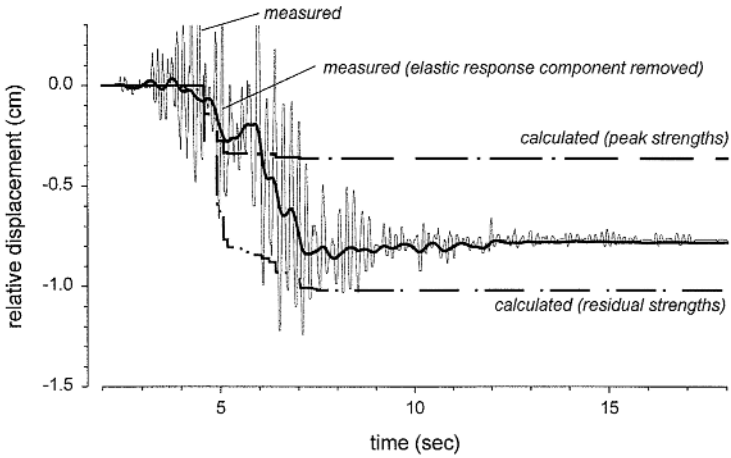

Figure 6 – Measured and calculated relative displacements versus time (negative displacement corresponds to downslope movement). Measured displacement recorded by monitor number 6 (see Figure 5a for location).

modeled seismic acceleration pulses in excess of the slope yield strength.

Test Results

Figure 5b depicts the post-shaking geometry of the slope. Deformations occurred primarily along a single well-defined shear surface with several secondary shear displacements occurring near the middle and rear of the model. The principal mode of permanent deformation was a deep rotational/translational displacement in the soft clay several centimeters above the stiff clay. The maximum displacement offset along this shear surface was 1.1 cm. Several secondary shear failures with offsets in the range of 0.3 to 0.7 cm were also observed to splay from the principal displacement plane in the upslope direction.

Newmark Analyses

The Newmark method assumes that seismically-induced permanent deformations occur along a single, well-defined slip surface. Thus, it was not possible to analyze the secondary shear planes and only the principal slip surface was considered in the analysis. Relative displacements were calculated based on the integration of relative velocities using the Franklin and Chang (1977) procedure. The analyses were performed assuming sliding occurred in only one direction, and for yield accelerations corresponding to peak and residual soil shear strengths. Figure 6 presents the results of the analyses, along with actual measured displacements, as a graph of relative displacement versus time. The high-frequency sinusoidal shape of the measured displacements reflects the elastic response component of the deformation of the soil column. For clarity, the measured displacement-time history is also shown without this elastic deformation component.

Based on analysis of the data, it is believed that sliding initiated near the toe of the slope along the principal shear plane. As shaking continued, displacements continued along the secondary shear planes near the middle and rear of the model. It is noted that the yield accelerations corresponding to the secondary shear planes range from 1.42g to 1.46g.

Although not observed in this test, shaking-induced deviatoric straining of the slope often contributes to total deformations. This deformation mechanism, described by Stewart et al. (1995), involves the accumulation of seismically-induced permanent shear deformations in distributed regions of the slope away from the distinct slip surfaces, and in some instances (e.g., Wartman et al. 1998), can be a significant part of the overall deformations.

CONCLUSIONS

The following conclusions are drawn from this study.

1. The Newmark rigid block assumption appears to be generally unconservative when the excitation

frequency is at or below the natural frequency of the deformable soil column across the range of frequencies tested. The additional sliding displacement of the soil column may be substantial, often exceeding rigid displacements by 50 to 500 percent.

2. The Newmark rigid block assumption is generally accurate or conservative when the excitation frequency is significantly greater than the natural frequency of the soil column. For these cases, the difference between rigid and deformable masses is typically small.
3. Seismically-induced slope deformations in this moderately sensitive soil were reasonably bounded by displacements estimated using peak and residual soil strengths in a Newmark analysis.
4. Displacements in actual slopes may occur along one or more distinct slip surfaces, as well as within the soil mass. This latter deformation mechanism is the result of deviatoric straining of the soil. The single shear surface assumption may be a significant oversimplification for slopes that do not contain a single preferential shear surface such as a pre-existing slip plane, a thin liquifiable layer, a soft clay seam or geosynthetic interface.

ACKNOWLEDGEMENTS

These studies were supported by funding provided by the California Department of Transportation (Grant RTA-59A130[4]), the National Science Foundation (Grant BCS-9157083), and the David and Lucile Packard Foundation. This support is gratefully acknowledged. The authors also wish to thank Chris Moy for his assistance in performing the shaking table studies.

REFERENCES

Chopra, A.K. and Zhang, L. (1991) "Earthquake-Induced Base Sliding of Concrete Gravity Dams," *J. of Struct. Engng.*, ASCE, Vol. 117, No. 2, pp. 3698-3719.

Elgamal, A. W., Scott, R. F., Succarieh, M. F., Yan, L. (1990). "La Villita dam during five earthquakes including permanent deformation,' *J. Geotech. Engrg Div.*, ASCE, 116(10) 1443-1462.

Franklin, A. G., and Chang, F. K. (1977). "Earthquake resistance of earth and rockfill dams," *Misc. Paper S-71-17,* U. S. Army Wtrwy Exp. Sta., Vicksburg.

Goodman, R. E. and Seed, H. B. (1966). "Earthquake-induced displacements in sand embankments," *J. Soil Mech. and Found. Div.*, 92(SM 2).

Idriss, I.M. and Seed, H.B. (1968) "Seismic Response of Horizontal Soil Layers," *J. of Soil Mech. and Found. Engng.*, ASCE, Vol. 94, No. SM4, pp. 1003-1029.

Kramer, S. L., and Smith, M. W. (1997). "Modified Newmark model for seismic displacements of compliant slopes," *J. Geotech. and Geoenvir. Engrg.*, 123 (7)

Kutter, B. L. (1982). "Centrifugal modeling of the response of clay embankments to earthquakes," Ph.D. Thesis, Cambridge University

Lazarte, C. and Bray, J. D. (1996). "A study of strike-slip faulting using scale models," *Geotech. Testing J.*, ASTM, 19(2), 118-129.

Makdisi, F. I. and Seed, H. B. (1978) "Simplified procedure for estimating dam and embankment earthquake-induced deformations," *J. Geotech. Eng. Div.*, ASCE 104(7), 849-867.

Marcuson, W. F, Hynes, M. E., and Franklin, A. G. (1992) "Seismic stability and permanent deformation analyses: the last twenty-five years." *Proc. ASCE Spec. Conf. on Stab. and Perf. of Slopes and Embankments - II,* ASCE, NY, 552- 592.

Newmark, N. M. (1965) "Effects of earthquakes on dams and embankments." *Geotechnique*, London, 15(2), 139-160.

Rathje, E.M. and Bray, J.D. (1999) "An Examination of Simplified Earthquake-InducedDisplacement Procedures for Earth Structures," Canadian Geotech J. 36(1), in press.

Seed, H. B. and Clough, R. W. (1963). "Earthquake resistance of sloping core dams," *J. of Soil Mech. and Found. Engrg.*, 899(SM 1), 209-241.

Stewart, J. P., Bray, J. D., McMahon, D. J., and Kropp, A. L. (1995). "Seismic performance of hillside fills," *Landslides Under Static and Dynamic Conditions-Analysis, Monitoring, and Mitigation,* ASCE, NY, 76-95.

Wartman, J. (1996) "The effect of fly ash on the geotechnical properties of a soft clay," M. Eng. Thesis, University of California, Berkeley.

Wartman, J., Riemer, M. F., Bray, J. D., and Seed, R. B. (1998) "Newmark analyses of a shaking table slope stability experiment," Proc. of ASCE Geo-Institute Spec. Conf. on Geot. Earthquake. Engng. and Soil Dyn., Seattle, WA, August.

Earthquake Geotechnical Engineering, Sêco e Pinto (ed.) © 1999 Balkema, Rotterdam, ISBN 90 5809 116 3

Centrifuge model studies of the seismic response of reinforced soil slopes

Lili Nova-Roessig & Nicholas Sitar
Department of Civil and Environmental Engineering, University of California, Berkeley, Calif., USA

ABSTRACT: Centrifuge tests were used to study the dynamic behavior of soil slopes reinforced with geosynthetics. The main objectives were to determine the failure mechanism and amount of deformations under seismic loading, and to identify the main parameters controlling seismically-induced deformations. Geosynthetically reinforced soil slopes (2V:1H) were subjected to earthquake motions with maximum foundation accelerations of up to 0.86g. The experimental results show that slope movement can occur under relatively small base accelerations, and significant lateral and vertical deformations can occur within the reinforced soil mass under strong shaking. However, no distinct failure surfaces were observed, and the magnitude of deformations is related to the backfill density and reinforcement stiffness.

1 INTRODUCTION

Field experience with recent seismic events shows that reinforced soil slopes and walls perform well during earthquake loading (Table 1; Nova-Roessig and Sitar, 1998). In general, reinforced soil structures tend to deform under seismic loading, and complete or catastrophic failures have not been observed. Seismically-induced damage, if any, has been minor, consisting of crest settlement, face bulging and minor cracking in the backfill. More importantly, however, field validated methods for the prediction of seismically-induced deformations of reinforced soil structures are rare (Nova-Roessig and Sitar, 1996). Thus, the purpose of our study was to develop an experimental data base of seismic behavior of reinforced soil slopes.

2 EXPERIMENTAL PROCEDURES

2.1 *Experimental Set Up*

All of the slopes in our study were inclined 63.4° from the ground surface (2V:1H). Monterey #0/30 sand was used for the backfill, and was placed via dry pluviation. The backfill in the first three models was placed at a relative density (D_r) of 55% and had a peak, plane strain friction angle and unit weight of 39.5° and 15.6 kN/m^3, respectively. The rest of the models were built with a denser backfill (D_r=75%), which had a friction angle of 42.5° and unit weight of 16.2 kN/m^3. The backfill was dilative in all cases.

The models were built using the same materials and construction methods as those used in previous, static centrifuge studies on reinforced soil slopes (Zornberg, 1994; Zornberg et al., 1998). The use of similar materials and building techniques enabled the models to be designed to a true, static factor of safety of about 1.5 (Nova-Roessig, *in preparation*).

The centrifuge facilities at University of California at Davis were used to perform the model studies. The Schaevitz centrifuge was used to test the first four models. These slopes were constructed to a height of 15.25cm (7.3m, prototype). The first three models had an initial backfill density of 55% and the fourth had an initial relative density of 75%. Three more larger-scale tests were performed at the national centrifuge. The large container allowed for the construction of two slopes, placed in opposing directions with enough unreinforced backfill in between to allow for the formation of potential failure surfaces. The slopes were built to heights of 38.1cm (7.3m, prototype). All of the larger-scale slopes, six total, were constructed using a backfill density of 75%.

Table 1: Observed Seismic Performance of Reinforced Soil Structures (Nova-Roessig and Sitar, 1998)

Earthquake Country, Year	M_L	Horizontal Acceleration	# Walls	Height (m)	Reported Damage
Gemona, Italy, 1976 (Reinforced Earth Co., 1990, 94, 95)	6.4		3	4-6	none
Liege, Belgium, 1983 (Reinforced Earth Co., 1990, 94, 95)	5	0.15g-0.2g	2	4-6	none
Honshu, Japan, 1983 (Reinforced Earth Co., 1990, 94, 95)	7.7	0.1g-0.3g	49		few centimeters of settlement in some of the walls
Edgecumbe, New Zealand, 1987 (Reinforced Earth Co., 1990, 94, 95)	6.3		1	6	vertical movement of the unsecured deck
Loma Prieta, CA, USA 1989 (RE Co., 1990, 94, 95, Collin, et al. , 1992)	7.1	0.1g-0.55g	>20	3-24	none
		0.1g	1	21	2% H movement at top
Northridge, CA, USA 1994 (Reinforced Earth Co., 1990, 94, 95, Stewart et al, 1994, Sandri, 1994)	6.7	0.1g-0.9g	20	4-17	panel spalling, minor cracking
		0.1g	1	16	bulged at center (3% H)
		0.2g	>2	3-15	none
		0.35g	1	12	cracking, 2.5 cm diffrtl settlement
Hyogoken-Nanbu, Japan 1995 (Sitar, 1995, Tatsuoka, et al., 1996)	6.9 (M_w)	up to 0.8g	3	3-8	none
		up to 0.8g	1	6	30 cm lateral deformation, minor panel spalling, cracking

Pellon Tru-Grid™ sheets were used to reinforce all of the slopes. The tensile strength and stiffness of this nonwoven fabric is highly anisotropic. The fabric was placed in the direction of lower stiffness, 8.3 kN/m/m, in all four Schaevitz models and in three of the larger-scale slopes. A stiffer batch of Pellon Tru-Grid™ was used in the three remaining larger-scale slopes. This material, which will be referred to as the "Tru-Grid new" in the paper, is about twice as stiff as the original used by Zornberg (1994). It was placed in the weaker, less stiff direction, 19.3 kN/m/m, in two slopes and in the stiffer direction (137.9 kN/m/m) in one slope.

The geotextile layers were wrapped at the slope face in all of the models, and all of the overlaps exceeded the minimum overlap length of 1.2 m, prototype (Christopher et al., 1990). The Schaevitz slopes had reinforcement length to height ratios of 70%. The larger-scale slopes had ratios of either 70% or 90%. In the smaller-scale models, 10 reinforcements were required to stabilize the slopes to a static factor of safety of 1.5 when using a backfill with an initial relative density of 55%. The denser model ($D_{r,ini}$=75%) required 9 reinforcement layers. 18 layers of Tru-Grid material and 14 layers of Tru-Grid new material were needed to maintain a static factor of safety of 1.5 in the larger-scale models ($D_{r,ini}$=75%). Finally, a model reinforced with the Tru-Grid new material (stiff direction) was constructed using 18 layers.

A larger-scale model is shown in Figure 1. White sand was placed at the transparent container wall along each reinforcement to identify the reinforced soil slopes. Green sand was placed in the backfill behind the slopes to help identify the location of a potential failure surface. Finally, black sand markers were placed at regular horizontal spacing to monitor lateral and horizontal displacements.

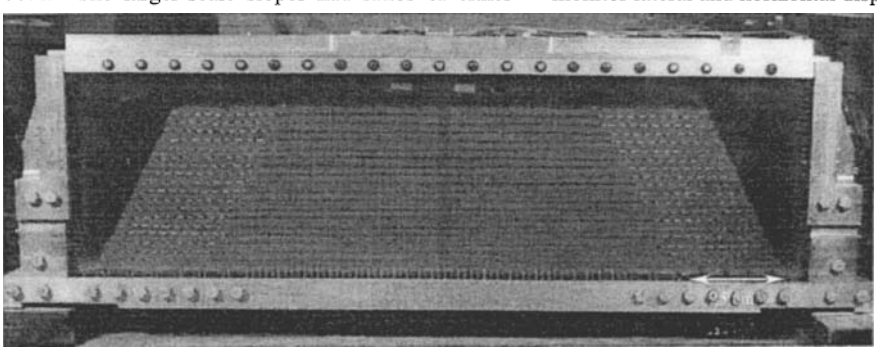

Figure 1: Larger-Scale Model with Two Reinforced Soil Slopes

2.2 *Input Motions and Instrumentation*

Various sinusoidal and earthquake motions were used to shake the models. Initially, the models were shaken with low amplitude sinusoids to observe elastic behavior and then shaken with 8 to 12 earthquakes. The slopes were also shaken with earthquakes having a broad range of frequency content and duration, including the El Centro, Loma Prieta and Kobe earthquakes. The maximum accelerations were scaled to produce peak foundation accelerations of 0.11g to 0.86g (prototype). Accelerations were recorded at the metal base, the foundation layer, along the slope height and along the top of the backfill. Lateral deformations and vertical settlements were also monitored.

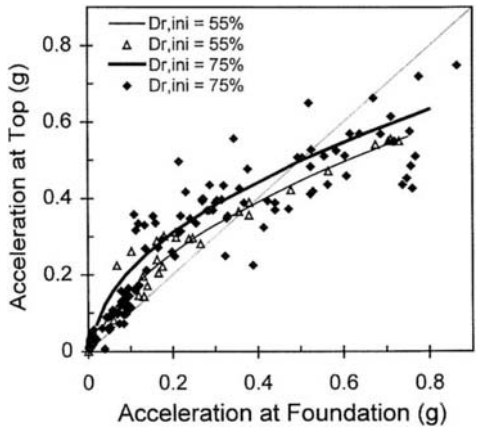

Figure 2: Amplification of the Input Motion

3 MODEL TEST RESULTS

3.1 *Amplification of Motions*

The peak accelerations measured at the foundation versus those measured near the top of the slopes are shown in Figure 2. Amplifications of about 2 were observed during peak foundation accelerations of 0.15g. Amplification of the input motion is accompanied with some shearing and occurs when the input motion at the foundation has a peak acceleration less than about 0.4g in the models with an initial backfill density of 55% and 0.5g in the denser models ($D_{r,ini}$=75%). Shaking the slopes with stronger base motions results in deamplification and significant vertical and lateral movement.

3.2 *Mode of Deformation*

None of the reinforcements ruptured in any of the models even though the slopes deformed significantly. In fact, a close examination of the reinforcement sheets during the post-testing dissection did not reveal any areas of localized straining. In general, the slopes deformed in a ductile manner without a distinct failure surface. Figure 3 shows the displacement vectors of the black sand markers before and after dynamically testing one of the models on the national centrifuge ($D_{r,ini}$=75%). Although some movement occurred in the backfill behind the slope, most of the shearing was found near the crest of the slope and distributed throughout the reinforced soil zone.

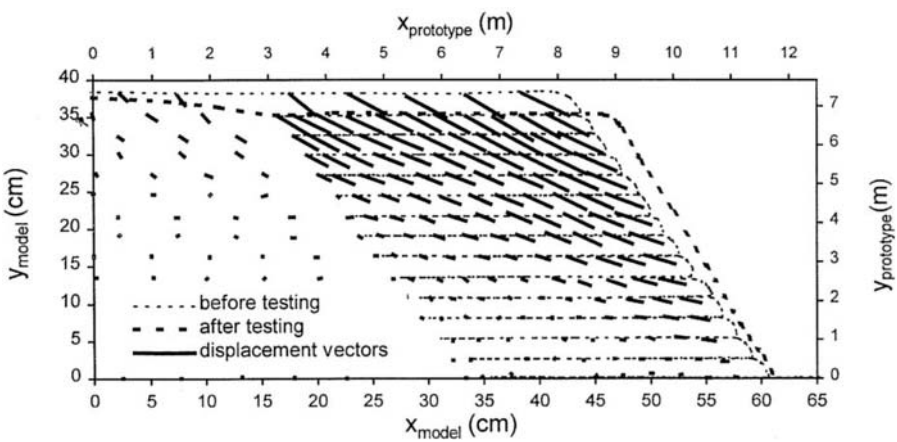

Figure 3: Displacement Vectors of Black Markers Before and After Shaking

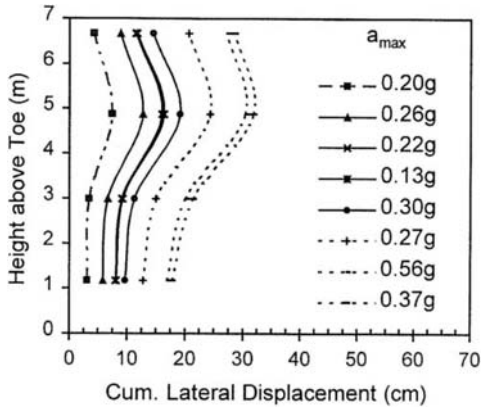

Figure 4: Cumulative Displacement of Slope Face

Figure 4 is a schematic of the cumulative displacements of the slope face after a series of earthquake events for a model reinforced with the Tru-Grid new material (L=70%H, $D_{r,ini}$=75%). Initially, horizontal deformations were greatest around the midheight of the slopes causing the face to curve outward, which is consistent with field reports which note bulging near the center of the walls.

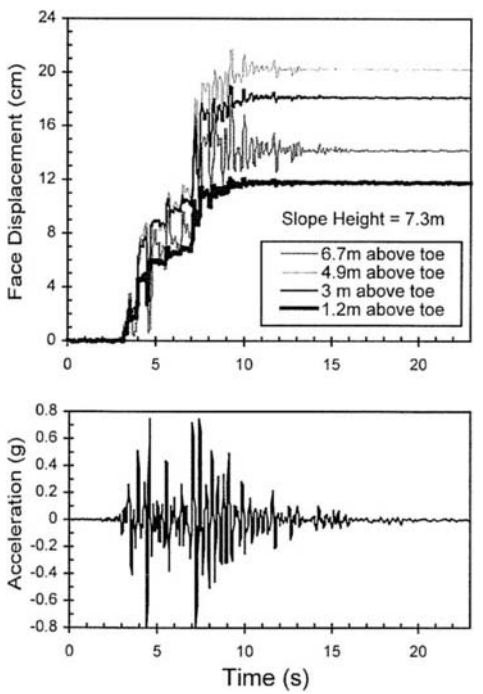

Figure 5: Displacement Behavior of Slope Face Under Seismic Loading

Time histories of the foundation acceleration and lateral displacements of the slope face are included in Figure 5 for a slope reinforced with the Tru-Grid material (L=90%H, $D_{r,ini}$=75%) and shaken with a Kobe event. The plot shows that lateral displacements occur in a step-like manner whenever the yield acceleration is exceeded.

3.3 *Lateral Displacements*

Effect of Backfill Density: Figure 6 shows a plot of the yield acceleration normalized by the maximum acceleration at the foundation versus the maximum observed lateral deformation normalized by the height of the structure. The data shows that the denser slopes ($D_{r,ini}$=75%) generally deform less than the slopes with an initial backfill density of 55%.

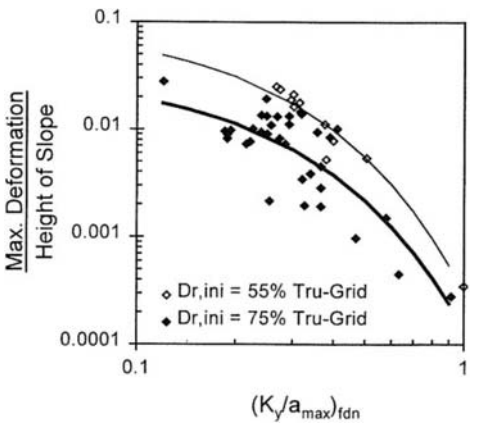

Figure 6: Effect of Backfill Density on Seismically-Induced Deformations

Effect of Reinforcement Properties: The effect of the reinforcement stiffness on the overall magnitude of deformations is illustrated in Figure 7. In general, seismically-induced deformations decrease with increasing reinforcement stiffness. Our data also indicate that deformations are not strongly affected by the reinforcement length for slopes with length to height ratios between 70% and 90%, which is typical for field conditions (Nova-Roessig, *in preparation*).

Implications for Design: The results of our studies do not support the assumptions of traditional limit equilibrium-based design methods. In fact, a discrete failure surface did not form behind the reinforced slope, the slope did not deform rigidly in

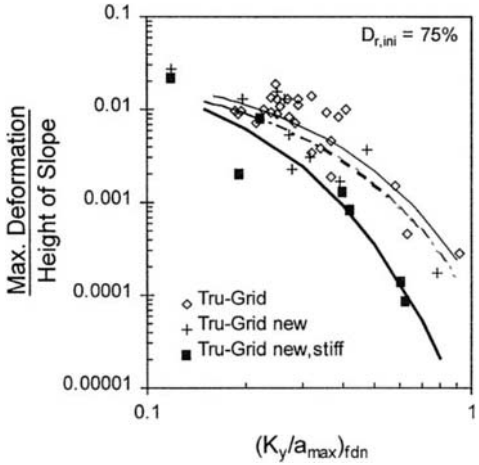

Figure 7: Effect of Reinforcement Stiffness on Seismically-Induced Deformations

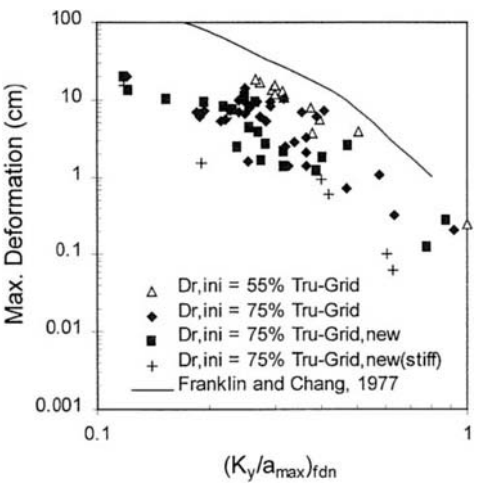

Figure 8: Deformation-Based Seismic Design

a block-like, outward motion, and deformations occurred throughout the reinforced zone near the crest. Figure 8 shows the data from the current studies and a correlation derived by Franklin and Chang (1977) for the response of dams and embankments at soil sites during the San Fernando earthquake. The Franklin and Chang data provide a relation between the expected deformation and the yield acceleration and peak ground acceleration, which can be used for a deformation-based design. The data presented here show similar trends and suggest that an empirically-based approach to the evaluation of seismically-induced deformations of reinforced soil slopes is feasible.

4 CONCLUSIONS

Amplification and deamplification effects should be considered in the seismic design of the reinforced soil structures. In general, amplification occurs when the maximum acceleration of the input motion is less than 0.4g to 0.5g, depending on the backfill density, and deamplification occurs when the input motion is stronger. These results compare well with similar seismic field data at soil sites.

Seismically-induced deformations are directly affected by the reinforcement stiffness and backfill density. Our results also indicate that the length of the reinforcement does not directly influence deformations. Slope deformations occur in a ductile manner, and lateral displacements can occur even under relatively small foundation accelerations. "Failure," defined as the development of very large deformations, occurrs as a result of shearing distributed throughout the reinforced soil mass, without the appearance of a distinct failure surface.

The seismic response of reinforced soil slopes observed in these studies is not consistent with limit equilibrium-based design methods, which assume a discrete failure plane in the backfill behind the reinforced soil mass and rigid outward movement of the slope. Thus, we propose that a deformation-based design method should be used for the design of reinforced soil slopes under seismic loading.

ACKNOWLEDGEMENTS

This research was done at the University of California, Berkeley as part of a research project funded by the California Department of Transportation, Award No. RTA-59A130-5. Special thanks is extended to the staff at the Schaevitz and National centrifuge facilities at University of California at Davis, especially Professor Bruce Kutter, Dr. Dan Wilson and Messrs. Tom Kohnke, Hideo Nakajima and Bill Sluis.

REFERENCES

Christopher, B.R., Gill, S.A., Giroud, J.P., Juran, I., Mitchell, J., Schlosser, F., and Dunnicliff, J. (1990). *Design and Construction Guidelines for Reinforced Soil Structures*, Vol. I, Report No. RD-89-043, FHWA, U.S. Department of Transportation.

Collin, J.G., Chouery-Curtis, V.E., and Berg, R.R. (1992). "Field Observations of Reinforced Soil Structures under Seismic Loading," *Proceedings*

of the International Symposium on Earth Reinforcement Practice, Fukuoka, Japan, A.A. Balkema, pp223-228.

Franklin, A.G., and Chang, F.K. (1977). *Earthquake Resistance of Earth and Rock-fill Dams: Permanent Displacements of Earth Embankments by Newmark Sliding Block Analysis*, Report No. 5, Corps. of Engineers, Waterways Experiment Station, Soils and Pavement Laboratory.

Nova-Roessig, L. and Sitar, N. (1996). "A Review of Seismic Design Methods for Reinforced Soil Walls and Slopes," Progress Report prepared for the California Department of Transportation, Geotechnical Report No. UCB/GT/95-06.

Nova-Roessig, L. and Sitar, N. (1998). "Centrifuge Studies of the Seismic Response of Reinforced Soil Slopes," *Proceedings of the Third Geotechnical Engineering and Soil Dynamics Conference*, Special Publication No. 75, ASCE, Vol. 1, pp458-468.

Nova-Roessig, L. (*in preparation*). "Centrifuge Studies of the Seismic Response of Reinforced Soil Slopes," Ph.D. Thesis, University of California, Berkeley.

The Reinforced Earth Company. (1990). *An Investigation of Reinforced Earth Structures Impacted by the Loma Prieta Earthquake*.

The Reinforced Earth Company. (1994). *Performance of the Reinforced Earth Structures Near the Epicenter of the Northridge Earthquake, January 17, 1994*.

The Reinforced Earth Company. (1995). *Reinforced Earth Structures in Seismic Regions*.

Sandri, D. (1994). "Retaining Walls Stand Up to the Northridge Earthquake," *Geotechnical Fabrics Report*, June/July issue, Industrial Fabrics Association International, pp30-31.

Sitar, N. editor (1995). "Geotechnical Reconnaissance of the Effects of the January 17, 1995, Hyogoken-Nanbu Earthquake, Japan," EERC, Rep. No. UCB/EERC-95/01, University of California.

Stewart, J.P., Seed, R.B., Riemer, M., and Zornberg, J.G. (1994). "Geotechnical Structures: Northridge Earthquake," *Geotechnical News*, BiTech Publishers, Ltd., pp59-62.

Tatsuoka, F., Tateyama, M., and Koseki, J. (1996). "Performance of Soil Retaining Walls for Railway Embankments," *Soils and Foundations*, Special Issue on Geotechnical Aspects of the January 17, 1995, Hyogoken-Nanbu Earthquake, pp311-324.

Zornberg, Jorge G. (1994). "Performance of Geotextile-Reinforced Soil Structures," Ph.D. Thesis, University of California, Berkeley.

Zornberg, J.G., Sitar, N., and Mitchell, J.K. (1998). "Performance of Geosynthetic Reinforced Slopes at Failure," *Journal of Geotechnical and Geoenvironmental Engineering*, Vol. 124, No.8.

Earthquake Geotechnical Engineering, Sêco e Pinto (ed.) © 1999 Balkema, Rotterdam, ISBN 90 5809 116 3

Evaluation of residual displacement of slopes during earthquake based on a simple cyclic loading model

A.Wakai & K.Ugai
Gunma University, Kiryu, Japan

ABSTRACT: A series of numerical analyses of slopes are presented. The horizontal acceleration is applied to the base of the ground. The histories of acceleration response and the residual displacement of slopes during excitation are predicted. Analyses are based on the 2D dynamic elasto-plastic FEM. A simple cyclic loading model, that simulates the $G-\gamma$ and $h-\gamma$ relationships commonly observed in soil element tests, is applied to the soft clayey ground. The results obtained by the analysis are useful to evaluate the safety of slopes against earthquakes.

1 INTRODUCTION

The dynamic elasto-plastic FEM makes it possible to evaluate the dynamic response of the system, considering the stress-strain relationships of soils. If a reasonable constitutive model is applied to the FEM, the sliding displacement of slopes caused by an earthquake can be predicted precisely.

There have been a few analytical approaches to this topic. Griffiths et al. (1988) has conducted 2D and 3D dynamic analyses of a fill dam. The multi-surface plasticity model, in which the hysteretic characteristics of soils were properly considered, was applied to the problem. The calculated residual deformation has not been referred to in the report. Woodward et al. (1994) has shown that similar results can be obtained by the elasto-perfectly plastic model. Rayleigh damping was introduced in the analyses. Toki et al. (1985) has analyzed the sliding displacement of slope, using a newly proposed 2D dynamic method. In these analyses, joint elements were inserted between each element. Ugai et al. (1996) has analyzed simple homogeneous slopes by the 2D and 3D dynamic FEM. The elasto-perfectly plastic model and Rayleigh damping were applied to the problem. It has been shown that the 3D end effects had great influence on the residual displacement of slopes.

Wakai et al. (1997) has reported numerical simulations for a dynamic centrifuge test of an embankment. The experimental results could be well simulated by the 2D dynamic elasto-plastic FEM. They applied a newly proposed undrained cyclic loading model to the soft clayey ground under the embankment. The $G-\gamma$ and $h-\gamma$ relationships of soils are properly considered in the model. They concluded that the hysteretic characteristics on the stress-strain relationships of soils were very important to analyze such a problem.

In this paper, numerical simulations for a series of dynamic centrifuge tests of an embankment (Tamoto et al., 1997) are presented. These experiments are similar to the one which has been referred to in the literature (Wakai et al., 1997). The model embankment was constructed on soft clayey ground. The horizontal acceleration was applied to the base of the ground. The residual displacement of the slope and the ground were observed and sketched after excitation.

The numerical analyses in this paper are based on the 2D dynamic elasto-plastic FEM in which the above-mentioned cyclic loading model (Wakai et al., 1997) is applied to the ground. The main objective of this study is to simulate the experimental results of the centrifuge tests.

2 ANALYTICAL MODEL

2.1 *Model embankment*

The embankment that consists of a mixture of clay and sand was constructed on the soft clayey ground. The centrifugal acceleration of the tests is 50G. Figure 1 shows the sketch of 2D finite element meshes in the prototype scale, that is, 50 times the size of the ground model. As seen in Figure 1, the ground is composed of 5.0m thickness of normally consolidated clay and 3.75m thickness of dense sand. The height of the embankment is 2.0m. It should be noted that a 0.25m thickness sand layer (sand mat) is

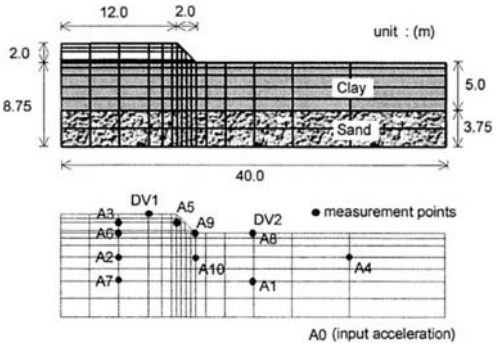

Figure 1. A diagram of ground and slope with the discretised finite element mesh for the analyses (**Case M1**).

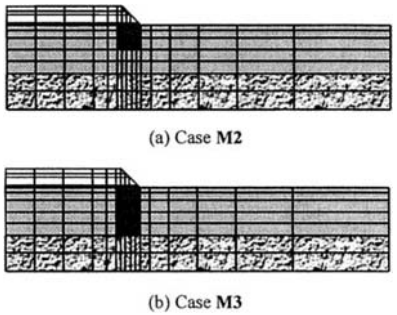

Figure 2. The discretised finite element meshes in **Cases M2** and **M3.**

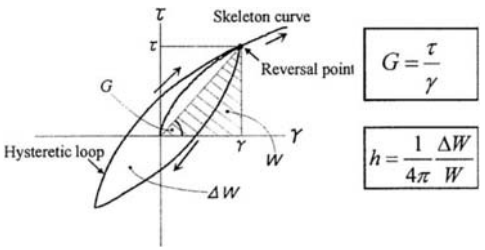

Figure 3. A typical $\tau-\gamma$ relationship of soil.

inserted at the bottom of the embankment, which has not been described in Figure 1. In the FE analyses, the bottom of the ground is perfectly fixed and both sides of the analytical region is fixed horizontally and can be moved vertically. The experimental case illustrated in Figure 1, which is no improvement case, is called as **Case M1** in this paper.

The rests of the experimental cases are **Case M2** (half improved case) and **Case M3** (fully improved case). The FE meshes correspond to each case are shown in Figure 2. In the figure the areas painted out as black indicate the soil improvements, i.e., the cement stabilized soil. In these two cases the soil improvements are inserted under the shoulder of the model embankment. The effect of the soil improvements can be evaluated in these cases.

2.2 *Constitutive model for the ground*

In dynamic analyses, it is very important to consider the hysteretic characteristics on the stress-strain relationships of soils. In this study the above-mentioned cyclic loading model is applied to the ground. The characteristics of this cyclic loading model have been examined by the 1D vibration analyses in the previous paper (Wakai et al., 1997). In these analyses, it was also indicated that the modified Hardin-Drnevich model (H-D model) with Masing's rule gave a much smaller displacement response value. Generally, experimental evidence from various soils have shown that even if the strain amplitude becomes larger, the value of h is usually $20\sim30\%$ at most. However, the value of h becomes more than 50% in the region of large strain when the H-D model is adopted. On the other hand, it was shown that the $h-\gamma$ relationships of soil were properly considered in this model.

In this study, the soils in the model ground are assumed to show the hysteretic characteristics based on the undrained $G-\gamma$ and $h-\gamma$ curves. These relationships can be easily determined by the element tests subjected to cyclic loading. G is the secant shear elastic modulus and h is the damping ratio. The concepts of these parameters are familiar. It should be noted that we assume that the liquefaction of soils will never occur during excitation. This is a basic assumption to apply this model.

Figure 3 shows typical hysteretic curves on the $\tau-\gamma$ relationships. τ and γ are given as follows :

$$\tau=\sqrt{\left(\sigma_x-\sigma_y\right)^2/4+\tau_{xy}{}^2} \tag{1}$$

$$\gamma=\sqrt{\left(\varepsilon_x-\varepsilon_y\right)^2+\gamma_{xy}{}^2} \tag{2}$$

The reversal of loading direction is judged by the sign of the γ increment, $d\gamma$.

The skeleton curves are given by the following hyperbolic equation.

$$\tau=\frac{G_0\gamma}{1+G_0\gamma/\tau_f} \tag{3}$$

Of course, it cannot predict a residual deformation that accumulates with the number of cycles under constant stress amplitude.

As seen in Figure 3, G_0 is the inclination of the initial part of the skeleton curve and τ_f is the undrained shear strength. The hysteretic loops are defined as Eq.(4).

$$\tau^* = \frac{a\gamma^{*n} + G_0\gamma^*}{1 + b\gamma^*} \tag{4}$$

$$\tau^* = \sqrt{\{(\sigma_x - \sigma_{xa}) - (\sigma_y - \sigma_{ya})\}^2 / 4 + (\tau_{xy} - \tau_{xya})^2} \tag{5}$$

$$\gamma^* = \sqrt{\{(\varepsilon_x - \varepsilon_{xa}) - (\varepsilon_y - \varepsilon_{ya})\}^2 + (\gamma_{xy} - \gamma_{xya})^2} \tag{6}$$

where b and n are material constants. The value of a is determined by b,n and the coordinates of the previous reversal point so that the hysteretic loop is exactly closed. The suffix 'a' attached to each component in Eqs.(4) and (5) indicates that these are the values at the previous reversal point.

G_0 and τ_f decide the $G-\gamma$ curve as shown in Figure 4. In this figure, the strain amplitude γ is normalized based on the reference strain γ_{G_0} $(=\tau_f / G_0)$ which gives $G = 0.5 \cdot G_0$. This is exactly the same in the H-D model. On the other hand, b and n decide the $h-\gamma$ curve as shown in Figure 5. In the graphs, the parameter b is expressed as $b \cdot \gamma_{G_0}$ which is the product of b and γ_{G_0}. The area of the enclosed hysteretic loops is calculated by numerical integrations to give these $h-\gamma$ relationships. It can be seen that the increase of b and n, decreases the magnitude of the damping ratio h. In general use, $b \cdot \gamma_{G_0} \geq 0.5$ and $n > 1$ are recommended. It is found that in cases where $b \cdot \gamma_{G_0}$ equals 0.5, $h-\gamma$ curve corresponds to the one derived from the H-D model with Masing's rule. As discussed before, if such a relationship is adopted, h is overestimated in the region of large strain. This curve is far removed from the actual property of soils.

3 SIMULATION OF THE CENTRIFUGE TESTS

3.1 *Material constants*

Table 1 shows the material constants for the 2D analysis. The embankment and the cement stabilized soil are assumed to be elasto-perfectly plastic material. The analyses are composed of 2 steps.

(1) The first step is to simulate the process of consolidation in which parameters under drained conditions are used. The increase of undrained shear strength of clay ground is estimated in this process. For the clayey layer, $\tau_f / p_v' = 0.520$ is adopted. This is based on the

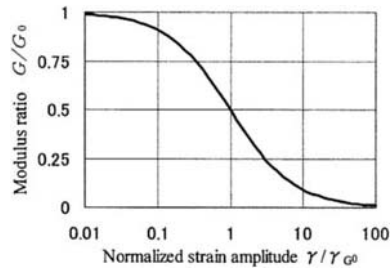

Figure 4. Assumed $G-\gamma$ relationships in the proposed model.

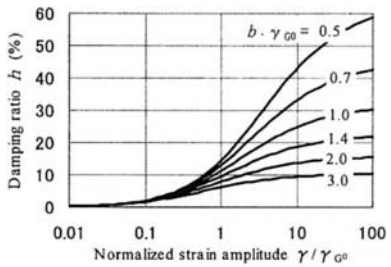

(a) $n = 2$

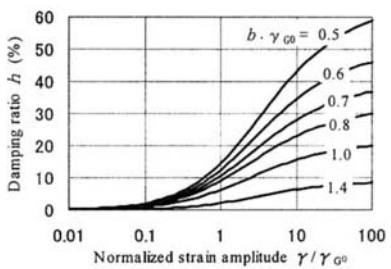

(b) $n = 3$

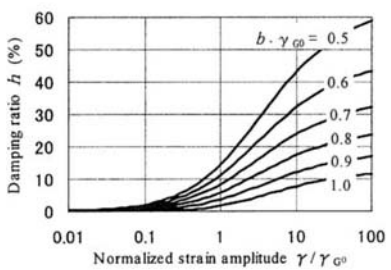

(c) $n = 5$

Figure 5. Variations of $h-\gamma$ relationships after parameter values have been altered.

Table 1. Material constants used in 2D analyses.

		E(kPa)	ν	c(kPa)	ϕ(deg)	ψ(deg)	$\gamma(kN/m^3)$	$b\gamma_{G_0}$	n	K_0
Embank-ment	consolidation	1820	0.3	13.0	6.65	0	16.7	—	—	—
	excitation	1960	0.4	13.0	6.65	0	16.7	—	—	—
Sand mat	consolidation	4550	0.3	9.8	30	0	17.2	—	—	—
	excitation	4910	0.4	9.8	30	0	17.2	—	—	—
Stabilized soil	consolidation	106700	0.286	235	0	0	5.3	—	—	0.4
	excitation	123600	0.49	235	0	0	15.1	—	—	—
Clay (ground)	consolidation	1960	0.286	*2	—	0	7.4	—	—	0.4
	excitation	*1	0.49	*2	—	0	17.2	0.80	3.0	—
Sand (ground)	consolidation	17100	0.3	0	40	10	7.4	—	—	0.43
	excitation	19600	0.49	49	—	0	17.2	0.80	3.0	—

*1 : $G_0/\tau_f = 516$, $E = 2(1+\nu)\cdot G_0$.

*2 : $\tau_f / p_v' = 0.520$.

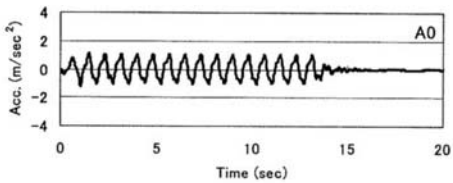

(a) input acceleration (**A0**)

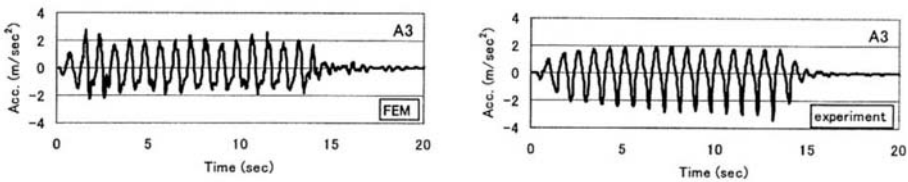

(b) calculated and observed acceleration history at **A3**

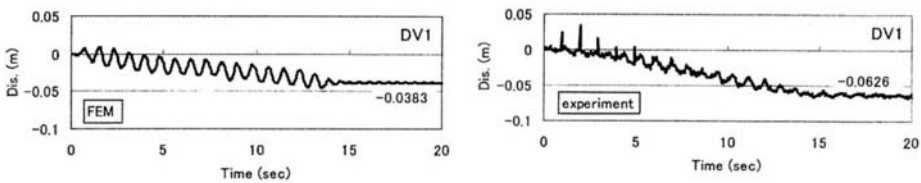

(c) calculated and observed displacement history at **DV1**

Figure 6. The histories of acceleration and displacement at each point (**1st** step, **Case M1**).

results of triaxial compression tests. p_v' is the vertical stress in the ground. To simplify the analyses, the relationship of $G_0/\tau_f = 516$ (Ishihara, 1976) is applied to the clay.

(2) The second step is the dynamic analysis. During this process, parameters under undrained conditions are used. Rayleigh damping is also adopted. The values of $b\cdot\gamma_{G_0}$ and n are assumed to be 0.8 and 3.0, respectively. However, it is desirable that the $h-\gamma$ relationships of soil are determined by the results of cyclic loading tests under undrained conditions. The input waves used in the analyses are the time history of horizontal acceleration on the shaking table (**A0**) observed in the centrifuge test.

3.2 *History of acceleration and displacement*

As stated before, we treat three experimental cases, **Cases M1**, **M2** and **M3**. Each case is composed of four steps of excitations (**1st**, **2nd**, **3rd** and **4th**). Each

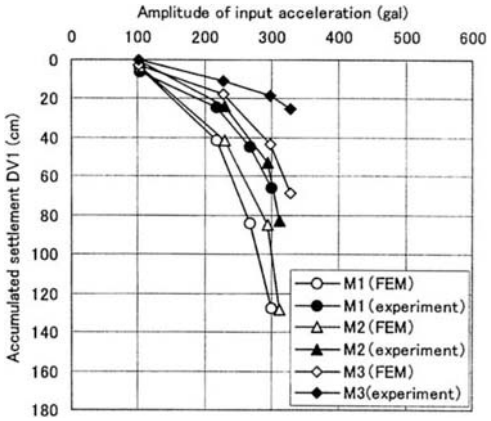

Figure 7. Accumulated residual displacement in each case.

step of excitation uses each different waves so that the amplitude of input sinusoidal waves gradually becomes larger, for example, 1st /100gal, 2nd/200gal, 3rd/300gal, 4th/400gal.

Figure 6 shows the time histories of horizontal acceleration at the center of the embankment (**A3**) and vertical displacement at the top of the embankment (**DV1**) at 1st step of **Case M1**. The location of these measuring points have already been shown in Figure 1. Both the calculated and the measured results are presented in Figure 6. Acceleration **A0** is the input wave for the analyses, which has been measured on the shaking table during the tests. A strong correlation between FEM and the centrifuge test can be seen in the histories of acceleration at **A3** and displacement at **DV1**.

The analytical and experimental results at other points are neglected here. Only the accumulated residual displacement (**DV1**) at each step is shown in Figure 7. The horizontal and vertical axes in the figure denote the amplitude of input sinusoidal waves and the accumulated settlement at the top of the embankment (**DV1**), respectively. It is found that the experimental results can be well simulated by the FEM. Also, it should be noted that the results in **Cases M1** and **M2** are similar to each other, while the result in **Case M3** gives very small residual displacement. It suggests that the effect of the soil improvement in **Case M2** is very small.

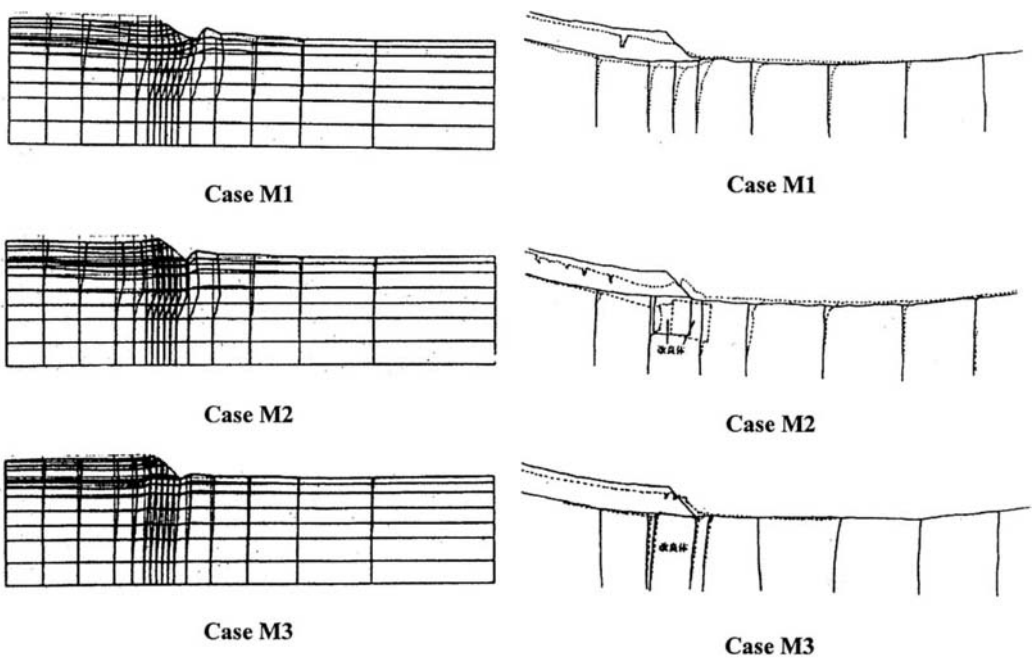

(a) FEM (2nd step in each case)

(b) centrifuge tests (4th step in each case) [after Tamoto et al. (1997)]

Figure 8. Residual deformation of the system after excitation.

The residual deformation after earthquakes in each case can be evaluated by the dynamic elasto-plastic FEM and the optimum depth of soil improvement can be determined by such analyses.

3.3 *Residual deformation of the whole system*

The residual deformations of the system calculated by the 2D dynamic FEM and observed in the centrifuge tests are sketched in Figure 8. Figure 8(a) shows the analytical results at 2^{nd} step in each case. In Figure 8(a), the dotted lines and the solid lines indicate the shapes before deformation and after excitation, respectively. On the other hand, Figure 8(b) shows the experimental results at 4^{th} step in each case. In Figure 8(b), the dotted lines and the solid lines indicate the shapes after excitation and before deformation, respectively. It should be noted that the deformation shown here includes the settlement caused by the self-weight of the ground before excitation.

It is found that the general tendency on the residual deformation of the system observed in the centrifuge tests is very close to the FE results. In **Case M1**, the sliding displacement can be seen under the slope. Large settlement and small upheaving can be seen at the top and the toe of the slope, respectively. The deformation of each element in the sandy layer is very small, while the clayey layer is found to be so much deformed after excitation. It suggests that the stiffness and the shear strength of the clayey layer under the slope have larger influence on the seismic stability of the embankment.

In **Cases M2** and **M3**, the soil improvement has been achieved. In these cases, the block of soil improvement was squeezed out during excitation. As for the deformation modes of the soil improvement, there is a large difference between **Cases M2** and **M3**. The block of soil improvement slid laterally in **Case M2**, while it rotated around the bottom in **Case M3**. This is why the effect of the soil improvement in **Case M2** is much smaller than in **Case M3**. In **Case M2**, the shear strength of the ground under the soil improvement is not sufficiently mobilized.

4 CONCLUSIONS

(1) The histories of acceleration and displacement observed in the centrifuge tests are well simulated by the 2D dynamic elasto-plastic FEM.
(2) A cyclic loading model presented in this study, that simulates the G- γ and h- γ relationships commonly observed in the element test, is very effective.
(3) The effect of soil improvements could be reasonably evaluated by the analyses proposed in this study.

ACKNOWLEDGEMENTS

The authors are grateful to Mr. Osamu Matsuo and Mr. Mitsu Okamura of the Public Works Research Institute, Ministry of Construction, Japan, for providing the valuable experimental data and to Mr. Takao Shimazu of Taisei Kiso-Sekkei Co., Ltd. for his great help in the research.

REFERENCES

Griffiths, D.V. and Prevost, J.N. (1988). Two- and three-dimensional dynamic finite element analyses of the Long Valley Dam. *Geotechnique* 38:3, 367-388.

Ishihara, K. (1976). *The Basis of Soil Dynamics*, Kajima-Pres., Japan, 196-202 (in Japanese).

Tamoto, S., Matsuo, O., Shimazu, T. and Yokokawa, S. (1997). Dynamic centrifugal model tests for embankment on clay ground (Part 2). *Proc. of the 32th JGS Domestic Conference*, pp.1021-1022 (in Japanese).

Toki, K., Miura, F. and Oguni, Y. (1985). Dynamic slope stability analyses with a non-linear finite element method. *Earthquake Engineering and Structural Dynamics*, 13, 151-171.

Ugai, K., Ida, H. and Wakai, A. (1996). Static and dynamic analyses of slopes by the 3-D elasto-plastic FEM. *Proc. of The 7th International Symposium on Landslides*, Trondheim, Norway, 1413-1416.

Woodward, P.K. and Griffiths, D.V. (1994). Non-linear dynamic analysis of the Long Valley Dam. *Computer Methods and Advances in Geomechanics*, Balkema, 1005-1010.

Wakai, A., Ugai, K., Li, Q., Matsuo, O. and Shimazu, T. (1997). Dynamic elasto-plastic analyses of the sliding displacement of embankment during earthquake. *Proc. of the International Symposium on Deformation and Progressive Failure in Geomechanics*, Nagoya, Japan, pp.635-640.

Earthquake Geotechnical Engineering, Sêco e Pinto (ed.) © 1999 Balkema, Rotterdam, ISBN 90 5809 116 3

Model tests on a seismic failure of an embankment due to soil liquefaction

Y. Sasaki – *Department of Civil and Environmental Engineering, Hiroshima University, Japan*

J. Ohbayashi – *Fudo Construction Company, Japan*

A. Shigeyama – *Penta-Ocean Construction Company, Japan*

Y. Ogata – *Graduate School, Hiroshima University, Japan*

ABSTRACT: A series of model tests on liquefaction induced settlement of an embankment was conducted. Liquefaction of the foundation layer was caused instantaneously by a single shock to the container. Test results revealed that the settlement of an embankment ceased in very short period while the shallow part of soil was in a full-liquefied state. When the liquefied thickness was large enough, model embankment settled with an oscillatory movement. From these observations, it was known that the soil in a post liquefaction state behaved like a viscous fluid.

1 INTRODUCTION

Severe failure of embankments during earthquake is often caused by the liquefaction of the foundation ground. The Yodogawa dike was extensively damaged due to the liquefaction of the 8-10 m thick sand deposit underneath the dike during the Hyogoken-nanbu Earthquake in 1995 (Sasaki & Shimada 1997). The Shiribeshi-toshibetsu-gawa dike failed during the Hokkaido-nansei-oki Earthquake in 1993, again due to the liquefaction of foundation ground (Kaneko et al. 1995). The Kushirogawa river dike and the Tokachigawa river dike experienced failures caused by liquefaction of the lower part of the embankments themselves during the Kushiro-oki Earthquake in 1992 (Sasaki 1994, and Finn et al. 1997). The Hachirogata dike failed due to the liquefaction of foundation ground during the Nihonkai-chubu Earthquake in 1983 (Sasaki et al. 1985). The Aganogawa dike was damaged by the Niigata Earthquake (PWRI 1965).

From these past experiences, although the ground conditions, seismic intensities, and the failure modes are different among each cases, the final settlement of the river dikes due to past earthquakes can be compiled against the initial height of the dikes as shown in Figure 1 (TCCRFE 1996). Even though this figure shows a wide scattering of the past settlements, it seems that there is an upper boundary which could not be exceeded by the observed settlements.

There are very limited data for confirming the rate and process of the dike settlement during the actual earthquake. However, there remains a testimony that the tilting of the Kawagishi-cho apartment house

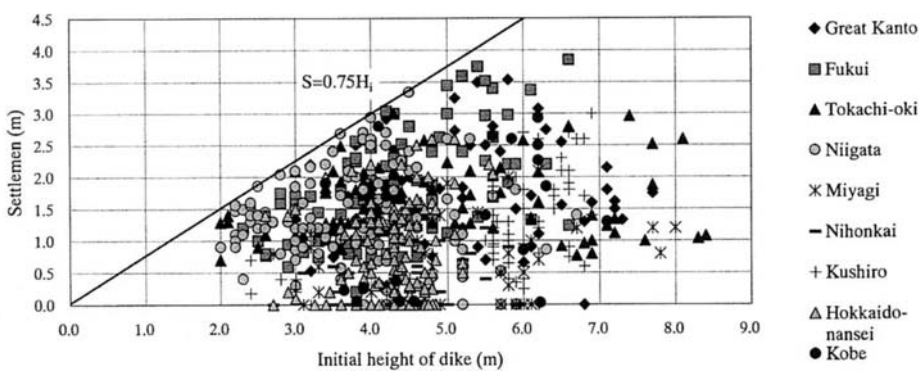

Figure 1. Settlement of dikes due to past earthquakes.

took place very gradually after the cease of the main shock during the Niigata Earthquake (PWRI 1965). Further it was also reported by an eye witness that the section on the Noshiro-minami By-pass, where the pavement failed as shown in Figure 2, was able to pass just after the main shock (Hoku-u Shinpo 1983).

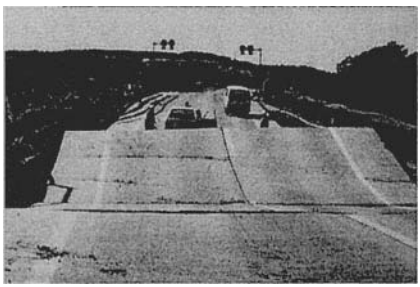

Figure 2. Damage of the Noshiro-minami By-pass.

These experiences imply that, in a certain circumstances, settlements of structures and the deformation of liquefied ground take place after the cease of the shaking.

On the contrary, from the observations during shaking-table tests in laboratories, the settlement of structures above liquefied ground even after the end of shaking is almost never reported to continue except the case reported by Kawasaki et al. (Kawasaki et al. 1998). Kawasaki employed viscous fluid for pore water in the centrifuge shaking test, and reported the continuation of the settlement of the foundation structures after the end of the shaking.

In general, the final settlement of an embankment on a liquefiable layer is considered to be brought about by the deformation of the embankment itself, large deformation of the liquefied layer, and the consolidation of the foundation layer. The large deformation of the foundation layer is consisted of two parts: one is caused during the shaking and the other is caused after the shaking. It is thought that the deformation after the shaking can take place only when the foundation layer loses its strength due to the upward seepage flow.

In order to establish a better method to predict the seismic damage of embankments, it is considered crucial to deeply understand the mechanism of the liquefaction induced deformation and to find out the governing factor which controls the degree of damage of embankments. Here in this paper, soil properties of post-liquefaction state, which may induce the large deformation of liquefied layer is discussed.

2 MODEL TEST

2.1 *Apparatus and Material used*

A loose liquefiable layer of Toyoura sand was made in a container of 30 cm wide 60 cm long and 40 cm deep as illustrated in Figure 3. Specific gravity of the sand used was 2.638, and e_{max} and e_{min} were 0.985 and 0.620 respectively.

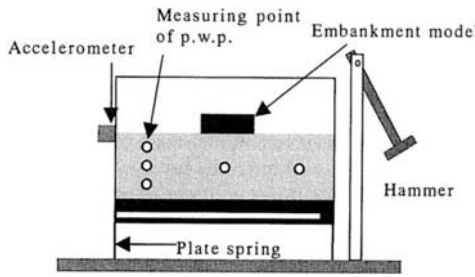

Figure 3. Schematic view of the small scale model test.

The thickness of the layer was varied from 10 cm to 24 cm. Relative density of the liquefiable layer was also varied from 20 % to 60 %.

Embankment loading was modeled by plastic block of 17.6 cm wide by 29 cm long, and its height was varied from 4 cm to 8 cm high as shown in Table 1.

Table 1. Model embankment.

MODEL	W×L(mm)	Height(mm)	Weight(kg)	Density
H	290×176	80	5.79	1.43
M	290×176	64	4.53	1.39
L	290×176	43	3.00	1.38

Liquefaction was caused instantaneously by giving a single shock by hitting the side wall of the container. Pore water pressures at three depths in liquefiable layer and the settlement of the loading block were monitored.

2.2 *Pore Water Pressure*

Pore water pressure measurement suggested that the intended full liquefaction state took place in liquefiable layer in almost every case as illustrated in Figures 4 and 5. In Figure 4, it is shown the case without an embankment and in Figure 5, the case with a model embankment is shown.

It should be noted that the initial pore water pressure just beneath the embankment for the case with an embankment was higher than that at free

field for about 0.2 sec. This is due to the increased initial overburden pressure just beneath the embankment by the dead weight of the embankment.

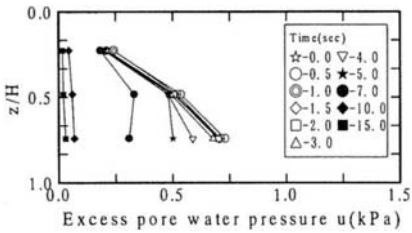

Figure 4. Example of the measured pore water pressure in case of the model ground without embankment.

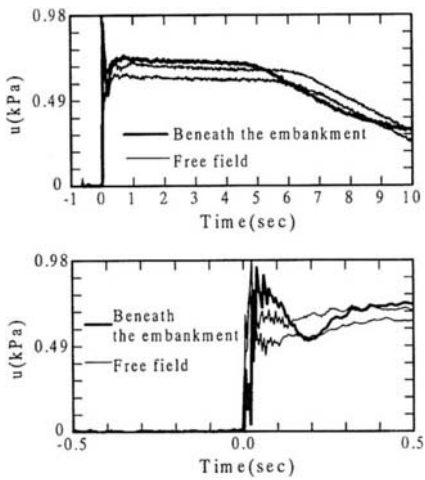

Figure 5 Example of the measured pore water pressure in case of the ground with embankment loading.

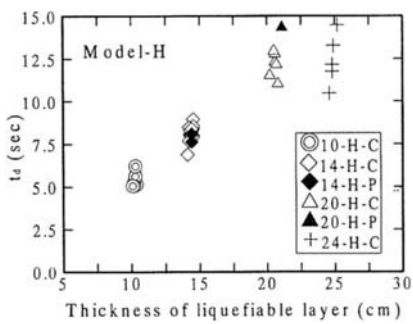

Figure 6. Duration of high pore water pressure versus the thickness of the liquefiable layer.

The pore water pressure was raised to the initial overburden pressure at depth instantaneously along with the given shock, then keeps the highest value for a while, and begins to decrease as consolidation proceeds. The duration of high pore water pressure at 1/4 depth of the liquefiable layer is plotted against the thickness of the liquefiable layer in Figure 6. From this figure, it is known that the duration of high pore water pressure is almost proportional to the liquefiable thickness.

2.3 *Final Settlement*

Final settlements of the heavy loading block (model H) are plotted against the liquefiable thickness in Figure 7. According to this figure, it is known that the final settlement increases with increase of the liquefiable thickness up to about 20 cm thick, however, the settlement does not increase further in the region beyond this thickness. This implies that the settlement amount of the embankment has a certain limit corresponding to its weight.

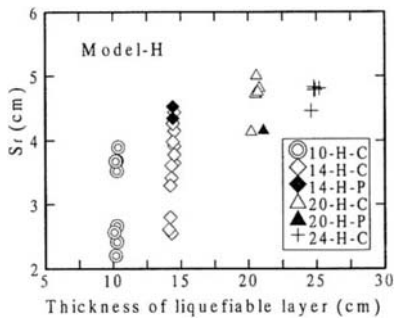

Figure 7. Final settlements versus thickness of the liquefiable layer.

The settlement ratios given by the test results on embankment model H are plotted against the relative density of the liquefiable layer in Figure 8.

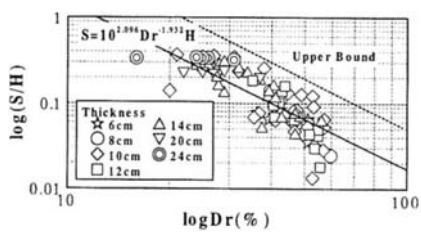

Figure 8. Settlement ratio versus the initial relative density of the liquefiable layer.

Following this figure, it is found that the final settlement can be expressed by the initial relative density and the thickness of liquefiable layer as follows.

$$S = 10^{2.096} \cdot Dr^{-1.932} \cdot H \qquad \cdots(1)$$

where S : settlement, Dr : the initial relative density and H : the thickness of liquefiable layer.
Figure 9 shows an example of the time history of the embankment settlement.

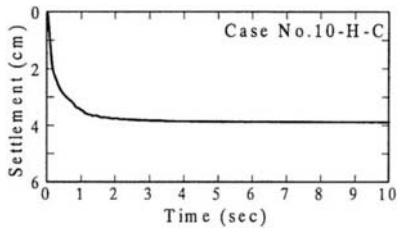

Figure 9. Time history of the embankment settlement.

It is known that the settlement took place in a very short time just after the shaking. The bending point (t_1, S_1) on the time history curve in logarithmic scale was measured as illustrated in Figure 10. As shown in Figures 11 and 12, it should be noted that 50-75 % of the final settlement took place in very short time. The time t_1 is much less compared to the duration of high pore water pressure mentioned before.

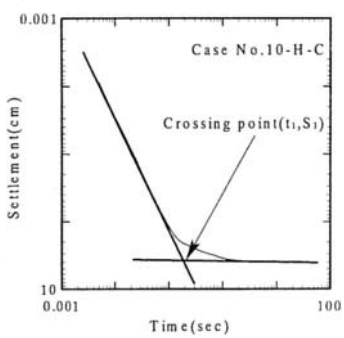

Figure 10. Definition of t_1 and S_1.

From these observations, it could be drawn that there exists a maximum settlement which is governed by the relative density of the layer and the weight of the embankment. If the thickness of the liquefied layer is large enough, which means that the liquefaction continues long enough, then the embankment settles to this amount. However, if the thickness of the liquefied layer is not thick enough, the amount of the settlement is less than this maximum value.

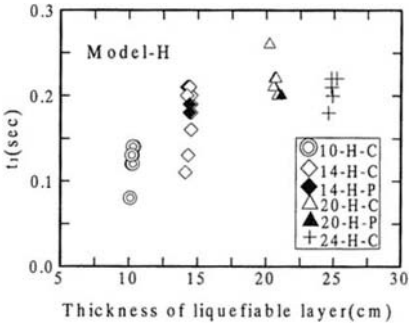

Figure 11. t_1 versus the thickness of the liquefiable layer.

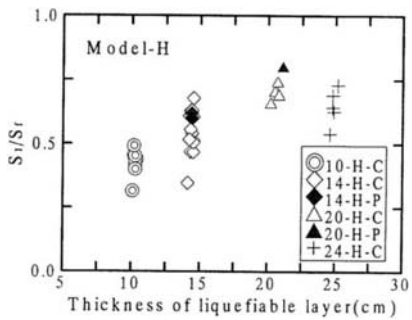

Figure 12. S_1/S_f versus the thickness of the liquefiable layer.

2.4 *Oscillatory Behavior of the Embankment during Settlement*

It should be noted that when the liquefied layer was thicker than 14 cm for light embankment and 20 cm for heavy embankment, the embankment showed the oscillating behavior during settlement as shown in Figures 13 and 14.

This oscillation continued for about 4-5 seconds, which is shorter than the duration of high pore water pressure, t_d. The observed period of the oscillation and the logarithmic decrement are summarized in Table 2.

Table 2. Logarithmic decrement and observed period.

MODEL	H	M	L
Δ	0.668	0.657	0.526
T(sec)	0.74	0.69	0.68

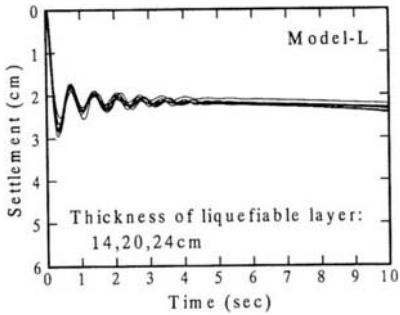

Figure 13. Oscillating time histories of the 9 cases for light embankment.

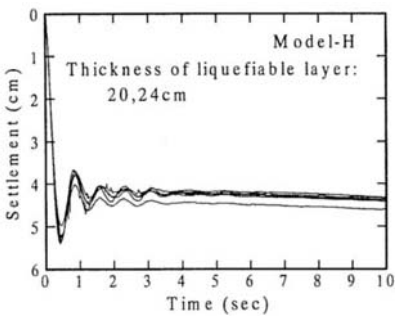

Figure 14. Oscillating time history of 6 cases for the heavy embankment.

3 ANALYTICAL MODELING OF THE EMBANKMENT SETTLEMENT

As mentioned previously, the pore water pressure in the foundation layer was suddenly raised to its initial overburden pressure by the single shock, and the model embankment began to settle into liquefied layer. When the duration of the liquefied state was long enough, the embankment reached to its maximum settlement in about 0.5 sec., then oscillated for a while. This implies that the liquefied layer behaves like a viscous fluid.

Therefore, assuming that the liquefied layer beneath the embankment could be treated as viscous fluid, an equation of motion of floating mass on viscous fluid was derived to simulate the settling behavior of the embankment.

$$W - W\cdot\frac{\ddot{\delta}_1}{g} = 2\rho_2\cdot(\delta_1+\delta_2)\cdot B\cdot g + 2\cdot\rho_2\cdot V\cdot\ddot{\delta}_1 + 2\cdot B\cdot u\cdot\eta \qquad \cdots(2)$$

where, W: weight of the embankment per unit length, ρ_2: density of fluid, δ_1: embankment settlement, δ_2: heaving height of the ground, $2B$: width of embankment, V: volume of fluid which moves with the embankment settlement, u: rate of the moving fluid, η: coefficient of viscosity.

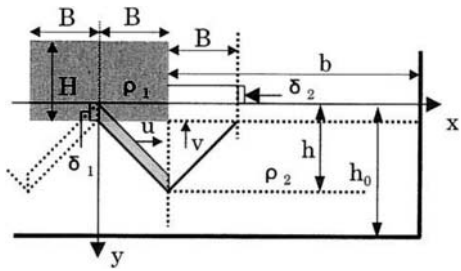

Figure 15. Modeling of the embankment settlement.

First term of the right hand side of the equation (2) is the buoyant force, the second term is inertia force of the moving fluid and the third term is the viscous resistance. If the moving fluid is assumed to be limited within a wedge shaped portion like a bearing capacity problem of smooth foundation on $\phi=0$ material as illustrated in Fig. 16, and $u=\dot{\delta}_1$, then (2) can be derived into equation (3).

$$\ddot{\delta}_1 + 2c\dot{\delta}_1 + \omega_0^2\delta_1 - \frac{H\rho_1}{H\rho_1+B\rho_2}\cdot g = 0 \qquad \cdots(3)$$

where $\omega_0^2 = \frac{2\rho_2 g}{H\rho_1+B\rho_2}$, $c = \frac{\eta}{2(H\rho_1+B\rho_2)}$

Thus the settling motion of the embankment can be given by the equation (4).

$$\delta_1 = \frac{H\rho_1}{2\rho_2}\left\{1 - \frac{\omega_0}{\sqrt{\omega_0^2-c^2}}e^{-ct}\cdot\cos\left(\sqrt{\omega_0^2-c^2}\cdot t - \tan^{-1}\frac{c}{\sqrt{\omega_0^2-c^2}}\right)\right\} \qquad (4)$$

In equation (2), the heaving width of the fluid is dealt to be B, however, at the final settlement state, heaving width should be b. If this is the case, solution of the equation of motion becomes (5).

$$\delta_1 = \frac{b\cdot H\rho_1}{(b+B)\rho_2}\left\{1 - \frac{\omega_0}{\sqrt{\omega_0^2-c^2}}e^{-ct}\cdot\cos\left(\sqrt{\omega_0^2-c^2}\cdot t - \tan^{-1}\frac{c}{\sqrt{\omega_0^2-c^2}}\right)\right\} \qquad \cdots(5)$$

Figure 16 shows the comparison between the measured motion and the calculated settlement. In this calculation, the motion until the first peak ($t<t_p$) was obtained by equation (4), and the motion after

this peak ($t>t_p$) was calculated by equation (6) which was derived from equations (4) and (5).

$$\delta_1 = S_2 - A_0 \cdot e^{-ct} \cdot \cos\left(\sqrt{\omega_0^2 - c^2} \cdot t - \tan^{-1}\frac{c}{\sqrt{\omega_0^2 - c^2}}\right) \quad (6)$$

where $S_2 = \frac{b \cdot H\rho_1}{(b+B)\rho_2}$,

$$A_0 = S_1 \cdot \left(\frac{1}{e^{-ct_P}} + a_0 \cdot \cos\left(\sqrt{\omega_0^2 - c^2} \cdot t_P - \tan^{-1}\frac{c}{\sqrt{\omega_0^2 - c^2}}\right)\right) - \frac{S_2}{e^{-ct_P}}$$

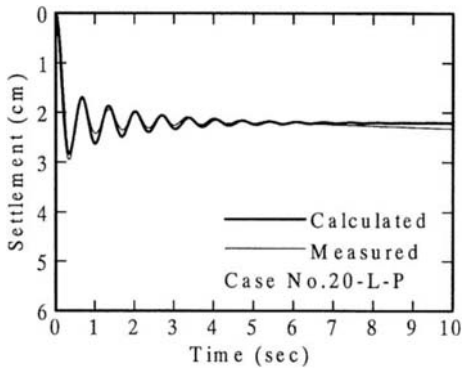

Figure 16. Comparison between measured and calculated motion of the embankment.

As shown by this figure, above mentioned modeling can well simulate the measured motion of the embankment. It is found that the viscosity coefficient of the liquefied soil calculated from measured period and logarithmic decrement is 40-50 Poise, which is equal to 4000-5000 times of water.

4 CONCLUSION

It was found that there is a fluid like zone near the surface of the liquefied layer for a while. This is a consequence of the upward seepage flow due to the built up pore water pressure. During this short stage, 50 to 75 % of the final settlement of the embankment is brought about.

It was seen that the settlement of an embankment is affected by the thickness of liquefied layer, the relative density of liquefiable layer, and the weight of the embankment on the liquefied layer.

Furthermore, it was found that the soil in a post liquefaction state behaves like a viscous fluid which has 4000 to 5000 times viscosity than that of water.

Although these findings are based upon the test results, that is caused after the cease of shaking, which might be an extreme case, it is considered that the viscous feature affects the settlement during the shaking in some cases. Therefore further study on the field condition which governs the embankment failure process is needed.

ACKNOWLEDGMENT

A part of this study was supported by a grant from the River Environment Fund. Authors are grateful for this support.

REFERENCES

Finn, W. D. L., Sasaki, Y. & Wu, G. (1997): Simulation of Response of the Kushiro River Dike to the 1993 Kushiro-oki and 1994 Hokkaido Toho-oki Earthquakes, Proc. 14th ICSMFE, pp. 99-102.

Hashimoto, H., Sasaki, Y., Matsuo, O. & Matsumoto, H. (1985): Damage to Facilities, Report on the Disaster caused by the Nihonkai-chubu Earthquake of 1983, Report of PWRI, MOC, pp. 147-207 (in Japanese).

Hoku-u Shinpo (1983): Record on the Disaster caused by the Nihonkai-chubu Earthquake, pp. 154 (in Japanese).

Kaneko, M., Sasaki, Y., Nishikawa, J., Nagase, M. & Mamiya, K. (1995): River Dike Failure in Japan by Earthquakes in 1993, Proc. 3rd Int. Conf. on Recent Advances in Geotechnical Engineering and Soil Dynamics, pp. 495-498.

Kawasaki, K., Sakai, T., Yasuda, S., & Satoh, M.(1998): Earthquake-induced Settlement of an Isolated Footing for Power Transmission Tower, Centrifuge 98 , Proc. Int. Conf. Centrifuge, pp. 271-276.

PWRI (Public Works Research Institute) (1965): Report on Niigata Earthquake, Report of the PWRI, MOC, vol. 125, pp. 51 (in Japanese).

Sasaki, Y., Oshiki, H. & Nishikawa, J. (1994): Embankment Failure caused by the Kushiro-oki Earthquake of January 15, 1993, Performance of Ground and Soil Structures during Earthquakes, Special Vol. 13th ICSMFE, pp. 61-68.

Sasaki, Y. & Shimada, K. (1997): Yodogawa Dike Damage by the Hyogoken-nanbu Earthquake, Seismic Behavior of Ground and Geotechnical Structures, Proc. Discussion Session 14th ICSMFE, pp. 307-316.

TCCRFE (Technical Committee on Countermeasure for River Facilities against Earthquake)(1996): Committee Report pp. 39 (in Japanese).

Earthquake Geotechnical Engineering, Sêco e Pinto (ed.) © 1999 Balkema, Rotterdam, ISBN 90 5809 116 3

Earthquake response analysis of a high embankment on an existing hill slope

S. Iai, K. Ichii & Y. Sato
Port and Harbour Research Institute, Japan

R. Kuwazima
Hokkaido Development Bureau, Japan

ABSTRACT: A 65 m high embankment constructed on an existing hill slope was shaken by an earthquake of magnitude 7.8 in 1993 in Kushiro, Japan. A complete set of seismic array records was obtained, registering a peak acceleration of 0.5g on the slope of the embankment. Despite the strong shaking, the high embankment suffered only minor damage. Two-dimensional non-linear seismic analysis is conducted to evaluate the performance of the embankment during the 1993 earthquake. The analysis is successful in approximating the residual displacements of the embankment, involving settlement at the shoulder and heave at the toe, with horizontal displacements from the shoulder to the toe in the order of 10 cm or less.

1 INTRODUCTION

An increasing number of high embankments have been constructed on existing hill slopes for projects expanding existing airports in mountainous areas in Japan. These embankments are massive soil structures, generally higher than 50 m. Because Japan is located in a very seismically active region, seismic design consideration is important for these embankments. In order to obtain field data on the seismic performance of these embankments, the authors have been operating a seismic array observation system at Kushiro Airport in Japan since 1988 (Fig.1). The response acceleration during the Kushiro-Oki, Richter-JMA magnitude 7.8, earthquake in 1993 registered a peak acceleration of 0.5g on the slope of the embankment, but damage to the embankment was minor. In this paper, the performance of this embankment during the 1993 earthquake is discussed through two-dimensional non-linear seismic analysis. Seismic response of the same embankment shaken with a weaker motion has been reported elsewhere (Iai & Kurata, 1990).

2 HIGH EMBANKMENT

The embankment was constructed in 1988 on the north slope of a hill, where Kushiro Airport was expanded to allow for operation of larger airplanes. The embankment is 65 m high and faces the N44E direction. As shown in Figure 2, the original hill slope at the site is formed of a firm deposit of Pleistocene origin, called Kushiro Group (K_1), overlain by gravel (D_g) and sandy soil (D_s) at and in

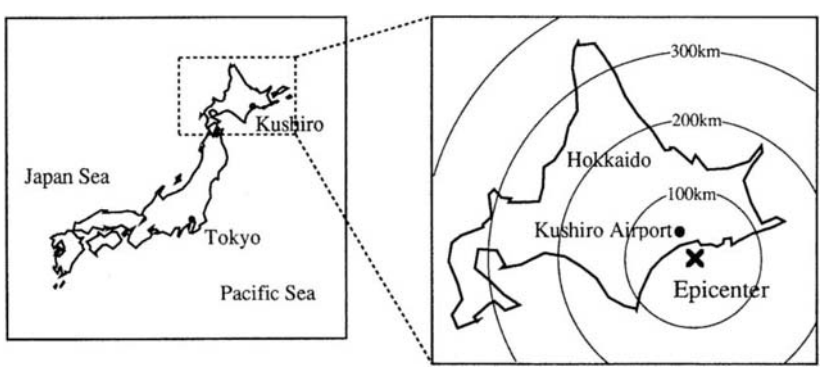

Figure 1. Location of high embankment and epicenter of 1993 Kushiro-Oki earthquake.

the vicinity of the toe of the embankment. Before the construction of the embankment, the original slope surface was covered with a loose talus deposit and the original toe of the slope was covered with a soft peat deposit. The material used for embankment was a mixture of sandy soil and gravel at a ratio of 1:4. A portion of the soft peat deposit below the embankment was improved using the gravel compaction method and the remaining portion of the soft peat deposit was replaced by sandy gravel as a shear key for increasing stability of the embankment (Fig.2). The loose talus deposit covering the original slope was removed before constructing the embankment. The upper 15 to 20 m portion of the embankment shows standard penetration test blow counts (SPT N-values) ranging from 20 to 40, below which the SPT N-values become higher than 50, indicating that a good engineered embankment was constructed at the site. The ground water level was maintained close to the level of the original hill slope by installing drainage layers where necessary.

3 SEISMIC PERFORMANCE & RESPONSE RECORDS

Despite the strong earthquake shaking during the 1993 Kushiro-Oki earthquake, damage to the embankment was limited to the opening of several cracks, 15 cm wide and about 10 m long, in the lower portion of the embankment. All of the cracks were shallow, limited to near the slope surface, and did not affect the overall stability of the embankment nor airport operation for incoming/outgoing air traffic. Displacements measured before and after the earthquake shown in Figure 3 indicate that the embankment displaced toward the toe about 2 to 3 cm, and settled at the shoulder and heaved at the toe both about 10 cm.

Strong motion seismometers are installed in the embankment at five locations, including the shoulder, mid and toe levels, ground surface and at the bedrock, as shown in Figure 2. Pore water pressure transducers are also installed in a sand layer (D_s) and a layer of sandy gravel replacing the original peat layer as a shear key (A_p replacement). The records for the N44E component obtained during the earthquake in 1993 are shown in Figure 4. The peak horizontal accelerations are 0.3g at the bedrock, 1.1g on the ground surface, and 0.5 to 0.6g on the slope of the embankment. The excess pore water pressures in the sand layer reached 4.0 to 4.2 m in water head, about 0.2 in terms of a ratio over an effective vertical stress, and dissipated quickly after the shaking subsided.

4 NON-LINEAR RESPONSE ANALYSIS

Earthquake response analysis was performed using a non-linear soil model based on a multiple simple shear mechanism representing a hyperbolic stress-strain relationship (Iai et al. 1992). The parameters needed for the analysis were determined as shown in Table 1 based on the results of the geotechnical investigations conducted at the site, including PS logging and standard penetration tests. Increase in the shear moduli within the embankment with increasing effective confining stresses becomes significant for an embankment as high as the one discussed in this paper, as shown in Figure 5. The solid line in this figure indicates the least squares fit of a function of the square root of effective confining stress. The variation of shear moduli discussed here was taken into account in the non-linear response analysis. The strain level dependency of shear modulus and hysteretic damping was taken into account through the use of the soil model representing a hyperbolic stress-strain relationship.

The non-linear seismic response analysis was

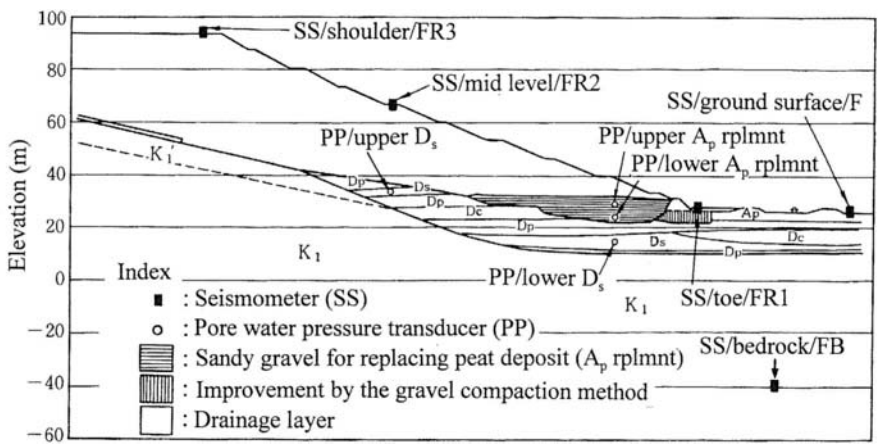

Figure 2. Cross section of high embankment, locations of seismometers & pore pressure transducers.

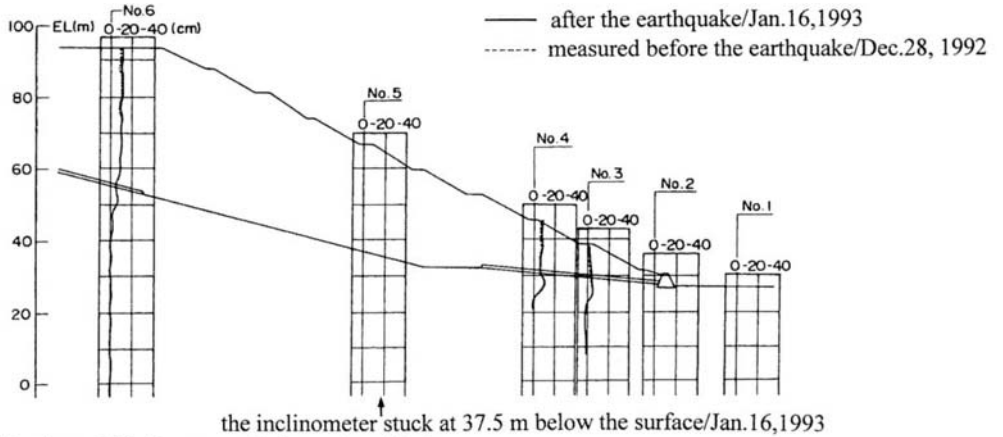

(a) horizontal displacement (rightward positive)

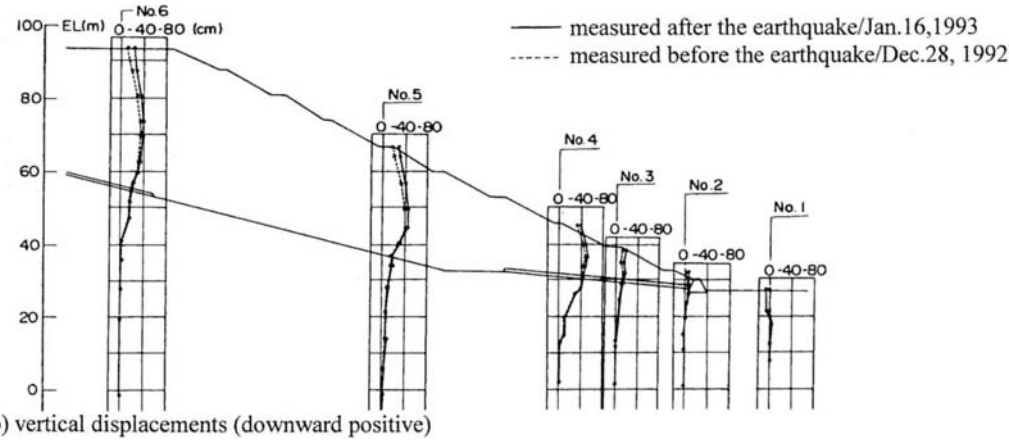

(b) vertical displacements (downward positive)

Figure3. Displacements of embankment before and after the earthquake.

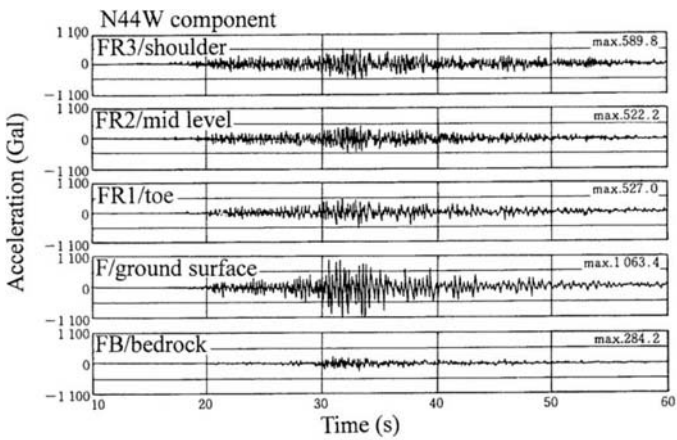

Figure 4. Acceleration records at Kushiro-Oki earthquake(N44W component).

Table 1. Model parameters for high embankment at Kushiro Airport.

Geological classification	Soil type	Mat No. (refer to Fig. 6)	γ_t (tf/m^3)	V_s (m/s)	σ_{ma}' (kPa)	G_{ma} (kPa)	K_{ma} (kPa)	c (kPa)	ϕ (degree)	h_m
Embankment	Surface deposit	①	1.50	93	10	13000	33800	19.6	42	0.24
	Upper layer	②	2.10	380	261	303200	790800	19.6	41	0.24
	Lower layer	⑥	2.20			317700	828500	19.6	40	0.24
Alluvial deposit	Peat, fill(A_p, B)	⑮	1.50	100	6	15000	39100	0.0	26	0.24
	Improved ground(A_p, B)	⑭	1.60	190	6	57800	150600	0.0	27	0.24
Shear key	Sandy gravel(Sk)	⑬	2.20	370	150	301200	785400	0.0	37	0.24
3rd upheaval deposit	Sandy gravel(T_{og})	③	1.90	400	102	304000	792800	49.0	35	0.24
Kushiro Group Upper layer	Sandy gravel(K_2)	④	2.15	550	212	650400	1696100	9.8	35	0.24
Lower layer	Sandy soil(K_1'')	⑦	1.95	360	196	252700	659100	9.8	35	0.24
	Sandy soil(K_1')	⑧	2.00			259200	676000	9.8	35	0.24
	Sandy soil(K_1)	⑤	2.10			272200	709800	49.0	42	0.24
6th upheaval deposit	Clay(D_s)	⑫, ⑱	1.70	360	196	220300	574600	49.0	30	0.20
	Sandy soil(D_s)	⑩, ⑰	1.90			246200	642200	29.4	35	0.24
	Sandy gravel(D_g)	⑨, ⑪, ⑯, ⑲	2.00			259200	676000	29.4	35	0.24

Mat No. : Material number used for analysis(shown in Fig.6)
γ_t : Unit weight
V_s : Shear wave velocity
σ_{ma}' : Reference confining stress
G_{ma} : Shear modulus
K_{ma} : Rebound bulk modulus
c : Cohesion
ϕ : Internal friction angle
h_m : Upper limit for hysteretic damping

performed using the finite element method, idealizing a cross sectional area of 650m by 140m in the horizontal and vertical directions respectively, using 7850 finite elements with 4472 nodes, as shown in Figure 6. The element size was chosen to allow response frequency components up to 10 Hz in the analysis. The shear moduli become very small near the slope surface because of the small confining stress there, resulting in the use of elements as small as about 1.5 m high. The input earthquake motion at the bottom of the analysis domain (i.e. bedrock) was assigned for both the horizontal and vertical directions from the recorded motion at the bedrock (FB) at the site. In order to save computation time, only the main portion of the time histories shown in Figure 4 (from 20 to 40 seconds from the triggering of the recording) was used for the response analysis. The side boundaries of the analysis domain were idealized using viscous dampers to allow incoming and outgoing waves to and from the free-fields. The time integration was done by Wilson-θ method (θ = 1.4), using Rayleigh damping (α = 0, β = 0.0005) to ensure stability in the time integration. The initial conditions were obtained by performing a static analysis with gravity using the same constitutive model as that used for the seismic response analysis.

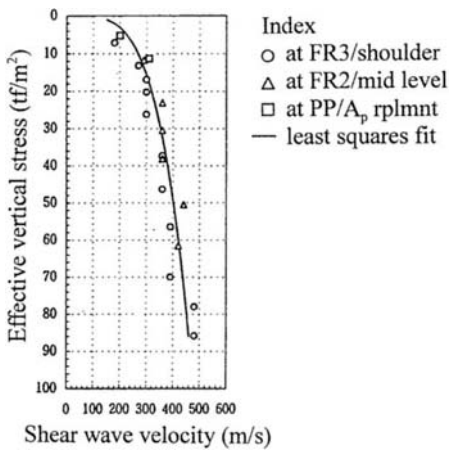

Figure 5. Shear wave velocity in embankment.

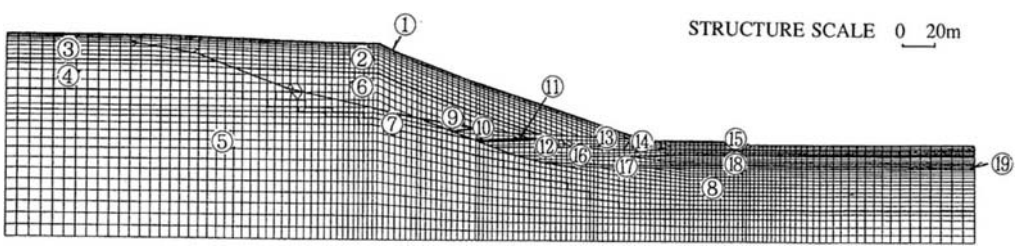

Figure 6. Mesh division for finite element analysis and zoning for material parameters.

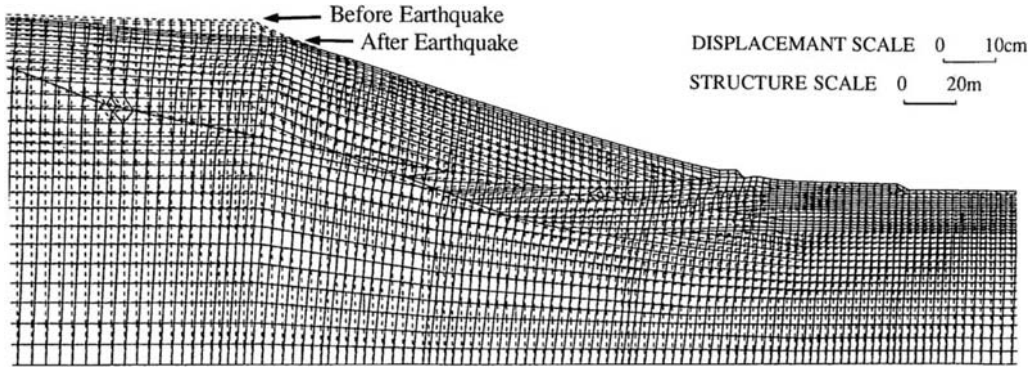

Figure 7. Computed residual displacements of high embankment after earthquake.

5 RESULTS OF RESPONSE ANALYSIS

The non-linear response analysis resulted in the residual deformation of the embankment shown in Figure 7. In this figure, the main portion of the embankment is depicted with an enlarged displacement scale of one hundred times magnification. The computed horizontal displacements are about 10 cm, whereas the measured ones are 2 to 3 cm. Both the computed and measured horizontal displacements are small in the sense that the damage to the embankment was minor. The computed vertical displacements show settlement at the shoulder and heave at the toe, thus the deformation mode is consistent with that observed in the field. The computed vertical displacements are about 3 cm for both settlement and heave, whereas those measured are about 10 cm. Both the computed and measured vertical displacements are small also in the sense that the damage to the embankment was minor.

The computed response accelerations are shown in Figure 8. The wave forms of the computed accelerations are similar to those measured from 20 to 40 seconds after the triggering of the recording (Fig. 4). The computed peak accelerations are consistent with those measured on the slope of the embankment (FR1 through FR3) except on the ground surface (F), where the analysis significantly underestimates the response as shown in Table 2. As shown in Figure 9, the Fourier spectra of the computed response accelerations are consistent with those measured at the toe and mid levels of the embankment, whereas the analysis results for the shoulder were about twice as large in spectral amplitude for the 1 to 4 Hz range. The analysis, however, resulted in about half of that measured on the ground surface for the 2 to 5 Hz range.

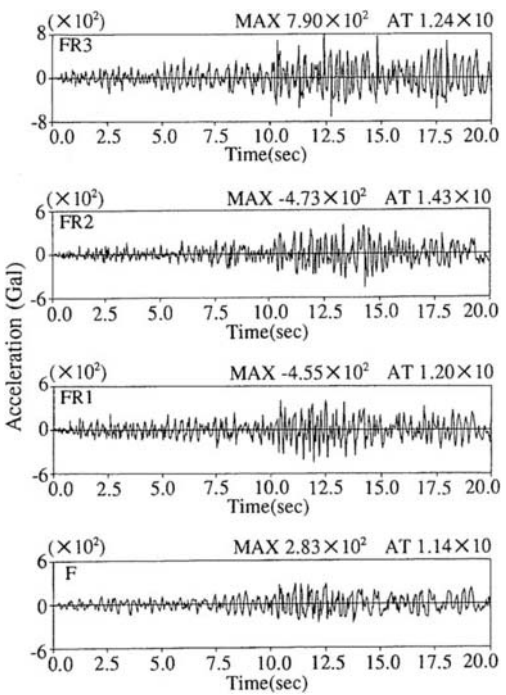

Figure 8. Computed response accelerations at high embankment.

Table 2. Maximum accelerations at high embankment.

Site	Peak acceleration(Gal)	
	computed	recorded
FR3	795	590
FR2	473	522
FR1	455	527
F	283	1063

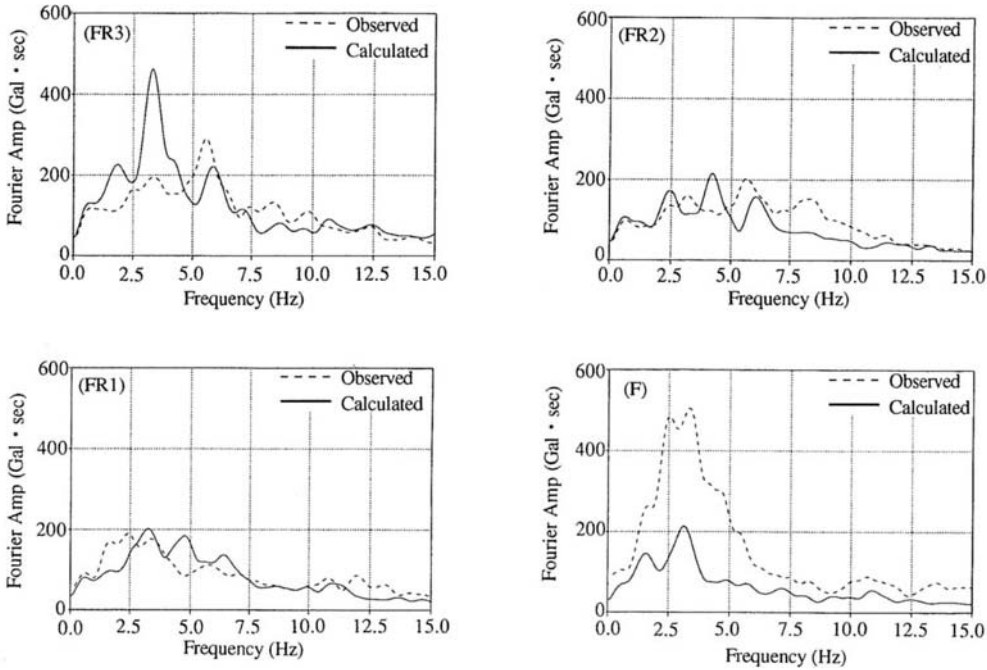

Figure 9. Recorded and computed Fourier spectra of response accelerations at high embankment.

To summarize, the computed results were consistent with those measured in the that both resulted in small displacements on the order of about 10 cm or less. An issue that remains to be studied is the fact that the analysis overestimated horizontal displacements whereas it underestimated vertical displacements. The analysis resulted in response accelerations consistent with those measured at the toe and mid levels of the embankment slope. Another issue for further study is the fact that the analysis was not successful in matching the observed acceleration response spectra at the shoulder and the ground surface.

6 CONCLUSIONS

A 65 m high embankment was shaken with a 0.5g earthquake motion and performed well during the 1993 Kushiro-Oki earthquake. Non-linear response analysis was conducted to evaluate the performance of the embankment. At the current stage of the study, the following conclusions may be drawn.

1) The computed residual displacements of the embankment showed settlement at the shoulder and heave at the toe, involving horizontal displacements from the shoulder toward the toe, consistent in the overall deformation mode with that measured.
2) The order-of-magnitude displacements obtained by the analysis were about 10 cm or less in both the horizontal and vertical directions, consistent with those measured in the sense that the displacements were small enough that damage to the embankment was minor.
3) The computed accelerations at the toe and mid levels on the embankment slope were consistent with those measured for the frequency range below 10 Hz. Further study is needed, however, to obtain more consistent results, especially at the shoulder and the ground surface.

REFERENCES

Iai, S. & E. Kurata, 1990. Seismic array observation and analysis of high embankment, *Proc. 8th Japan Earthquake Engineering Symposium*. 463-468 (in Japanese).

Iai, S., Y. Matsunaga & T. Kameoka, 1992. Strain space plasticity model for cyclic mobility, *Soils and Foundations*, JSSMFE, 32(2):1-15.

Earthquake Geotechnical Engineering, Sêco e Pinto (ed.) © 1999 Balkema, Rotterdam, ISBN 90 5809 116 3

Seismic design of lined face earth dams

J. H. Troncoso
Catholic University of Chile, Chile

A. J. Krause & P.G. Corser
TerraMatrix Incorporated, Colorado, USA

ABSTRACT : This paper presents experiences obtained in seismic design and construction of earth dams with lined upstream slope face, in Chile. Experiences included very high structures which shall undergo large amplifications of accelerations under the strong ground motions of major earthquakes. Influence of soil parameters, which are entered in predictive models, are discussed in relation with the characteristics of the design earthquakes. Details of construction are presented to demonstrate the importance of proper integration with design.

1 INTRODUCTION

Lined deposits of tailings or lined dams for water reservoirs are adequate structures to retain hazardous materials and to minimize the risks of discharge, seepage and contamination of the environment. Liners prevent seepage and pore water pressure increases inside the retaining dams. Seismic design of these dams have to consider deformations as well as stability to prevent ruptures of liners. Abandonment conditions are most demanding for tailings dams in seismic countries because maximum credible earthquakes have to be considered for verification of behavior in the long term periods following decommissioning and closure of mining operations.

Flexible membranes are specially adequate for lining of deposits with steep slopes. Depending of the degree of impermeability of the natural materials which form the bottom and the walls of the basin, the lining of a reservoir may need to be complete or limited to the retaining dam and its foundations.

Rockfill dams and earth dams with lined upstream face are cost effective alternatives to retain impoundments of mineral residues because they permit the use of almost any available geotechnical material for the construction of the dam. In fact, impermeable lines create a condition of high effective stresses and, as a result, they allow to design steep slopes with adequate safety margins for earthquake loadings.

Rock foundations and rockfill materials are best conditions for safe design in seismic zones. In effect, rock foundations warrant low compressibility and minimum amplifications of earthquake motions while rockfills have characteristic high shear strengths and permit to build stable steep slopes. The case of lined dams built with soils and founded on soils is more complicated as larger earthquake loadings, induced by amplified accelerations, combined with smaller shear resistances, may lead to smaller factors of safety and larger deformations. Strict quality assurance of construction is necessary in order to ensure adequate treatment of foundations and high degrees of compaction.

Tailings dams lined with geomembranes have to maintain their stable and also impermeable properties after suffering strong earthquake loadings in order to fulfill the environmental requirements. Therefore, accurate prediction of earthquake behavior and of resulting deformations are most important for adequate design of lining systems.

This paper presents experiences obtained in recent projects of lined dams in seismic zones and emphasizes the importance of construction controls, to back up the design assumptions, and instrumentation, to verify the adequate performance of the structural parts, impermeable barriers and drainage elements.

2 SEISMIC GROUND MOTIONS AND DYNAMIC RESPONSE OF A TAILINGS DAM

The dynamic response of a tailings dam to the ground motions induced by an earthquake is function of the geometric characteristics and of the dynamic properties of the materials which constitute the earth structure of the dam and the impounded sediments.

The closer the predominant period of the ground motions is to the natural period of the dam, the higher become the amplifications of accelerations throughout the body of the dam. This fact has been verified by dynamic finite element analyses of tailings dams of different heights subjected to diverse ground motions (Troncoso, 1990). Figure 1 illustrates this point showing the distributions of maximum shear stresses in tailings dams of 20 and 80 m heights for ground motions recorded in different sites for the same seismic event. Same effect has been found to explain the different seismic behavior of three tailings dams, two of which failed, in the Chilean earthquake of March 3, 1985 (Troncoso, 1988).

To predict the seismic response it is therefore necessary to start with an accurate theoretical model of the deposit and to enter in it the proper dynamic properties of the soils envolved. Most important data are the shear moduli and the damping ratios as functions of strain.

Confining stresses of impounded slimes over lined upstream face slopes reduce the amplification of accelerations and displacements and, therefore, they prevent detrimental deformations of the lining membranes. Higher strains are generated in the upper zones of a dam above the surface of the impounded slimes, therefore, if an earthquake occurs during operation, detrimental strains may be created in the uncovered portions of the liner.

The response of a dam to a seismic ground motion is very much dependent upon the dynamic properties of the soils which are used to build the dam and of the treatment of these soils during construction. Comparison of finite elements analyses performed in models of tailings dams constituted by homogeneous soils with those of dams formed by different soils in different zones, permit to verify that increases in degree of compaction, necessary to satisfy stability

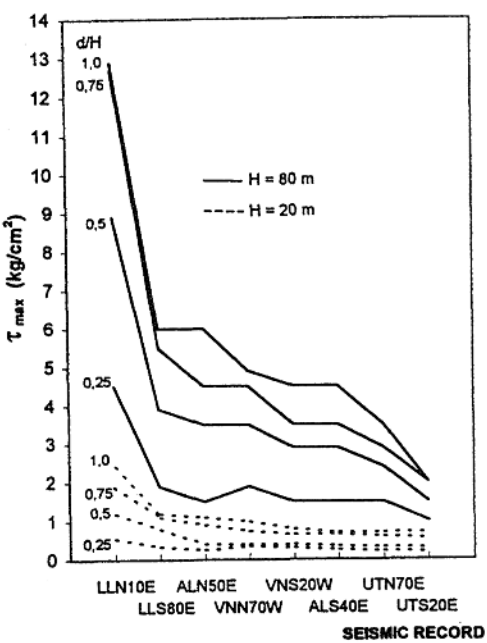

a. Different elevations beneath the crest

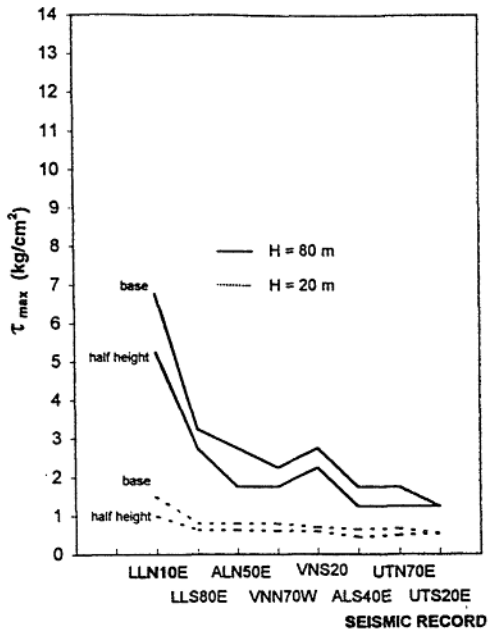

b. Different elevations beneath the center of the downstream slope

Figure 1. Maximum shear stress at different depths in a tailings dam for different ground motions

conditions may change unfavourably the dynamic response for a given seismic input movement leading to stronger inertia forces due to approximation to resonance period (TerraMatrix and I.G.L., 1997).

3 LINER AND LEAK DETECTION SYSTEMS FOR LINED TAILINGS FACILITIES

Increased regulations and concerns for environmental impacts from mine operators have lead to lining of many tailings facilities in recent years. The lining systems are intended to reduce the potential for release or contaminate the environment. Leak detection systems have been incorporated to identify and to control leaks in the main liner system, as part of the design of lined tailings facilities.

3.1 Liner and leak detection system components

Liner materials for most mining applications have consisted of low permeability soil materials, geomembranes (HDPE) and/or geosynthetic clay liners (GCLs). These elements have been used individually or in combination to form barrier layers. Leak detection materials have been used in conjution with barrier layers with the opposite functions of high permeability and rapid drainage, to intercept accidental seepages and to guide them to collection points. Materials that have been used as detection layers are :geotextile drainage layers and geocomposite drainage layers (combination of geonets and geotextiles). Figure 2 presents some typical configurations for barrier and drainage layers that are used for lined tailings facilities.

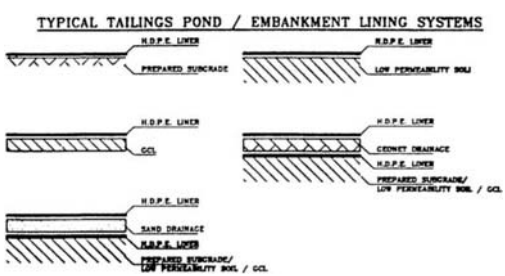

Figure 2. Typical liner sections for tailings dams and deposits.

3.2 Objectives of leak detection system

The primary objectives of the leak detection systems is to provide secondary containment to determine if leakage of the primary liner is occurring and to allow remedial measures to be implemented, if required. The system should allow rapid flow of liquids to a central collection point where the flows can be measured. If flows are detected in leak detection system, then a series of remedial measures are normally implemented. These measures include the following :

-If the flow is relatively small, the fluids can be collected and returned to the solution pond ;

-If the flow is relatively small and liquid is composed of uncontaminated water then it may be discharged :

-If the flow is relatively large, the source of the leak must be investigated and remedial measures implemented.

Due to the relatively thin nature of the leak detection layer, even small deformations within the embankment could result in disruptions to it. Therefore, accurate deformation analyses are necessary to be included in the design.

3.3 Design of liners and leak detection systems

The selection of a particular liner and drainage layer for a tailings application depends on a number of criteria. These criteria include both design and constructability factors. Some of the particular selection critera are : hydraulic properties (permeability of barrier layers), durability, deformation characteristics, internal and interface strength characteristics, and transmissivity characteristics of drainage layers.

Evaluation of the above selection criteria is critical to the performance of the lined tailings facility under dynamic loading conditions particularly where at least some displacements are expected. Historically, earthen and rockfil embankment were assumed to be able to withsland some deformations without any major stability impacts. Deformations in the range of 0.3 to 0.7 meters were considered acceptable. However, with the use of geosynthetic materials as barrier layers in tailings facilities, deformations of this magnitude may not be acceptable. Depending on the location within the embankment, the deformations may be limited to less than 0.3 meter to ensure performance of the leak detection system.

In general, the weakest components in a lined tailings embankment are the interfaces between the liner and the leak detection system. Therefore, any displacements that occur as a result of seismic events will result in displacements along or within the liner and/or the leak detection system. The interface strength characteristics of geosynthetic materials are vey dependent on a number of factors associated with the manufacture of the material. Manufacturing and/or resin characteristic that can affect strength properties include density and surface texture (smooth or rough).

Testing conditions to determine strength characteristics must simulate the actual field conditions in order to be representative. The factors to be evaluated include :

a) Range of expected normal loadings (previous testing programs have indicated that the interface strength properties will decrease with increased normal loading). At low normal loads interface strength properties are generally stronger.
b) Backing conditions for the interface being tested (steel plates have commonly been used) ; however, if soft soil layers (clay liners)are to be used in the constructed facility they must be used also in the testing program. Depending on the test being performed, soft backing conditions can result in conservative or unconservative results.
c) Most geosynthetic/geosynthetic or geosynthetic/soil interface will exhibit a strain-softening behavior. Therefore, all testing programs should be conducted to sufficient levels of strain to indentify both peak and residual strength characteristics.

3.4 Recommendations for seismic design of lined tailings facilities

a) Specific interface shear tests should be conducted on the proposed liner system and leak detection system materials ;
b) Interface shear tests should be conducted at the normal loads expected during ultimate operation of the facility ;
c) The tests should be conducted with the appropriate backing materials that reflect the field conditions ;
d) Based on the very limited amount of displacement that is required to achieve residual strength parameters and the amount of movement that is experienced within the liner systems during installation, it is recommended that residual strength parameters be used in the seismic design of lined facilites.

4 EXPERIENCES OF CONSTRUCTION OF A LINED GRAVEL DAM IN SEISMIC ZONE

Valuable experiences have been gained in CFGE, concrete face gravel dams, during design and construction of the recently commissioned Santa Juana dam built in Northern Chile. The senior author performed the soil mechanics studies for foundations and borrow materials as well as the slope stability analyses for static and seismic loadings of this dam. Main original characteristics, which differentiated this project from more traditional CFRD, were the use of rounded and subrounded gravel instead of rockfill, for the body of the dam, and foundation on fluvial sediments instead of bedrock. Figure 3 represents the cross section of the dam at maximum height of 106 m.

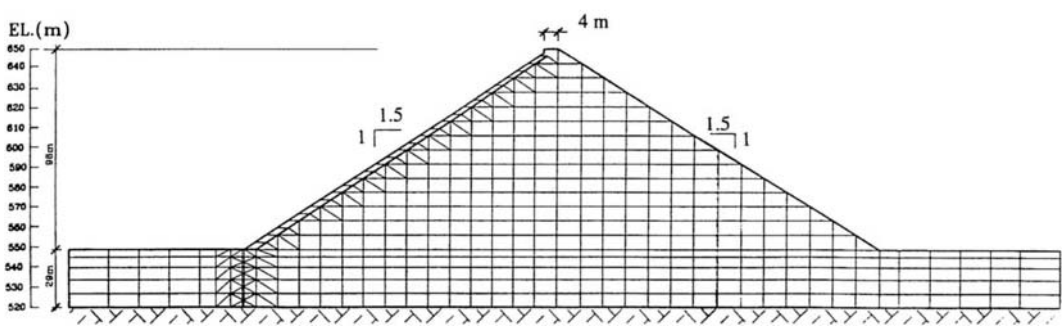

Figure 3. Santa Juana CFG dam schematic section and finite element mesh

Design performed by MN Ingenieros (1992) included : an 0.8-meter thick concrete cutoff wall, as impermeable barrier in the fluvial sediments, built to 0.5 m below rock surface ; a 6 m wide, 0.7 m thick plinth concrete slab at the base, between the cutoff wall and the lining slab ; and 5 m high cantilever retaining wall at the crest. The lining concrete face slab was 0.5 m thick at the base and 0.3 m at the crest.

Finite element models were used to calculate the distributions of deformations, stresses and strains under different kinds of seismic loadings.

Vertical and horizontal displacements of the dam after filling the reservoir, computed with ISBILD program, are shown in Figures 4 and 5. Maximum settlements of 0.3 m occur under the concrete slab while horizontal displacements amount to 0.2 m downstream at the crest of the dam and 0.16 m upstream of the heel. Flexible joints were therefore designed between the upstream concrete slab, the plinth at the base and the cut-off concrete wall.

Seismic analyses, performed with the QUAD-4 program, permitted to estimate the effects of different earthquakes such as induced accelerations, and derived stresses and strains, within the dam and the foundations. A seismic record obtained in similar soils, in the 1985 Magnitude 7.8 Chilean earthquake, named ALN50E, was used as base input motion. The dynamic characteristics of this ground motion record, with a predominant period of 0.9 sec, had been determined to be highly unfavourable for soil structures of long natural periods, in previous research (Troncoso, 1988). The acceleration of the base record were amplified to maximum value of 0.24, 0.3, 0.48 and 0.56 g to simulate events of different magnitudes. Corresponding natural periods of the dam were computed between 1.5 and 1.7 sec.

Maximum accelerations distribution in the dam, for 0.3 g maximum base acceleration, are shown in Figure 6. A 2.5 amplification factor is observed at the crest of the dam where the cantilever retaining wall is located. For such extreme unfavourable conditions displacements should occur in the uppermost wedges of the dam, Newmark (1965) procedure lead to 0.07 m estimated maximum permanent displacement in the upper 14 m of the downstream slope. Such displacements should not lead to a breach failure as probability of maximum water level in the reservoir combined with maximum foreseeable earthquakes are very low at the location of the dam.

Construction of the dam encountered only a few difficulties related to fulfilling hypothesis of design. These difficulties were overcome applying a successful integrated design and construction approach, as follows ;

a) Lenses of fine soils, discovered at depths of 8 to 11 m, below foundation level, were removed, in the zone located under the heel of the dam and replaced with compacted coarse sandy gravels. Dynamic stability analyses, based on cyclic triaxial and undrained compression tests, allowed to leave parts of these lenses under the central and downstream zones.
b) Sand contents in excess of specified percentage were found in parts of the borrow pits, requiring a tough supervision of placement and compaction procedures to ensure the obtention of adequate shear strength properties in the critical zones of the dam.

In-situ density measurements of compacted layers indicated high effectiveness of the 20 ton vibrator rollers supplemented with adequate routing of trucks over one meter thick layers. Evaluation of construction procedures was done with measurements of settlements with water cells on addition to topographic surveys Back calculated compressibilities were in good agreement with predicted values.

Accelerograph stations were installed at the crest and foot of the downstream slope and a third one in a rock outcrop on the left abutment. Moderate earthquakes MS < 6,5 have occurred in the two year period after commissioning, in 150 km distances, with no noticeable effects in the dam.

5 MONITORING THE BEHAVIOR OF LINED DAMS

The seismic and the environmental behaviours of lined dams depend upon the performance of the impermeable barriers. Leakages may occur through the membrane liners mainly due to : punctures, caused by sharp edges of base materials, ruptures under settlements and tensions, failures of seams. Seepage may occur along connecting permeable discontinuities in the abutments, such as faults, fractured rocks, joints, under the plinths, where the liners are anchored, or through the cut off walls.

Properly designed and built lined dams are very stable structures because large total stresses become effective stresses through the body of the

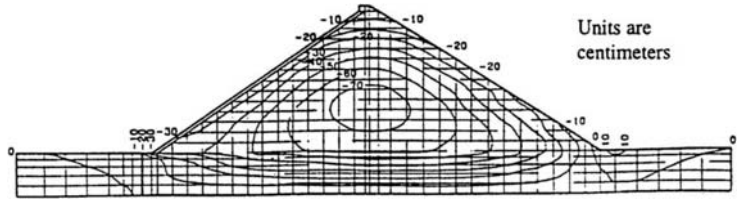

Figure 4. Settlements after filling

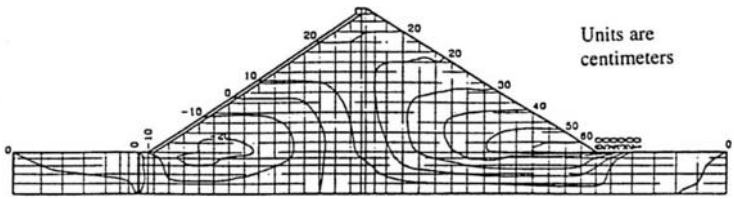

Figure 5. Horizontal displacements after filling.

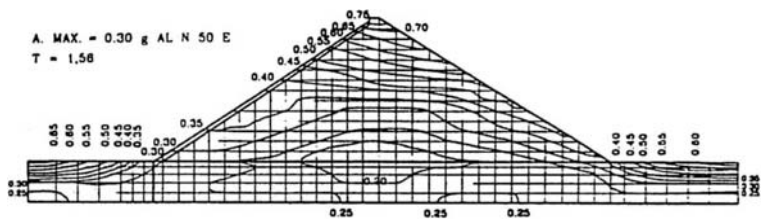

Figure 6. Maximum acceleration amplification ratio Santa Juana dam.

retaining structure which, therefore, is capable to develop high shear strengths. Detrimental increases in pore pressures are prevented to develop during earthquakes and a main cause of breaching is consequently eliminated.

Lined dams for impoundment of tailings are potentially less vulnerable to water seepage problems, in comparison with water reservoirs, both for stability and environmental impacts, because tailings sediments are fine soils which may seal causative openings. Proper knowledge of the index and hydraulic properties of the fine fraction of tailings, permits to program the discharge and the sedimentation of the slimes adequately to reinforce the impermeable barriers and to decrease the hydraulic gradients. Decant ponds and water reclaim barges or towers should be located as far as feasible upstream of the dam both to reduce gradients, to avoid accidental cuts to geomembranes and to create wide beaches over the upstream face and neighbour abutments.

Intermediate berms in the upstream face of a tailings dam are useful platforms to install discharge pipelines as well as to decrease tensional stresses in the liner. Support of plinth beams on the abutments is a most important task of construction. Sound rock or firm impermeable soils should be aimed for foundation of the plinths. Grouting injections should be provided to seal weaker sectors.

Monitoring instruments should be installed to check impermeability of liners and cut-off barriers.

Electric piezometers, buried in the lower parts of the upstream slope, are useful sensors to detect leakages through membranes and clogging of drain blankets. Settlement cells and extensometers serve to record deformations of the slopes and, particularly, of the upstream face. In-depth measurements of horizontal displacements, with inclinometer, vertical settlements, with magnetic probe, and water level, may be performed in single borehole, using grooved, telescopic and perforated casings.

Three or four deep wells, excavated downstream of a lined dam, permit to monitor seepage in quantity and quality. A six inch diameter casing is large enough to permit installation of submersible pumps to recirculate waters back to the reservoir or the treatment ponds, thus creating an effective hydraulic barrier, should the waters result inadequate for direct discharge into natural streams.

6 CONCLUSIONS

Use of impermeable liners is a convenient mode to mitigate environmental impacts of tailings and water deposits. Flexible liners are specially adequate to extend the barrier from the upstream face over part of the bottom of the reservoir upstream from the heel of the dam and to complete it with a vertical cut-off trench.

Static and seismic deformations have to be properly predicted to ensure the integrity of the barrier. Larger strains are generated on the slope, above the surface of the slimes, during strong earthquakes. As the reservoir is filled the confining stresses of the slimes reduce the deformability of the slope. These strains may be calculated by means of dynamic analyses as shown in this paper.

The most unfavourable combination of an strong earthquake with a low level of slimes have the smallest probability of occurrence because of the short time available for this situation. Construction in stages is, therefore, helpful for the integrity of the liner, as successive increases in height of the dam and corresponding extensions of the liner are followed by gradual filling of the reservoir with short intermediate periods of unconfined upper sections of the slope. On addition, such construction in stages is also helpful to prevent damage of plastic liners caused by UV radiation.

Construction of flexible liners is feasible in steep slopes as the membranes are unrolled from the crest or from intermediate berms. However, construction of foundation bases become more complicated in steeper slopes. Preparation of the bases is recognized as a most important task in lining technology to provide second lines of defense as well as to prevent excessive differential settlements and punctures.

Monitoring of the deformations of lined dams is important to evaluate the behavior of the geomembranes, to allow economic designs and to prevent failures. Leak detection systems monitored by piezometric readings are useful tools to control accidental flows.

7 ACKNOWLEDGMENTS

Thanks are extended to the Ministry of Public Works of Chile for the permission to publish results of the Santa Juana Dam Project. The senior author thanks the sponsorship of Fondecyt Project N° 1971259 which permitted to perform the seismic analyses of tailings deposits.

8 REFERENCES

MN Ingenieros Consultores, 1992. Proyecto Embalse Santa Juana. Informe Final. Dirección de Riego, M.O.P., Santiago, Chile.

Newmark, N.M. 1965. Effects of Earthquakes on Dams and Foundations. Geotechnique 15 :139-164.

TerraMatrix and IGL, 1997. Seismic Behavior of 230 m high Lined Earth Dam Built with materials of Different Compressibility. Internal Report.

Troncoso, J.H. 1996. Geotechnics of Tailings Dams and Sediments. Proc. 2nd International Congress on Environmental Geotechnics, Osaka, Japan.

Troncoso, J.H. 1992. Fundamentals of Earthquake Geotechnical Engineering Santiago : Ediciones Universidad Católica de Chile (in spanish).

Troncoso, J.H. 1990. Seismic Responses of Tailings Dams Built with Cohesionless Soils to Different Types of Ground Motions. Proc. International Symposium on Safety and Rehabilitation of Tailings Dams, ICOLD, Sidney, Australia.

Troncoso, J.H. 1988. Evaluation of Seismic Behavior of Hydraulic Fill Structures, ASCE's specialty Conference, Fort Collins, U.S.A.

This Page Intentionally Left Blank

Earthquake Geotechnical Engineering, Sêco e Pinto (ed.) © 1999 Balkema, Rotterdam, ISBN 90 5809 116 3

Seismic behavior of Shimagami pumping station and Seibu sewage treatment plant

J. Koseki
Institute of Industrial Science, University of Tokyo, Japan

O. Matsuo
Public Works Research Institute, Ministry of Construction, Tsukuba, Japan

T. Yoshizawa
Nippon Engineering Consultant Company Limited, Japan

ABSTRACT: By the 1995 Hyogoken-Nanbu earthquake, many structures were damaged by lateral flow of liquefied soil layers. This paper describes performance of Shimagami pumping station in Kobe City, which was not damaged irrespective of occurrence of the lateral flow, and results of simplified analyses of soil cement mixing walls which were surrounding the underground structures of the pumping station. It also presents performance of the second series of facilities in Seibu sewage treatment plant in Kobe City, which was free from any structural damage, and results of similar analyses of diaphragm walls supporting the facility partly. It was estimated that the earth pressure difference caused by the lateral flow of the liquefied soil layers was on the order of several percent of the total overburden pressure or less and that connecting the underground walls with the building would effectively increase their capacities against the lateral flow.

1 INTRODUCTION

During the 1995 Hyogoken-Nambu earthquake, a number of buildings and civil engineering structures located in the water front area were damaged by lateral flow of liquefied soil layers that were associated with lateral residual displacements of quay walls and revetments. They have been reported by several other researchers including Hamada and Wakamatsu (1996), Tokimatsu et al. (1996), Ishihara (1997) and Tokimatsu and Asaka (1998).

On the other hand, only a few case histories have been reported on undamaged structures which survived the earthquake irrespective of occurrence of the lateral flow in the surrounding soil layers. Such undamaged case histories are, however, of significant importance in analyzing the effects of the lateral flow on structures and in developing effective countermeasures against the lateral flow.

This paper reports good performance and results of simplified analyses of two sewage facilities, Shimagami pumping station and Seibu sewage treatment plant, which were free from any structural damage although they were located near revetments that moved laterally during the earthquake. Note that overall features on damage to sewage facilities in the area affected by the earthquake have been summarized by Kobe City (1995), Tohda et al. (1996) and Sasaki et al. (1997). Note also that effective stress based response analyses have been made by Kaneko et al. (1998) on Shimagami pumping station.

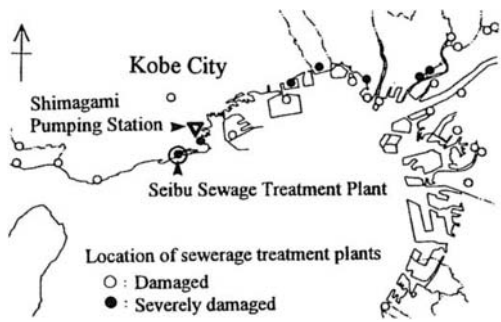

Figure 1. Location of investigated facilities (modified from Sasaki, et al., 1997)

2 SEISMIC BEHAVIOR AND SOIL CONDITION

2.1 *Shimagami pumping station*

Shimagami pumping station, located in Hyogo Ward, Kobe City (Figure 1), started its operation in 1994 as a discharging facility of storm water into Hyogo Port in case of high tides. The building, as typically shown in Figure 2, was supported by cast-in-place concrete piles having a diameter 1.0 to 1.5 m. For temporary earth retaining walls, soil cement mixing walls having a diameter of 0.55 m with a core using H-section steel rods (H-396*199*7*11 mm and H-350*350*12*19 mm) were constructed before the excavation work. They were left without connecting to the building after the completion of the construction work, as shown in Figure 3.

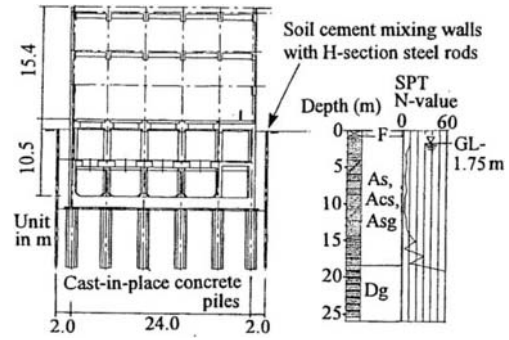

Figure 2. Typical cross section of Shimagami pumping station and bore hole survey results

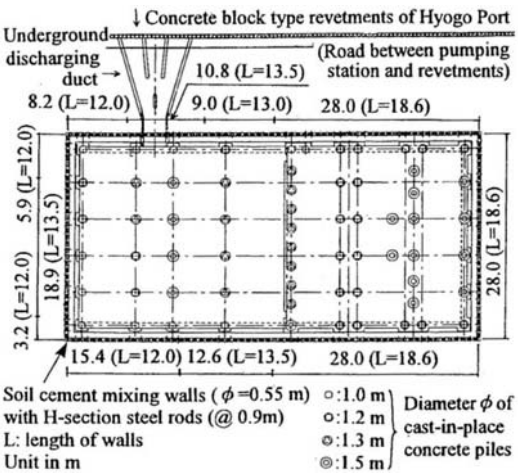

Figure 3. Plan of Shimagami pumping station

Typical boring survey and SPT results on original soil layers conducted before the earthquake are shown in Figure 2. Below very thin surface fill layer (denoted as F in the figure), Holocene sand layers (As) with alternative sandy gravel (Asg) and silt (Acs) layers were underlain by Pleistocene gravel layer (Dg). The foundation piles, 8.1 to 13.75 m long, were embedded in the Pleistocene gravel layer. On the other hand, the soil cement mixing walls were constructed to a depth of 12.0 to 18.6 m, which were not necessarily supported by the Pleistocene gravel layer when the excavated depth was relatively small.

As shown in Figure 3, concrete block type revetments were located on the south-eastern side of the building. These revetments were reported to have moved seawards permanently by about 1.4 to 1.8 m during the earthquake, causing a subsidence of a road located between the revetments and the building by several tens of centimeters. The above range of revetment movement is consistent with the results of aerial photo survey reported by Kaneko et al. (1998). Due possibly to effects of these movements, the discharging duct suffered opening by about 0.5 m at the connection to the building. Based on these behaviors, it was estimated that the Holocene sand layer liquefied during the earthquake and that lateral flow of the liquefied layer was induced on the seaside of the building by the permanent movement of the revetments.

According to survey results conducted after the earthquake, the top of the soil cement mixing wall on the seaside deformed seawards in an arch shape, resulting in the maximum horizontal displacement at the wall top of 24 cm and the maximum tilting angle near the wall top measured from the vertical direction of 3 degrees. The backfill soil on the seaside between the building and the soil cement mixing walls was deformed following the soil cement mixing wall, without showing any cracking. It subsided uniformly by about 1.1 to 1.5 m, while the backfill soil located on the other side showed smaller subsidence by about 0.1 to 0.2 m. It was, therefore, estimated that the earthquake caused the deformation of the soil cement mixing wall on the seaside, accompanied by the larger subsidence of the backfill soil between the wall and the building, which also liquefied during the earthquake.

2.2 *Seibu sewage treatment plant*

Seibu sewage treatment plant, located in Nagata Ward, Kobe City (Figure 1), started its operation in 1965. It consists of two series of facilities as shown in Figure 4. Among them, the seismic performance of the building for the second series of facilities which was supported by diaphragm walls having a thickness of 0.7 m and cast-in-place concrete piles having a diameter of 1.5 m, as typically shown in Figure 5, is reported and analyzed in this paper. The diaphragm walls were used as temporary earth retaining walls for the excavation work, and they were also employed as part of the foundation system to support the building.

Typical boring survey and SPT results conducted before the earthquake are shown in Figure 7. A reclaimed gravelly sand layer (denoted as B in the figure) was underlain by Holocene silt (Acs), clay (Ac) and sand (As) layers. Below these layers, there existed organic soil (O) and Pleistocene silt (Dcs), clay (Dc), gravel (Dg) and sand (Ds) layers. Both the foundation piles and diaphragm walls were embedded to a depth of 18.7 m in a dense sand layer with SPT N-value of about 50 or larger.

According to aerial photo surveys conducted by Hamada et al. (1995), revetments located on the south of the plant, as shown in Figure 4, moved seawards permanently by about 0.7 to 1.2 m during the earthquake, causing damage to the discharging ducts from both series of facilities by opening. Subsidence of the ground surface surrounding the

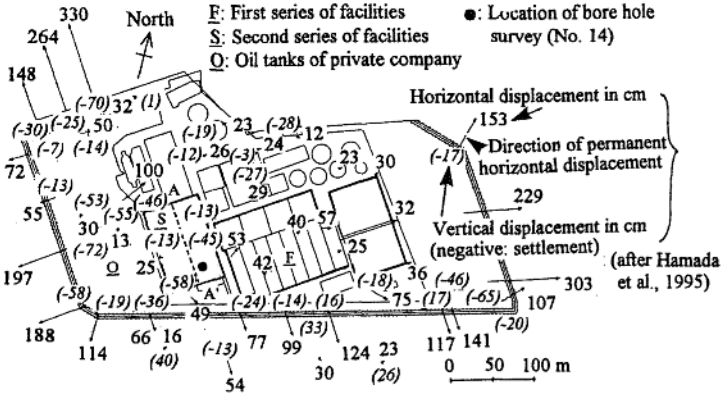

Figure 4. Plan of Seibu sewage treatment plant

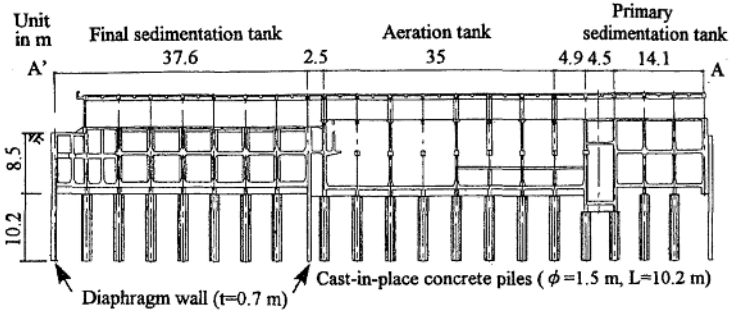

Figure 5. Typical cross section of the second series of facilities in Seibu sewage treatment plant (refer to Figure 4 for location of line A-A')

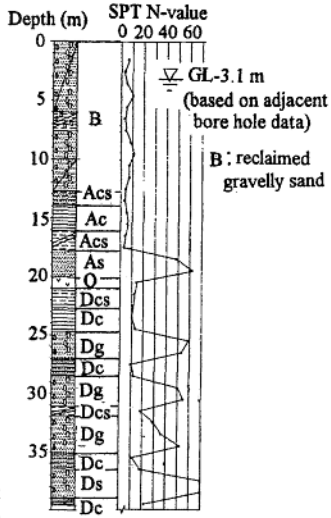

Figure 6. Typical bore hole survey results in Seibu sewage treatment plant (refer to Figure 4 for the location)

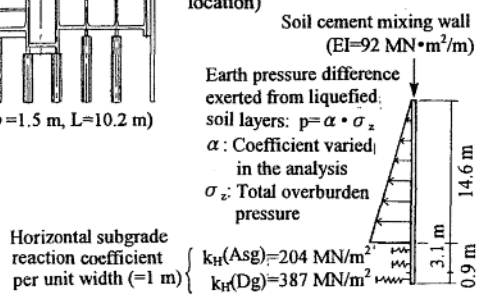

Figure 7. Modeling of wall for Shimagami pumping station

facilities was also observed by about 50 cm at largest.

Further, in the adjacent area located on the west of the facilities, oil tanks owned by a private company suffered extensive tilting damage. It was, therefore, estimated that the reclaimed soil layer liquefied during the earthquake and that lateral flow of the liquefied layer was induced on the seaside of the facilities by the permanent movement of the revetments. However, the second series of facilities including their building were free from any structural damage, and no residual displacement of the building was observed.

It should be added that several inflow ducts and pipes for the first series of facilities were broken during the earthquake, resulting in submergence of sewer pump which interrupted the operation of the first series. According to Kobe City (1995), this breakage was estimated to have been caused by different seismic responses among different facilities for the first series (i.e., a pump station, primary sedimentation tanks and aeration tanks) to which the damaged ducts and pipes were connected.

3 ANALYSES OF UNDERGROUND WALLS

In order to evaluate possible effects of the lateral flow on the performance of underground walls surrounding Shimagami pumping station and the second series of facilities in Seibu sewage treatment plant, simplified analyses were conducted on the bending capacity of these walls.

3.1 *Shimagami pumping station*

For Shimagami pumping station, the soil cement mixing walls were not connected to the building, and both the Holocene sand layers and the backfill soil, located outside and inside the walls, respectively, were estimated to have liquefied. The seaside wall was, therefore, modeled as a single beam as shown in Figure 7 for the wall with a length of 18.6 m, which was reported to have deformed as described in 2.1.

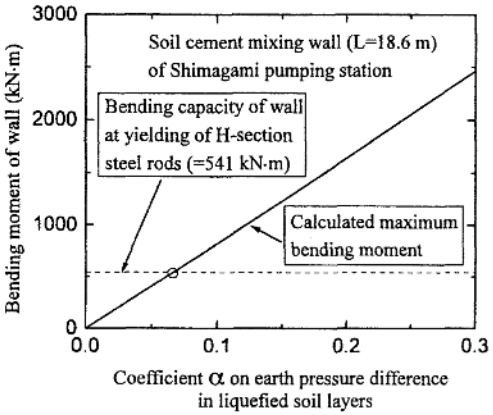

Figure 8. Calculated maximum bending moment of wall for Shimagami pumping station

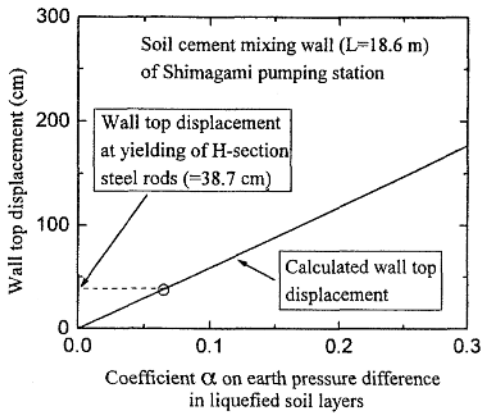

Figure 9. Calculated wall top displacement for Shimagami pumping station

In the model, the wall was supported by linear Winkler springs representing a horizontal subgrade reaction from nonliquefied soil layers that were located below the Holocene sand layers. Effects of the lateral flow were considered by applying a pressure on the upper part of the beam, which represented difference in earth pressures of liquefied soils acting from outside and inside of the wall. The earth pressure difference was assumed to be proportional to the total overburden pressure with a coefficient of α, which was varied in the analyses.

For simplicity, unsaturated soil layers, which were above the ground water level, and upper Holocene sandy gravel and silt layers, which were sandwiched in the Holocene sand layers, were regarded as part of the liquefied soils. On the other hand, lower Holocene sandy gravel and silt layers with SPT N-values larger than about 10 and Pleistocene gravel layers were regarded not to have liquefied. Values of subgrade reaction coefficient of these nonliquefied soil layers were evaluated based on their SPT N-values referring to specifications for highway bridges in Japan (JRA, 1994) and are shown in Figure 7.

By assuming that the lateral flow took place after the main shock of the earthquake motion, the inertia force of the wall was not considered.

Figure 8 shows a relationship between the coefficient α and the maximum bending moment of the wall with a length of 18.6 m, which was mobilized at the interface between the liquefied layers and the nonliquefied layers. The estimated bending capacity of the wall in a condition of reinforcement yielding was also indicated in the figure. It is seen that at a value of α as small as about 0.07, the wall is estimated to have yielded. At this condition, the wall top displacement is calculated to be about 39 cm as shown in Figure 9. Because the observed maximum wall top displacement was 24 cm, it could be concluded that the earth pressure difference caused by the lateral flow of the liquefied soil layers located outside the wall was on the order of several percent of the total overburden pressure or less.

Further investigation is required to evaluate the effects of the soil cement mixing walls in preventing possible damage to the building caused by the lateral flow. This would be made by comparing the estimated behaviors of the building with and without the walls.

3.2 *Seibu sewage treatment plant*

For the second series of facilities in Seibu sewage treatment plant, the diaphragm walls were connected to the building. The seaside wall was, therefore, modeled with a part of the building and its foundation piles as shown in Figure 10. The reclaimed soil layer was assumed to have liquefied during the earthquake, and the subgrade reaction from soil layers below the reclaimed soil was modeled by the linear Winkler springs similarly to the case with Shimagami pumping station. The stiffness of the cast-in-place piles was converted into an equivalent value considering their interval in the out-of-plane direction.

Although other parts of the building and the foundations that were connected to the analyzed part may have contributed to resist against the lateral flow, they were neglected in this simplified analysis. It should be noted that the effects of the out-of-plane diaphragm walls, which were not considered in the analyses either, would have been significantly large, and therefore the results presented below are conservative estimates.

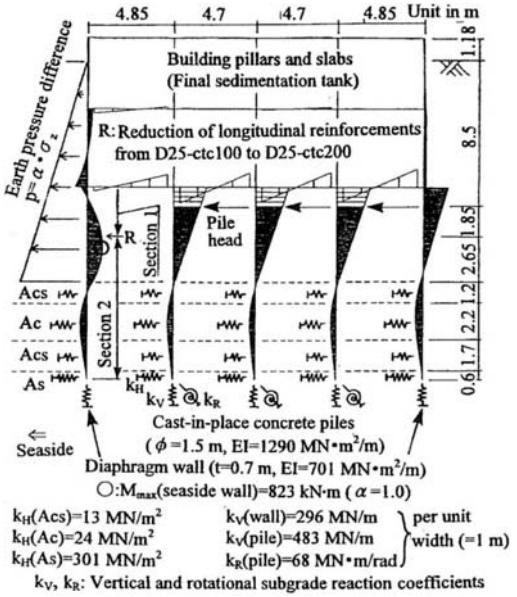

Figure 10. Modeling of wall-building-pile system for Seibu sewage treatment plant (2nd series) and bending moment distribution at α=1.0; refer to Figure 7 for common notations

Typical results on the distribution of bending moments at α=1.0 are also shown in Figure 10. Because the amount of longitudinal reinforcements in the diaphragm wall was reduced above a depth of 10.35 m from the ground surface, the maximum bending moments of the wall within two different sections (i.e., sections 1 and 2 as shown in Figure 10) were plotted versus the coefficient α in Figure 11, together with the estimated bending capacity at reinforcement yielding for each section. It is seen that the wall is estimated to have yielded at a value of α as large as about 1.0. On the other hand, the condition of α =1.0 may not be practically mobilized, since the liquefied soil located outside the wall should not exert any pressure to the wall in order to achieve this condition.

Figure 12 shows the relationship between the coefficient α and the maximum horizontal displacement of the building, which was mobilized at its top. It is seen that, even at α about 1.0, the horizontal displacement is limited to be about 3 cm. This is due to the extremely high bending stiffness of the wall-pile-building system, which is consistent with the field behavior that no residual displacement of the building was observed.

For comparison purpose, a trial analysis was added on the diaphragm wall by using a single beam model supported by the nonliquefied layers below the reclaimed soils, similarly to the case with the soil cement mixing wall of Shimagami pumping station

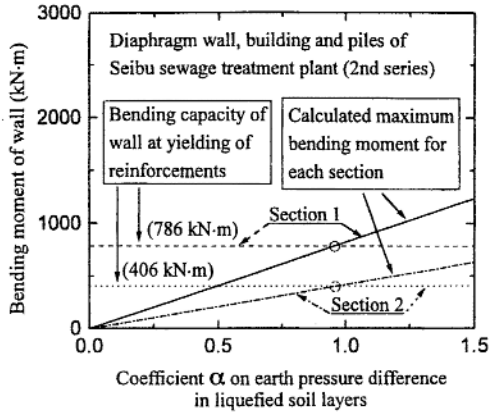

Figure 11. Calculated maximum bending moment of wall for Seibu sewage treatment plant (2nd series)

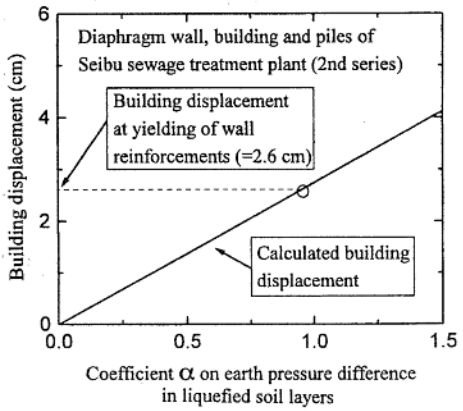

Figure 12. Calculated building displacement for Seibu sewage treatment plant (2nd series)

(refer to Figure 7). Results are shown in Figures 13 and 14. It is seen that, if the wall was not connected to the building, it would have yielded at the coefficient α about 0.05, resulting in the maximum wall top displacement about 6 cm. This hypothetical behavior is comparable to that of the soil cement mixing wall of Shimagami pumping station (refer to Figures 8 and 9).

Based on the above results, it could be concluded that the diaphragm wall for the second series of facilities in Seibu sewage treatment plant had a large resistance against the lateral flow, due mainly to its structural condition that it was connected to the building which was supported by cast-in-place concrete piles as well. It should be added that the location of the reduction in the reinforcement of the wall was partly at a depth of 7.35 m from the ground surface, whereas analyzed results in this condition did not largely change from those mentioned above.

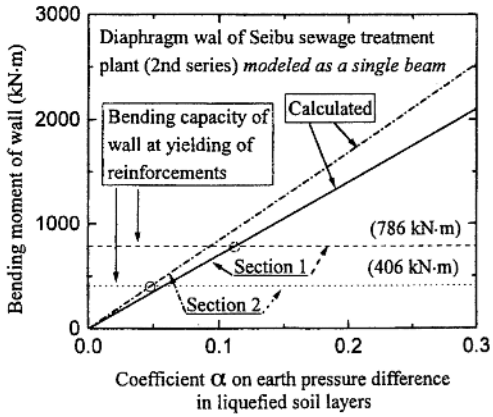

Figure 13. Calculated maximum bending moment of wall as a single beam for Seibu sewage treatment plant (2nd series)

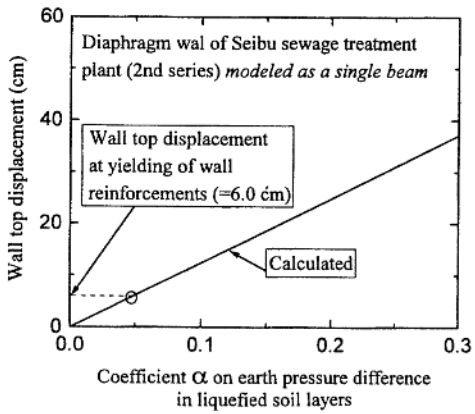

Figure 14. Calculated wall top displacement as a single beam for Seibu sewage treatment plant (2nd series)

4 SUMMARY AND CONCLUSION

Good performance of Shimagami pumping station in Kobe City against lateral flow of liquefied soil layers during the 1995 Hyogoken-Nanbu earthquake is reported, which was surrounded by soil cement mixing walls used for temporary soil retaining during excavation work to construct the facility building.

Based on simplified analyses of the wall located on the seaside of Shimagami pumping station that was deformed during the earthquake, it was estimated that the earth pressure difference caused by the lateral flow of the liquefied soil layers was on the order of several percent of the total overburden pressure or less.

Similar analyses of a diaphragm wall located on the seaside of the second series of facilities in Seibu sewage treatment plant in Kobe City revealed that, since it was connected to the building which was supported by both the wall and concrete piles, it was more effective against the lateral flow than the soil cement mixing wall of Shimagami pumping station that was not connected to the building.

ACKNOWLEDGMENTS

Assistance of Messrs. T. Nakai and K. Hata in Kobe City Office by providing information on the investigated sewage facilities is greatly acknowledged.

REFERENCES

Hamada, M., Isoyama, R. and Wakamatsu, K. 1995: The Hyogoken-Nanbu (Kobe) earthquake, liquefaction, ground displacement and soil condition in Hanshin area, *Association for Development of Earthquake Prediction*, p. 121.

Hamada, M. and Wakamatsu, K. 1996: Liquefaction, ground deformation and their caused damage to structures, *The 1995 Hyogoken-nambu Earthquake - Investigation into Damage to Civil Engineering Structures-, Committee of Earthquake Engineering, Japan Society of Civil Engineers*, pp.45-91.

Ishihara, K. 1997: Geotechnical aspects of ground damage during the Kobe-Awaji earthquake, *Earthquake Geotechnical Engineering, Proc. of IS-Tokyo 95', Ishihara (ed.)*, Vol. 3, pp.1327-1331.

Japan Road Association 1994: Specification for Highway Bridges, part IV: foundation, 430 p.

Kaneko, O., Isemoto, N., Yamaguchi, J., Funahara, H. and Fujii, S. 1998: Countermeasure effect of soil cement walls observed during the 1995 Kobe earthquake, submitted to *11th Japan Earthquake Engineering Symposium* (in Japanese).

Kobe City 1995: Earthquake damage to the Kobe City sewage system and restoration of the system's function, *Sewage Works Bureau*, pp. 11-13.

Sasaki, Y., Koseki, J., Shioji, K., Konishi, M., Kondo, Y. and Terada, T. 1997: Damage to Higashi-nada sewage treatment plant by the 1995 Hyogoken-Nanbu earthquake, *Special Volume of TC4 -Proc. of discussion special session on earthquake geotechnical engineering, Hamburg, 6-12 September 1997-, Seco e Pinto (ed.)*.

Tohda, J., Yoshimura, H. and Li, L. 1996: Characteristic features of damage to the public sewerage systems in the Hanshin area, *Special Issue of Soils and Foundations on Geotechnical Aspects of the January 17 1995 Hyogoken-Nambu Earthquake*, pp. 335-347.

Tokimatsu K., Mizuno, H. and Kakurai, M. 1996: Building damage associated with geotechnical problems, *Special Issue of Soils and Foundations on Geotechnical Aspects of the January 17 1995 Hyogoken-Nambu Earthquake*, pp. 219-234.

Tokimatsu K. and Asaka, Y. 1998: Effects of liquefaction-induced ground displacements on pile performance in the 1995 Hyogoken-Nambu earthquake, *Special Issue of Soils and Foundations on Geotechnical Aspects of the January 17 1995 Hyogoken-Nambu Earthquake, Vol. 2*, pp. 163-177.

Earthquake Geotechnical Engineering, Sêco e Pinto (ed.) © 1999 Balkema, Rotterdam, ISBN 90 5809 116 3

Near field earthquake synthesis

R.C.Câmara
National Laboratory for Civil Engineering, Lisbon, Portugal

ABSTRACT: This paper presents progress work on the synthesis of near field earthquakes and on the modelling of seismic sources.

1 INTRODUCTION

Structures sensitive to strong earthquakes need to have at design level a good characterisation of the Design Earthquake (D.E) and of the Maximum Design Earthquake (M.D.E.), usually assumed equal to the Maximum Credible Earthquake (M.C.E.) for high risk structures. On one hand the D.E. demands continuity of the operating conditions, namely the existence of no severe cracking on concrete and may be a result of both a probabilistic risk analysis and a stochastic generation of vibration time histories (Oliveira; C.S. 1974, Câmara; R.C. 1993). On the other hand the M.D.E. demands no failure of the structure and may be a result of both geotectonic considerations (Câmara; R.C. 1989) and a realistic method of generation of vibration time histories.

One way to generate near field (< 10 km) time histories once settled the dimensions of the fault and the spatial distribution of dislocations, it is by superposition of Green elastodynamics functions, assuming a given rupture pattern.

So, this is a procedure that takes into account the same data usually used at the definition of the M.D.E.

2 SCHEME FOR NUMERICAL EARTHQUAKE SYNTHESIS

The formulation of the earthquake source problem is based on the body force equivalent representation (Maruyama; T. 1963, Burridge; R. & Knopoff; L. 1964). The displacement at a point $\bar{x}$, due to discontinuity in the displacements across the fault surface Σ is given by

$$u_n(\bar{x},t) = \int_{-\infty}^{\infty} d\tau \int_{\Sigma} D_i(\bar{\xi},t)\, K_{in}(\bar{x},\bar{\xi},t-\tau)\, d\Sigma_{\xi} \quad (1)$$

where

$$K_{in}(\bar{x},\bar{\xi},t-\tau) = C_{ijpq}\, n_j(\bar{\xi}) \frac{\partial}{\partial \xi_q} G_n^p(\bar{x},\bar{\xi},t-\tau) \quad (2)$$

is the kernel of the integral equation (1). The quantity $u_n(\bar{x},t)$ is the n^{th} component of the displacement at the point $\bar{x}$ and at a time t due to the dislocation vector $\bar{D}(\bar{\xi})$, defined over the fault surface Σ. $G_n^p(\bar{x},\bar{\xi},t)$ is the dynamic Green tensor, $n_j(\bar{\xi})$ is the j^{th} component of the unit vector normal on the fault surface and C_{ijpq} is the elasticity tensor.

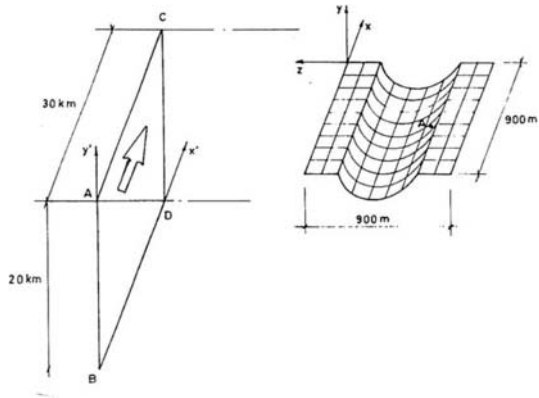

Fig. 1 – Faults characterisation

The dynamic Green tensor is only available for full space hypothesis so, in order to take into account the half space surface, it may be assumed a simplified scheme where the responses to the dislocations on a sub-area are filtered at time domains, assuming that the responses are plane volume waves (P,SH,SV) at the receiver at the surface of the half-space (Trifunac; M.D. 1989, Jordanovski; L.R, Trifunac; M.D. & Lee; V.V. 1986). The author developed a boundary element method that discretizes the canyon with the presented seismic sources.

In the present problem the rupture process for earthquakes must be defined . It may be used a kinematic self-similar rupture process for earthquakes (Herrero; A. & Bernard; P. 1974). In fact the basic assumption that the self-similarity and the spectral law of the seismic body-wave radiation (e.g., ω - square model) must find their origin in some simple self-similar process during the seismic rupture led to the construction of a kinematic, self-similar model of earthquakes. It is first assumed that the amplitude of the slip distribution high-pass filtered at high wavenumber does not depend on the size of the ruptured fault. This leads to the following "k-square" model for the slip spectrum for $k > 1/L$:

$$D(k) = C \frac{\Delta\sigma L}{\mu k^2} \qquad (3)$$

where L is the ruptured fault dimension, k the radial wavenumber, $\Delta\sigma$ the global stress drop, μ the shear modulus and C an adimensional constant of the order of 1.

The rupture front is assumed to propagate on the fault plane with a constant velocity v, and the rise time function is assumed to be scale dependent. The partial slip associated to a given wavelength 1/k is assumed to be completed in a time 1/(kv), based on simple dynamical considerations. Therefore, it was considered a simple dislocation model (instantaneous slip at the final value) which indeed correctly reproduces this self-similar characteristic of the slip duration at any scale. When the rupture front goes through the subarea the slips starts increasing but as soon as the rupture reaches its border a partial stopping phase is expected to travel back in the subarea due to the local and temporary slip velocity decrease at this barrier (when the subarea stops slipping the next subarea begins slipping). The "k-square" model for the slip leads to the "ω-square" model, with the assumption above. The "ω square" model assumes a displacements Fourier spectrum constant till the corner frequency and than decaying like ω^{-2}. The velocity and acceleration Fourier spectrum are equal to the displacement Fourier spectrum respectively times ω and ω^2. The corner frequency is aproximately

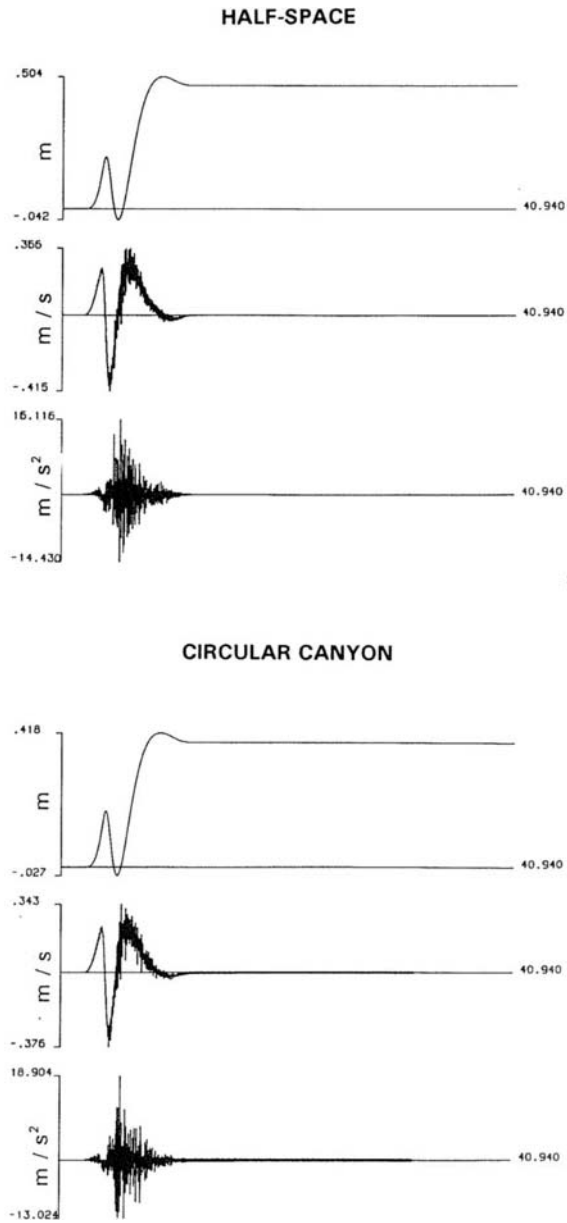

Fig. 2 – Component X of synthetic earthquakes

$f_o = \frac{2{,}34\, C_s}{R}$ where R is the fault radius and C_s the S wave velocity.

Based on this theory the final dislocations on a rectangular fault, fig.1, are assumed to be given by

$$D(x,y) = C\, 2\sqrt{2}\, \frac{\Delta\sigma}{\mu} \sqrt{L_x\, L_y} \sum_{n=N}^{M} \frac{1}{n^3} \operatorname{sen}\left(\frac{n\pi x}{L_x} + \theta_n\right) \operatorname{sen}\left(\frac{n\pi y}{L_y} + \theta_n'\right) \quad (4)$$

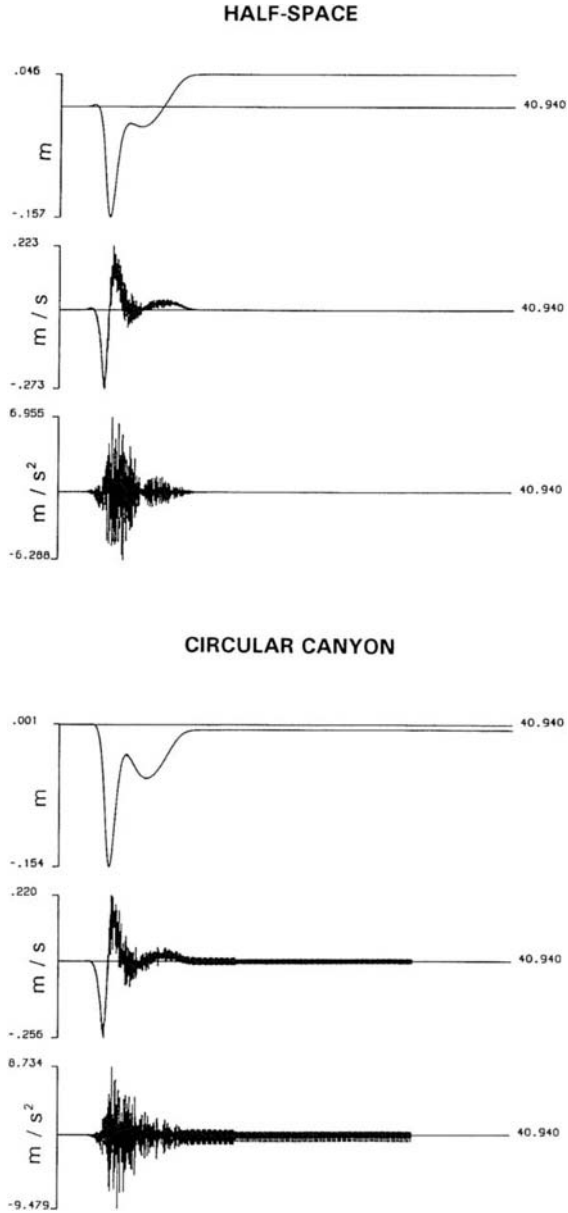

Fig. 3 – Component Y of synthetic earthquakes

Where θ_n and θ_n' and random number between 0 and 2π, L_x is the length of the rectangle and L_y its height. It is assumed that the dislocations are always positive with a direction at the rectangle surface given "à priori". For $1 \leq n < N$ it's assumed the same

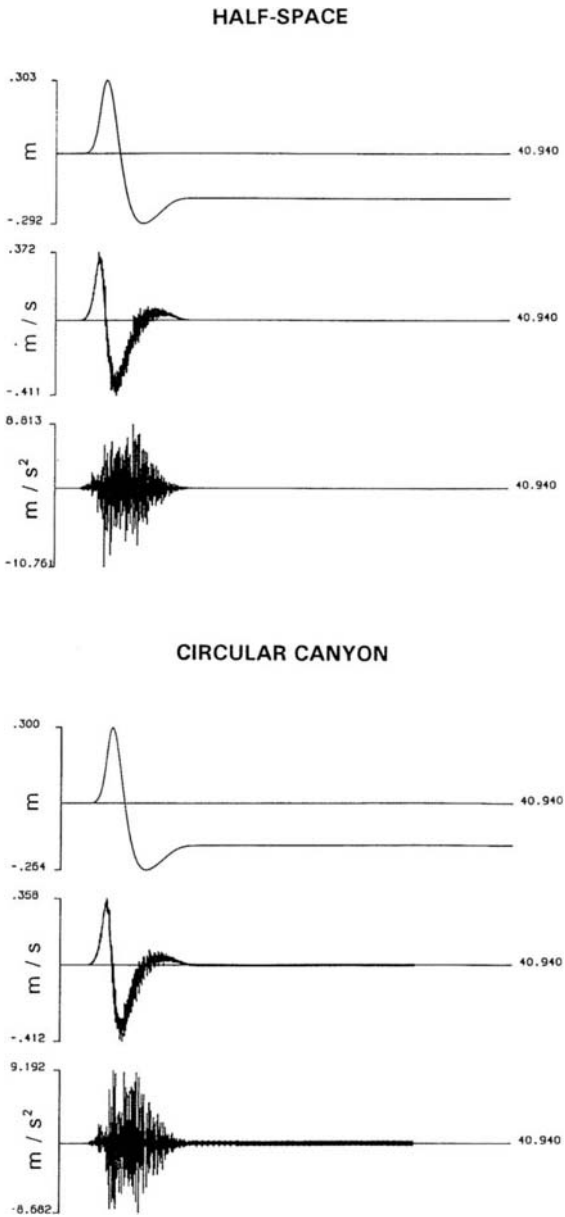

Fig. 4 - Component Z of synthetic earthquakes

equation (4) with other weights rather than n^3, and for the very first n, $\theta_n = \theta'_n = 0$, in order to control the surface displacement.

We must notice that each sub-area creates a stopping phase, so it is expected a uniform density power spectrum of accelerations even for very high frequencies. On the other hand the velocity histories controls the density power spectrum of accelerations at lower frequencies.

3 PROGRESS RESULTS

It was assumed a vertical rectangular fault (transverse slip) with rupture length 30 km and depth 20 km, and two hypothesis: 1) station at half-space; 2) station at half-circular canyon, fig. 1.

The final offset of dislocations was assumed to be generated by (4) with N = 1 and M = 40. The phase of the first three harmonics was assumed zero. These hypothesis result in a average slip of 1.567 m and 0.047 m at the edge AC. The shear modulus was assumed $\mu = 4.5 \times 10^{11}$ dyne / cm^2.

The velocity of P waves was assumed 7500 m/s and the Poisson coefficient $\nu = 0.25$ so $C_p/C_s = \sqrt{3}$ where C_s is the S wave velocity. The value of $C\,\Delta\sigma$ was assumed 2.5 MPa. The rupture front was assumed a straigth line travelling with a velocity of 4.0 km/s form AB to CD. With this hypothesis the seismic moment is $M_o = 4.5 \times 30 \times 20 \times 10^{21} \times 156.7 = 4.23 \times 10^{26}$ dyne/cm
and the moment magnitude

$$M_w = \left(\frac{\log_{10} M_o}{1{,}5}\right) - 10.73 = 7$$

This value compares well with the estimation of the magnitude from the rupture area S

$$M_s = \log_{10} S + 4.15 = 6.9 ; \qquad S - Km^2$$

Two earthquakes were generated for both hypothesis at station A located at 5 km from the fault trace with the half-space. The results are presented in figs 2 to 4.

4 CONCLUSION

The synthetized earthquakes are rich in high frequencies (>10Hz), owing to the existence of a high number of stopping phases (100×100 subareas). These high frequencies are expected to be damped with distance in real earthquakes.

When active faults are near the dam site the usual procedure is to generate accelerograms from a response spectrum. However this procedure takes not into account the non-stationary nature of real accelerograms and so the need of earthquake synthesis like the proposed scheme.

5 BIBLIOGRAPHY

Oliveira, C.S. 1974. Seismic risk analysis. Report No. EERC 74-1, Berkeley.

Câmara, R.C. 1993. Coupled arch dam-foundation-reservoir seismic behaviour. Safety evaluation for rupture scenarios. PH.D.Thesis, Porto.

Câmara, R.C. 1989. Finite element models for dynamic analysis of concrete dams. Specialist Thesis, LNEC, Lisbon.

Maruyama, T. 1963. On the force equivalent of dynamic elastic dislocation with reference to the earthquake mechanics. Bull. Of Earthq. Res. Inst. Vol 41, 467-468.

Burridge; R.&. Knopoff L.1964. Body force equivalent for seismic dislocation. Bull. Seism. Soc. Amer., Vol. 54,6, 1875-1888.

Trifunac, M.D. 1989. Inversion of earthquake source mechanism using near field strong motion data. 4th International Conference on Computational Methods and Experimental Measurements, Capri.

Jordanovski; L.R & Trifunac M.D. & Lee, V.V. 1986. Investigation of numerical methods in inversion of earthquake source. Dept.of Civil Eng. Report No. 86-01, Univ. Southern California, Los Angeles.

Herrero; A. & Bernard, P 1994. A kinematic self-similar rupture process for earthquakes. Bull. Seism. Soc. Amer., Vol. 89, No 4,1216-1228.

7 Codes, standards and safety evaluation

This Page Intentionally Left Blank

Earthquake Geotechnical Engineering, Sêco e Pinto (ed.) © 1999 Balkema, Rotterdam, ISBN 90 5809 116 3

Reduction of seismic vulnerability by geomaterial attenuation procedures

A.d'Onofrio & C.Mancuso
Dipartimento di Ingegneria Geotecnica, Università di Napoli Federico II, Italy
F.Silvestri
Dipartimento di Difesa del Suolo, Università della Calabria, Italy

ABSTRACT: Analytical and experimental studies in literature have shown that the liquefaction hazard of soft soil sites can be substantially reduced by ground improvement or replacement of the uppermost portion of a subsoil profile. The paper summarises the most recent advances in these studies, addressed to verify the applicability of the so-called *Geomaterial Attenuation Procedure* (GAP) to simplified subsoil patterns, characterised by different kinds of heterogeneity in terms of shear wave velocity profiles. Preliminary design criteria were first formulated, then summarised in synthetic charts, and finally tested on actual subsoil profiles subjected to strong-motion seismic shaking. The GAP demonstrated most effective in the range of natural periods pertaining to medium-height buildings, made by either masonry walls or r.c. frames.

1 BACKGROUND

Many case histories in literature demonstrate that earthquake-induced damage can be largely affected by small variations of mechanical properties in a deformable subsoil profiles (e.g. Mexico City, 1985; Loma Prieta, 1989; Kobe, 1995). Observations of recorded events (Yasuda et al., 1996), experiences in physical modelling (Kimura et al., 1997) and numerical studies (Fukutake, Ohtsuki, 1995) also suggest that most of the site amplification occurs across the uppermost layers. This behaviour suggested that reduction of the seismic risk of soft soil sites can be achieved by ground improvement of the shallowest layers or by replacing them with a stiffer geomaterial.

This paper first summarises some results of preliminary studies carried out at University of Naples Federico II (Mancuso et al., 1997), addressed to verify the effectiveness of this *Geomaterial Attenuation Procedure* (GAP) on a specific soft clay subsoil. Thereafter, the effort towards a rational approach to design is documented by synthetic charts for the preliminary selection of the GAP system, based on the simplified assumption. Finally some tests are presented considering actual Italian seismic sites.

2 PRELIMINARY STUDIES

The soil profile constituted by a thick and apparently homogeneous lacustrine Fucino clay, was used as a model site to quantitatively appreciate the influence of small details in the soil profile on the site seismic response and the effectiveness of the GAP systems.
The geotechnical characterisation of the selected subsoil was obtained from high-quality in-situ and laboratory tests (A.G.I. 1991). Despite the apparent uniformity of the clay deposit, a careful inspection of the variation of G_0 with depth (Fig. 1a) reveals some heterogeneity factors: close to surface, an upper desiccated stiff crust (~5 m thick) below which the stiffness suddenly drops; then, the shear modulus increases regularly, down to around 20 meters, where a sharp variation in the stiffness profile is observed, associated to a consistent increase in $CaCO_3$ content.

To account for the above heterogeneity factors, several subsoil models were considered in the analyses (Festa, Girardi, 1996). In particular, the two $G_0(z)$ and $D_0(z)$ profiles marked with S and C in Fig. 1a wished to reproduce:

S) a profile based on cross-hole measurements below the desiccated crust, extrapolated up to the surface. This model simulates the absence of information on the shallowest properties of soil, like that which might have resulted from laboratory tests alone;
C) the complete subsoil profile, including both the desiccation and $CaCO_3$ content effects.

In the study, the top of the bedrock was fixed at 40 m (maximum depth of the available data). To account for non-linearity, the $(G/G_0):\gamma$ and $D:\gamma$ curves from RC tests were taken (Pane, Burghignoli, 1988); the initial damping were assumed equal to 2 % within and 4 % below the desiccated crust, while the normalised $G:\gamma$ curve was unique for the whole profile.

Numerical predictions of 1D non-linear seismic response were carried out using the SHAKE '91 code (Sun et al. 1991). The analyses were based on a reference input motion from the accelerogram recorded on a rock outcrop during Irpinia earthquake (1980).

To simulate the variations of the input motion with the distance from a causative fault, the seismic record

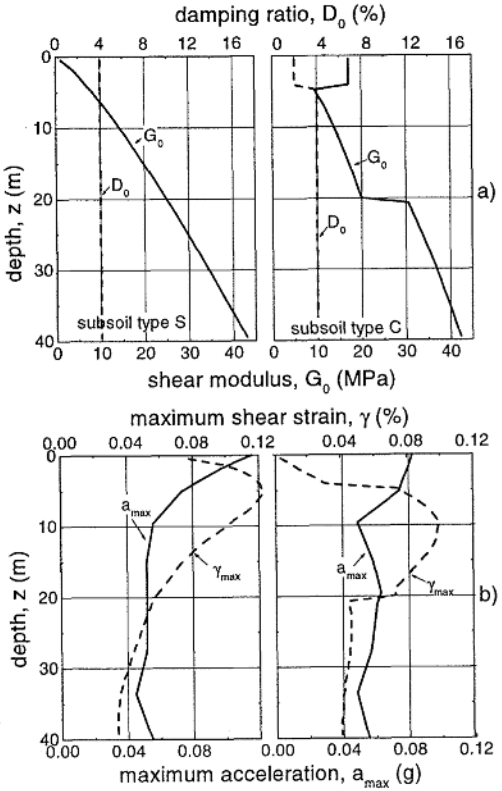

Fig. 1. a) Variations of G_0 with depth; b) Profiles of maximum accelerations and shear strains.

was introduced in the analyses both unmodified, and scaled in terms of amplitude and frequency contents Mancuso et al. (1997). Table I summarises the main parameters of the resulting reference input motions.

The results are reported in Fig. 1b in terms of profiles of maximum accelerations (a_{max}) and shear strains (γ_{max}). The effects of the stratigraphic details can be clearly argued comparing the values of a_{max} for profiles S and C, the latter presenting a considerable deamplification close to the surface. From the analysis of other soil patterns, it was also noted that the variation of stiffness due to increasing $CaCO_3$ content was about ineffective on the ground response (Mancuso et al., 1997). Therefore, the beneficial effect should be ascribed to the presence of the desiccated crust.

This confirmed that the variations of soil properties at large depths play a much less significant role on the ground shaking than the shallow heterogeneity factors. This suggest that, in order to reduce the surface shaking, shallow heterogeneous elements can be introduced into the subsoil profile, using low cost technologies or geomaterials such as compacted soil.

This idea has been supported from literature evidence and previous Authors' experience. Laboratory data reported by d'Onofrio et al. (1995) show that, after appropriate treatments, compacted silty sands

Table I. *Reference input motions adopted in the study.*

Seismogram	Distance from causative fault (km)	Duration (s)	Maximum Acceleration (g)
I, not scaled	80	70.0	0.06
II	50	63.0	0.10
III	30	52.5	0.20

can exhibit higher stiffness and damping values than the above considered desiccated crust: as a consequence, their adoption can improve the static and seismic performance of the foundations of any structure to be constructed or protected. The principle is justified by the observation that a shallow stiff screen compels most of the seismic waves energy to remain trapped within the soft subsoil without outcropping at surface.

In order to verify the feasibility of such a '*Geomaterial Attenuation Procedures*' (GAP), some preliminary analyses were run considering three types of low-cost systems: (1) homogeneous layer of compacted soils; (2) alternate layers of compacted soils and soft clay; (3) alternate layers of compacted soils and concrete. These GAP systems were located on the top of the S profile, the most unfavourable situation for the examined clay deposit. Due to the reduced space, in this paper only the first type (GAP1) is considered. The profile reported in Fig. 2a was subjected to the above mentioned accelerograms. The results are reported in Fig. 2b in terms of amplification ratios (i.e. the maximum acceleration at depth divided by the corresponding bedrock value) comparing the response of the GAP1 system to that of the S profile. It can be observed that the GAP1 reduces the ground acceleration along its thickness, with negligible effects at higher depths. Some evidence of non-linearity also appears in Fig. 2b: analysing the amplification ratios close to the surface, the plots confirm that the larger the seismic shaking, the smaller the average amplification.

The results are also summarised in Fig. 3 in terms of spectral accelerations at surface (structural damping ξ=5%) with and without *GAP*. Fig. 3b reports the *effectiveness*, E(T), as defined by the ratio between the amplitudes of surface response spectra of the deposit with the attenuation system, $Sa_{ON}(T)$, and the same values for the S profile, $Sa_{OFF}(T)$:

$$E(T) = \frac{Sa_{ON}(T)}{Sa_{OFF}(T)} \qquad (1)$$

The capability of the GAP to reduce the seismic shaking can be measured by this ratio, being the effectiveness higher as E(T) reduces. Overall, the values of E(T) are significantly lower than unity through a range of periods (0.1÷1 sec). The GAP1 shows particularly effective between 0.2 and 0.5 s, i.e. the range of natural periods pertaining to medium-height constructions, including buildings with a limited number of storeys, made by masonry walls or r.c. frames; for such a range, the seismic motion can be reduced down to 60%.

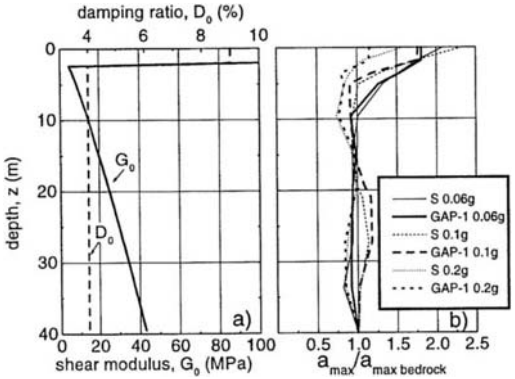

Fig. 2. a) Subsoil profile; b) Amplification ratios.

3 PRELIMINARY DESIGN CRITERIA

As previously forwarded, one of the main targets of this research was to formulate simplified criteria for the preliminary design of a GAP system. In practice, it is required to optimise mechanical and geometrical parameters of the soil layer to be placed at the top of the existing subsoil, according to the known geotechnical characteristics of the natural profile. In this stage, the non-linear response of the subsoil to strong-motion earthquake shaking is not accounted for, and the attenuation system is dimensioned hypothesising a linear site amplification.

The set of basic properties of the top 'attenuating' layer is constituted by the vector (ρ_G, V_G, D_G, H_G), where: ρ_G is the mass density, V_G is its shear wave velocity, D_G is the damping and H_G is the thickness.

The procedure requires the choice of a parameter appropriate to describe the coupling between the seismic impedances of a tentative GAP and the subsoil. After some trials, the choice fell on the ratio between impedance, η, and the thickness ratios, ζ:

$$\frac{\eta}{\zeta} = \frac{(\rho_G \cdot V_G)/(\rho_S \cdot V_S)}{H_G / H_S} \qquad (2)$$

where ρ_S, V_S, H_S are reference values of mass density, shear wave velocity and thickness for the existing subsoil. These can take in due account the heterogeneity of the soil profile, for instance selecting the most appropriate average values.

To express the effectiveness of the GAP system, an 'Attenuation Coefficient' was defined as:

$$I = \frac{1}{\Delta f} \int_0^{\Delta f} \frac{A_{ON}(T)}{A_{OFF}(T)} \cdot df \qquad (3)$$

with $[A_{ON}(f)]$ and $[A_{OFF}(f)]$ the transfer functions of the subsoil, respectively with and without the GAP system. Both these functions can be computed with simple calculations under the simplified assumptions of a regular layering and linear amplification.

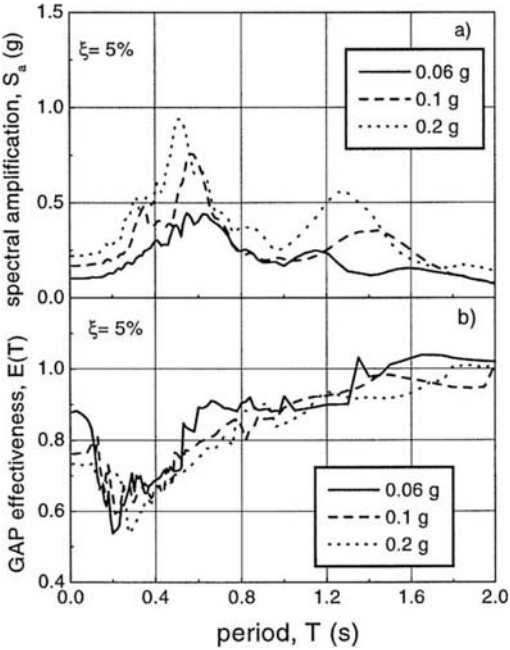

Fig. 3. a) Spectral accelerations at surface (ξ=5%); b) GAP effectiveness.

Using the above quantities, a set of charts was produced for various subsoil profile models, each one characterised by different reference values and profile shapes of shear wave velocity (Crisci 1997).

Fig. 4 plots the variation of the attenuation coefficient, I, with the logarithm of the ratio η/ζ, with reference to an homogeneous profile on the top of which a 4 m thick attenuation layer is placed. Each data set refers to a different value of the reference shear wave velocity, V_S, and is fitted by a regression line. In all cases, the attenuation coefficient I decreases with the ratio η/ζ (i.e. the effectiveness increases with the impedance of the attenuating layer). Also, the relative effectiveness appears higher for softer reference subsoils (lower V_S).

The data reported in Fig. 5 pertain to the case of a 4m thick attenuation blanket resting on a two layers (equal thickness) profile. The degree of heterogeneity is moderate, being equal to 4 the shear wave velocity ratio between the bottom and the top layer.

The same general considerations relevant to the case of the homogenous subsoil can be drawn; moreover, this time for high η/ζ values I seems to stabilise towards an asymptotic value, which increases with the average density and shear wave velocity of the soil.

By comparing these values of I with those obtained on a homogeneous profile with the same average value of V_S (recalled in Fig. 5 by the same regression lines plotted in Fig. 4), the GAP appears more effective in the double layered profile.

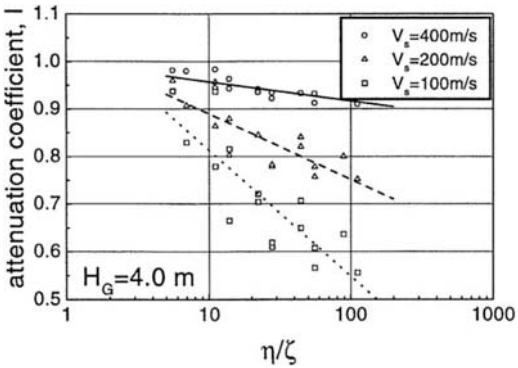

Fig. 4. Attenuation coefficient I of an homogeneous profile (4 m thick attenuating layer).

To model typical lithologically-homogeneous subsoil, the solutions pertaining to velocity profiles with linear variation of V_s with depth (see Gazetas 1982) where computed. Several cases have been considered (see Table II), each one identified by the values of the shear wave velocity at zero-depth (V_0) and of the degree of heterogeneity, represented by the slope of variation of V_S versus depth (α).

In Fig. 6 all the cases relevant to a GAP thickness of 4 m are plotted. Irrespective of the α value, all the data pertaining to a given V_0 plot close together. This seems to indicate that V_0 is the parameter which the effectiveness depends on, with the heterogeneity of the profile (α) playing a more limited role.

This conclusion was confirmed by the results of analyses of parabolic V_S:z profiles. An example, again relevant to the case of 4m, can be found in Fig. 7, in which two profiles with 40 and 80 m thickness are separately considered. For both of them, the shear wave velocity is equal to zero at surface, and reaches 600 m/s at the 'bedrock'. The attenuation coefficient I are proportional to the subsoil thickness, decreasing to limit values of 0.72 and 0.81 for 40 m and 80 m respectively.

4 VALIDATION STUDIES

4.1 *Full design procedure*

The above charts can be useful for the design of GAP systems by the following schematic procedure:
step 1: the actual layered soil profile is reduced to the most appropriate simplified pattern of variation of shear wave velocity with depth;
step 2: the most suitable treatment is chosen according to the soil nature, the type, the state and the importance of the structure to be protected. In fact, the choice of the most suitable ground improvement technique is conditioned by the structural issues: if the building or infrastructure is already present, the choice can be limited to few methods (e.g. grouting), if the building is monumental the tolerable costs can be higher, and so on;

Table II. *Reference linear subsoil profiles.*

PROFILE	V_0 (m/s)	α [(m/s)·m^{-1}]
A | A′ | A″	200 | 300 | 400	2.5
B | B′	200 | 300	5.0
C | C′ | C″	200 | 300 | 400	7.5
D | D′	200 | 300	10.0
E | E′	200 | 300	12.5

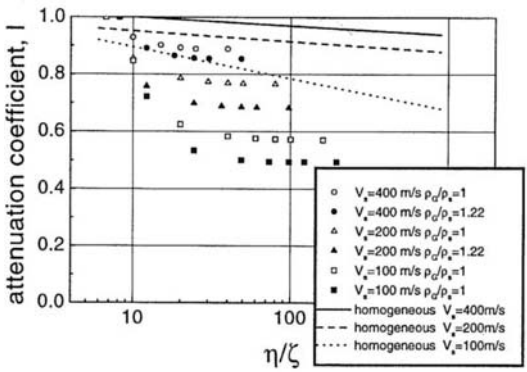

Fig. 5. Attenuation coefficient of a two layers profile (4m thick attenuating layer).

step 3: the impedance and the maximum possible thickness of the attenuating blanket are determined according to the technology selected and the properties of the shallowest soil to be treated or replaced;
step 4: by using the most appropriate charts, the thickness of the attenuation layer can be found which gives the optimum balance between the cost and the effectiveness of the countermeasure (i.e. the value of H_G beyond which no appreciable reduction of the attenuation coefficient I is observed);
step 5: if the thickness selected is technologically acceptable, non-linear seismic response analyses can be run without and with the GAP at the top of soil profile, to confirm the performance of the attenuation system, or to suggest different solutions.

4.2 *Verification*

As a preliminary verification, some seismic response analyses were attempted on a particular GAP system (with fixed geometry and mechanical properties) placed on different subsoil profiles, to be subjected to various reference input motions. This allowed to compare the attenuation coefficients predicted by the design charts to the non-linear response of the complex layered soil model shaken by a strong motion event (Crisci, 1997). 1-D analyses were again run by SHAKE '91 on three Italian sites struck by the 1980 Irpinia earthquake (Garigliano, Mercato S. Severino, S. Severo), for which both accelerometric records and geotechnical characterisation were available.

Table III. *Attenuation coefficients from the analysis.*

	ATTENUATION COEFFICIENTS					
	H	D	L	P	SHAKE '91	
					M=6.5	M=7.5
G	0.85	0.83	0.80	0.58	0.69	0.89
MSS	0.87	0.85	0.99	0.73	0.81	0.74
SS	0.81	-	0.89	0.70	0.87	0.86

LEGEND: H – Homogeneous profile; D – Double layer profile; L – Linear profile; P – Parabolic profile; G - Garigliano site; MSS – Mercato San Severino site; SS – San Severo site.

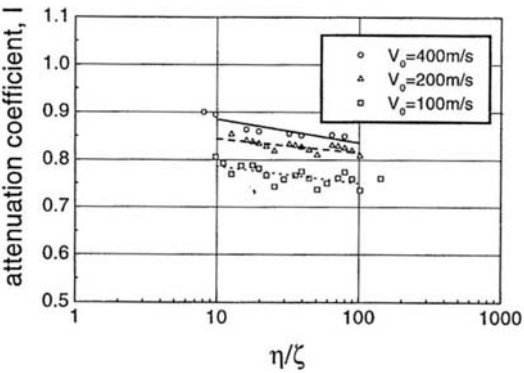

Fig. 6. Attenuation coefficients of linear V_s:z profiles (4 m thick attenuating layer).

Like in the pilot study on Fucino clay, a variability in amplitudes and frequency contents of the reference input motions was considered, scaling the seismic records as described in Crisci (1997).

On the basis of the in situ and lab experimental data, it was possible to define detailed shear wave profiles and reduce them to the simplified patterns of the design charts. The value selected for the thickness H_1 of the GAP system was 6 m, the shear wave velocity fixed to 600 m/s and the mass density to 2.2 kNs^2/m^4. Such conditions can be realised by using intensive grouting of the shallow soil layer.

In Table III the attenuation coefficients, predicted using four different heterogeneity patterns, are compared to those computed by non-linear seismic response analyses (with two earthquake magnitudes, M=6.5 and M=7.5). It is worth noting that the estimates of the attenuation coefficients which yield the best agreement with the numerical predictions (underlined in Table III) pertain to different heterogeneity patterns according to the site considered.

Due to the lack of space, only the example of S. Severo is described. The soil is lithologically rather homogeneous, formed by silty sands (100 m) thick, with an average V_S of about 500 m/s. Fig. 8a reports the transfer functions computed for the site, with and without GAP, adop-ting both the linear/simplified and the non-linear/complex predictions.
The effect of non-linearity is not evident in this case: the amplification curves match quite well.

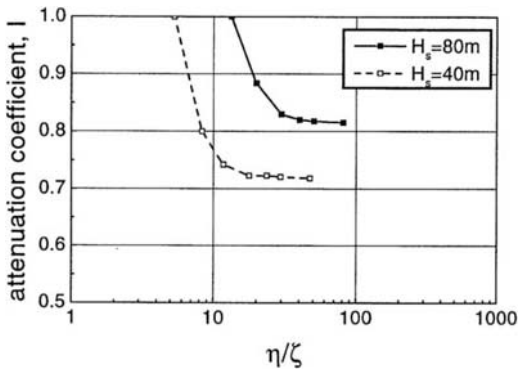

Fig. 7. Attenuation coefficients of parabolic V_S:z profiles (4 m thick attenuating layer).

In Fig. 8b the ratio R(f) between the transfer functions computed with and without GAP are reported for the design and the verification schemes. A good agreement between them is observed throughout the frequency range 0-10 Hz. The average values of R(f), i.e. the attenuation coefficients I (horizontal lines in the figure), are equal to 0.85 in the chart design and 0.86 in the refined calculation. It can be noted that the frequency shift between the transfer functions, causes the attenuation ratio R(f) oscillating around an average value, overcoming unity around the frequencies amplified by the GAP.

The results of the verification analyses are finally plotted in Fig. 9 in terms of: (a) acceleration spectra (M=6.5, ξ=0) and (b) efficiency factor (M=6.5 and 7.5). The range of periods is limited to the values 0-1s, pertaining to r.c. or masonry buildings of moderate height (less than 10 storeys). The comparison between the spectra pertaining to the bedrock and surface shaking first shows that, in absence of any treatment, the site effect results in a strong amplification of the reference motion throughout the whole range of periods. The subsoil response with the GAP produces a less pronounced amplification, even though some anomalous amplifications occur between 0.60 Hz and 0.85 Hz, i.e. where the attenuation ratio R(f) presents its first peak values (compare Fig. 8b). The analysis of the effectiveness (Fig. 9b) confirms that the spurious peaks in R(f) can produce some local amplification; nevertheless, the overall behaviour of GAP, at least in this case, is considerably beneficial, since it induces an attenuation of spectral ordinates as high as 30% in the range of low periods. It is worth underlining that higher reductions must be expected for softer subsoils than that examined in this specific case.

5 CONCLUDING REMARKS

The examples shown in this paper demonstrate that the introduction of an even relatively thin stiff layer at the top of a soft to medium stiff soil profile can attenuate the ground shaking at surface.

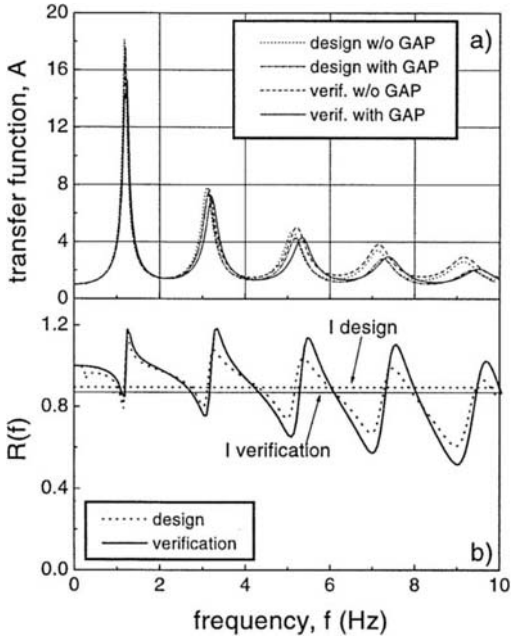

Fig. 8. Transfer functions computed for S. Severo site (with and without GAP).

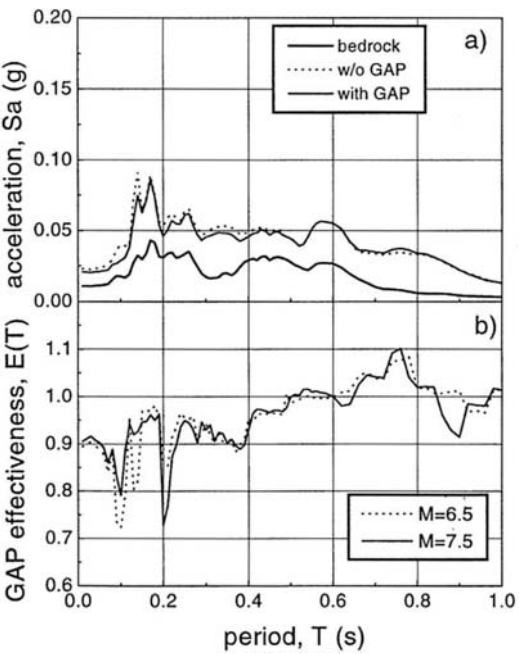

Fig. 9. a) Acceleration spectra for M=6.5 (ξ=0) and b) efficiency factor (M=6.5 and 7.5).

The first numerical checks of the effectiveness of GAP highlighted an acceptable consistency between the preliminary design and the results of numerical 1D non-linear predictions. The GAP confirmed to be particularly effective in the range of natural periods pertaining to medium-stiff constructions, including masonry walls or r.c. buildings with a limited number of storeys, monuments, infrastructures. For the reduction of seismic vulnerability of such constructions, the low-technology systems can represent a valuable solution, as an alternative to the more efficient, yet more costly, elastomeric 'base isolators'. Nevertheless, an effort to improve the rationality of the design approach still need to be pursued, as well as more verifications on an extended range of vulnerable soil profiles. 2D analyses and model tests can further help the assessment of validity of the GA P. Developments in this sense are now taken under consideration by the Authors.

REFERENCES

A.G.I. 1991. Geotechnical characterisation of Fucino clay. *Proc. X ECSM FE*, Florence, Italy, 1991.

Crisci M., 1997. Sistemi di attenuazione del moto sismico in superficie: criteri preliminari di progetto. *M. Sc. Thesis*, Università di Napoli.

d'Onofrio A., Santucci de Magistris F., Silvestri F., F. Vinale, 1995. Behaviour of compacted sand-bentonite mixtures from small to medium strains. *Proc. I Int. Symp. on Eart. Geotechnical Eng., Tokyo.*

Festa M. ,and G. Girardi, 1996. Sistemi di isolamento sismico a basso contenuto tecnologico: primi studi di fattibilità. *M. Sc. Thesis*, Università di Napoli.

Fukutake K., Ohtsuki A., Y. Yoshimi, 1995. A new cement block system for protecting piles in liquefiable ground. *Proc. I Int. Symp. Earth. Geot. Eng., Tokyo.*

Gazetas G., 1982. Vibrational characteristics of soil deposits with variable wave velocity. *Int. Journ. for Numerical and Analytical Met. in Geomechanics.*

Kimura T., Takemura J., Hiro-oka A., Okamura M., Matsuda T., 1997. Countermeasures against liquefaction of sand deposits with structures. *Proc. I Int. Symp. on Earthquake Geotechnical Eng., Tokyo.*

Idriss J. ,and J. I. Sun, 1992. SHAKE91 - A computer program for conducting equivalent linear seismic response analyses of horizontally layered soils deposits. *University of California*, Davis.

Mancuso C., Silvestri F., F. Vinale, 1997. Soil properties relevant to seismic microzonation. *Proc. I Japanese-Turkish Conf. Earth. Eng.* Istanbul 1997

Pane V. ,and A. Burghignoli, 1988. Determinazione in laboratorio delle caratteristiche dinamiche dell'argilla del Fucino - Conv. GNCSIG – Monselice, Italy.

Seed ,and Idriss. 1969. Influence of soil conditions on the ground motion during earthquakes. Int. J. Soil Mech. and Found. Eng., ASCE, v 95., n SM1.

Yasuda S., Ishihara K., Harada K. ,and N. Shinkawa, 1996. Effect of soil improvement on ground subsidence due to liquefaction. *Soils & Foundations, Special Issue on Geotechnical Aspects of the January 17 1995 Hyogoken-Nambu Earthquake.*

Earthquake Geotechnical Engineering, Sêco e Pinto (ed.) © 1999 Balkema, Rotterdam, ISBN 90 5809 116 3

Effect of sheet piling as a measure against liquefaction-induced embankment failure

M. Okamura & O. Matsuo
Public Works Research Institute, Tsukuba, Japan

Y. Koga
Onoda Chemico Company Limited, Tokyo, Japan

ABSTRACT: After the Hyogoken-Nanbu Earthquake in 1995, the seismic safety concerning the potential of liquefaction-induced river dikes failure have been evaluated nationwide and measures to prevent failure have been applied if necessary. Various types of preventive measures including densification, deep mixing, gravel drain and sheet pile driving have been adopted. Among these measures, the sheet piling method is often used especially in urban areas where construction space is limited.

In this study a series of large shaking table tests was carried out in order to study the behavior of dikes and sheet piles installed vertically at the toes of dikes and its effect as a countermeasure against liquefaction-induced embankment failure. Particular attention was paid to earth pressures acting on the sheet piles during shaking.

1 INTRODUCTION

River dikes in Japan have been constructed and increased in height step-by-step since late 19th century without receiving proper consideration on the potential of liquefaction of foundation soil. After the Hyogoken-Nanbu Earthquake in 1995, the seismic safety of the river dikes concerning the potential of liquefaction-induced failure have been evaluated nationwide and measures to prevent failure, if necessary, have been applied. Various types of preventive measures including densification, deep mixing, gravel drain and sheet pile driving have been adopted in practice. Among these measures, the sheet piling method is often used especially in urban areas where construction space is limited.

In the current design practice for sheet piling method, averaged vertical pressure along the base of embankment is applied as uniformly distributed horizontal pressure on the sheet pile, which pressure might be thought to be considerably on the safe side. A type of sheet piles is selected so that sheet piles do not yield under the horizontal load. Thus, the horizontal load should be re-examined.

Model tests on the effects of sheet pile enclosure technique were carried out by some researchers (Yoshimi and Tokimatsu, 1977; Matsuo et al., 1994; Kimura et al., 1995; Adalier et al., 1998) and results of them have contributed to understand the mechanisms of reducing damage during quakes. But the number of tests conducted so far is limited and there may be many influential factors on the horizontal load acting on the sheet pile during an earthquake, such as geometry of dikes, depth of liquefied layer, intensity and dominant frequency of earthquake acceleration, flexural rigidity of sheet piles and so on.

In this study a series of shaking table tests was carried out in order to verify the validity of current design procedure and to study the behavior of dikes and sheet piles installed vertically at the toes of dikes and its effect as a remediation countermeasure against liquefaction-induced embankment failure. Particular attention was paid to earth pressures acting on the sheet piles and influences of flexural rigidity, slope of dikes and dominant frequency of input acceleration were experimentally examined.

2 SHAKING TABLE TESTS

2.1 Soil properties and test procedures

Silica sand and gravel with properties shown in

Table 1 Index properties of the sand used

	Silica sand	Gravel
Specific gravity	2.65	2.65
Mean grain size (mm)	0.17	5.0
Permeability coefficient (m/s)	7.6×10^{-5}	—
Maximum void ratio	1.11	—
Minimum void ratio	0.626	—

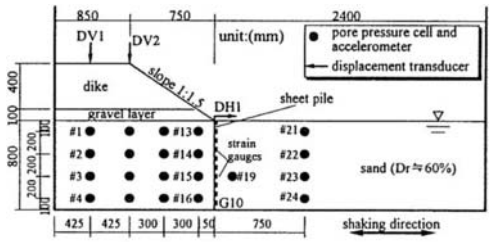

(a) model for tests C1-C4 (sheet pile was not installed for the model C1)

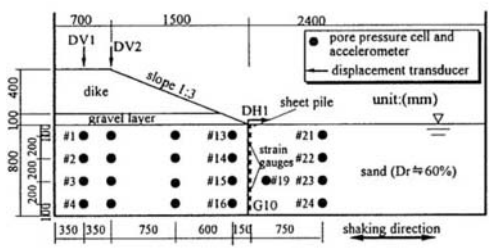

(b) model for test C5

Fig.1 Model setup and location of transducers

Table 1 were used for the tests. A rigid container with inner size of 4.0m in width, 1.0m in breadth and 2.0m in height was used for the tests. A model sheet steel pile wall which was instrumented with ten strain gauges and five earth pressure cells on the both sides was made use of. The model was prepared in the following way. Firstly, the model sheet pile was fixed to the base of container. Channels with internal dimensions of 10mm × 10mm, filled with colored sand were attached to the plexiglass side of the container which made it possible to observe deformation of foundation soil. Dry silica sand was then pluviated into the container. The pluviation was continued intermittently so that pore pressure cells and accelerometers could be installed at the locations indicated in **Fig.1** and the channels could be removed.

Table 2 Test conditions

Case	Thickness of sheet pile	Frequency of input motion	Slope of dike
C1	---	5Hz	1:1.5
C2	6.0mm	5Hz	1:1.5
C3	6.0mm	3Hz	1:1.5
C4	4.5mm	5Hz	1:1.5
C5	4.5mm	5Hz	1:3.0

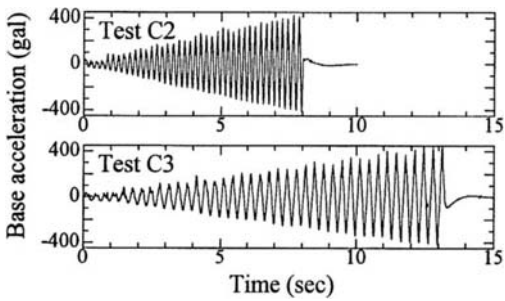

Fig.2 Observed base acceleration

On completion of preparation of sand bed with 800mm deep, de-aired water was introduced from the bottom of the container to saturate the sand. Finally, gravel mound of 100mm thickness, which prevents model dike from sucking water from foundation soil, was placed and silica sand with water content of 15% was tamped to build a model dike. A half the width of an embankment was modeled due to space limitation. Displacement transducers were installed as shown in **Fig.1** and dynamic base excitation was imparted.

2.2 Test conditions

A total of six tests was performed. Test conditions are summarized in **Table 2**. A relative density of the sand bed was very close to 60% in all tests.

Test C1 was the benchmark model test without sheet pile, while in the rest of models sheet pile was applied. Two model sheet piles with different thickness were used. The flexural rigidity of these sheet piles were 5.54×10^5 and 1.83×10^5 kN/cm^4/cm, respectively. The input acceleration time history is shown in **Fig.2**. Sinusoidal waves

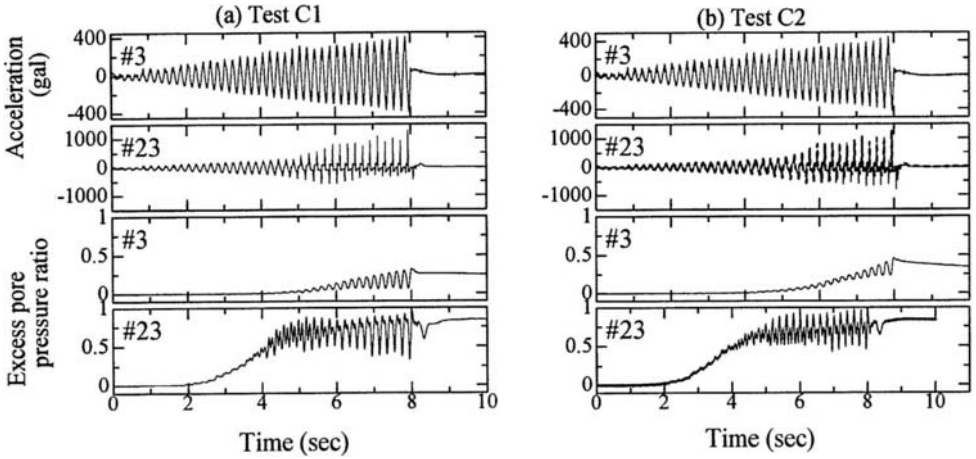

Fig.3 Typical acceleration and excess pore water pressure responses observed in Test C1 and C2

with an amplitude increasing linearly from zero to approximately 400gal were imparted. The dominant frequency of the input motion was 5Hz with an exception for case C3, in which 3Hz was tested. The slope of the dikes was 1:1.5 or 1:3.

It should be noted that sand used in tests C1 to C4 was uniformly mixed in advance, and it was air dried under the sun, after those tests and used again in test C5. Although the unit weight of foundation soil for C5 was almost the same as the preceding tests, liquefaction resistance appeared to be apparently lower than preceding models. Results of sieve analysis conducted after the tests revealed finer content inclusion for sand used in C5 as a result of particle crushing.

3 TEST RESULTS AND DISCUSSION

3.1 Mechanism of embankment damage mitigation

Figure 3 shows recorded excess pore pressures and accelerations at locations indicated as #3 and #23 in **Fig.1** for Test C1 and C2. In the figure, excess pore water pressure was normalized with regard to initial effective vertical stresses calculated from the weight of foundation soil and embankment only directly above these points. At free field (#23), on the one hand, the response of excess pore pressure was generally similar for C1 and C2. Excess pressure was gradually accumulated and it reached the initial effective vertical stress at around t=5(sec), corresponding to initial liquefaction. Recorded responses with pore pressure cells at #21 to #24 indicated that foundation soil in the free field liquefied in all depth. Thereafter clear dips in pore pressure record was found. The acceleration records at this location showed clear spikes during each cycle of excitation. The timing of the spikes coincided to that of pore pressure dips and this responses are believed to be associated with dilative nature of soil skeleton at large strains (Dobry et al., 1995).

It is interesting to note that a peculiar asymmetric acceleration spikes occurred during test C1, while spikes were relatively symmetric for test C2. Such asymmetric response is attributed to the occurrence of down-slope or right-hand side oriented deformation under a static driving shear stresses due to embankment load (Dobry et al., 1995; Adalier et al., 1998). In fact, accumulated lateral deformation in the direction away from embankment was much larger for test C1 in this vicinity, as will be shown later.

On the other hand, observed excess pore pressure at #3 were considerably lower than initial effective vertical stress and accelerations in the vicinity were found not to decay throughout the event, indicating that the soil in this locality did not liquefy. It has also been reported that excess pore pressures were highest in the free field and lowest just beneath the embankment and this fact may be due to existence of surcharge loading (Matsuo et al., 1994; Adalier et al., 1998). The excess pore pressure below the embankment was higher for test C2 than C1. This may be attributed to the fact that sheet piles restrain the soil below the embankment to undergo horizontal displacement and thereby, reducing driving shear stress, resulting in higher pore pressure accumulation. Indeed, results of model tests with highly constrained

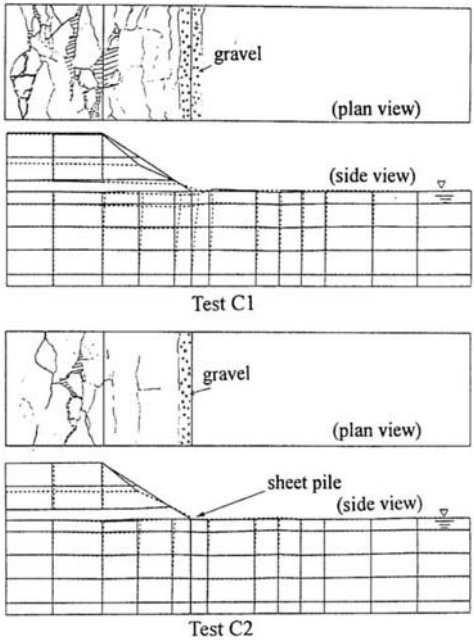

Fig.4 Sketches of grids of colored sand and cracks

foundation soil below embankments using a pair of sheet piles connected their head with tie-rods (Matsuo et al., 1994; Adalier et al., 1998) showed that foundation soil liquefied in almost all locations below embankment.

Sketches of grids of colored sand before and after the tests are shown in **Fig.4**. Overall, deformation of foundation soil was larger and embankment was more heavily damaged for test C1 as compared with C2. Vertical settlement of the embankment observed with DV1 and DV2 for test C2 was reduced by approximately 25% and 50% respectively, but lateral displacement at the toe was only 25% that for test C1. In addition, for test C2, vertical settlement was relatively uniform along the embankment base except around toe. Higher excess pore pressure generated below the embankment in test C2, resulting in reduction of soil stiffness and bearing capacity more effectively, may be responsible for relatively uniform base settlement for C2. While for C1, vertical settlement was found to have increased with distance from embankment center line (i.e. rigid container wall). Large lateral displacement plus this uneven settlement is considered to have caused large tensile strain and cracks to the model C1. It can be concluded that lateral displacement of sheet piles,

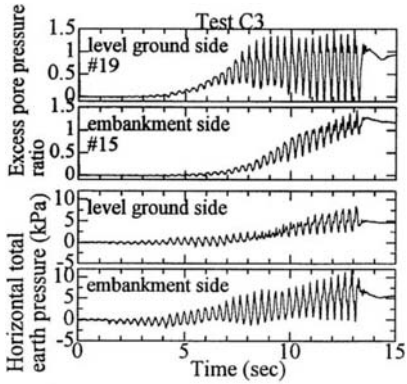

Fig.5 Time history of observed horizontal earth pressure at a depth of 550mm from ground surface

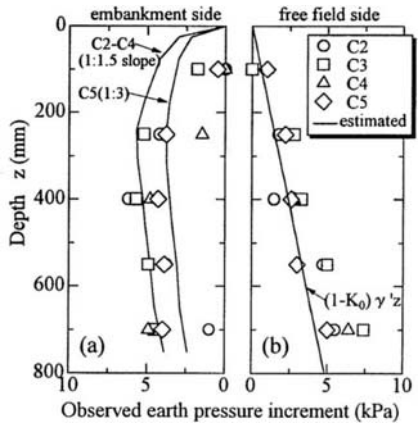

Fig.6 Observed maximum horizontal earth pressure profile

which may be governed by earth pressures as well as flexural rigidity and fixity condition, is a determining factor of mitigated settlement and preserved embankment integrity. Hence, it is important to study the lateral load acting on the sheet piles in order to account for embankment settlement and integrity in the course of design.

3.2 Lateral load acting on sheet piles

Time histories of horizontal earth pressures on the sheet pile observed in test C3 with earth pressure cells and excess pore pressure in the vicinity of the earth pressure cells are shown in **Fig.5**. It can be seen that the mean value of the earth pressure

increased with time, and thereafter tended to level off in the later stage, indicating similar responses to the generated excess pore pressure. In the following discussion, mean values of the earth pressure are focussed on and a fluctuation component is not concerned in this paper.

The mean values of earth pressure increment profile at the end of excitation are depicted in **Fig.6**. On the free field side, a straight line corresponding to the prediction, which equals to initial effective vertical stress minus horizontal earth pressure at rest with K_0=0.4, are provided, where γ' is effective unit weight of sand and z is depth. Since relatively large scatter can be seen in the figure, quantitative discussion on the measured earth pressure should be avoided. The earth pressure increment appear to increase approximately linearly with depth in the free field side. While on the embankment side, earth pressure increment increased rapidly with depth at shallower depth and decreased in deeper portion.

3.3 Estimation of horizontal load

It should be noted that horizontal displacement of the top of the sheet pile obtained by double integrating measured bending strain profiles along the sheet pile agreed quite well with displacement measured with transducer DH1. For the purpose of evaluating horizontal load on the sheet pile, utilization of the bending moment is believed to be more reliable than that of measured earth pressure.

Mean values of bending moment of the sheet pile at a depth of 750mm (G10 in Fig.1) are plotted against averaged pore pressure ratio (APPR) beneath the embankment in **Fig.7**. Horizontal axes of Fig.7(a) and (b) are averaged mean value of measured excess pore pressure ratio at four locations, that is #1 to #4 and #13 to #16, respectively. In Fig.7(b) the relationship between bending moment and APPR is observed to be different for different slope angle. For test C5 with gentle slope of embankment virtually no residual moment generated until APPR exceeded unity, while bending moment started to increase at lower APPR for the rest of tests. On the other hand, the bending moment increased with APPR below the embankment top. These observation may indicate that the settlement of embankment starts to accumulate when the degradation of effective stress of foundation soil occurs, not only in the vicinity of sheet pile but in whole area beneath embankment.

In this study, an attempt was made to evaluate an

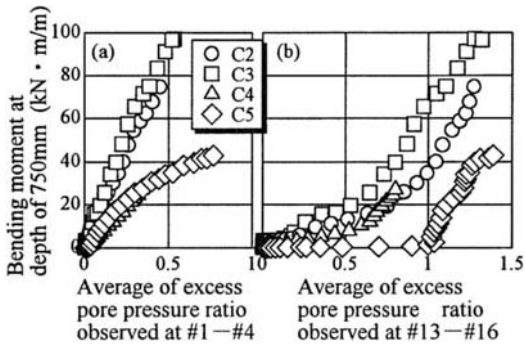

Fig.7 Relationship between bending moment of sheet pile and averaged excess pore pressure ratio

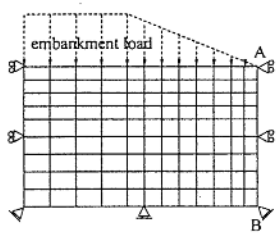

Fig.8 Finite element mesh for embankment with 1:1:5 slope

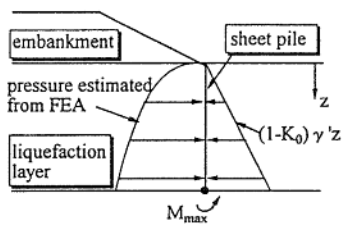

Fig.9 A sheet pile is subjected to earth pressures on both side to generate maximum bending moment M_{max}

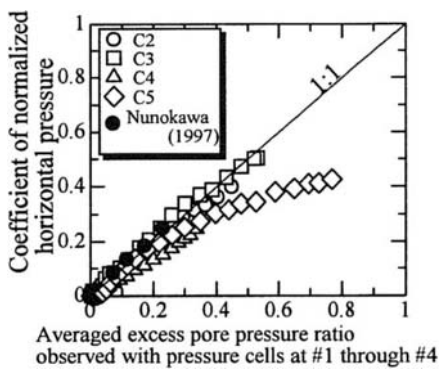

Fig.10 Relationship between coefficient of mobilized horizontal pressure and averaged excess pore pressure ratio beneath embankment

upper limit of the earth pressure on the embankment side for design purpose. Considering extreme situation that foundation soil liquefies in all area, foundation soil is assumed to be an almost incompressible (poisson's ratio = 0.495) elastic media with uniform modulus. The earth pressure on the sheet pile on the embankment side was estimated from finite element analysis using a FE Mesh shown in **Fig.8**. In the analysis embankment load was vertically applied on the surface of foundation soil. In order to estimate pressure before shaking an analysis of foundation soil with poisson's ratio of 0.29, corresponding to K_0 of 0.4, was also conducted. The difference of the horizontal stress obtained from the two calculations with different poisson's ratio on the boundary A-B depicted in **Fig.8** are assumed to be the increase in horizontal pressure due to liquefaction of whole foundation soil, which is plotted in **Fig.6**. The calculated profile of earth pressure on the sheet pile of embankment side appears to be similar to that observed.

A coefficient of mobilized horizontal pressure, α, defined by eq.(1) were introduced,

$$\alpha = \frac{M_{obs}}{M_{\max}} \tag{1}$$

where M_{obs} is observed bending moment at the bottom of liquefied layer. $M_{\max}$ is the bending moment at the bottom of liquefied layer when the sheet pile is subjected to the calculated maximum horizontal pressure on the embankment side and to $(1-K_0)\gamma' z$ on the free field side, as indicated in **Fig.9**. The coefficient are plotted against APPR below the embankment top (#1-#4) in **Fig.10**. It can be seen that test results are laid on a 1:1 slope straight line for all tests until APPR reached about 0.5. Results of centrifuge test (Nunokawa, 1997) are also shown in **Fig.10**. The corresponding prototype of the centrifuge model was a high embankment with steep slope supported on 10 meter deep liquefiable sand bed with sheet piles installed at the embankment toes. A 20 cycles of sinusoidal base acceleration was imparted to the model. The results of centrifuge test were also laid on the straight line. These observation may indicate the possibility that horizontal load acting on the sheet pile can be reasonably evaluated in combination with appropriately estimated excess pore pressure beneath embankment crest.

4 CONCLUSION

A series of shaking table tests was conducted on models of an embankment supported on liquefiable sand deposit with and without sheet pile as a measure of liquefaction induced embankment failure.

The mechanisms of reducing damage by sheet piling were studied in detail. It was found that higher excess pore pressure being generated in a foundation soil with sheet pile beneath an embankment and displacement containment by the sheet pile caused relatively uniform settlement along the base of embankment with smaller horizontal displacement, which contributed to preserve embankment integrity.

It appeared that mean value of horizontal earth pressure on the sheet pile on the embankment side increases almost linearly with averaged excess pore pressure beneath the top of embankment. Vertical profiles of earth pressure on the embankment side was reasonably estimated by finite element analysis. A unique relationship between earth pressure on the embankment side normalized with the pressure estimated from FEA and the averaged excess pore pressure was found, irrespective of the slope of embankment, the frequency of imparted base acceleration, the flexural rigidity of sheet pile and liquefaction resistance of the foundation soil.

REFERENCES

Adalier, K., Elgamal, A.-W. and Martin G.R. 1998. Foundation liquefaction countermeasures for earth embankments. *Proc. ASCE, Vol. 97, No.GT6,* 500-517

Dobry, R., Taboada, T. and Liu, L. 1995.Centrifuge modeling of liquefaction effects during earthquakes, *First Int. Conf. On Earthquake Geotech. Engrg.*, Vo.3, pp.1291-1324

Kimura, T., Takemura, J. Hiro-oka, A. Okamura, M. and Matsuda, T. 1995. Countermeasures against liquefaction of sand deposits with structures. *First Int. Conf. On Earthquake Geotech. Engrg., Preprint Volume*, 1203-1224

Matsuo, O., Koga, Y., Koseki, J. and Washida, S. 1994. Study on cut-off sheet pile method as a countermeasure against liquefaction of embankment foundation. *Proc. Fourth U.S.-Japan Workshop on Soil Liquefaction*, 203-222

Nunokawa, O. 1977. Master thesis of Tokyo Institute of Technology (in Japanese)

Yoshimi, Y. and Tokimatsu, K. 1977. Settlement of buildings on saturated sand during earthquakes. *Soils and Foundations, Vol.17, No.1, pp.23-38*

8 Recent earthquakes

This Page Intentionally Left Blank

Earthquake Geotechnical Engineering, Sêco e Pinto (ed.) © 1999 Balkema, Rotterdam, ISBN 90 5809 116 3

Geotechnical aspects of the 1995 Aegion, Greece, earthquake

G.D. Bouckovalas, G.Gazetas & A.G. Papadimitriou
National Technical University, Athens, Greece

ABSTRACT: Results are presented from multidisciplinary studies regarding the M_S=6.2, 15 June, 1995 Aegion Earthquake (Gulf of Corinth, Greece). From a seismological point of view this event deserves attention since it is the first well documented earthquake resulting from low angle (33°) normal faulting. From a geotechnical point of view, attention is focused upon the high acceleration (0.54g), long period (0.40-50s) ground motion recorded in the city of Aegion, which is attributed to the coincidence of a number of independent factors: directivity of rupture, soil amplification and topography effects. In addition, the analysis of structural damage within the city of Aegion and ground failures along both coasts of the Gulf provides new insight to earthquake-induced failure mechanisms.

1 INTRODUCTION

The June 1995 Aegion earthquake ruptured the western part of the Gulf of Corinth, in southern Greece. With a magnitude M_S=6.2, the earthquake caused significant destruction, including structural damage, liquefaction and ground ruptures. The most severe effects occurred at Aegion, a town located at an epicentral distance of about 15 km on the southern coast of the Gulf. Namely, about 1000 buildings suffered major damage and had to be repaired or even rebuilt, while 26 people were killed from the collapse of two multi-story buildings.

This paper summarizes the findings from a number of multidisciplinary studies performed in the wider area, with the aim to assess the factors which contributed to the severity of the earthquake. Emphasis is placed upon geotechnical issues (soil and topography effects, liquefaction and related ground failures). However, attention is also focused on some unusual seismological evidence, which had crucial effect on the seismic excitation.

2 FAULT RUPTURE AND DIRECTIVITY

The Gulf of Corinth has long been recognised as one of the most active rifts in the highly seismic Aegean. The 1995 Aegion earthquake is the largest event recorded in the Gulf since the 1981 sequence which ruptured its eastern part. To identify the rupture mechanism of the earthquake, a two-week seismotectonic field study was initiated by Bernard et al (1997), including: the temporary installation of a seismological array, aftershock studies, the surveying of GPS points whose monitoring had been initiated in 1991-1994 and a detailed investigation for surface breaks along the well known onshore active faults.

The final fault model established from this study is shown in Figs. 1 and 2, together with the aftershocks and the active faults in the wider area. In brief:

a) The rupture initiated at 10km depth, 15km away from the damaged city of Aegion. It lasted 4 to 5 s and propagated southward, on a north-dipping normal fault, with 33° dip angle. This is an unusually low angle normal faulting, apparently one of the first well-documented cases of its kind.
b) The seismic moment estimated from GPS and InSAR data is 3.9×10^5 kNm and provides a 0.87 m mean slip over a fault area of 9.5km x 15km.
c) The fault plane is probably connected to the surface by a steeper segment cutting through the thick sediments of the Gulf and reaching the sea floor within the active submarine slumps of the southern coast.
d) The aftershock seismicity is concentrated to the west of the rupture area, suggesting that the crustal stress state in that part is closer to failure than the eastern part which has been relaxed earlier, by the Galaxidi 1992 earthquake.

The above description of the rupture mechanism already implies considerable directivity effects, a hypothesis which is further substantiated by the few available recordings of the main shock. For instance, Fig. 3 compares acceleration records at two stations, at comparable epicentral distances from the fault

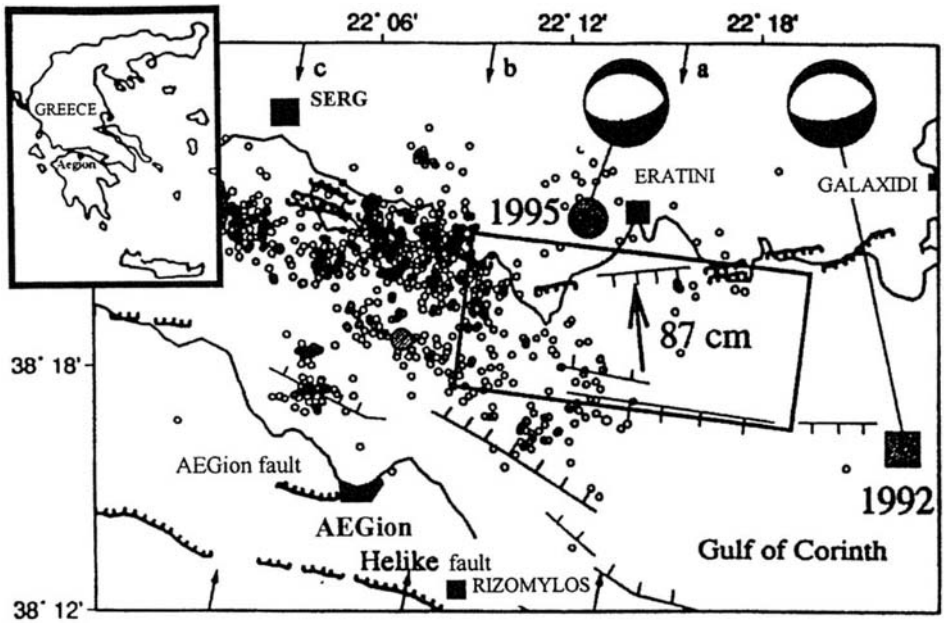

Figure 1. Epicenter and rupture zone of the 1995 Aegion earthquake (based on Bernard et al. 1997).

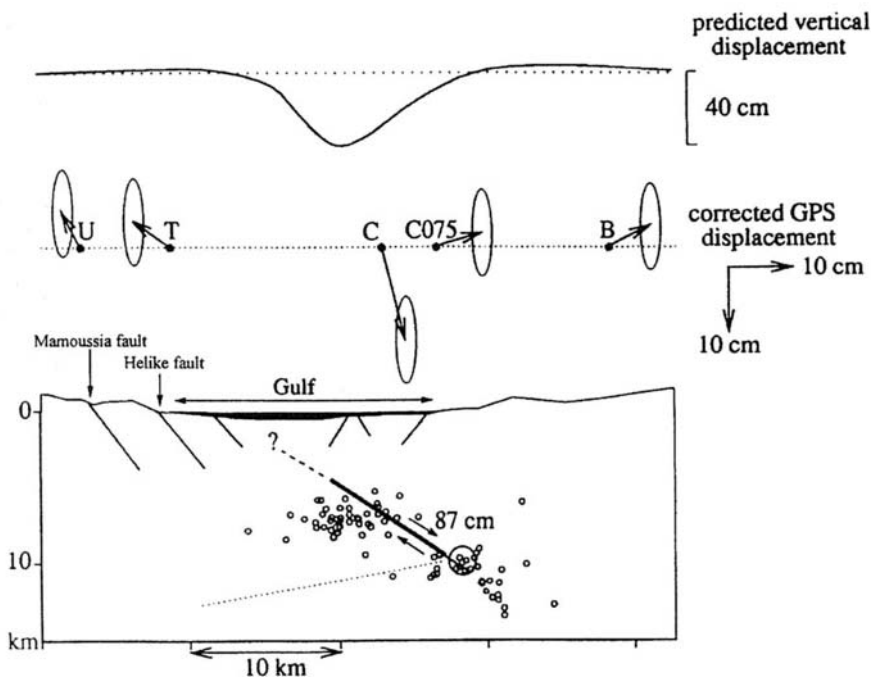

Figure 2. Cross section of the fault plane of the 1995 Aegion earthquake (based on Bernard et al. 1997).

(Fig. 1): SERG to the W-NW of the fault plane and AEGion (at the center of the town of Aegion) to the S-SW. It is readily observed that peak horizontal accelerations in Aegion station, in the hypothesized direction of rupture, are more than quadraple the peak horizontal acceleration in SERG station, opposite to the direction of rupture. Furthermore, the duration of very strong shaking in AEGion station is about 1s as compared to 2 s in SERG station.

Fig. 4 shows the time histories of acceleration, velocity and displacement, as well as, the elastic response spectra (5% damping) of all seismic motions recorded at AEGion station. This recording is characterized by high horizontal PGA (0.54g and 0.50g) and a long predominant period of about 0.50s. This long-period pulse results in high horizontal PGV values (51.8 and 40.3 cm/s) and an especially high velocity step ĆV≈ 80 cm/s. There is ample evidence in the literature that such long-period pulses are related to directivity phenomena (Singh, 1985, Somerville & Graves, 1993, Naeiem, 1993). However, it is shown next that the soil conditions and the topography at AEGion station may have also contributed to the creation of this high acceleration, long period seismic recording.

3 GEOLOGICAL AND GEOTECHNICAL DATA

Fig. 5 shows a N-S geological section passing through the center of Aegion. It is observed that the northern side of the city is essentially bounded by a normal fault running on an E-W direction, parallel to the nearby coast. This fault produces an almost vertical drop of about 90 m. The residential part of Aegion lies mostly on the upthrow region of the fault, while the harbor is built on the downthrow region. It is emphasized here that this geologic fault was only indirectly related with the causative fault of this earthquake. Nevertheless, in its western part it produced a small surface breakout, 1 km in length and 10mm in width.

The figure also shows two typical soil profiles for the upthrow and downthrow regions: one at AEGion station within the city, and the other at the harbor. In brief, the subsoil in the city area consists of 20 - 40 m of alternating layers of relatively stiff low-plasticity sand-silt-clay mixtures, overlying 100-150 m of conglomerate. Under the conglomerate, there is a bed of neogene marl that reaches great depths. The shear wave velocity at the surface layers ranges between 200 and 600m/s while in the conglomerate it increases gradually with depth from 800 to 1200m/s. The soil conditions at the harbor area are similar, with one important exception: the recent soil deposits on the surface are of marine origin, having a larger percentage of fines, a larger thickness (in excess of 50m) and a much smaller shear wave velocity (less than 200m/s).

4 SOIL AND TOPOGRAPHY EFFECTS

The only available recording of the main event within the city limits comes from AEGion station, installed at the basement of the two-story telecommunications building. Hence, the investigation of possible soil and topography effects during the earthquake has been based on analytical predictions rather than actual data from recorded motions. The analyses were performed with computer codes SHAKE (Schnabel et al 1972) and QUAD4M (Hudson et al 1994), for 1-D and 2-D conditions respectively. The soil parameters were mostly evaluated from geological and geophysical data, as well as data from in-situ SPT, Crosshole and Downhole measurements (Tsiambaos et al 1996). In many cases, the available data were supplemented via empirical correlations from the literature (Imai and Tonuchi 1982, Kalteziotis et al 1992, Zervoyannis et al 1987, Vucetic and Dobry 1991).

As a first step, soil effects were decoupled from topography effects and evaluated assuming 1-D wave propagation, from the seismic bedrock upwards. Fig. 6 shows typical results obtained for the recording site, in the form of elastic response spectra (5% damping) and peak ground accelerations for all three components of motion: TRANSverse (N150° E), LONGitudinal and VERTical. The results are shown for the ground surface and at the top of the conglomerate and the marl. Attention is drawn on the following points:

a) At the marl-conglomerate interface, the elastic response spectra for both horizontal components are practically identical and in remarkable agreement with the frequency content of the spectrum for the vertical motion. This is an indication that the seismic ground motion at this level bears the source characteristics, with a minimum effect from the overlying soil. In that case, the strong motion from the source arrived rich in periods around 0.10s and between 0.25 and 0.50s.
b) Passing through the conglomerate layer, the horizontal elastic spectra are amplified uniformly by an average factor of 1.50, while spectral accelerations at periods between 0.40 and 0.70s may be amplified even more, forming a well defined peak at 0.50s.
c) The top 24m of recent soil deposits amplify spectral amplifications by another 50% on average. The amplification appears to be more intense at periods between 0.10 and 0.30s, resulting in a second local peak at 0.20s.

Subsequently, the effects of topography were computed from 2-D seismic response analyses, for a representative N-S section through AEGion recording station (Fig. 6). The seismic excitation was estimated from 1-D deconvolution of the recorded motion and assigned to the top of the neogene marl.

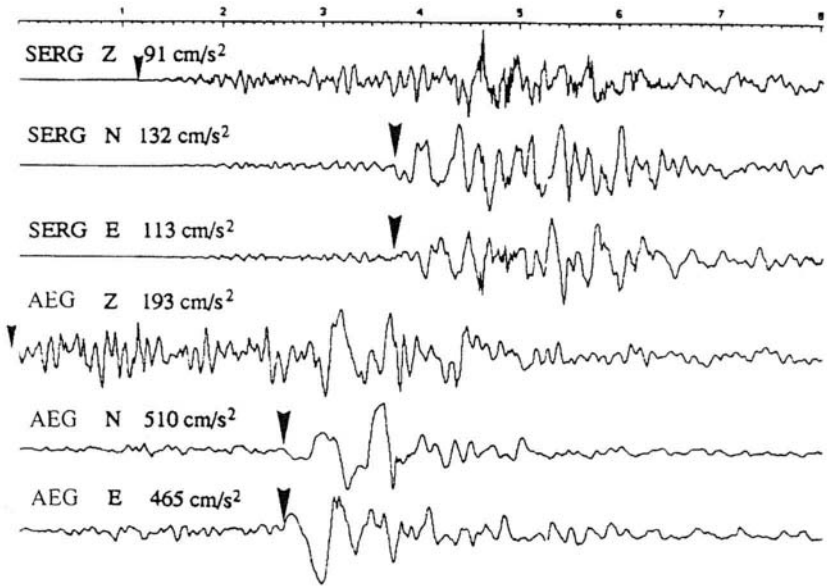

Figure 3. Acceleration records at SERG and AEGion stations (from Bernard et al. 1997).

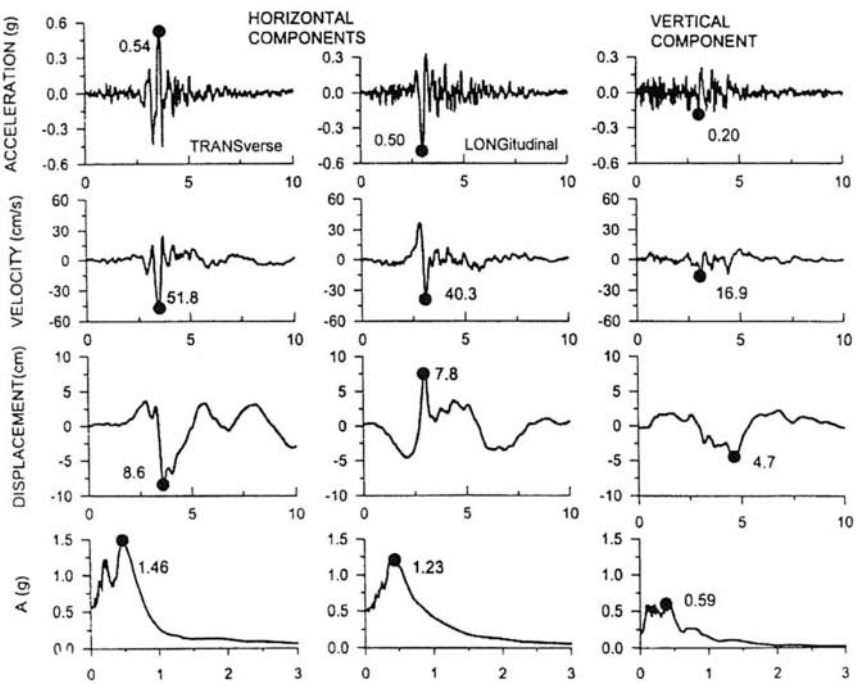

Figure 4. Recored ground motions and corresponding elastic response spectra at AEGion station (from Gazetas 1995).

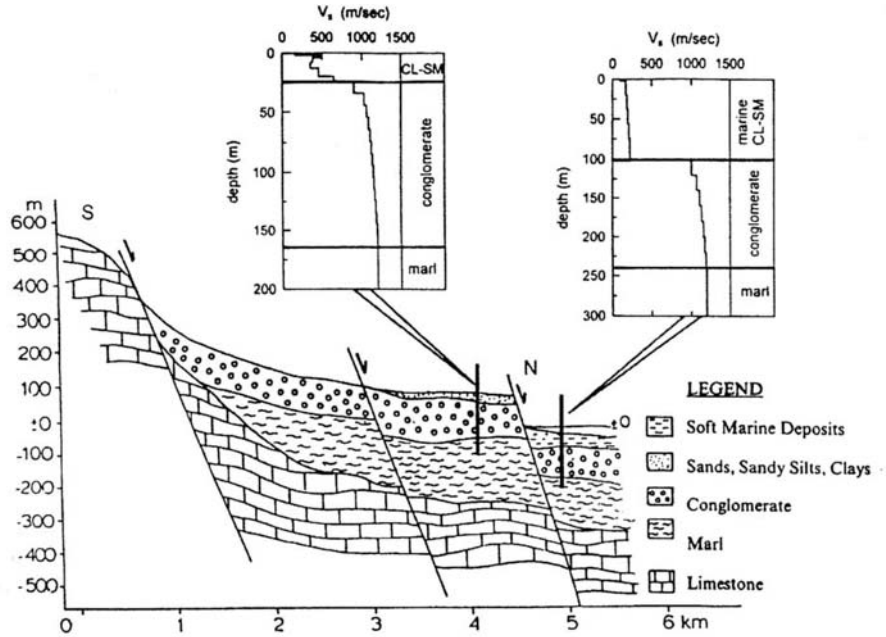

Figure 5. N-S geological cross section of the Aegion area.

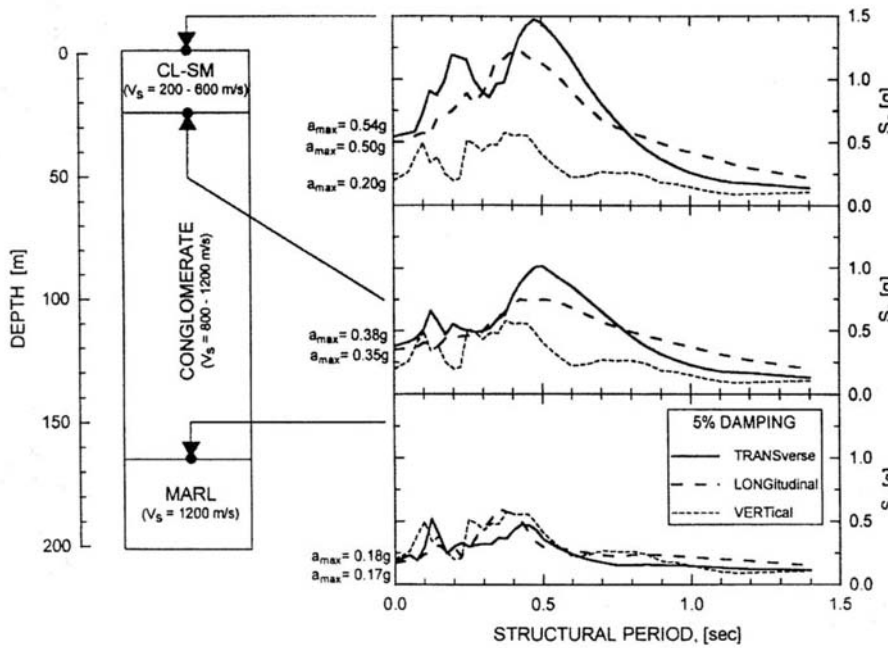

Figure 6. Computed effect of soil conditions on AEGion main shock recording.

The results of the 2-D analyses were finally calibrated against the peak ground acceleration of the recorded motion.

Fig. 7 shows the N-S variation of computed peak ground acceleration, as well as elastic spectral acceleration (5% damping) for a structural period of 0.40s. To distinguish topography from soil effects, the results of the 2-D analyses are compared to results from 1-D analyses performed in the previous step. It is observed that the role of topography is neither simple nor uniquely defined. Still, there is clear evidence that the presence of the fault escarpment may have amplified the intensity of ground shaking in its vicinity, i.e. 50 to 600m to the south and up to 100m to the north. In addition, it is important that Aegion station falls within one of these zones and consequently the main shock recording has sustained a frequency dependent amplification. This is shown in Fig. 8 where computed elastic response spectra in the area of the recording have been normalized against the spectrum at a large distance (to the south) from the fault, where topography effects vanish. In this way, it is seen that the harmonic components of motion with periods between 0.20 and 0.45 may have been amplified disproportionally due to the presence of the fault escarpment.

Combined site (soil and topography) effects in the entire city area were assessed by performing 1-D analyses for 14 borehole sites, and consequently correcting the results for the topography effects implied by the 2-D analysis. (Bouckovalas et al, 1996, Papadimitriou and Bouckovalas, 1997). Final ground motions show considerable spatial variability that may explain, in part at least, the non-uniform distribution of observed structural damage. Similar conclusions had been reached by Gazetas (1995) and Athanasopoulos et al (1998) who analyzed the seismic response of distinct sites within the city and the harbor area.

Of particular interest is the substantial overall de-amplification of ground motions that apparently took place in the soft and deep clayey deposits in the harbor area. The resulting reduced intensity of motion (PGA computed to be in the range of 0.10-0.20g) literally saved the gravity-type, 10m-high harbor quaywall, which displaced merely by 5 to 10cm. Such a de-amplification of motion by the 60m or more soft clayey deposit is reminiscent of: (a) the reduced acceleration levels recorded at the surface of the Port Island 80m-deep borehole array during the 1995 Kobe earthquake (Iwasaki & Masaru, 1997), and (b) the reduced macroseismic intensity documented for the coastal deep alluvial sites during the 1996 Kalamata, Greece, earthquake (Gazetas et al 1990).

5 STRUCTURAL DAMAGE

Among the 1159 reinforced concrete (RC) buildings of the town, 30 had to be evacuated and another 231 had to be repaired. Damage was more severe in masonry buildings. In a sample of 706 masonry houses, 361 had to be evacuated and 212 required major repair. In general, the structural damage was concentrated in the central and eastern parts of the city. On the contrary, very little damage was observed in the harbor and the western parts of the city. These findings agree well with the analysis of site effects discussed earlier. For instance, the difference in the intensity of damage between the harbor and the city center could be readily foreseen based on the variation of the peak ground and spectral accelerations along the N-S section presented in Fig. 7.

Particularly sensitive to the long-duration, high-amplitude pulse of the ground motion proved to be the flexible low-rise buildings with a "soft" first story. Namely, in three cases the first story of such buildings collapsed (Gazetas, 1995). The sensitivity of elastoplastic flexible structures to near field, directivity affected ground excitations has been well documented in the literature following the pioneering work of Bertero after the 1971 San Fernando earthquake (Bertero et al, 1978).

Following the earthquake, an extensive effort was initiated to map and evaluate structural damage in the wider area of Aegion (Fardis and Karantoni, 1999). The results demonstrate the severity of ground shaking, but they also provide indirect evidence in support of site effect analyses presented earlier. It is noted that this study is still in progress and consequently all results presented herein should be considered preliminary.

Table 1. Scale of structural damage to masonry buildings

Degree of Damage (D.D.)	Description of damage
0	no damage
1	a few fissures of 1mm width
2	a number of cracks with 5mm average width or isolated cracks with 10mm average width
3	intense cracking, masonry walls beginning to disintegrate
4	disintegration of masonry walls, total or partial collapse

Table 2. Categorization of masonry buildings

Category	building type (No. of stories)	fundamental period
MAS1	adobe(1), stone(1), brick (1&2)	0.1s
MAS2	adobe(2), stone(2)	0.4s

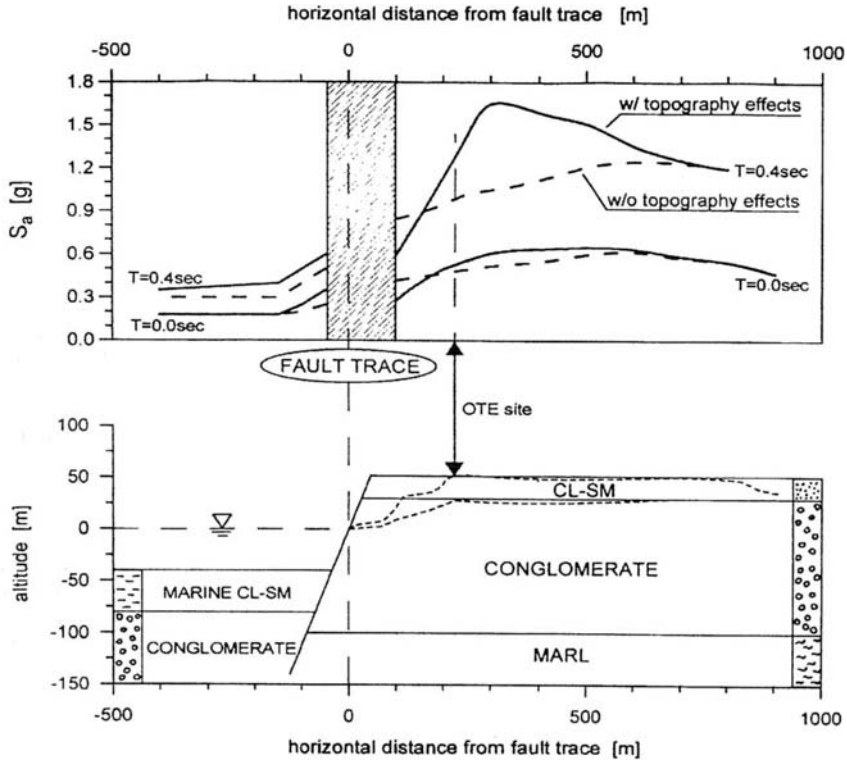

Figure 7. Computed soil and topography effects along a typical N-S cross section of Aegion.

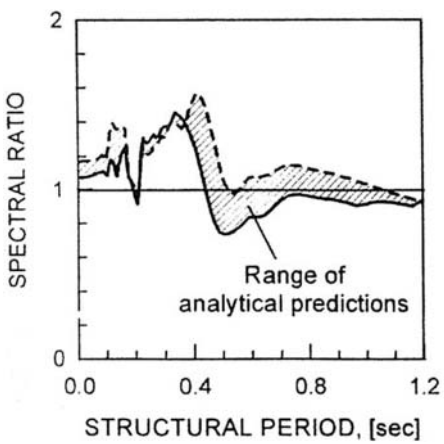

Figure 8. Computed topography effects on horizontal spectral acceleration (5% damping) at AEGion station.

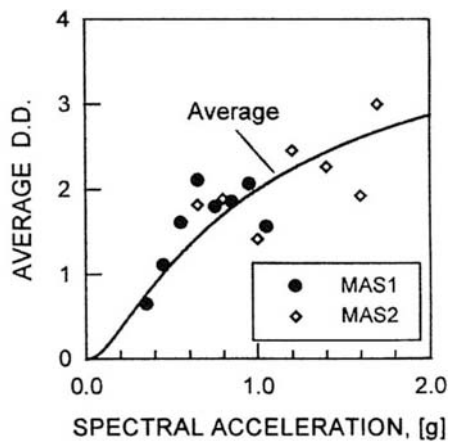

Figure 9. Correlation between structural damage to masonry buildings and seismic ground motion intensity.

For a systematic correlation of observed damage and ground motion intensity, the average Degree of Damage (D.D.) of masonry buildings has been related to elastic spectral accelerations (Fig. 9). The average D.D. has been evaluated according the criteria listed in Table 1, while spectral accelerations have been estimated based on the fundamental period of vibration of the building and the analytical computations of site effects. However, no similar evaluation of structural damage was available for RC buildings to generalize the above conclusion.

In the analysis presented herein, all masonry buildings are grouped into two categories, MAS1 and MAS2, according to their fundamental period of vibration (Table 2). The number of buildings in the two categories are very similar, so that the two statistical samples data are equally reliable.

As shown in Fig. 9, the correlation between observed damage and spectral acceleration, computed taking into account site effects, is satisfactory since:

- it portrays the expected increase of the average D.D. with spectral acceleration for both categories of masonry buildings, and
- the scatter is fairly small, given the uncertainties of the analysis.

One point of further interest in this plot, is that buildings in category MAS2 sustained larger accelerations and suffered relatively greater structural damage. This may be attributed to the proximity of their fundamental structural period to the predominant period of the earthquake (0.40 - 0.50 s).

6 GROUND FAILURES

In addition to structural damage, the earthquake caused extensive ground failures in the form of liquefaction and lateral terrain movement. These phenomena have been systematically investigated for two locations (Fig. 1):

a) Rizomylos, a village located on the south coast of Corinthian Gulf, at a distance of 8km southeast of Aegion and 18km south of the epicenter (Athanasopoulos et al, 1998).
b) Eratini, a small town located on the north coast of the Gulf, within the epicentral distance of the earthquake (Bouckovalas et al 1998).

The occurrence of liquefaction at Rizomylos was manifested by sand boils, expulsion of ground water at the ground surface, sand blows, as well as limited lateral spreading and ground rupture parallel to the coast line. Fortunately, the damage caused by these phenomena was minor: cracking of the concrete floors and the walls of coastal buildings and also settlement, tilting and cracking of a RC walk way along the water front.

Geotechnical investigations at this area revealed that the subsoil consists of a 5m thick layer of sand and gravel, followed by a loose to medium dense layer of sand (N_{SPT}=10-20) of about the same thickness, and a layer of clay. The liquefaction resistance of sand, estimated empirically according to Seed et al (1985), corresponds to a horizontal peak ground acceleration of 0.16 to 0.18g. These values are likely to have been much lower than the actual seismic accelerations at the site.

Ground failures in Eratini were far more intense. In four sites, one within the fishing harbor of Eratini and three along the nearby 2 km beach, the coastline advanced 5 to 15 m inland. In addition, water front barriers collapsed, paved park areas cracked and sunk into the sea, while the seaside retaining wall of a coastal road was threatened by scouring of the foundation soil.

Submarine geophysical surveys have shown that, in three of the above sites, the earthquake caused extensive landslides accompanied by debris flows and block rotations (Fig. 10). Reconstruction of the pre-earthquake topographic profiles along the main axis of the landslides indicates that the failure zones extended to a maximum depth of 6 to 10m within the loose alluvial deposits which cover the seabed.

Geotechnical exploration, based on static cone penetration with skin friction measurement, revealed that the soil profile at the failure sites is characterized by a continuous interchange between silty-sand and clay layers. This profile favors the development of excess pore pressures which may remain trapped within the clay-sealed silty sand layers for a long time after the end of shaking. Thus, zones of reduced shear resistance are created into the soil leading to a static massive failure, even for relatively small surface gradients.

Table 3 summarizes some characteristic data obtained from the geophysical and geotechnical exploration of the area, as well as, from the liquefaction and slope stability analyses. From a practical point of view, the following points are worthy of attention:

a) Post-earthquake landslides occurred for ground slopes as low as 12.0 %, corresponding to a static factor of safety of 2.0.
b) At all sites, except from A, ground failures were triggered by excess pore pressure build up in very thin silty sand layers, with average thickness between 0.24 and 0.36m. Such layers can be easily missed during a conventional geotechnical exploration or intentionally overlooked on the grounds that they probably luck lateral continuity.
c) Assuming complete liquefaction of the silty sand layers, the relevant analyses indicate that the horizontal peak ground acceleration in the area must have exceeded 0.29g. This is a relatively high value, but it is readily justified by the small epicentral distance of Eratini.

Table 3. Summary of results from the analysis of Eratini earthquake-induced ground failures

SITE	THICKNESS OF LIQUEFIABLE LAYERS (m)		MINIMUM LIQUEFACTION RESISTANCE[1]		AVERAGE SLOPE OF SEABED[2]	SF[3]	GROUND FAILURE	
	MAX.	AVERAGE	$a_{max,l}$(g)	DEPTH (m)	(%)		ERROSION (m)	LAND-SLIDE
A	3.00	1.10	0.29	8.5	17.0	3.3	5.0	YES
B	0.40	0.24	0.15	6.3	12.0	2.0	5.0	YES
C	0.60	0.34	0.20	8.0	12.0	2.5	10.0	NO
D	0.80	0.36	0.21	9.4	18.0	1.5	10.0 - 15.0	YES

(1) According to Seed et al. (1985), (2) Prior to the earthquake, (3) Estimated from infinite slope stability analysis.

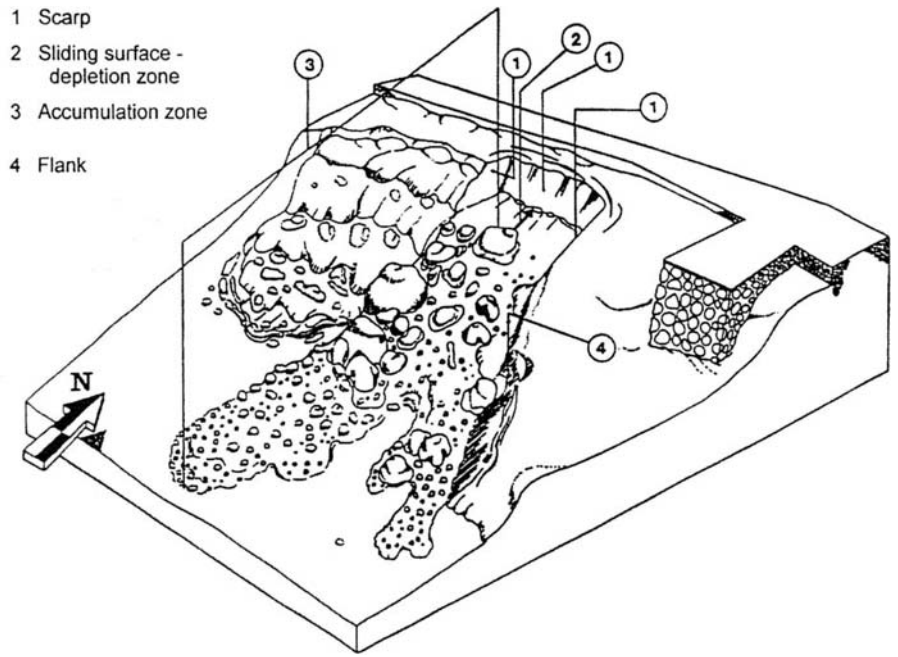

Figure 10. 3-D perspective of a typical earthquake-induced landslide at Eratini Gulf.

d) The depth of minimum liquefaction resistance, ranging between 6.3 and 9.4 m, compares well with the maximum depth of the failure surface estimated from reconstruction of the pre-earthquake topography.
e) Sites B and C developed different forms of ground failure, despite an apparent similarity in soil conditions and topography. This is an indication that, although the prediction of liquefaction per se has become a rather trivial issue, prediction of liquefaction-induced ground failures may still pose a challenge to geotechnical engineers.

Concluding this brief overview, it is noted that similar ground failures have been reported for a number of other locations along both coasts of the Gulf. However, they did not affect human activity and consequently they did not become the subject of systematic investigation.

7 CONCLUSION

Despite its moderate size (M_S=6.2), and the fact that it stroke a thinly populated area, the earthquake event of 15-06-1995 revealed to some extent many of the important seismological, geotechnical and structural aspects observed in the far more destructive earthquakes of Northridge 1994 and Kobe 1995. Furthermore, this event shed light to seismotectonic and geotechnical factors which interacted over the past centuries to shape the wider zone of the Corinthian Gulf, and will probably affect the area in the future.

ACKNOWLEDGEMENTS

The data of structural damage in the city of Aegion were used after permission of Professor M. Fardis

and Dr. T. Karantoni, of the Civil Engineering Dept. of Patras University. The first author wishes also to acknowledge the Hellenic Organization for Earthquake Planning and Protection for financing the research on site effects, and the Ministry of Public Works (Port Division) for financing the analysis of ground failures along the coast of Eratini.

REFERENCES

Athanasopoulos G. A., Pelekis P. C. & E. A. Leonidou 1998. Effects of surface topography and soil conditions on the seismic ground response - including liquefaction - in the Egion (Greece) 15/6/1995 earthquake. *Proceedings, Eleventh European Conference on Earthquake Engineering*. Paris, France, (in CD-ROM), Rotterdam: Balkema.

Bernard P., Briole P., et al 1997. The Ms=6.2, June 15, 1995 Aegion earthquake (Greece): evidence for low angle normal faulting in the Corinth rift. *Journal of Seismology 1:131-150.*

Bertero V.V. 1978. Aseismic design implication of San Fernando earthquake records. *Intern .Journal of Earthq. Engineering and Struct. Dynamics*. Vol. 6.

Bouckovalas G. D., Papadimitriou A. G. & D. N. Gatzis 1996. Analysis of the Effect of Local Soil Conditions during the Aegion Earthquake of June 15th 1995. *Research Report, E.P.P.O.*. September, (in Greek).

Bouckovalas G. & A.D.K. Consultants 1998. Analysis of earthquake-induced ground failures along the Eratini - Tolofon eroding coast. *Technical Report, Hellenic Ministry of Public Works*. April.

Ferentinos G. & A.D.K. Consultants 1997. Submarine geophysical exploration along the Eratini - Tolofon eroding coast. *Technical Report, Hellenic Ministry of Public Works*. December.

Gazetas G. 1995. Aegion earthquake of 15-06-95: Analysis of damage to buildings with a flexible pilotis. *Journal of the Technical Chamber of Greece, (1883)* November 27 (in Greek).

Gazetas G., Dakoulas P. & Papageorgiou A.S. 1990. Source and soil effects in the 1986 Kalamata, Greece, earthquake. *Earthquake Engineering and Structural Dynamics*.19:431-456.

Hudson M., Idriss I. M. & M. Beikae 1994. A computer program to evaluate the seismic response of soil structures using finite element procedures and incorporating a compliant base. *User's manual*, CGM, Davis, California.

Imai I. & K. Tonuchi 1982. Correlation of N value with S-wave velocity and shear modulus. *Proceedings, Second European Symposium on Penetration Testing*. Amsterdam, 1: 67-72.

Iwasaki Y., Masaru T. 1996. Strong motion records at Kobe Port Island. *Soils and Foundations*. Special Issue: 29-40, January.

Kalteziotis N., Sabatakakis N., Vassiliou J. 1992. Evaluation of dynamic characteristics of Greek soil formations. *Proceedings, 2nd Hellenic Conference on Geotechnical Engineering*. 2: 239-246 (in Greek).

Naeim F. 1995. On seismic design implications of the 1994 Northridge earthquake records. *Earthquake Spectra, 11(1):91-110.*

Papadimitriou A. G. & G. D. Bouckovalas 1997. Numerical simulation of seismic ground response in the case of the Aegion (Greece) earthquake of June 15th, 1995. *Proceedings, Eleventh Young Geotechnical Engineers' Conference*, Madrid, Spain, September.

Schnabel P. B., Lysmer J. & H. B. Seed 1972. A computer program for earthquake response analysis of horizontally layered sites. *User's manual*, EERC, Berkeley, California.

Seed H.B., Tokimatsu K., et al 1985. Influence of SPT procedures in soil liquefaction resistance evaluation. *Journal of GED, ASCE, 112(11):1016-1032*

Singh J. P. 1985. Earthquake ground motions; implications for designing structures and reconciling structural damage. *Earthquake Spectra, 1(2).*

Sommerville P. & R. Graves 1993. Conditions that give rise to unusually large, long period ground motions, *Structural design of tall buildings, 2:211-232.*

Stavrakakis G. 1996. Characteristic properties of the seismic strong motion of the Aegion earthquake. *Technical Report*, Observatory of Athens (in Greek).

Tsiambaos G., Sabatakakis N., Vassiliou J. & S. Devenes 1996. Geotechnical Investigation of the city of Aegion. *Technical Report, Ministry of the Environment, City Planning and Public Works - Center of Research for Public Works* (in Greek).

Vucetic M. & R. Dobry 1991. Effect of Soil Plasticity on Cyclic Response. *Journal of Geotechnical Engineering*, ASCE. 117(1): 89-107.

Zervoyannis C., Bouckovalas G. & St. Christoulas 1987. Correlations of mechanical characteristics and classification of soil formations. *Journal of the Center of Research for Public Works*. 4: 255-265 (in Greek).

Earthquake Geotechnical Engineering, Sêco e Pinto (ed.) © 1999 Balkema, Rotterdam, ISBN 90 5809 116 3

Nasca earthquake, November 12, 1996, Peru

J. E. Alva Hurtado & D. Vasquez Lopez
CISMID, National University of Engineering, Lima, Peru

ABSTRACT: The main features of the November 12, 1996 earthquake produced in the Nasca region in southern Peru are presented. A summary of damage evaluation and seismic microzonation undertaken by several national and international institutions is also presented.

INTRODUCTION

A moderated earthquake occurred on Tuesday, November 12, 1996 in the Nasca-Acari region, 450 km. south of Lima. The earthquake was produced by the subduction of the Nasca plate underneath the South American plate. The epicenter was located 135 km. south west of the city of Nasca

Nasca and Acari were the cities most affected, as well as several towns in the highlands where damage was extensive in adobe buildings. Many new and old adobe houses collapsed. Damage was observed in concrete buildings mainly recently built state schools.

Seventy five percent of the houses in the region were built with adobe. Official damage reports indicated that 14 persons dead, 624 were injured, 4,000 houses were destroyed, 11,000 were partially damaged, 91 schools and 100 health centers were damaged in the epicentral area.

SEISMOLOGY

The earthquake started at 11:59 a.m., local time, on the border between the Departments of Ica and Arequipa in southern Peru. The Geophysical Institute of Peru (IGP, 1977) calculated a magnitud of 6.3 based on duration of the earthquake (1'58"), with epicentral coordinates at 15.47°S and 75.94° W and a focal depth of 40 km. The corresponding USGS magnitudes are mb= 6.5, Ms = 7.3 and Mw = 7.7, with a focal depth of 33 km and epicentral coordinates at 14.99°S and 75.68°W. Figure 1 presents IGP's epicentral calculation.

This earthquake originated at the southern end of the seismic gap between the August 24, 1942 and October 3, 1974 earthquakes. Aftershocks progressed to the south, towards the 1942 earthquake area. The event was complex with at least two major events that occurred 20 and 33 seconds after the first shock (IGP, 1997).

According to historical seismicity data (Silgado, 1978, Alva Hurtado et al., 1984) a maximum intensity of IX in the Mercalli Modified scale was produced in the region by the August 24, 1942 earthquake. This subduction earthquake had a magnitud M_s= 8.1 and a focal depth of 60 km. with epicenter in the sea.

Strong motion records were obtained in Lima during the 1996 earthquake with maximum acceleration from 7 to 10 gals because of the long distance to the epicenter. No records closer to the epicenter were obtained.

REGIONAL AND LOCAL INTENSITIES

A regional intensity map, MSK scale (Figure 2) for the November 12, 1996 earthquake was presented by the Geophysical Institute of Peru (Ocola et al, 1997).

The maximun intensity of 7^+ (MSK scale) was observed in the Yauca river estuary. Along the shore line between Yauca and San Nicolas, cracks were observed as well as along the shoulders of the adjacent Panamerican Highway. Soil liquefaction

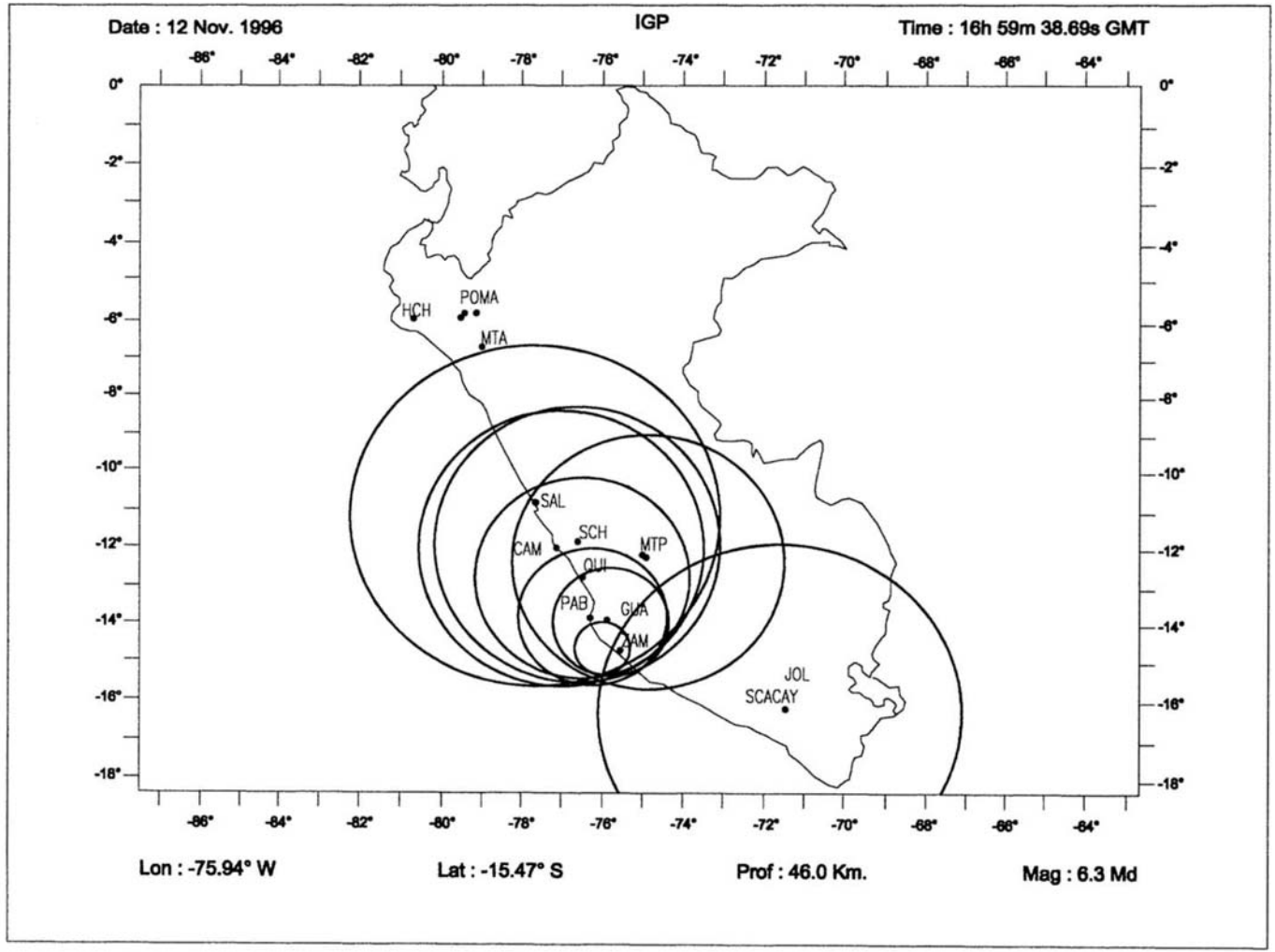

FIGURE N°1 : EPICENTER OF NOVEMBER 12,1996 NASCA EARTHQUAKE (IGP, 1997)

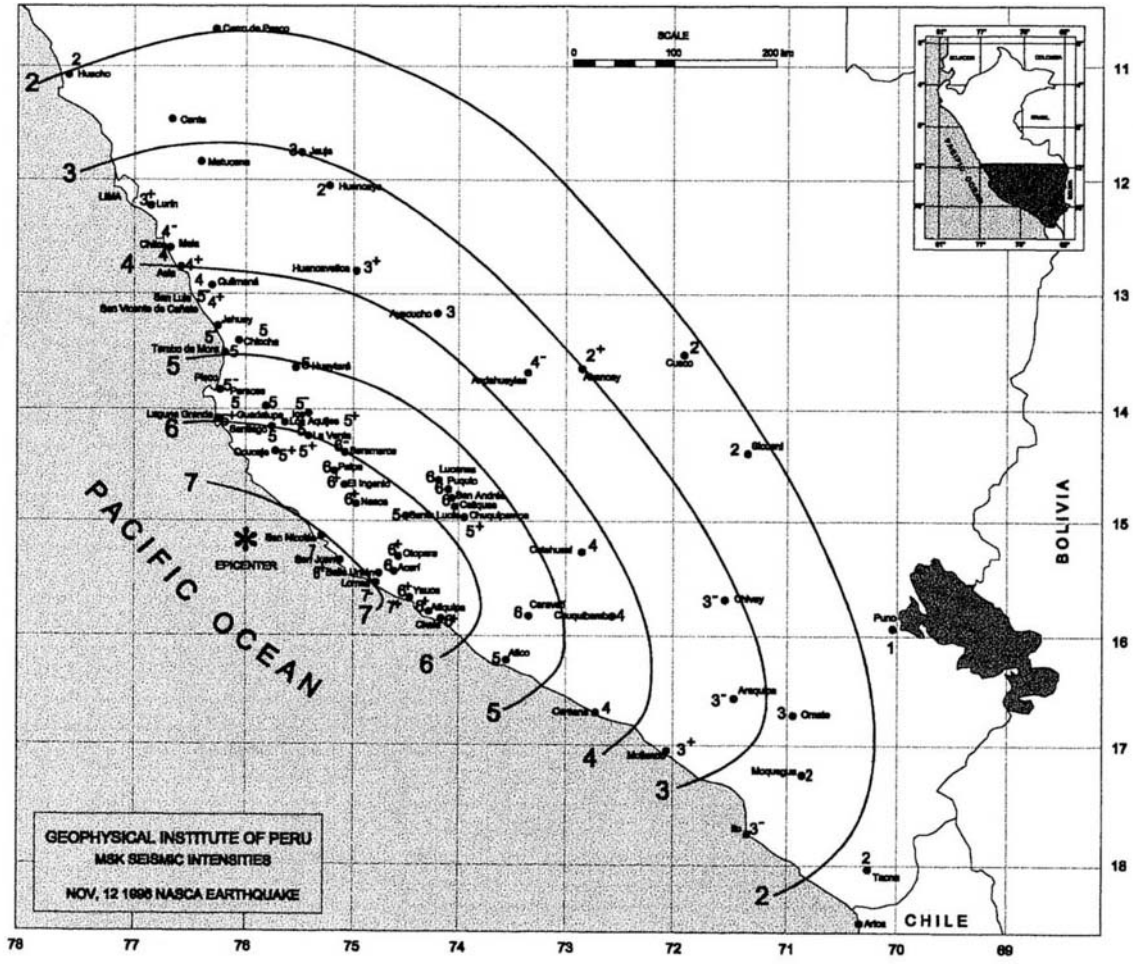

FIGURE N° 2 : ISOSEISMAL INTENSITY MAP OF NASCA NOV 12, 1996 EARTHQUAKE (IGP, 1997)

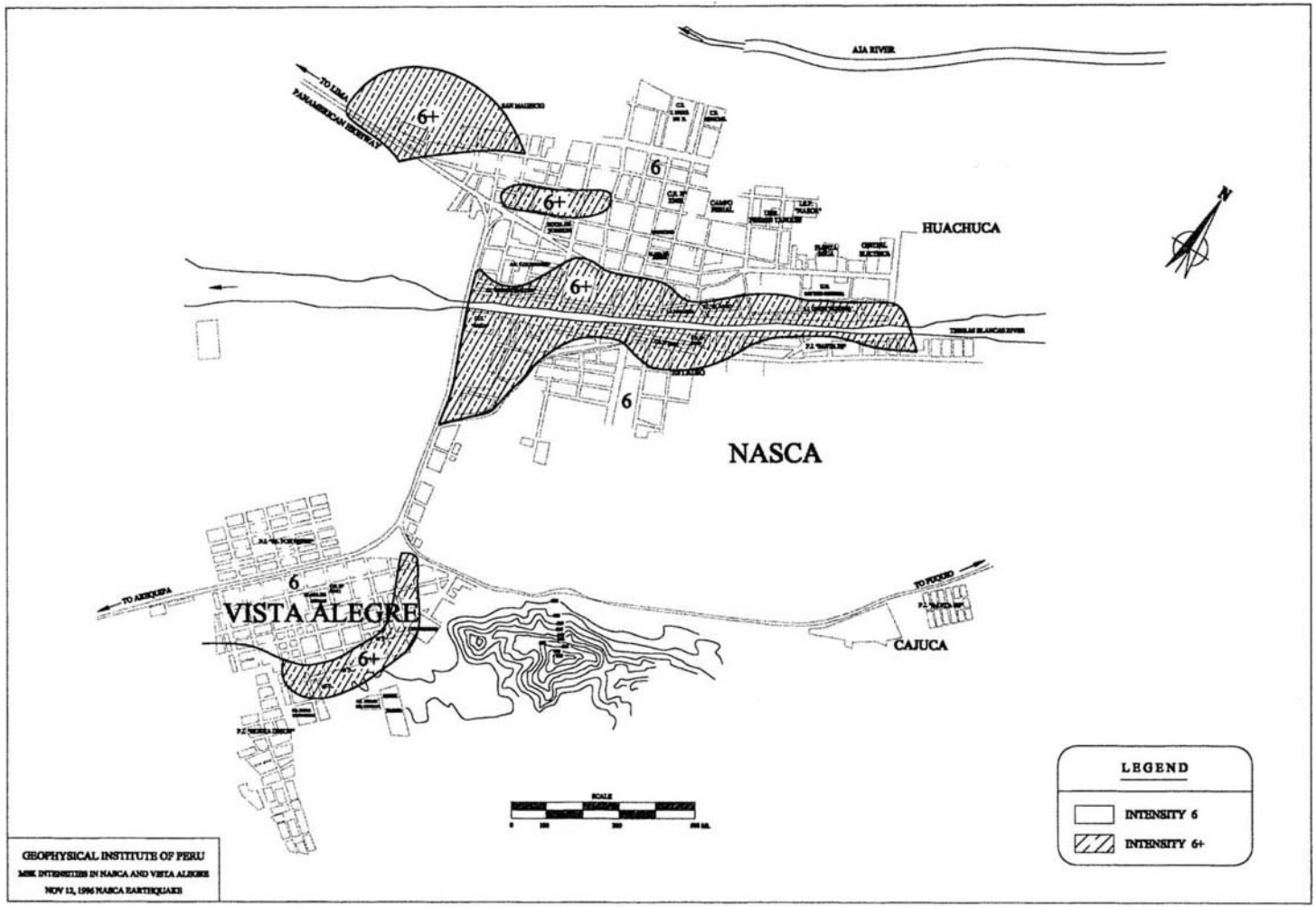

FIGURE N° 3 : LOCAL INTENSITIES OF 12 NOV 1996 NASCA EARTHQUAKE IN NASCA CITY (IGP, 1997)

occurred in the estuary of the Yauca river where saturated and sandy soil deposits exists. Cracking was observed in loose deposits of sand and gravel over ground slopes.

Intensities in cities and towns were estimated from building damage. In Acari, Bella Union and Vista Alegre district of Nasca, higher intensity values were observed closer to the surrounding mountains, indicating a topography effect in soil amplification. Isoseismal countour lines have ellipsoidal shape with some asymmetry towards the southeast, reflecting the direction of rupture propagation in the epicentral zone.

The Geophysical Institute of Peru prepared local intensity maps for several localities: Chincha, Pisco, Ica and Nasca. Figure 3 presents the local intensities for Nasca, including the Vista Alegre district (Ocola et al, 1997).

DAMAGE EVALUATION

Nasca Downtown

A great percentage of adobe houses collapsed because of its low tensile strength and low bond between adobe and mortar. Adobe is made with clayey - silty sand with brittle failure. Most of failures were produced by separation of walls at their intersection. There was not a collar beam around the upper part of the walls. The roof was light without anchorage with walls. Failure was by tension with flexure. Unconfined and confined masonry buildings had light damage, mostly in partition walls. Very few had structural damage. Most of these buildings were built without engineer's supervision and without confinement. Mixtures of adobe and masonry walls were noted, as well as adobe walls with concrete roofs. Damage in concrete framed structures is related mostly to partition walls due to structural deformation, without structural damage.

Schools

During this earthquake, as in previous earthquakes, higher percentage of damage was produced in schools as compared with other types of buildings. Main reason being its architectural vulnerability to faulty construction. In recently built Fermin del Castillo and Jose Carlos Mariategui schools in Vista Alegre district, extensive structural damage was produced in concrete structures and confined masonry. Besides, important construction defects were observed. Soil conditions are good. The topography suggests soil amplification. Short column effect was notorious.

Lifeline Systems

An elevated water tank in Nasca suffered damage. It was supported by a reinforced concrete framed structure. Water and sewage lines were not affected in the city. Landslides and rock falls were produced in secondary highways. No major damage in the Panamerican highway. Soil Liquefaction was reported near of Yauca bridge foundation. Damage ocurred in the upper beam of the central pier.

LOCAL GROUND EFFECTS

Soil liquefaction occurred in the riverbed of the Yauca river. One of the river piers suffered cracking of the upper beam and columm, as well as displacement of the bridge slab. Traffic was interrupted across the bridge and repair and restoration was inmediately undertaken. In the riverbed sand volcanoes and cracking was observed. The bridge foundation consisted of caissons (Pique, 1997).

The Geophysical Institute of Peru (IGP, 1997) reported generalized liquefaction in the Yauca river estuary. Sand volcanoes and mud ejection were observed. Landslides and rock falls were produced along highways towards the highlands in the Andes.

A very important phenomena was the collapse of tailing dams due to liquefaction and flow. The dams were located in Acari, Jaqui and Chala. The collapsed dams were built by the upstream method of construction and were in operation during the earthquake. The Acari river was contaminated by one of the tailing dams that collapsed.

The city of Nasca is located on fluvio-aluvial soils partially covered in some places by fine soils on the surface. The water level was 5.0 meter below the surface at the moment of the earthquake. Vista Alegre district is to the south of Nasca and has rolling ground surrounded by mountains. For this reason soil amplification developed.

In Palpa there is silty-clay material at the surface, medium stiff with different water content. Gravel is located 5.0 m. below surface. In Acari and Bella Union gravel material is present in the ground with the exception of Old Acari where fine material exists at the surface.

In general no important ground effects were noted in the main cities affected by the earthquake.

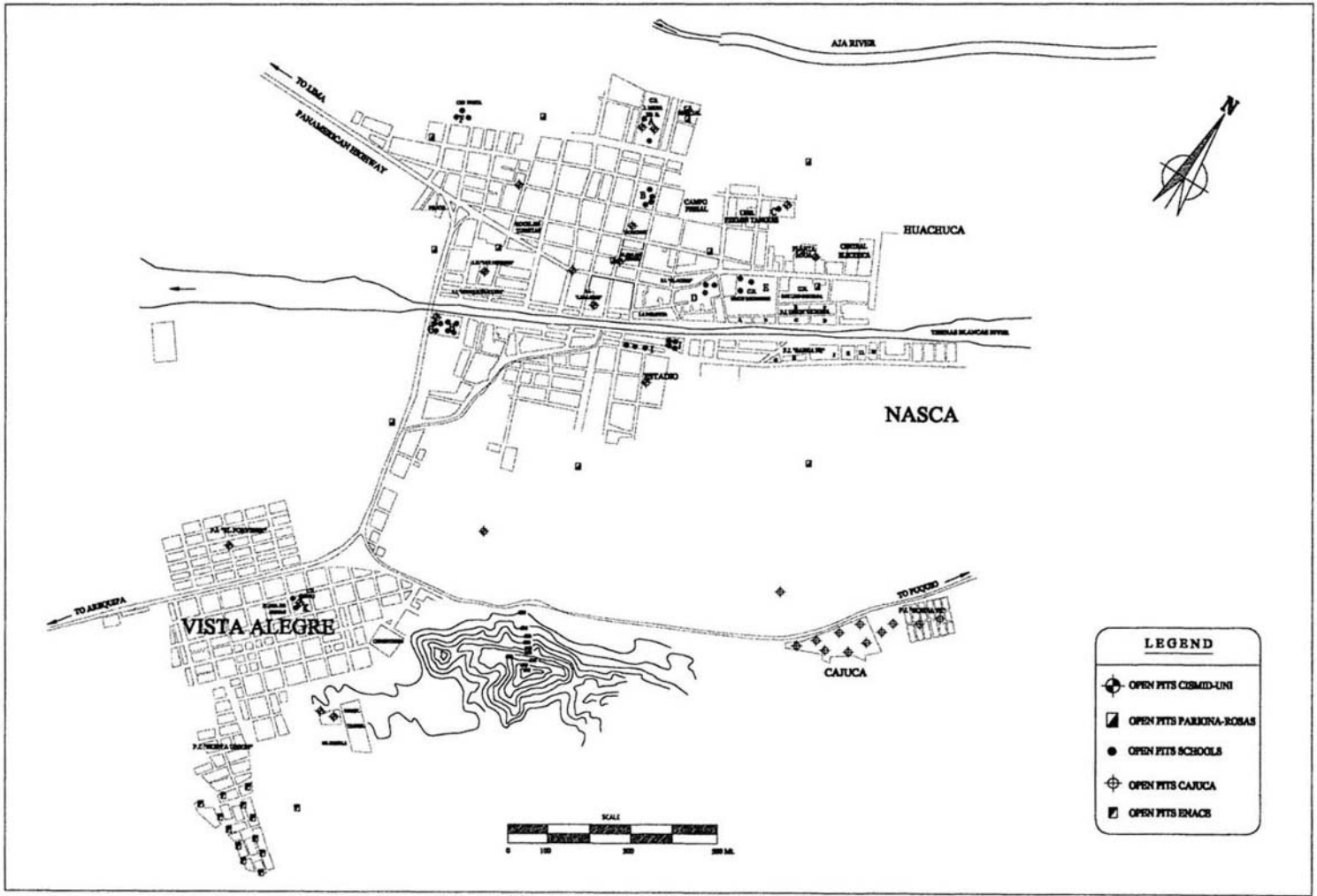

FIGURE N° 4 : SOIL EXPLORATION PROGRAM FOR NASCA MICROZONATION

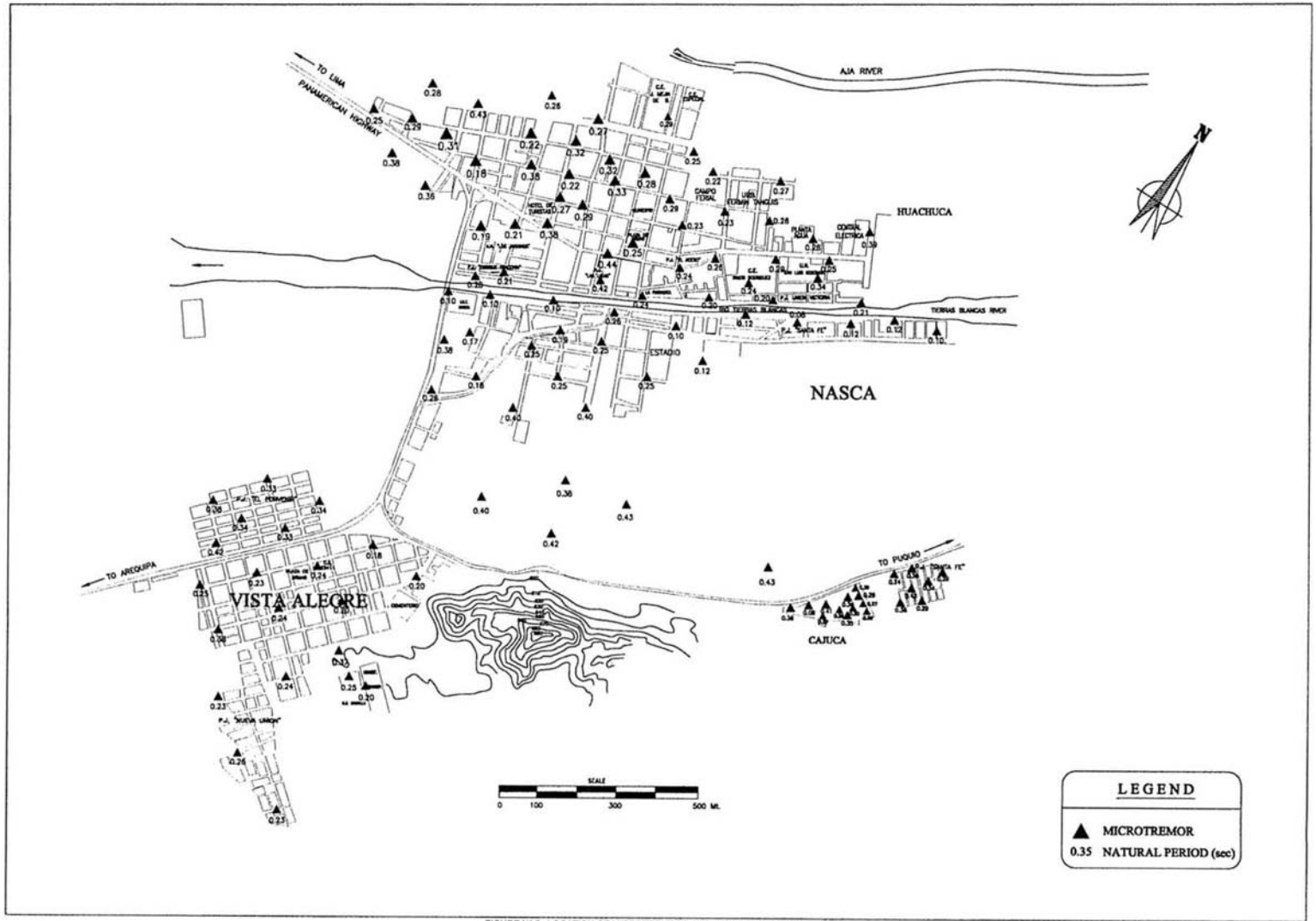

FIGURE N° 5 : LOCATION OF MICROTREMORS AND NATURAL PERIODS

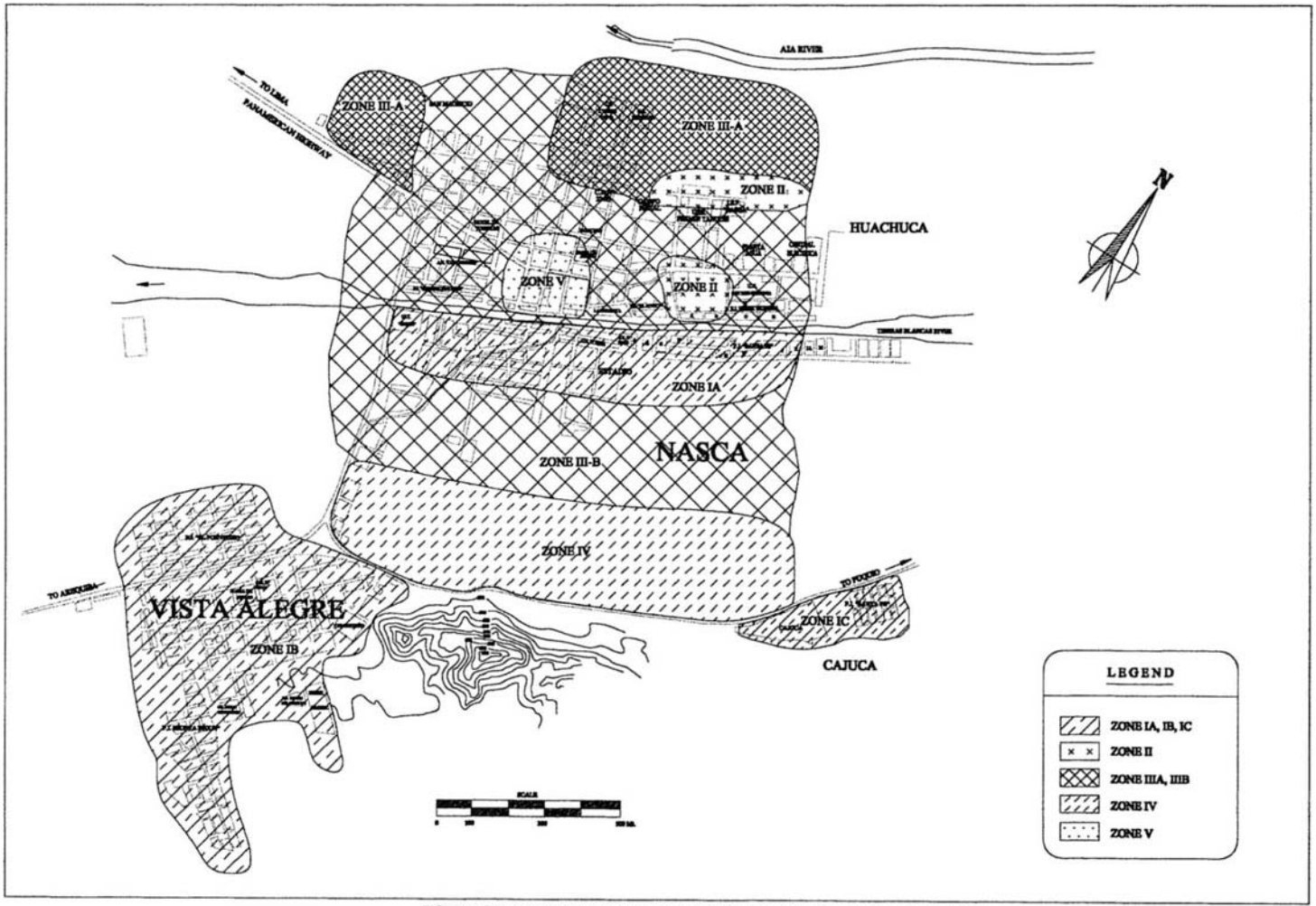

FIGURE N° 6 : SEISMIC MICROZONATION OF NASCA CITY (Vásquez and Alva-Hurtado, 1997)

SEISMIC MICROZONATION OF NASCA

To contribute with the reconstruction of Nasca, a microzonation of the city was undertaken, Available information was compiled (Pariona and Rosas, 1993, Huiman, 1996) and a soil exploration and microtremor measurement program was undertaken (Vasquez and Alva-Hurtado, 1997). A study involving microtremor and aftershocks measurements was also reviewed (Bondoux, et al, 1997).

Figure 4 present the location of open pits compiled and executed in Nasca and Vista Alegre. Because of the nature of the ground, hand made open pits up to 5.0 meters in depth were made. Figure 5 presents the locations of the microtremor measurements and their natural periods under ambient vibration.

The city was divided into five zones as presented in Figure 6.

Zone I. This zone has the best geotechnical conditions. The ground is composed of compacted gravel with boulders up to 10" in diameter. Bearing capacity is over 2 kg/cm^2 and the predominant period of soils is between 0.1 and 0.2 seconds. This zone was subdivided in 3 subzones.

Zone II. This zone is similar to zone I, with gravel down to 1.5 meters in depth. Fine material exists at the surface. Bearing capacities are from 1.5 to 2.0 kg/cm^2 and the predominant periods of soils are from 0.20 to 0.25 seconds.

Zone III. A medium thick layer of fine soils exists at the suface. Below the superficial layer, the gravel layer appears. For shallow foundations settlements are expected. It is recommended to reach the gravel layer for founding important buildings. Bearing capacities range from 1.0 to 1.5 kg/cm^2 and soil predominant period varies from 0.25 to 0.40 seconds.

Zone IV. The superficial layer consists of silty and clayey soils with thickness greater than 5.0 meter. The gravel layer is located beneath this layer. Bearing capacity of 1.0 kg/cm^2 is expected for shallow foundations. Predominant period is greater than 0.4 seconds. This zone is not developed. Soil amplification is expected because of the presence of nearby mountains.

Zone V. This is a critical zone because there is loose thick fill on the surface. This area is near Nasca downtown where adobe houses collapse was total during the earthquake. It is recommended to use this area for public recreation and parks.

CONCLUSIONS

1) Even though this earthquake had a moderate intensity, 75% of adobe buildings suffered severe damage or collapse. Main damages in adobe buildings are related to poor unions between walls and weak roof diaphragms, extended cracking along adobe joints in walls and overturning of fences and main walls.

2) Masonry buildings had light damage, mostly in partition walls.

3) Concrete framed structures presented non-structural damage. A special case was the recently built state schools where short columns developed because of large structure deformations and faulty construction

4) Future development of Nasca is recommended towards zones I and II, where the ground is composed of compact sandy gravel. Flood protection structures along the river banks should be provided. Zone III has second priority because the gravel layer is deeper.

5) Zone IV and V are critical because the gravel is below 5.0 meters. Zone IV is close to the nearby mountains and could develop soil amplification. Zone V has loose fill at the surface providing weak foundations.

6) Based upon damage produced by the earthquake some modifications to the peruvian earthquake code were proposed.

REFERENCES

Alva Hurtado J.E., Meneses J.F. and Guzman V. (1984), "Distribution of Maximum Seismic Intensities Observed in Peru", V National Conference on Civil Engineering, Tacna, Peru (Spanish).

Bariola J. (1997), "Retroffiting of Schools Damaged by the 1996 Nasca Earhquake", XI National Conference on Civil Enginnering, Trujillo, Peru, pp. 168-171 (Spanish).

Bondoux F., Chatelain J.L., Guerguen P. and Guillier B (1997), "Report of the ORSTM Mission to Nasca", Quito, Ecuador (Spanish)..

Huiman P. (1996), "Microzonation for Disaster Mitigation in Nasca", Professional Degree Thesis, National University of Engineering, Lima, Peru (Spanish).

IGP (1997), "Nasca Earthquake of 12.11.96. Preliminary Report", Lima, Peru (Spanish).

Muñoz A., Montalbetti A. and Tinman M. (1997), "Damage in Reinforced Concrete Structures due to the November 1996 Nasca Earthquake", XI National Conference on Civil Enginnering, Trujillo, Peru, pp. 58-63 (Spanish).

Ocola L., Monge F., Huaco P. and Agüero C. (1997), "Shaking Severity of the 1996 Nasca Earthquake", Geophysical Institute of Peru (Spanish).

Ocola L., Agüero C., Monge F., Huaco P. and Fernandez E. (1997) "Vulnerability of Housing, Mining and Highways to the 1996 Nasca Earthquake", Geophysical Institute of Peru (Spanish).

Pariona H. and Rosas M. (1993), "Bearing Capacity of Nasca Soils", Professional Degreee Thesis, San Luis Gonzaga National University, Ica, Peru (Spanish).

Pique J. (1997), "The Nasca Earthquake of November 12, 1996", Editor of the CISMID-UNI Report on the Nasca Earthquake, El Ingeniero Civil, Año 16, N° 107-108, March and June, Lima, Peru (Spanish).

Quiun D., San Bartolome A., Torrealva D. and Zegarra L. (1997), "Damage in Buildings produced by the November 12, 1996, Nasca Earthquake", XI National Conference on Civil Engineering, Trujillo, Peru, pp. 64-69 (Spanish).

Silgado E. (1978), "History of the Most Important Earthquakes that Occurred in Peru (1513-1974)", Institute of Geology and Mining, Journal N° 3, Series C., Lima, Peru (Spanish).

UNSA (1996), "Damage Evaluation of the November 12, 1996, Nasca Earthquake", Geophysical Institute, San Agustin National University, Arequipa, Peru (Spanish).

Vasquez D. and Alva Hurtado J.E. (1997), "Seismic Microzonation of Nasca", XI National Conference on Civil Engineering, Trujillo, Peru, pp. 87-93 (Spanish).

Earthquake Geotechnical Engineering, Sêco e Pinto (ed.) © 1999 Balkema, Rotterdam, ISBN 90 5809 116 3

Amplification characteristics of earthquake motion and damage during 1997 Kagoshihmaken-hokuseibu earthquake, Japan

H. Kiku, I. Suetomi & N. Yoshida
Sato Kogyo Company Limited, Tokyo, Japan

ABSTRACT: The 1997 Kagoshimaken-hokuseibu earthquake struck the southern part of Kagoshima prefecture, Japan, on March 26 and May 13, 1997. The earthquake motions were recorded at many sites by K-net strong motion observation networks. Peak ground accelerations greater than 0.5 g were observed at several sites. The earthquake brought many damages to various facilities such as buildings, port facilities and soil structures. These damages were mainly caused by soil liquefaction and landslide at the Sirasu ground. Soil liquefaction was occurred not only at the reclaimed land in the port but also at the embankment made from Sirasu.

1 INTRODUCTION

An earthquake of Magnitude 6.3 struck the northwest part of Kagoshima prefecture, Japan on March 26, 1997. The epicenter is located near the Izumi City and depth to focus was about 8 km. The JMA seismic intensity scale in Akune and Miyanojo was VI. It was the first earthquake by which seismic intensity greater than 6 was observed after JMA intensity scale was revised after the 1995 Kobe earthquake. The JMA seismic intensity scale greater than 5 was observed at several sites in Izumi and Sendai Cities and its vicinity.

After this earthquake, an earthquake with Magnitude 6.2 occurred in May 13, 1997 in nearly the same area. In order to distinguish two earthquakes, the notations I and II are used in the earthquake name. Significant damage was observed at port facilities and roads in the first earthquake. In addition to damage to these structures, damage to reclaimed lands and structures were observed in the second earthquake. Heavy rainfalls continued from March in this area, which may loosened the subsoil causing significant ground failure.

This paper describes ground motions in two earthquakes and damages observed in the second earthquake.

2 GROUND MOTIONS

The ground motions were observed at many K-net sites that was installed in whole Japan after the 1995 Kobe earthquake by Science and Technology

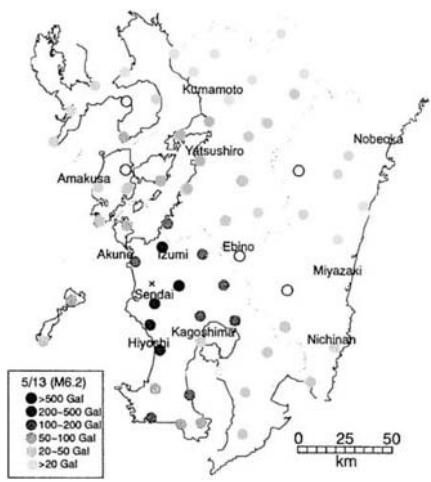

Figure 1 Peak accelerations at K-net sites

Table 1 Ground motion indices in the vicinity of epicenter

Earthquake	Location	PGA (cm/s^2)	PGV (cm/s)	PGD (cm)	I_J
I (March)	Izumi	859.8	17.4	4.08	5.25
	Ohkuchi	320.7	18.0	2.66	4.90
	Akune	295.6	43.7	11.45	5.68
	Miyanojo	548.5	36.9	5.99	5.54
	Sendai	238.2	29.3	5.14	5.18
II (May)	Izumi	736.9	24.2	4.59	5.30
	Ohkuchi	188.1	10.3	1.35	4.60
	Akune	173.9	18.4	4.14	4.80
	Miyanojo	953.0	46.8	6.39	5.90
	Sendai	340.7	32.0	7.57	5.40

I_J: JMA seismic intensity scale

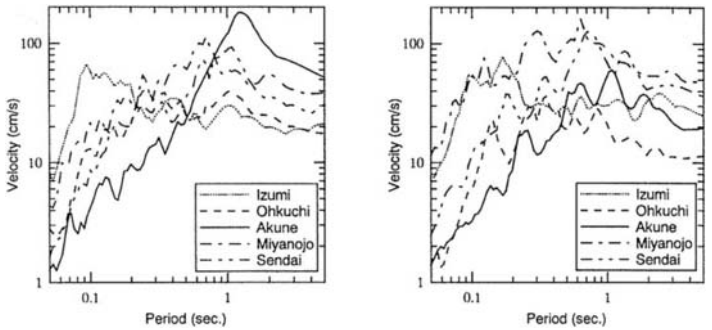

Figure 2 Velocity response spectra at the sites near the epicenter (h=5%)

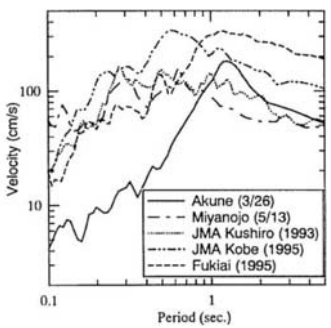

Figure 3 Comparison of velocity response spectra (h=5%)

Agency. Figure 1 shows peak acceleration distribution in the southern area of Kyushu Island, The third largest Island in Japan during the second earthquake.

2.1 *Ground response in epicentral region*

Several indices of ground motions such as peak ground acceleration (PGA), velocity (PGV) and displacement (PGD), and seismic intensity scale calculated from the observed records are shown in Table 1 at the sites close to the epicenter. They are computed from two horizontal components after filtering within 0.1 to 30 Hz. Numerical integration was made by Fourier integration. Peak acceleration is the largest at Izumi, but peak velocity and displacement are small. On the other hand, peak acceleration is small at Akune, but peak velocity and displacement are large. This indicates ground condition may affect the ground motions.

Velocity response spectra (5% damping) at these five sites are shown in Figure 2, in which significant differences are observed in the frequency characteristics. At Izumi where peak acceleration is the largest, frequency component at high frequency region is predominant and these at 0.5 to 2 sec. are small compared with other sites. Earthquake records at hard deposits such as Izumi and Ohkuchi was affected by the ground amplification at the surface

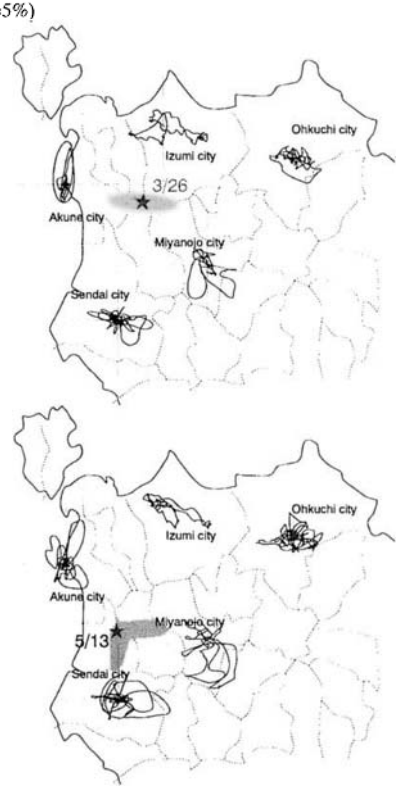

Figure 4 Orbit of displacement of earthquake motion near the epicenter in two earthquakes

deposit only in the frequency region higher than several Hz. Compared with these sites, response at Akune shows different feature. Response about 1.2 Hz is predominant and those at high frequency region are much smaller than other sites.

Comparison of velocity response spectra with other earthquakes is shown in Figure 3. Compared with the JMA Kobe record during the 1995 Kobe earthquake, velocity spectrum at Miyanojo is larger in period less than 0.13 sec. and smaller in period greater than 0.13 sec, resulting in larger acceleration and lower JMA seismic intensity scale. This feature

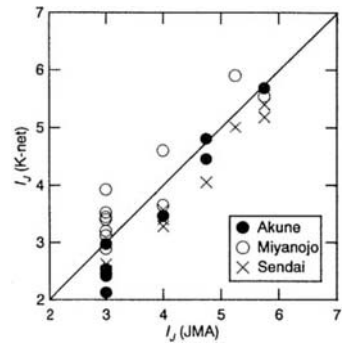

Figure 5 Comparison between seismic intensity scales

resembles to the spectrum characteristics at JMA Kushiro during the 1993 Kushiro earthquake. Both sites are located on the hilltop with volcanic ash. This geological similarity may result in the similar wave characteristics.

Velocity spectrum at Akune site is predominant at period of about 1 second and the shape is similar with that at Fukiai during the 1995 Kobe earthquake although magnitude at Akune is small.

Orbit of displacement of the observed records are shown in Figure 4. Here, each figures is normalized by its maximum value, resulting in different scale in each trajectory; we are interested at only the predominant direction. From these trajectories, fault rapture is supposed to travel from the epicenter toward the east-west direction during the first earthquake. Large ground motion in NS direction at Akune site was caused by the directivity effect. The predominant direction of displacement trajectory in the second earthquake is nearly the same with the first earthquake.

Records by both K-net and JMA are obtained at Akune, Miyanojo and Sendai. Figure 5 compares seismic intensity scale by two records for both main shock and aftershocks. Seismic intensity scale by K-net is always larger at Miyanojo, whereas it is always small at Sendai. In contrary, that by K-net is smaller under small earthquake at Akune City, but both records become similar in magnitude under the large earthquake. These characteristics seem to come from the differences of ground condition. We, therefore, will investigate the difference at Akune in detail.

2.2 *Amplification characteristics at Akune*

Seismometer of K-net in Akune is installed at the city hole, which is located south from the Akune port where liquefaction-induced damage was observed as described later. However, proof of liquefaction such as sand boil was not found at this site. On the other hand, seismometer of JMA is installed on the hard deposit in the mountain area.

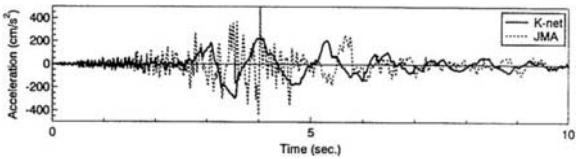

Figure 6 Comparison of waveforms at two sites in Akune during the first earthquake

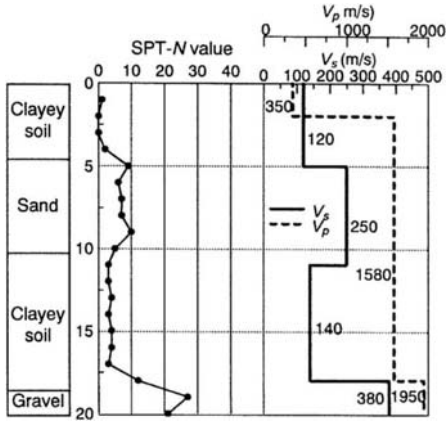

Figure 7 Soil profiles at Akune K-net site

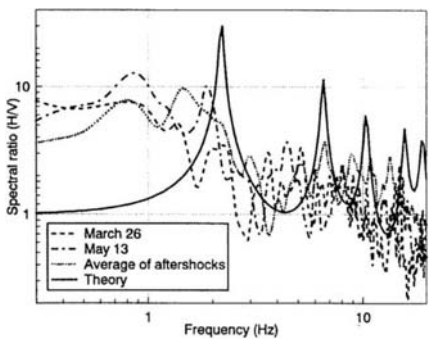

Figure 8 Spectral ratio at Akune K-net site

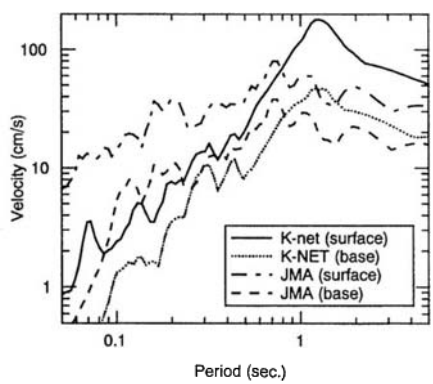

Figure 9 Comparison of velocity response spectrum at Akune

Figure 6 compares acceleration time history at both sites. Acceleration by JMA includes many high frequency component whereas frequency of about 1Hz is predominant and there is no high frequency component wave in the record by K-net. Since this difference is supposed to come from the difference of surface ground, we first obtain the waveform at the engineering base layer.

Figure 7 shows soil profiles at K-net site. Spectral ratio of horizontal component to vertical component computed from this soil profiles is shown in Figure 8 with the ones of computed from the observed records. Comparison between main shock and aftershock indicates that spectral ratio is not very large even at high frequency range and that predominant period at the main shock is a little smaller in frequency and a little smaller in magnitude. Spectral ratio at high frequency region is also not large even in the theoretical calculation. This may be caused by the existence of soft clayey layer at GL-10~17 m.

Velocity response spectrum (5% damping) is shown in Figure 9. As pointed out in the preceding, responses spectrum at the ground surface are quite different to each other. On the other hand, that at the seismic base layer is similar to each other in shape. This indicates that difference of surface deposit brought the significant difference of the ground motions at the surface although two sites are only several km distant. This difference may be supposed to be caused by the liquefaction at K-net site. This is, however, not true because not only sand boil was not observed but also the site is far from the port area where sand boils were observed. In addition, this kind of difference is observed even in small earthquake, which cannot be explained by the liquefaction. Moreover, waveform caused by cyclic mobility was not seen in the strong motion record. Therefore, the difference comes from the existence of soft clay layer.

3 DAMAGE CAUSED BY THE SECOND EARTHQUAKE

3.1 *General*

The authors made field survey after the second earthquake at Miyanojo, Tsuruta, Akune and Seidai areas especially focusing on liquefaction induced damage, damage to road embankment, and slope failure in Shirasu (volcanic gravelly soil) region. Figure 10 shows various damages caused by the second earthquake. The damaged regions are nearly the same with the ones damaged during the first earthquake. Over 5000 houses were damaged, which is much larger than the damage during the first earthquake. Damaged property reached more than 5 billion Japanese Yen, and more than half of them were damage to civil engineering structures.

In this paper, we focus on the damage at several ports and damage caused by the failure of Shirasu.

3.2 *Damage to port facilities*

3.2.1 *Akune port*

Damage at Akune port is shown in Figure 11.

Figure 10 Locations of damaged site

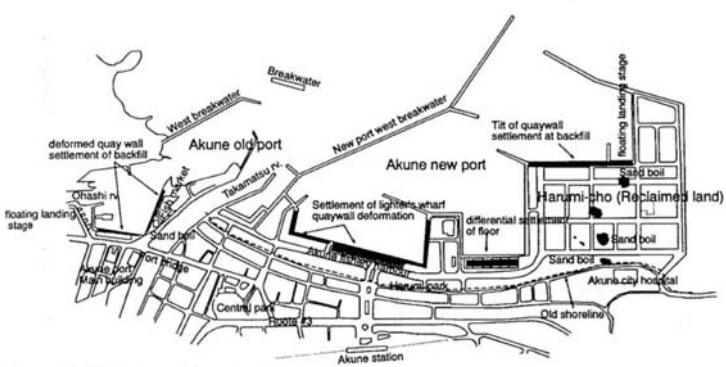

Figure 11 Damage at Akune port

Damage at the new port was the most severe. Settlement in the backfill ground and cracks between quay walls were observed at many places (Figure 12). At some places, cracks expanded more than 100 m and differential settlement reached 50 cm. According to the interview to the resident, cracks and differential settlement appeared firstly during the first earthquake, and increased at the time of aftershocks and the earthquake of May 13. Sand boils were observed nearby.

Same types of damage were also observed at the old port. Columns of the fish market were damaged and the differential settlement was observed on the floor (Figure 13). Muddy water were observed to flow up on the floor at the first earthquake, which indicates soil liquefaction was the main reason of the damage.

In the Harumi-cho district, a new reclaimed land, a new quay wall tilted towards the sea and backfill ground subsided. Moreover, cracks toward the quay walls were observed in the interior road. There are many sand boils inside the road. These sand boils were colored blue-gray and include many fines; they are probably dredged soil. Generally, sand boils and liquefaction-induced damage were observed in the new fill region and neither liquefaction nor damage due to inertia force was hardly seen in the areas inside the old shoreline.

3.2.2 *Sendai Port*

Settlement and cracks of the quay wall were observed at new quay walls (Figure 14). Settlement of about 3cm and crack with 10 cm were observed during the first earthquake. Settlement increases to 20 cm during the second earthquake. The ground surface in the backfill ground was paved, therefore sand boils was not observed. Similar damage was observed at several locations.

3.3 *Damage to road*

Damage to road embankment was frequent, but not heavy. Cracks on the boundary between fill and original ground are typical pattern.

Fallen rocks and slope failures were frequently seen on the road in the Shibi mountain area, and road closed at many places because of them. Slopes in this area are made from weathered diorite granite. Near the Second Tsuruta dam, large scaled slope failure occurred; failed rock flowed into the dam lake (Figure 15).

Many slope failures occurred at the cut slope along Route 324, national road connecting Izumi City and Miyanojo-cho.

Shoulders of the road were heavily damaged in the areas facing the Sendai River in Tsuruta-cho. This region is Alluvial lowland, therefore damage pattern is different with that of granite slope.

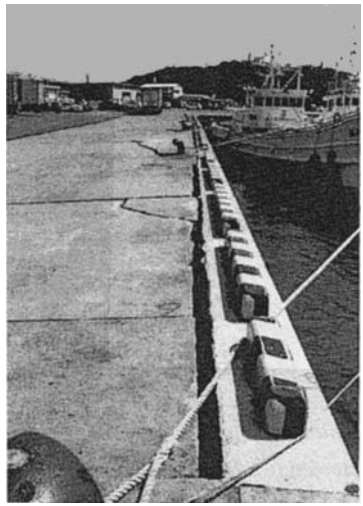

Figure 12 Settlement of backfill ground and separation

Figure 13 Damage to column and differential settlement of ground

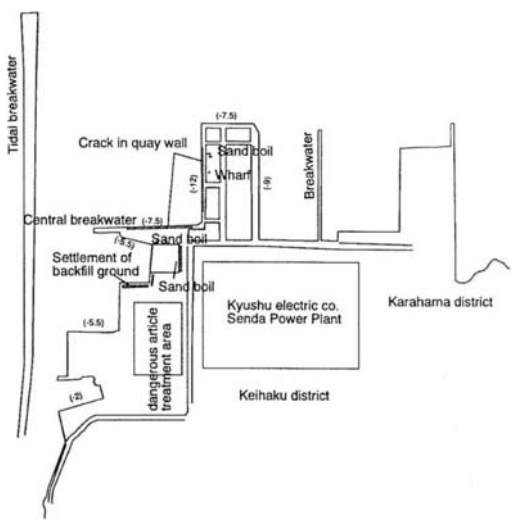

Figure 14 Damage at Sendai port

Figure 15 Failure of cut slope and flow into lake

Figure 16 Collapsed house due to slope failure

3.4 *Damage in Shirasu ground*

Kagoshima prefecture is famous because of the Shirasu (volcanic gravelly soil) that is the deposit made by pyroclastic flow. Firstly deposited Shirasu is a good material because of its high load carrying capacity and high permeability. As it is not harden, however, the possibility of failure increases very much when disturbed. Many failures has been seen not only by the earthquake but also by rainfalls.

Slope with about 15m high and located at the back of residential houses failed and collapsed houses at Haneda district, Sendai city (Figure 16). Similar failure was also seen at several places.

Liquefaction of Shirasu was also observed at several places (Figure 17). They are mainly secondly deposited Shirasu. Liquefaction-induced damage was occurred at Atago district in Iriki-cho where streams flow both side of fill area as shown in Figure 18. As seen sand boils were observed at many places. In addition, float-up of manhole were observed, too, which probably caused by the settlement of surrounding ground. According to the interview to the resident, settlement reached about 50 cm in total by two earthquakes. Similar damage was also observed nearby.

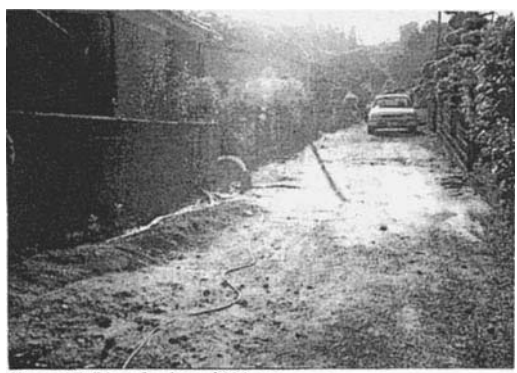

Figure 17 Liquefaction of Shirasu

Figure 18 Map of Iriki district

4 CONCLUSING REMARKS

Significant damage occurred during the 1997 I and II Kagoshimaken-hokuseibu earthquakes in the Kagoshima prefecture. Earthquake motions were recorded at many sites by the K-net system. Through the investigation of the records, the ground conditions are shown to play an important role on the earthquake motion at the ground surface.

New reclaimed land was severely damages same as past earthquakes. The local soil Shirasu was shown to be responsible in many landslides and liquefaction.

Earthquake Geotechnical Engineering, Sêco e Pinto (ed.) © 1999 Balkema, Rotterdam, ISBN 90 5809 116 3

Seismological, geological, geotechnical and engineering of the July 9, 1997 Cariaco Venezuela earthquake

J. Murria & A. Hernández
Venezuelan Foundation for Seismological Research, Caracas, Venezuela

ABSTRACT: On July 9, 1997, at 15:24:10.8 local time (19:24:10.8 GMT) an Mw 6.9 earthquake shook eastern Venezuela between the towns of Cariaco and Casanay. The epicenter is located in the El Pilar fault system which is of the boundary between the South American and the Caribbean plates. A total of 73 persons were killed, and 531 persons were injured. About 1.000 dwellings were destroyed and 3 buildings collapsed, affecting more than of 5.000 persons. Extended damage was reported to lifelines and structures. This damage was mainly associated with fault rupture and liquefaction (including lateral spread) and, in some cases, landslides. This paper will discuss in detail the geological, geotechnical and engineering aspects being studied and evaluated at the time of this writing.

1 INTRODUCTION

On July 9, 1997, at 15:24:10.8 local time (19:24:10.8 GMT) an earthquake with a magnitude Mw 6.9 shook eastern Venezuela between the towns of Cariaco and Casanay in the state of Sucre. The earthquake was strongly felt in Cumaná the state capital some 70 km west of the epicenter and as far as Caracas about 400 km west of the epicenter. (Figure 1)

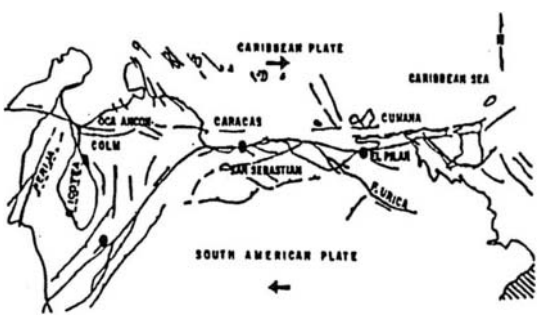

Figure 1. Main active faults in Venezuela

The Cariaco earthquake is the most important seismic event in Venezuela since the July, 1967 Caracas earthquake.

The epicenter was located at latitude 10.545° north and longitude 63.515° west at a depth of about 10 km. This places the epicenter at the El Pilar fault system which is the easternmost section of the boundary between the South American and the Caribbean plates. It is a right lateral strike-slip earthquake with a coseismic displacement of 0,25 m.

The main characteristic of the Cariaco earthquake is the more than 30 km right lateral surface rupture of the El Pilar fault, from Muelle de Cariaco on the west to the village of Las Varas east of Casanay (Figure 2).

The actual length of the surface rupture could be more than the 30 km mentioned above as its west end is under water in the Gulf of Cariaco and its east end is in an area of heavy tropical vegetation (FUNVISIS 1997b).

A total of 73 persons were killed, most of them in Cariaco, and 531 persons were injured. About 1.000 dwellings were destroyed within 70 km of the epicenter affecting more than of 5.000 persons.

The town that suffered the most damage was Cariaco, 10 km west of the epicenter. A grammar school and a high school collapsed killing 30 students and teachers (FUNVISIS 1997b).

Structural damage occurred in the city of Cumaná where a six-story building "pancaked" killing 21 persons. Only a few other buildings were seriously damaged but no fatalities were reported.

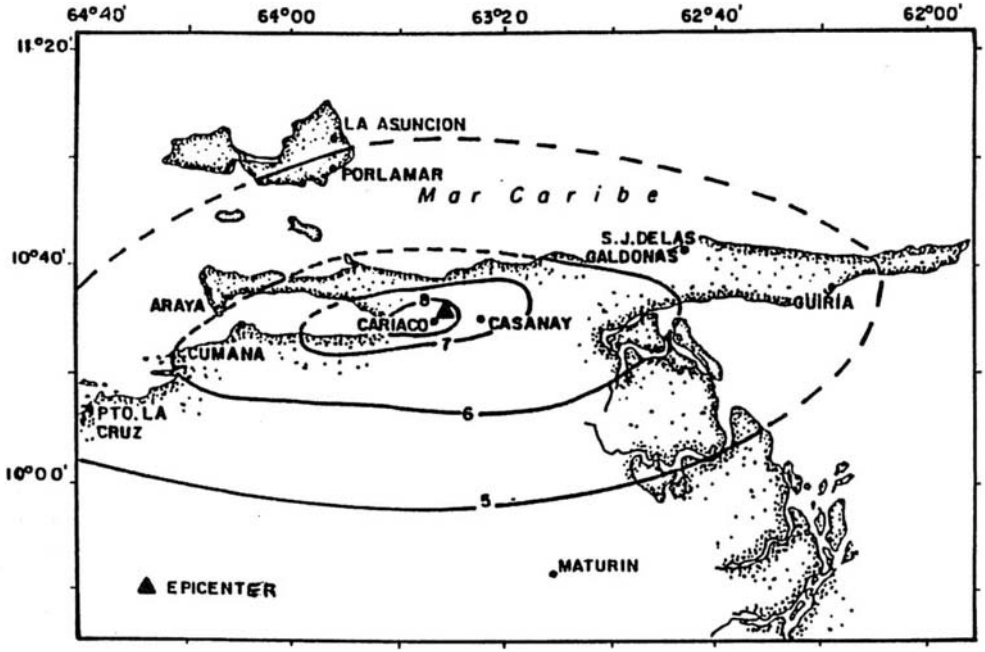

Figure 2. Isoseismal map (MMI)

Extensive damage was reported to lifelines and structures. This damage was mainly associated with fault rupture and liquefaction (including lateral spreading) and, in some cases, landslides.

Lateral spreading was observed in the fishing wharf in the mouth of Rio Manzanares in Cumaná as well as at a shrimp farm near Chiguana where some earth dikes of the shrimp farm ponds collapsed (FUNVISIS 1997b).

Evidences of liquefaction (sand boils) were detected, near Marigüitar, some 50 km west of the epicenter, as well as near the margins of the Manzanares river in Cumaná (Murria 1999).

2 GEOLOGICAL AND TECTONIC SETTING

Venezuela is the boundary between the Caribbean and the South American plates. A continuous system of right lateral strike-slip faults extends across the country from the Andes in the southwest to the Gulf of Paria close to Trinidad in the northeast. This system comprises the Boconó fault in the southwest, the San Sebastián fault in the north central region and the El Pilar fault in the east (Figure 1). The July 9 Cariaco earthquake epicenter is located on the central portion of the El Pilar fault, east of the segment than was activated during the 1929 Cumaná earthquake (FUNVISIS 1997b)).

3 SEISMIC HISTORY

The first historically documented earthquake occurred in September 1530, shortly after the first Spanish settlements were established in Cumaná. This earthquake destroyed the Spanish fortress and generated the first recorded tsunami in América (EERI 1997).

The largest earthquake ever known in this region occurred in October 1766. It was felt as far at Maracaibo, 800 km to the west and caused some damage in Caracas, 300 km to the west (Figure 2).

In July 15, 1853 another earthquake shook the region causing heavy damage and hundred of casualties.

The January 17, 1929 Cumaná earthquake was the last strong earthquake felt in the region. Heavy damage was reported in Cumaná. An Ms 6.3 magnitude and MMI XI for Cumaná and VII for Cariaco have been assigned to this earthquake. Minor earthquakes have been recorded in the area in 1939, 1944 and 1974 (FUNVISIS 1997a).

4 SEISMOLOGICAL ASPECTS

4.1 General

As mentioned in the introduction the main shock took place on July 9, 1997 at 15:24:10.8 local time (19:24:10.8 GMT). The epicenter was located at Lat. 10.545° north and Long. 63.515° west at a depth of about 10 km. The magnitude was given as Ms 6.8, Mm 6.9 and Mo 2.53E + 26 dyne-cm.

The preliminary focal mechanism, calculated by the Seismological Laboratory of the University of California at Berkeley using the seismic moment tensor method, indicates a dextral strike-slip movement with the following values: strike 266°, rake 176°, and dip 86°. Body and surface waves from 5 stations of the seismic world network were used (EERI 1997; FUNVISIS 1997b).

In addition to the seismological stations of FUNVISIS and UDO, the portable network displayed after the earthquake included 9 stations, of which two were broadband, from Northwestern University/IRIS, Illinois, USA; 6 stations from the University of Chile/CERESIS, Santiago; and 18 stations from the German Task Force for Earthquakes, GFZ Potsdam. For the investigation of site effects, engineering purposes and better location of strong aftershocks the Civil Engineering Task Force (Bauhaus-University Weimar) installed 10 digital strong motion stations. The installation of 5 GPS stations (GFZ Potsdam) was aimed at monitoring fault movements due to afterslip or slip induced by the aftershocks.

During the first weeks, the daily number of recorded aftershocks decreased rapidly, from about 350 to 50 by the end on July.

The number of felt shocks (over Ms 3.5) decreased from about 5 per day during the first days to one every 2-3 days in the same period (Murria 1999).

4.2 Intensities, attenuation relationships and ground motions

Figure 2 shows the isoseismal map which was the result of an intensity survey carried out by FUNVISIS in the days following the earthquake.

The isoseismals show a clear EW trend, following the valley formation related to the El Pilar fault rupture orientation. Local amplification effects were not considered (FUNSIVIS 1997b). Only two strong motion records were obtained at Cumaná, 70 km west of the epicenter with peak accelerations of 0.10g and 0.17g and 23 and 43 seconds, respectively. The other six strong motion instruments did not produce any records. However from the regional attenuation law, the epicentral acceleration is estimated at 0.20 - 0.25g. (EERI 1997)

5 GEOLOGICAL ASPECTS

One of the most salient aspects of the Cariaco earthquake is the east-west trending surface rupture of the El Pilar fault which has been preliminarely mapped for approximately 30 km, although it seems that a considerable portion of the surface rupture is missing at both ends. On the west the fault seems to continue west into the Gulf of Cariaco (Figure 2). On the east it is masked by very thick tropical vegetation (Figure 2).

Most of the rupture shows a rather constant coseismic slip of about 0.25 m. The fault rupture is generally less than 4 m wide as is basically expressed by synthetic Riedle shears. At some sites, the rupture exhibits en echelon folds (INCEDE NEWLETTER 1997).

6 GEOTECHNICAL CONSIDERATIONS

6.1 General

As mentioned in the introduction extensive liquefaction and lateral spreading were observed, particularly on or near the coast and along river margins. Small landslides were also reported. These manifestations were to a large extent concentrated along the coastline.

This was to be expected for an earthquake of this magnitude given the geomorphology of the region and the origin and composition of the soils.

6.2 Subsurface soil conditions

The soil in the east-west trending topographic depression where the El Pilar fault is located (see 2. above) are alluvial of fluvio-marine origins.

Old river beds, abandoned meanders, oxbow lake formations, alluvial fans and alluvial cones are typical geomorphic manifestations in this area (FUNVISIS 1997c; Gámez & Hernández 1998). This results in considerable soil heterogeneity, although it can be stated that the soils in the area are generally nonplastic, loose, and easily removable (FUNVISIS 1997c).

6.3 Liquefaction and lateral spreading

Extensive liquefaction occurred along the coastline in the form of sand boils and vents in river deltas, along river banks and flood plains (FUNVISIS 1997a).

Sand boils near the banks of the Manzanares river as far as 2 km upstream of Cumaná have been reported (FUNVISIS 1997b).

Liquefaction occurred mainly in hydraulically filled reclaimed areas but extensive liquefaction was also detected along sandy beaches were sandboils of up to 1 m in diameter have been reported.

Certain areas of the town of Cariaco (Figure 2) also showed evidences of liquefaction particularly along old meanders and old river deltas.

Many evidences of lateral spreading were detected along the coastline between Cumaná to the west and Casanay to the east of the epicenter.

The fishing port of Cumaná also showed considerable lateral spreading.

It is interesting to note that all these cases of lateral spreading occurred within the MMI 6 isoseism (Figure 2).

7. ENGINEERING ASPECTS

7.1 General

As it is to be expected most of the damage occurred near the epicentral area (Figure 2) where 360 of the 531 victims were reported.

The damage to the built environment took place mostly in cane and mud type of construction, know locally as "bahareque".

Preliminary report indicate that damage to engineered structures was due to the combination of site effects, building configuration and, in some cases, faulty construction (detailing and/or non suitable materials). (EERI, 1997)

7.2 Damage in Cumaná

As mentioned above, Cumaná, the state capital, is located some 70 km west of the epicenter. MMI intensities in Cumaná were estimated at between band (Figure 2).

Of the more than 200 buildings higher than two stories existing in Cumaná only a handful suffered structural damage: four multistory building (two of them under construction) suffered severe structural damage, while other three sustained only minor damage.

These buildings were located fairly close to each other in or near the avenue that runs parallel to the coast and about 2 km from it particular interest is the case of Residencias Miramar a six story reinforced convert building that collapsed killing 31 persons.

The structural system of this buildings was a concrete frame with deep beams in one direction (parallel to the Avenue) and shallow beams along the other. The plan of the building was irregular with a large opening (40% of the areas) in the first two stories.

On the basis of interviews to the witnesses of the collapse it can be inferred that torsional and lateral movements preceeded the pancake type collapse (FUNVISIS, 1997b).

Legal and insurance problems have delayed the publication of the final official reports of the ongoing investigations but, with the information ar hand, it can be preliminary concluded that localized site effects, building configuration and faulty detailing contributed to the building collapse.

7.3 Damage in Cariaco

In Cariaco, less than 10 km from the epicenter and a few hundred meters from the fault rupture, one high school and one grammar school collapsed killing 30 students and teachers.

The "Raimundo Martínez" high school was a 4 story modular reinforced concrete structure built in 1989. The central module collapsed completely while the side modules suffered less severe damage. The use of short columns, irregular plan and lack of transverse reinforcement may have contributed to the failures of this structure (EERI, 1997).

The "Valentín Valiente" grammar school had a regular rectangular plant and one way slabs. This school had been built around 40 years ago so it reflected the state-of-art at that time. Examination of the material showed the use of gravel instead of crushed stone. Defective detailing of the reinforcement may have also contributed to the collapse of the structure.

As to the rest of the damage in Cariaco it was mainly in one story dwellings of very light construction of mud and cane ("bahareque") type or unreinforced masonry.

7.4 Other communities affected

Structural damage was reported in the villages of muelle de Cariaco, San Antonio del Golfo and Chiguana among other, all located within the MMI 6 isosist (Figure 2). Again most of the damage occurred in one story light construction dwellings not

properly designed or constructed. Very little damage was detected in properly designed and built one or two story mostly reinforced concrete structures.

8. CONCLUSIONS

-The most salient characteristic of the Cariaco earthquake was the surface rupture of more than 30 Km a long the El Pilar fault zone.

-Extensive liquefaction, lateral spreading and, to a lesser extent, landslides are the outstanding geotechnical manifestations. These phenomena were to be expected given the earthquake characteristics and the soil properties and contributed in many cases to the damage to lifelines and structures (buildings and one story dwellings).

-Structural damage was concentrated in the epicentral area. The earthquake affected mainly those buildings which structural configuration and/or construction quality was not in accordance with the present building code. Typical dwellings in the region, mud and cane ("bahareque") and unreinforced masonry suffered extended damage.

REFERENCES

EERI 1997. The July 9, 1997, Cariaco, eastern Venezuela earthquake, *EERI Special earthquake report*, October, 1997.

FUNVISIS 1997b. Evaluación preliminar del sismo de Cariaco del 9 de julio de 1997, Estado Sucre, Venezuela (Versión revisada), José A. Rodríguez, *Editor*. Caracas, October 1997, 123p + annexes.

FUNVISIS 1997c. Geomorfología del Centro Poblado de Cariaco, Estado Sucre. Informe preliminar. Internal FUNVISIS report (Undated) 4 p.

Gamez, M. & R. Hernández 1998. Microzonificación sísmica de Cariaco, BCE thesis, IUPFAN, Caracas, Venezuela, 135 pages + 15 annexes.

INCEDE NEWSLETTER 1997. Preliminary geological report on the Cariaco earthquake July 9, 1997, Venezuela, Juan Murria, incede network member, Venezuela. *Incede Newsletter, volume 6, number 2*, July-September 1997, page 7.

Murria, J. 1999. Earthquake geotechnical engineering aspects of the July 9, 1997 Cariaco, eastern Venezuela earthquake. Submitted to the Organizing Committee of the Second International Conference on Earthquake Geotechnical Engineering, Lisbon, Portugal, June 21-25, 1999.

Singer, A., C. Rojas & M. Lugo 1983. Inventario Nacional de Riesgos Geológicos, Estado Preliminar, FUNVISIS, Serie Técnica 03-83, Dpto. Ciencias de la Tierra, Caracas, August 1983 126 p + map.

This Page Intentionally Left Blank

Earthquake Geotechnical Engineering, Sêco e Pinto (ed.) © 1999 Balkema, Rotterdam, ISBN 90 5809 116 3

A down-hole experiment and geotechnical investigations at Fabriano, Italy

Teresa Crespellani
Dipartimento di Ingegneria Civile, Università di Firenze, Italy

Roberto De Franco & Alberto Marcellini
Istituto di Ricerca sul Rischio Sismico, CNR, Milano, Italy

Michele Maugeri
Facoltà di Ingegneria, Università di Catania, Italy

ABSTRACT: The paper presents some findings of a multidisciplinary research, begun after the two main shocks of the seismic sequence that initiated in September 1997 in the Marches and Umbria Italian regions. In the city of Fabriano, the observed damage was, on the whole, light and concentrated in a few areas. In some of them, observation favoured the hypothesis that damage might be due mainly to site effects. Thus, with the perspective to retrofit the damaged buildings and to prevent the existing heritage, a study of microzonation, based on extended seismological measures and geotechnical testing, was set up. The results presented here are concerned with the measurements obtained on a site where a down-hole accelerometric experiment (DHE) has been operating since April 1998. The system recorded many aftershocks characterised by magnitude M_D and ranging from 2.5 to 4. These records are interpreted here in the light of in situ and laboratory dynamic tests and of numerical seismic response analyses.

1. INTRODUCTION

On 26th September 1997, two seismic shocks, having magnitudes respectively of M_S =5.5 and M_S = 5.9, struck an area of Central Italy, causing considerable damage in a wide zone situated on the boundary between the Marches and Umbria. In a few villages the macroseismic intensity reached values of IX MCS; in a broad area of about 450 km^2, the intensity was greater than VII (Camassi et al., 1997). Also at Fabriano the intensity reached VII MCS (Figure 1).

The two shocks occurred at 2.33 and 11.40 a.m., and during the subsequent months were followed by a large number of other shocks. The seismic events were recorded by all accelerometric stations of the Italian accelerometric network situated in Central Italy; unfortunately, however, none of them is located at Fabriano.

Lying in a wide valley, Fabriano is an important town of the Marches, with ancient origins, which still preserves high and noble traces of its past in the narrow streets and in the ancient, medieval and of the 16th-17th century fabrics of its historic centre. Because of its geographic location, it has played a leading role in the territory between the Marches and Umbria. At present, it is also an important industrial centre for the region.

After the earthquake, damage observation favoured the hypothesis that site effects could be a cause of the damage observed. In fact, no evidence of particularly poor quality in the buildings was observed.

Figure 1 – Location of Fabriano, Italy

Therefore, with a view to interpreting damage and especially to retrofitting the historical and existing heritage, a study of microzonation, extended to the whole area of the municipality, was set up by GNDT (Gruppo Nazionale per la Difesa dai Terremoti) and SSN (Servizio Sismico Nazionale) (Marcellini, 1998). An analysis of the regional and historical seismicity indicated that more severe shocks than those that occurred in the recent seismic sequence can be expected in the area (Marcellini & Tento, 1998).

As the reliability of a microzoning map depends on both the quality and the density of the experimental data, the area was the object of seismological and geophysical surveys and of numerous in situ and laboratory geotechnical testing. Since the most reliable way to identify site effects is the installation of seismological instruments, in order to capture the aftershocks an extended temporary horizontal array covering the most damaged and significant sites was implanted immediately after the earthquake. The location of the all instruments was established after an examine of the intensity of the damage, of the morphology and of the geotechnical properties of the soils. As available geological information did not cover the urban centre at scales useful for seismic microzoning, a detailed geological survey was also conducted and as a result a map at scale 1:5000 was made.

A programme of soundings and geotechnical in situ and laboratory dynamic tests was set up in a more restricted target areas. As far as the shear strain levels investigated by means of dynamic testing are concerned, since site effects appeared to be the most plausible cause of damage (no strong evidence of soil collapse was observed) attention was mainly focused on low and medium levels of shear strain amplitude. In situ, geophysical testing with various techniques (Down-hole, SASW, FTAN) were carried out, while in laboratory, cyclic dynamic tests, in addition to conventional testing, were carried out. All these experimental investigations attracted a substantial amount of attention from many Italian researchers for more than an year (Marcellini, 1998).

For a better insight on site effects, in April 1998 a down-hole accelerometric array (De Franco et al., 1998) was located in a part of the city that had suffered severe damage and which is of particular interest for urban planning purposes. This down hole experiment (DHE) is the object of the present study. The data obtained are presented and discussed in the light of the in situ and laboratory geotechnical dynamic testing and modelling.

2. INSTRUMENTATION

The down hole accelerometric experiment (DHE) is located in the north western part of Fabriano, in an urban expansion area called Borgo.

From a stratigraphic point of view, in correspondence with the DHE, the soil is characterised by 1 m of organic material, 6 m of inorganic clays of high plasticity, 6.6 m of silty clays with intercalation of sandy strata and 2 m of intercalation of clays and marls that overly the Gessoso-Solfifera bedrock formation.

Two holes (Figure 2), located at a relative distance of 1m, were equipped with three accelerometers, situated as follows: a) the first, on the free surface, in an intermediate position between the holes (n.1); b) the second, at a depth of 5 m in the right hole in Figure 2 (n.2) c) the third, in the left hole at a depth of 25 m (n.3). In this way, the response of the three soil layers were obtained. The spectral ratios considered here are the ratios between the spectra of the recordings obtained on surface to the spectra obtained at a depth of 25 m and the ratios between 5 m to 25 m spectra.

The hole measurements were performed using two 3D down-hole force balance Kinemetrics FBA13-DH accelerometers and a 3D FBA23 surface accelerometer controlled by a SMA3 central unit. The instrumental full scale is 1g and the proper frequency of accelerometers is 50 Hz with a damping of 0.7.

The sensorial coupling was guaranteed by a pneumatic system controlled on the surface. A 1 Hz Mark L4C/3D velocimeter (0.7 damped) was installed on the surface near the FBA23 accelerometer, in order to control the trigger system. The accelerometric analogic signals were amplified 10 times and DC component conditioned. The acquisition system consisted of 4 Lemnartz Mars88-FD working in a master-slave configuration and operating with a sampling rate of 62.5 Hz. The velocimetric master station trigger is based on a short time-long time analysis algorithm (*STA/(LTA+ level)>threshold; LTA=12s, STA=1s, level=2 and threshold=3*), and the accelerometric slave stations were activated by an external input trigger derived from the master station. The pre-event and post-event triggers were set at 16 s and 48 s, respectively. The experiment has been operating since April 1998. Between April and June 1998, the system recorded mainly the Gualdo Tadino aftershock sequence located about 20 km westward and characterised by M_D ranging from 2.5 to 4. A selection of 19 events allowed us to perform a preliminary evaluation of the amplification in the DHE site.

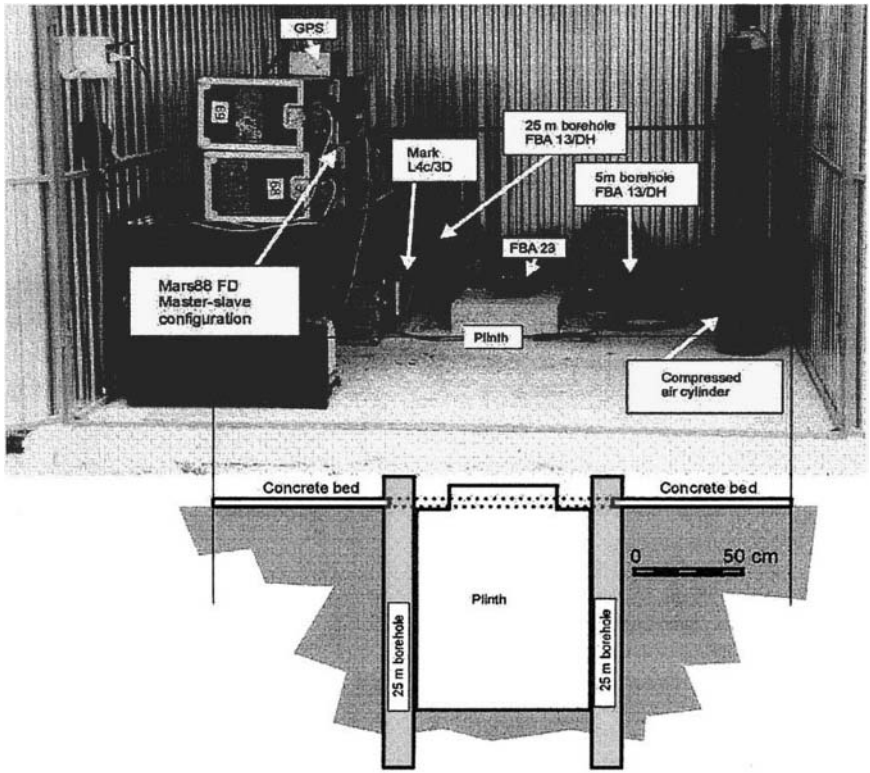

Figure 2 – Fabriano DHE characteristics

The analysis was carried out using the spectral ratio method by means of the following procedure. The spectra were evaluated by using a time window of 16 s starting from the S arrival.
The time window was 5% tapered at the ends, by using a cosine function. The spectra were convoluted with a triangular frequency window, 1 Hz long, thus obtaining the smoothed spectra. After the spectral ratio calculation, for each event and with respect to the 25m recordings, the geometric mean and the 95% error band were calculated for each component. Figure 3 reports the spectral ratios for the three DHE components.

3. GEOTECHNICAL INVESTIGATIONS

Synthetically, in the site of Borgo, where the DHE is located, the stratigraphy consists of three main layers:

a) layer 1 (up to 6.00 ÷7.00 m) composed by silty inorganic clays of high plasticity with small percentiles of gravely sands;
b) layer 2 (between 6.00÷7.00 to about 15.00 m) prevalently constituted of clayey silts;
c) bedrock (at a depth of about 15.00 m) composed by the marls of the Gessoso - Solfifera formation.

The geotechnical properties of these strata were investigated by means of soundings, field and laboratory testing (Marcellini, coord., 1998). Their main physical properties are shown in Table 1 (Crespellani et al.,1998a and 1998b). In the following only the results of interest for interpreting the DHE data will be illustrated in detail. They refer to the sounding 2MS, nearest to the DHE site. Its stratigraphy is shown in Figure 4. The laboratory tests refer to an undisturbed sample extracted in this sounding at the depth of 6.00-6.70. This sample is practically at the same depth as the accelerometer n. 2 in the DHE and is just in correspondence with

the transition between the inorganic clays (layer 1) and the silty clays (layer 2). According to USCS, the sample is classified as CH. Its index properties are summarised in Table 2. In Table 3 other significant parameters derived from the conventional tests are reported. This said sample was the object of an interlaboratory experiment, that, in particular, made possible for the results obtained with various dynamic tests to be compared (Crespellani et al., 1998b; Ciulli, 1998). The laboratories involved were the University of Florence and the Polytechnic School of Turin.

A) Field testing

Two different techniques were used to determine the shear wave velocities, V_S, in correspondence with hole 2MS: down hole (DH) and Spectral Analysis of Surface Waves (SASW). The data obtained were very similar; however, for the specific purpose of interpreting the DHE recordings, the DH technique gives more significant and locally precise results. The V_S-values against depth obtained by DH testing are shown in Figure 4. This diagram indicates that, in the layer 1, that is in the inorganic clays, the shear velocity had a mean value of 146 m/s; in the silty clays, it increased gradually up to 300 m/s, and finally in the marls, it had an average value of about 500 m/s, passing from values of 400 m/s of the weathered levels to 800 m/s in correspondence with the wealthy rock. It must be noted that, at the sampling depth the value of V_S measured in situ was 185 m/s and the corresponding value of shear modulus was 69.8 MPa.

B) Laboratory dynamic testing

In order to investigate the dynamic behaviour under different conditions and test techniques, three Resonant Columns (RC) and two Torsional Shear tests (TS) were performed. The values of the initial shear modulus, G_0 , and of the damping ratio, D_0, are shown in Table 4. Figure 5 and Figure 6 show respectively the normalised values of the shear modulus, G, and of the damping ratio, D, versus the amplitude of shear strain, γ. The average value of the linear threshold is $\gamma_l = 0.002$ %, while γ_v ranges between 0.054 and 0.07%. As Table 4 clearly indicates, G_0 varied with the confining pressure and with the testing apparatus. The values obtained by TS apparatus were inferior to those obtained using the RC. These results agree with those obtained by other authors (Zavoral et al., 1994; Lo Presti et al., 1998).

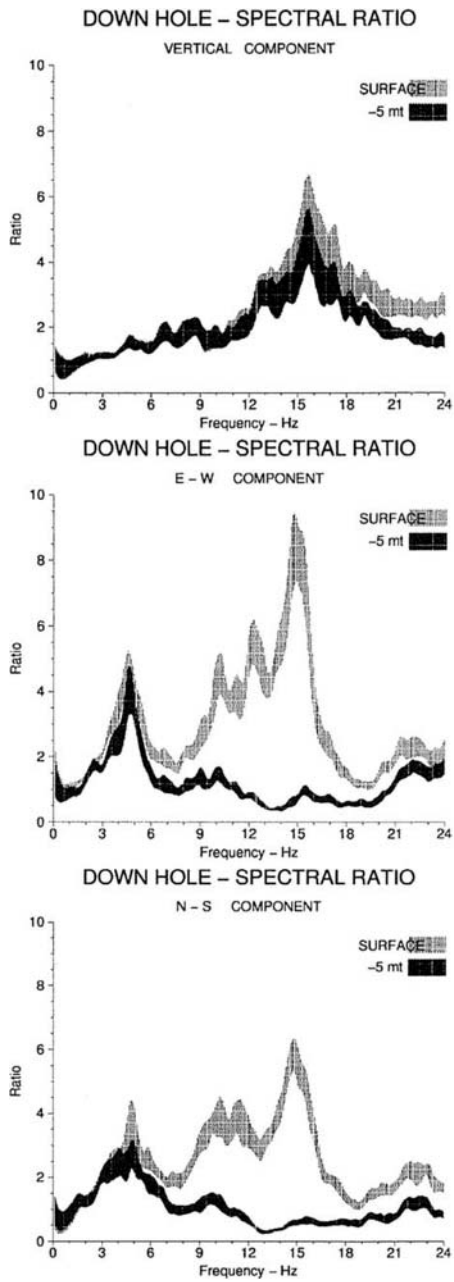

Figure 3 - Mean spectral ratios, together with 95% error interval, computed on 19 selected events recorded at the DHE site. Dark band: spectral ratios 5 m to 25 m depth. Light band: spectral ratios surface to 25 m depth.

Table 1 - Average values of the physical properties

Layer	γ kN/m^3	γ_n kN/m^3	e -	S_r %	w %	w_L %	w_P %	I_p %	I_c -	%C	%L	%S	% G
Layer 1	27.0	18.91	0.810	99.9	30.2	73.0	27.7	45.2	0.9	49.0	34.0	12.0	5
Layer 2	26.77	20.18	0.605	95.8	22.1	48.1	20.8	26.5	1.1	41.0	53.2	5.8	0
marls	26.22	21.74	0.320	100.	12.4	53.8	24.0	29.8	1.3	29.4	65.0	7.0	0

C = clay
L = silt
S = sand
G = gravel

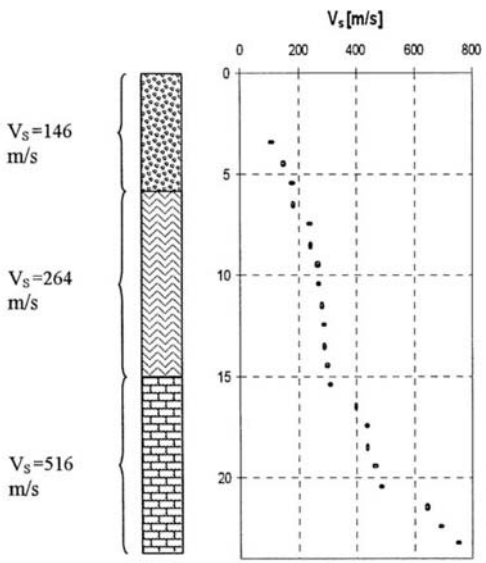

Figure 4 – V_S – versus depth profile

Table 4 shows that also the initial damping ratio, D_0, varied greatly with the testing apparatus and proce¸dures (amplitude decay method, ADM, or steady state method SSM), ranging from 1% to 8%.

4. SEISMIC RESPONSE ANALYSIS

With these data, a twofold modelling of the seismic ground response was carried out. Firstly, the response to a design earthquake with a return period of 475 years was determined. Secondly, site effects due to the same design earthquake but scaled to a peak value equal to maximum peak value obtained in the DHE, were evaluated.
An hazard analysis conducted by Marcellini & Tento (1998) led to defining at Fabriano an expected value of peak ground acceleration of 0.3 g on the rock. As no accelerometric stations of the Italian network exist, by assembling actual records on analogous soil conditions these authors suggested two possible accelerograms for the site. These accelerograms were utilised for computing the ground response by means of the SHAKE code. Since uncertainties about the actual depth of bedrock and the input motion existed, various models were analysed under different soil conditions and the two input motions given by Marcellini and Tento (1998) (Ciulli, 1998; Crespellani et al., 1998a and 1998b). One of these profiles and its results are illustrated in Figure 7, whereas the main results obtained by changing the input motion and the bedrock depth are synthesised in Table 5 .
For a comparison of ground response models with the data provided by the DHE, the results of the second analysis, in which the input accelerogram at the bedrock was scaled to the PGA-value of 0.1g (that is the maximum value of PGA of the aftershocks) appear more significant. They are shown in Figure 8.

Table 2 - Mean values of physical parameters

Parameter	Unity	Mean value
w	[%]	25.73
γ	[kN/m^3]	20.08
γ_s	[kN/m^3]	27.63
e_0	[-]	0.715
w_L	[%]	56.0
w_P	[%]	27.5
I_p	[%]	28.5
I_c	[-]	1.04

Table 3 - Geotechnical properties

Property	Unity	Mean value
c_u	[kPa]	97.25
C_c	[-]	0.24
C_r	[-]	0.05
OCR	[-]	4.3
K_0^*	[-]	0.99

* = estimated

There are a few considerations that follow from all these results.

Although more work will be necessary, a first consideration is that these findings appear to be consistent with those of Figure 2. Without a loss of generality, in all cases site effects appeared to be considerable. It can be argued that more severe seismic actions than the ones assumed by the Italian code could be transmitted to the structures at Borgo during the earthquake expected with a return period of 475 years.

The second consideration is that, by observing the results of Figure 7, since the volumetric threshold, γ_v, ranges between 0.05% and 0.07%, in the upper strata between 1 m to 7.00, the maximum shear strain amplitudes largely exceeded this value. Thus, under the design earthquake soil behaviour became non linear. In the case of Figure 8 maximum shear strain amplitudes did not exceed the volumetric threshold and soil behaviour remained in the linear field.

Finally, from all data collected, it is possible to advance the hypothesis that during the two main shocks occurred on 26th September 1997, the peak acceleration values at bedrock were less than 0.3 g. Therefore, the damage produced by the two destructive shocks, that also involved retrofitted structures, might have been be due to soil amplification effects (and to the consequently increased actions on the buildings) rather than to other causes concerned with either the non linearity of soils (e.g. settlements) or with the structural quality of buildings.

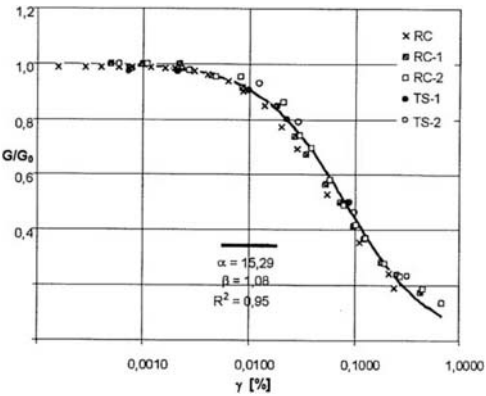

Figure 5 - Normalised G-values against shear strain amplitude γ and coefficient of the relationship $\frac{G}{G_0} = \frac{1}{1+\alpha \cdot \gamma^{\beta}}$

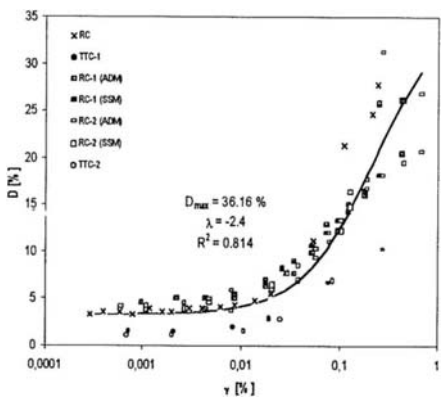

Figure 6 - Damping ratio D versus amplitude of shear strain γ and coefficients of the relationship $D = D_{max} e^{\lambda \cdot \frac{G}{G_0}}$

Table 4 - G_0 and D_0 values

Parameter	RC	RC	RC	TS-1	RC-1	TS-2	RC-2
G_0 [MPa]	38.5	43.6	53	36	46	37	43
σ_0' [MPa]	65	80	120	98	98	98	99
D_0 [%]	3.28	1.45	8.54	4.55	5.71	1	4.11

Table 5 – Parameters of the seismic response

Property	Unity	Values
Fundamental period T_0	[s]	0.29-0.36
Amax at surface	[g]	0.61-0.67
Shear strain amplitude γ_{max} [%]		0.22- 0.49

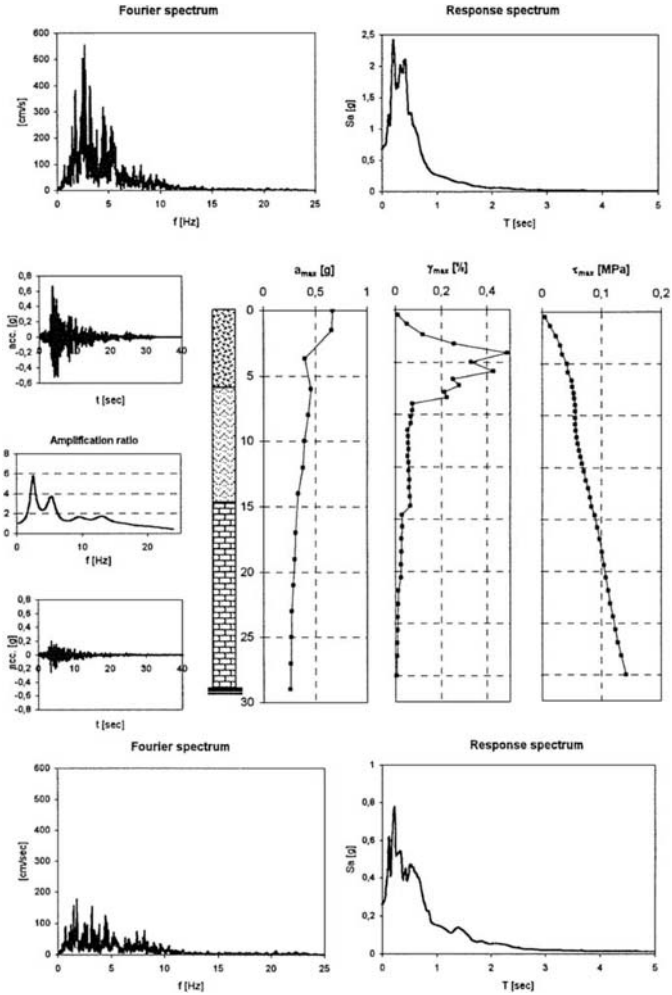

Figure 7 – Seismic response of the alluvial deposit under a design earthquake given by Marcellini & Tento (1998) having PGA=0.3 g: Fourier spectra, transfer function and accelerograms (on the left); response spectra (on the right) and a_{max}, γ_{max} , τ_{max} versus depth

5. CONCLUSIONS

While more work will be needed in order to assess the actual causes of building damage, the empirical findings reported here provide support for < the thesis that the damage which occurred at Borgo during the earthquake of September 1997 is closely linked also to soil amplification. Although the most visible effects on damage were not immediately attributable to them, as no strong evidence of soil collapses or of large settlements was found, the DHE results and the geotechnical modelling performed show that soil conditions played a fundamental role.

Within this perspective, DHE data have offered a very significant contribution to our knowledge of local phenomena which might have been produced at Borgo by recent seismic events and of those that may occur in future.

ACKNOWLEDGEMENTS

The research was supported by the GNDT. The Authors wish thank Eng. B. Ciulli, Eng. C. Madiai and Dr. A. Tento for their help with computations.

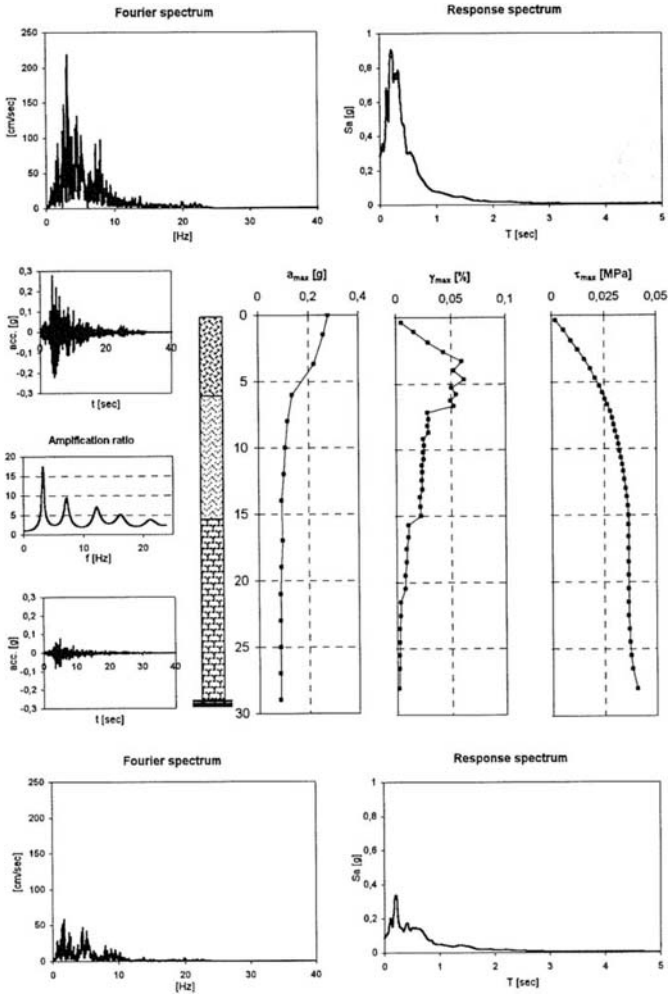

Figure 8 – Seismic response of the alluvial deposit under the design earthquake given by Marcellini & Tento (1998) but scaled to PGA=0.1 g.

BIBLIOGRAPHY

Camassi, R., Galli, P., Molin,D., Monachesi, G., Morelli G., 1997. *Rilievo macrosismico preliminare del terremoto umbro-marchigiano di settembre - ottobre 1997.* Ingegneria sismica, XIV (3), 5-11.

Ciulli, B. 1998. *Caratterizzazione dinamica dei terreni e analisi della risposta sismica locale in alcuni siti di Fabriano finalizzate alla microzonazione simica.* Graduated Thesis. Firenze.

Crespellani, T. (Coord.). 1998a, *Rapporto n.12,* http// seism. cnr.mi.it.

Crespellani, T. (Coord.), 1998b. *Proprietà dinamiche dei terreni di Fabriano,* Poster, Convegno Nazionale G.N.D.T., Roma.

Lo Presti, D.C.F., Pallara, O., Cavallaro, A., Maugeri, M., 1998. *Non linear stress-strain relations of soils for cyclic loading*. Proc. 11th Conf. on Earth. Eng. Paris, 6-11 September, 1998.

Marcellini A. (coord.), 1998. http// seism. cnr.mi.it.

Marcellini, A. & Tento A., 1998. Personal comunication.

De Franco, R., Morrone, A., Biella, G., Boniolo, G., Corsi, A., Demartin, M.,Franceschina, G. L., Maistrello, M., Marcellini, A., pierni, G., Stoppoloni, R., Tento, A., Tiberi, P., 1998. *Misure accelerometriche in pozzo: località Borgo-Fabriano, Ancona, Rapporto N.10.* http// seism. cnr.mi.it.

Zavoral, D.Z. & R.G. Campanella, 1994. *Frequency effects on damping/modulus of cohesive soil,* in Dynamic Geotechnical Testing II, ASTM, R. ed. . J. Ebelhar, V.P. Drnevich and B.L. Kutter, 191-201.

Earthquake Geotechnical Engineering, Sêco e Pinto (ed.) © 1999 Balkema, Rotterdam, ISBN 90 5809 116 3

The Faial, Pico, São Jorge Azores earthquake of July 9, 1998

C.S.Oliveira
Instituto Superior Técnico, Technical University of Lisbon, Portugal

A. M. Malheiro
Laboratório Regional de Engenharia Civil, Ponta Delgada, Açores, Portugal

ABSTRACT: On the morning of July 9, 1998, the volcanic islands of Faial, Pico and São Jorge in the archipel of Azores were shaken by a m_d=6 earthquake with epicenter localized in the northern sector of the canal which separates Pico from Faial. The ground motion caused by this earthquake was recorded in a SMA-1 accelerograph located at 15 km from the epicenter, with a PGA of 0.40 g. Macroseismic intensity of VIII/IX (IMM) was assigned to the areas close to the epicenter (5 km). This earthquake caused important damage, including many collapses, in the zones close to the epicenter (5 to 10 km), in the housing stock constituted essentially by 1-2 story rubble rural masonry buildings, and moderate damage to 3-4 story urban masonry housing (15 km) and to churches. Important landslides took place in the steep areas close to the epicenter and a large rockflow developed over more than 600 m. In many locations, damage in the road system due to collapse of retaining walls, compactation, differential settlement and lateral spreading of soil formations, occurred. Amplification of strong ground motions, possibly due to soft deposits, were observed at several places causing extensive damage.

1. INTRODUCTION

On the morning of July 9, 1998, the islands of Faial, Pico and São Jorge in the archipel of Azores were shaken by a m_d=6 earthquake with epicenter localized in the northern sector of the canal which separates Pico from Faial, Figure 1. This earthquake, with a focal depth not larger than 10 km, was felt with maximum Mercalli Modified Intensity VII/IX, causing 8 deaths, 150 injuries and important damage to the built housing stock, road lines and monuments. About 1500 persons were homeless.

The observed damage is located essentially in the island of Faial, close to the epicentral region, and in the island of Pico. In São Jorge the damage is much smaller. Even though the attenuation of ground

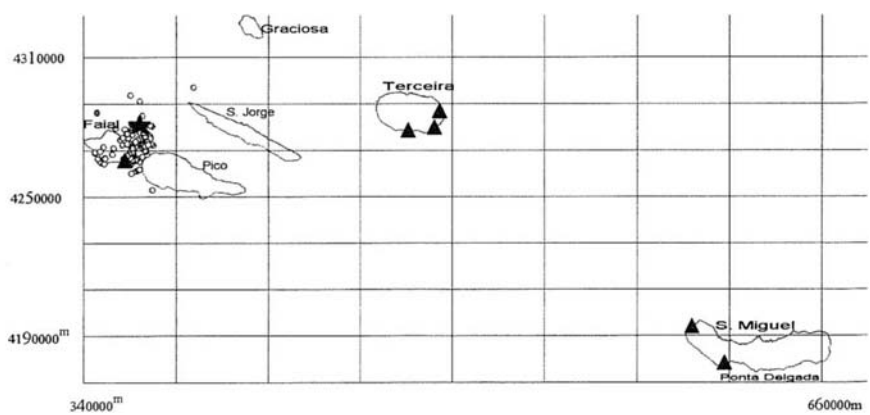

Figure 1. The islands of Archipel of Azores with the strong motion stations (▲), the epicenter of the July 9, 1998 earthquake (★), and the main aftershocks recorded at the strong motion network.

shaking, measured through MMI, is in average decaying regularly with distance, there are several locations of increased anomalies, denoting the influence of soil amplification and the existence of local preferencial directions for wave propagation.

This event is of great relevance because two other important events occurred already in this century, one in 1926 and the other in 1973, not to speak about the Capelinhos Volcano which erupted in 1952. The building stock was repaired after these events using different techniques and behaved differentely now.

2. GENERAL DESCRIPTION

2.1. *Seismology and strong motion*

The earthquake occurred in an area of intense seismic activity, near the Azores Triple Junction. The epicenter is probably associated to the crossing of two main faults, one with expression WNW-ESE coinciding with the principal direction of faults in Faial, and the other in NNW-SSE. The fault mechanism indicated by Harvard, 1998, was NP1: strike=241°, dip=82°, slip=-180° and NP2: strike=151°, dip=90°, slip=-8°. According to Madeira, 1999, the most probable rupture seems to be a left lateral in the NNW-SSE direction.

The main shock occurred at 5.19 h and was followed by a large number of aftershocks, the largest one with m_d=4.2, almost two days after the main shock. Until December 1998 more than 11000 events were recorded in the seismographic network of Azores (SIVISA, 1999); from these 400 were felt.

The ground motion was recorded in a Kinemetrics SMA-1 analogic strong motion instrument, located at the Observatório Príncipe de Mónaco, Horta, Faial, at the top of a 59 m high pyroclastic hill, at 15 km from the epicenter (Oliveira *et al.*, 1998). The digitized record of the most intense part (out of a total 22 s duration) is shown in Figure 2; peak ground values for acceleration, velocity and displacement for each component are given in Table 1, where the value of 391 cm/s^2 stands out. A MM intensity of VI was assigned to this zone.

Table 1. Peak ground values for acceleration, velocity and displacements.

Component	W-E	S-N	Vertical
Acc. [mg]	372	399	327
Vel. [cm/s]	37	30	8
Despl. [cm]	2.8	3.9	0.8

Response spectra for the three components and 5% damping are presented in Figure 3, showing a concentration of energy towards the frequencies 0.8 to 3 Hz for the two horizontal components and around 3 to 6 Hz for the vertical one.

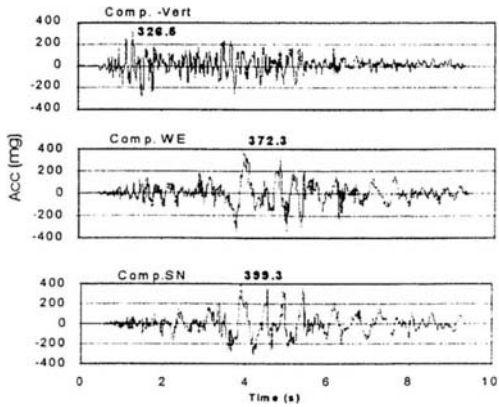

Figure 2. Most important part of the record obtained at the SMA-1 instaled at the Observatório Príncipe de Mónaco, Horta.

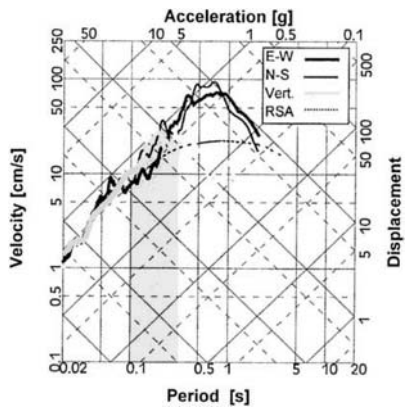

Figure 3. Response spectra for ground motion above; comparison with code (RSA,1983) for the same type of soil; 5% damping.

The analysis of the horizontal orbit corresponding the strong motion record indicates an important impulse in the NNW-SSE direction, which is in agreement with the observation made on different objects and structures exhibiting movement in that direction. However, other structures, such as the "Torre do Relógio" in Horta, exhibit an important movement in the E-W direction. This information,

together with strong motion information obtained 100 km away (Oliveira *et al*, 1999) plus GPS data prior and post earthquake (Pagarete, 1999), is of maximum interest for assessing the fault rupturing mechanism in the near field. Data from the seismological stations in the Archipel are not available as these instruments were completely saturated.

One case of great importance to calibrate the possible acceleration values produced in this earthquake was the lighthouse of Ribeirinha, an old masonry construction of good quality built around 1918 on the top of an almost vertical cliff of *Pyroclast lava* 100 m high, located at approximately 5 km from the epicenter (Sincraian *et al*, 1999). The structure is composed by a tower with 13.5 m high with a thick cross-section almost constant in elevation (outside - rectangle with 5.8x6.2 m at the base; inside – circle with 4.0 m diameter), topped by an optical system, surrounded by an H-shape house, 2-storey high.

The masonry is made of cut limestone blocks in the 4 corners and rubble inside with a good connecting mortar. The lighthouse was subjected to the strong shaking of 1926 which may have caused some damage to the optical system, denoting an important movement in the NNE-SSW direction.

The July 9, 1998 event caused extensive damage to the tower, to the house, to the outside facilities including land property walls, and to the embankment on the southern part. The tower has suffered important deformation, leading to the formation of large inclined cracks passing through the openings, very consistent throughout all the four sides. The general appearance is of an overall counterclockwise rotation of the tower (view from above), with peripheral enlargement at mid height. The tower was broken into several solid blocks, which show relative horizontal displacements above 50 cm. At the top, the optical system suffered slight denoting again intense movement in the above referred direction.

The main results of a recent work (Sincraian *et al*, 1999), indicate that the observed rotation of the tower was modelled without introducing any rotational component of ground motion. The record in Horta should be multiplied by a factor of 2.0 in order to give approximately the same range of relative displacement (about 48 cm in the model compared to about 50 cm in the real structure), meaning that the PGA at the lighthouse site was about 0.8 g. This number is in good agreement with the attenuation law for m_d=6 (Oliveira, 1999).

The above estimative, in direction and in amplitude of movement, is also supported by other evidences such as the permanent displacement of flower pots observed at cemiteries (17 cm to the South at 5 km from the epicenter).

2.2. *Damage to housing and other structures*

In the island of Faial, from a total of about 3950 housing units, 54% had no problem and 10% had total collapse; the other 36% had some type of damage statistically distributed with a mode around the 25% damage ratio.

But the damage inflicted to the housing stock was very selective. The older rubble masonry units, 1-2 story high, in the rural areas near the epicenter (5 to 10 km) were very much affected by the shaking. In some places collapse attained almost 100%, Figure 4. In the town of Horta, 15 km away from the epicenter, the housing stock of 3-4 story high old masonry suffered moderate damage with slight opening of walls towards the exterior. Low-rise modern reinforced concrete structures in Horta suffered no damage or just a few minor cracks. Only one case of a short column at the Hospital of Horta had slight minor diagonal cracking. At larger distances there were a few sites of higher shaking intensity and damage inflicted to rural housing. They reflect the presence of soft sites, Figure 5, or the existence of channels for easier propagation of seismic waves.

In Pico, the damage was much less extensive, but exhibited the same type of pattern. However, there were differences in behaviour, denoting the smaller amplitude of the vertical component compared to the horizontal ones: distances to the epicenter are larger, but older masonry construction is in general of less quality than in Faial. In Pico, two locations, Valverde and Almagreira, showed intensities larger, than the average tendency, probably due to channelled energy. At an epicentral distance of 35 km, a diagonal crack in a short reinforced concrete column of a modern 2-story fireman headquarters was formed.

Besides the anomalies already referred, a general explanation to the observed structural behaviour is as follows. (i) In locations close to the epicenter (5 to 10 km), the heavy damage to masonry structures is due to the large amplitude of ground motion (PGA=0.8 g). (ii) In locations 10 to 15 km from the epicenter, even though a PGA=0.4 g was recorded and energy is above the Code value for a certain range of frequencies, the little damage observed might be due to the non existence of structures with low frequency mode shape (they are always greater than 3 Hz). The pattern of damage inflicted to the

Figure 4. Typical damage at zones 5 to 10 km from the epicenter to rural houses of rubble masonry and to houses with some reinforced concrete beam elements.

Figure 5. Typical damage at zones 15 km from the epicenter to block masonry houses; amplification due to soil layers.

Figure 6. Differential soil settlement at road side on top of hill.

Figure 7 a. Landslide at Lomba Grande, Pedro Miguel: general view.

Figure 7 b. Detailed view of landslide at Lomba Grande, showing the large volume of displaced material.

Figure 8. Collapse of road retaining wall.

masonry in the area close to the epicenter seems to be indicate the importance of the intense high frequency vertical motion which has reduced quite heavily the friction in horizontal joints between blocks, and consequently, eliminating the good behaviour of interlocking blocks.

Damage to other structures include several churches (two collapsed two in great ruin), schools, roads, bridges, water lines and wells.

3. SITUATIONS INVOLVING IMPORTANT GEOTECHNICAL ASPECTS

Most soils in the islands affected by the earthquake are associated to different volcanic origins (Forjaz *et al.* 1990). Water level was down due to a dry winter season.

The effects of the strong ground shaking on geotechnical structures were various, related to the aspects:

- Mass movements related to the presence of alignements/fault scarps and to the presence of inclined areas;
- Soil amplification in zones of thick soil layers;
- Superficial instability with fall of material;
- Compactation of land-fill formations.

In the following, the most significative examples are presented.

• Ribeirinha Fault – Espalhafatos: Along this important fault one can observe various offsets, some of them quite significant. The zone showing larger damage is the village located along the rural road which coincides with the fault line. Also the road giving access to the Ribeirinha Lighthouse follows the fault which shows a scarp with a maximum vertical offset of approximately 100 m. Its betuminous pavement has settled in a few places around 1 m, Figure 6. The phenomenon has occurred due to the fault movement and the lack of lateral support on the down hillside. In other locations of the road along the same scarp, at the edge, offsets of 10 to 20 cm were observed.

• One of the most frequent phenomena occurred as a consequence of this event are landslides, located essentially along the abrupt coast lines of Faial and São Jorge Islands, in zones of high cliffs. They are in general surperficial landslides not envolving large amounts of displaced material. However, there are two significant landslides in Faial envolving large dimensions and extensions, the one taking place in the cliff of the Lomba Grande Fault, in Pedro Miguel, and the other on the northern border of the Caldera in the center of the Island.

The zone in Pedro Miguel, Figures 7 a) and b), is particularly vulnerable to mass movements, due to its geomorphologic characteristics and to the type of volcanic materials forming the cliffs. Old eruptive sequencies from the Volcanic Complex of Ribeirinha can be observed, including lavic flows mixed with pyroclast deposits, generally much altered. The referred landslide took place in the scarp of the Lomba Grande fault, a cliff with 200 meters high, and the material was displaced for several tens of meters.

In relation to the second case, several landslides were triggered, but the dramatic case occurred upstream Ribeira Funda (in the county of Cedros) is the most spectacular. This mass movement, in the form of a detritic flow, had origin at the border of Caldera in the center of Faial, evolved through 1400 m and could have pose a great threat to the populations downstream.

Another case of interest was in the road connecting Pedro Miguel to Ribeirinha (Estrada Regional), where several collapses, involving blocks of large dimensions, affected the retaining wall.

• Areas affected by amplification of ground motion, due to the soft underlying soil, were the counties of Castelo Branco, Salão and Flamengos, in Faial, and Valverde and Almagreira in Pico.

The localities in the first two counties are essencially sited on thick pyroclastic fall deposits (ashes and pumice *lapilli*) and of stream type, with origin at the central volcano, whereas the majority of Flamengos county is sited on pyroclastic flow deposits (mudflow and pyroclastic flows); the remaining parts are sited on epiclastic deposits. In the more deep water lines one can observe a few basaltic lavic flows from the Almoxarife Formation and from the Cedros Complex.

The localities referred in Pico (Valverde and Almagreira) are both sited on basaltic *aa* flows, which usually present strong fronts and thick layers of clinker (detritic material, under and above a layer of massive rock formation). This material, not well consolidated, has a tendency to exhibit compactation when subjected to strong shaking.

• Southern Coast Line in Faial (Feteira): The zone is primarily formed by mixture of basaltic flows, normaly of small thickness, with levels or pockets of clinker. This last material, with poor aggregating cement, is easily eroded by the action of the sea. Consequentely, various cavities were formed in that zone, a few of them with large dimensions spreading underneth the road (Estrada Regional). After the main shock several cracks were visible at the upper surface, runing paralel to

the coast, between the road and the cliff, some very near the road, creating safety concerns to the public authorities.

• Monte Queimado (City of Horta): The hill Monte Queimado consists of a strombolian volcanic cone. In the existing outcrops it is possible to identify its internal formation: a predominance of red basaltic pyroclasts, intercalated with basaltic lava flows. This type of material, mainly formed by desaggregated components, is easily eroded, causing some instability to the lavic layers already fractured. The occurred strong motion has aggravated this natural erosion process, causing mass movements involving pyroclast layers and a few basalt blocks, and instability problems in other situations. On top of this the fault crossing the volcanic cone, may have contributed to the increase of the potential scenario of landslide, putting at risk facilities and the circulation at the base of the this hill.

Numerous other cases of damage to geotechnical structures were observed: (i) small dimension landslides, as the result of collapse of retaining walls, Figure 8 and (ii) damage to bridges and aqueducts, such as the cases of the bridges connecting Ribeirinha to Espalhafatos, Espalhafatos to Salão, and the bridge in Flamengos, due to compactation of embankments retaining walls. These damages, clearly visible at the pavement surface on the embankments zones, were the result of a strong compactation of the land infills under the seismic action, which also increased the soil lateral impulse.

ACKNOWLEDGEMENTS

The authors would like to thank the many experts who worked in the field collecting data which is indirectly referred here and the institutions such as CPR. CM Horta. SIVISA and the University of Azores, for providing the information on the housing damage, damage to lifelines, seismicity and geology data, respectivelly.

This work was partially supported by the Project PPERCAS, "Projecto Praxis para o Estudo do Risco/Casualidade Sísmica do Grupo Central do Arquipélago dos Açores", Praxis / Ciência e Tecnologia 3/3.1/CEG/2531/95.

REFERENCES

Forjaz, V. H., A. Serralheiro & J. C. Nunes 1990. Carta Vulcanológica dos Açores, Centro de Vulcanologia, Universidade dos Açores.

Harvard Seismology 1998. Harvard CMT Catalog. http://www.harvard.edu. December.

Madeira, J. 1999. Personnal Communication.

Nunes, J. C., Z. França, C. S. Oliveira & R. Ortiz 1998. Distribuição das Intensidades Sísmicas na Ilha do Pico Referentes ao Sismo de 9 de Julho de 1998: Condicionantes Morfológicas, Geológicas e Tectónicas. *Proceedings, 1º Simpósio de Meteorologia e Geofísica da APMG*, Lagos, Novembro.

Oliveira, C. S., L. N. Sousa, J. H. Correia Guedes, A. Martins & A. Campos-Costa 1998. A Crise Sísmica do Faial/Pico/São Jorge Iniciada com o Sismo de 9 de Julho de 1998 vista na Rede Acelerográfica dos Açores, *Proceedings, 1º Simpósio de Meteorologia e Geofísica da APMG*, Lagos, Novembro.

Oliveira, C. S. et al. 1999. O Sismo do Faial/Pico/São Jorge de 9 de Julho de 1998 e o Comportamento Estrutural de Algumas Estruturas de Alvenaria, *Report for PPERCAS Project, in Progress*, ICIST, Lisbon.

Pagarete, J. 1999. Personnal Communication.

RSA 1983. Regulamento de Segurança e Acções em Estruturas de Edificios e Pontes. Decreto 235/83, Imprensa Nacional.

Sincraian, G., C. S. Oliveira & J. V. Lemos 1999. Seismic Behaviour of an old Light-House under Strong Ground Shaking, *Proceedings, 1st Spanish Assembly of Earthquake Engineering*, Murcia, Spain, April.

SIVISA 1999. Carta de Epicentros de 09/Julho/1998 – 31/Dezembro/1998. Document not Published, Instituto de Meteorologia/ Universidade dos Açores.

Earthquake Geotechnical Engineering, Sêco e Pinto (ed.) © 1999 Balkema, Rotterdam, ISBN 90 5809 116 3

Damages due to Northern Iwate Prefecture Earthquake, September 3, 1998

Susumu Nakamura – *School of Engineering Nihon University, Koriyama, Japan*
Motoki Kazama – *Tohoku University, Sendai, Japan*
Akira Kobayashi – *Iwate University, Morioka, Japan*
Tsuneo Osumi – *Nihon Koei, Tokyo, Japan*

ABSTRACT: The characteristics of the Northern Iwate Prefecture Earthquake, September 3,1998 are mainly as follows;i)slope failures around epicentral region and the structural damages due to the vertical dislocation of ground caused by the fault movement were main damages.ii)building structure itself was damaged very slight. However facilities equipped with the building were failed. iii)the strong motion records were observed around the epicentral region. The maximum acceleration is more than 700gal. The characteristics of the seismic records were influenced by the the fault mechanism as dip slip.

1.INTRODUCTION

The Northern Iwate Prefecture Earthquake (Mj=6.1) occurred in September 3,1998. The epicenter ,where is Lat.39° 48'N. and Long.140° 55'E. and 7 km deep, is located at distance of 10 km from Iwate mountain to south-west direction. The maximum seismic intensity specified by Japan Meteorological Agency was recorded 6.0 Lower as well as that of the 1997 Northern Kagoshima Prefecture Earthquake. The source mechanism has been estimated as inverse dip slip occurred at the Nisine fault. The vertical dislocation of the ground surface was observed to be more than 30 cm. It has been supposed to be caused by the fault movement. The damages due to this earthquake are mainly land slides of natural slope around epicentral region and the damages of underground structure due to the vertical dislocation of ground caused by the fault movement. Furthermore, it was noted for important information about inter-plate earthquake that the dislocation of surface ground caused by the seismic fault movement was appeared and that the strong motion records near the epicenter was observed.

After the 1995 Hyogoken-Nambu Earthquake, it has been important for not only seismic design but also disaster prevention to estimate a design input motion taking into account of the rapture process of the identified seismic fault. On the other hand, in order to estimate the earthquake motion, we have to make model for three factors such as source, path and site which are depend on the characteristics of local area. Therefore, it will be necessary to estimate a design input motion based on the factors inherent in the local area. Furthermore, the similar relationship between the seismic fault and Morioka where has prefecture office is found in the other middle town in the inland area like that between Fukushima and Fukushima fault.

This earthquake will give us the essential information for mitigation due to the earthquake ground motion of inter-plane earthquake. Then, the characteristics of the earthquake ground motion around the source area and the damages are described in this paper.

2.DAMAGES

Damages of ground system such as slope failure and structure damages caused by the fault movement around ground surface were mainly occurred around epicentral region shown in Fig.1. Fortunately, persons who were injured in National Vacation Center(herein called as Nagayama) were less than 10. Furthermore, in spite of the magnitude less than 6.8 , it is important to appear the vertical dislocation on the ground surface due to the fault movement.

On the other hand, building structure was not damaged itself but such facilities as ceiling plate of National Vacation Center(shown in Photo.1) and sprinkler at rest house for skiing ground were damaged. Furthermore, wooden houses and small retaining wall made of stone in lodging area were damaged slightly. These structures are located in epicentral region and the maximum acceleration observed at National

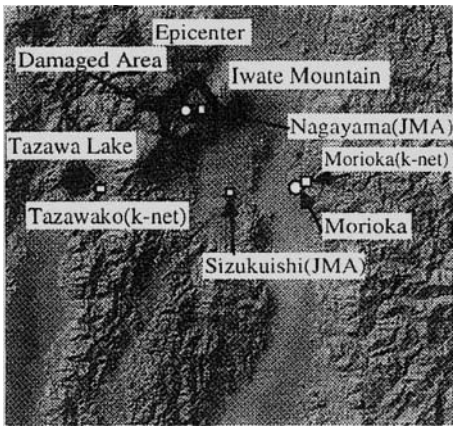

□ :Seismic Observation sites(JMA,K-net)

Figure.1 Geography around Damaged Area and Seismic Observation Sites for evaluating the Characteristics of Earthquake Ground Motion

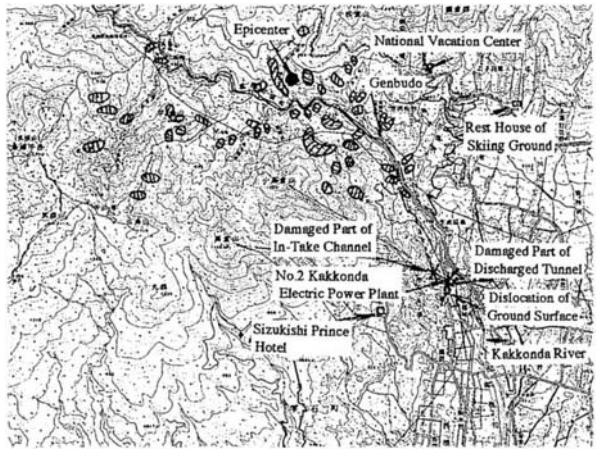

Figure.2 Location of Damages around Epiceral Region

▨ : Land Slide Area

Vacation Center is more than 700gal. This evidence indicates not to be able to evaluate the damage of building structures based on only maximum acceleration.

2.1 Dislocation of Surface Ground

The vertical dislocation generated by the fault movement appeared on the surface ground along the west edge of Sizukuishi basin shown in Fig.2. A part of dislocation was observed 200 m long from No.2 Kakkonda electric power plant to north-east direction shown in Photo.2 and 200m long to south-south east direction. Furthermore, from the south end of that, that was obserbed 350m long to Yamagami shrine shown in Photo.3. Then, the observed dislocation was 750m in total length. The west side ground of dislocation was lifted between 20cm and 30cm in comparison with the east side.

It has been pointed out in Japan that the dislocation of ground surface due to the fault movement appear for the earthquake whose magnitude was more than 6.8. Only one evidence has been reported that the dislocation on the ground surface was appeared for the 1959 Teshikaga earthquake occurred in Hokkaido. Therefore, This earthquake gives us the important information to evaluate the earthquake damages based on the identified earthquake for seismic design.

2.2 Slope failure

More than 50 land slides were observed around Kakkonda river close to epicenter. Furthermore, some land slides were also observed around Matsu river. The road along Kakkonda river was intercepted by the slope failure shown in Photo.4 and the electric pole was fallen down. Amang them, as a result of land slide of the upper slope around Genbudo where is the sightseeing place, a large amount of earth and sand fell into Kakkonda river and dammed up the river shown in Photo.5. Not only the high intensity of this earthquake motion but also the high water content of surface deposit due to heavy rain fall at the end of August are seemed to be the reason why so many land slides occurred. The total amount of rain fall in the upper part of Kitakami river which is main river of Kakoonda river is more than 240mm.

2.3 Damages of Facilities of Electric Power Plant

Facilities of No.2 Kakkonda electric power plant such as in take channel and discharge water tunnel were damaged. The plant occupied by Tohoku electric power Coop. has been operated since 1953.

In take channel consists of open and closed channel made of RC. A part of the open channel close to the plant was damaged about 12m length and is shown in Photo.5. As shown in Photo.6, damages were widely opened diagonal cracks generated on both side walls. The discharged water tunnel consists of culvert and tunnel made of RC and its shape is a horse's hoof. A part of tunnel close to the plant was damaged about 30m length and is shown in Photo.7 and 8. The cracks generated at side walls and ceiling slab along the tunnel were observed at length of 23m in the damaged portion. The width of the cracks were between 1 and 3mm. The right side wall and invert in the other damaged tunnel were completely failed. Then, stones and sand were flowed into the tunnel. This damage part was just located around the ground dislocation due to fault movement. Therefore, this damages supposed to be caused by the ground deformation.

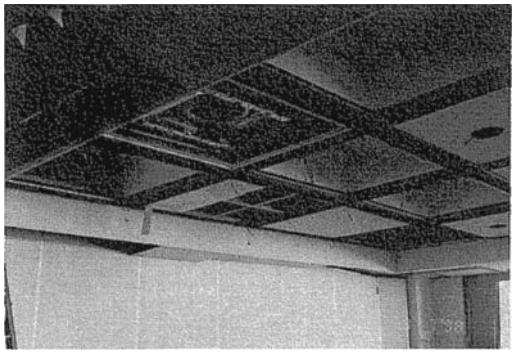

Photo.1 Falling down of Ceiling Plate at Nationl Vacation Center

Photo.2 Dislocation of Ground Surface (From South-South East of No.2 Kakkonda Electric Power Plant)

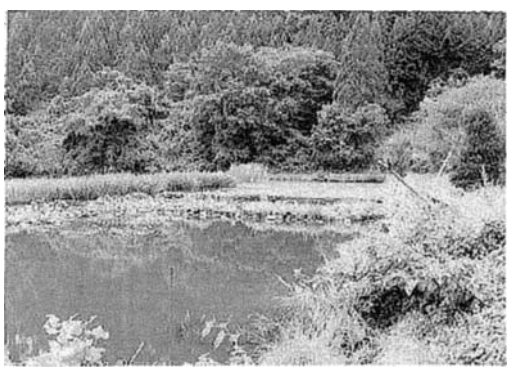

Photo.3 Dislocation of Ground Surface (Lifted up the Back side of Water Pond for Yamagami shrine)

Photo.4 Intercept of the road along Kakkonda river due to Land Slide (Povided by Prof.Ohota of Iwate University)

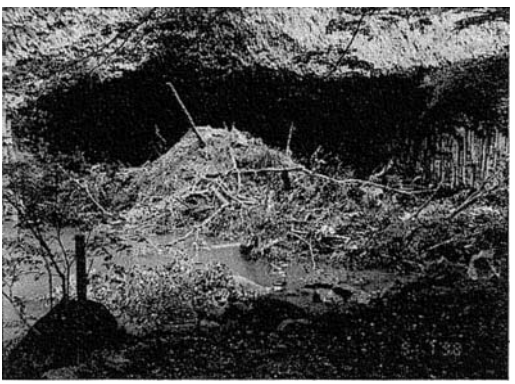

Photo.5 Dam in front of Genbudo made of Sand and Stone Generated by Land Slide over the Slope

Photo.6 Damage of Side Wall of In Take Channel

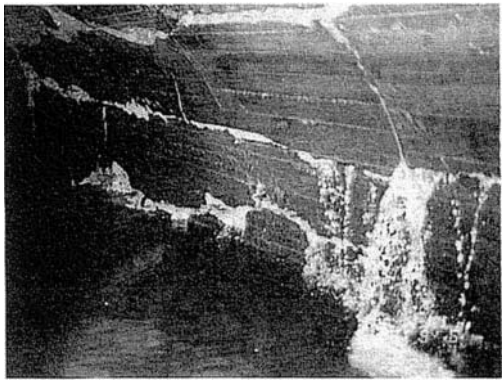

Photo.7 Cracks along Tunnel Axis of Discharged Tunnel

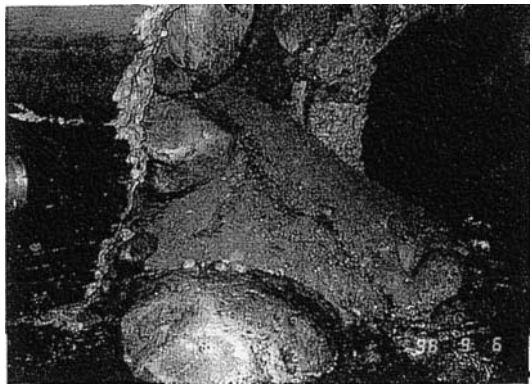

Photo.8 Failure of Side Wall at Discharged Tunnel

3. CHARACTERISTICS OF EARTHQUAKE GROUND MOTION

Nishine fault group on the east side of sizuishi basin has been estimated as the seismic fault of the earthquake. The mechanism has also been estimated to be inverse dip slip. Because the craters of Iwate mountain whose volcanic activity has been higher was lined along east-west direction and Nishine fault group along north-south direction was perpendicular to the compression axis along east-west direction due to crustal activity. These evidence were correspond with the results observed by GPS about the shrinkage of the distance between Tazawa lake point and sizukuishi point after the earthquake.

First of all, the distribution of maximum acceleration

Figure.3 Distribution of Maximum accelaration in Tohoku Region of Honsyuu, Japan

(URL: htrp://www.k-net.bosai..go.jp/ provided by National Research Institute for Earth Science and Disaster Prevention)

in northern honsyuu area in Japan based on kyosin-net(so called K-net) installed by National Research Institute for Earth Science and Disaster Prevention(NIED) is shown in Fig.3. As for the shape of the counter line around the epicenter shown in symbol X, the maximum acceleration on the upper side of the fault, in other word, east direction from the epicenter is larger than that of the other side. This tendency shows the general evidence for the radiation pattern of the seismic wave generated by the inverse dip slip fault. In order to make clear this tendency, the attenuation characteristics of the peak horizontal ground acceleration values(PHGA) based on the data observed at Nagayame and Sizukuishi by JMA and those on K-net is shown in Fig.4. PHGA values were obtained as the square root of square of maximum values with respect to NS and EW component respectively. Hence Nagayama is very close to the epicenter. Solid line presents the attenuation relationship proposed by Joyner and Boore(1981). Hence, it was assumed that moment magnitude Mw was 6.1 and that the closet distance from the fault line was equal to the epicentral distance. According to PHGA at the distance between 10km and 30km from the epicenter, the values on the upper side of

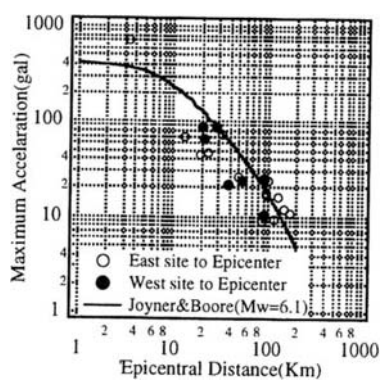

Figure.4 Attenuation Characteristics of PGHA

fault shown in symbol ● are lager than those on the other side shown in symbol ○. The typical characteristics for the inverse dip slip fault mentioned above is made sure by this evidence. Furthermore, the observed value at Nagayama is about 1.8 times to the estimated value.

Acceleration time histories for three components observed at Nagayama(JMA), Sizukuishi(JMA), Tazawako(K-net) and Morioka(K-net) shown in Fig.1 are shown in Fig.5. In this figure, amplitude scale without Nagayama is twice to that of Nagayama. The maximum amplitude at Nagayama is 714.9gal in NS component and 708.3gal in UD component. These are so large values that these are correspond with the values observed on the 1995 Hyogoken-Nambu Earthquake. However, the duration time in the main portion is so short that it is about 5 seconds. At Tazawako on west side of the epicenter, the characteristics about shape of envelope and duration time are the almost same with those of Nagayama. On the other hand, the other two points on the east side of epicenter has the characteristics that the duration times are longer than the other side although the amplitudes are smaller. It is noted that, according to EW component at Sizukuishi, the maximum amplitude appear at 10 seconds after arriving P wave and that long period component seems to be predominant as the frequency characteristics after the time. Next, particle orbits in horizontal plane with respect to velocity component obtained by numerical integration of the acceleration time history for Nagayama and Sizukuishi are shown in Fig.6. The predominant vibrating direction at Nagayama is southeast direction from northwest. On the other hand, that at Sizukuishi up to 10 seconds after arriving P wave shown as solid line is the almost same with Nagayama. However, that after the time changes to the east and west direction shown as dash line.

Next, the comparison of vector Fourier spectrum (Susumu Nakamura 1995) based on two horizontal components for four sites shown in Fig.4

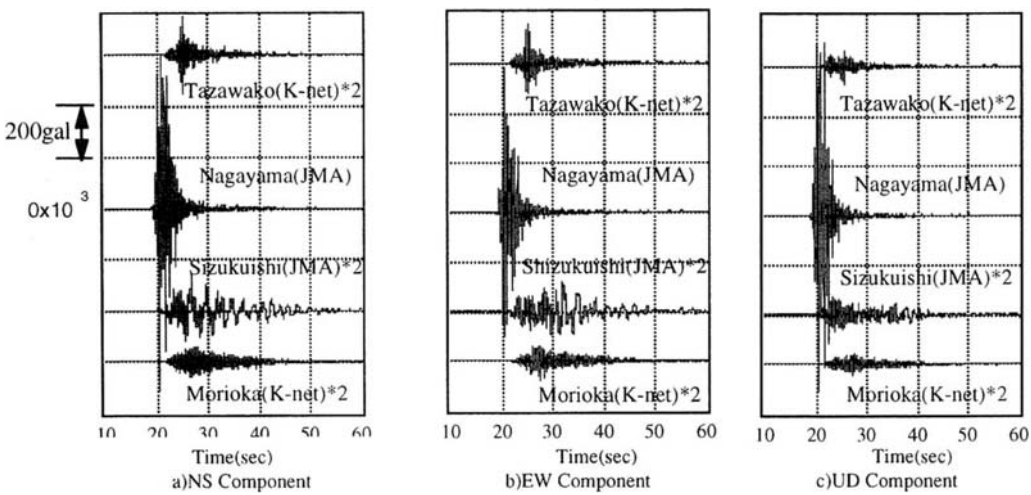

Figure.5 Accelaration Time History at 4 sites

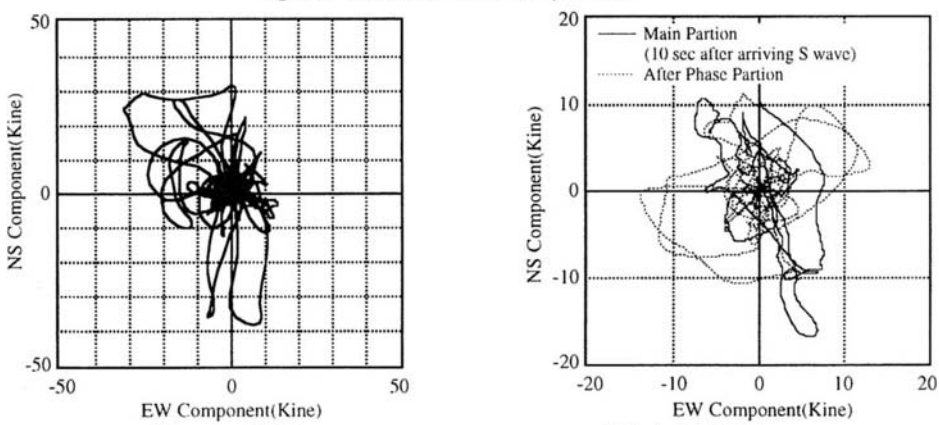

Figure.6 Particle Orbits in Horizontal Plane with respect to Velocity Component

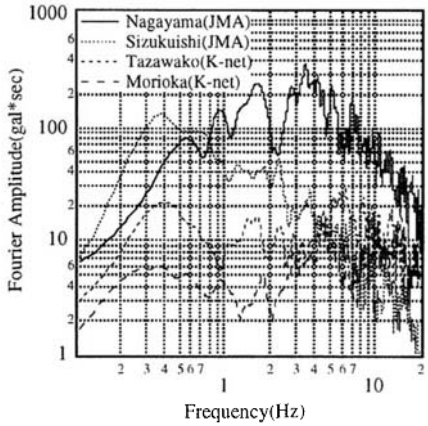

Figure.7 Comparison of Vector Spectrum at 4 Site

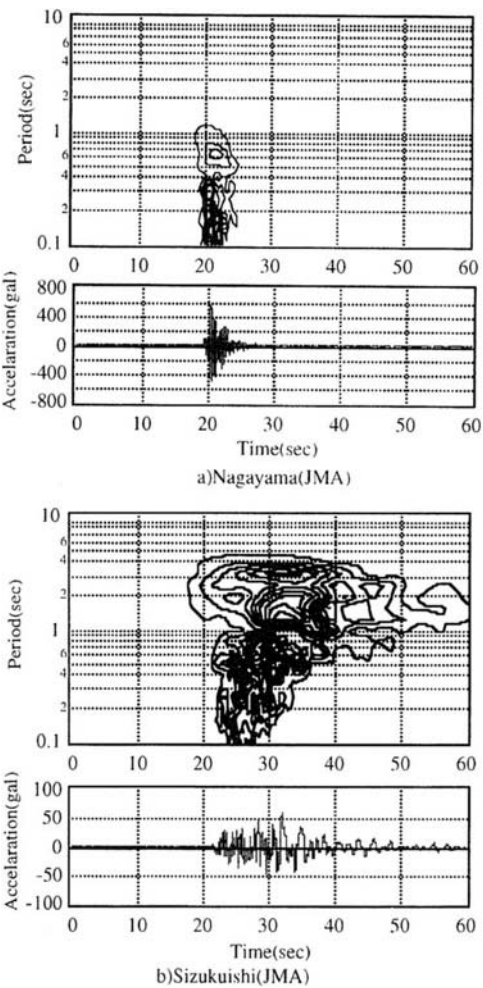

Figure.8 Comparison of Non-Stationary Spectrum

are shown in Fig.7. It is found that the predominant frequencies are 1.7 Hz and 3.4 Hz for Nagayama, around 0.4 Hz for Sizukuishi, respectively. At the other two site, it is found that the Fourier amplitude is predominant at 0.4Hz. Furthermore, The Fourier amplitude at 0.4 Hz for Sizukuishi is lager than that for Nagayama. In order to make clear the wave component, nonstationary spectrum for EW component at Nagayama and Sizukuishi are compared in Fig.8. As for the frequency characteristics at Sizukuishi, the effect of surface wave is remarkably found in the frequency component longer than 1.0 second. However, the tendency is not found that at Nagayama. These evidences indicate that the long period component at Sizukuishi more than 1.0 second was generated inside of Sizukuishi basin.

4.CONCLUDING REMARKS

The characteristics of the Northern Iwate Prefecture Earthquake, September 3,1998 are mainly as follows;

i) land slides around epicentral region and the structural damages due to ground deformation caused by the fault movement were main damages.

ii) In spite of very large amplitude of earthquake ground motion around epicentral region, damage of building structure itself was very slight. However facilities equipped with the building were failed.

Furthermore, one of the major characteristics is to obtain the strong motion records around the epicentral region. As the characteristics of the records, the influence of the mechanism as inverse dip slip fault is observed at the characteristics of the seismic records by NIED along the perpendicular direction to the fault and the later phase which has large amplitude is observed at the seismic observation point of JMA in Sizukuizi basin and is seemed to be surface wave generated around edge of the basin.

Finally, I thank Prof. Ohota of Iwate University and Mr.Kano of Tohoku Electric Power Coop. very much for providing us some data and Photograph for land slide and damages of facilities of electric power plant.

REFERENCE

Joyner,W.B.,D.M.Boore,Peak horizontal acceleration and velocity from strong motion records including records from the 1979 imperial valley, California, Earthquake, B.S.S.A., No.6,pp.201-238,1981.

Susumu Nakamura,Proposal of vector frequency response function of ground based on vector spectrum and its application, Journal of structural mechanics and earthquake engineering,J.S.C.E..No.519/I-32,pp.161-173,1995.7(in Japanese)

Earthquake Geotechnical Engineering, Sêco e Pinto (ed.) © 1999 Balkema, Rotterdam, ISBN 90 5809 116 3

Author index